

UNIVERSITÀ
DEGLI STUDI
DI PADOVA

Head Office: Università degli Studi di Padova

Department of Industrial Engineering

Ph.D. course in Science and Engineering of Materials and Nanostructures

Series XXXVI

SOLUTION-BASED OXIDE FILMS FOR CLEAN ENERGY APPLICATIONS

Coordinator: Ch.mo Prof. Stefano Agnoli

Supervisor: Ch.mo Prof. Alessandro Martucci

Ph.D. student: Maria Basso

Thesis written with the financial contribution of Cariparo Foundation

Abstract (English)

The reduction of the energy consumption is currently one of the most critical global challenges, which applies to an extensive number of fields. Heating, ventilation, and air conditioning (HVAC) systems account for up to 20% of the global energy consumed by developed countries.[1,2] Several HVAC systems rely on condensation heat exchangers, which harness the liquid-vapor phase change for the thermal transfer. Considering the air conditioning (AC) systems, the challenge posed by the systemic cooling poverty underscores the necessity of exploring new approaches with respect to conventional AC systems.[3] An alternative and/or complementary solution is offered by thermochromic smart windows, which exhibit a passive modulation of the solar irradiation without requiring active energy inputs for activation.

In addition to HVAC systems, the shortage of drinkable water poses an additional challenge affecting the global energy consumption. According to the FAO reports, nearly one-sixth of the world's entire population are daily plagued from severe water scarcity.[4] Among the various approaches, from solar-driven desalination plants[5,6] to distillation systems for contaminated water[7], a promising solution is offered by the vapor collection from humid air. As emerges from these reports, even slight improvements in the efficiency of heat exchangers, water collectors, and smart windows could have a powerful impact on reducing the massive global energy consumption. The optimization of the latter three applications has been the focus of this doctoral research.

Several oxide coatings were prepared following a chemical solution deposition (CSD) method, which will be introduced in Chapter 1. In the first experimental part (Chapter 2), the functional properties of hybrid silica (SiO_2) coatings were tuned and exploited to control the efficiency of heat exchangers and moisture collectors. In the second part (Chapters 3-6), vanadium dioxide (VO_2) thin films were employed for the fabrication of thermochromic smart windows. The temperature-dependent nature of the optical and electrical properties of VO_2 provides a passive means to modulate the solar irradiation without relying on active energy inputs. The numerous parameters influencing the CSD method were optimized in Chapter 4, from which homogeneous and thermochromic VO_2 thin films were obtained.

Concerning the latter material, a currently unsolved challenge involves the reduction of the crystallization temperature below 400°C. In Chapter 5, an unconventional nanosecond pulsed laser annealing method was exploited to remarkably reduce the crystallization temperature of VO_2 thin

films. Additional challenges regarding VO_2-based smart windows pertain to two essential features that must be ensured for real-world application, namely the transmission of visible light and the resistance against weatherability. Both challenges were addressed in Chapter 6, though the combination of VO_2 with titanium dioxide (TiO_2) and hybrid SiO_2 coatings in bilayer configurations.

In the final Chapter 7, the efficiency of VO_2 thin films towards H_2 gas detection was considered. The latter is becoming increasingly important in the field of decarbonization and implementation of low-impact renewable energy.[8] Different morphologies and degrees of crystallinity were considered by tuning the laser-annealing and conventional furnace-annealing parameters, and the latter impact on the H_2 gas sensing efficiency was investigated.

Sommario (Italiano)

La riduzione del consumo energetico è attualmente una delle sfide globali più critiche e coinvolge un'ampia gamma di settori. I sistemi di riscaldamento, ventilazione e condizionamento dell'aria (HVAC) sono responsabili fino al 20% dell'energia globale consumata dai paesi sviluppati.[1,2] Diversi sistemi HVAC si basano su scambiatori di calore a condensazione, che sfruttano il cambiamento di fase liquido-vapore per il trasferimento termico. Considerando i sistemi di condizionamento dell'aria (AC), la sfida posta dalla povertà sistemica legata ai sistemi di raffreddamento ("systemic cooling poverty") evidenzia la necessità di trovare nuovi percorsi rispetto ai sistemi AC convenzionali.[3] Una soluzione alternativa e/o sinergica è offerta dalle finestre intelligenti termocromiche, che mostrano una modulazione passiva dell'irraggiamento solare senza la necessità di input attivi di energia per la loro attivazione.

Oltre ai sistemi HVAC, la carenza di acqua potabile è un'ulteriore sfida che influisce sul consumo energetico globale. Dai rapporti della FAO, quasi un sesto dell'intera popolazione mondiale è quotidianamente afflitto da gravi carenze d'acqua.[4] Tra i vari approcci, dalla desalinizzazione solare[5,6] alle centrali a distillazione per l'acqua contaminata[7], una soluzione promettente è offerta dalla raccolta del vapore dall'aria umida. Come emerge da questi rapporti, anche lievi miglioramenti nell'efficienza degli scambiatori di calore, dei raccoglitori d'acqua e delle finestre intelligenti potrebbero avere un forte impatto sulla riduzione del massiccio consumo energetico globale.

L'ottimizzazione di queste tre applicazioni è stata l'obiettivo di questa ricerca di dottorato. Diversi rivestimenti a base di ossidi sono stati preparati seguendo un metodo di deposizione da soluzione chimica (CSD), che verrà introdotto nel Capitolo 1. Nella prima parte sperimentale (Capitolo 2), le proprietà funzionali dei rivestimenti ibridi di silice (SiO_2) sono state ottimizzate e utilizzate per controllare l'efficienza degli scambiatori di calore e dei raccoglitori di umidità. Nella seconda parte (Capitoli 3-6), sottili film di diossido di vanadio (VO_2) sono stati impiegati per la fabbricazione di finestre intelligenti termocromiche. La dipendenza dalla temperatura delle proprietà ottiche ed elettriche del materiale VO_2 offre una soluzione passiva per modulare l'irraggiamento solare senza fare affidamento su input attivi di energia. I numerosi parametri che influenzano il metodo CSD sono stati ottimizzati nel Capitolo 4, da cui sono stati ottenuti film sottili omogenei e termocromici di VO_2.

Riguardo a quest'ultimo materiale, una sfida attualmente irrisolta riguarda la riduzione della temperatura di cristallizzazione al di sotto dei 400°C. Nel Capitolo 5, è stato sfruttato un metodo non

convenzionale di trattamento laser, basato su impulsi con durata di 22 nanosecondi, per ridurre notevolmente la temperatura di cristallizzazione dei film sottili di VO_2. Riguardanti alle finestre intelligenti basate su VO_2, due ulteriori sfide affrontate sono legate a due caratteristiche chiave che devono essere garantite per un'applicazione reale delle stesse, ovvero la trasmissione della luce visibile e la resistenza alle condizioni atmosferiche. Entrambe le sfide sono state affrontate nel Capitolo 6, combinando i film di VO_2 con il biossido di titanio (TiO_2) e rivestimenti ibridi di SiO_2 in formando dei bilayer.

Nel capitolo finale (Capitolo 7), è stata presa in considerazione l'efficienza dei film sottili di VO_2 verso il rilevamento di idrogeno (H_2). Diverse morfologie e gradi di cristallinità sono stati considerati, ottimizzando i parametri del trattamento laser e di quello convenzionale, ed è stato studiato il loro impatto sull'efficienza del rilevamento di idrogeno.

References

1. Davis, L. W. & Gertler, P. J. Contribution of air conditioning adoption to future energy use under global warming. *Proc Natl Acad Sci U S A* **112**, 5962–5967 (2015).

2. Cao, X. *et al.* Challenges and Opportunities toward Real Application of VO2-Based Smart Glazing. *Matter* **2**, 862–881 (2020).

3. Mazzone, A. *et al.* Understanding systemic cooling poverty. *Nature Sustainability 2023* 1–9 (2023).

4. FAO. *The State of Food and Agriculture 2020. Overcoming water challenges in Agriculture*. *Fao* (2020).

5. Prado de Nicolás, A., Molina-García, Á., García-Bermejo, J. T. & Vera-García, F. Desalination, minimal and zero liquid discharge powered by renewable energy sources: Current status and future perspectives. *Renewable and Sustainable Energy Reviews* **187**, 113733 (2023).

6. Jonhson, W. *et al.* Fabrication of 3D-Printed Ceramic Structures for Portable Solar Desalination Devices. *ACS Appl Mater Interfaces* **13**, 23220–23229 (2021).

7. Aijaz, M. O. *et al.* Recent Progress, Challenges, and Opportunities of Membrane Distillation for Heavy Metals Removal. *The Chemical Record* **22**, e202100323 (2022).

8. Hren, R. *et al.* Hydrogen production, storage and transport for renewable energy and chemicals: An environmental footprint assessment. *Renewable and Sustainable Energy Reviews* **173**, 113113 (2023).

Preface

The results of this doctoral project have been published or are currently being prepared for publications. Some of the results have been presented at international conferences. In this Preface, the list of the published papers, as well as the manuscripts submitted or under preparation is reported.

Part of the experimental work discussed in this PhD thesis has been carried out at overseas facilities, which are reported below, along with the attended conferences and schools.

Refereed Journal Publications

1) Basso, M., Colusso, E., Sacco, A. *et al.* Bioinspired silica-based sol–gel micropatterns on aluminium for humid air condensation. *J Sol-Gel Sci Technol* 102, 466–477 (2022). https://doi.org/10.1007/s10971-022-05771-7

2) Tancon, M., Mirafiori, M., Bortolin, S., Basso, M., Colusso, E., Del Col, D. Dropwise condensation mechanisms when varying vapor velocity, *Applied Thermal Engineering* (2022). https://doi.org/10.1016/j.applthermaleng.2022.119021

3) Basso, M., Colusso, E., Tancon, M., Bortolin, S., Mirafiori, M., Guglielmi, M., Del Col, D., Martucci, A. Hydrophobic hybrid silica sol-gel coating on aluminium: Stability evaluation during saturated vapour condensation, *Journal of Non-Crystalline Solids: X*, Volume 17, 100143, (2023). ISSN 2590-1591 https://doi.org/10.1016/j.nocx.2022.100143

4) Basso, M., Colusso, E., Bombardelli, G. *et al.* Rapid laser-induced low temperature crystallization of thermochromic VO2 sol-gel thin films. *Applied Surface Science*, Volume 631, 157507 (2023). ISSN 0169-4332 https://doi.org/10.1016/j.apsusc.2023.157507

5) Colusso, E., Basso, M., *et al*. Pulsed laser crystallization of sol-gel derived cerium oxide thin films. *J Sol-Gel Sci Technol* (2023) https://doi.org/10.1007/s10971-023-06225-4

6) Basso, M. *et al*. Ultrafast laser crystallization dynamics of thermochromic VO_2 thin films by simple moisture-assisted sol-gel. *Submitted.*

7) Basso, M. *et al*. Influence of morphology and crystalline degree of VO_2 thin films on H_2 gas sensing. *Under preparation.*

8) Basso, M. *et al*. Antireflective thermochromic multilayers for weather-resistant smart windows. *Under preparation.*

9) Tancon, M., Colusso, E., Basso M. *et al*. Enhanced atmospheric water vapor condensation through superhydrophobic surfaces. *Under preparation.*

10) Facco, E., Colusso E., Parin, R., Basso M., *et al*. Passive ice prevention system for unmanned aerial vehicles applications: a review. *Under preparation.*

11) Riaz, A.A., Kalha, K., Basso, M., Furedi, M., Regoutz, A. The influence of stabiliser concentration on the formation of In_2O_3 thin films. *Under preparation*.

Oral presentations during national and international conferences

1) Basso, M.* *et al.,* "Laser crystallization of thermochromic VO_2 thin films". 30 years of INSTM: past, present and future of the Consortium. Conference. Brixen, Italy, 2023.

   Winner of the "G. Gusmano" award for the Best Oral Presentation.

2) Basso, M.* *et al.* "Laser crystallization of thermochromic VO_2 thin films obtained by an environmentally friendly sol gel approach". SolGel 2022 conference. Lyon, France, 2022.

3) Basso, M.* *et al.* "Laser crystallization of thermochromic VO_2 sol gel coatings". InoMat – International School on Inorganic Materials. Bardonecchia, Italy, 2021.

4) Basso, M.* *et al.* "Tuned wettability of sol-gel coatings for saturated vapor condensation". NewTimes – New Trends in Materials Science and Engineering. Virtual conference, 2021.

Overseas visits

1) Monash University – Melbourne, Australia – 2.5 months – 2023
   Host: Prof. Jacek Jasieniak

2) University College London (UCL) – London, United Kingdom – 6 months – 2022
   Host: Dr. Anna Regoutz

The CARIPARO Foundation is acknowledged for the scholarship which funded this PhD research.

The Gini Foundation is acknowledged for the scholarship which funded the visit to UCL, London.

Specialization schools and workshops

1) International workshop on Photonic Glasses by Sol-Gel – Lyon, France – July 2022

2) Dielectrics 2022 – London, United Kingdom – April 2022

3) International School on Inorganic materials – Bardonecchia, Italy – December 2021

Acknowledgments

I would like to deeply acknowledge my supervisor, Prof. Alessandro Martucci, for his constant support, encouragement, and mentoring throughout this doctoral project. All the Nanoeng research group, including Elena, Alessandro, Michele, Lorenzo, Riccardo, Marco, and the MSc and BSs students, are acknowledged for creating a supportive and stimulating work environment.

I am sincerely grateful for all the inspiring and motivating scientists I had the opportunity to meet within these three years, starting with Prof. Jacek Jasieniak and Dr. Anna Regoutz, who hosted me at Monash University and University College London, respectively. Prof. Massimo Guglielmi is kindly acknowledged for the fruitful discussions on the sol-gel process. Prof. Enrico Napolitani is acknowledged for the discussions on the laser effects and for the temperature simulations. The STET research group is acknowledged for the ongoing collaboration on dropwise condensation and for performing the thermal exchange tests. Dr. Emily Cheng is acknowledged for the TEM measurements, Dr. Laura Ratcliff is acknowledged for the DFT simulations, Carlo Scian is acknowledged for his help with the XRD measurements, Dr. Francesco Sgarbossa is acknowledged for the RBS analysis. Prof. Carlo Cantalini and Dr. Valentina Paolucci are acknowledged for the ongoing collaboration and for performing the electrical gas sensing tests. Dr. Curran Kalha is acknowledged for the fruitful discussions and help on XPS. The research groups of Prof. Jasieniak and Dr. Regoutz are acknowledged for the support and for making my overseas visits a wonderful experience.

Finally, I would like to especially thank my family and friends for their constantly supportive and caring presence.

To my family.

Table of contents

1 Chapter 1 – The Sol-Gel method 1

1.1 Introduction 3

1.2 Aqueous sol-gel 4

1.2.1 Silica from Silicon alkoxides 4

1.2.1.1 Precursor 5

1.2.1.2 Catalyst (pH) 5

1.2.1.3 Alkoxo group/water ratio and solvent 6

1.2.2 Metal oxides 7

1.2.2.1 Precursor reactivity 8

1.2.2.2 Oligomerization 8

1.2.2.3 Viscosity and volatility 9

1.2.2.4 Solvent 9

1.2.3 Strategies to reduce reactivity of transition metal alkoxides 9

1.2.3.1 Titania from Titanium alkoxides and β-diketones 10

1.2.4 Inorganic-organic hybrids 11

1.2.5 Gelation 12

1.2.6 Aging, drying and annealing 12

1.3 Nonaqueous sol gel 13

1.3.1 Precursors and principal NASG routes 14

1.3.2 Solvent or surfactant-assisted routes 15

1.3.2.1 Surfactant-controlled route 15

1.3.2.2 Solvent-controlled route 17

1.4 Vanadium oxides 20

1.4.1 Sputtering 21

1.4.2 Chemical vapor deposition (CVD) 21

1.4.2.1 Mist / aerosol CVD (metal-organic decomposition, MOD) 21

1.4.2.2 Direct liquid injection CVD 22

1.4.3 Pulsed laser deposition (PLD) 22

1.4.4 Chemical solution deposition (CSD) 23

1.4.4.1 Moisture-assisted aqueous sol gel from alkoxides 23

1.4.4.2 Moisture-aided polymer-assisted deposition (PAD) from metal salts 23

1.4.4.3 Metal-acetylacetonates and alcohol 24
1.4.4.4 Hydrothermal 27
1.5 Conclusions 28
2 Chapter 2 – Humid air and saturated vapor condensation 37
2.1 Introduction 39
2.1.1 Surface wettability 40
2.1.2 Condensation theory 42
2.1.3 Dropwise condensation 44
2.1.3.1 Spatial-temporal evolution of dropwise condensation 44
2.1.3.2 Heat exchanged through single and multiple droplets 45
2.1.3.3 Dropwise condensation challenges 48
2.1.4 Surface functionalization and nanostructuring 49
2.1.4.1 Saturated vapor condensation 51
2.1.4.2 Humid air condensation 54
2.1.4.3 Low hysteresis of the contact angle 57
2.2 Durability and heat exchange efficiency of hybrid sol-gel coatings during saturated vapor condensation 60
2.2.1 Synthesis and deposition of hybrid coatings 62
2.2.2 Optimization of hybrid-silica coating 62
2.2.3 Saturated vapor condensation experiments 63
2.2.4 Coating degradation tests 68
2.2.5 Considerations on heat transfer and coating durability 72
2.2.6 Durability and heat exchange efficiency of hybrid sol-gel coatings during saturated vapor condensation – conclusions 74
2.3 Bioinspired sol-gel micropatterns for humid air condensation 75
2.3.1 Synthesis and deposition of patterned, silica and CH_3-silica coatings on aluminum substrates 77
2.3.1.1 Patterned coatings 77
2.3.1.2 Plain reference silica coatings 78
2.3.1.3 Characterization of the plain silica and plain CH_3-silica coating 78
2.3.1.4 Optimization of patterned morphology 80
2.3.2 Coating durability under high relative humidity conditions 83
2.3.3 Humid air condensation tests 84
2.3.4 Bioinspired sol-gel micropatterns for humid air condensation – conclusions 89
2.4 Conclusions 90
3 Chapter 3 – Vanadium dioxide (VO_2) 103

3.1 Introduction **105**
3.2 Vanadium oxides **105**
3.3 Crystallographic structures of VO_2 polymorphs **106**
3.4 Electronic structures of VO_2 **109**
3.5 Metal-insulator transition mechanism of VO_2 **111**
3.5.1 Mott-Hubbard transition 112
3.5.2 Peierls transition 112
3.5.3 Current perspectives 113
3.6 Optical and electrical properties of VO_2 **114**
3.6.1 Luminous transmittance 115
3.6.2 Solar modulation 116
3.6.3 Hysteresis and transition temperatures of heating/cooling cycles 117
3.7 Applications and challenges of VO_2 **118**
3.7.1 VO_2 applications 118
3.7.2 VO_2 challenges 121
3.7.2.1 Transition temperature 121
3.7.2.2 Thermochromic performance 122
3.7.2.3 Long-term stability 123
3.7.2.4 Environmental friendliness 124
3.7.2.5 Color and skin-comfort design 124
3.7.2.6 Flexible fabrication 125
3.7.2.7 Current work 125
4 Chapter 4 – Sol-gel synthesis of VO_2 thin films **137**
4.1 Introduction **139**
4.2 V_2O_5 precursor **140**
4.2.1 Solution stability 144
4.2.2 Film aging and moisture influence 146
4.2.3 Deposition over hot substrates and influence of drying temperature 147
4.3 $VO(acac)_2$ precursor **149**
4.3.1 Solvent 149
4.3.2 Synthesis 152
4.3.2.1 Chemical composition of the solution 152
4.3.2.2 Solution aging 155
4.3.3 Thin film deposition and drying 157
4.3.4 Annealing atmosphere 161
4.3.5 Annealing temperature 166

4.3.6 Thin film thickness 170
4.3.7 Solution aging time 176
4.3.8 Atmosphere during synthesis and deposition 179
4.3.8.1 Inert atmosphere vs air 179
4.3.8.2 Moisture influence on synthesis and deposition 181
4.3.8.3 Moisture influence – conclusions 193
4.4 Conclusions 194
5 Chapter 5 – Laser annealing of VO_2 thin films 203
5.1 Introduction 205
5.2 Photonic annealing 207
5.2.1 UV continuous lamps 207
5.2.1.1 DUV lamp crystallization of MO sol gel thin films 209
5.2.1.2 DUV lamp crystallization of VO_2 thin films 209
5.2.2 Laser annealing 210
5.2.2.1 Laser irradiation of sol gel MO thin films 215
5.2.2.2 KrF excimer laser irradiation of VO_2 thin films 216
5.3 Laser-induced crystallization of VO_2 thin films 216
5.3.1 Synthesis and deposition of VO_2 thin films 217
5.3.2 Laser annealing 217
5.3.3 Low temperature drying 218
5.3.4 Laser-thin film interaction 219
5.3.5 Substrate influence 228
5.3.6 Laser-crystallization of VO_2 thin films – conclusions 236
5.4 Moisture influence on laser annealed VO_2 thin films 236
5.4.1 Synthesis, deposition, and laser-annealing of VO_2 thin films 237
5.4.2 Optimal working window for laser-processing of VO_2 thin films 237
5.4.3 Moisture influence and optimal working window – conclusions 247
5.5 Laser-induced crystallization mechanism of VO_2 thin films 247
5.5.1 GIXRD, SEM, TEM and AFM results 248
5.5.2 Laser-induced crystallization mechanism of VO_2 thin films 254
5.5.3 Laser-induced crystallization mechanism of VO_2 thin films – conclusions 257
5.6 Conclusions 258
6 Chapter 6 – Multifunctional bilayers 271
6.1 Introduction 273
6.1.1 Principles of antireflective layers 275

6.2 TiO_2 – VO_2 bilayers **276**
6.2.1 Synthesis, deposition and annealing of VO_2 thin films 276
6.2.2 Synthesis and deposition of TiO_2 films 276
6.2.3 Crystallization of TiO_2 films 279
6.2.4 TiO_2 – VO_2 bilayers 282
6.2.4.1 Structural and morphological analysis of TiO_2 – VO_2 bilayers 282
6.2.4.1.1 Influence of VO_2 on the anatase-rutile transition of TiO2 282
6.2.4.1.2 Elemental interdiffusion 284
6.2.4.1.3 Influence of TiO_2 on VO_2 crystallization 287
6.2.4.2 Optical and electrical properties of TiO_2 – VO_2 bilayers 288
6.2.4.2.1 Simulations of luminous transmittance of TiO_2 – VO_2 bilayers 288
6.2.4.2.2 TiO_2 thickness influence on luminous transmittance of bilayers 290
6.2.4.2.3 Optical properties of "low diffusion" bilayers 291
6.2.4.2.4 Optical properties of "high diffusion" bilayers 292
6.2.4.2.5 Optical and electrical hysteresis of bilayers 293
6.3 VO_2 – SiO_2 bilayers **295**
6.3.1 Synthesis and deposition of VO_2 films 296
6.3.2 Synthesis and deposition of hybrid SiO_2 coatings 296
6.3.2.1 Methyl-modified SiO_2 coating 296
6.3.2.2 Octyl-modified SiO_2 coating 297
6.3.3 Optical properties of VO_2 – hybrid SiO_2 bilayers 297
6.3.4 Durability tests 301
6.4 Multifunctional bilayers – conclusions **303**
7 Chapter 7 – VO_2 thin films for H_2 gas sensing **311**
7.1 Introduction **313**
7.1.1 Properties of gas sensors 314
7.1.2 Gas sensing mechanism 314
7.1.3 Vanadium oxides as gas sensors 315
7.2 VO_2 thin films for H_2 gas sensing **316**
7.2.1 Device fabrication 316
7.2.2 Device characterization 317
7.2.3 Electrical and optical H_2 gas sensing 322
7.2.4 H_2 gas sensing – discussion 327
7.3 Conclusions **329**
8 Conclusions and future perspectives **337**

A Appendix **349**

A.1 Materials recipes **351**

A.1.1 Optimized recipe for the synthesis and deposition of octyl-modified SiO_2 coatings 351

A.1.2 Optimized recipe for the synthesis and deposition of methyl-modified SiO_2 coatings 351

A.1.3 Optimized recipe for the synthesis and deposition of VO_2 thin films from V_2O_5 353

A.1.4 Optimized recipe for the synthesis and deposition of VO_2 thin films from $VO(acac)_2$ 353

A.1.5 Conventional thermal annealing of VO_2 thin films 353

A.1.6 Laser annealing of VO_2 thin films 354

A.1.7 Optimized recipe for the synthesis Pt nanoparticles 355

A.2 Characterizations **355**

A.2.1 Dynamic contact angle and contact angle hysteresis 355

A.2.2 Saturated vapor condensation tests 355

A.2.3 Coating degradation tests 357

A.2.4 Durability tests under high moisture conditions 358

A.2.5 Humid air condensation tests 358

A.2.6 Grazing incidence X-ray diffraction (GIXRD) 359

A.2.7 Raman spectroscopy 359

A.2.8 Optical spectroscopy 359

A.2.9 Ellipsometry 360

A.2.10 Four point probe characterization 361

A.2.11 Electron microscopy and image analysis 361

A.2.12 Atomic force microscopy (AFM) 362

A.2.13 X-ray photoelectron spectroscopy (XPS) 363

A.2.14 Density-functional theory (DFT) 363

A.2.15 Temperature profile simulations 364

A.2.16 Rutherford Backscattering Spectrometry (RBS) 364

A.2.17 Gas sensing tests 364

Chapter 1

The Sol-Gel method

Table of contents

1 Chapter 1 – The Sol-Gel method 1

1.1 Introduction 3

1.2 Aqueous sol-gel 4

1.2.1 Silica from Silicon alkoxides 4

1.2.1.1 Precursor 5

1.2.1.2 Catalyst (pH) 5

1.2.1.3 Alkoxo group/water ratio and solvent 6

1.2.2 Metal oxides 7

1.2.2.1 Precursor reactivity 8

1.2.2.2 Oligomerization 8

1.2.2.3 Viscosity and volatility 9

1.2.2.4 Solvent 9

1.2.3 Strategies to reduce reactivity of transition metal alkoxides 9

1.2.3.1 Titania from Titanium alkoxides and β-diketones 10

1.2.4 Inorganic-organic hybrids 11

1.2.5 Gelation 12

1.2.6 Aging, drying and annealing 12

1.3 Nonaqueous sol gel 13

1.3.1 Precursors and principal NASG routes 14

1.3.2 Solvent or surfactant-assisted routes 15

1.3.2.1 Surfactant-controlled route 15

1.3.2.2 Solvent-controlled route 17

1.4 Vanadium oxides 20

1.4.1 Sputtering 21

1.4.2 Chemical vapor deposition (CVD) 21

1.4.2.1 Mist / aerosol CVD (metal-organic decomposition, MOD) 21

1.4.2.2 Direct liquid injection CVD 22

1.4.3 Pulsed laser deposition (PLD) 22
1.4.4 Chemical solution deposition (CSD) 23
1.4.4.1 Moisture-assisted aqueous sol gel from alkoxides 23
1.4.4.2 Moisture-aided polymer-assisted deposition (PAD) from metal salts 23
1.4.4.3 Metal-acetylacetonates and alcohol 24
1.4.4.4 Hydrothermal 27
1.5 Conclusions 28

1.1 Introduction

Inorganic and organic coatings or thin films are widely employed in most of our technologies and permeate our everyday life, from antireflection displays and micro/nano electronic devices to protection barriers against corrosion or abrasion.[1–6] Several techniques have been developed to allow their synthesis and deposition, each possessing advantages and disadvantages. Generally, the methods are divided into two main categories, *vapor phase* deposition and *solution-based* deposition:

- Vapor phase deposition includes techniques such as evaporation, molecular beam epitaxy, sputtering, physical and chemical vapor deposition, pulsed laser deposition;
- Solution-based deposition includes electrochemical deposition, chemical solution deposition, self-assembled monolayers, and sol-gel.

In this work, most of the thin films or coatings were obtained by exploiting the advantages of the sol gel process, which offers a great synthesis versatility along with the possibility to profoundly tune the chemical composition of the material. The method is based on simple and straightforward procedures, it does not require the use of expensive vacuum-based equipment and it is scalable at industrial level. Usually, amorphous glass-based oxides are obtained from rapid cooling of melted materials, which prevents the crystallization from happening by instead favoring the thermodynamically more stable phase. The sol-gel process offers an alternative path based on a "bottom-up" approach: the final amorphous material is obtained by gradually connecting molecular building blocks, such as SiO_4 tetrahedra or TiO_6 octahedra, via irreversible reactions.

According to Schubert[7], a *sol* is intended as a stable suspension of colloidal particles within a liquid medium, with dimensions ~1-1000 nm. The particles can either be amorphous or crystalline, based on building blocks that can be porous, dense, or polymeric. The sol particles interact and agglomerate via attractive Van der Waals forces and tend to minimize the system surface energy. The sol stability is key during sol-gel, therefore repulsive forces must be introduced to prevent undesired sol agglomeration, exploiting organic additives to create steric or electrostatic barriers. A *gel* is a solid, porous, and continuous network, developed over three-dimensions which holds within it a percolating liquid phase. In most cases, gelation is reached via covalent bonds between the sol particles, whereas a reversible gel is formed when Van der Waals forces or hydrogen bonds are involved. According to the final goal and application, the gel can be tuned to evolve into aerogels, xerogels, dense ceramic bulks or thin films.[8]

The sol-gel process can be principally divided into two categories: aqueous, or hydrolytic, and nonaqueous. This work has been focused on three types of materials, vanadium dioxide (VO_2), titanium dioxide (TiO_2) and silicon dioxide (SiO_2). The formation of silica coatings from silicon

alkoxides represents one of the most widely studied sol-gel process, which is based on hydrolytic reactions. Regarding the formation of vanadium or titanium oxides, several reactions mechanisms could occur, even concurrently, depending on the type of precursor used and on the synthesis conditions, therefore a panoramic of the most fitting ones will be presented. The principal categories which the sol-gel process include, along with the key parameters affecting them, will be presented in the following sections.

As defined by Niederberger and Pinna[9], not all the examples included in sol-gel chemistry are based on the mere transformation of a molecular precursor first into sol and then into a gel. They generalized the *sol-gel* definition to "any process in which the transformation of a molecular precursor into the final oxidic compound involves chemical condensation reactions in liquid phase under mild conditions".

1.2 Aqueous sol-gel

The aqueous sol-gel chapter will be discussed in two separate sections: the first part will be devoted to silicon alkoxides precursors, whereas the second section will be devoted to metal oxide precursors.

1.2.1 *Silica from Silicon alkoxides*

According to the definition by Brinker and Scherer[8], during *aqueous* sol-gel a starting precursor solution is turned into an inorganic solid via inorganic polymerization reactions induced by water.[8] Silica-based sol-gel materials can be principally obtained from two precursor types, silicates and silicon alkoxides. In the latter case, which is relevant to this work, the initial $Si(OR)_4$ precursor is hydrolyzed by water during the first step, leading to the formation of silanol groups (Si-OH), which are then condensed to form siloxane bonds (Si-O-Si).

The hydrolysis reaction is schematized as represented in Eq. (1.1):

$$Si(OR)_4 + H_2O \leftrightarrow (OR)_3Si–OH + R–OH \quad (1.1)$$

Whereas condensation reactions can proceed either by alcohol elimination (Eq. (1.2)) or by water elimination (Eq. (1.3)):

$$Si(OR)_4 + (OR)_3Si–OH \leftrightarrow (OR)_3Si–O–Si(OR)_3 + R–OH \quad (1.2)$$

$$(OR)_3Si–OH + HO–Si(OR)_3 \leftrightarrow (OR)_3Si–O–Si(OR)_3 + H_2O \quad (1.3)$$

Hydrolysis and condensation reactions compete during the sol-gel process of alkoxides. Their kinetic is influenced by multiple parameters, among which the most relevant are:

a. Precursor type,
b. Acid or basic catalysis,
c. Alkoxide/water ratio,
d. Solvent type,
e. Temperature,
f. Concentration.

1.2.1.1 *Precursor*

Steric hindrance influences the hydrolysis of alkoxides, i.e., a higher branching or higher chain length determines a reduction in hydrolysis rate. For example, $Si(OMe)_4$ undergoes a faster hydrolysis respect to $Si(OEt)_4$ and $Si(O^nPr)_4$, and the latter is faster than $Si(O^iPr)_4$.[8]

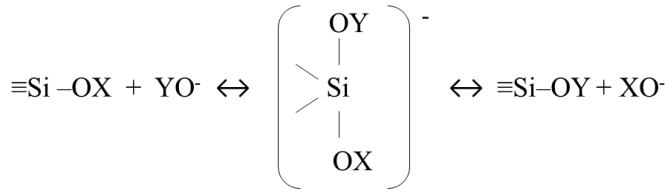
1.2.1.2 *Catalyst (pH)*

The pH of the solution, i.e., the acidity or basicity induced by the catalyst, has a different effect on hydrolysis and condensation. The lowest reaction rate is found at pH=7 for hydrolysis and at pH=4.5 (which is the PZC for silica) for condensation. At pH<5 the hydrolysis is faster, with condensation being the rate determining step, whereas at pH>5 the Si-O-Si bonds are immediately formed from the hydrolyzed parts, which are consumed due to the more rapid condensation.[8]

$$\equiv Si\text{–}OX + H^+ \leftrightarrow \equiv Si\text{–}O^+\begin{matrix}H\\X\end{matrix} \tag{1.4}$$

$$Y\text{–}OX + \equiv Si\text{–}O^+\begin{matrix}H\\X\end{matrix} \leftrightarrow Y\text{–}O\text{–}Si\equiv + XOH \tag{1.5}$$

Considering the silica reactions as an example, during acid catalyzed sol-gel, the oxygen atom in either ≡Si–OR, ≡Si–OH or $\equiv Si\text{–}O^-$ is quickly protonated (Eq. (1.4)). This determines a reduction in electron density in the Si center, which increases its electrophilicity and susceptibility towards water or silanol attack (Eq. (1.5)), during hydrolysis (X=R, Y=H) or condensation (X=R or H, Y=Si≡), respectively.



(1.6)

Under basic catalyzed sol-gel, deprotonation of H_2O or ≡Si–OH leads to the formation of OH^- and ≡Si–O^- (Eq. (1.6)). The central silicon atom undergoes a nucleophilic attack by either OH^- (hydrolysis, X=R, Y=H) or ≡Si–O^- (condensation, X=R or H, Y=Si≡) with a S_N2 mechanism.[7]

Transition or intermediate states are stabilized or destabilized in function of the reagents that are present in the reacting solution, that are responsible of inductive effects. The electron density near the central Si increases as Eq. (1.7):

$$\equiv Si–O–Si\equiv \; < \; \equiv Si–OH \; < \; \equiv Si–OR \; < \; \equiv Si–R^- \qquad (1.7)$$

Under acid catalysis, hydrolysis and condensation reactions increase in reaction rate with the same order of the electron density, because the positively charged transition state is better stabilized by a higher electron density on the silicon atom. Under basic catalysis, the reaction rate increases with the inverse of the order in Eq. (1.7), because the negatively charged transition state needs to be stabilized.[7]

While hydrolysis and condensation reactions are developed, the central Si increases the electrophilicity due to the higher -OH and -OSi- bonded to it. This determines favored reactions at the central Si atoms under acidic conditions, leading to chain-like network formation. Basic conditions are favored at terminal Si, which possess only one Si-O-Si bond, leading to a higher branching and ramifications of the network. Moreover, $Si(OR)_4$ have a slower reaction kinetics respect to alkoxysilanes which are organically substituted $R'Si(OR)_3$ if under acidic condition, whereas the opposite happens under basic conditions.[7]

1.2.1.3 *Alkoxo group/water ratio and solvent*

If tetraalkoxysilanes ($Si(OR)_4$) are used as precursors, two equivalents of water are required for their full conversion into SiO_2. Generally, if the water amount is increased, the formation of Si-OH groups over condensed Si-O-Si is favored, with the complete hydrolysis reached with four equivalents of water.

The solvent properties, such as viscosity, polarity, protic behavior, volatility, and dipole moment can play a major role upon stabilizing the liquid system or balancing/boosting the reactions. As depicted

in Eq. (1.1-1.3), solvent is rarely an inert component, since is participates in both hydrolysis and condensation reactions as a product.

1.2.2 *Metal oxides*

With respect to silicon, a semimetal, metals display a higher Lewis acidity (i.e., are more electropositive) and are more reactive towards a nucleophilic attack. Additionally, while in the case of silicon the coordination number coincides with its valence (4), metals and transition metals are more stable with a coordination number higher than their valence. The higher coordination number is obtained by coordination with any Lewis base nucleophile component.[7]

The higher coordination number of transition metals has consequences on how they arrange within the forming sol-gel network. For example, SiO_2 and TiO_2 polymorphs share the same valence of 4. While Si is a 4-coordinate, forming tetrahedral SiO_4 components, Ti is a 6-coordinate, forming octahedral TiO_6 blocks when in rutile form, which is the most stable. To form a stoichiometric SiO_2 material, each oxygen bridges 2 Si atoms, with the tetrahedra sharing corners with the neighboring blocks. In the case of TiO_2, since 2 O are present in the formula, each O atom must coordinate 3 Ti atoms to satisfy the 6-fold coordination requirement ($TiO_{6/3}$), leading to edge-sharing octahedra connected with the corners of an adjacent string. The SiO_2 structural arrangement has a higher degree of freedom respect to the TiO_2 one. This results in an amorphous structure in the former case, and a semi- or microcrystalline gels in the latter.[7]

Widely used precursors for metal oxides (MOs) include inorganic metal salts, such as chlorides, nitrates, or sulfates, and metal-organic compounds, among which the alkoxide family has been extensively investigated.[9] Starting from these precursors, a homogeneous solution is formed. A direct dissolution of an inorganic salt can be performed if water is employed as the main solvent; if metal-organic precursors are used, organic solvents miscible with water can be chosen instead. As described for silica materials, the hydrolysis reaction is generally schematized as represented in Eq. (1.8):

$$M(OR)_n + H_2O \leftrightarrow M(OR)_{n-1}–OH + R–OH \quad (1.8)$$

Whereas condensation reactions can proceed either by alcohol elimination (Eq. (1.9)) or by water elimination (Eq. (1.10)):

$$M(OR)_n + M(OR)_{n-1}–OH \leftrightarrow (OR)_{n-1}M–O–M(OR)_{n-1} + R–OH \quad (1.9)$$

$$M(OR)_{n-1}–OH + HO–M(OR)_{n-1} \leftrightarrow (OR)_{n-1}M–O–M(OR)_{n-1} + H_2O \quad (1.10)$$

As for the silicon alkoxide process, the kinetics of these reactions are greatly affected by several factors, including water/precursor ratio; steric hindrance of the organic group R; type, polarity, and volatility of the solvent; acid or basic catalysis; temperature.[8] Key factors that influence the chemical and physical properties are:

a. the difference in electronegativity between the metal atom and oxygen, which influences the degree of ionic character of the M-O bond;
b. the electronic density of the organic group R, which can modify the polarity of the M-O bond by donation or extraction of electrons through the interaction with the oxygen atom;
c. the possible expansion of the metal coordination sphere, which can lead to the formation of oligomers with the adjacent alkoxide through dative bonds with donor atoms.[10]

1.2.2.1 *Precursor reactivity*

As described earlier, metal alkoxides are stronger Lewis acids respect to their silicon counterparts, which determines an extreme reactivity towards hydrolysis due to the higher metal sensitivity towards a nucleophilic attack.[7] Silicon alkoxides require the addition of catalysts to increase the reaction rates of hydrolysis and condensation, that would otherwise be excessively slow. In the case of metal alkoxides the problem lies at the opposite side: to properly control the evolution and formation of the wet gel, avoiding precipitates, the requirement is to reduce the high reaction rate of hydrolysis. For example, $Si(OR)_4$ displays a $\sim 10^5$ slower hydrolysis rate respect to the corresponding $Ti(OR)_4$ counterpart, with R being the same.

The chemical reactivity of metal alkoxides varies according to the different type of metal center[7]:

$$Si(O^iPr)_4 << Sn(O^iPr)_4, Ti(O^iPr)_4 < Zr(O^iPr)_4 < Ce(O^iPr)_4 \quad (1.11)$$

Strategies to reduce the reactivity of transition metal alkoxides will be discussed in the following paragraph 1.2.3.

1.2.2.2 *Oligomerization*

The oligomerization of metal alkoxides originates from the general tendency of metals to maximize their coordination number, which in turn raises with increasing size of the metal atom. While $Si(OR)_4$ precursors display a monomeric structure, a bridging ligand can coordinate 2 or 3 metal atoms with metal alkoxides precursors. The degree of oligomerization is also influenced by the complexity of the organic ligand, the solvent type, and the solute concentration. The higher the ramification or spatial

obstruction of the alkoxy group, the lower the degree of oligomerization. As a general trend, the molecular complexity tends to increase if the metal size increases and if the steric hindrance of the alkoxy group decreases.[10]

1.2.2.3 *Viscosity and volatility*

The viscosity of the solution is affected by the concentration and steric hindrance of the precursors, the type of solvent, and the volatility of all reagents. An increase in oligomerization generally leads to a lower precursor volatility, which influences the homogeneity and viscosity of the solution. In sol-gel, alcohols are widely used solvents and their behavior is hardly inert, since even in the most straightforward case they are formed as reaction products during hydrolysis and condensation.

1.2.2.4 *Solvent*

The alcoholic solvent can be chosen to match the reaction product of the starting alkoxide or can be chosen to be different due to volatility or polarity goals. For example, the hydrolysis of zirconium alkoxides ($Zr(O^nPr)_4$) was compared in n-propanol and in cyclohexane. While in the former the hydrolysis was fast and led to precipitates, in the second it led to a gel. Different intermediate complexes were formed: in the first case, the parent alcohol ROH was preferentially coordinated, while in cyclohexane OR-bridged oligomers were formed. The ROH can be easier released respect to the OR- bridge.[7] In either way, exploiting a preferential coordination of the parent/different alcohol instead of adjacent alkoxides, zirconium alkoxides can concurrently increase their coordination number and reduce the molecular complexity.[10]

In the case of a different solvent respect to the parent one, alcoholysis can play a role by changing the reaction equilibrium (Eq. (1.12)):

$$M(OR)_n + xR'OH \leftrightarrow (OR)_{n-1}M–O–M(OR')_x + xR–OH \qquad (1.12)$$

In line with the previous considerations, alcoholysis is influenced by steric hindrance effects, strength of the metal-oxygen bond, volatility of the alcohol product.

1.2.3 *Strategies to reduce reactivity of transition metal alkoxides*

The aqueous sol-gel process offers great advantages when precursors like silicon alkoxides are employed, which allow to effectively control the reactivity of the hydrolysis and condensation reactions. However, when transition metal alkoxides are concerned, the aqueous pathway constitutes

a challenge to be performed, due to the extremely high reactivity of these precursors towards water. Strategies developed to solve this problem, allowing for the use metal alkoxides with an aqueous approach, include[9]:

a. Introduction of organic additives which act as chelating agents, effectively slowing the reactivity of the metal alkoxide. These chelating agents include carboxylic acids, β-diketones and functional alcohols;
b. Employment of chemical/physical processes to slowly release H_2O within the system, to induce a more controlled hydrolysis kinetic by locally controlling the H_2O amount.

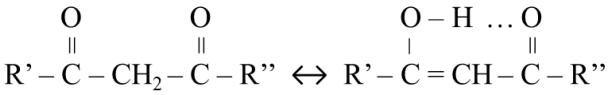
Chelated complexes possess a higher stability respect to their starting alkoxide, so *m* multidentate ligands (Y) can substitute n monodentate ligands (X) as depicted in Eq. (1.13):

$$M–X_n + mY \leftrightarrow M–Y_m + nX \tag{1.13}$$

Thermodynamically, bidentate ligands were confirmed to hold a higher *K* respect to their monodentate version. The thermodynamic equilibrium is influenced by the donor atom and by how the chelating agent coordinates around the metal ion, in terms of size and geometry.[10]

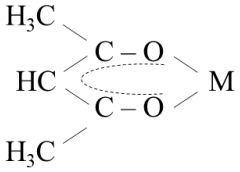
1.2.3.1 *Titania from Titanium alkoxides and β-diketones*

Titanium alkoxides are more reactive towards a nucleophilic attack respect to silicon alkoxides, due to their capability of increasing the coordination number to a highly stable six-fold geometry. To reduce their rapid reactivity and thus control the hydrolysis, β-diketones have been used as chelating agents. The latter show an enol-keto tautomerism (Eq. (1.14)):



(1.14)

By chelating the transition metal exploiting the reactivity of the –OH group, the enol form is stabilized. In the case of acetylacetone (Hacac), the resulting chelated complexed (Eq. (1.15)) are considered stable against hydrolysis.



(1.15)

Upon chelation of the metal ion, acetylacetone undergoes a molecular structural change, which leads to the closure of the ring. The elevated complex stability against hydrolysis is attributed to the redistribution of the electronic charges within the six-member ring configuration.[10]

$$Ti(OPr^i)_4 + Hacac \leftrightarrow Ti(OPr^i)_3(acac) + Pr^iOH \quad (1.16)$$

Even if the hydrolysis is far less rapid when compared to the original transition metal alkoxides, chelation with Hacac does not totally impede the interaction of the complex with water. In the case of titanium isopropoxide, the chelation with Hacac was proven to increase the coordination number of Ti to six (Eq. (1.16)). When exposed to water, the -OR groups are preferentially removed, subsequently followed by acac ligand removal. This was demonstrated by the partial charge distribution. Acac ligands possess a high negative charge (δ_{acac} = - 0.65) when bound to Ti centers. During hydrolysis, the ROH species are positively charged (δ_{ROH} = + 0.17) and therefore easier to be removed respect to Hacac (δ_{Hacac} = - 0.46).[11]

1.2.4 *Inorganic-organic hybrids*

The classic ceramic route involves elevated process temperatures, which do not allow for the introduction of organic components into the inorganic matrix. The latter allows for beneficial effects to the final sol-gel product, due to the introduction of specific functionalities such as hydrophobicity or to the increase in material's flexibility. Applied examples will be presented in Chapter 2 (SiO_2 coatings for vapor condensation) and Chapter 6 (protective SiO_2 coatings for VO_2-based smart windows).

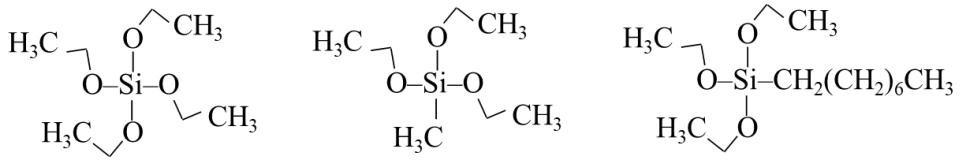
Hybrid organic-inorganic materials are classified into two categories:

a. Class I hybrids: organic molecules are incorporated into the overall inorganic gels without chemical bonds;
b. Class II hybrids: covalent bonds are employed to chemically link the organic molecules to the gel.

In class I, the organic components are dissolved within the precursor solution, to induce a matrix formation around them which leads to a weak interaction between the inorganic matrix and the trapped organic materials.

In class II, functional or non-functional organic precursors are covalently bonded to the developing oxide network. In hybrid SiO_2 gels, this is usually reached by mixing conventional silicon alkoxides ($Si(OR)_4$) with organotrialkoxysilanes ($R'Si(OR)_3$), which include Si-C bonds. The latter are not

sensitive towards hydrolysis, therefore they are not expelled as reaction products, allowing the organic functionalities to be maintained within the gel network.[7]



TEOS **MTES** **OTES**

Figure 1.1. Tetraethylorthosilicate (TEOS), methyltriethoxysilane (MTES), octyltriethoxysilane (OTES).

Examples of organotrialkoxysilanes which were employed in this work are reported in Figure 1.1.

1.2.5 *Gelation*

Generally, thermodynamics favors the crystalline state over the amorphous one, which in turn is favored when the structural building blocks have a high number of possible configurations to arrange among themselves, i.e., a high degree of freedom, as for silica amorphous gels.[7]

The gelation path can follow multiple alternatives, which lead to totally different structural configurations. In function of the system properties (pH, solvent, concentration, temperature, …), the nanoparticles (NPs) formed in the early stages of sol-gel can either continue to grow or begin to aggregate. In the latter case, the agglomerated compounds can form a 3D network (wet gel) or remain stable and suspended in the solution. The particles could be polymeric or dense, amorphous or crystalline, in the case of non-silicate materials.

Gelation is reached when the 3D solid, continuous and percolating network is formed, which pores contain liquid along with unbound oligomers and monomers. When thin films are considered, instead of monoliths, gelation happens during the final phase of the deposition step, after a major solvent evaporation.

1.2.6 *Aging, drying and annealing*

After the gelation phase, the elevated increase in viscosity induces the structure to retain its shape. During the following step, defined as “aging”, the development of chemical reactions does not stop. The initial flexibility of the gel is progressively reduced by the reaction between adjacent M-OH and M-OR unreacted groups, which increase the gel stiffness inducing structural modifications within the network.

During the drying step, which usually follows the aging one, densification and elimination of the residual solvent in the pores is induced by a temperature increase or pressure decrease. The rising stresses can be caused by two phenomena: solvent shrinkage and film contraction, when films/coatings are considered. During drying, menisci are formed at the interface between the shrinking liquid and the gas due to the progressive solvent decrease. This induces capillary pressure gradients due to the non-uniform curvature of different pores, which in turn determines tensile stress on the film. The solvent removal leads to a progressive increase in stiffness and volume decrease, since superficial -OH groups come in contact and form condensed bonds with other unreacted pairs.

The progressive liquid reduction induces a volume contraction in the coating. The contraction of the latter is not free in every direction: due to the substrate-coating interfacial contact, the latter is constrained by the contraction capacity of the former. The difference in coefficients of thermal expansion (α) creates compressive or tensile stress on the film, depending on whether the coefficient α_{film} is respectively lower or higher than $\alpha_{substrate}$. When the stiffness overcomes the network deformability induced by the surface tension, gel cracking may occur. During the final drying stages, the remining liquid within the gel ends the percolation state and is isolated inside the residual pores. The residual liquid removal can be achieved through gas diffusion.[7,8]

Finally, an annealing step is performed if organic removal or crystallization is required. According to the different requirements, the atmosphere can be oxidizing, inert or reducing.

1.3 Nonaqueous sol-gel

Under some circumstances, aqueous sol-gel (ASG) lacks feasibility due to:

i. the extremely high reactivity of transition metal alkoxides towards hydrolysis;
ii. the elevated number of reaction parameters to control;
iii. most of the as-synthesized materials are amorphous and would require a post-deposition thermal treatment to be gain a crystalline structure.

If an aqueous route is desired or required, possible solutions can be the slow release of water in the system and the use of chelating ligands to reduce the reactivity of the precursors. However, due to the high reactivity of some precursors, these options do not always guarantee an effective result.

Nonaqueous sol gel (NASG) has been developed as a successful alternative when the presence of water must be avoided in the system.

According to Niederberger and Pinna[9], NASG is based on the precursor transformation in organic solvents, under the exclusion of water. The oxygen for the metal-oxide formation is either supplied by the solvent or by the organic precursors. The definition of *nonaqueous*, rather than *nonhydrolytic*, guarantees a higher precision, since in some cases hydrated precursor could be used and/or water could be generated by *in situ* reactions.

1.3.1 *Precursors and principal NASG routes*

The number of possible precursors in NASG is higher respect to the aqueous route: while the latter is based on metal salts and metal alkoxides, the former includes other metal-organic and organometallic compounds, such as metal acetates, acetylacetonates, halides, carboxylates. Metal-organic compounds display a heteroatom, mostly oxygen, in between the metal and the organic ligand, whereas organometallic compounds are based on direct bonding between carbon and metal. The latter transformation to a metal oxide can mainly be related to a thermal decomposition, which may or may not be considered a nonaqueous sol gel.[9]

As for the aqueous route, the formation of the fundamental M-O-M units during NASG can be summarized into seven principal paths[9]:

i. Alkyl halide elimination: based on the condensation between a metal halide (≡M–Cl) and a metal alkoxide (≡M–OR), which leads to an alkyl halide (R–Cl) product formation deriving from the condensation (Eq. (1.17)):

$$\equiv M–Cl + RO–M\equiv \rightarrow \equiv M–O–M\equiv + R–Cl \quad (1.17)$$

ii. Ether elimination: based on the reaction of two metal alkoxides (Eq. (1.18)):

$$\equiv M–OR + RO–M\equiv \rightarrow \equiv M–O–M\equiv + ROR \quad (1.18)$$

iii. Metal carboxylate precursor, during which the condensation of carboxylate groups could be performed via:
   a. Ester elimination: reaction between a metal carboxylate and a metal alkoxide (Eq. (1.19)):

$$\equiv M–O–C(=O)R' + RO–M\equiv \rightarrow \equiv M–O–M\equiv + RO–C(=O)R' \quad (1.19)$$

   b. Amide elimination: reaction between an amine and a metal carboxylate.

iv. C-C coupling of benzylic alcohols and alkoxide molecules, in which the C-C bonds derive from two alkoxy groups.

v. Aldol or ketimine condensation: based on the reaction among two carbonyl groups, employing a ketone as the solvent. The oxygen source derives from the release of H_2O as a reaction product. Solvolysis could happen prior to aldol/ketimine condensation, as in the case of acetylacetonates.
vi. Oxidation of metal nanoparticles.
vii. Thermal decomposition.

1.3.2 *Solvent or surfactant-assisted routes*

The nonaqueous sol gel method offers the possibility to tune and control the metal-oxide formation via two routes: the surfactant-controlled and the solvent-controlled route.

1.3.2.1 *Surfactant-controlled route*

During surfactant-controlled route, the formation of the metal-oxide from the initial precursor is performed by exploiting the action of stabilizing ligands, under temperatures of 250-350°C. This route allows for a meticulous control of the crystal size and a good control of the crystal shape, leading to a narrow size distribution along with a reduced agglomeration tendency and a well-balanced redispersibility.[9]

Some of the most important processes based on a surfactant-control will be briefly reviewed, based on the work by Niederberger and Pinna[9]:

i. *Hot-injection*: first developed by Murray and Bawendi[12], room-temperature precursor solution is rapidly injected into a hot solvent, under the presence of surfactants. An initial fast nucleation is induced by the supersaturation resulting from the rapid injection. Further nucleation is the prevented, due to temperature reduction deriving from the cold precursor addition and to the decrease in precursor concentration deriving from the nucleation itself. Growth is controlled by a gradual raise in temperature. Surfactants are used to stabilize the nanoparticles in solution due to the presence of reversible capping layer. Through nonsolvent addition, the precipitation of the nanocrystals can be induced, with a subsequent redispersion in mostly apolar organic solvents. Semiconductor nanocrystals II-IV, IV-VI and III-V are suitable to be prepared with this method, as well as metals and metal oxides.[12–14] Metal oxide sols or amorphous particulates could be used as alternative ways for the rapid injection, respect to the conventional molecular precursors. For example, aqueous sol-gel was used to initially prepare the MO sol, during which acetylacetone allowed to control the

polymerization of the inorganic oxide. The sol was injected into tetradecane at 160°C, containing an amine. The amine surfactant plays two competing roles: it can exchange the acac ligands and promote M-O-M condensation from M-OH on the surface of the particles, as well as acting as a steric stabilization agent.[15]

ii. *Heating-up*: the starting solution is prepared at room temperature, followed by a raise in temperature to induce the crystallization in solution. Differently from the hot-injection, the heating-up route does not involve supersaturation conditions and is easier to be performed.

iii. *Solvothermal*: closed vessels are employed to perform reactions at temperatures above the solvent boiling point. Temperature and pressure are key parameters to control the reactions, besides the reagents and the solvent involved. Advantages are the greener approach, sustained by the use of common laboratory solvents and by mild reaction temperatures with a reduced energy consumption. The former could however limit the synthesis of nanoparticles, due to the generally low boiling point.

iv. *Microwave*: it offers an efficient source of homogeneous solution heating. The energy employed (2.45 GHz, corresponding to a photon energy of 0.0016 eV) is too low to cause bond breaking or even Brownian motion, therefore chemical reactions cannot be induced. The heat is generated by oscillations of the applied field, which lead to a continuous re-alignment of the dipoles/ions involved generating friction of molecules and dielectric losses. This technique is applicable with compatible solvents, which possess strong dielectric properties and can be polarized by electric fields, such as ethanol, isopropanol or dimetylsulfoxide (DMSO). Metal acetates or acetylacetonates are suitable precursors.[16]

v. *Seed-mediated growth*: mostly employed for metal nanoparticles, but it can be used for metal oxide nanoparticles as well. Preformed nanocrystals are introduced as nucleation seeds within the solution, on which monomers can preferentially nucleate, following a heterogeneous nucleation and preventing a homogeneous nucleation.

vi. *Self-assembled nanoparticles*: the shape, size and structural organization of the nanoparticles is controlled by the presence of surfactants. These amphiphilic molecules arrange the nanoparticles into 1D or 2D morphologies, in which the inorganic matrix is connected by the organic component.

vii. *Heterostructures/multicomponent nanoparticles*: hybrid nanocrystals can be prepared via this route, composed by two or more materials which are different in terms of composition, connected at the interface by a fixed inorganic component. Several subunits can be connected, each with a specific optical, magnetic, electronic, or catalytic property. Core-shell materials are a well-known example.

viii. *Nonaqueous with water traces*: as mentioned in Paragraph 1.2.3, the high reactivity of transition metals during aqueous sol gel can be solved by either employed chelating agents or by slowly controlling the water addition in the system. Water vapor was also successfully used to induce a controlled hydrolysis.[14,17,18] This route is set at the edge between aqueous and nonaqueous sol-gel.

1.3.2.2 *Solvent-controlled route*

Besides the surfactant-controlled route, coordinating organic solvents can be used as an alternative route to control the formation and growth of metal oxide nanoparticles. The solvent-controlled route offers a higher simplicity of the synthesis, the lower process temperatures (~50-200°C), and the higher purity of the products. The simplicity derives from the starting reaction solution, usually consisting of the mere MO precursor and a commonly used organic solvent. The higher purity derives from the removal of surfactants or other additives from the solution, which in turn reduces the nanoparticle's toxicity and surface accessibility for sensing or catalysis.

The organic solvent acts as an oxygen source and/or as a capping agent, either participating as a reaction reagent in the first case or as a growth limiting agent in the second case. Suitable precursor compounds are metal halides, acetates, acetylacetonates and alkoxides. Suitable solvents can either contain oxygen (alcohols, ketones and aldehydes) or not (amines, acetonitriles, toluene).

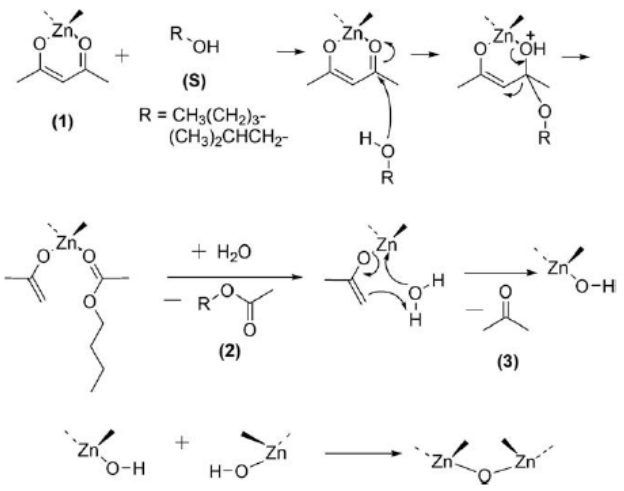
A possible disadvantage deriving from this route is the complexity of the final solution mixture, which can comprise unreacted organic components from the initial precursor, excess of organic solvent, unexpected products deriving from the reaction of the organic parts. Regarding the experimental set-up, oil baths with stirrer and eventually reflux columns are employed if the reaction temperature is well below the solvent boiling point. If the molecular precursor conversion into MO requires temperatures close or above the solvent boiling point, autoclave is usually preferred. Microwave heating can also be employed for a homogeneous solution heating.

Some of the most important processes based on a solvent-control will be briefly reviewed, based on the work by Niederberger and Pinna[9]:

i. *Metal halides and alcohols*: a simple beaker in an oil bath can be used to convert metal halides, mostly chlorides, in MO nanoparticles. Common precursors are $FeCl_3$, $VOCl_3$, WCl_6, $TiCl_4$. TiO_2 nanoparticles were obtained by the reaction of $TiCl_4$ with ethanol[19] or benzyl alcohol (C_6H_5-CH_2-OH)[20]. Semiconducting $VO_{1.52}(OH)_{0.77}$ single crystal nanorods were created from the reaction between $VOCl_3$ and benzyl alcohol.[20]

ii. *Metal alkoxides/acetates/acetylacetonates and alcohols*: a disadvantage of the metal halide route is the presence of halide impurities in the final product. Metal alkoxides, acetates, or acetylacetonates can instead offer a halide-free path. The reaction of metal salts with polyols, i.e., solvents containing multiple -OH groups, has been extensively employed. The solvothermal reaction between metal acetylacetonates and benzyl alcohol is another popular route. In most of the reactions, the addition of a certain H_2O amount is required for the precursor evolution into MO. This complicates the definition of a boundary between aqueous and nonaqueous sol gel. An alternative to water addition is the use of hydrated precursors: for example, ZnO was obtained from the reaction between zinc acetate dihydrate and diethyleneglycol at 100-120°C. On the other hand, the use of a dehydrated precursor along with an anhydrous solvent did not lead to the metal oxide formation.[22]

Example I – zinc acetylacetonate hydrate reaction with 1- or 2-butanol: Ambrozic *et al*.[23] studied the formation mechanism of ZnO nanoparticles, by refluxing a solution of $Zn(acac)_2$ hydrate in 1- or 2-butanol at 130-120°C. From the NMR results, they proposed a single-pathway alcoholysis reaction, resulting in the cleavage of the C-C bond of the acetylacetonate ligand with consequent formation of butyl acetate or isobutyl acetate products (Figure 1.2). An initial dissociation of the Zn-O bond by alcohol nor water did not occur since they refluxed acetylacetone in both solvents and the latter was not active towards alcoholysis. The non-occurrence of ligand exchange, a possible competitive reaction, was also proved since the formation of Zn alkoxide and/or Zn hydroxide intermediates was not detected.



Scheme 1. Proposed mechanism of Zn–O–Zn bond formation from the precursor **1** and 1-butanol or isobutanol.

Figure 1.2. Proposed mechanism of Zn-O-Zn formation from the $Zn(acac)_2$ hydrate precursor with 1-butanol or isobutanol.[23]

Example II – zinc acetylacetonate: Liu *et al*.[24] synthetized different ZnO NCs morphologies (dendritic branches, hexagonal pyramids, needles, or pinecones) starting from the same precursor, zinc acetylacetonate ($Zn(acac)_2$), and varying solvent type, additives, and temperature (Figure 1.3). A surfactant-controlled heating up route was developed in the first part, whereas a solvent-controlled route was tested in the second part. Dendritic branched ZnO NCs were obtained by thermolysis of the precursor at 285-300°C. By reducing the precursor concentration, amorphous or semi-crystalline ZnO NPs would be formed instead of the crystalline dendritic branches. Amorphous NPs would be formed by reducing the temperature to 250°C. They highlighted the critical role of both precursor concentration and temperature, from a thermodynamic and kinetic point of view. A critical radius for a stable NP formation decreases if the monomer concentration or the temperature are increased.

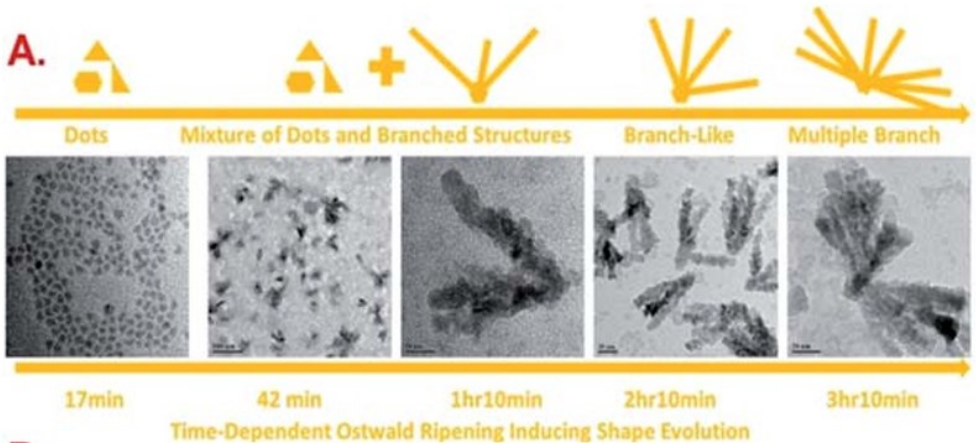


Figure 1.3. Time dependent Ostwald ripening inducing a shape evolution.[24]

iii. *Metal alkoxides and aldehydes/ketones*: the cations in some Cu-, Ni-, Pb-containing compounds are susceptible to a reduction to their corresponding metal form operated by

alcohols. The benzyl alcohol route is not applicable to obtain metal oxides based on these cations. Non-reducing solvents such as ketones or aldehydes offer an alternative as oxygen supplier for the MO formation.[25]

iv. *Metal acetylacetonates and amines/nitriles*: the oxygen source can be represented by the molecular precursors, such as metal acetylacetonates. In this case, oxygen-free solvents such as amines or nitriles can be employed, among which benzylamine is the most frequently used.[21] Additionally, ZnO was prepared though the solvothermal reaction of the corresponding metal acetylacetonate, which acted as the oxygen source, by acetonitriles at 100°C.[26]

1.4 Vanadium oxides

The most used vanadium precursors include vanadium alkoxides, vanadium pentoxide, $VOSO_4$, NH_4VO_3, and vanadyl/vanadium acetylacetonates. Many vanadium sources, despite being widely employed, are linked to high levels of toxicity, carcinogenicity, mutagenicity, damages to the reproductive system or the aquatic environment.[27,28] This highlights the need for a safer process, in terms of both precursor and solvent, which will be addressed in Chapter 4. Moreover, many processes rely on remarkable energy consumption, which should as well be minimized by exploiting or combining several solutions, as will be discussed in Chapter 5.

Different techniques can be used for the deposition of VO_2 or other vanadium oxides, including sputtering, chemical vapor deposition (CVD), pulsed laser deposition (PLD) and chemical solution deposition (CSD). In the case of smart windows application, the thermochromic properties will be reported and expressed in terms of luminous transmittance (T_{lum}) and solar modulation (ΔT_{sol}) (see Chapter 3 for further details). These two parameters are conventionally used in literature to compare the performance of the different thermochromic smart windows.

A general overview of different processes and vanadium sources will be presented below. Particular focus will be devoted to different synthesis route involving the precursor chosen for this work ($VO(acac)_2$).

1.4.1 *Sputtering*

Sputtering involves the strike of a target materials by highly energetic ions from a plasma state, inside a vacuum chamber. The impact results in ion ejection from the original target, with subsequent re-deposition onto a substrate under optimized pressure conditions, generally within the mTorr range.

Cai *et al*.[29] first attached 10 μm colorless and transparent polyimide films to a silica glass and then used DC magnetron sputtering to deposit VO_2 films, starting from a V_2O_3 target. The chamber conditions were maintained at 7 mTorr and room temperature, with an argon and oxygen ratio of Ar/O_2 = 35:15. Rapid thermal annealing (RTA) was used to post-anneal the films at 325–350°C for 5 min under 5 Torr. The VO_2 thin films on CPI had a ~45% T_{lum} and ~12% ΔT_{sol}, whereas the optimized multilayer with ITO films below and above the VO_2 film had a ~40% T_{lum} and ~16% ΔT_{sol}, besides offering a remarkable durability of 70 days under 60°C and 90% RH.

1.4.2 *Chemical vapor deposition (CVD)*

Chemical vapor deposition is based on the vapor phase transport of metal oxide precursors to the substrate, employing a gas carrier stream. Decomposition and/or reactions between the reagents involved is performed directly at the substrate surface, leading to the formation of the desired metal-oxide films or coatings. Temperature, pressure, carrier gas type, post annealing steps can be properly tuned in function of the initial reagents and the final material.

1.4.2.1 *Mist / aerosol CVD (metal-organic decomposition, MOD)*

Piccirillo *et al*.[30] investigated by AACVD (aerosol-assisted CVD) the influence of precursor, solvent, and flow rate on the formation of different oxides. They compared two metal-organic precursors, vanadium (III) acetylacetonate ($V(acac)_3$) and vanadyl (IV) acetylacetonate ($VO(acac)_2$). Methanol, ethanol, water, or different ratios between an alcohol and water were used as the solution solvent, whereas the nitrogen flow rate was set at 1.5 or > 3 L/min. It is important to note that $VO(acac)_2$ is soluble in methanol and ethanol but is insoluble in water. The glass substrate was maintained at 450°C to induce the crystallization. Any combination of ethanol/water led to the formation of V_2O_3, for both precursors. Under a flow rate of 1.5 L/min, $VO(acac)_2$ and ethanol led to VO_2(M1), and to a mix of VO_2 and other oxides if $V(acac)_3$ was employed. However, if the flow rate was increased to > 3 L/min, the combination of $VO(acac)_2$ and ethanol did not lead to , but to instead. This evidenced that the gas carrier is not just a transporter but can actively change and influence the growth conditions.

Matamura *et al.*[31] used the same metal-organic precursor ($VO(acac)_2$) and compared the effect of water and methanol during mist-CVD, under nitrogen stream of 3 L/min and at substrate temperatures between 400-750°C. Differently from Piccirillo *et al.*[30], they obtained V_2O_3 above 400°C when methanol was employed as the solvent, while VO_2 was detected above 450°C with water as the solvent. The differences between the two studies highlights the extreme sensitivity of vanadium oxides to the experimental settings, during which even small variations can lead to the formation of different results.

1.4.2.2 *Direct liquid injection CVD*

Kumar *et al.*[32] employed vanadium (V) oxytriisopropoxide to create VO_2 or V_2O_5 thin films by direct liquid injection MOCVD. An initial liquid solution, consisting of the vanadium (V) oxytriisopropoxide precursor and cyclohexane solvent, was maintained under nitrogen, and then vaporized. The injection stream consisted of the vaporized solution and nitrogen carrier gas. The substrate was maintained at 200°C for 2 h during the deposition. The as-deposited thin films did not show diffraction patterns from XRD, but did show Raman shifts, revealing a nano-VO_2 crystalline structure. Post-annealing was performed for 1 h at 600°C under $p_{O2} = 1*10^{-2}$ mbar, leading to V_2O_5 from both XRD and Raman. Additional 4 h at 600°C under vacuum (~0.6 mbar) reduced the oxidized film to crystalline VO_2.

1.4.3 *Pulsed laser deposition (PLD)*

Pulsed laser deposition involves the vapor phase deposition deriving from the ablation of a solid target material, which results in the vaporization of the latter and the creation of a plasma, generally under vacuum conditions. The vaporized material is then deposited on the substrate, which is maintained at optimized conditions of temperature, pressure, and oxidizing/reducing gases.

In the work by Chen *et al.*[33], V_2O_5 and Al_2O_3 targets were ablated by a KrF excimer laser, under a fluence of 2–3 J/cm^2 and 50 Hz repetition rate. The silicon or soda lime substrates were maintained at 600°C under 1.4 mTorr O_2 process gas to induce the deposition of pure and Al-doped VO_2 thin films. At the same temperature, higher oxygen partial pressure (47 mTorr) led to V_2O_5 formation, whereas vacuum induced a mixed oxide composition. Lowering the deposition temperature to 400°C or 500°C at 1.4 mTorr O_2 led to a lower crystallinity, whereas 600°C induced a highly oriented (011) monoclinic VO_2 (M1). Behera *et al.*[34] obtained VO_2 thin films by ablating a V_2O_5 target with a laser energy of 220–240 mJ for each pulse at 5 Hz. The substrates were kept at 630°C inside a chamber at

$p < 5 \times 10^{-8}$ Torr, with p_{O2} of 1 mTorr. The as-deposited films were then annealed at 660 °C for 1 hour under p_{O2} of 100 mTorr. Xiang *et al*[35]. deposited VO_2 thin films on Kapton substrates, ablating a VO_2 target at room temperature under $\sim 10^{-6}$ Torr. Post annealing was performed at 390°C under p_{O2} = 70 mTorr and gas flow of 2 sccm for 2-12 h.

1.4.4 *Chemical solution deposition (CSD)*

From a thermodynamic point of view, during physical vapor deposition methods the most widely used route is to vary the oxygen partial pressure in the growth chamber, which allows to tune the final vanadium oxide type at a fixed growth temperature. Contrarily, chemical solution deposition methods usually anneal the samples at fixed oxygen partial pressures, and the oxide type is changed in function of the processing temperature.[36] Here, examples of different chemical solution deposition processes will be presented, based on various vanadium precursors. Emphasis will be devoted to $VO(acac)_2$, which was employed during the experimental part of this PhD thesis. When appropriate, the effect of moisture will be highlighted since the benefits of the latter were also exploited in this work.

1.4.4.1 *Moisture-assisted aqueous sol gel from alkoxides*

In the work by Chae *et al*.[37], vanadium triisopropoxide ($VO(OC_3H_7)_3$) was mixed with isopropanol and acetic acid and spin coated in air on sapphire substrates, to induce hydrolysis by environmental moisture. Following a drying step at 250°C in air, the films were annealed 30 min at 410°C in air, followed by 10 min at 400-500°C under 32 mTorr, leading to the formation of VO_2 (M1).

1.4.4.2 *Moisture-aided polymer-assisted deposition (PAD) from metal salts*

During polymer assisted deposition, water-soluble polymers which are bound to inorganic metal ions are used to favor the latter dissolution in a water solvent. The polymer-metal bond prevents hydrolytic reactions from happening, since water cannot reach the metal ion due to the polymer shielding.

With other oxides, moisture was previously used to balance the possible formation of oxygen vacancies and avoid the reduction to V^{3+},[38] while at the same time preventing the oxidation to V^{5+} due to the very low oxidation capability.[39,40] An additional advantage is that the introduction of moisture is not a complicated task to perform during CSD.

In the work by Liang *et al*.[36], polyethyleneimine (PEI) and ethylenediaminetetraacetic acid were dissolved in water, along with ammonium metavanadate (NH_3VO_3). Since the green aspects of the

synthesis process were considering during work, it should be mentioned that NH_3VO_3 is considered toxic for reproductive organs and a chronic aquatic hazard. The solution was spin coated on sapphire and pre-annealed at 450°C for 1 h to remove the organic component. Annealing under reducing atmosphere (98.5% N_2 + 1.5% H_2) around ~500°C was balanced by a 5.5% moisture introduction, which allowed an expansion of the growth window temperatures from 4°C to 36°C to obtain stoichiometric VO_2 (M1). They exploited the role of moisture to improve the VO_2 (M1) crystallinity and reduced the hysteresis to less than 1°C.

1.4.4.3 *Metal-acetylacetonates and alcohol*

As discussed in paragraph 1.4.2.1, metal acetylacetonates can be employed for the deposition of metal oxides by CVD. An alternative approach is offered by CSD.

The CSD deposition of VO_2 thin films from a solution of $VO(acac)_2$ and methanol was first proposed by Pan *et al*.[41] The precursor solution was aged at room temperature for 1 week, spin coated on silicon and dried at 80°C for 20 min. The films were then annealed for 30 min at 550°C under nitrogen, which led to the formation of a detectable (011) peak at 2Θ~27.8°, not visible at 500°C. Further annealing for 5 min at 600°C remarkably improved the intensity of the (011) peak. Each layer had a 20-30 nm thickness and refractive index *n* ranging between 1.96-2.17. The average grain size was calculated from the Scherrer equation to be ~20-30 nm, corresponding to the thickness value. This highlights the thickness influence on the crystal grain size. The authors did not investigate the possibility of precursor oxidation induced by the preparation of the synthesis in uncontrolled atmosphere, i.e., in air.

In 1997, Grybos *et al*.[42] proposed a mechanism for the oxidation of $VO(acac)_2$ by atmospheric oxygen in a methanolic solution (Eq. (1.20)):

$$4V^{(4+)}O(acac)_2 + 4MeOH + O_2 + 2H_2O \rightarrow 4V^{(5+)}O(OH)(OMe)(acac) + 4Hacac \qquad (1.20)$$

When exposed to environmental air, which contains both O_2 and H_2O, the solution gradually turns from blue-green, due to the precursor's original color, to brown, orange, and bright red at the final state. As visible in Figure 1.5 (a), they compared the UV-Vis absorption spectra of the precursor dissolved in commercial methanol (containing 0.04% v/v H_2O) or in anhydrous methanol with the spectra of acetylacetone (Hacac) and the oxidized compound, which they propose to be $V^{5+}O(OH)(OMe)(acac)$.

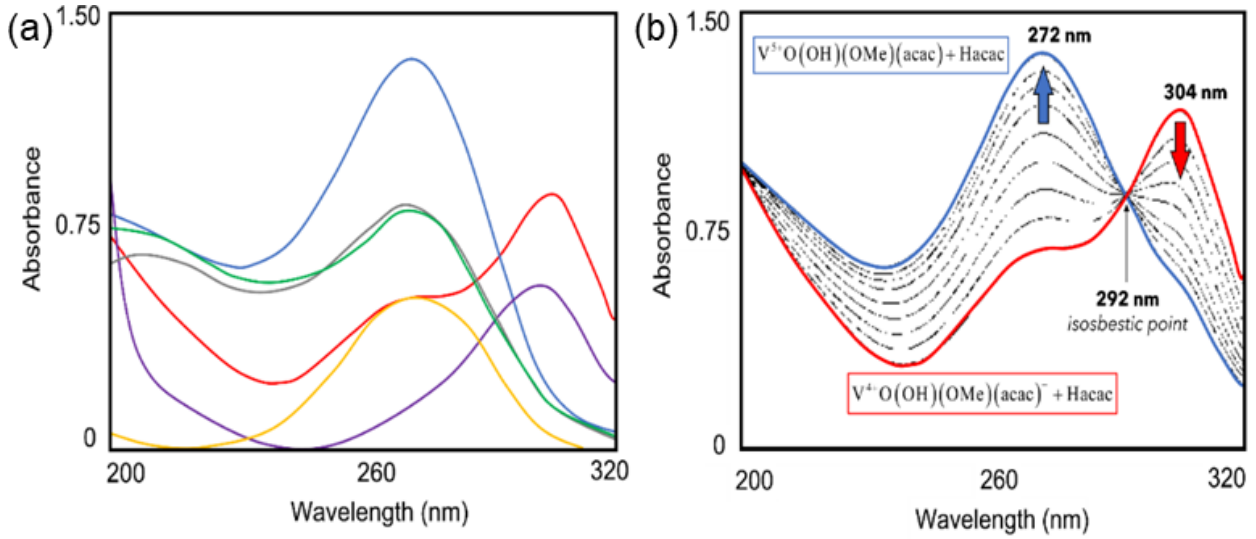


Figure 1.4. UV-Vis spectroscopy of the different compounds. (a) at fixed time, (b) evolution over time of $V^{4+}O(OH)(OMe)(acac)^-$ and $V^{5+}O(OH)(OMe)(acac)$.[42]

From the comparison of the spectra of the precursor in anhydrous methanol (purple line in Figure 1.4 (a)) and in commercial methanol (red line) at time zero, the authors propose the solvolysis of the precursor due to the presence of H_2O. This leads to release of one acetylacetonate ligand (acac) as acetylacetone (Hacac), while the precursor remains under a 4+ oxidation state as $V^{4+}O(OH)(OMe)(acac)^-$ (Eq. (1.21)):

$$V^{(4+)}O(acac)_2 + MeOH + 2H_2O \rightarrow V^{(4+)}O(OH)(OMe)(acac)^- + Hacac + H^+ \qquad (1.21)$$

The presence of O_2 in the alcohol solvent induces a change in oxidation state from V^{4+} to V^{5+} (Eq. (1.20)), leading to the formation of $V^{5+}O(OH)(OMe)(acac)$. The latter is shown in the gray line in Figure 1.4 (a), which coincides with the green line, in turn obtained by the subtraction of the blue line ($V^{5+}O(OH)(OMe)(acac)$+Hacac) and yellow line (Hacac).

In Figure 1.4 (b), the authors showed the evolution over time of the solution containing the precursor and the commercial methanol, i.e., with both O_2 and H_2O. At time zero, the solution contains $V^{4+}O(OH)(OMe)(acac)^-$, therefore, according to the authors, the release of one acac ligand happens immediately upon mixing with the H_2O containing alcohol, while the precursor is still under a V^{4+} oxidation state. Over time, the 304 nm peak progressively decreases, consequently to an increase of the 272 nm peak, indicating the evolution of the solution into a coexisting mixture of $V^{(4+)}O(OH)(OMe)(acac)^-$ e $V^{(5+)}O(OH)(OMe)(acac)$.

The mechanism proposed by Grybos *et al*. was not supported by other complementary techniques and did not consider the reversibility of the oxidation state of vanadium, which was experimentally seen during this work under certain conditions. By employing TGA analysis, Nenashev *et al*.[43] suggested that ligand detachment could happen only above temperatures around 150-180°C. Moreover, when

other metal acetylacetonates were considered ($Zn(acac)_2$), the authors of the work suggested the mechanism of alcoholysis by 1- or 2-butanol to be based on C-C cleavage rather than Zn-O cleavage.[23] Therefore the exact mechanism underlying the interaction between $VO(acac)_2$ and methanol, as well as the exact role of water and oxygen, has yet to be fully determined.

Starting from the same precursor ($VO(acac)_2$) and solvent (MeOH), Yu *et al.*[44] studied the effect of solution aging at 70°C under reflux for 7 days on the final film properties. They correlated the color change of the solution to a gradual precursor oxidation, citing the previous work by Grybos *et al.*[42], and they showed that acac ring opening could be detected by FTIR on the solution after several days of solution aging. Higher film quality, in terms of surface coverage, was obtained by 7 days of solution aging, as opposed to the formation of isolated particles with 1 day of solution aging. The increasing solution aging corresponded to a decrease in the visible transmittance but an increase in thermochromic efficiency ($T_{500\ nm} \sim 45\%$ and $\Delta T_{500\ nm} \sim 50\%$ after 7 days of solution aging).

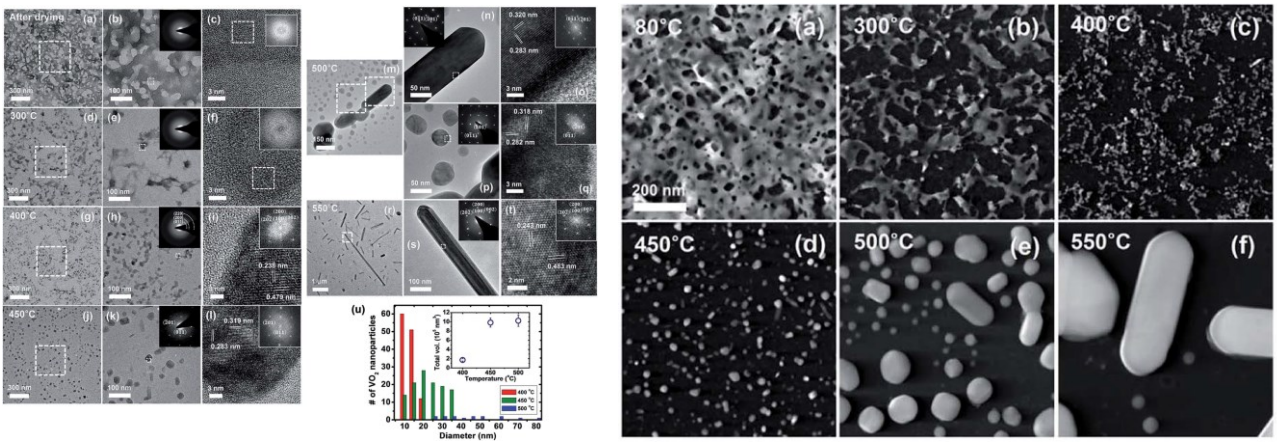


Figure 1.5. TEM investigation of the synthesis based on $VO(acac)_2$ and methanol, under the exclusion of oxygen and water.[44]

The interaction between $VO(acac)_2$ and methanol, under exclusion of water and oxygen, was studied by Jo *et al.*[45], who employed *in situ* TEM investigation to evaluate the metal-insulator transition in function of the annealing temperature. They spin coated a 250 mM solution, ultrasonically mixed and aged for 25 days in a glovebox and compared morphology and selected area electron diffraction (SAED) patterns by annealing between 80°C and 550°C in argon (Figure 1.5). Amorphous and spiderweb resembling morphologies were shown at 80°C and 300°C, with no visible diffraction from SAED. The first diffraction patterns were seen at 400°C, along with a highly fragmented morphology. The formation of isolated small (13-35 nm) nanoparticles was first seen at 450°C, which then grew in dimension at 500°C (25-84 nm). At the latter temperature, the beginning of the transformation from nanoparticles to nanowires was seen, which was completed by annealing at 550°C. From the total particle volume evolution, the authors observed that precursor conversion progressed until 450°C, above which the total volume remained constant and the particles were subjected to atomic diffusion.

They observed an increase in V/O ratio with annealing temperature, from 0.2 at 80°C (coherent with the precursor, $C_{10}H_{14}O_5V$) to 0.3 at 200°C to 0.35 at 300°C. At and above temperatures of 400°C, the ratio stabilized to 0.5, coherently with the formation of VO_2. By comparing Raman, XRD and electrical resistance in function of temperature, they found a transition temperature of 75 ± 2°C.

1.4.4.4 *Hydrothermal*

The hydrothermal route has been widely used for the synthesis of VO_2 nanocrystals of a wide range of morphologies (nanobelts, nanoplatelets, nanorods, nanoparticles) at mild temperature conditions, generally below 250°C. The hydrothermal method is based on heterogeneous reactions developed at temperatures and pressures higher than ambient ones. Generally, a sealed stainless-steel autoclave is filled with the starting solution and heated above the boiling point of the solvent. This generates a remarkable increase in pressure, which, synergistically with temperature, allows for the formation of well-defined crystalline nanoparticles without the need for post-annealing heat treatments.

The hydrothermal route has mainly been exploited for the synthesis of crystalline VO_2 (A) and VO_2 (B) polymorphs at mild temperature conditions, around 200-250°C. Similarly to VO_2 (M1), VO_2 (B) undergoes a phase transition but below 0°C, from 300 K to 27 K, with notable changes in the magnetic susceptivity.[46] In agreement with the VO_2 polymorphs diagram, VO_2 (B) is stable at low temperature conditions and can be transformed to VO_2 (M1) around 400-450°C. Detailed description of the different vanadium oxides and VO_2 polymorphs will be provided in Chapter 3.

VO_2 (A) nanoplatelets were hydrothermally synthesized after 24 h at 220°C from a solution of $VO(acac)_2$ in H_2O,[47] whereas VO_2 (B) nanobelts were obtained from $VO(acac)_2$ in H_2O with HCl.[48] Wu *et al*.[49] were among the few to report the hydrothermal formation of VO_2 (M1) at low temperature, instead of (A) and (B) polymorphs. They heated at 180°C for 24 h a stainless steel autoclave containing $VO(acac)_2$ in H_2O with HCl. The similarities between these examples highlight the extreme precision that is required to control and obtain the desired VO_2 polymorph or vanadium oxide.

Another hydrothermal synthesis that successfully led to VO_2 (M1) nanoparticles was reported by Xu *et al*.[50], who mixed a NH_4HCO_3 aqueous solution with a $VOSO_4$ aqueous solution. The precipitate, after centrifugation and washing, was heated in autoclave at 280°C for 24 h.

Liu *et al*.[51] employed the V_2O_5 precursor to synthesize VO_2 (B) nanoparticles by combining the hydrothermal method with microwave heating. They heated at 120°C for 2 h a solution containing the V_2O_5 precursor in H_2O, with citric acid as the reducing agent, which led to VO_2 (B) formation. It

should be mentioned that V_2O_5 powder is considered highly toxic and cancerogenic. Additionally, they showed the possibility to transform VO_2 (B) into VO_2 (M1), by post-annealing in vacuum at 560-600°C for 2 h. A similar route, employing the V_2O_5 precursor in H_2O, was used to obtain VO_2 (A) or (B) nanorods: the length of the nanorods and the polymorph type were tuned by changing the ratio with the reducing agent (oxalic acid, quinol or 4-butylaniline), the temperature (180-230°C) and the reaction time (24-48 h).[52]

Bergerud *et al*.[53] synthetized metastable V_2O_3 (V^{3+}) NCs, that oxidize to VO_2 (V^{4+}) over months if exposed to air. The proposed an aminolysis solvothermal process to happen during the reaction of $VO(acac)_2$ in squalene, with the presence of oleic acid as the capping agent and oleylamine as the reducing agent. They refluxed and heated the solution at 310-370°C for 1 h, after degassing to exclude oxygen and water presence. Stable V_2O_3 was synthesized by hydrothermal method at 220°C, starting from a mixture of $VO(acac)_2$ in H_2O with N_2H_4 as a reducing agent.[54] VOOH was obtained after 6-12 h, while a mixture of VOOH and V_2O_3 was seen after 24 h, with a complete conversion to after 48 h. The authors proposed the reaction to proceed first with the removal of both acac ligands and the formation of VO^{2+}. The latter would than react with N_2H_4 and OH^- to form VOOH, along with the release of H_2O and N_2. VOOH would finally lead to the formation of V_2O_3 and H_2O. They highlighted that both the acac ligands and the NH_4^+ inorganic ions affected the morphology, but the latter had a minor influence respect to the crucial role played by the former.

1.5 Conclusions

As mentioned in the introduction, most of the thin films or coatings employed in this work were obtained by the sol gel process. Three types of materials were considered, i.e., silicon dioxide (SiO_2), vanadium dioxide (VO_2), and titanium dioxide (TiO_2).

In Chapter 2, hybrid SiO_2 coatings were exploited to control the condensation dynamics of water vapor, which constitutes a crucial aspect when heat exchangers are considered. The former were obtained starting from an acid-catalyzed synthesis based on a tetraethylortosilicate precursor (paragraph 1.2) The same typologies of coatings were then employed in Chapter 6, to improve the luminous transmittance and durability of VO_2 films exploiting a bilayer configuration.

The research work presented in Chapters 3-7 was centered on thermochromic VO_2 films. V_2O_5 powder was initially chosen as a reference starting point but was then substituted by $VO(acac)_2$ (paragraph 1.4). Finally, TiO_2 films were exploited in Chapter 6 to improve the luminous transmittance VO_2 films in a bilayer configuration. The TiO_2 films were obtained via a sol-gel method

based on a Titanium alkoxide precursor, which reactivity was decreased with the aid of a chelating agent (paragraph 1.2.3.1).

References

1. Son, J. *et al.* A practical superhydrophilic self cleaning and antireflective surface for outdoor photovoltaic applications. *Solar Energy Materials and Solar Cells* **98**, 46–51 (2012).

2. Yarali, E. *et al.* Recent Progress in Photonic Processing of Metal-Oxide Transistors. *Adv Funct Mater* **30**, 1–37 (2020).

3. Li, Y. *et al.* Direct Laser Writing of Multishaped VO2 Microactuators Based on Freestanding VO2 Film. *Adv Mater Technol* **8**, 2200977 (2023).

4. Xie, B., Zhang, W., Zhao, J., Zheng, C. & Liu, L. Design of VO2-based spacecraft smart radiator with low solar absorptance. *Appl Therm Eng* **236**, 121751 (2024).

5. Khodakarami, S., Zhao, H., Rabbi, K. F. & Miljkovic, N. Scalable corrosion-resistant coatings for thermal applications. *ACS Appl Mater Interfaces* **13**, 4519–4534 (2021).

6. Nanda, D. *et al.* Single step method to fabricate durable superliquiphobic coating on aluminum surface with self-cleaning and anti-fogging properties. *J Colloid Interface Sci* **507**, 397–409 (2017).

7. Schubert, U. Chemistry and Fundamentals of the Sol–Gel Process. *The Sol-Gel Handbook* **1–3**, 1–28 (2015).

8. Brinker, C. J. & Scherer, G. W. Sol-Gel Science: The Physics and Chemistry of Sol-Gel Processing. *Sol-Gel Science: The Physics and Chemistry of Sol-Gel Processing* 1–908 (2013) doi:10.1016/C2009-0-22386-5.

9. Niederberger, M. & Pinna, N. *Metal Oxide Nanoparticles in Organic Solvents: Synthesis, Formation, Assembly and Application*. (Springer, 2009). doi:10.1007/978-1-84882-671-7.

10. Guglielmi, M. & Carturan, G. Precursors for sol-gel preparation. *J Non Cryst Solids* **100**, 16–30 (1988).

11. Sanchez, C., Livage, J., Henry, M. & Babonneau, F. Chemical modification of alkoxide precursors. *J Non Cryst Solids* **100**, 65–76 (1988).

12. Murray, C. B., Norris, D. J. & Bawendi, M. G. Synthesis and Characterization of Nearly Monodisperse CdE (E = S, Se, Te) Semiconductor Nanocrystallites. *J Am Chem Soc* **115**, 8706–8715 (1993).

13. Narayanaswamy, A., Xu, H., Pradhan, N. & Peng, X. Crystalline Nanoflowers with Different Chemical Compositions and Physical Properties Grown by Limited Ligand Protection. *Angewandte Chemie International Edition* **45**, 5361–5364 (2006).

14. Monge, M., Kahn, M. L., Maisonnat, A. & Chaudret, B. Room-Temperature Organometallic Synthesis of Soluble and Crystalline ZnO Nanoparticles of Controlled Size and Shape. *Angewandte Chemie International Edition* **42**, 5321–5324 (2003).

15. Epifani, M. *et al.* Nanocrystalline Metal Oxides from the Injection of Metal Oxide Sols in Coordinating Solutions: Synthesis, Characterization, Thermal Stabilization, Device Processing, and Gas-Sensing Properties. *Adv Funct Mater* **16**, 1488–1498 (2006).

16. Panda, A. B., Glaspell, G. & Samy El-Shall, M. Microwave synthesis and optical properties of uniform nanorods and nanoplates of rare earth oxides. *Journal of Physical Chemistry C* **111**, 1861–1864 (2007).

17. Yang, S. & Gao, L. Controlled synthesis and self-assembly of CeO2 nanocubes. *J Am Chem Soc* **128**, 9330–9331 (2006).

18. Kahn, M. L., Monge, M., Snoeck, E., Maisonnat, A. & Chaudret, B. Spontaneous Formation of Ordered 2D and 3D Superlattices of ZnO Nanocrystals. *Small* **1**, 221–224 (2005).

19. Wang, C., Deng, Z. X. & Li, Y. The synthesis of nanocrystalline anatase and rutile titania in mixed organic media. *Inorg Chem* **40**, 5210–5214 (2001).

20. Niederberger, M., Bartl, M. H. & Stucky, G. D. Benzyl alcohol and transition metal chlorides as a versatile reaction system for the nonaqueous and low-temperature synthesis of crystalline nano-objects with controlled dimensionality. *J Am Chem Soc* **124**, 13642–13643 (2002).

21. Pinna, N., Garnweitner, G., Antonietti, M. & Niederberger, M. A general nonaqueous route to binary metal oxide nanocrystals involving a C-C bond cleavage. *J Am Chem Soc* **127**, 5608–5612 (2005).

22. Jezequel, D., Guenot, J., Jouini, N. & Fiévet, F. Submicrometer zinc oxide particles: Elaboration in polyol medium and morphological characteristics. *J Mater Res* **10**, 77–83 (1995).

23. Ambrožič, G., Škapin, S. D., Žigon, M. & Orel, Z. C. The synthesis of zinc oxide nanoparticles from zinc acetylacetonate hydrate and 1-butanol or isobutanol. *J Colloid Interface Sci* **346**, 317–323 (2010).

24. Liu, X. & Swihart, M. T. A general single-pot heating method for morphology, size and luminescence-controllable synthesis of colloidal ZnO nanocrystals. *Nanoscale* **5**, 8029–8036 (2013).

25. Garnweitner, G., Antonietti, M. & Niederberger, M. Nonaqueous synthesis of crystalline anatase nanoparticles in simple ketones and aldehydes as oxygen-supplying agents. *Chemical Communications* 397–399 (2005) doi:10.1039/B414510K.

26. Buha, J., Djerdj, I. & Niederberger, M. Nonaqueous Synthesis of Nanocrystalline Indium Oxide and Zinc Oxide in the Oxygen-Free Solvent Acetonitrile. *Cryst Growth Des* **7**, 113–116 (2007).

27. Rehder, D. Vanadium. Its role for humans. *Met Ions Life Sci* **13**, 139–169 (2013).

28. Fatola, O. I., Olaolorun, F. A., Olopade, F. E. & Olopade, J. O. Trends in vanadium neurotoxicity. *Brain Res Bull* **145**, 75–80 (2019).

29. Cao, C. *et al.* Sputtering Flexible VO2 Films for Effective Thermal Modulation. *ACS Appl Mater Interfaces* **14**, 28105–28113 (2022).

30. Piccirillo, C., Binions, R. & Parkin, I. P. Synthesis and Functional Properties of Vanadium Oxides: V2O3, VO2, and V2O5 Deposited on Glass by Aerosol-Assisted CVD. *Chemical Vapor Deposition* **13**, 145–151 (2007).

31. Matamura, Y., Ikenoue, T., Miyake, M. & Hirato, T. Mist CVD of vanadium dioxide thin films with excellent thermochromic properties using a water-based precursor solution. *Solar Energy Materials and Solar Cells* **230**, 111287 (2021).

32. Kumar, S., Maury, F. & Bahlawane, N. Electrical Switching in Semiconductor-Metal Self-Assembled VO2 Disordered Metamaterial Coatings. *Sci Rep* **6**, (2016).

33. Chen, B., Yang, D., Charpentier, P. A. & Zeman, M. Al3+-doped vanadium dioxide thin films deposited by PLD. *Solar Energy Materials and Solar Cells* **93**, 1550–1554 (2009).

34. Behera, M. K., Williams, L. C., Pradhan, S. K. & Bahoura, M. Reduced Transition Temperature in Al:ZnO/VO2 Based Multi-Layered Device for low Powered Smart Window Application. *Scientific Reports 2020 10:1* **10**, 1–11 (2020).

35. Xiang, W., Le Drogoff, B., Koch, D., Margot, J. & Chaker, M. High-quality VO2 films synthesized on polymer substrates using room-temperature pulsed laser deposition and annealing. *Ceram Int* (2023) doi:10.1016/J.CERAMINT.2023.10.168.

36. Liang, W. *et al.* Enhanced Metal-Insulator Transition Performance in Scalable Vanadium Dioxide Thin Films Prepared Using a Moisture-Assisted Chemical Solution Approach. *ACS Appl Mater Interfaces* **10**, 8341–8348 (2018).

37. Chae, B.-G. *et al.* Highly oriented VO 2 thin films prepared by sol-gel deposition method. *Electrochem. and Solid-State Letters* **9**, (2005).

38. Zhang, H., Yang, J., Liu, H. & Wang, S. Meter-long CeO2/YSZ/Y2O3 buffer layers for YBCO coated conductors using DC reactive sputtering. *Physica C Supercond* **470**, 1998–2001 (2010).

39. Liu, J., Li, Q., Wang, T., Yu, D. & Li, Y. Metastable Vanadium Dioxide Nanobelts: Hydrothermal Synthesis, Electrical Transport, and Magnetic Properties. *Angewandte Chemie* **116**, 5158–5162 (2004).

40. Son, J. H., Wei, J., Cobden, D., Cao, G. & Xia, Y. Hydrothermal synthesis of monoclinic VO2 micro- and nanocrystals in one step and their use in fabricating inverse opals. *Chemistry of Materials* **22**, 3043–3050 (2010).

41. Pan, M. *et al.* Properties of VO2 thin film prepared with precursor VO(acac)2. *J Cryst Growth* **265**, 121–126 (2004).

42. Samotus, A., Grybos, R., Popova, N. & Bogolitsyn, K. Kinetics of oxidation of vanadyl acetylacetonate by oxygen in methanolic solution. **64**, 2–5 (1997).

43. Nenashev, R. N., Mordvinova, N. E., Zlomanov, V. P. & Kuznetsov, V. L. Thermal decomposition of vanadyl acetylacetonate. *Inorganic Materials* **51**, 891–896 (2015).

44. Yu, J. H. *et al.* Thermal aging effect of vanadyl acetylacetonate precursor for deposition of VO2 thin films with thermochromic properties. *Mater Res Bull* **82**, 11–15 (2016).

45. Jo, Y. R., Myeong, S. H. & Kim, B. J. Role of annealing temperature on the sol–gel synthesis of VO2 nanowires with in situ characterization of their metal–insulator transition. *RSC Adv* **8**, 5158–5165 (2018).

46. Zhang, Y. *et al.* Phase B vanadium dioxide: characteristics, synthesis and applications. *CrystEngComm* **24**, 518–542 (2022).

47. Zhang, L. *et al.* Synthesis and formation mechanism of VO2(A) nanoplates with intrinsic peroxidase-like activity. *RSC Adv* **5**, 61371–61379 (2015).

48. Nie, G. *et al.* Monocrystalline VO2 (B) nanobelts: large-scale synthesis, intrinsic peroxidase-like activity and application in biosensing. *J Mater Chem A Mater* **2**, 2910–2914 (2014).

49. Wu, F. *et al.* A 3D flower-like VO2/MXene hybrid architecture with superior anode performance for sodium ion batteries. *J Mater Chem A Mater* **7**, 1315–1322 (2019).

50. Lu, X. *et al.* A novel method to modify the color of VO2-based thermochromic smart films by solution-processed VO2@SiO2@Au core–shell nanoparticles. *RSC Adv* **6**, 47249–47257 (2016).

51. Liu, Y. *et al.* Effect of W-Mo doping on the phase transition temperature of VO2 synthesized by hydrothermal microwave method. *Mater Res Express* **10**, 035008 (2023).

52. Beidelman, B. A. *et al.* Influence of water concentration on the solvothermal synthesis of VO2(B) nanocrystals. *CrystEngComm* **24**, 6009–6017 (2022).

53. Bergerud, A., Buonsanti, R., Jordan-Sweet, J. L. & Milliron, D. J. Synthesis and phase stability of metastable bixbyite V2O 3 colloidal nanocrystals. *Chemistry of Materials* **25**, 3172–3179 (2013).

54. Bai, Y., Jin, P., Ji, S., Luo, H. & Gao, Y. Preparation and characterization of V2O3 micro-crystals via a one-step hydrothermal process. *Ceram Int* **39**, 7803–7808 (2013).

Chapter 2

Humid air and saturated vapor condensation

Table of contents

2 Chapter 2 – Humid air and saturated vapor condensation 37

2.1 Introduction 39

2.1.1 Surface wettability 40

2.1.2 Condensation theory 42

2.1.3 Dropwise condensation 44

2.1.3.1 Spatial-temporal evolution of dropwise condensation 44

2.1.3.2 Heat exchanged through single and multiple droplets 45

2.1.3.3 Dropwise condensation challenges 48

2.1.4 Surface functionalization and nanostructuring 49

2.1.4.1 Saturated vapor condensation 51

2.1.4.2 Humid air condensation 54

2.1.4.3 Low hysteresis of the contact angle 57

2.2 Durability and heat exchange efficiency of hybrid sol-gel coatings during saturated vapor condensation 60

2.2.1 Synthesis and deposition of hybrid coatings 62

2.2.2 Optimization of hybrid-silica coating 62

2.2.3 Saturated vapor condensation experiments 63

2.2.4 Coating degradation tests 68

2.2.5 Considerations on heat transfer and coating durability 72

2.2.6 Durability and heat exchange efficiency of hybrid sol-gel coatings during saturated vapor condensation – conclusions 74

2.3 Bioinspired sol-gel micropatterns for humid air condensation 75

2.3.1 Synthesis and deposition of patterned, silica and CH_3-silica coatings on aluminum substrates 77

2.3.1.1 Patterned coatings 77

2.3.1.2 Plain reference silica coatings 78

2.3.1.3 Characterization of the plain silica and plain CH_3-silica coating 80
2.3.1.4 Optimization of patterned morphology 83
2.3.2 Coating durability under high relative humidity conditions 84
2.3.3 Humid air condensation tests 89
2.3.4 Bioinspired sol-gel micropatterns for humid air condensation – conclusions **90**
2.4 Conclusions

3.1 Introduction

As reported in the Abstract section, heating, ventilation, and air conditioning (HVAC) systems are responsible for up to 20% of the global energy consumed by developed countries.[1,2] Even slight improvements in the efficiency of the former could have a powerful impact on reducing the massive global energy consumption.[3,4] The heat exchanged during condensation, along with the droplet dynamics, remarkably impact a wide range of applications, from heat exchangers to desalination systems[5,6], from humidity collectors to anti-icing devices. Moreover, surface properties such as self-cleaning, anti-bacterial, and corrosion-resistance are greatly influenced by the condensation dynamics.[7,8]

The condensation heat exchange of saturated vapor or humid air is considerably influenced by the way the condensation is developed, namely in form of a liquid film or in form of liquid droplets. The preferential formation of liquid droplets (i.e., "dropwise" condensation), instead of a uniform film ("filmwise" condensation), can lead to enhancement of the heat transfer coefficient (HTC) of one order of magnitude.[9,10] Both the chemical and physical properties of the substrate affect the condensation mode. Among the several influencing parameters, particular importance is attributed to the surface wettability of the substrate. In general, a high surface wettability enhances the droplet's nucleation, whereas a low surface wettability favors the droplet's removal by decreasing the latter adhesion to the surface. The surface wettability is affected by the surface energy of the involved liquid and solid phase, gravity, external forces, environmental conditions, substrate morphology and eventual presence of defects.[11] Concerning condensation heat exchange, the heat exchangers are typically based on metallic materials such as copper, aluminum, and stainless steel, which all display high surface energy (γ). The high γ values lead to a filmwise condensation, which severely limits the heat exchange due to the additional thermal resistance of the liquid layer developed on the metallic surface. A rapid removal of the latter is crucial for the heat exchange, to allow for a renewed condensation cycle due to the availability of the exposed cooling surface.[12]

Several techniques have been employed over the past years to favor a dropwise condensation, which rely on the decrease of the substrate's surface tension with the aid of surface functionalization and morphological modifications.[13–15] The control of the droplet formation and removal was obtained through the creation of superhydrophobic surfaces, possessing high surface roughness and/or low contact angle hysteresis. Before addressing some past key work, a brief overview on the different modes of surface wettability and on the most relevant condensation theories will be presented in paragraphs 2.1.1-2.1.2.

3.1.1 *Surface wettability*

The surface wettability is described through the water contact angle (θ) parameter, defined as the intersection between the liquid-solid interface and the liquid-vapor interface.[16] The surface wettability is usually defined according to four possible categories, from a total wettability to a total liquid repulsion[17]:

- Superhydrophilic surface: $\theta < 10°$;
- Hydrophilic surface: $10° < \theta \leq 90°$;
- Hydrophobic surface: $90° < \theta \leq 150°$;
- Superhydrophobic surface: $150° < \theta \leq 180°$.

The Young equation[18] (Eq. 2.1) valid for an ideal solid substrate, correlates the water contact angle (θ) with the interfacial tensions within a solid-liquid-vapor system:

$$cos\theta = \frac{\gamma_{sv} - \gamma_{sl}}{\gamma_{lv}} \tag{2.1}$$

In which γ_{sv} is the solid-vapor interfacial tension, γ_{lv} the liquid-vapor interfacial tension, and γ_{sl} is the solid-liquid interfacial tension.

Real surfaces lack to fulfill the requirement of total smoothness and chemical homogeneity, but rather display surface roughness and/or defects, as well as chemical heterogeneity. The latter additional parameters are considered by the Wenzel and Cassie-Baxter equations, respectively. The apparent contact angle (θ_W) from the Wenzel equation[19] (Eq. 2.2):

$$cos\theta_W = f cos\theta \tag{2.2}$$

Is function of the surface roughness f, which is varied within $f \geq 1$ with increasing surface roughness.

The Cassie-Baxter equation[20] for the apparent contact angle (θ_{CB}) considers the presence of chemical heterogeneities (chemical species f_1 and f_2) and/or surface defects (Eq. 2.3):

$$cos\theta_{CB} = f_1 cos\theta_1 + f_2 cos\theta_2 \tag{2.3}$$

In which θ_1 and θ_2 are the local contact angles of the chemical species f_1 and f_2.

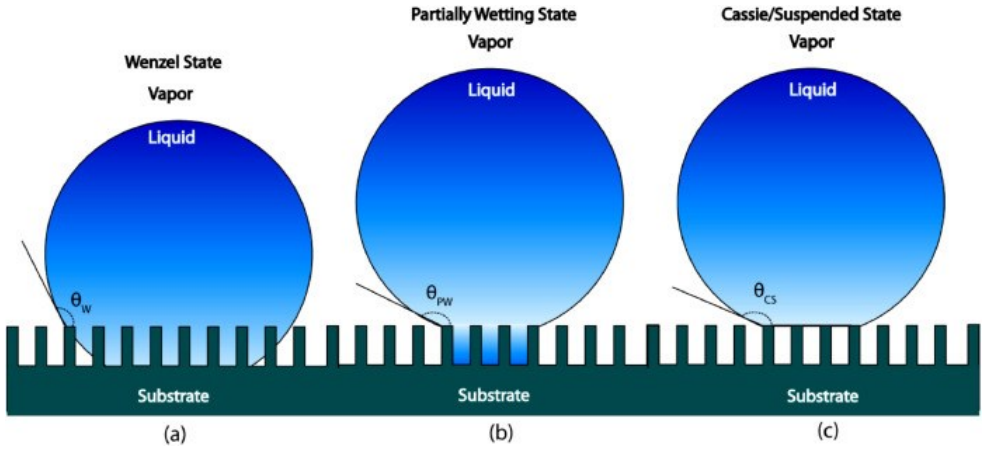


Figure 2.1. Different wettability states of a liquid droplet on a solid surface.[21]

Following the previous discussion, three different modes are commonly employed to describe how a liquid droplet can wet a solid surface (Figure 2.1), among which the Wenzel (Figure 2.1 (a)) and Cassie (Figure 2.1 (c)) state represent the edge conditions among non-ideal modes. Considering the former, the effect of surface roughness can either enhance the hydrophilicity or the hydrophobicity, in function of the contact angle. On hydrophilic surfaces, which thermodynamically favor the liquid diffusion, a higher surface roughness leads to an increase of the surface area, with a consequent increase of hydrophilicity. Hydrophobic surfaces penalize the liquid adhesion, therefore a higher surface roughness thermodynamically leads to a higher hydrophobicity.[22]

Air fractions can be trapped within the roughness features on non-flat surfaces, which can be described according to the Cassie-Baxter model with the surface being the first chemical specie f_1 and air being f_2. The Cassie-Baxter equation is then modified as Eq. 2.1:

$$cos\theta_{CB} = f_{CB}cos\theta + (1 - f_{CB})cos\theta_0 \qquad (2.1)$$

In which f_{CB} is the fraction of contact area between liquid and solid, respect to the total horizontal area, and θ_0 is the contact angle between air and liquid, which is 180° if the microcavities are in sufficient proximity. In such configuration, the liquid interacts with the upper part of the surface protrusions, which allows the creation of superhydrophobic surfaces through the exploitation of the partial liquid-solid contact.

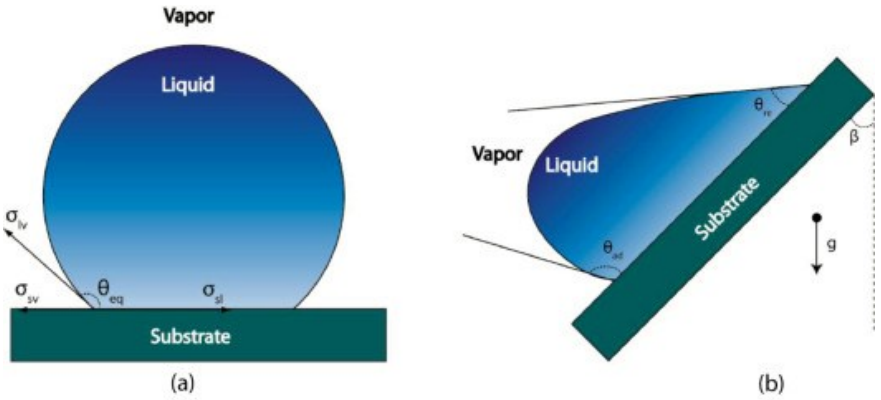


Figure 2.2. Schematic of (a) static and (b) dynamic contact angles.[21]

The static contact angle (Figure 2.2 (a)), which describes a liquid wetting a solid while the latter is set to be on a horizontal position and still, fails to describe real condensation applications such as heat exchangers or water collectors. During the latter, the liquid often evolves on the surface and is subjected to several changes of volume, speed, and direction. Dynamic contacts angles (Figure 2.2 (b)) are employed to allow for a more proper description of the wetting phenomenon. The eventual expansion and retraction of a liquid droplet is described through the advancing (θ_a) and receding (θ_r) contact angles, respectively.[16] The difference between the advancing (θ_a) and receding (θ_r) contact angles is defined as the hysteresis of the contact angle (H, Eq. 2.2):

$$H = \theta_a - \theta_r \tag{2.2}$$

The hysteresis of the contact angle is null (H = 0) for totally smooth and chemical homogeneous surfaces. A difference between θ_a and θ_r could originate from the presence of chemically heterogeneous surfaces, eventual defects, and surface roughness. The presence of multiple areas which display different chemical behavior and/or morphology can lead to a preferential pinning of condensed droplets on specific regions, as well as to droplets sweeping on others. The method employed for the estimation of the advancing and receding contact angles is reported in Appendix A.2.1.

3.1.2 *Condensation theory*

The vapor condensation relies on a phase change from a vapor phase to a liquid phase, upon which the condensation latent heat is exothermically released. The pressure gradient between the vapor and liquid phase favors the transformation of the former into the latter. Condensation can either be homogeneous or heterogeneous, according to the presence or absence of additional external materials. Heterogeneous condensation is induced when an external material, such as particles or liquid/solid

substrates, are characterized by a lower temperature respect to the vapor saturation temperature. Heterogeneous condensation is typically favored with respect to the homogeneous one, as it requires a lower activation energy for nucleation.[23,24]

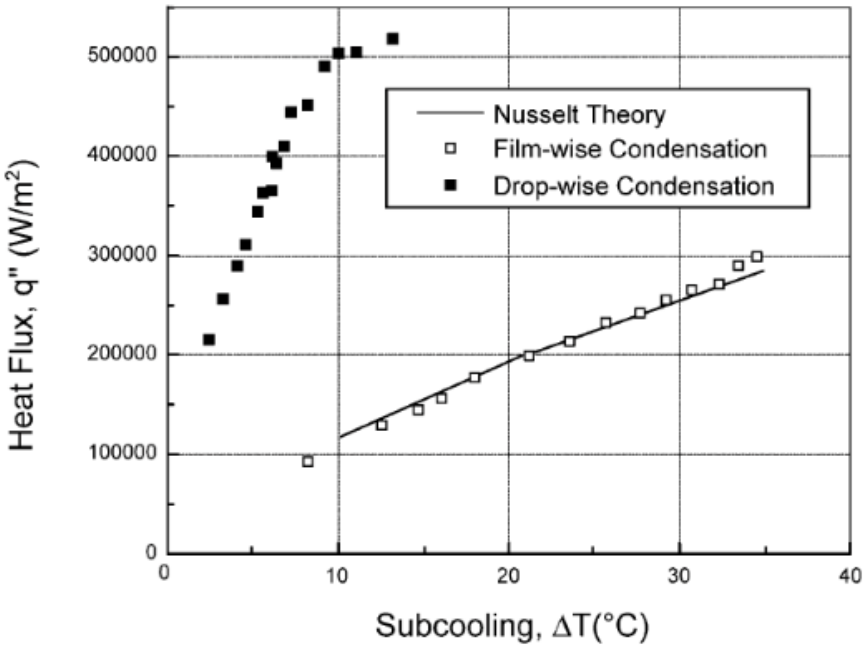


Figure 2.3. Influence of the subcooling degree on the heat flux, for either dropwise or filmwise condensation.[25]

Heterogeneous condensation is manifested in either a filmwise or a dropwise mode. During filmwise condensation, vapor condenses on the subcooled surface by forming a continuous liquid film on the latter. The liquid layer leads to the formation of an additional thermal resistance, which negatively impacts on the heat exchange. Industrial heat exchangers typically consist of metallic materials, which hydrophilicity favor the formation of a condensed liquid film, with a consequent decrease in heat transfer efficiency. The formation of isolated condensed droplets during dropwise condensation allows for a reduced area that could increase the thermal resistance, which allows for increases in HTC up to one order of magnitude.[9,10,23]

Dropwise condensation can be induced on metallic surfaces with the aid of functional coatings and/or morphological features. The additional coatings or nanostructures are required to sustain considerable high temperatures and long exposure times, besides displaying a solid mechanical resistance to impact or abrasion and low manufacturing costs.

3.1.3 *Dropwise condensation*

For an accurate control and maximization of the heat exchanged during condensation, the spatial-temporal evolution of the condensing droplet should be considered, along with the way the heat is exchanged through the droplets.

3.1.3.1 *Spatial-temporal evolution of dropwise condensation*

Dropwise condensation is a cyclic phenomenon over both time and space. As reported in Figure 2.4, nucleation of droplets is followed by growth by direct vapor condensation, as well as consecutive coalescence.[26] The initial nucleation is developed over local minima of surface tension and, according to Sikarwar *et al.*[27], the heat is transferred through the condensing droplet, while the surface among the isolated droplets is not involved in the heat exchange.

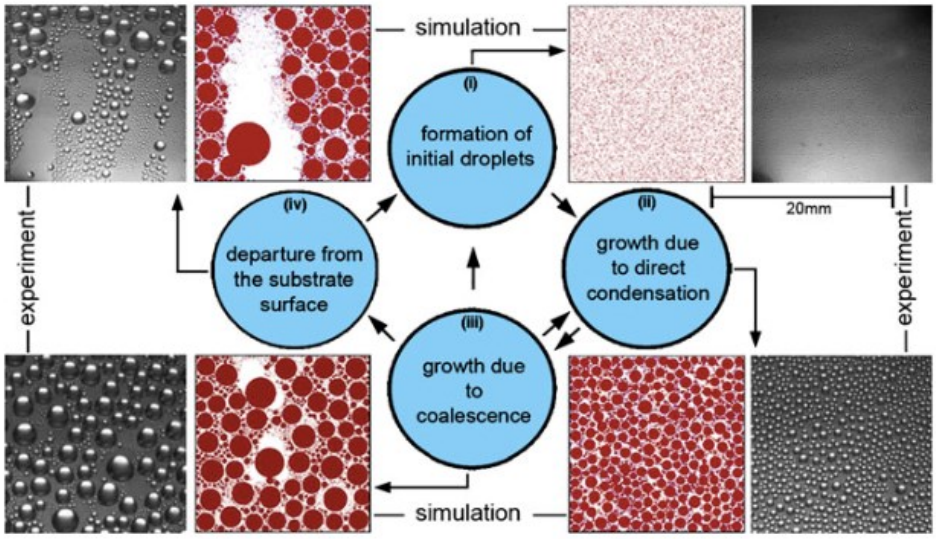


Figure 2.4. Cyclical evolution of the vapor condensation on an inclined substrate in function of time:(i) nucleation and droplet growth, (ii) droplet growth to direct condensation and (iii) coalescence, (iv) droplet departure from the substrate.[26]

After a critical radius is overcome, droplet removal is induced due to the removal of equilibrium between the capillary force, gravity, and additional forces specific of the system. The removal of the droplet can be developed by either sweeping or detachment, which leads to a renewed exposure of available condensing surface. The cyclic behavior of nucleation, growth, and removal of droplets positively enhances the heat exchange efficiency.[28,29]

Dropwise condensation is influenced by numerous parameters, among which the density of nucleation sites and the minimum nucleation radius are of particular importance. The former depends on the thermal, physical, and chemical properties of both liquid and solid, besides on the substrate

morphology and on the subcooling degree. Rose[24] proposed that the nucleation density (N) could be expressed in function of the minimum radius for droplet nucleation (r_{min}) according to Eq. 2.3:

$$N = \frac{0{,}037}{r_{min}^2}\ cm^{-2}\ ; \qquad r_{min} = \frac{x\ T_w}{(T_{sat} - T_w)} \tag{2.3}$$

In which x represents the thermophysical parameters of the system, including surface roughness, and T_{sat} and T_w are respectively the saturation temperature and the condensing surface temperature. The nucleation density is therefore influenced by the subcooling degree and substrate morphology.[24,30]

Another critical aspect during dropwise condensation is the distribution of droplet dimension within the condensing substrate.

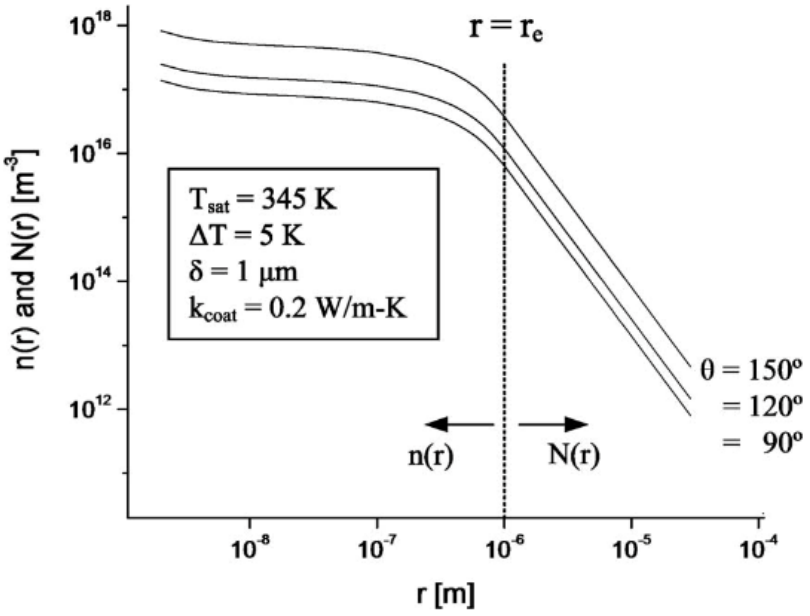


Figure 2.5. Droplet distribution according to the model of Kim et al.[29]

According to the model of Kim *et al.*[29] two different categories can be detected during the condensation, which are grouped respectively below and above a critical radius r_e. The first group ($n_r < r_e$) describes the direct vapor condensation, whereas the second group ($N_r > r_e$) is relative to the growth by coalescence. From Figure 2.5, lower radius values allow for a higher nucleation density, which decreases with higher r. The latter behavior can be explained by the coalescence and sweeping phenomena, which lead to the aggregation and removal of multiple droplets.

3.1.3.2 *Heat exchanged through single and multiple droplets*

During dropwise condensation, the cyclic removal of condensed droplets allows for a higher efficiency in the heat transfer.[31–33] Several models on dropwise condensation have been proposed over the years[8,21], starting from the fundamental one by Le Fevre and Rose.[31] From successive studies, droplets with low radius were found to be crucial to improve the efficiency, as most of the heat was found to be exchanged through the former with respect to bigger droplets.[8,21,32,34]

Respect to previous models, Kim *et al.*[29] addressed the evaluation of dropwise condensation of saturated vapor on hydrophobic surfaces with $\theta > 90°$. As a case study, the authors considered a droplet with radius r, condensing on a coated substrate with $\theta > 90°$ and coating thickness δ. At fixed subcooling degree (ΔT) between the vapor saturation temperature and the substrate temperature, the thermal resistance was expressed by finite degrees ΔT_x, the sum of which led to ΔT. The authors identified four main thermal resistances ΔT_x, respectively to the vapor-liquid interface (ΔT_i), to the heat conduction through the liquid droplet (ΔT_{drop}), to the hydrophobic coating presence (ΔT_{coat}), and to the droplet's curvature (ΔT_c). They assumed a sufficiently small droplet dimension, to allow for conduction to be the principal heat transport mechanism, respect to convection. The four thermal resistances were described as reported in Eq. 2.4-2.7:

$$\Delta T_i = \frac{q_d}{h_i 2\pi r^2 (1 - cos\theta)} \tag{2.4}$$

With q_d heat transfer rate through the droplet and h_i interfacial heat transfer coefficient, in which h_i depends on the vapor pressure.

$$\Delta T_{drop} = \frac{q_d \theta}{2k_c \pi d} \tag{2.5}$$

With k_c thermal conductivity through the droplet and $d = 2r\ sin\Theta$.

$$\Delta T_{coat} = \frac{q_d \delta}{k_{coat} \pi r^2 sin^2 \theta} \tag{2.6}$$

With k_{coat} thermal conductivity though the coating.

$$\Delta T_c = \frac{r_{min}}{r} \Delta T \tag{2.7}$$

With r_{min} the minimum viable droplet radius.

The total thermal resistance was then expressed as Eq. 2.8:

$$\Delta T = T_{sat} - T_{surf} = \Delta T_i + \Delta T_{drop} + \Delta T_{coat} + \Delta T_c \tag{2.8}$$

and the influence of the overall parameters on the thermal flux was found to be (Eq. 2.9)[29]:

$$q_d = \frac{\Delta T \pi r^2 (1 - \frac{r_{min}}{r})}{\frac{\delta}{k_{coat} sin^2\theta} + \frac{r\theta}{4k_c sin\theta} + \frac{1}{2h_i(1 - cos\theta)}} \tag{2.9}$$

As a fundamental outcome, the dependency of the thermal flux on the droplet dimension *r,* contact angle Θ, and coating thickness δ was evidenced. The results by Kim *et al.*[29] confirmed previous models by Wu *et al.*[3333] and Neumann *et al.*[34], who demonstrated that a higher heat flux could be transferred through lower dimension droplets.

The dropwise condensation efficiency is highly influenced by the sweeping rate. The latter allows for the detachment of condensed droplets, which incorporate neighboring droplets during the sliding path along the inclined surface and induce a renewed surface exposure for nucleation.[34] Dropwise condensation is influenced by the droplets' dimension and distribution, as well as by the contact angle. Droplets with high dimension are considered inefficient from a heat exchange point of view. At fixed droplet radius, the heat flux was found to be higher with increasing contact angle, which supports the extensive research towards the creation of stable superhydrophobic surfaces.[29]

Following the heat transfer through a single droplet, the overall heat transfer per unit area was obtained considering the distribution density of the droplets' population.[29] Considering the discussion of paragraph 2.1.3.1, two separate subgroups were defined in function of a limit radius r_e. The first subgroup ($n(r)$, $r < r_e$) accounts for smaller droplets which grow under direct vapor condensation, whereas the second subgroup ($N(r)$, $r > r_e$) accounts for bigger droplets, deriving from coalescence.[29] The heat flux per unit area q was defined as (Eq. 2.10):

$$q = \int_{r_{min}}^{r_e} q_d(r) n(r) dr + \int_{r_e}^{r_{max}} q_d(r) N(r) dr \tag{2.10}$$

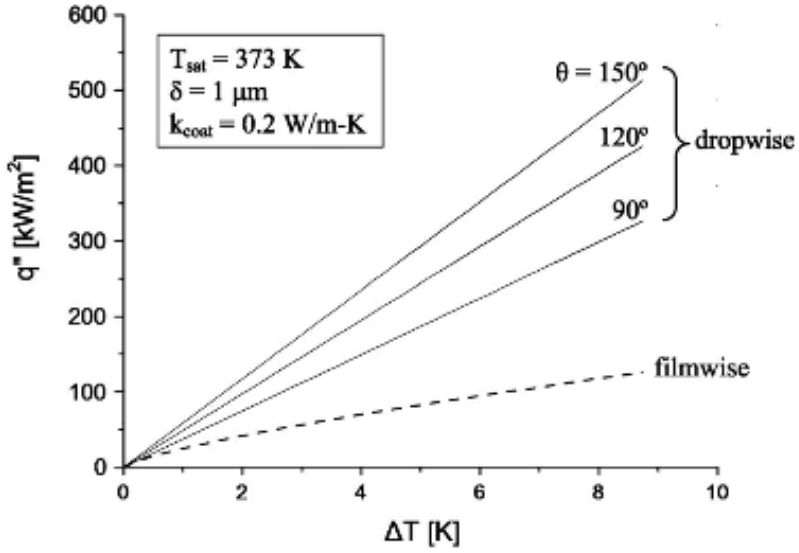


Figure 2.2.6. Heat flux in function of subcooling degree, for different water contact angles.[29]

The influence of condensation mode, subcooling degree, and water contact angle is reported in the example of Figure 2.6. Dropwise condensation clearly emerges in terms of providing a higher heat transfer efficiency, respect to the filmwise mode. The increasing subcooling degree has a different influence on q, in function of the condensation mode. During dropwise condensation, the increasing ΔT favors an increased droplet growth rate and sweeping rate but does not influence the distribution of droplet dimension. During filmwise mode, the increased condensation rate due to higher ΔT leads to increases in thickness of the condensed liquid layer, which in turns deteriorates the heat transfer efficiency. The water contact angle determines an increase in heat flux during dropwise condensation, since a higher Θ leads to a lower critical droplet radius required for the droplet's detachment. Overall, Θ can influence both the droplet dimension distribution and the heat flux through a single droplet. Reaching a superhydrophobicity condition on the surface allows for a lower droplet radius for detachment, with the consequent presence of smaller droplets and more extended surface area available for condensation.[29]

3.1.3.3 *Dropwise condensation challenges*

The multiple advantages of inducing a controlled dropwise condensation, with respect to a filmwise mode, were highlighted in the previous paragraphs. However, the former condensation mode is marked by some critical issues, which must be resolved to guarantee a successful applicability for heat exchangers, water collectors or desalination plants.

According to Sikarwar *et al.*[35], the principal criticalities for dropwise condensation applicability concern the coating durability, the complexity of the phenomenon, the precise measurement of the

HTC, and the multiscale levels over which the condensation is developed. The coatings are required to sustain a considerable amount of heat transfer cycles, while guaranteeing a low thermal resistance. Ideally, they should be simultaneously characterized by high chemical, thermal and mechanical durability, low surface energy, and low thermal resistance. The condensation phenomenon is influenced by multiple interconnected parameters, which do not favor the creation of reliable heat transfer models. Considering the third issue, the experimental measurement of the HTC requires high precision degree, which is however difficult to guarantee, especially at low subcooling degrees. Finally, condensation involves multiple scales, from the atomic level to the macroscopic one. Several open questions are still under investigation, concerning under which conditions nucleation is truly favored, the role of surface roughness, the influence of the distribution of droplet dimensions, how the sweeping rate could be modified to aid for a more efficient droplet removal.[8]

3.1.4 *Surface functionalization and nanostructuring*

As emerges from the previous paragraphs, a precise control of the condensation mode allows to favorably increase the heat exchange. In literature, surface functionalization techniques have been combined with surface nano- or micro-structuring, to induce the modification of the surface energy of the pristine substrate.

A key point that affects the optimization process is that the different steps of dropwise condensation often require chemical and/or morphological modifications that are in contrast with each other. The higher droplet nucleation requires different surface properties respect to a faster droplet removal. Over the past years, research has mainly focused on the development of hydrophobic or superhydrophobic surfaces. With respect to a smooth hydrophobic surface, a higher surface roughness was confirmed to increase the static contact angle above 150°.[23,36] On the latter superhydrophobic nanostructured surfaces, the critical droplet radius for detachment was found to be ~10-100 μm, two orders of magnitude lower than the values required for smooth hydrophobic surfaces.[37] The detachment could be induced independently from gravity, exploiting coalescence and release of surface energy.[36,37] The presence of smaller droplets, through which most of the heat is transferred, enhanced the heat transfer efficiency when the former was combined with a fast droplet removal before unnecessary growth.[38–40]

Superhydrophobic were proved to offer great advantages, but critical unsolved issues were simultaneously evidenced, including a higher thermal barrier for nucleation and a lower nucleation density, especially during the preliminary phases of the latter. The vapor film trapped within the

nanostructured asperities, which allowed a Cassie state, constituted an additional thermal barrier. Moreover, an evolution of the wettability state from a Cassie state to a Wenzel one was noticed over time, due to the Laplace instability.[41] A few years ago, the crucial role of the hysteresis of the contact angle was highlighted, which was found to independently offer remarkable advantages with respect to the presence of high absolute values of the contact angle (i.e., superhydrophobicity). The reduction of the hysteresis of the contact angle to almost zero values was proved to facilitate the droplet sweeping and provide new available surface for condensation.[14,23,42,43]

Alongside with superhydrophobic surfaces, another vastly investigated way to modify the surface wettability is represented by hybrid surfaces. In literature, the term "hybrid" is employed to highlight two separate aspects, which should be clarified. When the physical-chemical properties of a surface are concerned, the term "hybrid" indicates the presence of multiple and distinct areas, displaying different morphology and/or functionalization type and are hence characterized by a different wettability. For example, a hybrid surface can be constituted by an overall flat hydrophobic layer, patterned by hydrophilic channels or bumps. When CSD methods are considered, particularly the sol-gel method, the term "hybrid" indicates the simultaneous presence, at the molecular scale, of organic and inorganic components within the same network. The latter case was discussed in paragraph 1.2.4 of Chapter 1. The sol-gel method allows for a simple and straightforward combination of organic and inorganic compounds, as the low processing temperatures can often be maintained below 200°C to preserve the organic part.

A critical aspect of dropwise condensation hence lies in balancing the several aspects involved in the process optimization. The employed coatings and/or nanostructuring should guarantee a low thermal resistance, an efficient dropwise condensation mode, along with low manufacturing costs and high chemical, thermal and mechanical stability. Moreover, several techniques involve the use of fluorinated compounds for the creation of superhydrophobic surfaces, which are commonly used precursors but pose severe hazards concerning both the environment and human health. In this paragraph 2.1.4, past key research on the functionalization techniques and morphological modifications to induce a dropwise condensation will be discussed. The focus will be particularly devoted to the employed materials and nanostructuring techniques, besides the thermal exchange efficiency. The coating's synthesis method, durability, and costs will be considered in combination with parameters such as HTC values, water collection efficiency, contact angle and critical sweeping radius. For the sake of a higher clarity, the different functionalization techniques and/or morphological modifications will be divided according to the application, i.e., condensation of saturated vapor (paragraph 2.1.4.1) or humid air condensation (paragraph 2.1.4.2). The final

paragraph 2.1.4.3 will be devoted to a focus on the most up to date models, which highlight the crucial influence of the hysteresis of the contact angles on dropwise condensation.

3.1.4.1 *Saturated vapor condensation*

Miljkovic *et al*.[44] studied the influence of droplets' morphology on the mass and heat transfer during dropwise condensation of saturated vapor. The superhydrophobic surface, composed by vertically aligned nanopillars with nanoscale roughness, was obtained by e-beam lithography and deep reactive ion etching (DRIE) of silicon (Figure 2.7 (a)). A (tri-decafluoro-1,1,2,2-tetrahydrooctyl)-1-trichlorosilane precursor was deposited by CVD on the nanopillars, leading to a static contact angle of $\Theta_s = 164 \pm 4°$.

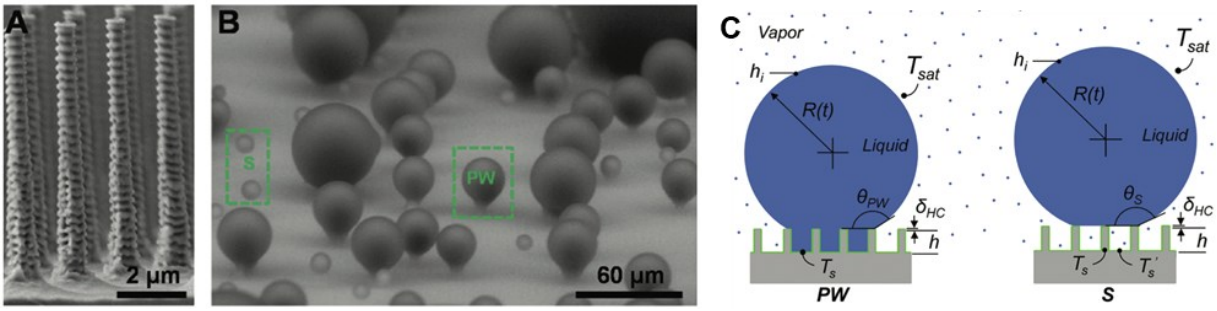


Figure 2.7. (a) Superhydrophobic morphology, with nanocolumns possessing nanoscale roughness. (b, c) Cassie-state condensation, in either suspended "S" or partial wetting "PW" state.[44]

Two different condensation modes were noticed, during which the condensed droplets were either suspended ("S") or partially wetting ("PW") the surface (Figure 2.7 (b, c)). The growth rate of the "S" droplets was found to be lower respect to the "PW" ones, which was explained by a higher thermal resistance of the former. Within the development of the condensation tests, the authors found a progressive conversion of the first mode into the second one. The heat transfer efficiency of the nanostructured surface was considered with respect to a flat hydrophobic reference surface. The "PW" condensation mode allowed for a 56% increase of the heat flux, with respect to the reference surface. The "S" mode, on the other hand, induced a 71% decrease of the heat flux. In the latter condensation mode, the advantages deriving from the suspended condensed droplets, which allow a faster droplet removal at lower dimensions respect to the capillary size, were not enough to compensate for the higher thermal resistance, which in turn decreases the growth rate. This study highlighted that a stable Cassie state is not sufficient by itself to gain an increase in the heat transfer efficiency. The creation of nanostructured superhydrophobic surfaces should be combined with a fine tuning of the morphology of the condensed droplets.

As previously mentioned, an alternative to superhydrophobic surfaces is provided by hybrid substrates. Chen *et al.*[45] exploited a hierarchical microstructure, composed by different areas with variable wettability. A multiscale surface roughness was created by photolithography and DRIE of silicon substrates. The inclined side walls of the micropyramids were covered by *nanograss*, i.e., small and aligned nanocolumns. Higher wettability areas were created on the vertical side walls of the micropyramids, to favor the droplets' growth and coalescence (Figure 2.8 (a, b)). A fluoride polymer film was deposited on the surface and several passivation and chemical attack were performed with C_4H_8 and SF_6, respectively, inducing the formation of random fluoride polymer particles as nanomasks. A perfluorooctyl trichlorosilane solution was employed to reach the superhydrophobicity. The static contact angle and the hysteresis were measured to be 160–165° and 0.4–3°, respectively. The performance of the hybrid superhydrophobic surface was compared to three surfaces: a flat surface, covered with nanograss; a flat surface, displaying hydrophilic flat areas surrounded by nanograss; a two-level microstructured surface, composed of vertically aligned microcolumns without nanograss.

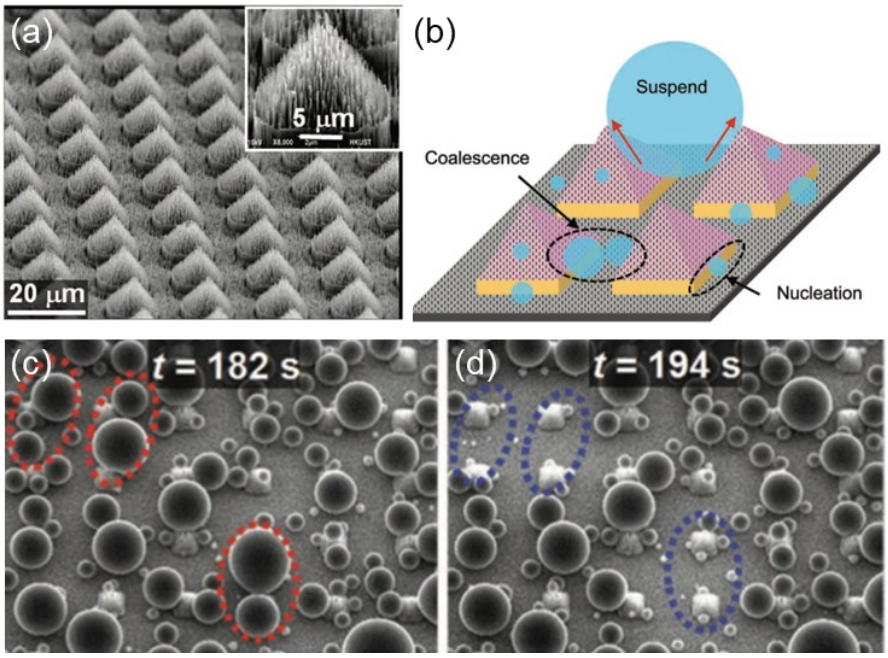


Figure 2.8. (a, b) Hierarchical micro and nanostructure. (c, d) saturated vapor condensation on the hierarchical surface.[45]

A spontaneous sweeping effect was proved on the hybrid superhydrophobic surface, which displayed a ~50 μm droplet departure radius, considerably lower than the ~2 mm of capillary length.[45] Comparing the hybrid superhydrophobic surface with the two-level roughness one, the presence of hydrophilic areas on the former positively enhanced the nucleation of droplets. The hydrophilic areas also allowed for the formation of spherically shaped and isolated droplets. The droplet growth rate was found to be lower on the hybrid superhydrophobic surface with respect to the surface composed

by hydrophilic flat areas surrounded by nanograss. This was attributed to the fact that, on the nanograss, the latter tips were the only available nucleation sites, which convexity is not energetically favored. The hybrid superhydrophobic surface guaranteed higher efficiency in both the nucleation rate and the droplets' removal (Figure 2.8 (c)). The behavior was explained by the coalescence, which was engineered to happen on preferential sites and not randomly, and by the low contact angle hysteresis, favored by the inclined side walls of the pyramids.

Another hybrid surface was proposed by Park *et al.*[46], which was inspired by the biological world (Figure 2.9 (a)), specifically by a Namib desert beetle, cactus, and carnivorous plants. Slippery asymmetric bumps were created, starting from asymmetric millimetric convex bumps, on which friction was reduced at the molecular scale by depositing a lubricant layer on the nanoscale roughness. A thin aluminum sheet was roughened with sandpaper and subsequently molded to create the bumps. The superhydrophobicity was reached by liquid-phase surface treatment with 0.1 wt% CPE-K in water, followed by spin coating Carnation® mineral oil to create the slippery surfaces. The apices of the bumps were changed from spherical to rectangular, to maintain a constant growth rate and a low curvature radius (Figure 2.9 (b)).

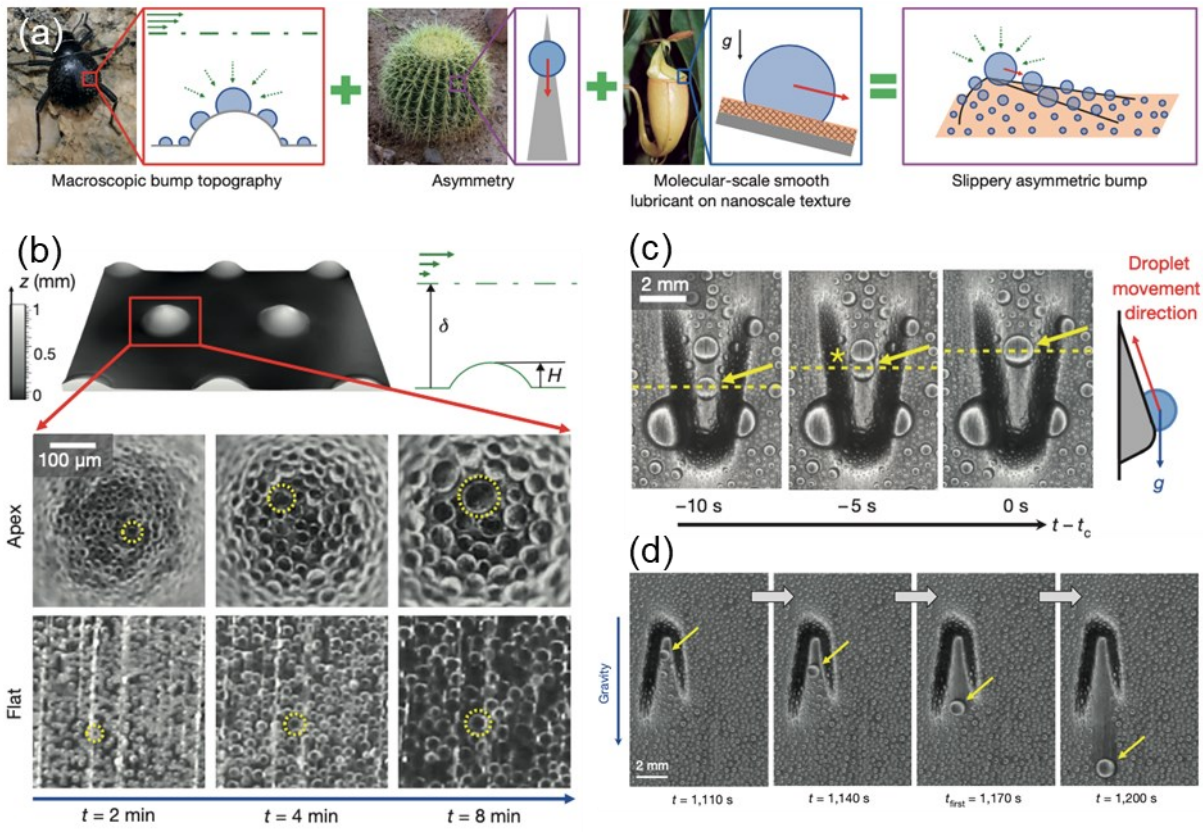


Figure 2.9. (a) Animal and plant-based models for the hybrid surface. (b) Vapor condensation on the hybrid surface. (c, d) Temporal evolution of the droplets' growth, on asymmetric bumps, with different orientations.[46]

As visible in Figure 2.9 (b), condensation on the convex apices led to the formation of bigger droplets with respect to the flat surrounding areas. The asymmetricity of the bumps, covered with lubricant slippery layer, allowed for capillary forces to prevail on gravity, as can be seen by the sweeping direction opposite to gravity (Figure 2.9 (c)). The higher diffusive thermal flux at the apices was confirmed by the bigger dimensions of the droplets on the latter. A higher growth rate was found in the configurations shown in Figure 2.9 (d), attributed to the synergy between capillary forces and gravity, since the sweeping direction was aligned with the latter. The configuration allowed for considerable decreases in critical departure radius, besides higher water collection values with respect to flat slippery surfaces.[46]

3.1.4.2 *Humid air condensation*

Hybrid surfaces displaying different wettability were employed to enhance the humid air condensation as well. Yang *et al*.[47] compared four different wettability configurations, started from analogous copper substrates: hydrophobic, hydrophilic, superhydrophilic, and hybrid hydrophobic-hydrophilic (Figure 2.10 (b)). The bare polished substrate was used as the hydrophilic surface, whereas hydrophobicity was obtained by spraying an ethyl nonafluorobutyl ether organic solution on the polished substrate. Superhydrophilicity was reached by immersing the substrate in a sodium hydroxide and potassium persulfate aqueous solution at 60°C for 15 min. The hybrid surface consisted of aligned V shape hydrophilic/hydrophobic channels, employed to direct and remove the condensate towards vertical hydrophilic channels (Figure 2.10 (a)). The air humidity was varied between 40-60-85% at 30°C, whereas different air flux speed was tested, between 0.5-4 m/s.

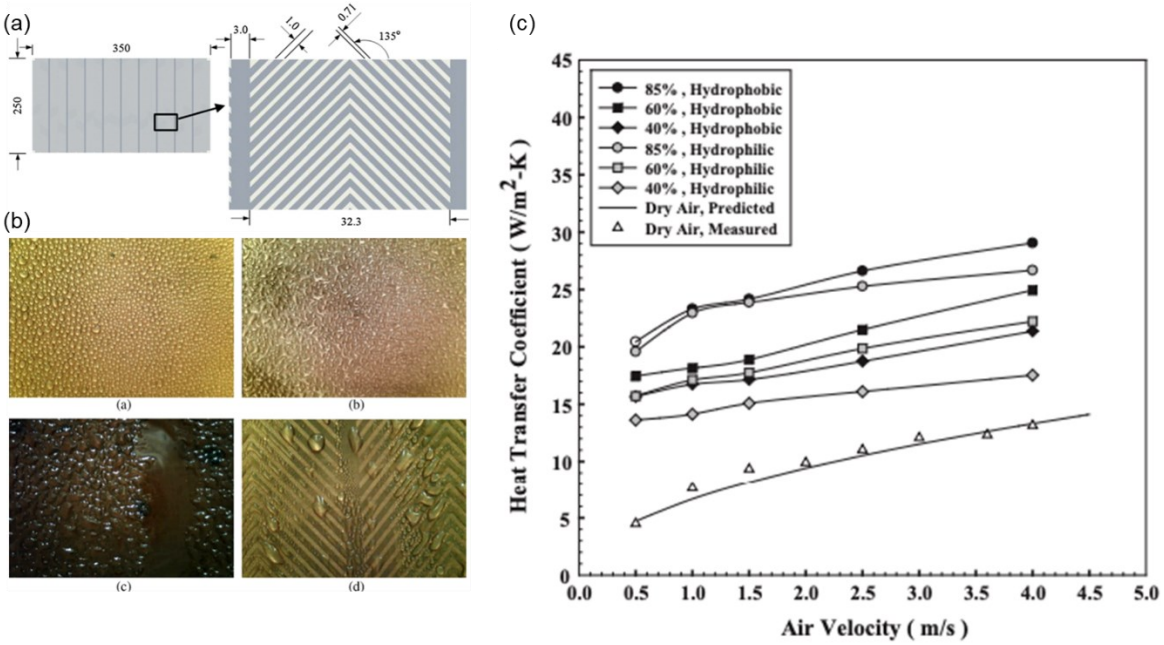


Figure 2.10. (a) Schematization of the hybrid surface. (b) Condensation modes on the different surfaces. (c) Correlation between the HTC and the air velocity, at different relative humidity conditions (RH), for the hydrophilic and hydrophobic surface, respectively.[47]

As visible from Figure 10 (c), the HTC was proved to increase with both increasing RH and increasing air speed. The HTC values on the hydrophobic surfaces were found to be higher under every tested condition, with respect to the hydrophilic surface. The former surface displayed a lower droplet dimension and higher nucleation density, with respect to the hydrophilic one. With increasing RH values, the hydrophobic surface withstood dropwise condensation, whereas coalescence of droplets and consequent formation of bigger agglomerates was seen on the hydrophilic one. The latter led to a decrease in HTC due to the higher surface covered by the condensed liquid. The superhydrophilic surface displayed the lowest HTC values, whereas the hybrid one displayed the highest values, both respect to both hydrophobic (+3-9%) and hydrophilic (+6-16%). The hybrid behavior was attributed to faster condensation cycles of nucleation, growth, and removal.

Another bioinspired coating was proposed by Gosh *et al.*[15], to favor the dropwise condensation of humid air under the presence of non-condensable gas (NCG). The authors chose an approach which did not involve the use of fluorinated compounds, which are commonly used precursors but pose severe environmental and human health related hazards. A mirror-finish aluminum plate was coated with a protective polymer sheet and ablated to create different patterns with the aid of a CO_2 laser. The exposed lasered surface was etched by immersing the sample in a 3 M HCl solution for 15 min, followed by immersion in boiling water for 1 h. This led to the formation of micro- and nanoscale roughness, with superhydrophilic channels surrounded by hydrophilic regions. Two different hybrid surfaces were considered, a “straight” (Figure 2.11 (a)) and a “interdigitated” one (Figure 2.11 (b)). The first consisted of aligned vertical channels, whereas the second one was bioinspired by banana

leaves and consisted of edge-shaped superhydrophilic tracks to transport the condensate from the narrow end to the wider end.[15] Two different humid air conditions were tested, namely 80% RH at 20°C (C_1) and 80% RH at 35°C (C_2), with a substrate temperature of 0°C. The overall goal was to decrease the critical detachment radius, optimize the nucleation density, and increase the droplet removal rate. Both the HTC values and the water collection rate were considered for the efficiency evaluation.

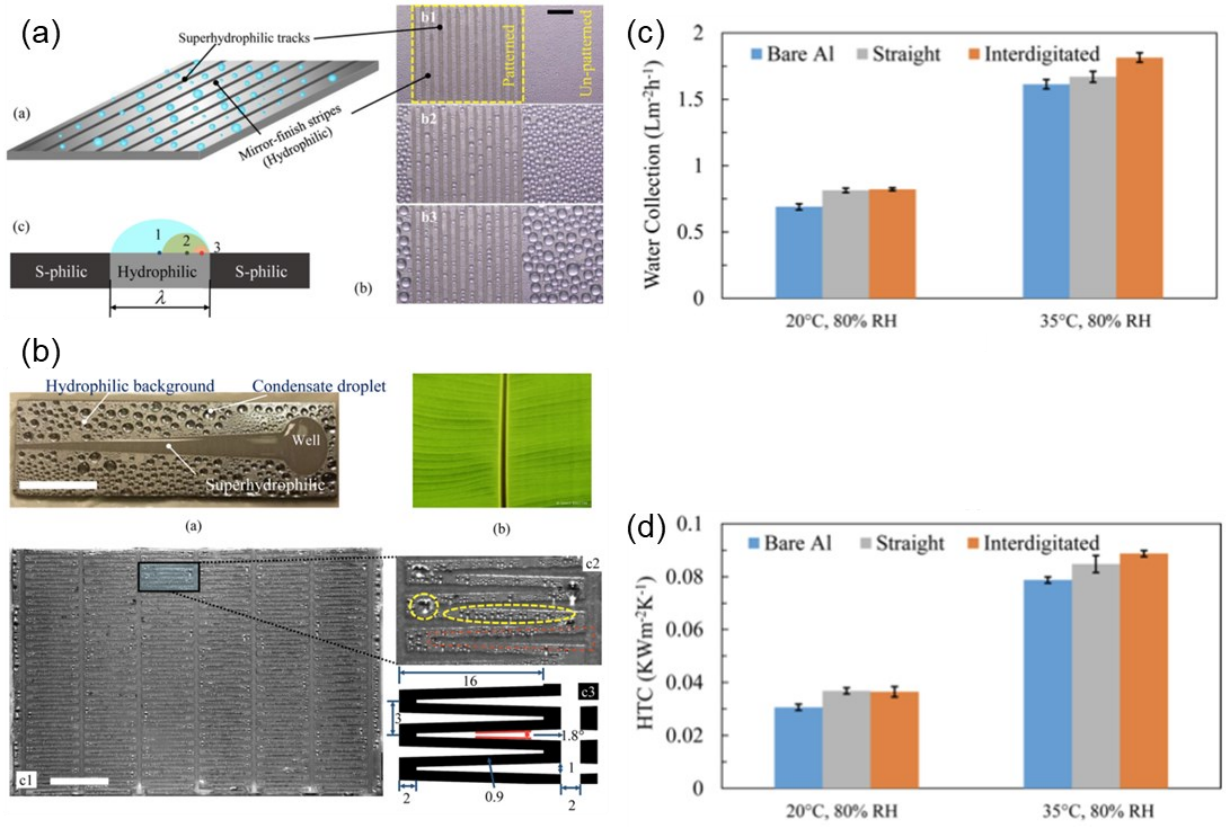


Figure 2.11. (a) "Straight" type of hybrid surface scheme and comparison between humid air condensation on the latter and on flat surfaces. (b) "Interdigitated" type of hybrid surface scheme and comparison between humid air condensation on the latter and on flat surfaces. (c, d) Water collection and HTC values of the bare Al, straight and interdigitated hybrid surfaces, at different humid air conditions.[15]

The hydrophilic areas favored the initial nucleation step during the dropwise condensation, whereas the superhydrophilic channels guaranteed a faster removal of the condensed droplets with the aid of filmwise condensation. The hybrid patters allowed for a reduction of the critical detachment radius and a faster condensation cycle. Under both humid air conditions (C_1 and C_2), the hybrid patterns favored a higher efficiency with respect to the flat hydrophilic surface, even though the increase was higher under C_2 (+18%) respect to C_1 (+4%). This was attributed to the maximum drainage capacity, which was reached during the high moisture conditions and constitutes a limiting factor. Finally, the interdigitated hybrid surface provided for a more efficient water collection and HTC values, with respect to the straight one. In the former, the optimized geometry consisted of edge-shaped

superhydrophilic tracks, which allowed a more efficient transport of the condensate from the narrow end to the wider end of the tracks, with a consequent faster removal.

3.1.4.3 *Low hysteresis of the contact angle*

In 2019-2020, two research works proposed an alternative pathway to superhydrophobic surfaces, for the control and optimization of the dropwise condensation dynamics. Kaneko *et al.*[43] developed a surface which showed improving sliding properties with decreasing contact angle, i.e., with increasing hydrophilicity. Cha *et al.*[48] highlighted the key effect of a lower contact angle hysteresis on dropwise condensation, with respect to targeting superhydrophobic absolute values of Θ_s. The authors successfully induced a dropwise condensation on a hydrophilic surface, which displayed $\Delta\Theta \sim 0°$.

Generally, the simultaneous presence of low hysteresis of the contact angle and surface hydrophilicity is challenging to be obtained. Previous works already evidenced the remarkable importance of the contact angle hysteresis, employing liquid-like surfaces to favor the droplets' sweeping, such as lubricant infused surfaces (LISs) and slippery liquid-infused porous surfaces (SLIPSs).[42,49,50] However, these surfaces typically displayed a hydrophobic state, whereas low Θ_s and low $\Delta\Theta$ could be obtained through the presence of low surface tension liquids on the surface.[51,52] The work by Kaneko *et al.*[43] and Cha *et al.*[48] allowed to obtain a simultaneous reduction of both Θ_s and $\Delta\Theta$ on solid substrates, without the need of additional liquid lubricants.

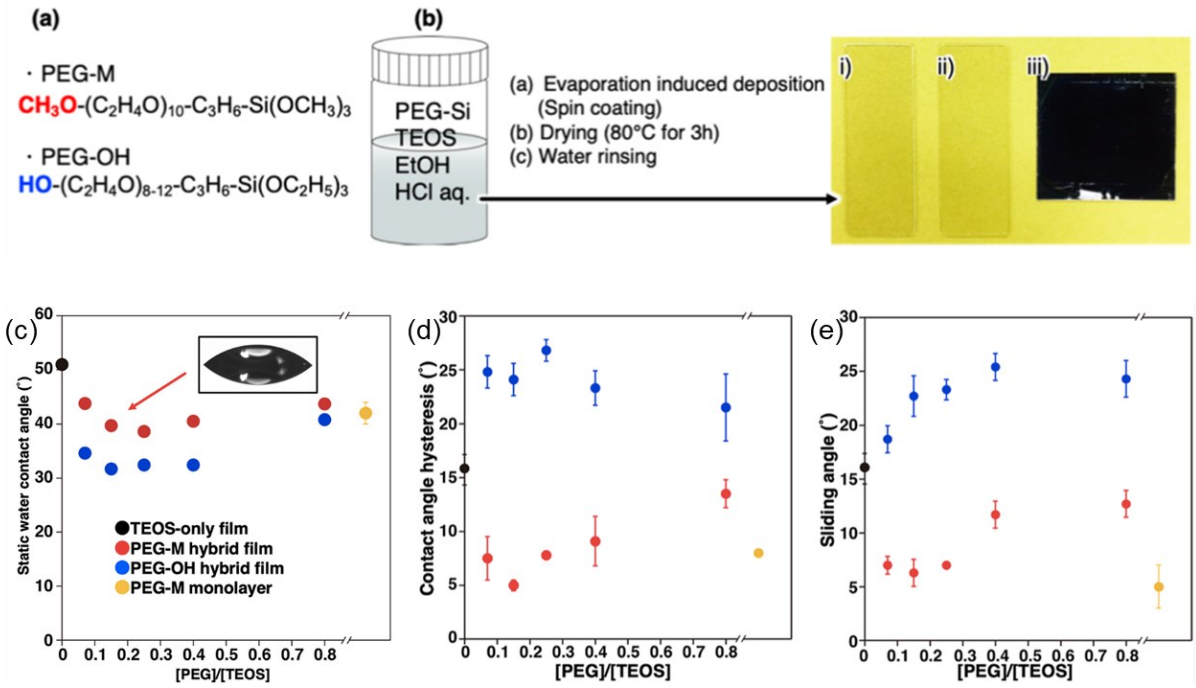


Figure 2.12. (a) Molecular structures of two different types of PEG-silanes (PEG-Si), namely PEG-M and PEG-OH. (b)Coating process and appearances of samples. (c) Static contact angle, (d) hysteresis of the contact angle and (e) sliding angle of four samples, in function of the [PEG]/[TEOS] ratio. TEOS-only (black), hybrid PEG-M (red), hybrid PEG-OH (blue), PEG-M monolayer (yellow).[43]

Kaneko *et al.*[43] deposited PEG-hybrid films on silicon and aluminum, starting from sol−gel solutions containing hydrophilic pegylated organosilane (PEG-Si) and tetraethoxysilane (TEOS) as precursors (Figure 2.12 (a, b)). They compared different terminal groups, such as methoxy (CH_3O−) or hydroxy (HO−) terminated PEG chains and named the samples "PEG-M" and "PEG-OH", respectively. The authors initially compared the static contact angle (Θ_s), hysteresis of the contact angle ($\Delta\Theta$) and sliding angle (Θ_{sl}) among the different samples, optimizing the [PEG]/[TEOS] ratio (Figure 2.12 (c-d)). The optimized ratio [PEG-Si]/[TEOS] = 0.15 for the PEG-M sample displayed the lowest $\Theta_s \sim 40°$, simultaneously with the lowest $\Delta\Theta \sim 6°$. Traditionally, hydrophilic surfaces are considered to induce pinning of the condensed droplets, whereas the sol-gel PEG-M coating allowed to reach considerably low $\Delta\Theta$ values on a hydrophilic surface.

The authors investigated the dropwise condensation efficiency on aluminum substrates, by comparing the hybrid PEG-M coating with two reference samples, namely a hydrophobic perfluorinated monolayer and a hydrophilic uncoated substrate. The perfluorinated monolayer was deposited from the perfluoroalkylsilane FAS13. The PEG-M coating required sliding angles to induce the droplet detachment, which were half with respect to the bare substrate. The minimum droplet volume required for sliding was found to be 3 μL, considerably lower than the 8 μL required by the hydrophobic reference coating. As a key result, an optimized hydrophilic surface with low hysteresis of the contact angle facilitated the droplets' detachment during condensation, with respect to a hydrophobic surface.

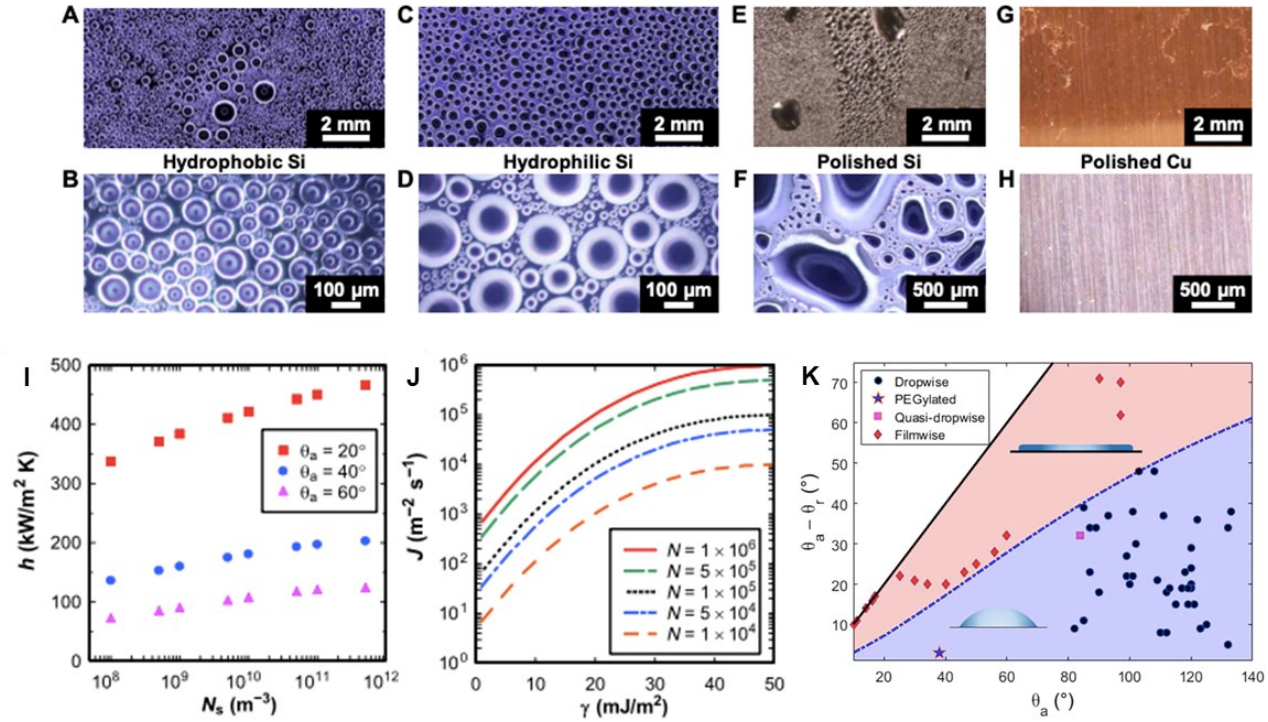


Figure 2.13. Droplets distribution during vapor condensation. (A,B) Hydrophobic fluorinated coated silicon, (C, D) hydrophilic PEGylated coated silicon, (E, F) polished silicon, (G, H) polished copper. (I, J) Parameters affecting condensation heat transfer coefficient (h): model results of h as a function of nucleation density (Ns) for varying advancing contact angle with departure radius r_{max} = 1 mm. (J) Condensation nucleation rate (J) as a function of condensing surface energy. (K) Condensation regime map as a function of advancing contact angle and contact angle hysteresis.[48]

Further confirming the findings by Kaneko *et al.*[43], Cha *et al.*[48] reported a dropwise condensation on a solid PEGylated surface, displaying high chemical homogeneity and sub nanoscale roughness, with an overall hydrophilic behavior (Θ_a = 38°) and almost null contact angle hysteresis ($\Delta\Theta$ < 3°). The authors developed a physical model demonstrating that stable dropwise condensation is mainly influenced by the contact angle hysteresis, rather than by the surface intrinsic wettability or advancing contact angle as assumed on previous models. The PEGylated coating on silicon was compared with a hydrophobic fluorinated coating on silicon, polished silicon, and polished copper (Figure 2.13 (a-h)). The former was obtained by immersing the silicon substrate in a solution consisting of 2-[methoxy (polyethyleneoxy)6-9propyl]trimethoxysilane and hydrochloric acid in anhydrous toluene, whereas the hydrophobic layer was obtained by chemical vapor deposition (CVD) of octafluorocyclobutane (C_4F_8).

The development of condensation on hydrophilic surfaces was found to be advantageous in terms of lower nucleation barrier, with respect to a hydrophobic surface, leading to a higher nucleation (Figure 2.13 (i, j)). The hydrophilicity was also found to increase the heat transfer coefficient (h) values. The flatter spherical cap-shaped morphology of the droplets induced by the hydrophilic surface allowed a reduction of the conduction thermal resistance through the droplet. The latter was found to be the dominant thermal resistance for droplet radius below 100 μm.[48] As discussed in paragraph 2.1.3.2,

previous theories already demonstrated that most of the condensation heat is exchanged through small-sized droplets.[32,34] As a result, the minimization of the advancing contact angle, simultaneously with the development of a dropwise condensation mode appear as key parameters for improving the heat exchange efficiency.

From the condensation tests, the hydrophilic PEGylated surface displayed a 10x increase in the initial nucleation density, with respect to the hydrophobic fluorinated one. In the former surface, remarkably, the condensed droplets maintained a spherical shape during the coalescence step. To demonstrate the irrelevant role of the advancing contact angle, if the $\Delta\Theta$ is not considered, the condensation mode was studied on the polished silicon and polished copper substrates (Figure 2.13 (e-h)). The former displayed $\Theta_a \sim 46°$ and $\Delta\Theta \sim 23°$, whereas the latter $\Theta_a \sim 97°$ and $\Delta\Theta \sim 70°$. A filmwise condensation was noticed on the polished copper substrate, whereas the silicon substrate, despite the hydrophilicity, displayed a simil-dropwise condensation with irregularly shaped droplets. Finally, the hydrophilic PEGylated surface allowed for a ~500% increase in heat exchange, with respect to the hydrophobic fluorinated one.

3.2 Durability and heat exchange efficiency of hybrid sol-gel coatings during saturated vapor condensation

Author disclosure statement. The data and discussion reported in paragraph 2.2 in Chapter 2 were published in the article "Basso, M., *et al*. Hydrophobic hybrid silica sol-gel coating on aluminum: Stability evaluation during saturated vapor condensation, *Journal of Non-Crystalline Solids: X*, Volume 17, 100143, (2023). ISSN 2590-1591. https://doi.org/10.1016/j.nocx.2022.100143"[53]

As previously discussed, the efficiency of liquid-vapor phase change (LVPC) has a major influence on both industrial productivity and environmental pollution. Vapor condensation has been extensively investigated within the LVPC systems, due to the involvement in processes such as water harvesting and heat exchange.[54–56] High efficiency of the latter can be reached by controlling the condensation dynamics, avoiding filmwise condensation and exploiting the dropwise mode. LVPC processes are usually related to metallic substrates, which typical hydrophilicity is unfavorable when heat exchange efficiency is considered.[57] However, the condensation mode can be controlled through the surface modification of both chemical composition and morphology. Among the different techniques, silica-

based sol-gel coatings offer an efficient trade-off between cost, time, and chemical-mechanical resistance, besides the possibility to properly tune the coating's properties. Their wettability can be controlled through a hybrid organic-inorganic composition, introducing organic groups to decrease the hydrophilicity of plain silica coatings. Experimental results recently demonstrated that such coatings represent a valid strategy for the promotion of dropwise condensation (DWC) on aluminum substrates.[58]

The high length of the precursor's organic chain is known to increase the hydrophobicity along with the decrease of the contact angle hysteresis,[59] therefore an octyl-modified silica sol gel coating was selected for the control of saturated vapor condensation. Reductions in the average droplet dimension was expected, along with the improvements in HTC, since most of the heat exchanged during DWC is associated to small droplets,[60]

Besides the heat exchange, the introduction of long organic chains in silica networks was recently proven to favor the durability of sol-gel coatings in water-based environments.[61] A major challenge for future works is the durability of such coatings, since they face severe environmental conditions when employed in real-life applications, such as fouling, scratching, corrosion or high thermal stresses.[62] Among the numerous studies on the control of surface wettability for LVPC devices, the majority primarily focus on developing new paths for surface modification, without considering the coatings' stability over time. On the other side, when the durability is studied, the possible negative influence on the heat exchange is often not examined. An increase in coating's thickness could improve its resistance to harsh conditions but could simultaneously lead to a higher thermal barrier.[57,62] The coatings employed in LVPC applications are therefore required to simultaneously satisfy several requirements, which is a demanding challenge since improving one requisite often implicates worsening another one.

In the case of the hybrid octyl-modified silica coating, the global performance was evaluated during saturated vapor condensation, in terms of both thermal exchange and coating's durability. The heat exchanged over time was examined on aluminum substrates in a custom-made heat exchange apparatus. The coating's stability was studied by separating the different influencing factors on its degradation, from temperature to steam-air coexistence to nucleation and growth phenomena. The coating's degradation, which led to variations in thickness, wettability, chemical and morphological properties, was monitored with scanning electron microscopy (SEM), Fourier-transformed infrared spectroscopy (FTIR), ellipsometer and contact angle goniometer characterizations. For the sake of a higher clarity, in paragraphs 2.2.1-2.2.4 the outcomes of the distinct tests and characterizations will

be individually presented. In paragraph 2.2.5 a general discussion will provide an overall explanation of the thermal exchange efficiency and coating's durability.

3.2.1 *Synthesis and deposition of hybrid coatings*[53]

Tetraethyl orthosilicate (TEOS, 98%; Sigma Aldrich), octyltriethoxysilane (OTES, 98%; Sigma Aldrich), absolute ethanol (EtOH, Emsure; Sigma-Aldrich), concentrated hydrochloric acid (HCl, 37%; Sigma Aldrich), milliQ water (H_2O, 18.2 MΩ). All employed materials were used as purchased, except for hydrochloric acid which was diluted to obtain a 1 M concentration. Silicon wafers, aluminum with high purity (AW1050, 99.50% minimum aluminum content), 20 x 20 mm^2 and 20 x 50 mm^2 dimensions. Aluminum was polished to obtain a smooth mirror-like surface, following a standard metallographic technique. The octyltriethoxysilane-based solution was prepared adapting a recipe from De Ferri *et al*.[59] TEOS, OTES, EtOH, HCl 1 M and H_2O were mixed in molar ratios of (TEOS+OTES):EtOH:H_2O:HCl=1:2:2:0.01, respectively, with varied TEOS:OTES molar ratio. The solution was stirred for 2 h at 400 rpm at room temperature, during which additional solvent was added after 30 min, to reach a theoretical final concentration of SiO_2 of 1.3 M. The solution was aged still for 2 additional hours and then filtrated with syringe filters of 0.2 μm pores prior to the deposition. The sol-gel coatings were deposited on polished aluminum substrates and silicon wafers, both previously cleaned through sonication in ethanol followed by atmospheric plasma treatment (Plasma Cleaner, PDC-002-CE, Harrick Plasma). The deposition was done inside a custom-made dip-coater, by withdrawing the substrates from the solution at 4.8 cm/min. The solvent evaporation was induced gradually, together with the evolution of condensation reactions, by aging the coatings at room temperature for 24 h. The coatings were then annealed in a furnace at 200°C for 2 h, with a heating ramp of 10°C/min.

3.2.2 *Optimization of hybrid-silica coating*[53]

The effect of the OTES/TEOS ratio and the deposition parameters on the wettability, thickness, and adherence to the substrate were considered. Preliminary experiments were performed on silicon by tuning the moles of OTES to TEOS from a minimum of 10% (O_1T_9) to a maximum of 50% (O_5T_5). Different withdraw speeds were tested, from 2.5 cm/min to 10 cm/min. As dewetting of the coatings was observed for O_4T_6 and O_5T_5, these compositions were discarded.

Table 2.1. Thickness, advancing contact angle (Θ_a) and receding contact angle (Θ_c) of the coatings on silicon for different OTES/TEOS molar ratio and withdrawal speed.[53]

Sample	Withdrawal speed (cm/min)	Thickness (nm)	Θ_a (°)	Θ_c (°)
O_1T_9 – 5 cm/min	4.8	216 ± 2	100 ± 2	88 ± 1
O_1T_9 – 7.5 cm/min	7.4	248 ± 8	101 ± 1	89 ± 1
O_2T_8 – 5 cm/min	4.8	227 ± 5	101 ± 1	88 ± 1
O_2T_8 – 10 cm/min	10.4	330 ± 7	103 ± 1	91 ± 1
O_3T_7 – 2.5 cm/min	2.5	207 ± 6	105 ± 1	96 ± 1
O_3T_7 – 5 cm/min	4.8	343 ± 9	106 ± 2	96 ± 2

As reported in Table 2.1, the amount of OTES affected the surface wettability by increasing the advancing contact angle (Θ_a) from 100 ± 2° to 106° ± 2°, as well as the receding contact angle (Θ_r) from 88 ± 1° to 96 ± 2°. With respect to previous hybrid silica-based systems[63,64], an HTC enhancement was expected, due to the higher Θ_a and low contact angle hysteresis ($\Delta\Theta$) of the OTES/TEOS coatings. For all samples, the $\Delta\Theta \sim$ 10-14° was found to be slightly lower with respect to other hybrid organic-inorganic coatings, which were obtained by different molecular precursors such as phenyltriethoxysilane and methyltriethoxysilane.[65] The thickness of the films was found to be within 200-400 nm from ellipsometry measurements (Table 2.1). These values offer a good compromise, ensuring adequate robustness under high temperature and heat flux, while minimizing the intrinsic thermal resistance of the coating. Hybrid silica-coatings with thickness < 200 nm have been proven to degrade within the first 15 hours of condensation.[64] Considering a film thickness between 200 and 400 nm and a thermal conductivity of 0.2 W m^{-1} K^{-1}, the thermal resistance per unit area of the coatings can be estimated in the range 1.5-2 m^2 K MW^{-1}.[65]

Further samples were deposited on polished aluminum substrates (2 × 2 cm^2), selecting O_2T_8 and O_3T_7 compositions at a fixed withdrawal speed of 4.8 cm/min. As previously observed[66], the different substrate causes a slight increase in thickness, found to be about 300 nm for O_2T_8 and 380 nm for O_3T_7. The wettability was similar for both the compositions, with average Θ_a = 102 ± 3°, and Θ_r = 89 ± 3°. Following these results, the O_2T_8 composition was selected as a good compromise in terms of wettability, thickness, and reproducibility. Following the same protocol, the O_2T_8 coating was deposited on a larger aluminum substrate (5 × 2 cm) for steam condensation tests.

3.2.3 *Saturated vapor condensation experiments*[53]

The hybrid silica coatings deposited on aluminum substrates were tested in a two-phase thermosyphon designed for the investigation of water vapor condensation on vertical metallic

substrates. The experimental apparatus consists of three main components: a boiling chamber, a test section, and a post-condenser (Figure 2.14).

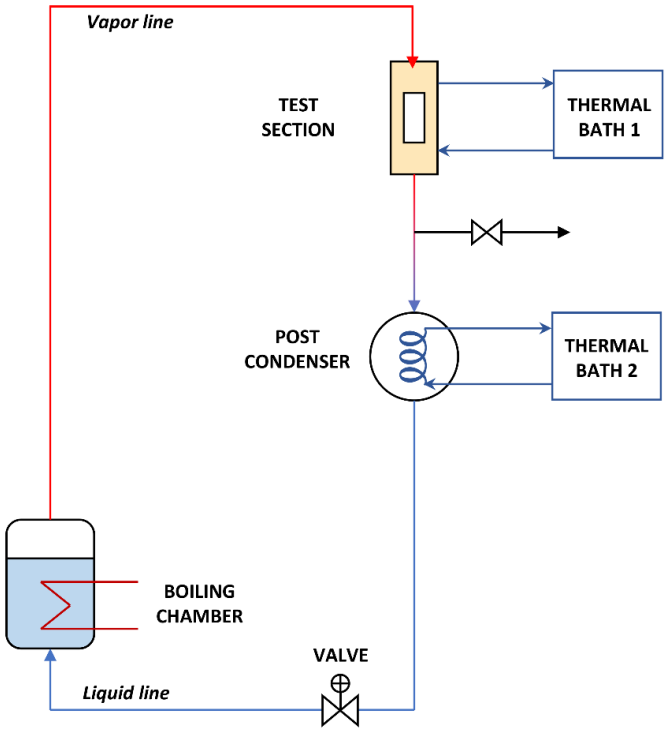


Figure 2.14. Scheme of the experimental apparatus for saturated vapor condensation tests.[53]

The vapor produced inside the boiling chamber flew into the test section where it was partially condensed over a metallic sample, with condensing area of 50 mm height, 20 mm width. Inside this component, condensation was driven by the action of the cooling water supplied on the back surface of the sample by a thermostatic bath at controlled temperature and flowrate. Downstream the test section, the two-phase mixture of vapor and liquid was completely condensed in the post-condenser before returning to the boiling chamber. The detailed description of the experimental apparatus is reported in Appendix A.2.2. The condensation tests were performed at the following thermodynamic conditions: 106°C of saturation temperature (which corresponds to a saturation pressure of 1.24 bar), 2.9 m s^{-1} of steam velocity, heat flux in the range 250-550 kW m^{-2}.

The heat transfer performance of the hybrid silica sol-gel coating, selected to be O_2T_8 from the previous section, was assessed during steam condensation in the custom-build experimental apparatus described above (Figure 2.14). During the test runs, the heat flux was varied between 250 kW m^{-2} and 550 kW m^{-2}, while saturation temperature and steam velocity were kept constant at 106°C and 2.9 m s^{-1}, respectively. The experimental results of the vapor condensation test (VC-Al) are shown in Figure 2.15 (a), in which the HTC is plotted versus time.

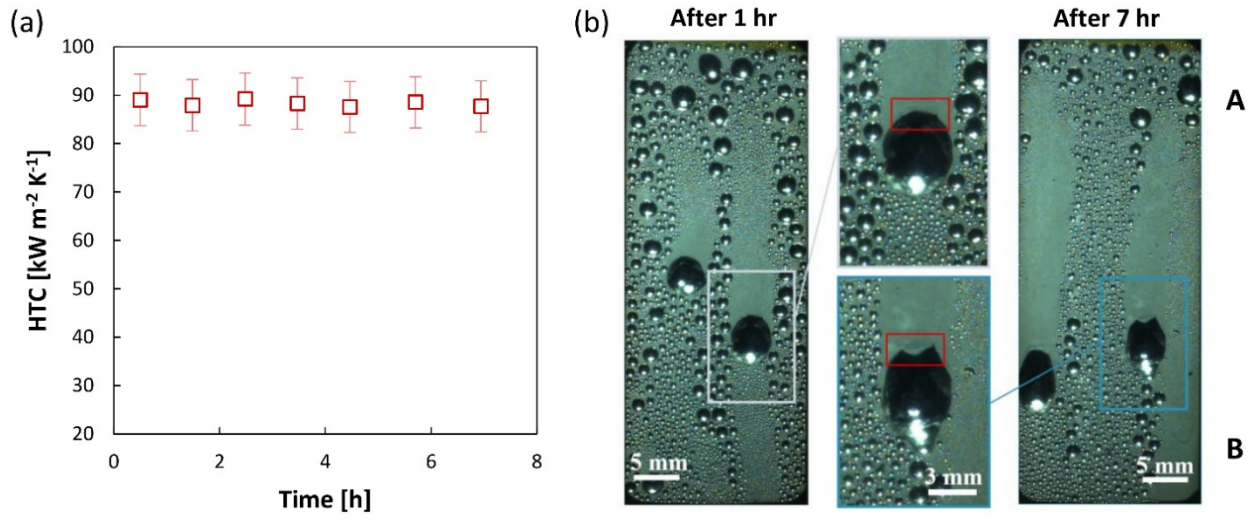


Figure 2.15. (a) Heat transfer coefficient (HTC) measurements obtained during DWC of steam on the sol-gel coated aluminum sample versus time. (b) Images recorded at the beginning and at the end of the condensation test. An example of droplet pinning is shown. The position of the two examined areas of the coated surface (top and bottom) is highlighted by the letters A and B, respectively.[53]

The functionalized surface sustained DWC for the entire duration of the condensation tests of 7 h, exhibiting a stable thermal performance with HTC values of ~90 kW m^{-2} K^{-1}. No changes of the coated surface were detected from the thermal measurements since the HTC remained almost constant for the whole endurance tests. During the test runs, the heat flux was reduced from 550 to 250 kW m^{-2} to assess the effect of the heat flux on HTC (Figure 2.15 (a)). Due to the fixed value of the saturation temperature, the temperature of the cooling water supplied to the test section was varied between 25°C and 85°C to control the heat flux. The latter increases with the increasing saturation-to-coolant temperature difference. In accordance with literature[67,68], the HTC measured during DWC was found to be constant in the heat flux range here investigated (250-550 kW m^{-2}), despite the considerable variation of coolant temperature. Interestingly, similar heat flux values could be obtained during FWC only with the HTC being significantly lower (8-12 kW m^{-2} K^{-1} according to the FWC model described in Del Col *et al.*[69]). The promotion of DWC on aluminum substrates resulted in an average 9-fold increase of the condensation HTC compared to values measured during filmwise condensation (FWC) under similar heat flux conditions.[69] Compared to other sol-gel coatings with slightly higher wettability (average $\Theta_a \sim 90°$), similar film thickness, and tested during DWC under the same heat flux condition, the developed coating showed an increase in the HTC of about 10%.[65]

The images taken at the beginning and end of VC-Al tests showed an evolution of the condensation phenomenon, specifically of the droplet population (Figure 2.15 (b)). The droplet's departing radius, which is a key parameter of the DWC heat transfer mechanism, showed a moderate increase after 7 hours in some areas of the sample, from 1.1 mm to 1.5 mm. Being the thermodynamic conditions

constant[70], the droplet's departing radius depended on the surface wettability, therefore a variation of the contact angles was expected. This variation could also be related to an increase of the droplets' pinning, which affects their motion on the condensing surface (Figure 2.15 (b), zoomed images). Even though no variations in the HTC were detected after 7 hours of continuous condensation, the experiments were stopped to investigate the evolution of the coated surface before that irreversible and complete degradation could be reached.

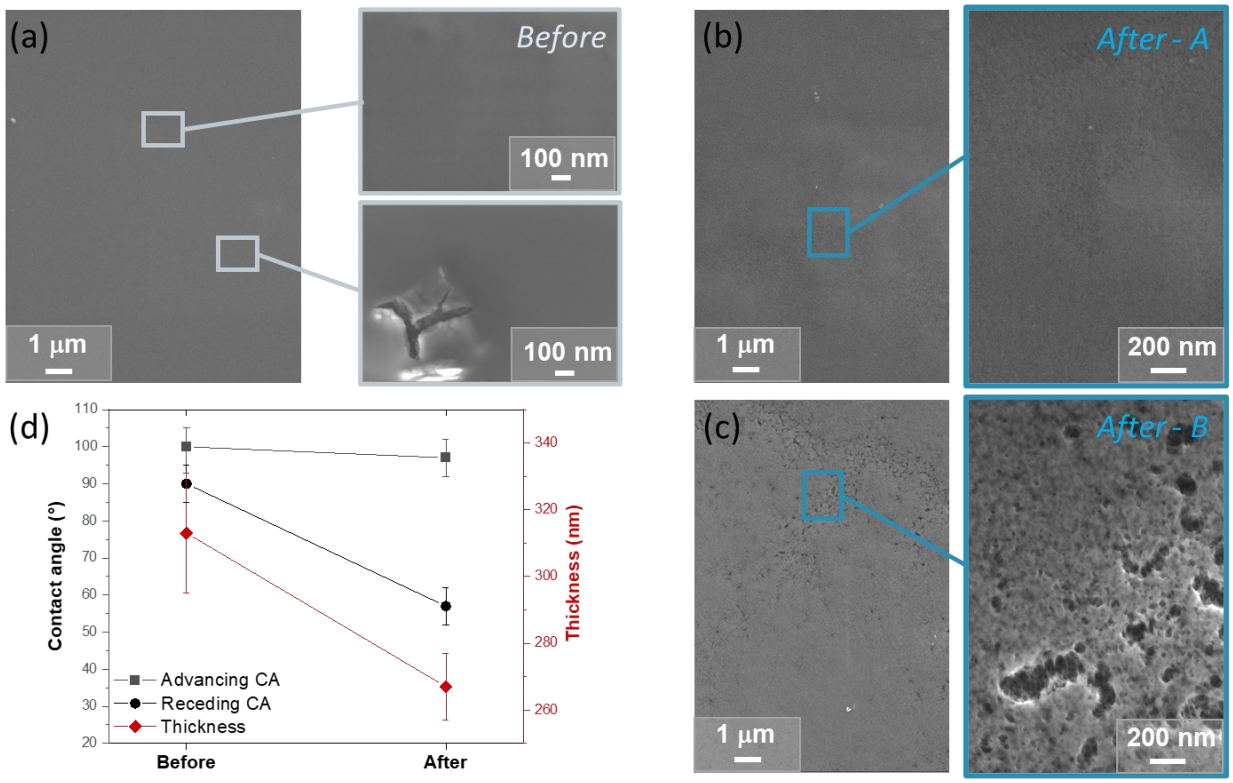


Figure 2.16. (a-c) SEM images of the octyltriethoxysilane-based coating on aluminum: (a) reference sample; (b) sample after the 7 h condensation tests (VC-Al), on zone A; (c) sample after the 7 h condensation tests, on zone B. The scale bar of each figure is reported on the bottom right. (d) Variation of the dynamic contact angles and of the coating's thickness after the 7 h VC-Al tests. Each experimental result is the average value of three distinct measurements in different areas of the sample. The standard deviation is reported for each result.[53]

The changes in the dynamic contact angles, thickness, and morphology of the coatings after 7 hours of continuous condensation are reported in Figure 2.16, while the FTIR spectroscopy results are visible in Figure 2.17 and Table 2.2. Before the VC-Al tests, the coated aluminum surface was hydrophobic, with $\Theta_a = 100 \pm 5°$ and $\Theta_r = 90 \pm 5°$ (Figure 2.16 (d)). The ellipsometry measurements revealed an initial coating thickness of 310 ± 18 nm. After the condensation tests, the thickness moderately decreased by ~46 nm, along with a decrease of ~33° of the Θ_r (Figure 2.16 (d)).

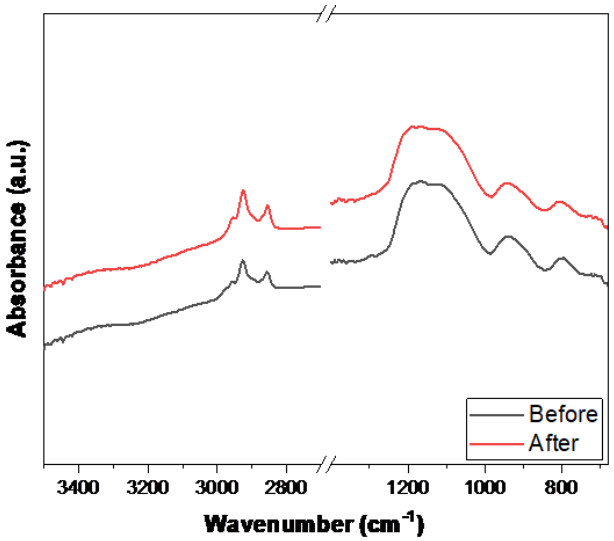


Figure 2.17. FTIR spectroscopy absorption spectra of the coating on aluminum before and after the 7 h condensation tests in the experimental apparatus.[53]

Table 2.2. Peak intensity and ratio between Si-OH peak and Si-O-Si peaks from FTIR spectroscopy, before after the 7 h degradation tests of the coatings on aluminum.[53]

Vibrations	Before	After
Si-OH	238	237
Si-O-Si	492	492
Si-OH/Si-O-Si (%)	48	48

According to FTIR spectroscopy (Figure 2.17), no variations in the vibrational modes of the peaks could be observed. The vibrational peak at ~1180 cm^{-1}, corresponding to the bond between octyl-groups and silicon ($Si\text{-}CH_2\text{-}(CH_2)_6\text{-}CH_3$), was covered by the intensity of Si-O-Si bonds, therefore it could not be used to evaluate the possible disappearance of the organic groups.[59] Nonetheless, the persistence of a hydrophobic character was shown by the Θ_a, which was not affected after 7 hours of condensation ($\Theta_a = 97 \pm 5°$, Figure 2.16 (d)). FTIR spectroscopy is commonly used to monitor the evolution of hydrolysis and condensation reactions, via the ratio between the peak of asymmetric stretching of Si-O-Si (~1120 cm^{-1}) and Si-OH peak (~940 cm^{-1}).[71] The ratio between the Si-O-Si and Si-OH peaks did not vary after the condensation experiments (Table 2.2), therefore no evident variation was found.

Significant changes in the coating's morphology after the exposure to saturated vapor were instead highlighted by SEM (Figure 2.16 (a-c)). During the VC-Al tests, droplet pinning was not observed as a global and homogeneous phenomenon but was instead present only at isolated locations. In the afterwards characterizations, several macro-areas were explored to detect possible morphological variations and wettability differences. Two different representative areas were individuated, namely at the top (zone A - Figure 2.16 (b)) and at the bottom (zone B - Figure 2.16 (c)) of the sample, and

their position is reported in Figure 2.15 (b). As shown in the insights at higher magnification (Figure 2.16 (a-c)), the interaction with saturated vapor during condensation led to an evolution of the coating. Prior to the tests, the sample's surface was globally smooth and uniform, presenting only a few isolated and small defects such as nanocracks (Figure 2.16 (a)). After the 7 hours condensation tests, local spots of the surface were found to gradually evolve into a spiderweb-like morphology characterized by a higher porosity (Figure 2.16 (a-c)). Similar morphologies were found by Metroke *et al.*[61], who studied the corrosion resistance in salt-containing environments. Here, the spiderweb morphology of the coating was found to be more pronounced on the bottom (Figure 2.16 (c)) with respect to the top part (Figure 2.16 (b)) of the sample. The $\Theta_a = 63 \pm 5°$ on zone B was slightly lower respect to the $\Theta_a = 70 \pm 5°$ on zone A. A thickness decrease of ~ 60 nm was detected in the bottom area from ellipsometry, slightly higher respect to the average value of ~46 nm.

3.2.4 *Coating degradation tests*[53]

From the characterizations carried out before and after condensation experiments (paragraph 2.2.3), the evolution of the hybrid silica sol-gel coating seemed to be related to the combined effect of mechanical-chemical interaction with water, high temperature of the environment, and presence of defects/voids on the coating. To investigate the effect of steam condensation on the coating's stability, ad-hoc tests were performed to separate the different variables of influence.

Additional hybrid coatings were deposited on silicon substrates, following the same procedure as described in paragraph 2.2.1. The samples were tested under five different environments that could affect the coating's degradation and could be related to the conditions present during the condensation experiments. The tests were chosen to be straightforward to perform and easily replicable. The exposure time of each tested condition was set to 7 h, to be comparable to the condensation experiments. Three main factors were considered separately and then combined: the chemical-mechanical interaction with water, the effect of temperature and the role of defects. The effect of the hot water on the coatings was considered both in the case of liquid and vapor phase (i.e., steam-air mixture). The five different tests are summarized in Figure 2.18.

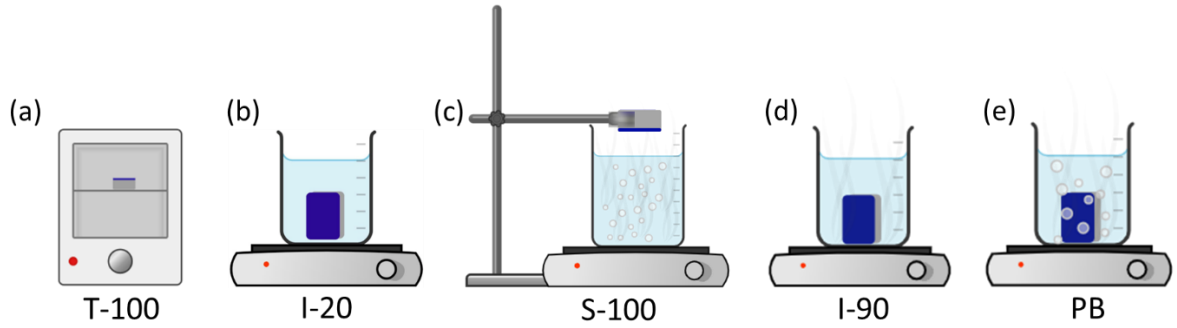


Figure 2.18. Different conditions used in the degradation tests on silicon substrates: (a) heat treatment at 100°C in furnace (T-100); (b) immersion in deionized water at 20°C (I-20); exposure to mixed air-steam (S-100); (d) immersion in deionized water at 90°C (I-90); (e) immersion in boiling water at 100°C (I-100).[53]

A first sample was heat treated at 100°C in a standard heating furnace (T-100). A second specimen was exposed to an air-steam mixture, during which the coated surface was held downside in a horizontal position, 3 cm above a glass beaker containing boiling deionized water (S-100). The third and fourth samples were fully immersed in a glass beaker containing deionized water at 20°C (I-20) and 90°C (I-90), respectively, whereas the last sample was immersed in boiling water (pool boiling, PB). To further correlate the influence of the substrate type on the coating's stability, the PB test was carried on a reference coated aluminum sample as well (PB-Al).

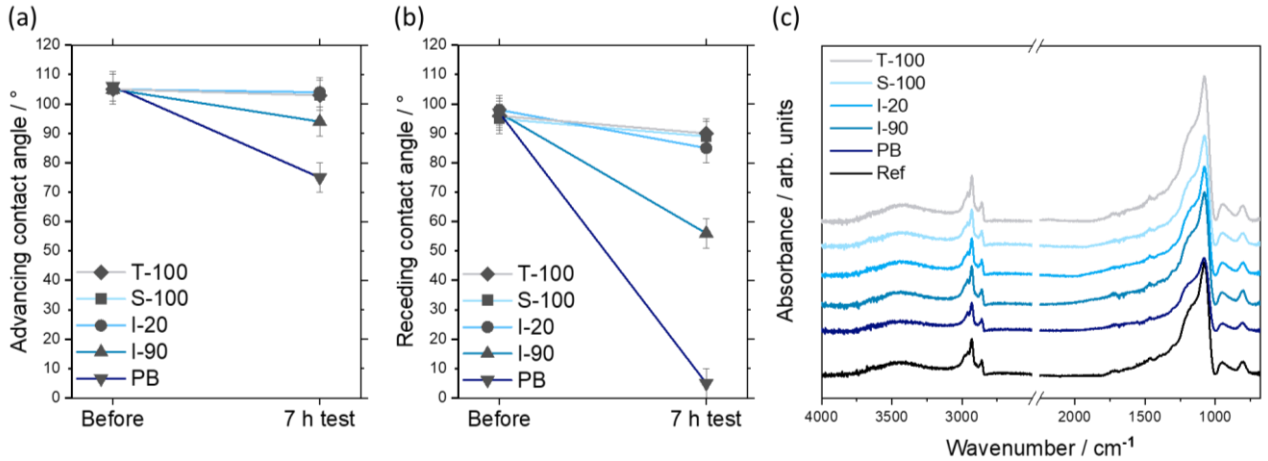


Figure 2.19. (a, b) Dynamic water contact angles of the hybrid silica coatings deposited on silicon, before and after the degradation tests: (a) advancing contact angles (Θ_a); (b) receding contact angles (Θ_r). (c) FTIR spectroscopy absorption spectra of the reference sample and of the coatings after the degradation tests.[53]

The evolution of advancing and receding contact angles is reported in Figure 2.19 (a, b). Coherently for both Θ_a and Θ_c, the wettability was affected the most by the pool boiling test (PB), in which vapor bubbles nucleated on the coated surface. The Θ_a decreased by ~30° and by ~10° after pool boiling (PB) and immersion at 90°C (I-90), respectively, whereas the other tests did not lead to significant variations. Analogously, the Θ_r showed a similar trend, but with enhanced variations. After PB test, the Θ_r decreased below the measurable limit, while I-90 and I-20 tests led to reductions of ~ 41° and ~13°, respectively. The exposure to hot steam-air mixture (S-100) and the heat treatment at 100°C

(T-100) did not affect the Θ_r. The latter result was expected since the hybrid coatings were exposed to temperatures of 200°C during the annealing treatments (paragraph 2.2.1).

Table 2.3. Peak intensity and ratio between Si-OH peak and Si-O-Si peak from FTIR spectroscopy, before and after the 7 h degradation tests of the coatings on silicon wafers.[53]

Vibrations	S-100	PB	I-90	I-20	T-100	Ref
Si-OH	1,76	0,95	1,62	1,55	2,21	1,69
Si-O-Si	29,69	21,14	31,51	29,65	41,81	31,34
Si-OH/Si-O-Si (%)	6	5	5	5	5	5

As for the aluminum sample, FTIR spectra were collected on the coated silicon samples to detect eventual chemical modifications caused by the degradation tests (Figure 2.19 (c)). The ratio between the intensities of the Si-O-Si peak (~1078 cm^{-1}) and the silanol peak (~950 cm^{-1}) was monitored to detect changes in the network, but no evident variations were noticed (Table 2.3).

Table 2.4. Ellipsometry measurements of the thickness before and after the degradation tests for each sample, with the corresponding standard deviation value.[53]

Test	Before (nm)	After (nm)	Delta (nm)
T-100	319 ± 1	320 ± 1	-
I-20	324 ± 7	324 ± 4	-
S-100	324 ± 4	323 ± 1	-
I-90	324 ± 1	328 ± 7	-
PB	323 ± 1	243 ± 19	- 80 ± 20

The thickness before and after the degradation tests is reported in Table 2.4. Globally, the tests did not lead to changes in thickness, except for the pool boiling test, after which the coating's thickness decreased by ~80 nm.

The morphologies of the coatings after PB and I-90 tests are reported in Figure 2.20 (b, c) in comparison to a reference sample (Figure 2.20 (a)).

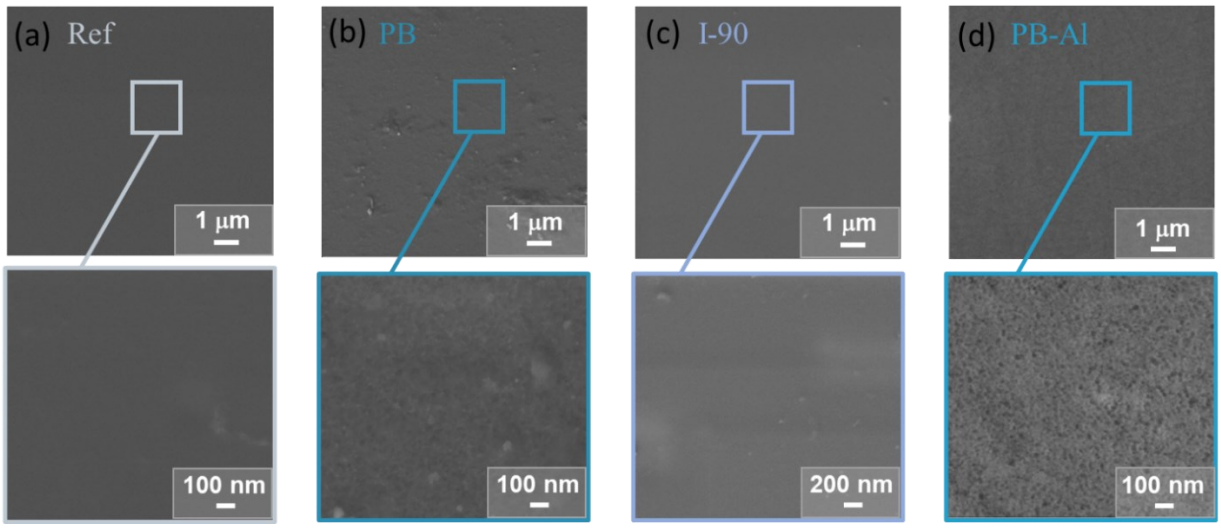


Figure 2.20. SEM images of the hybrid silica coating on silicon and aluminum substrates after the 7 h degradation tests, at 2 different magnifications. (a) reference sample on silicon; (b) coating on silicon after pool boiling immersion test (PB); (c) coating on silicon after immersion test at 90°C (I-90); (d) coating on aluminum after pool boiling immersion test (PB-Al). The scale bar of each figure is reported on the bottom right.[53]

As visible from the SEM images, the reference sample was found to be smooth, flat, and uniform at both the nano and microscale. After the degradation tests, the pool boiling led to the highest deterioration of the coating's quality, with the appearance of surface features on the nanoscale (Figure 2.20 (b)). With respect to the I-90 test, the PB test led to nucleation and growth of vapor bubbles on the coated surface, which accelerated the formation of the nanofeatures visible in Figure 2.20 (b). The latter were only slightly detectable after the immersion test at 90°C, whereas the S-100, I-20 and T-100 tests did not induce significant variations of the surface morphology.

Table 2.5. Water contact angles (Θ_a, Θ_r) and thickness before and after the PB test on the coated aluminum sample, with the corresponding standard deviation value.[53]

	Before	After
Θ_a (°)	96 ± 5	97 ± 5
Θ_r (°)	87 ± 5	< 10°
Thickness (nm)	266 ± 10	228 ± 7

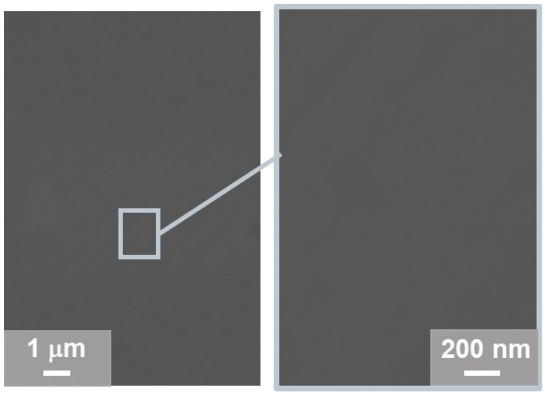


Figure 2.21. SEM images of the reference small aluminum sample. The scale bar is reported on the bottom right corner of each image.[53]

To consider the possible influence of the substrate on the coating's degradation, the PB test was repeated on a coated aluminum sample (PB-Al). The variations in contact angles, thickness and morphology are reported in Figure 2.20 (d), Figure 2.21 and Table 2.5, respectively. In analogy with the PB test on silicon, the Θ_r decreased below the measurable limit (from 87 ± 5° to < 10°), whereas the Θ_a remained unchanged. As for both PB test on silicon and VC-Al test, the thickness decreased by ~40 nm, from 266 ± 10 to 228 ± 7 nm (Table 2.5). The initially smooth surface morphology evolved after the test, after which the formation of nanofeatures was detected (Figure 2.20 (d)).

3.2.5 *Considerations on heat transfer and coating durability*[53]

As discussed in the Introduction section, coatings employed in heat transfer applications are simultaneously required to fulfil two main purposes: the control of condensation dynamics and the durability during their industrial employment.

The thermal performance of the optimized hybrid silica sol-gel coating was initially tested in a custom-made apparatus (VC-Al test). The coating, deposited on aluminum substrate, induced DWC with HTC values of ~90 kW m^{-2} K^{-1}, ~9 times higher with respect to HTC measured on hydrophilic aluminum at similar heat flux conditions (Figure 2.13 (a)).[69] HTC values above 100 kW m^{-2} K^{-1} and extended durability were reported for copper-modified surfaces.[72,73] Compared to copper, studies about DWC on aluminum are limited. Paxson *et al*.[74] reported HTC value of 35 kW m^{-2} K^{-1} stable for up to 48 h on aluminum substrates covered with an ultrathin polymer film deposited by iCVD. Raush *et al*.[75] demonstrated a duration of DWC for 8 months on ion-implanted aluminum, but the HTC was only double compared to FWC. Steam or liquid at high temperature (>100°C) promotes the formation of boehmite on the aluminum surface, enhancing the wettability and thus affecting the durability of the DWC conditions.

Despite the morphological and functional variations of the hybrid silica sol-gel coating during steam condensation, the HTC remained stable for the entire duration of the condensation experiments without any significant variation of the thermal performance, in accordance with previous results on similar hybrid coatings.[65] The VC-Al test was stopped after 7 hours to properly characterize the coating variation and avoid its total failure. A decrease in thickness of ~46 nm was found, along with morphological and wettability variations. Two different representative areas were individuated on the coating, indicating a non-uniform degree of degradation on its surface (Figure 2.14 (b, c)). Since the vapor flow was almost constant along the sample, the different evolution among the two areas could be attributed to the non-uniform interaction with the condensate. Due to the vertical orientation of the

sample, the upper area was less affected by the sweeping of falling drops as compared to the lower part. On this lower part, the chemical-mechanical interaction between the coating and the water was higher due to a higher condensate mass flow rate. The presence of small defects such as microcracks or pinholes, which were seen in a few spots on the initial coating (Figure 2.14 (a)), contributed to locally accelerate the coating's degradation as found in previous studies.[65,76,77] Droplets' nucleation on pre-existing defects, along with shear stress applied by their sweeping over the defects, can enlarge the dimensions of the latter leading to the gradual delamination of the coating. In the lower area of the sample, the frequency of droplets' nucleation was higher, as well as their sweeping, which could have contributed to the enhanced modifications of the coating's morphology. Moreover, the presence of unreacted hydrophilic silanol groups on the surface can promote the interaction with condensing saturated vapor. Respect to other hybrid sol-gel coatings[62], the low temperature of thermal degradation of octyl-groups does not allow to perform the coating's annealing above 200°C[59], leading to the presence of residual hydrophilic Si-OH groups. The durability of surface hydrophobicity is therefore a crucial factor to reduce the affinity and interaction with condensed vapor, as found by Juan-Diaz *et al.*[78] Breakage of organic-silica bond and/or partial removal of the coating on the underlying substrate could lead to the decrease of contact angles[78,79], since both the factors lead to the exposure of hydrophilic spots among the surrounding hydrophobic area. However, as shown in Figure 2.15, no major chemical variations were noticed from FTIR spectroscopy, so the major cause of the RCA decrease was attributed to the local morphological changes (Figure 2.14 (c)).

In the second part of the work, ad-hoc degradation tests were performed to separate the different influencing factors on the coating's durability. Neither the chemical interaction with water (I-20) or air-vapor stream (S-100) nor the exposure to high temperatures (T-100) induced significant variations in the coating's properties (Figure 2.17). The tests evidenced how these factors, if applied singularly, were not sufficient to induce remarkable changes in the coatings. Variations in wettability and morphology were seen when the interaction with water was combined with higher temperatures (I-90), whereas the maximum deterioration was reached when bubble nucleation was induced (PB and PB-Al, Figure 2.18). The simultaneous presence of all factors led to the highest degradation, as confirmed by the substantial decrease of dynamic contact angles and thickness (Figure 2.17 (a, b), Table 2.4). On both silicon (PB) and aluminum (PB-Al) substrates, the formation of features at the nano-microscale led to pinning of water droplets and affected the Θ_c at the macroscopic scale, leading to its decrease below the measurable level.

Analogously to bubble nucleation during PB and PB-Al tests, during the condensation experiments nucleation, growth and sweeping of condensed vapor droplets were identified as crucial factors for

the coating's degradation. After the VC-Al test, the formation of the nanofeatures was not detected on the whole surface, except for local spots on the lower area, in which a porous spiderweb morphology was found. Globally, the pool boiling test was found to be more aggressive on both silicon (PB) and aluminum (PB-Al) with respect to the VC-Al test, in terms of changes in wettability and overall morphology (Figures 2.14, 2.17, 2.18). The PB test was found to induce similar variations in wettability, thickness, and morphology on both the silicon and aluminum substrates (Figures 2.14, 2.17, 2.18, Table 2.4), whereas the wettability changes induced by the I-90 test were similar to the ones found after the VC-Al test (Figures 2.14, 2.17). A non-identical behavior between PB-Al and VC-Al tests was expected, due to the different nature of the two processes: on the former, the coatings were fully immersed in boiling water and air bubble nucleation was developed, whereas on the latter, the sample was exposed to a saturated vapor flux and water droplets condensed on its surface. However, the changes in thickness and morphology found on the two samples showed interesting similarities (Figures 2.14, 2.18, Table 2.5).

The stability tests on silicon or metallic substrates were therefore proven to be a useful tool to induce an accelerated degradation on the coatings, to evaluate their resistance under harsh conditions before their employment on larger scale applications. Based on a reproducible and straightforward approach, the proposed tests allow to separately study the different influencing factors, that can be then partially (I-90) or totally (PB) combined according to specific performance requirements.

3.2.6 *Durability and heat exchange efficiency of hybrid sol-gel coatings during saturated vapor condensation – conclusions*[53]

The heat transfer performance of a hybrid silica sol-gel coating was tested in a custom-made apparatus during the condensation of saturated vapor. The coating successfully promoted DWC with HTC values of ~90 kW m^{-2} K^{-1}, an average 9-fold increase with respect to FWC under similar heat flux conditions.[4] The heat transfer performance remained stable during the overall duration of condensation experiments, which were stopped prior to a possible failure to investigate the detected changes in wettability and morphology. Straightforward accelerated degradation tests were performed to separate the different influencing factors, to evaluate the coating's resistance prior to its real industrial application. If singularly applied, the possible degradation conditions did not lead to significant variations on the coating's properties, whereas the interaction with water at high temperature induced different degrees of degradation whether if bubble nucleation was present (PB) or avoided (I-90). Owing to the similar variations, in terms of wettability and morphology, which

were found between the coatings deposited on aluminum and silicon substrates, the latter tests could successfully provide an estimation of the coating's durability during a broad range of LVPC applications.

3.3 Bioinspired sol-gel micropatterns for humid air condensation[100]

Author disclosure statement. The data and discussion reported in paragraph 2.3 in Chapter 2 were published in the article "Basso, M., *et al.* Bioinspired silica-based sol–gel micropatterns on aluminium for humid air condensation. *J Sol-Gel Sci Technol* 102, 466–477 (2022). https://doi.org/10.1007/s10971-022-05771-7"[100]

As discussed in the introduction to this Chapter, the global drinkable water scarcity urges the need to find alternative paths to sustain the increasing water demand. As reported in the FAO 2020 publication, 1.2 billion people, meaning almost one-sixth of the world's entire population, are daily plagued to live in agricultural areas which suffer from severe water scarcity.[4] Urgent solutions are required to solve this problem and several hypotheses have been proposed in the recent years, from solar-driven desalination plants[80] to membrane-based distillation systems for contaminated water[81]. Among the various approaches, a promising solution to refill the water supplies is given by the collection of water from the vapor present in the humid air. Water condensation on a surface is subjected to nucleation and growth phenomena, which are influenced by the wettability of the surface. By acting on the latter, it is possible to favor specific dynamics during the condensation and increase the water collection efficiency. The surface wettability is strictly related to the surface energy and can be principally controlled via two factors, chemical composition and surface roughness[57]. Hydrophilic surfaces favor the nucleation of droplets but can lead to the formation of a liquid film on the cooled surface as the condensation proceeds, negatively affecting both the heat transfer and the water collection mechanism. Hydrophobic substrates, on the contrary, are characterized by the formation of isolated liquid droplets and their subsequent roll-off from the surfaces, allowing an efficient water collection and favoring the renewal of the surface for cyclic condensation and droplet removal. The surface morphology is capable to enhance both the hydrophilic and the hydrophobic properties of a substrate, as evidenced by the Young's equation[82].

The joint effort between the surface functionalization and the nano-micro structuring has been widely investigated, from superhydrophobic surfaces to hybrid surfaces with mixed hydrophilic-hydrophobic wettability.[83–86] Generally, the nano or micropatterning of surfaces has been employed to enhance the efficiency in a wide range of applications, including memory-devices, microfluidics, cell-culture systems, heat exchangers and water-collectors.[87–90] The daily phenomena of humid air condensation involving external surfaces can be manipulated with the aid of patterned films, to gain a precise control of the quantity of water collected and heat exchanged.

Considering the already existing solutions in nature, hybrid patterned coatings were developed by Colusso *et al*.[91] taking inspiration from the exoskeleton of a Namib desert beetle. The back of the beetle is covered with hydrophilic bumps that favor the humid air condensation in harsh environments, while the hydrophobic wax surrounding the bumps allows the droplets to detach and roll-off into the beetle's mouth. Hydrophobic organic-modified silica coating with hydrophilic bumps was developed via a sol-gel process, and the dewetting mechanism was exploited to gain the patterned morphology.[91] The sol-gel method offered lower costs and facile controllability of the synthesis respect to other vacuum-based processes, along with chemical inertness and higher resistance provided by the inorganic components respect to polymer-based coatings. Regarding the dewetting mechanism, extensive research is available in literature when polymers are considered[92–95], but only a few researchers[96] address the dewetting of sol gel inorganic materials. The *dewetting* indicates the spontaneous breakage of an unstable liquid coating on the surface of a non-wetting substrate, determined by the difference in the surface tensions of the two.[91,93]

In a preliminary work[91], the beetle's patterned morphology was reproduced by initially spin coating a plain sol-gel silica film on a hydrophobic CH_3-silica layer, which was previously deposited on a monocrystalline silicon wafer. The increased hydrophobicity of the bottom layer respect to the top silica film was enabled by the introduction of organic -CH_3 group inside the inorganic silica network. The instability of the hydrophilic top-layer was induced by enclosing it in a solvent-saturated atmosphere, causing the already labile bonds to break apart due to the instability of Rayleigh and leading to the formation of growing holes. This was possible due to the permeability of the freshly spun xerogel to the solvent vapors, since the latter holds an active role in the condensation reactions during the sol-gel process.[91] After several seconds, the originally uniform film was transformed into isolated droplets, which autonomously distributed themselves following the Voronoi geometry.[92,95]

In paragraph 2.3, the efficiency of the hybrid patterned morphology, obtained by sol-gel dewetting, was tested during humid air condensation. The influence of a different substrate on the reproducibility of the sol-gel dewetting method was investigated. A change in the substrate determines a variation in

its surface tensions and morphological properties, therefore a variation in the forces exerted on the above unstable coating. To verify the reliability of the pattern's application in real environments, the hybrid coating was deposited and optimized on metallic aluminum surfaces with larger dimensions with respect to the silicon substrates used in our previous study, confirming the possibility of tuning the size and the density of distribution of the hydrophilic bumps.

In paragraph 2.2, hybrid organic-inorganic sol-gel coatings were confirmed to enhance the heat exchanged during dropwise condensation of saturated vapor. The possible degradation of the silica-based films due to the interaction with saturated water vapor was evidenced in both paragraph 2.2 and in literature[97–99]. In paragraph 2.3, the possibility offered by the patterned morphology to enhance the drainage rate during condensation from humid air was assessed in a custom-made apparatus. The patterned coating's efficiency was expressed in terms of condensed mass and compared with a bare aluminum substrate and with a plain hydrophobic CH_3-silica coating. The hybrid silica coatings' durability was also assessed, under static environmental conditions of high relative humidity.

3.3.1 *Synthesis and deposition of patterned, silica and CH_3-silica coatings on aluminum substrates*[100]

All the employed materials were used as received, except if otherwise stated: TEOS (98%; Sigma Aldrich), MTES (98%; Sigma Aldrich), absolute ethanol (EtOH, Emsure; Sigma-Aldrich). The hydrochloric acid dilution (1 M) was obtained from concentrated hydrochloric acid (HCl, 37%; Sigma Aldrich) and milliQ water (18.2 MΩ). The metallic substrates used were made of aluminum with high purity (AW1050, 99.50% minimum aluminum content). The dimensions of the squared aluminum substrates were 20 x 20 mm^2 in the case of the static tests and 40 x 40 mm^2 for the humid air condensation tests, respectively. The side exposed to the condensation phenomenon was polished following a standard metallographic technique to obtain a smooth mirror-like surface.

3.3.1.1 *Patterned coatings*[100]

The patterned coatings were synthetized following the procedure described by Colusso *et al.*[91] The patterned coatings were developed starting from a sol-gel bilayer. To synthetize the bottom CH_3-silica layer, an acid-catalyzed solution was prepared by mixing tetraethylortosilicate (TEOS), methyltriethoxysilane (MTES), ethanol (EtOH), hydrochloric acid 1 M (HCl) and water (H_2O) for 1 h at 400 rpm at room temperature, in molar ratios of (TEOS+MTES):EtOH:H_2O:HCl=1:2:4:0.01,

respectively, with a TEOS:MTES molar ratio of 1. After the first 30 min of mixing, the solvent was additionally added to reach a theoretical final concentration of SiO_2 of 1.3 M. Following the first hour of stirring, the solution was aged for 30 min, filtrated with syringe filters with 0.2 μm pores and deposited on the polished aluminum substrates, which were previously cleaned through sonication in ethanol followed by atmospheric plasma cleaning (Plasma Cleaner, PDC-002-CE, Harrick Plasma). The deposition was done by spin coating at 2000 rpm for 30 s, after which the film was aged at room temperature for 24 h to allow a gradual solvent evaporation and a proper evolution of the condensation reactions and then annealed at 200°C for 4 h. The above hydrophilic silica-layer was synthetized following an analogous acid-catalyzed sol gel process. The solution was prepared by mixing EtOH:TEOS:H_2O:HCl of 2:1:4:0.01, respectively, which was stirred for 30 min and diluted with the solvent to gain a final theoretical concentration of silica between 0.75 M and 2 M. After 24 h of aging, the solution was filtered (0.2 μm pore size) and deposited on the bottom hydrophobic layer. To induce the dewetting, the as-deposited unstable film was exposed to a solvent-saturated atmosphere by enclosing the bilayered sample inside a closed-cell. The destabilization of the upper film determined the formation of growing holes, which eventually allowed the evolution of the film into isolated droplets. The as-created patterned coatings were aged at room temperature for 24 h in air to favor a gradual solvent evaporation. The films were then annealed at 200°C to reach the film densification while avoiding the thermal degradation of the organic groups. The elimination of the latter would compromise the hydrophobicity of the coating, leading to an increase of the coating wettability.

3.3.1.2 *Plain reference silica coatings*[100]

To extend the comprehension and control of the dewetting mechanism and to gain a deeper knowledge on how different morphologies and chemical compositions influence the condensation from humid air, plain silica and plain CH_3-silica coatings were also deposited on the aluminum substrates. The plain CH_3-silica coating was synthetized and deposited following the same procedure as described for the bottom-layer of the patterned coating. Regarding the plain silica films, the synthesis described for the top-layer in the pattern was identically reproduced, but after the deposition by spin coating, the silica films of different concentrations were aged for one day and then annealed in a furnace for their densification and stabilization.

3.3.1.3 *Characterization of the plain silica and plain CH_3-silica coating*[100]

The variations in wettability of the coated surfaces compared to the bare aluminum sample were verified by measuring the dynamic contact angles and detecting the characteristic FTIR peaks. The advancing (Θ_a) and receding contact angles (Θ_r) of the CH_3-silica coating were 89° ± 3° and 72° ± 2°, respectively. The bare aluminum contact angles were Θ_a = 65° ± 3° and Θ_r = 10° ± 3°, and the plain silica ones were Θ_a = 58 ± 3° and Θ_r = 45° ± 2°. The generally accepted definition considers a surface to be hydrophobic if the static contact angle is above 90°, but no general agreement can yet be found in the literature on how to consider the influence of the dynamic evolution of a droplet on a surface. In the present case, indeed, the general definition would lead to defining both the surfaces as hydrophilic, but a favored droplet removal from the surface is allowed by the plain CH_3-silica coated sample and impeded on the bare aluminum. Recently, several authors[57,86] started to describe the overall phenomenon during the droplet-substrate interaction with the aid of the dynamic contact angles. The difference between the Θ_a and Θ_r, i.e., the hysteresis of the contact angle, provides an estimation of how easily the droplet is allowed to be removed from the surface. Regarding the present surfaces, the bare aluminum sample was characterized by a high hysteresis of the contact angle (ΔH) of 55° ± 3°, which is considerably higher than the ones of the coated samples, namely ΔH = 17° ± 3° for the plain CH_3-silica film and ΔH = 20° ± 3° for the plain silica. Considering the recent literature and the droplet evolution during its deposition and removal from the surface, the CH_3-silica coating was classified as hydrophobic, while the bare aluminum was defined as hydrophilic.

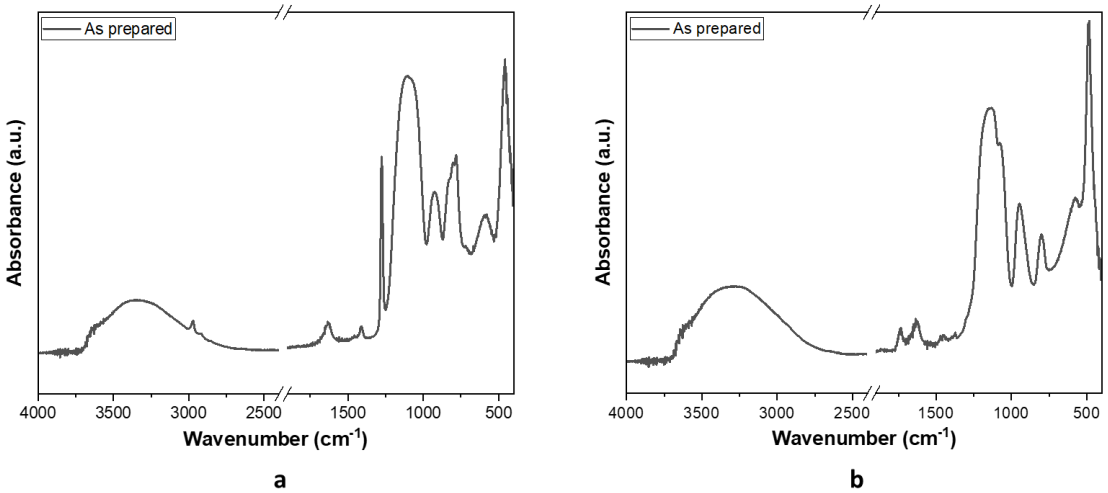


Figure 2.22. FTIR spectra of the (a) as-deposited plain CH_3-silica coating; (b) as-deposited plain silica coating on aluminum.[100]

The successful introduction of the organic methyl group inside the silica network of the CH_3-silica coating was verified with the aid of FTIR. As reported in Figure 2.22 (a), the presence of the characteristic CH_3-Si bond was visible at the 1250 cm^{-1} peak, together with the C-H bond vibration of CH_3 at 2970 cm^{-1}. All the sol-gel coatings showed the typical silica peaks at 1150-1070, 790 and 450 cm^{-1}, which correspond respectively to the longitudinal-transversal optical components of the Si-

O asymmetric stretching, the Si-O symmetric stretching and the Si-O-Si rocking vibrations. The 930 cm^{-1} peak indicates the presence of the O-H stretching vibrations of the unreacted Si-OH or $Si-O^-$ groups, while the wideband at 3600-3000 cm^{-1} arises from the water adsorption which leads to the Si-OH bonds.[101] When compared to the plain silica coating (Figure 2.22 (b)), the -OH vibrations of the CH_3-silica coating at the 3600-3000 cm^{-1} band decreased in intensity respect to the stronger vibrations detectable in the plain silica film. The weaker intensity of the adsorbed water constituted an additional confirmation of the presence of the methyl group inside the silica network, since organic group increase the hydrophobicity of a coating while reducing the percentage of adsorbed water.[101,102]

3.3.1.4 *Optimization of patterned morphology*[100]

Considering that the condensation mode and dynamics can be greatly influenced by the morphological and chemical properties of the condensing surface.[55,97] Previous studies exploited the sol-gel dewetting process to create patterns on silicon wafers.[91] In paragraph 2.3.1.4, the reproducibility of the patterned coatings on metallic substrates, which could be used for real applications, was assessed.

The concentration of the TEOS-based solution was varied to study the dewetting process on aluminum substrates. In the sol-gel process, the sol concentration is directly related to the thickness of the resulting thin film and therefore to the morphology of the dewetted droplets. The silica concentration of the initial colloidal solution was varied from 0.75 M to 2.0 M, which led to the corresponding patterns reported in Figure 2.23.

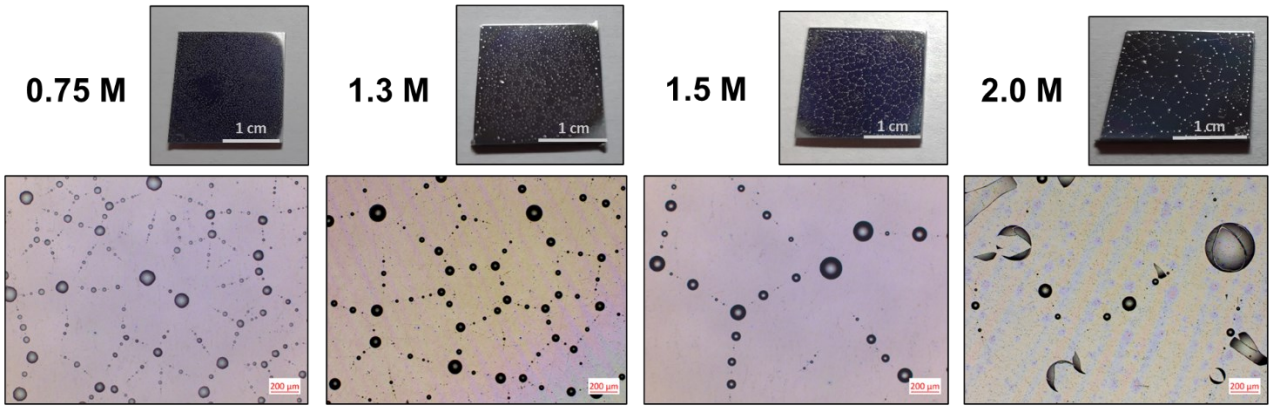


Figure 2.23. Photographs and optical microscope micrographs of patterned films on aluminum for different top silica layer concentrations. At 2.0 M cracks begin to form.[100]

The dewetting process was successfully reproduced and scaled on substrates with larger dimensions with respect to previously studied silicon wafers. Coherently with the latter, the linearity of the

correlation between the concentration or thickness with the mean diameter was confirmed for the aluminum substrates, as well as the correlation with the particle density (Figure 2.24 (a, b)).

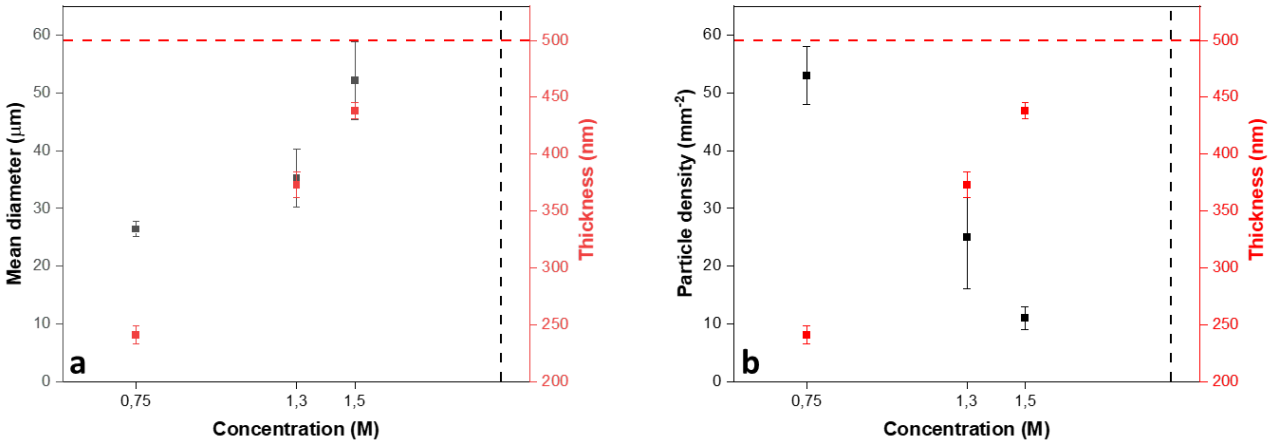


Figure 2.24. Correlation between (a) mean diameter, (b) particle density of each pattern with the corresponding concentration and thickness of the top silica layer. The dotted lines indicate the concentration and thickness limit above which the silica particles crack after the thermal treatment. Each value derives from the average of three different measurements with the standard deviation.[100]

The increasing concentration of the precursor solution led to an increase in the plain silica films' thickness and therefore to bigger mean diameters and lower particle densities (Figure 2.24 (a, b)). The mean diameter of the particles varied from 26.4 ± 1.3 µm to 52.1 ± 6.8 µm when the concentration increased from 0.75 M to 1.5 M, which simultaneously led to the variation of the particle density from 53 ± 5 to 11 ± 2 mm^{-2}. Analogously to previous patterns on silicon wafers[91], the existence of a lower limit in the tunability range was confirmed for the aluminum substrates. At concentrations below 0.75 M, the dewetting of the film occurred during the deposition step by spin coating and could not be controlled via exposure to the solvent saturated atmosphere. The higher value of the lower concentration limit determined a decrease in the tunability range of the droplets' sizes on aluminum respect to the one previously obtained for the silicon wafers. On the latter, the diameters could be varied by one order of magnitude (7.3 ± 1.3 - 59 ± 12 µm range) between 0.3 M and 1.3 M.[91] For 0.75 M concentration, nearly the same particles' diameter was found on both aluminum and silicon, despite the film's thickness being almost the double on aluminum (241 ± 8 nm) compared to the corresponding one on silicon (nearly 140 nm)[91]. By increasing the concentration to 1.3 M, the initial film's thickness was similar on both the substrates, but the diameter of the particles was nearly the double on aluminum (35 ± 5 µm) with respect to the ones on silicon (59 ± 12 µm).

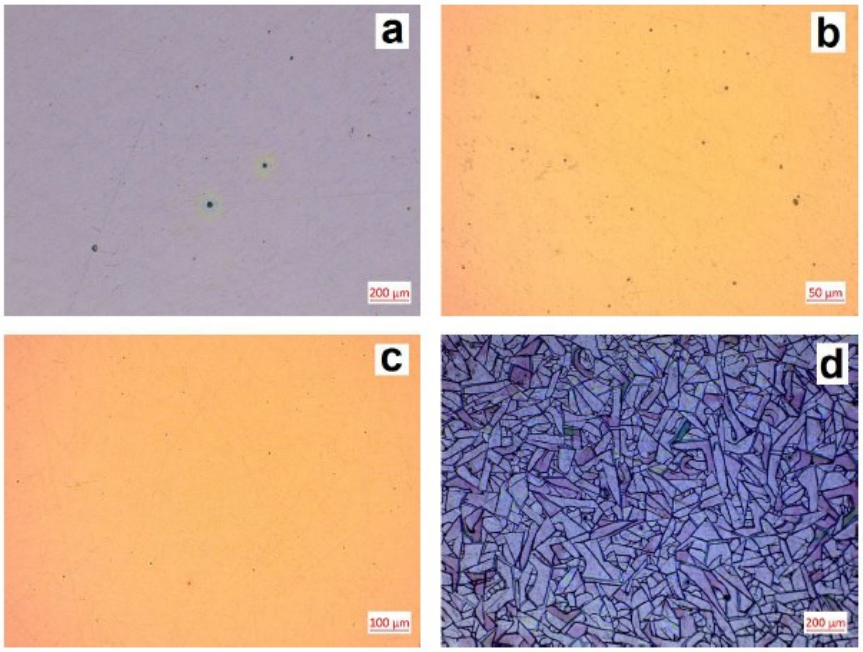


Figure 2.25. Optical micrographs of the plain silica films at different concentrations: a 0.75; b 1.3; c 1.5; d 2.0 M.[100]

To better mimic the 500 µm hydrophilic bumps of the beetle, the concentration was further increased up to 2.0 M compared to the values considered for the previous silicon substrates. As visible in Figure 2.25 (d), the corresponding plain silica film obtained from a 2.0 M solution was subjected to elevated stresses during the thermal treatment, which led to the formation of cracks throughout the film. Analogously, the cracks' formation is detectable on the dewetted particles obtained from 2.0 M solution (Figure 2.23). Therefore, an upper limit in the solution concentration was found, which limits the further increase of the particles' mean diameter.

An explanation of the different behavior, in terms of particles' size and dimension, between the silicon wafer and the aluminum substrate can be related to the surface properties of the two substrates. The two materials are characterized by substantially different surface tensions (around 0.07 J/m^2 for silicon wafers[103] and around 0.9 J/m^2 for pure aluminum[104]) and roughness, which strongly influence their interaction with the coatings. The surface roughness of the samples was evaluated by AFM. The root-mean-square roughness (rms) of the bare aluminum surface was 6.56 ± 0.69 nm, which is one order of magnitude higher with respect to the rms of the plain silicon wafer (0.2-0.3 nm)[91]. The higher roughness of the metallic surface is caused by the mechanical polishing procedure used to reach a mirror-like quality, which cannot completely guarantee the removal of impurities and asperities from the surface. The latter determines the formation of unwanted preferential nucleation sites, which influence, together with the physical-chemical surface properties, the final morphology of the dewetted droplets and could explain the increased particle densities with respect to the silicon

substrates. Globally, the reproducibility and scalability of the dewetting process were confirmed on the aluminum substrates.

3.3.2 *Coating durability under high relative humidity conditions*[100]

A fundamental prerequisite regarding the employment of the patterned coatings for industrial purposes is their resistance under the harsh conditions which often characterize the real working applications. The recent literature evidenced the critical interaction between the water molecules and the silane-based films, which suffer from delamination after a prolonged exposure to the water vapor.[78,97,105] As evidenced by Miljkovic and co-workers, the coating degradation initiates at specific pinholes present in the films, in which the osmotic pressure determines the rupture of the Si-O-X bonds due to the hydrolysis reactions.[97]

Before the humid air condensation tests, the coatings were preliminary tested in static conditions of high relative humidity, to verify the resistance prior to the condensation experiments. The patterned coatings and the plain CH_3-silica films, deposited on the squared smaller samples, were enclosed inside a home-made humidity test chamber for increasing exposure times of 1 day, 14 days and 30 days, respectively. The chamber consisted of a sealed glass vessel and the humidity was controlled by a saturated salt solution (Potassium Nitrate, 94-96% RH, 20-25°C)[106]. The RH was monitored by a commercial sensor (Bel-Art, Scienceware digital hygrometer). Three samples for each type of coating were tested.

As a representative patterned coating, the concentration of 1.3 M was chosen to be investigated, since the range of the sizes and distributions of the droplets on aluminum was substantially inferior to the one obtained on silicon wafers (paragraph 2.3.1). The corresponding mean diameter, particle density and percentage of the occupied surface of the patterned coatings, obtained from the image analysis of the optical micrographs, were reported in Table 2.6.

Table 2.6. Particle density, mean diameter, occupied surface, advancing, and receding contact angles of the as prepared sample before the condensation tests. The values derive from the average of three measurements with the standard deviation.[100]

	As prepared sample
Mean diameter (μm)	31.3 ± 8.5
Particle density (mm^{-2})	45.1 ± 17.3
Occupied surface (%)	3.4 ± 0.2
Θ_a (°)	82 ± 1
Θ_r (°)	70 ± 2

The hydrophilic bumps displayed a mean diameter of 31.3 ± 8.5 μm and were distributed on the surface with a density of 45.1 ± 17.3 particles/mm^2. The advancing and receding contact angles were 82° ± 1° and 70° ± 2°, respectively, similar to the plain CH_3-silica coating (paragraph 2.3.1.3). This can be explained by considering the percentage of surface occupied by the hydrophilic droplets on the bottom hydrophobic layer. The former was only nearly 3%, therefore the hydrophilic bumps provided a marginal contribution to the global dynamic contact angles. Moreover, the hysteresis of the contact angle of the patterned coating was similar to the plain CH_3-silica coating, confirming that the presence of the hydrophilic bumps on the surface does not constitute an obstacle to the liquid droplet's detachment during the vapor condensation.

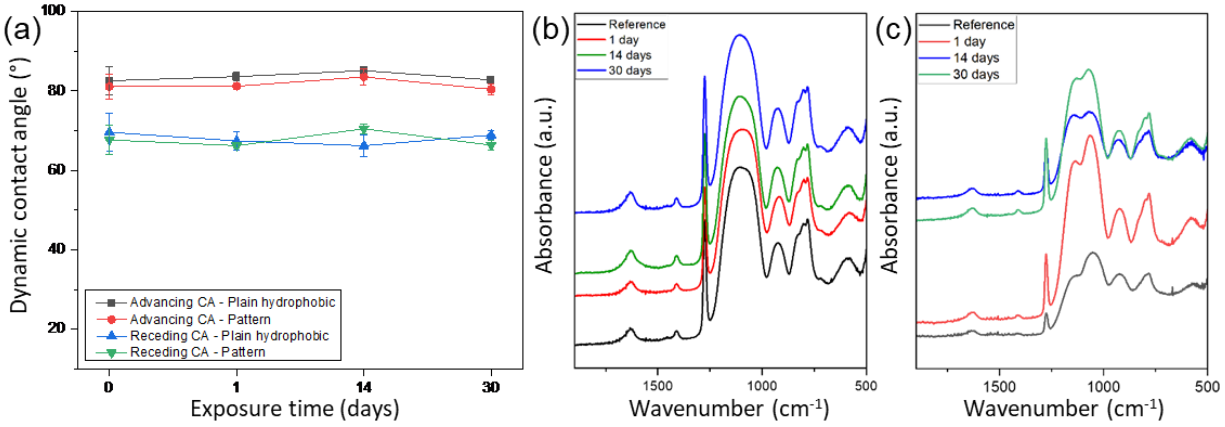


Figure 2.26. (a) Evolution of the dynamic contact angles, namely the advancing (Θ_a) and receding (Θ_r) contact angle, of the patterned coating and the plain CH_3-silica coating during the static tests of high relative humidity exposure (T=28°C, 95% RH). Each value derives from the average of three different measurements with the standard deviation. FTIR spectra of (b) as-deposited plain CH_3-silica coating; (c) as-deposited patterned coating on aluminum, before and after the static tests of exposure to high relative humidity (T=28°C, 95% RH).[100]

Following the static high humidity durability tests, the degradation was evaluated in terms of variation of the dynamic contact angles, vibrational FTIR peaks and morphology from the optical microscope. Both the patterned coating and the plain CH_3-silica film successfully proved their resistance to the high values of relative humidity for up to 30 days, demonstrating no variation in the dynamic contact angles (Figure 2.26 (a)). The FTIR measurements confirmed the presence of the vibrations of the bonds of the organic groups even after 30 days of tests (Figure 2.26 (b, c)).

3.3.3 *Humid air condensation tests*[100]

Having assessed the coatings' durability, the bigger squared aluminum substrates (see paragraph 2.3.1) were placed in a wind tunnel to study the humid air condensation over vertical metallic surfaces. After the stage of conditioning, the air enters the wind tunnel and it flows over the aluminum surface (A = 16 cm^2), where a fraction of the water vapor present in the airflow is condensed. The

condensate water is collected in a receiver that is weighed continuously by a high precision balance scale. Condensation tests were performed at constant air conditions (temperature of 28°C, relative humidity of 50%, and velocity of 1 m s^{-1}), while the dew-to-wall temperature difference (ΔT) was varied in the range 4–10 K by controlling the air-cooled Peltier device connected to the substrate. The tests start with the condensing surface dry. After the air inside the wind tunnel reached steady-state conditions, the Peltier element was activated to lower the temperature of the substrate. At this point, all experimental data, in particular the mass of the condensate produced, were recorded for 90 minutes. Each experimental data was given as the average of 30 measurements recorded over 1 minute with error bars representing the combined uncertainty, calculated considering the "Type A" and "Type B" components as described in the ISO Guide[107].

As shown in Figure 2.27, three samples were compared in terms of condensation dynamics, namely a bare aluminum sample, a plain hydrophobic sample (plain CH_3-silica film), and a patterned sample (hybrid patterned coating).

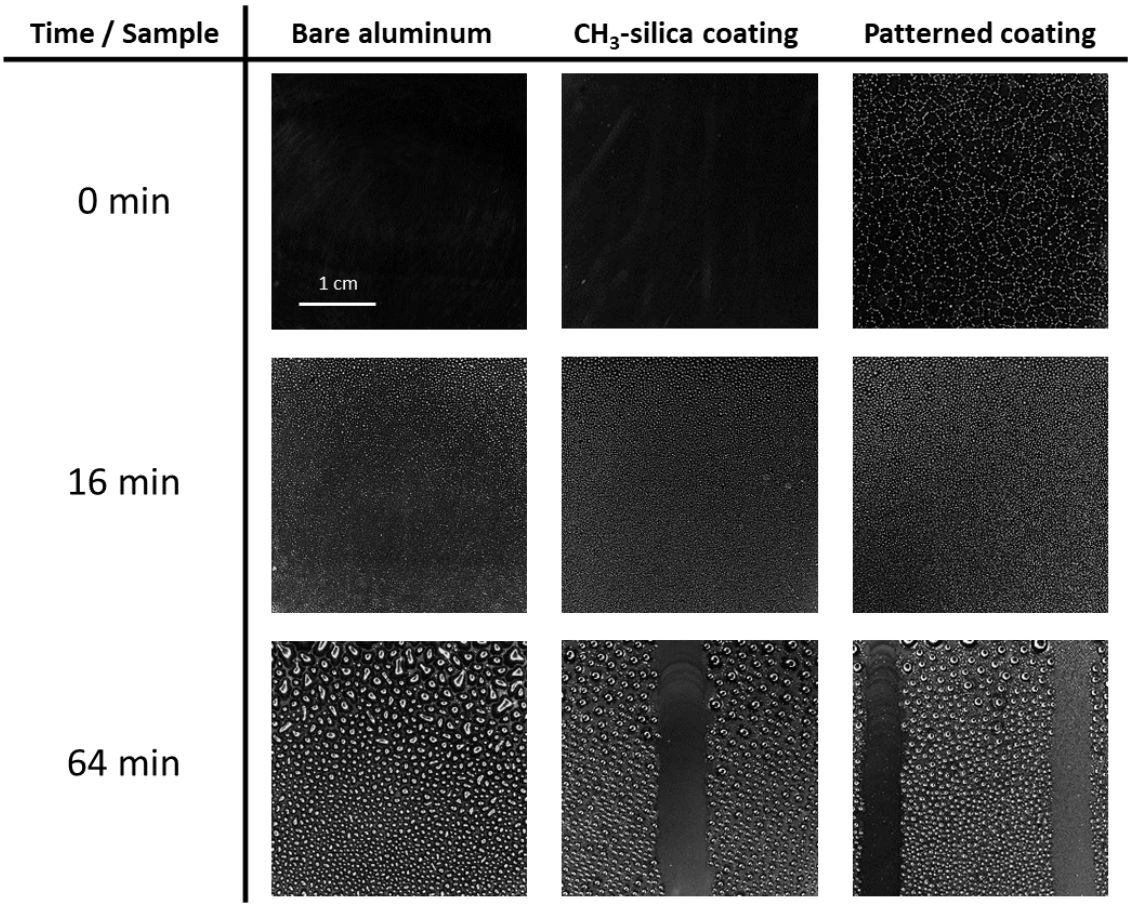


Figure 2.27. Evolution of the condensation process observed on the bare aluminum, the CH_3-silica coating and the patterned coating at the same operating conditions (ΔT = 4 K, T = 28°C, v_{air} = 1 m s^{-1} and RH = 50%).[100]

During the temporal evolution of the test, the condensate formed irregular liquid droplets on the bare aluminum surface. Due to the hydrophilicity of such substrate, the droplets exhibited a substantial

adhesion to the surface and a flat irregular morphology. The elevated affinity and superficial contact of the liquid droplets with the bare aluminum determined their gradual aggregation into non-uniform large droplets. On the contrary, the presence of a hydrophobic coating led to the promotion of dropwise condensation on the two coated substrates, with the formation of spherical-shaped isolated droplets. The increased hydrophobicity favored the liquid droplets' detachment from the sample and the renewal of the underlying surface, which were not allowed on the bare aluminum due to the subsequent aggregation of the droplets (Figure 2.27, 64 min).

During the first instants of the interaction between a surface and a water vapor, it is known that the nucleation of the droplets is enhanced on hydrophilic surfaces respect to hydrophobic ones.[85,86] After 60 seconds, the density of the small condensed droplets was considerably higher on the hydrophilic bumps respect to the surrounding hydrophobic areas (Figure 2.28). The presence of a hybrid morphology, composed of hydrophilic spots surrounded by hydrophobic areas, allowed to enhance both the nucleation and the removal of the liquid droplets, which is not possible to obtain on surfaces characterized by a single type of wettability. The hydrophilic bumps favored the increase in the nucleation density, but due to their small percentage with respect to the total surface area, they did not affect the condensation mode.

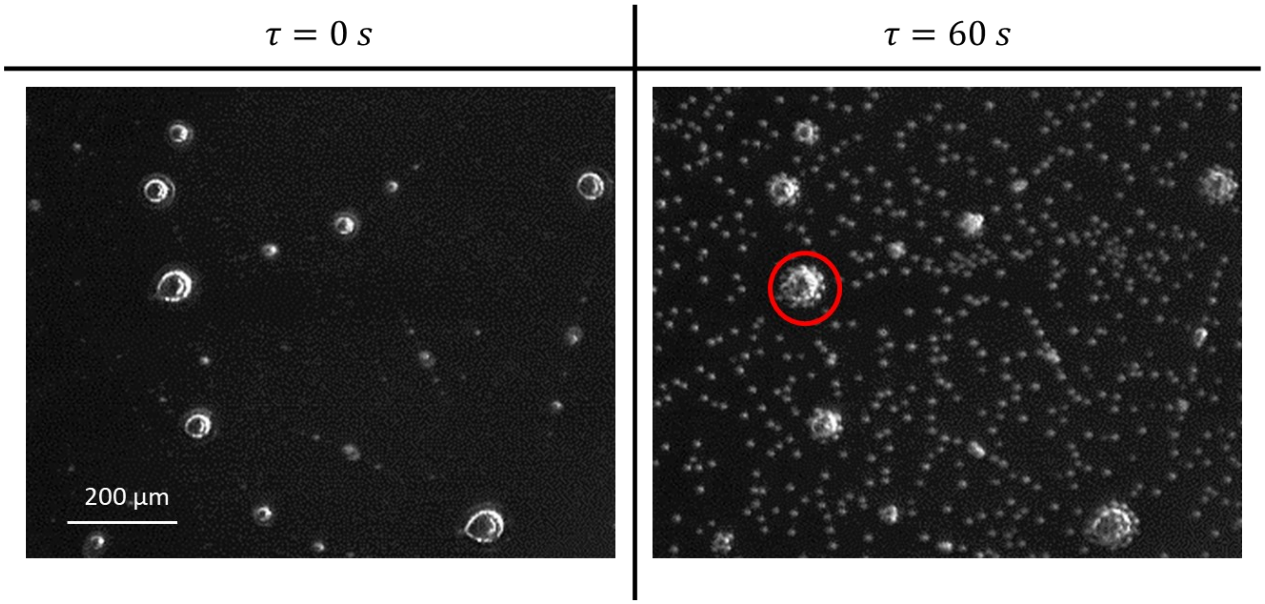


Figure 2.28. Evolution of the condensation process observed on the patterned coating. The images, obtained at the same operating conditions (T = 28°C, RH = 50%, v_{air} = 1 m s^{-1}, ΔT = 4 K), were recorded by using the high-speed camera coupled with microscopic lens (12x). Visualized area of ~1 mm^2. The red circle underlines a hydrophilic silica droplet where it is visible an increased density of condensed water droplets.[100]

The condensed mass collected during the condensation of humid air was evaluated at two different subcooling conditions (ΔT = 4 K, 10 K), namely at increasing differences between the dew temperature and the condensing surface temperature. The two conditions were selected to reproduce distinct industrial working conditions. The condensation performance was analyzed at increasing

times of 15, 30 and 60 minutes. From the results reported in Figure 2.29**,** the advantages provided by the presence of the hydrophobic coatings on the metallic surfaces were confirmed.

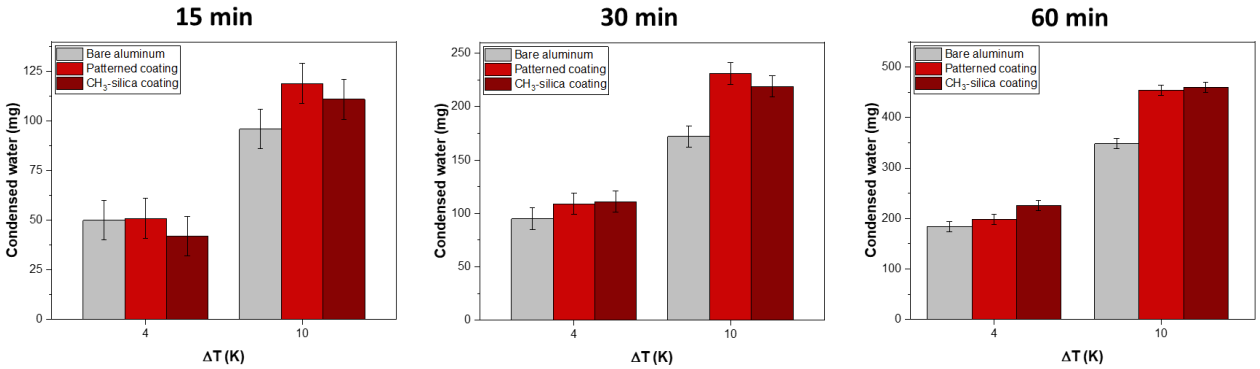


Figure 2.29. Condensed mass as a function of the subcooling degree of the bare aluminum, the patterned coating and the plain CH_3-silica coating, at the same operating conditions (T = 28°C, RH = 50%, v_{air} = 1 m s^{-1}, ΔT = 4-10 K). The error bars represent the experimental uncertainties calculated as described at the beginning of paragraph 2.3.3.[100]

For each subcooling degree, the condensed mass obtainable on the bare aluminum was far below the values reached in the case of both the hydrophobic films. During the first 15 minutes at ΔT = 4 K, the patterned coating and the bare aluminum substrate allowed an increase of the condensed mass by 20% with respect to the plain hydrophobic surface (Figure 2.29, 15 min). This behavior confirms the theoretical studies on the condensation dynamics, which stress that hydrophilic surfaces favor the nucleation of the liquid droplets.[57] During condensation in the presence of humid air, non-condensable gases strongly limit the overall condensation performance compared to the case of pure steam condensation.[56] Therefore, droplets nucleation and growth are slower and involve a significantly lower amount of condensed mass. Compared to the saturated vapor condensation, in the case of humid air the dynamics of the nucleation and growth are slower and involve a significantly lower amount of condensed mass. As shown in Figure 2.29, the bare aluminum substrate represented a typical hydrophilic material, which was also supported by the dynamic contact angles reported in paragraph 2.3.1.3. The surface of the patterned coating, despite the global hydrophobicity, was characterized by the presence of hydrophilic bumps, which favored the nucleation of the liquid droplets as visible in Figure 2.28. After 15 min at ΔT = 10K the patterned coating reached a 24% increase of the collected mass with respect to the bare aluminum, and a 9% increase with respect to the plain hydrophobic film. By increasing the subcooling degree, the driving force for the mass transfer mechanism increases and the condensation of the water vapor in humid air is favored, explaining the higher values of the condensed mass. With the raising of the interaction time between the humid air and the condensing surfaces at 30 minutes (Figure 2.29, 30 min) and subsequently at 60 minutes (Figure 2.29, 60 min), the condensation performance of the pattern started to be comparable to the plain CH_3-silica coating. The similar efficiencies promoted by the plain and the

patterned coatings can be explained by considering the weak wettability contrast in the pattern. The difference in wettability between the hydrophilic drops and the surrounding hydrophobic areas may be not sufficient to induce evident enhancements of the collected mass. Moreover, since the hysteresis of the contact angle was recently found to be a fundamental factor for the control of the condensation dynamics[108], besides the static contact angle, the similar values of both the parameters for the two samples, can also provide an explanation of the similar efficiencies of the two hydrophobic coatings. As confirmed by the literature[109], the formulation of a hybrid wettability requires careful optimization of both the morphology of the surface and the degree of the wettability contrast between the highly hydrophilic areas and the highly hydrophobic ones. Moreover, the optimized parameters of morphology and wettability may change as a function of the humid air conditions. In previous work[91], the patterned coating on the silicon substrate allowed to reach the maximum performance at very low degrees of subcooling (70% RH, $\Delta T_{d-w} = 3.3°C$), which represent the typical conditions found in arid environments. By changing the type of substrate, the different interactions with the coating led to a variation of the patterned morphology, namely of the particle size and density of distribution, and therefore to a change in the condensation performance. Nonetheless, the enhancement of the condensed mass provided by the presence of a hydrophobic coating on the metallic surface was confirmed also at increasing times of 30 and 60 minutes, together with the opportunity to control the condensation dynamics.

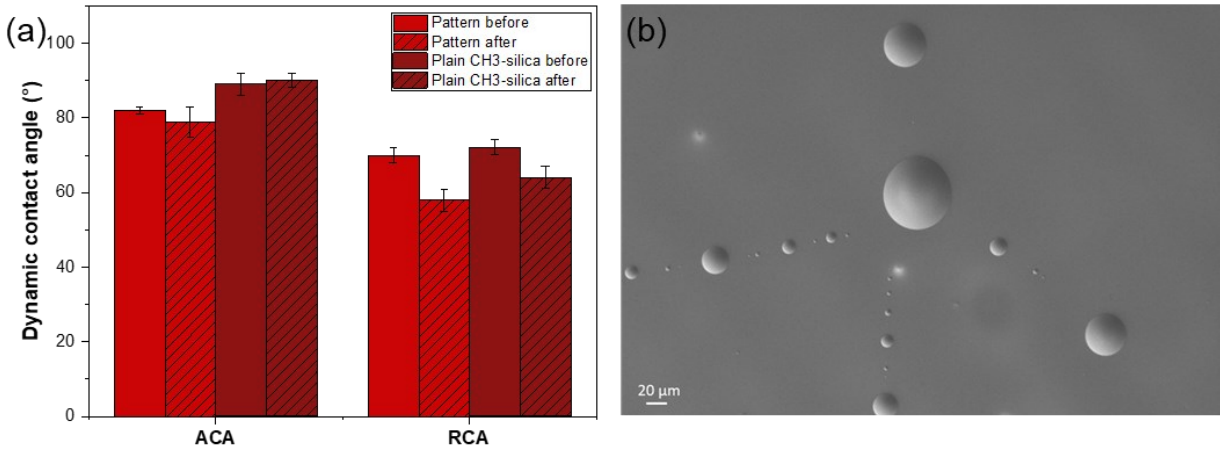


Figure 2.30. (a) Dynamic contact angles of the patterned coating and the plain CH_3-silica film, before and after the humid air condensation tests. Each value derives from the average of three different measurements with the standard deviation. (b) SEM images of the coated sample, after the humid air condensation.[100]

Following the humid air condensation tests, both the patterned coating and the plain hydrophobic films were characterized to verify any variation of their chemical and physical properties. Considering the dynamic contact angles (Figure 2.30 (a)), the unchanged value of the advancing contact angles confirmed the presence of the $-CH_3$ organic groups inside the hybrid silica network after the

condensation tests. A slight decrease of the receding contact angle was found after the condensation tests for both the hydrophobic samples.

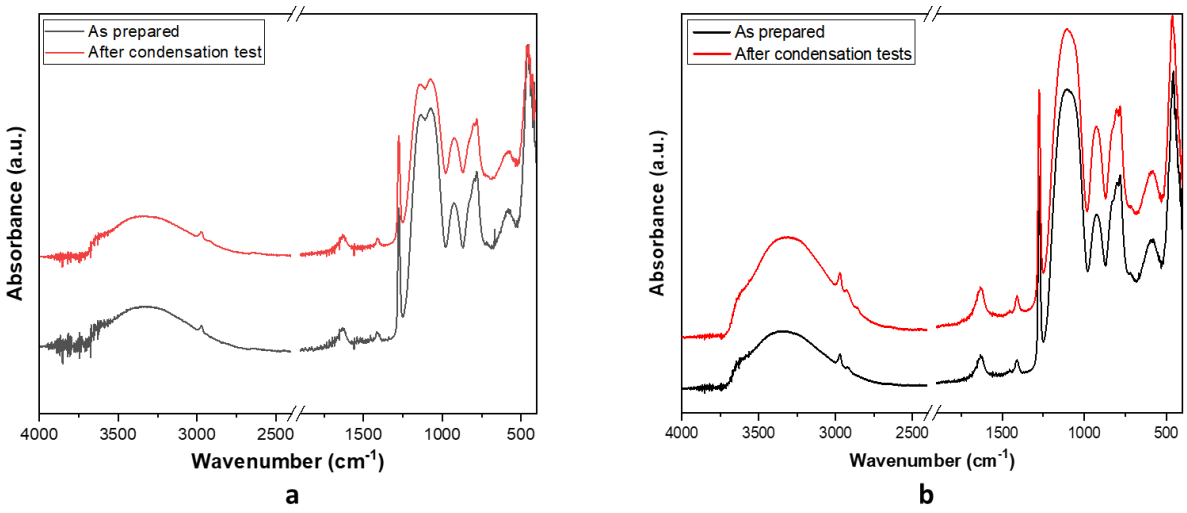


Figure 2.31. FTIR spectra before and after the humid air condensation tests on (a) the patterned coating and (b) the plain CH_3-silica coating. The tests were carried at the same operating conditions (T = 28 °C, RH = 50%, v_{air} = 1 m s^{-1}, $\Delta T_{d\text{-}w}$ = 4-13 K).[100]

Table 2.7. Ellipsometry measurements of the plain CH_3-silica film before and after the humid air condensation tests. Each value derives from the average of three different measurements with the standard deviation.[100]

	CH_3-silica coating
Before	360 ± 10 nm
After	370 ± 10 nm

Further confirmation of the presence at 1250 cm^{-1} of the characteristic peak of the organic groups, which are responsible for the hydrophobicity of the coatings, was provided by the FTIR spectra (Figure 2.31). The ellipsometry measurements on the plain CH_3-silica film confirmed that the thickness did not significantly vary after the condensation tests (Table 2.7), while the integrity of the coatings' surface was verified by the SEM analysis (Figure 2.30 (b)), since no cracks nor degradation signs appeared after the exposure to the high relative humidity environment. Therefore, the resistance to humid air condensation was verified for both the hydrophobic coatings.

3.3.4 *Bioinspired sol-gel micropatterns for humid air condensation – conclusions*[100]

In paragraph 2.3, the successful scalability and reproducibility of the dewetting process of silica-based sol-gel bilayers on metallic substrates was assessed. The diameter and the density of distribution of the dewetted droplets was controlled and tuned between nearly 26-52 μm and 53-11 particles/mm^2, respectively. To verify the feasibility for industrial applications, the influence of the patterned morphology during condensation from humid air was assessed in terms of condensed in a

custom-made apparatus. During the first 15 minutes of the condensation tests at 50% RH and ΔT=4-10K, the hydrophilic bumps of the pattern favored the formation of droplets compared to the surrounding hydrophobic areas, and respect to the bare aluminum, the patterned coating at subcooling degrees of 4-10 K enhanced the condensation performance by 21-24%, confirming the crucial role of the coatings in the control of the condensation dynamics. Future goals will be devoted to the investigation of different geometries and wettability contrasts of the pattern, to evaluate their influence on the condensation dynamics of the humid air.

3.4 Conclusions

In Chapter 2, the functional properties of hybrid silica (SiO_2) coatings were tuned and exploited to control the efficiency of heat exchangers and moisture collectors. As previously mentioned, several HVAC systems rely on metallic substrates, which typical hydrophilicity is unfavorable in terms of heat exchange efficiency due to the formation of a liquid film upon vapor condensation (filmwise condensation, FWC). In this Chapter, the condensation mode was controlled through the modification of both the chemical composition and the morphology of the substrate's surface, to induce a dropwise condensation (DWC). Silica-based sol-gel coatings were employed to control the condensation mode of both saturated vapor and humid air. The wettability of the coatings was optimized exploiting a hybrid organic-inorganic composition, in which organic groups were introduced to increase the hydrophobicity of plain SiO_2 coatings. The introduction of organic chains within the silica networks was proven to enhance the durability of the latter in water-based environments.[61] Indeed, a major challenge regarding the real-life application of heat exchangers is the durability of such coatings, as they face severe environmental conditions such as fouling, scratching, corrosion or high thermal stresses.[62]

In paragraph 2.2, the efficiency of hybrid octyl-modified SiO_2 coatings was evaluated during saturated vapor condensation, in terms of both thermal exchange and coating's durability.[53] The heat exchanged over time was examined on aluminum substrates in a custom-made heat exchange apparatus. The coatings successfully promoted the DWC with heat transfer coefficient (HTC) values of ~90 kW m^{-2} K^{-1}, an average 9-fold increase with respect to FWC under similar heat flux conditions.[5] The heat transfer performance remained stable during the overall duration of condensation experiments, which were stopped prior to a possible failure to investigate the detected changes in wettability and morphology. Straightforward accelerated degradation tests were performed on silicon substrates, to separate the different influencing factors, to evaluate the coating's

resistance prior to its real industrial application. If singularly applied, the possible degradation conditions did not lead to significant variations on the coating's properties, whereas the interaction with water at high temperature induced different degrees of degradation whether if bubble nucleation was present or avoided. Owing to the similar variations, in terms of wettability and morphology, which were found between the coatings deposited on aluminum and silicon substrates, the latter tests could successfully provide an estimation of the coating's durability during a broad range of LVPC applications.

In the second part of Chapter 2 (paragraph 2.3), bioinspired hybrid patterned coatings were employed to optimize the collection of moisture from humid air.[100] Hydrophobic methyl-modified SiO_2 coatings with hydrophilic bumps were developed via a sol-gel process, exploiting a dewetting mechanism to gain the patterned morphology. To verify the reliability of the pattern's application in real environments, the hybrid coatings were deposited and optimized on metallic aluminum surfaces. The diameter and the density of distribution of the dewetted droplets was controlled and tuned between nearly 26-52 μm and 53-11 particles/mm^2, respectively. The drainage rate of the patterned coatings during condensation from humid air was assessed in a custom-made apparatus and expressed in terms of condensed mass. During the first 15 minutes of the condensation tests at 50% RH 28°C and ΔT = 4-10K, the hydrophilic bumps of the pattern favored the formation of droplets with respect to the surrounding hydrophobic areas. With respect to the bare aluminum, the patterned coating at subcooling degrees of 4-10 K enhanced the condensation performance by 21-24%, confirming the crucial role of the coatings in controlling the condensation dynamics. Future goals will be devoted to the investigation of different geometries and wettability contrasts of the pattern, to evaluate their influence on the condensation dynamics of the humid air.

References

1. Davis, L. W. & Gertler, P. J. Contribution of air conditioning adoption to future energy use under global warming. *Proc Natl Acad Sci U S A* **112**, 5962–5967 (2015).

2. Cao, X. *et al.* Challenges and Opportunities toward Real Application of VO2-Based Smart Glazing. *Matter* **2**, 862–881 (2020).

3. Mazzone, A. *et al.* Understanding systemic cooling poverty. *Nature Sustainability 2023* 1–9 (2023) doi:10.1038/s41893-023-01221-6.

4. FAO. *The State of Food and Agriculture 2020. Overcoming water challenges in Agriculture*. *Fao* (2020).

5. Prado de Nicolás, A., Molina-García, Á., García-Bermejo, J. T. & Vera-García, F. Desalination, minimal and zero liquid discharge powered by renewable energy sources: Current status and future perspectives. *Renewable and Sustainable Energy Reviews* **187**, 113733 (2023).

6. Jonhson, W. *et al.* Fabrication of 3D-Printed Ceramic Structures for Portable Solar Desalination Devices. *ACS Appl Mater Interfaces* **13**, 23220–23229 (2021).

7. Aijaz, M. O. *et al.* Recent Progress, Challenges, and Opportunities of Membrane Distillation for Heavy Metals Removal. *The Chemical Record* **22**, e202100323 (2022).

8. Wang, X. *et al.* Review of droplet dynamics and dropwise condensation enhancement: Theory, experiments and applications. *Adv Colloid Interface Sci* **305**, 102684 (2022).

9. Rose, J. W. Dropwise condensation theory and experiment: A review. *Proceedings of the Institution of Mechanical Engineers, Part A: Journal of Power and Energy* **216**, 115–128 (2002).

10. Carey, V. P. *Liquid-Vapor Phase-Change Phenomena: An Introduction to the Thermophysics of Vaporization and Condensation Processes in Heat Transfer Equipment*. *Liquid-Vapor Phase-Change Phenomena* (CRC Press, 2020). doi:10.1201/9780429082221.

11. Snoeijer, J. H. & Andreotti, B. A microscopic view on contact angle selection. *Physics of Fluids* **20**, (2008).

12. Oestreich, J. L., van der Geld, C. W. M., Oliveira, J. L. G. & da Silva, A. K. Experimental condensation study of vertical superhydrophobic surfaces assisted by hydrophilic constructal-like patterns. *International Journal of Thermal Sciences* **135**, 319–330 (2019).

13. Goswami, A., Pillai, S. C. & McGranaghan, G. Surface modifications to enhance dropwise condensation. *Surfaces and Interfaces* **25**, 101143 (2021).

14. Miljkovic, N. & Wang, E. N. Condensation heat transfer on superhydrophobic surfaces. *MRS Bull* **38**, 397–406 (2013).

15. Ghosh, A., Beaini, S., Zhang, B. J., Ganguly, R. & Megaridis, C. M. Enhancing dropwise condensation through bioinspired wettability patterning. *Langmuir* **30**, 13103–13115 (2014).

16. Yuan, Y. & Lee, T. R. Contact angle and wetting properties. *Springer Series in Surface Sciences* **51**, 3–34 (2013).

17. Wu, X., Chu, F., Ma, Q. & Zhu, B. Frost formation and frost meltwater drainage characteristics on aluminum surfaces with grooved structures. *Appl Therm Eng* **118**, 448–454 (2017).

18. Thomas Young, B. & For Sec, M. D. III. An essay on the cohesion of fluids. *Philos Trans R Soc Lond* **95**, 65–87 (1805).

19. Wenzel, R. N. Resistance of solid surfaces to wetting by water. *Ind Eng Chem* **28**, 988–994 (1936).

20. Cassie, A. B. D. & Baxter, S. Wettability of porous surfaces. *Transactions of the Faraday Society* **40**, 546–551 (1944).

21. El Fil, B., Kini, G. & Garimella, S. A review of dropwise condensation: Theory, modeling, experiments, and applications. *Int J Heat Mass Transf* **160**, 120172 (2020).

22. Blossey, R. Self-cleaning surfaces — virtual realities. *Nature Materials 2003 2:5* **2**, 301–306 (2003).

23. Enright, R., Miljkovic, N., Alvarado, J. L., Kim, K. & Rose, J. W. Dropwise Condensation on Micro- and Nanostructured Surfaces. *Nanoscale and Microscale Thermophysical Engineering* **18**, 223–250 (2014).

24. Rose, J. W. Condensation Heat Transfer Fundamentals. *Chemical Engineering Research and Design* **76**, 143–152 (1998).

25. Bum-Jin, C., Sin, K., Min Chan, K. & Ahmadinejad, M. Experimental comparison of film-wise and drop-wise condensations of steam on vertical flat plates with the presence of air. *International Communications in Heat and Mass Transfer* **31**, 1067–1074 (2004).

26. Sikarwar, B. S., Khandekar, S. & Muralidhar, K. Mathematical modelling of dropwise condensation on textured surfaces. *Sadhana - Academy Proceedings in Engineering Sciences* **38**, 1135–1171 (2013).

27. Sikarwar, B. S., Battoo, N. K., Khandekar, S. & Muralidhar, K. Dropwise condensation underneath chemically textured surfaces: Simulation and experiments. *J Heat Transfer* **133**, (2011).

28. Leipertz, A. *Dropwise Condensation*. *VDI Heat Atlas* vol. J3 (Springer, Berlin, Heidelberg, 2010).

29. Kim, S. & Kim, K. J. Dropwise condensation modeling suitable for superhydrophobic surfaces. *J Heat Transfer* **133**, (2011).

30. Mu, C., Pang, J., Lu, Q. & Liu, T. Effects of surface topography of material on nucleation site density of dropwise condensation. *Chem Eng Sci* **63**, 874–880 (2008).

31. Fevre, E. J. Le & Rose, J. W. A theory of heat transfer by dropwise condensation. *International Heat Transfer Conference 3* 362–375 (1966) doi:10.1615/IHTC3.180.

32. Ma, X., Rose, J. W., Xu, D., Lin, J. & Wang, B. Advances in dropwise condensation heat transfer: Chinese research. *Chemical Engineering Journal* **78**, 87–93 (2000).

33. Wen, H. W. & Jer, R. M. On the heat transfer in dropwise condensation. *The Chemical Engineering Journal* **12**, 225–231 (1976).

34. Neumann, A. W., Abdelmessih, A. H. & Hameed, A. The role of contact angles and contact angle hysteresis in dropwise condensation heat transfer. *Int J Heat Mass Transf* **21**, 947–953 (1978).

35. Sikarwar, B. S., Khandekar, S., Agrawal, S., Kumar, S. & Muralidhar, K. Dropwise condensation studies on multiple scales. *Heat Transfer Engineering* **33**, 301–341 (2012).

36. Lafuma, A. & Quéré, D. Superhydrophobic states. *Nat Mater* **2**, 457–460 (2003).

37. Boreyko, J. B. & Chen, C. H. Self-propelled dropwise condensate on superhydrophobic surfaces. *Phys Rev Lett* **103**, 184501 (2009).

38. Dietz, C., Rykaczewski, K., Fedorov, A. G. & Joshi, Y. Visualization of droplet departure on a superhydrophobic surface and implications to heat transfer enhancement during dropwise condensation. *Appl Phys Lett* **97**, (2010).

39. Mirafiori, M., Parin, R., Bortolin, S. & Del Col, D. Experimental analysis of drop-size density distribution during dropwise condensation of steam. *J Phys Conf Ser* **1599**, (2020).

40. Rose, J. W. On the mechanism of dropwise condensation. *Int J Heat Mass Transf* **10**, 755–762 (1967).

41. Hou, Y., Yu, M., Chen, X., Wang, Z. & Yao, S. Recurrent filmwise and dropwise condensation on a beetle mimetic surface. *ACS Nano* **9**, 71–81 (2015).

42. Cha, H. *et al.* Nanoscale-Agglomerate-Mediated Heterogeneous Nucleation. *Nano Lett* **17**, 7544–7551 (2017).

43. Kaneko, S., Urata, C., Sato, T., Hönes, R. & Hozumi, A. Smooth and Transparent Films Showing Paradoxical Surface Properties: The Lower the Static Contact Angle, the Better the Water Sliding Performance. *Langmuir* **35**, 6822–6829 (2019).

44. Miljkovic, N., Enright, R. & Wang, E. N. Effect of droplet morphology on growth dynamics and heat transfer during condensation on superhydrophobic nanostructured surfaces. *ACS Nano* **6**, 1776–1785 (2012).

45. Chen, X. *et al.* Nanograssed Micropyramidal Architectures for Continuous Dropwise Condensation. *Adv Funct Mater* **21**, 4617–4623 (2011).

46. Park, K. C. *et al.* Condensation on slippery asymmetric bumps. *Nature* **531**, 78–82 (2016).

47. Yang, K. S., Lin, K. H., Tu, C. W., He, Y. Z. & Wang, C. C. Experimental investigation of moist air condensation on hydrophilic, hydrophobic, superhydrophilic, and hybrid hydrophobic-hydrophilic surfaces. *Int J Heat Mass Transf* **115**, 1032–1041 (2017).

48. Cha, H. *et al.* Dropwise condensation on solid hydrophilic surfaces. *Sci Adv* **6**, (2020).

49. Cheng, D. F., Urata, C., Yagihashi, M. & Hozumi, A. A Statically Oleophilic but Dynamically Oleophobic Smooth Nonperfluorinated Surface. *Angewandte Chemie International Edition* **51**, 2956–2959 (2012).

50. Xiao, R., Miljkovic, N., Enright, R. & Wang, E. N. Immersion Condensation on Oil-Infused Heterogeneous Surfaces for Enhanced Heat Transfer. *Scientific Reports 2013 3:1* **3**, 1–6 (2013).

51. Wong, T. S. *et al.* Bioinspired self-repairing slippery surfaces with pressure-stable omniphobicity. *Nature 2011 477:7365* **477**, 443–447 (2011).

52. Rykaczewski, K. *et al.* Dropwise Condensation of Low Surface Tension Fluids on Omniphobic Surfaces. *Scientific Reports 2014 4:1* **4**, 1–8 (2014).

53. Basso, M. *et al.* Hydrophobic hybrid silica sol-gel coating on aluminium: Stability evaluation during saturated vapour condensation. *Journal of Non-Crystalline Solids: X* **17**, 100143 (2023).

54. Hou, Y., Yu, M., Chen, X., Wang, Z. & Yao, S. Recurrent filmwise and dropwise condensation on a beetle mimetic surface. *ACS Nano* **9**, 71–81 (2015).

55. Ghosh, A., Beaini, S., Zhang, B. J., Ganguly, R. & Megaridis, C. M. Enhancing dropwise condensation through bioinspired wettability patterning. *Langmuir* **30**, 13103–13115 (2014).

56. Huang, J., Zhang, J. & Wang, L. Review of vapor condensation heat and mass transfer in the presence of non-condensable gas. *Appl Therm Eng* **89**, 469–484 (2015).

57. Rose, J. W. Dropwise condensation theory and experiment: A review. *Proceedings of the Institution of Mechanical Engineers, Part A: Journal of Power and Energy* **216**, 115–128 (2002).

58. Bortolin, S., Tancon, M. & del Col, D. Heat Transfer Enhancement During Dropwise Condensation Over Wettability-Controlled Surfaces. *The Surface Wettability Effect on Phase Change* 29–67 (2022) doi:10.1007/978-3-030-82992-6_3.

59. De Ferri, L., Lottici, P. P., Lorenzi, A., Montenero, A. & Vezzalini, G. Hybrid sol-gel based coatings for the protection of historical window glass. *J Solgel Sci Technol* **66**, 253–263 (2013).

60. Tancon, M. *et al.* Dropwise condensation mechanisms when varying vapor velocity. *Appl Therm Eng* **216**, 119021 (2022).

61. Metroke, T. L., Gandhi, J. S. & Apblett, A. Corrosion resistance properties of Ormosil coatings on 2024-T3 aluminum alloy. *Prog Org Coat* **50**, 231–246 (2004).

62. Jin, H. *et al.* Recent advances in emerging integrated antifouling and anticorrosion coatings. *Mater Des* **213**, 110307 (2022).

63. Parin, R., Sturaro, M., Bortolin, S., Martucci, A. & del Col, D. Heat transfer during dropwise condensation of steam over a mirror polished sol-gel coated aluminum substrate. *International Journal of Thermal Sciences* **144**, 93–106 (2019).

64. Parin, R., Rigon, M., Bortolin, S., Martucci, A. & del Col, D. Optimization of Hybrid Sol-Gel Coating for Dropwise Condensation of Pure Steam. *Materials* **13**, 878 (2020).

65. Parin, R. *et al.* Heat transfer and droplet population during dropwise condensation on durable coatings. *Appl Therm Eng* **179**, 115718 (2020).

66. Basso, M. *et al.* Bioinspired silica-based sol–gel micropatterns on aluminium for humid air condensation. *J Solgel Sci Technol* **102**, 466–477 (2022).

67. Sharma, C. S., Stamatopoulos, C., Suter, R., Von Rohr, P. R. & Poulikakos, D. Rationally 3D-Textured Copper Surfaces for Laplace Pressure Imbalance-Induced Enhancement in Dropwise Condensation. *ACS Appl Mater Interfaces* **10**, 29127–29135 (2018).

68. Torresin, D., Tiwari, M. K., Del Col, D. & Poulikakos, D. Flow condensation on copper-based nanotextured superhydrophobic surfaces. *Langmuir* **29**, 840–848 (2013).

69. Del Col, D., Parin, R., Bisetto, A., Bortolin, S. & Martucci, A. Film condensation of steam flowing on a hydrophobic surface. *Int J Heat Mass Transf* **107**, 307–318 (2017).

70. Kim, S. & Kim, K. J. Dropwise condensation modeling suitable for superhydrophobic surfaces. *J Heat Transfer* **133**, 1–8 (2011).

71. Innocenzi, P., Falcaro, P., Grosso, D. & Babonneau, F. Order-disorder transitions and evolution of silica structure in self-assembled mesostructured silica films studied through FTIR spectroscopy. *Journal of Physical Chemistry B* **107**, 4711–4717 (2003).

72. Wen, R., Xu, S., Ma, X., Lee, Y. C. & Yang, R. Three-Dimensional Superhydrophobic Nanowire Networks for Enhancing Condensation Heat Transfer. *Joule* **2**, 269–279 (2018).

73. Preston, D. J., Mafra, D. L., Miljkovic, N., Kong, J. & Wang, E. N. Scalable graphene coatings for enhanced condensation heat transfer. *Nano Lett* **15**, 2902–2909 (2015).

74. Paxson, A. T., Yagüe, J. L., Gleason, K. K. & Varanasi, K. K. Stable dropwise condensation for enhancing heat transfer via the initiated chemical vapor deposition (iCVD) of grafted polymer films. *Advanced Materials* **26**, 418–423 (2014).

75. Rausch, M. H., Fröba, A. P. & Leipertz, A. Dropwise condensation heat transfer on ion implanted aluminum surfaces. *Int J Heat Mass Transf* **51**, 1061–1070 (2008).

76. Guglielmi, M. Sol-gel coatings on metals. *Journal of Sol-Gel Science and Technology 1997 8:1* **8**, 443–449 (1997).

77. Ma, J. *et al.* Condensation Induced Delamination of Nanoscale Hydrophobic Films. *Adv Funct Mater* **29**, 1905222 (2019).

78. Juan-Díaz, M. J. *et al.* Study of the degradation of hybrid sol-gel coatings in aqueous medium. *Prog Org Coat* **77**, 1799–1806 (2014).

79. Ruiz-Cabello, F. J. M. *et al.* Testing the performance of superhydrophobic aluminum surfaces. *J Colloid Interface Sci* **508**, 129–136 (2017).

80. Jonhson, W. *et al.* Fabrication of 3D-Printed Ceramic Structures for Portable Solar Desalination Devices. *ACS Appl Mater Interfaces* **13**, 23220–23229 (2021).

81. Yarlagadda, S., Gude, V. G., Camacho, L. M., Pinappu, S. & Deng, S. Potable water recovery from As, U, and F contaminated ground waters by direct contact membrane distillation process. *J Hazard Mater* **192**, 1388–1394 (2011).

82. Wen, R., Ma, X., Lee, Y. C. & Yang, R. Liquid-Vapor Phase-Change Heat Transfer on Functionalized Nanowired Surfaces and Beyond. *Joule* **2**, 2307–2347 (2018).

83. Yang, K. S., Lin, K. H., Tu, C. W., He, Y. Z. & Wang, C. C. Experimental investigation of moist air condensation on hydrophilic, hydrophobic, superhydrophilic, and hybrid hydrophobic-hydrophilic surfaces. *Int J Heat Mass Transf* **115**, 1032–1041 (2017).

84. Park, K. C. *et al.* Condensation on slippery asymmetric bumps. *Nature* **531**, 78–82 (2016).

85. Durán, I. R. & Laroche, G. Water drop-surface interactions as the basis for the design of anti-fogging surfaces: Theory, practice, and applications trends. *Adv Colloid Interface Sci* **263**, 68–94 (2019).

86. Miljkovic, N., Enright, R. & Wang, E. N. Effect of droplet morphology on growth dynamics and heat transfer during condensation on superhydrophobic nanostructured surfaces. *ACS Nano* **6**, 1776–1785 (2012).

87. Pan, T. & Wang, W. From cleanroom to desktop: Emerging micro-nanofabrication technology for biomedical applications. *Ann Biomed Eng* **39**, 600–620 (2011).

88. Kim, S. H., Lee, S. Y., Yang, S. M. & Yi, G. R. Self-assembled colloidal structures for photonics. *NPG Asia Mater* **3**, 25–33 (2011).

89. He, F. *et al.* Femtosecond laser fabrication of monolithically integrated microfluidic sensors in glass. *Sensors (Switzerland)* **14**, 19402–19440 (2014).

90. Lei, Y., Yang, S., Wu, M. & Wilde, G. Surface patterning using templates: Concept, properties and device applications. *Chem Soc Rev* **40**, 1247–1258 (2011).

91. Colusso, E., Martucci, A. & Neto, C. Fabrication of Biomimetic Micropatterned Surfaces by Sol–Gel Dewetting. *Adv Mater Interfaces* **6**, 1–11 (2019).

92. Zhao, J. *et al.* Effects of molecular weight, solvent and substrate on the dewetting morphology of polystyrene films. *Appl Surf Sci* **236**, 131–140 (2004).

93. Telford, A. M., Thickett, S. C. & Neto, C. Functional patterned coatings by thin polymer film dewetting. *J Colloid Interface Sci* **507**, 453–469 (2017).

94. Thickett, S. C., Neto, C. & Harris, A. T. Biomimetic surface coatings for atmospheric water capture prepared by dewetting of polymer films. *Advanced Materials* **23**, 3718–3722 (2011).

95. Al-Khayat, O., Hong, J. K., Geraghty, K. & Neto, C. 'The Good, the Bad, and the Slippery': A Tale of Three Solvents in Polymer Film Dewetting. *Macromolecules* **49**, 6590–6598 (2016).

96. Kwon, S. J. & Park, J. G. Dewetting of a sol-gel-derived thin film. *Langmuir* **22**, 3895–3898 (2006).

97. Khodakarami, S., Zhao, H., Rabbi, K. F. & Miljkovic, N. Scalable corrosion-resistant coatings for thermal applications. *ACS Appl Mater Interfaces* **13**, 4519–4534 (2021).

98. Ma, J., Cha, H., Kim, M. K., Cahill, D. G. & Miljkovic, N. Condensation Induced Delamination of Nanoscale Hydrophobic Films. *Adv Funct Mater* **29**, 1–10 (2019).

99. Parin, R. *et al.* Heat transfer and droplet population during dropwise condensation on durable coatings. *Appl Therm Eng* **179**, 115718 (2020).

100. Basso, M. *et al.* Bioinspired silica-based sol–gel micropatterns on aluminium for humid air condensation. *J Solgel Sci Technol* **102**, 466–477 (2022).

101. Innocenzi, P., Abdirashid, M. O. & Guglielmi, M. Structure and properties of sol-gel coatings from methyltriethoxysilane and tetraethoxysilane. *J Solgel Sci Technol* **3**, 47–55 (1994).

102. Yang, J., Chen, J. & Song, J. Studies of the surface wettability and hydrothermal stability of methyl-modified silica films by FT-IR and Raman spectra. *Vib Spectrosc* **50**, 178–184 (2009).

103. Pasquariello, D., Lindeberg, M., Hedlund, C. & Hjort, K. Surface energy as a function of self-bias voltage in oxygen plasma wafer bonding. *Sens Actuators A Phys* **82**, 239–244 (2000).

104. Bainbridge, I. F. & Taylor, J. A. The surface tension of pure aluminum and aluminum alloys. *Metall Mater Trans A Phys Metall Mater Sci* **44**, 3901–3909 (2013).

105. Dalmoro, V. *et al.* Improving the corrosion performance of hybrid sol-gel matrix by modification with phosphonic acid. *Prog Org Coat* **80**, 49–58 (2015).

106. Greenspan, L. Humidity fixed points of binary saturated aqueous solutions. **81**, (1977).

107. Evaluation of measurement data — Guide to the expression of uncertainty in measurement. (2008).

108. Kaneko, S., Urata, C., Sato, T., Hönes, R. & Hozumi, A. Smooth and Transparent Films Showing Paradoxical Surface Properties: The Lower the Static Contact Angle, the Better the Water Sliding Performance. *Langmuir* **35**, 6822–6829 (2019).

109. Ghosh, A., Beaini, S., Zhang, B. J., Ganguly, R. & Megaridis, C. M. Enhancing dropwise condensation through bioinspired wettability patterning. *Langmuir* **30**, 13103–13115 (2014).

Chapter 3
Vanadium dioxide (VO_2)

Table of contents

3 Chapter 3 – Vanadium dioxide (VO_2) 103

3.1 Introduction 105

3.2 Vanadium oxides 105

3.3 Crystallographic structures of VO_2 polymorphs 106

3.4 Electronic structures of VO_2 109

3.5 Metal-insulator transition mechanism of VO_2 111

3.5.1 Mott-Hubbard transition 112

3.5.2 Peierls transition 112

3.5.3 Current perspectives 113

3.6 Optical and electrical properties of VO_2 114

3.6.1 Luminous transmittance 115

3.6.2 Solar modulation 116

3.6.3 Hysteresis and transition temperatures of heating/cooling cycles 117

3.7 Applications and challenges of VO_2 118

3.7.1 VO_2 applications 118

3.7.2 VO_2 challenges 121

3.7.2.1 Transition temperature 121

3.7.2.2 Thermochromic performance 122

3.7.2.3 Long-term stability 123

3.7.2.4 Environmental friendliness 124

3.7.2.5 Color and skin-comfort design 124

3.7.2.6 Flexible fabrication 125

3.7.2.7 Current work 125

4.1 Introduction

As mentioned in the Abstract section, the challenge posed by the systemic cooling poverty requires new paths with respect to conventional air conditioning systems.[1-3] An alternative or synergic solution is represented by thermochromic smart windows, which offer a passive modulation of the solar irradiation without the need of active energy inputs for activation. The modulation of the solar radiation offers great advantages in terms of energy-saving applications. Within the latter, vanadium dioxide (VO_2) has emerged as a promising material regarding the creation of passive thermochromic smart windows. In this chapter, the crystallographic and electronic structure of VO_2 will be presented, along with the metal-insulator transition mechanism, the optical and electrical properties. In the final part, the current challenges and applications of VO_2 will be highlighted.

4.2 Vanadium oxides

Vanadium ($[Ar]3d^3 4s^2$) forms nearly 20 types of the corresponding oxide phases. The strong electron-lattice interactions and electron-electron correlations of several vanadium oxides have been extensively exploited for a wide range of applications, as will be addressed in paragraph 3.6.[4,5]

Among the multiple available oxides (Figure 3.1), V_2O_5, VO_2 and V_2O_3 are sensible to external stimuli such as temperature, electromagnetic radiation, or electric fields. Stoichiometries such as V_6O_{13}, V_4O_9, or VO, $V_{10}O_9$, are often metastable as they display small decomposition energies into stable phases (≤ 100 meV / atom).[4,5]

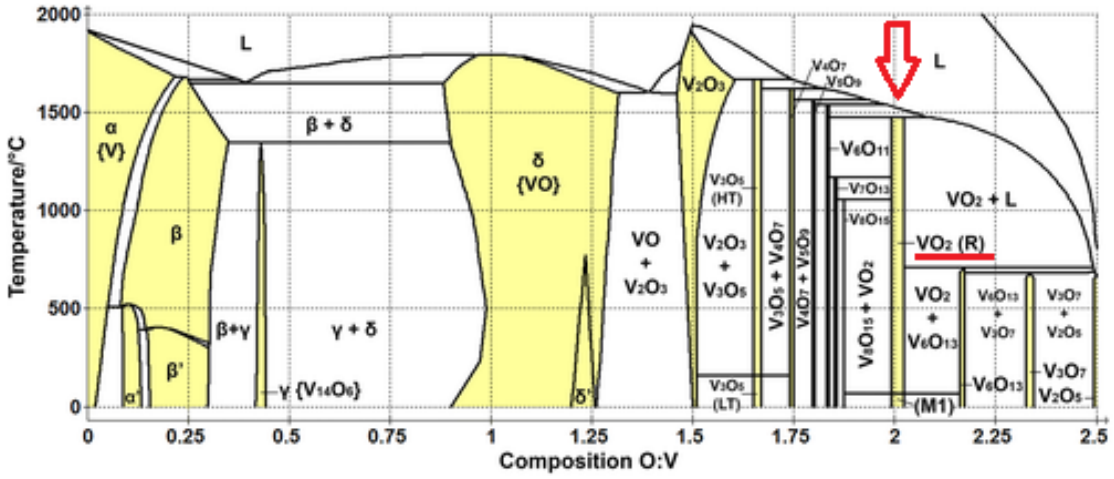


Figure 3.1. Vanadium-oxygen phase diagram.[6]

Among the several oxide phases, vanadium dioxide (VO_2) displays more than 10 polymorphs, such as VO_2 (M), VO_2 (A) or VO_2 (B), which share the same chemical formula but hold totally different

crystalline structure, optical and electrical properties.[7] The vanadium-oxygen system is known to be highly influenced by the synthesis and growth conditions, for all deposition methods.[8] Minimal deviations with respect to the optimal V:O ratio are capable to induce the formation of long-range order defects or additional and unwanted oxide phases. Oxygen deficiencies during the growth of VO_2 lead to Magnelì phases (V_nO_{2n-1}), with n = 3–9, whereas oxygen-rich environments favor the formation of Wadsley phases (V_nO_{2n+1}), with n = 2, 3, 6.[4,9]

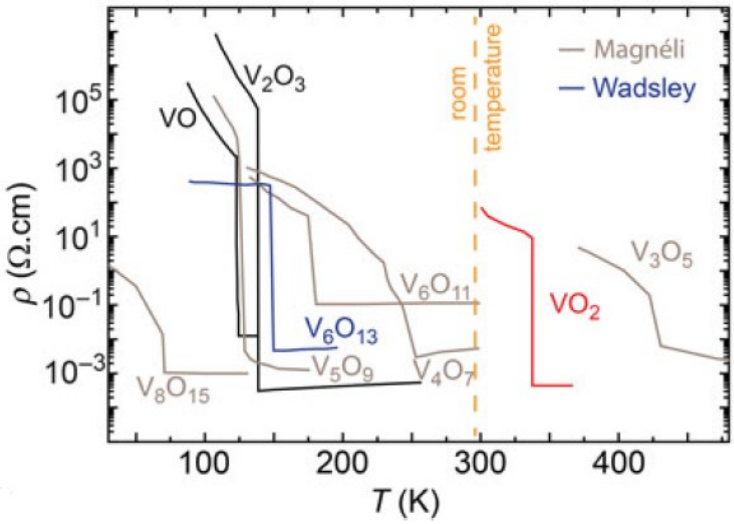


Figure 3.2. Resistivity versus temperature for various V–O phases, with a MIT at different temperatures. [9]

Several vanadium oxides are phase change materials (PCM), as they display a phase change upon external variations of temperature, pressure, electric or magnetic field.[4] While the transition temperatures to activate the phase change vary within a ~300 K range, the remarkable abundance of research studies on VO_2 is explained by the transition temperature (T_c) of the oxide (Figure 3.2). The latter is ~68°C for bulk VO_2, which is sufficiently close to room temperature, with respect to other oxide phases.[2]

4.3 Crystallographic structures of VO_2 polymorphs

As previously mentioned, vanadium dioxide exhibits various polymorphs, including VO_2 (M) ($P\,2_1/c$), VO_2 (R) ($P\,4_2/mnm$), VO_2 (A) ($P\,4_2/nmc$), VO_2 (B) ($C\,2/m$), VO_2 (C) ($I\,4/mmm$), VO_2 (D) ($P\,2/c$) and VO_2 (P) ($Pbnm$) (Figure 3.3).[10] The polymorphs share the same chemical formula, but substantially differ in terms of crystalline and electronic structures, along with optical, electrical and chemical properties. VO_2 (A), (B), (D) display a phase change, but the transition is not reversible. For the latter oxides, immense strain or stress transformations are required to induce the phase change, which cannot be reversed once applied.[11] On the contrary, monoclinic VO_2 (M1) and rutile VO_2 (R)

are characterized by a fully reversible phase transition, with the additional advantage of a T_c close to room temperature. The crystallographic structure of the latter is displayed in Figure 3.4.

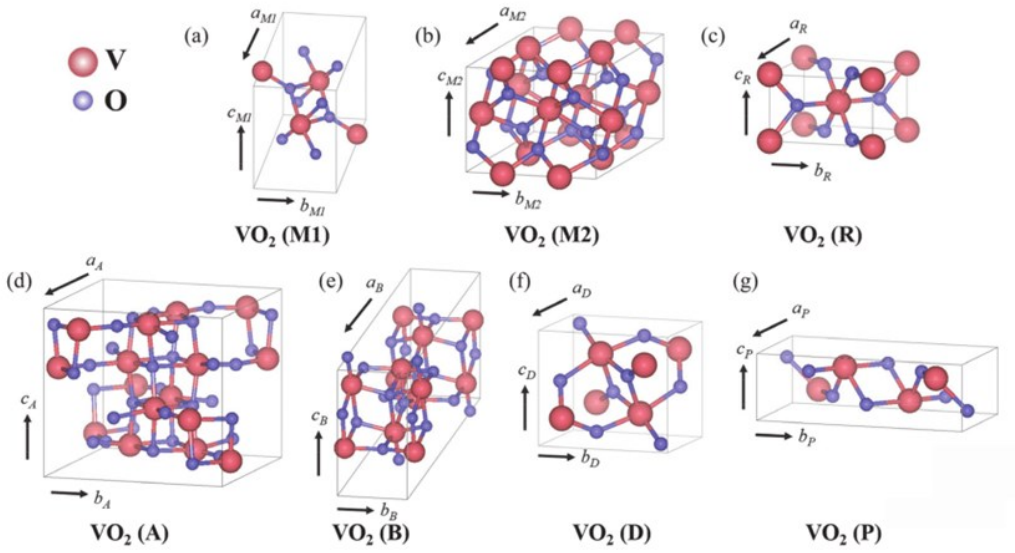


Figure 3.3. Crystalline structures of several polymorphs of VO_2.[10]

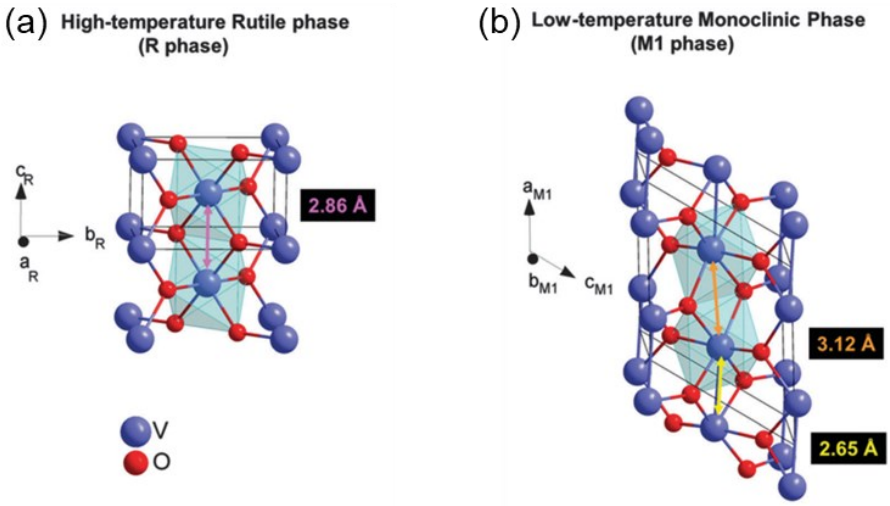


Figure 3.4. Crystallographic cells of (a) tetragonal rutile (R, space group $P4_2/nm$, $a_R = b_R = 4.55$ Å, $c_R = 2.86$ Å) and (b) monoclinic (M1, space group $P2_1/c$, $a_M = 5.75$ Å, $b_M = 4.52$ Å, $c_M = 5.38$ Å, $\beta = 122.6°$) VO_2.[12]

At room temperature, VO_2 is stable in the monoclinic (M1) structure, whereas at temperatures above the T_c, the phase transition to rutile VO_2 (R) is favored. In the latter (Figure 3.4 (a)), the tilted VO_6 octahedra exhibit a body-centered cubic structure, in which the hexacoordinated vanadium atoms are located at the center positions. The edge-sharing VO_6 octahedra, which display a V-V spacing of ~2.86 Å, are oriented linearly along the crystallographic c axis and share corners in the a-b plane. Upon the metal-insulator transition (MIT) from VO_2 (R) to VO_2 (M1), the crystal symmetry of the tetragonal phase is broken as the V atoms move along the V-V direction. With respect to the rutile structure, the monoclinic VO_2 (M1) is stable at room temperature (Figure 3.4 (b)) and the unit

cell volume is doubled. The two structures are linked by the following unit vector relations: $a_{mono} = 2c_{tetra}$, $b_{mono} = a_{tetra}$, and $c_{mono} = a_{tetra} - c_{tetra}$.[13] The MIT from R to M1 induces a structural distortion and a consequent change the V-V distances along a_M axis. Two different V-V distances are displayed in the monoclinic structure, namely ~3.12 Å and ~2.65 Å (Figure 3.4 (b)). The shorter V-V distance of ~2.65 Å was found to be lower with respect to the critical value for 3*d* electron coupling interaction, which is $R_c \sim 2.93 \pm 0.04$ Å.[14] This was phenomenologically deduced in the pioneering studies by Goodenough[14], from the observation of the physical properties of several isostructural compounds. The atomic displacement of the longer V-V distance (3.12 Å > R_c) interrupts the electron delocalization, with a resulting insulating/semiconductor behavior. Contrarily to the rutile state, in the monoclinic structure the 3*d* valence electrons of V atoms are no longer delocalized along the whole axis, but only between the closest V-V pairs.[12,13]

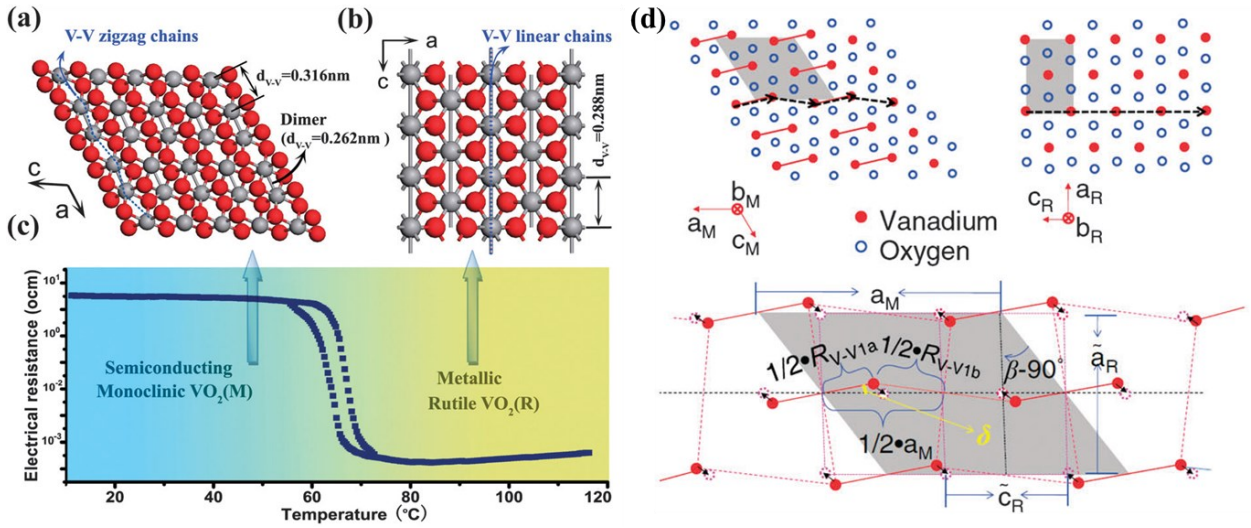


Figure 3.5. Atomic crystal structure of VO_2 (M): (a) projected along the b-axis of the monoclinic cell with the zigzag-type vanadium atom chains; (b) projected along b-axis of the rutile cell with the infinite linear V–V chains. (c) Temperature dependence of the resistivity based on the fully-reversible phase transition. (d) In situ XAFS investigation into the MIT process in VO_2 (M). (a) The top panel shows the microscopic atomic structures of VO_2 (M) and VO_2 (R) projected along [010]. The distortion of vanadium atoms is outlined by black arrows along the aM axis (c_R). The bottom panel shows the motions of the V atoms and the relations of the unit cell parameters between the two phases. The twisted angle of the V–V pairs is noted as δ.[15]

In the monoclinic structure, the V atoms are displaced with respect to the center of the octahedra. The V atoms dimerization along the a_M axis (Figure 3.5 (a)) is an example of antiferromagnetic displacement.[14,16] Upon the R → M1 transition, besides the dimerization, the V–V pairs undergo tilting from the c-axis and twisting from the linear chains to the zig-zag configuration (Figure 3.5 (d)).[15] The rutile phase displays well-aligned V-V chains, which distance along the rutile *c*-axis (c_R-axis) is lower with respect to R_c (Figure 3.5 (b)). From a structural point of view, the metallic behavior of the rutile phase is explained by the $3d^1$ electrons, which are shared by the V atoms along the c_R axis.[17] VO_2 (M1) is transparent in the infrared (IR) region and displays a high electrical resistivity,

whereas VO_2 (R) is opaque to IR wavelengths and displays a low electrical resistivity, with values more than 3 orders of magnitude lower with respect to VO_2 (M1).[17,18]

4.4 Electronic structures of VO_2

The structural transition in VO_2 is manifested along with a concurrent change in the electronic band structure near the Fermi level. In his pioneering studies, Goodenough proposed a qualitative explanation of the VO_2 electronic structure with the aid of crystal-field theory (CFT).[14,19]

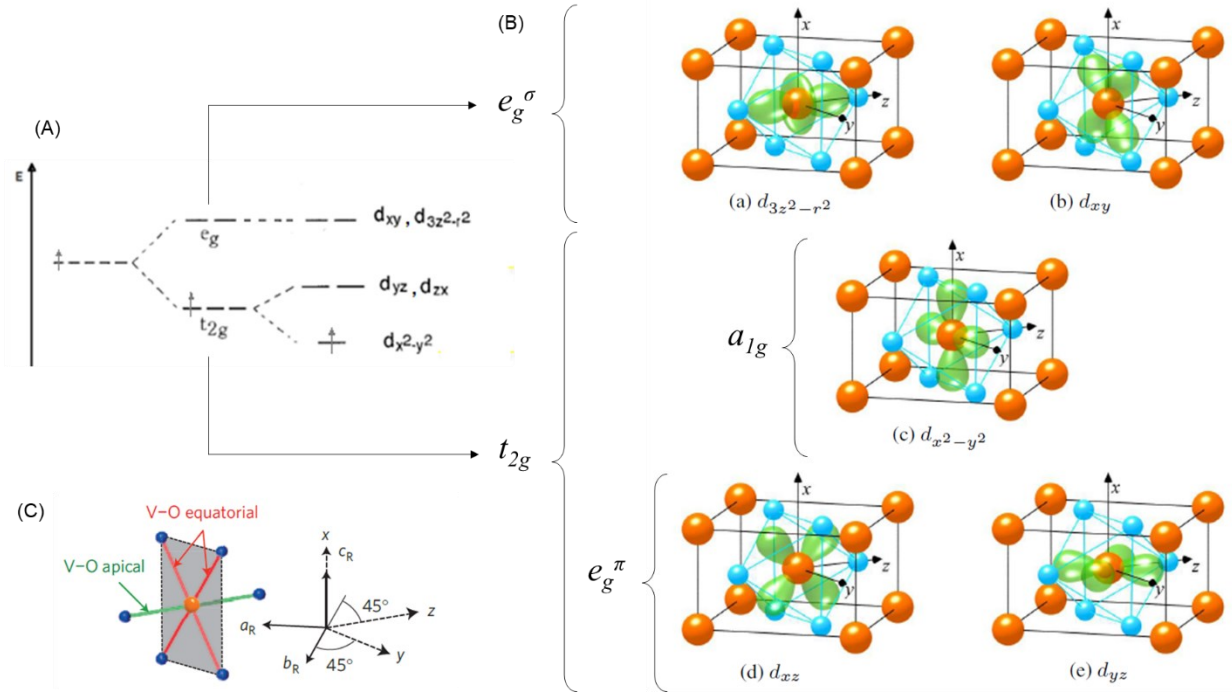


Figure 3.6. (A, B) Schematic of $3d^1$ system of VO_2, with t_{2g} splitting associated with a small orthorhombic field for VO_2. Adapted from[20,21] (C) *Orthorhombic distortion and the different apical and equatorial V–O bond lengths, in the octahedron at the center of the rutile unit cell of VO_2. Adapted from*[22]

Considering the spherical crystal field, the *d* band of the V atom is divided into five degenerate energy levels (Figure 3.6 (A)). When the V^{4+} state from octahedral VO_2 configuration (d^1) is analyzed, the *d* levels are split in lower-energy t_{2g} symmetry orbital and higher-energy e_{2g} symmetry orbital (Figure 3.6 (B)). An additional *d*-band splitting is considered due to a small orthorhombic distortion in the VO_2 (M1) octahedra (Figure 3.6 (C)). The t_{2g} symmetry orbital is triple degenerated into a single a_{1g} orbital ($d_{x^2-y^2}$) and a double degenerate e_g (Figure 3.6**)**. Due to the alignment along the c_R axis, the non-bonding a_{1g} symmetry orbital is often defined as $d_{//}$ (Figure 3.7), since it points towards the direction of the nearest V atom of the neighboring unit cell.[20,21]

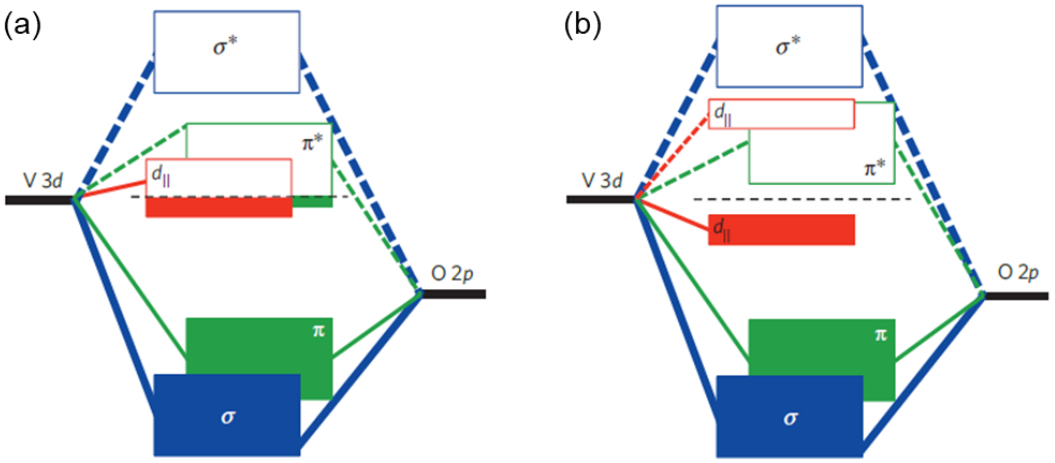


Figure 3.7. Schematic of the VO_2 band structure in the (a) metallic and (b) insulating state.[22]

The high-energy e_{2g} symmetry is double degenerated into d_{xy} and d_{z2} orbital, which point towards the O atoms. The d_{xy} and d_{z2} orbitals combine with the e_g symmetry adapted linear combinations (SALCs) of the six $2p$ O^{2-} orbitals. This leads to the creations of cylindrically symmetrical bonding (σ) and anti-bonding (σ*) orbitals (Figure 3.7). From the band model, bonding σ and π of metal oxides display energy values close to the O $2p$ ones, whereas anti-bonding σ and π display a higher V $3d$ character. The d_{xz} and d_{yz} orbitals point towards the faces of the octahedron and combine with the t_{2g} oxygen SALCs, leading to π and π* (e_g^{π}) orbitals (Figure 3.7).[22] The combined V $3d$ / O $2p$ result in a p-d hybridization, as the latter orbitals are involved in the V-O bonds. The electronic properties of VO_2 were found to be highly dependent on d_{xz}-p and d_{yz}-p (π*).[19,20,22]

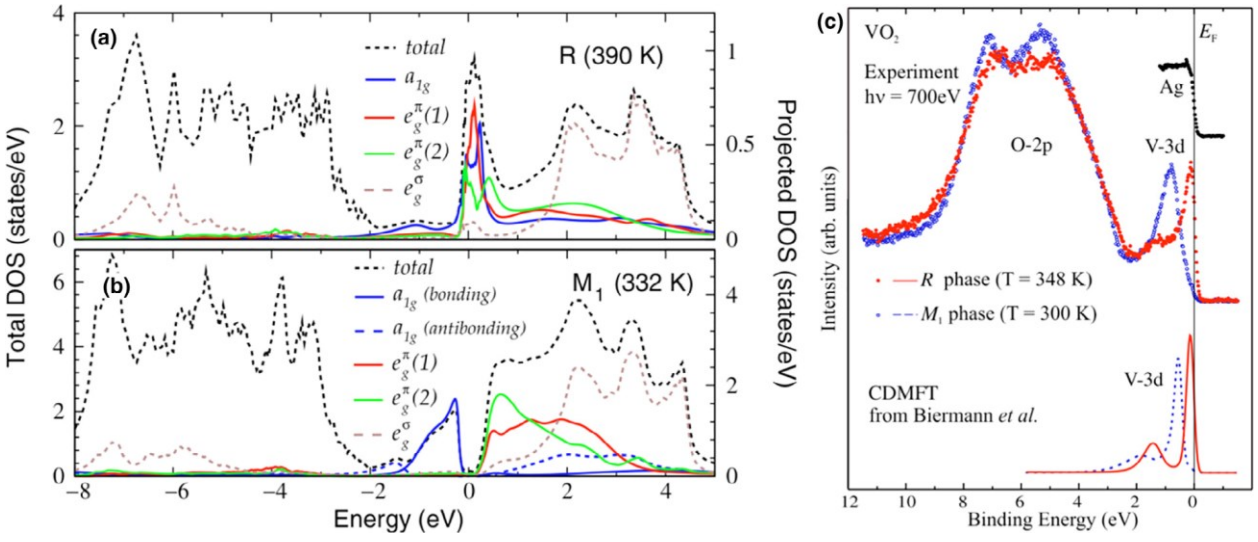


Figure 3.8. (a, b) Total and orbital-projected electron DOS for M1 and R phases, obtained from DFT + DMFT. (c) X-ray photoemission spectra of rutile (red) and monoclinic (blue) phases below the Fermi level. (a-c) adapted from references[8,23–25]

Figure 3.8 reports the density of states for both calculated metallic and insulating VO_2, which was obtained exploiting density functional theory (DFT) and dynamical mean-field theory (DMFT).[25] Upon the metal-insulator transition, the $3d_{//}$ band of VO_2 is divided into a filled band, at lower energy

values, and an empty antibonding $d_{//}^*$ band, at higher energy values (Figure 3.7). The resulting band gap between the π* and $d_{//}$ bonds was found to be $E_g \sim 0.6–0.7$ eV.[26] The displaced cations along the c_R axis, caused by the tilting of the VO_6 octahedra, enhances the π (*d-p*) overlap between V^{4+} and O^{2-} orbitals. The π orbital is hence stabilized and the anti-bonding π* orbitals are upshifted in energy.[14,20,22]

4.5 Metal-insulator transition mechanism of VO_2

The metal-insulator transition of VO_2 is a fully reversible first order mechanism, which involves a concurrent electronic and structural phase transition.[8] The underlying mechanism of the VO_2 MIT is still an open question, due to the extreme complexity of the phenomenon involving multiscale factors. Up to date, the proposed calculations based on local density approximation (LDA) and generalized gradient approximation (GGA) are considered insufficient to explain the change of properties upon the MIT.[27] During the latter, a concurrent variation of structural, electronic, and magnetic properties is induced, which complicate the understanding of the phenomenon, particularly regarding the band gap opening of the monoclinic VO_2 (M1).[28]

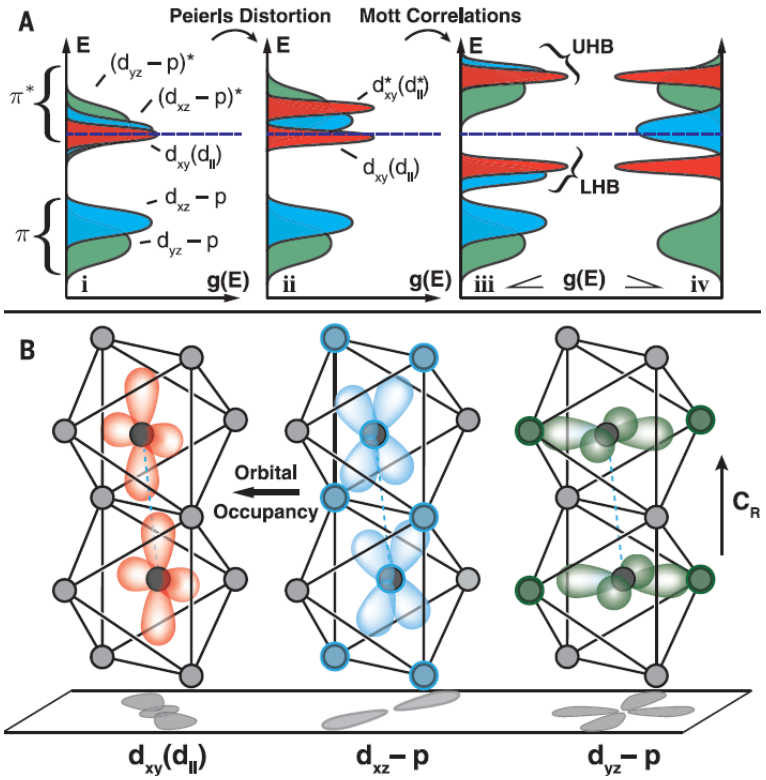


Figure 3.9. Effective band diagrams for states of t_{2g} symmetry. (A) i: Band diagram for the rutile, metallic phase. ii: Band diagram modified as a result of the PLD. iii: The effect of electron-electron correlations. UHB and LHB are upper and lower Hubbard bands, respectively. iv: Schematic band diagram indicating partial Mott melting of the dxz band. (B) Illustrations of the d_{xy}, d_{xz}, and d_{yz} molecular orbitals.[29]

Traditionally, two principal theories have been accepted for the explanation of the MIT, i.e., the electron correlation-induced transitions (Mott theory) and the lattice deformation-induced transitions (Peierls theory). A schematic of the two models is reported in Figure 3.9. Recent theoretical works proposed to merge the two theories within a single model, leading to a "Mott-assisted Peierls transition" or "correlation assisted Peierls transition".[25,27,29,30]

4.5.1 *Mott-Hubbard transition*

At low temperatures, the $3d^1$ electrons of VO_2 are strongly localized around the V cations, resulting in an insulating behavior. Electrons in *d* orbitals display a lower degree of delocalization with respect to *s* and *p* orbitals, leading to bands with high curvatures and low electron effective masses.[9,31] With the classical band theory, the behavior of multiple bodies is approximated to single-particle models, in which only electron-periodic lattice interactions are considered, whereas electrons are considered to be free and independent. As transition metal oxides (TMOs) are characterized by remarkably strong electronic correlations, classical band theory cannot be applied.[8]

In partially filled d^n systems, the coulombic potential and the kinetic energy of electrons display the same order of magnitude, which prevents the former to be discarded from the Hamiltonian.[9,32] In the Mott-Hubbard theory, the Hubbard term (*U* potential) was proposed better simulate the insulating behavior of VO_2 (M1). For narrow bandwidth ($U < W$), which represents a localized electrons case, the electron correlation splits the conduction band in two parts, with a consequent formation of a band gap.[32,33] The latter bands are respectively the lower and fully occupied Hubbard band (LHB) and the upper and unoccupied Hubbard band (UHB), which are separated by energy values proportional to the Coulomb energy of interacting electrons.[33] In Mott's insulators, the d^1 electron of V atoms do not possess sufficient energy to hop from one site to another (*d*-*d* hopping), due to the strong electronic repulsions. With increasing the temperature, electrons are allowed to escape their site, which leads to an increasing carrier density in the conduction band. The latter is raised until a metal-like conduction behavior is reached. The Mott-Hubbard transition can be tuned by *d*-band filling, i.e., varying the carrier concentration, or through the bandwidth, by compressing the lattice.[32]

4.5.2 *Peierls transition*

According to the theory of Peierls, the VO_2 MIT is induced by a spontaneous displacive distortion of a regular atomic array in a quasi-one-dimensional metal, which breaks the system symmetry.[34] The

distortion is induced by electron-phonon coupling, i.e., by the interactions of electrons with crystal lattice, differently from the Mott transition, which is driven by electronic interactions. From a thermodynamic point of view, the atomic array distortion is favored at low temperatures. The quasi-one dimensional metal indicated a three-dimensional metal in which the atoms form chains in a single direction. The latter direction determines the electrical conductivity of the material. Below the transition temperature , the periodic deformation of the lattice induces a variation of the electronic charge density. The insulator behavior of is qualitatively explained by the formation of the energy gap between the filled $d_{//}$ bonding and the empty π^* orbitals.[14,34]

Upon the monoclinic to rutile transition, the dimerization of V atoms due to the zig-zag orientation along c_R axis is concurrently induced with a major $d_{//}$-$d_{//}$ overlapping. This increases the strength of the V-V bonds into vanadium pairs, in which electrons are localized. The states near the Fermi level vary in configuration, with a splitting of the $d_{//}$ band in bonding and anti-bonding bands and a upshifting of the π^* bands (d_{yz}-p , d_{xz}-p), following the decrease in V-O distance.[14,22]

4.5.3 *Current perspectives*

Recently, the Peierls theory was considered insufficient to fully describe the VO_2 MIT, as the latter was proven to be induced through optical excitation as well, which therefore excludes a structural-induced transition.

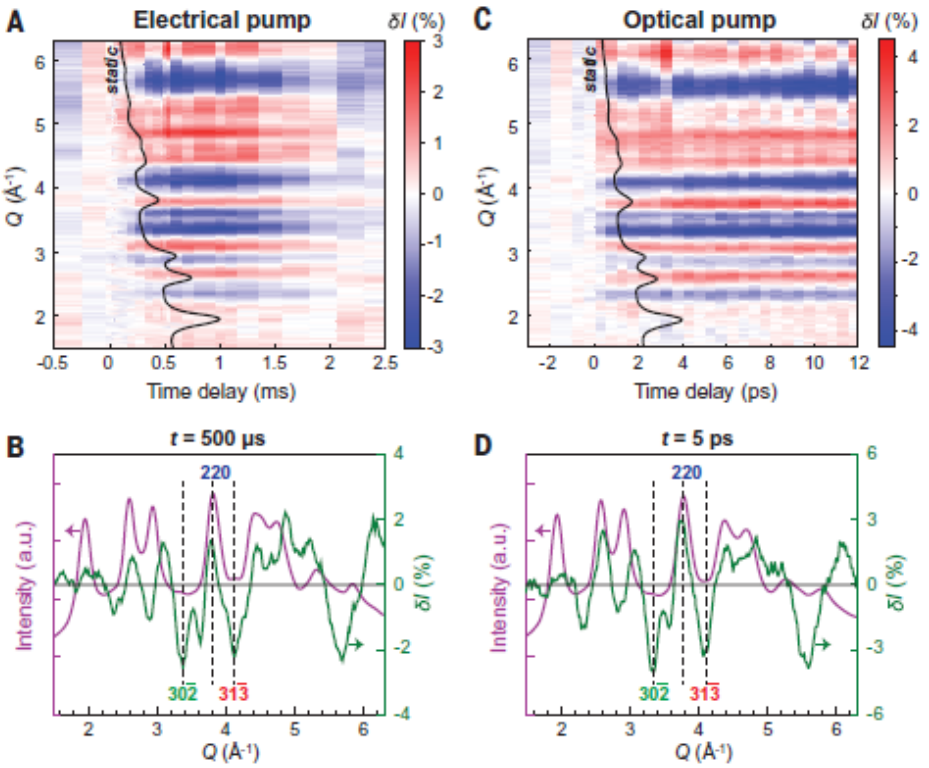


Figure 3.10. Similarity of transient structures formed under electrical and optical excitation. (A) Normalized intensity changes during E-IMT with a 5.6-V, 500-ms pulse. (B) Lineout at a delay of 500 ms showing the static pattern and the normalized intensity change. (C) Normalized intensity changes during P-IMT with a ~100-fs pulse at a fluence of ~49 mJ cm^{-2}. (D) Lineout at a delay of 5 ps.[28]

Sood *et al.*[28] recently employed ultrafast operando diffraction to investigate the phase dynamics of VO_2 at the ps scale. The authors discover an electrically triggered, isostructural state that forms transiently on microsecond time scales. The latter was shown by phase-field simulations to be stabilized by local heterogeneities and interfacial interactions between the equilibrium phases. As the metastable phase, electrically triggered, was similar to the one formed under photoexcitation within ps, the group suggested a universal transformation pathway (Figure 3.10). Other studies showed that metal-like IR optical properties could be induced through photoexcitation of monoclinic VO_2 films.[35] The optical properties were demonstrated to vary in a timescale significantly shorter with respect to the one required for the structural transition to occur.[29,35,36]

4.6 Optical and electrical properties of VO_2

The thermochromic behavior of VO_2 can be triggered by variations of temperature, pressure, strain, or electrostatic fields.[5] The monoclinic to rutile transition in induced concurrently to drastic variations in optical, electrical, and magnetic properties. In the low temperature state, the VO_2 films allow a full transmission of the NIR wavelengths, whereas above the transition temperature, the latter range is reflected owing to a metal-like behavior. The modulation of the solar radiation offers great advantages

in terms of energy-saving applications. Within the latter, the MIT of VO_2 has been exploited for the creation of passive thermochromic smart windows, which do not require active energy inputs for the activation.

Regarding the application field of smart windows, several key parameters have been established in literature to properly compare the solar modulation ability of different configurations. As a general requirement, a thermochromic smart window is required to satisfy high luminous transmittance (T_{lum}) values, simultaneously with a high solar modulation (ΔT_{sol}). Moreover, a low hysteresis (H) during heating and cooling cycles is demanded, along with a low phase-transition temperature (T_c). All parameters will be defined as follows.

4.6.1 *Luminous transmittance*

The luminous transmittance (T_{lum}) describes the ability of the smart window to transmit the visible transmittance. The parameter is calculated by integrating the transmittance in the visible range while applying a weight parameter, based on the photopic sensitivity of the human eye (Eq. 3.1):

$$T_{lum} = \frac{\int \emptyset_{lum}(\lambda)\, T(\lambda) d(\lambda)}{\int \emptyset_{lum}(\lambda)\, d(\lambda)} \tag{3.1}$$

in which Φ_{lum} represents the photopic vision luminous efficiency function and T_λ represents the transmittance at wavelength λ. The standard integration range for luminous transmittance is 380 to 780 nm.

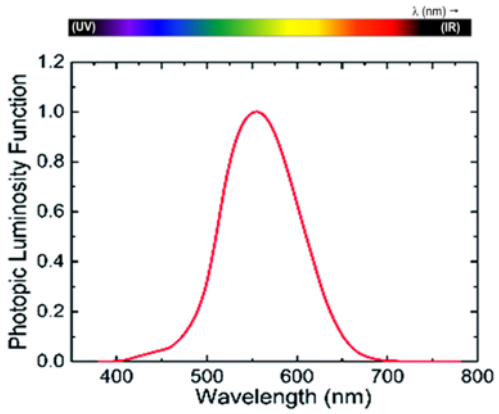


Figure 3.11. Standard CIE photopic vision luminous efficiency function.[37]

The photopic vision efficiency (Φ_{lum}) in function of the visible wavelength is reported in Figure 3.11.

4.6.2 *Solar modulation*

The ability to modulate the solar radiation (ΔT_{sol}) of a smart window is defined as (Eq. 3.2):

$$\Delta T_{sol} = T_{sol,lt} - T_{sol,ht} \tag{3.2}$$

in which $T_{sol,lt}$ is the solar transmittance at low temperature (i.e., semiconducting state – 20°C) and $T_{sol,ht}$ is the solar transmittance at high temperature (i.e., metallic state – 90°C). The solar transmittance (T_{sol}) is defined as Eq. 3.3:

$$T_{sol} = \frac{\int \emptyset_{sol}(\lambda)\, T(\lambda) d(\lambda)}{\int \emptyset_{sol}(\lambda)\, d(\lambda)} \tag{3.3}$$

where $\emptyset_{sol}$ is the standard solar radiation spectrum for the air mass 1.5 (AM 1.5, shown in Figure 3.12) and the standard integration range is 250 to 2500 nm.

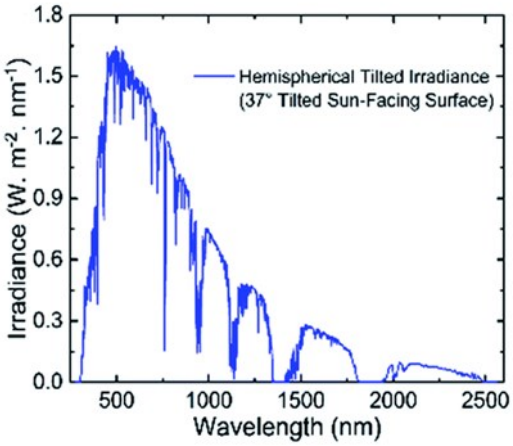


Figure 3.12. Hemispherical 37° tilted solar irradiance.[37]

The solar modulation ability is often calculated at a fixed wavelength of 2000 nm by $\Delta T_{2000\,nm} = T_{20°C} - T_{90°C}$, rather than integrating over the entire solar spectrum. This value qualitative estimates the NIR modulation offered by the smart window.

Regarding the "high temperature" state, the commonly used temperature in literature is 90°C, chosen to be sufficiently higher with respect to the transition temperature of bulk VO_2, which is usually ~68°C. In this study, the high temperature state was sometimes increased above 90°C, as higher T_c values were experimentally found in the case of some VO_2 thin films. The temperature was raised to verify the full potential of the solar modulation.

4.6.3 *Hysteresis and transition temperatures of heating/cooling cycles*

Besides the modulation of the optical transmittance, a remarkable drop in electrical conductivity is induced upon the MIT of VO_2. For VO_2 single crystals, resistivity variations up to 10^5 can be reached, along with hysteresis values of only a few degrees (Figure 3.13 (a)).[38] The crystalline state of materials crucially influences both the electrical properties and the hysteresis. Polycrystalline materials suffer from a wider hysteresis with respect to single crystals and display less pronounced conductivity variations.[39] Besides the former advantages, VO_2 single crystals display a considerably low durability to MIT cycles, which induce structural distortions upon the transition. While single crystals were reported to break after a few MIT cycles, VO_2 polycrystalline films can withstand the stress variations above 10^8 cycles, which make them suitable for smart windows applications.[40]

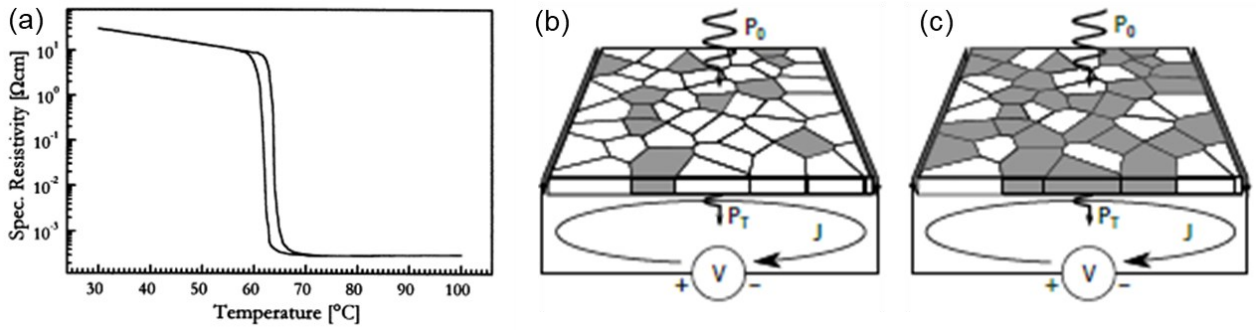


Figure 3.13. (a) Specific electrical resistivity for a single crystal VO_2 sample on sapphire substrate.[38] (b, c) Schematic transition in a thin film with (a) 20% fraction transformed and (b) 60% fraction domains transformed (grey).[41]

The composite-medium model is usually employed to explain the presence of the hysteresis during heating and cooling cycles. According to the former, the film is approximated to be formed by several small domains, which may coincide with individual crystalline grains. Upon the MIT, each domain is singularly subjected to the first-order phase transition, resulting in a domain growth.[18,41] As each domain may possess slightly different properties, structural arrangement, or defects, MIT does not occur at the same time in all domains, which leads to the presence of a hysteresis.

Optical and electrical hysteresis are measured according to two different methods. Even if the characterizations are performed on the same sample, the two hysteresis types often do not display the same value.[41] Optical transmissivity is measured through the light transmittance through the film, along the normal direction with respect to the surface (P_T/P_0 in Figure 3.13 (a)). Differently, electrical resistivity is measured through the current passage within the film, in the parallel direction with respect to the surface (V/J in Figure 3.13 (a)). While during optical characterizations each light ray interacts with a single domain, during electrical analysis each current streamline passes through multiple domains. The optical transmittance change upon the MIT is directly influenced by the

percentage of VO_2 which is or is not yet transformed between the monoclinic and the rutile state. On the contrary, a percolation path is required for electrical conduction, the absence of which leads to the deterioration of the electrical properties.[42,43]

The transition temperature is usually determined from the optical and/or the electrical hysteresis, according to the final application. While for bulk VO_2 the T_c was reported to be ~68°C[44], the latter determination for the thin film form is not trivial, as the transition usually displayed within a range of temperatures, instead of a single value. Different approaches for the T_c estimation can be found in literature, among which one of the most acknowledged T_c is to average the transition temperatures during heating and cooling processes. The latter correspond to the inflection point of the respective curve and, for narrow hysteresis values, $T_{heat} = T_{cool} = T_c$. A narrow and sharp hysteresis, along with univocal transition temperatures, are usually targeted for VO_2 thin films, to allow a satisfactory application of the latter for smart windows and electronic devices.[45]

4.7 Applications and challenges of VO_2

Vanadium dioxide offers great opportunities in terms of exploitation of the solar modulation capability. As previously discussed, the metal-insulator transition can be triggered by multiple stimuli, including temperature, pressure, strain, electric fields, and laser photons.[2,8,46]

4.7.1 *VO_2 applications*

Besides the smart windows application, the multiple activation possibilities favored the application of VO_2 in a wide range of fields, including radiative space applications, thermal controllers, cathode materials for aqueous batteries, H_2 production by photocatalysis, electrocatalytic water splitting, neuromorphic memristors, microactuators, optical filters, polarization converters, and gas sensors.[40,42,47–68]

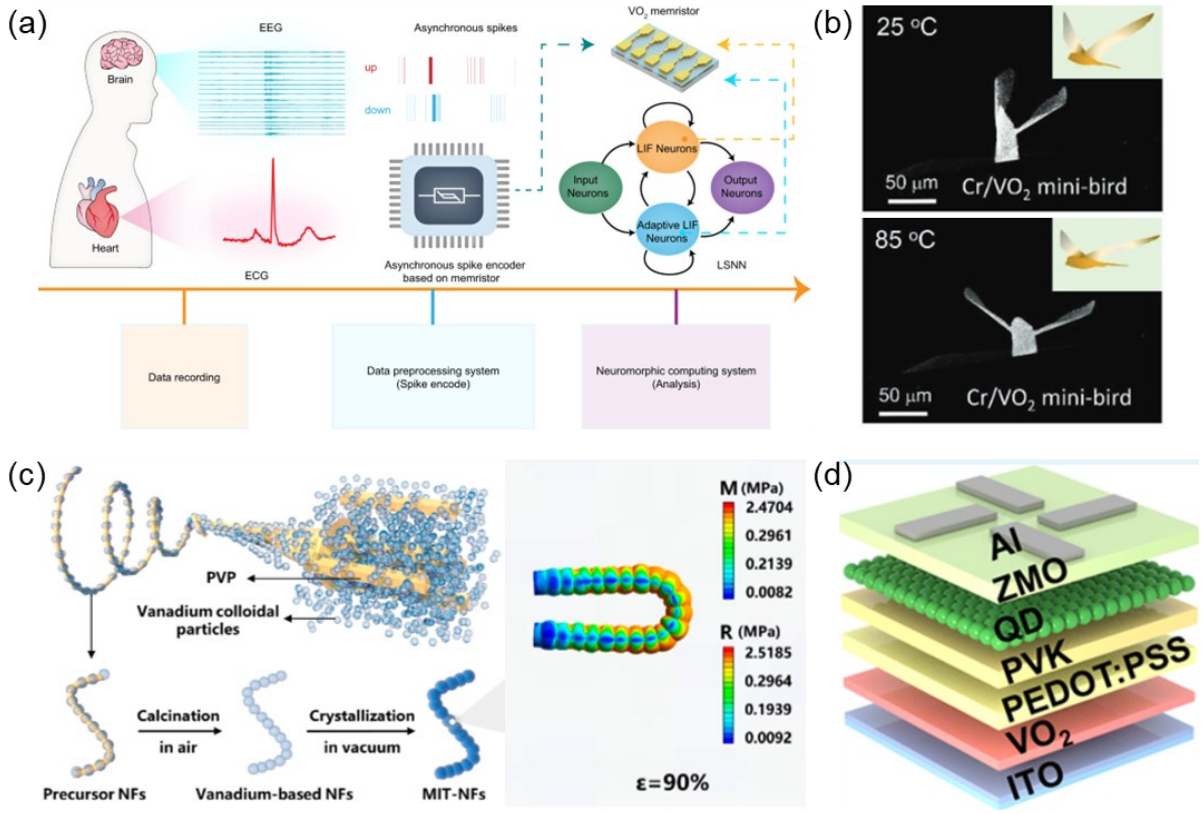


Figure 3.14. (a) Neuromorphic physiological signal processing system based on VO_2 memristor for the next-generation human-machine interface.[57] (b) SEM images of bird shaped VO_2 microactuator at 25°C and 85°C.[56] (c) Fabrication of MIT nanofibers and simulation of the stress distribution of bending crystalline MIT-NFs (M) and MIT-NFs(R) with strain (ε) of 90%.[49] (d) Illustration of the QLED structure using VO2 as a hole injection layer.[55]

Since its discovery in 1959 by Morin[44], the increasing interested sparked by VO_2 over multiple fields clearly emerges considering the most recent publications. Yuan *et al.*[57] created a neuromorphic physiological signal processing system based on VO_2 memristors, which promotes next-generation interfaces between human bodies and machine devices (Figure 3.14 (a)). In the field of displays, the efficiency of quantum dot light-emitting diodes (QLEDs) was increased by exploiting VO_2 as a hole injection layer (Figure 3.14 (d)).[55] Regarding the control of encrypted imaging for key encoding, a chirality-selective meta-absorber based on VO_2 was developed by Xiong *et al.*[47] The developed material exploited the temperature tunable phase change of the vanadium oxide. VO_2 metasurfaces were also employed to achieve THz cross polarization converters.[61]

The simultaneous presence of shape stability, temperature resistance, microscale continuity along with sufficient phase-change performance is a current challenge for VO_2 applications. By phase-engineering epitaxial VO_2 metamaterials, Guo *et al.*[49] fabricated nanofibers, self-standing 2D membraned and 3D aerogels (Figure 3.14 (c)). The materials demonstrated high structural robustness, surface stiffness, temperature resistance between -196°C and 300°C, besides offering thermal reallocation properties.

VO_2-based microactuators, which are key components in microelectron-mechanical systems, were developed by direct laser writing on freestanding VO_2 films, overcoming the disadvantages of conventional microfabrication techniques (Figure 3.14 (b)).[56] In space-related applications, the thermal control during launching and mission life of satellites is a crucial challenge. VO_2 has been proposed as a smart passive radiator, as it is able to withstand complex interactions with various types of space radiation.[50,59]

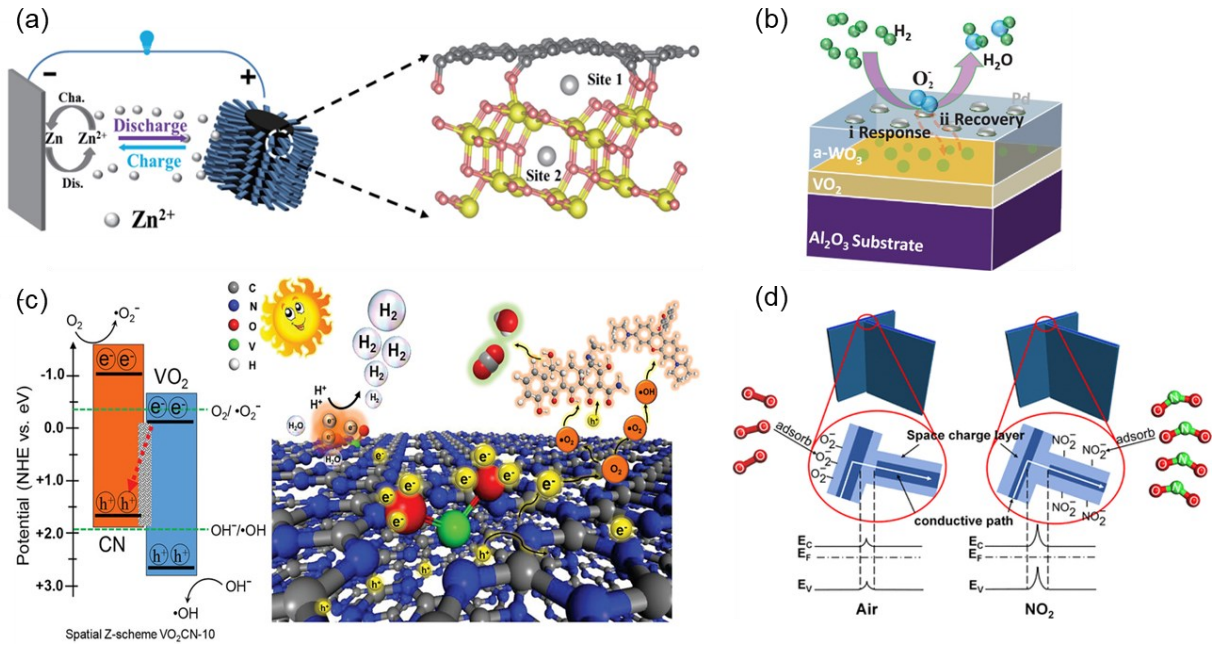


Figure 3.15. (a) Schematic illustration of Zn2+ storage sites in H-VO2@CC.[51] *(b) A schematic of hydrogen sensor using Pd nanoparticles on a-WO_3/VO_2 thin-film heterostructure.*[66] *(c) A schematic energy band diagram of VO_2 and CN and a schematic of the photodegradation mechanism of TC/RhB and hydrogen production over the VO_2 CN−10 photocatalyst.*[54] *(d) Schematic diagram of the grain boundary barrier model.*[64]

Regarding aqueous batteries, the zinc-ion storage in aqueous zinc-ion batteries was enhanced by designing a self-standing VO_2/carbon cloth composite cathode, exploiting the heterostructure interface of the latter (Figure 3.15 (a)).[51] In aqueous iron-ion batteries, a tunnel-like VO_2 as cathode material allowed to considerably increase the capacity. The cathode morphology consisted of stacked VO_2 nanosheets.[52] VO_2 was combined with MXene in form of flower-like hybrid architectures to enhance the efficiency in sodium-ion batteries.[58] The modulation properties of VO_2 were also exploited for photocatalytic H_2 production, organic pollutant degradation, and electrocatalytic water splitting (Figure 3.15 (c)).[53,54]

Different VO_2 polymorphs, including VO_2 (M1), were exploited for gas sensing applications. The advantages of a nanostructured morphology, offering high surface area, was combined with the variable oxidation state of vanadium to enhance the gas sensitivity to multiple gas types. The latter included H_2, NH_3, NO_2, CH_4, CO_2, and moisture (Figure 3.15 (b, d)).[62–68] The VO_2 application in

biosensing was proved, as VO_2 (B) nanobelts were found to possess intrinsic peroxidase-like activity.[48] Colorimetric and fluorometric sensing of catecholamines was also developed exploiting 2D VO_2 nanosheets sensors.[60]

In this PhD work, smart windows were chosen as the primarily field of application of VO_2 films. The optimization of the latter parameters, along with the analysis of different crystallization pathways, was thoroughly investigated in Chapters 4-5. An additional application of VO_2 films for gas sensing of H_2 was also considered, as will be discussed in Chapter 7.

4.7.2 *VO_2 challenges*

As emerges from a general agreement within the literature[2,5,8,69,70], the real applicability of VO_2 smart glazing requires the simultaneously fulfilling of seven principal challenges, which involve:

- transition temperature,
- thermochromic performance,
- long-term stability,
- environmental friendliness,
- color,
- skin-comfort design,
- flexible fabrication.

The explanation of the challenges, along with the existing solutions offered in literature, are reported in the paragraphs below.

4.7.2.1 *Transition temperature*

The transition temperature (T_c) that activates the metal-insulator transition of bulk and chemically homogeneous VO_2 is ~68°C.[44] Even though the latter value is close enough to room temperature, with the respect to other phase-change vanadium oxides[4], a reduction towards ~30-35°C is required a real applicability. Several strategies have been proposed to decrease the T_c, among which elemental doping and the introduction of strain are the most common.

Regarding elemental doping, the dopant choice has been performed with the aim of either increasing the carrier concentration or introducing structural distortions in the atomic configuration. The objective of the former was to boost the phase transition from an electronic point of view, whereas

the latter aimed to assist the phase transition from a structural point of view.[2] The two approaches are often debated, and the controversy originates from the currently unsolved problem of the mechanism underlying the phase transition, which was addressed in paragraph 3.4. Besides the exact mechanisms which lies beneath the doping effect, interstitial or substitutional doping has been proved to effectively reduce the T_c. Multiple doping elements have been theoretically and/or experimentally proposed, including H[71], Li[72], Mg[73], Ca[74], F[75], W[76], Zr[77] and Ti[78]. In the latter studies, besides the increase in electrons or holes concentration, doping has also been exploited to modify the distanced within V-V chains and hence the MIT temperature. It should be noted that these effects are often induced simultaneously, which limits the exact comprehension of the dopant effect.

An alternative strategy to decrease the T_c is to apply compressive or tensile strain or pressures on the deposited films/particles. For example, post deposition treatments such as three-point bending or uniaxial compression have been proposed[79,80], or deposition of epitaxial VO_2 films on non-matching buffer layers.[81,82]

4.7.2.2 *Thermochromic performance*

Thermochromic smart windows are required to simultaneously guarantee a high transparency in the visible range and a high modulation of the solar irradiation. As introduced in paragraph 3.6, the former is expressed as T_{lum} in literature, whereas the latter as ΔT_{sol}. Multiple studies highlighted that the two parameters follow an anti-synergic behavior, as increases in ΔT_{sol} usually lead to decreases in T_{lum}, and viceversa. The minimum values generally required are $\Delta T_{sol} > 10\%$ along with $T_{lum} > 50\%$.[2]

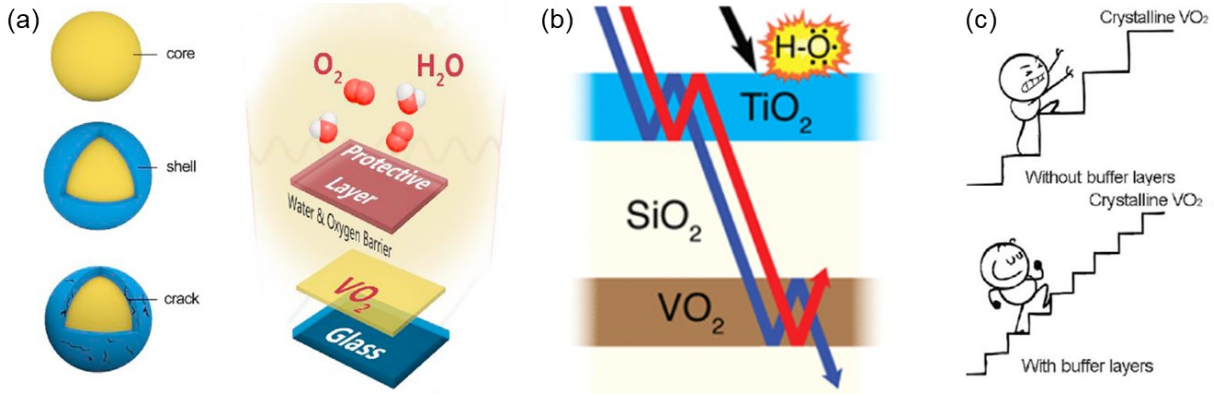


Figure 3.16. (a) Diagram of the core-shell structure of VO_2 nanoparticles.[2] (b) Diagram of the protective layer of VO_2 thin films.[83] (c) Diagram of the degree of difficulty of fabricating crystalline VO_2 without/with buffer layers.[2]

In single VO_2 thin films, the increasing thickness allows for a higher ΔT_{sol}, but inevitably leads to a lower T_{lum}. With respect to the former, several strategies have been proposed to increase simultaneously T_{lum} and ΔT_{sol}. Most solutions involved morphological modifications, in terms of

micro- or nanostructuring, as well as combinations of multiple materials. Besides doping, which was also employed to enhance the optical performance of VO_2, successful solutions included multilayered structures[83,84], nanocomposites based on VO_2 nanoparticles, core-shell particles[85], porous coatings[86], laser texturing[87], nano stripe morphologies[88], hybrid organic-inorganic coatings[89,90], and bioinspired patterns. The latter include nano cones[91], wood-based devices[92], and cephalopod-inspired[93] morphologies. As will be discussed in Chapter 6, many effective strategies exploited the gradient refractive index principle or tuned the destructive interferences by properly combining thickness and different material properties.[94] TiO_2 and SiO_2 particularly emerge when multilayers or core-shells are considered to improve the properties of VO_2 films. TiO_2 is often chosen as a buffer layer, to improve VO_2 crystallization owing to the similar lattice parameters, and/or as an antireflective and self-cleaning layer, which leads to the creation of a multifunctional smart window (Figure 3.16 (b, c)). The multifunctionality is allowed by SiO_2 coating as well, which improves the antireflection as well as the mechanical and chemical resistance of VO_2, especially the durability under high moisture conditions. Powell *et al.*[83] combined the three materials in a $VO_2/SiO_2/TiO_2$ configuration, with overall high ΔT_{sol} = 15.29% but low T_{lum} = 17.81%. Wu *et al.*[84] deposited VO_2/TiO_2 bilayers by magnetron sputtering and, following simulations on the optimal thicknesses, obtained T_{lum} = 42.29% and ΔT_{sol} = 16.03%. Core-shell VO_2/SiO_2 particles were mixed with mesoporous silica nanospheres by Wang *et al.*[85], leading to T_{lum} = 71.02% and ΔT_{sol} = 14.31%.

4.7.2.3 *Long-term stability*

As mentioned in the previous paragraph 3.6.2.2, protective coatings are often applied on thermochromic VO_2 films. As will be experimentally shown in Chapter 5, a thin layer of oxidized V^{5+} state naturally tends to form on the surface of VO_2 films, when the latter are exposed to air.[95] Depending on its thickness, the oxidized layer can partially or totally deteriorate the thermochromicity of VO_2 films.[90,96] The application of protective coatings was demonstrated to be effectful in preventing the oxidation and remarkably prolonging the life cycles of smart windows (Figure 3.16 (a)).[2] Moreover, most protective coatings offer an additional mechanical protection against wear and impacts. SiO_2 is among the most exploited materials, both in terms of multilayered and core-shell structures, as it offers great visible transparency and chemical and mechanical stability (Figure 3.16 (b)).[97–100] Additionally, it can act as a diffusion barrier and provide a blocking layer during high temperature treatments of CSD methods.[83]

4.7.2.4 *Environmental friendliness*

The most used vanadium precursors include vanadium alkoxides, vanadium pentoxide, $VOSO_4$, NH_4VO_3, and vanadyl/vanadium acetylacetonates. Many vanadium sources, despite being widely employed, are linked to high levels of toxicity, carcinogenicity, mutagenicity, damages to the reproductive system or the aquatic environment.[101,102] This highlights the need for a safer process, in terms of both precursor and solvent.

4.7.2.5 *Color and skin-comfort design*

The natural color of VO_2 films is yellow, which must be modified to guarantee colorless or color-tunable smart windows. Color tuning is often pursued along with the improvement of the thermochromic performance. The most effective strategies have been found to be organic thermochromic materials, doping, metal nanoarrays and core-shell structures (Figure 3.17 (a, b)).[2]

Smart windows should also be designed to favor a higher skin-comfort. The solar spectrum includes both beneficial and harmful wavelength ranges, which transmission through the window should be modulated accordingly.[2] As visible in Figure 3.17 (c), the human skin is composed of epidermis, dermis, and hypodermis. UVB (280-320 nm) and UVA2 (320-340 nm) rays only reach the epidermis, whereas UVA1 (340-400 nm) reach the dermis layer and infrared radiation can penetrate up to the hypodermis layer.[103] The smart window's properties should be tailored to block UV light, while allowing the transmission of both visible and infrared light.

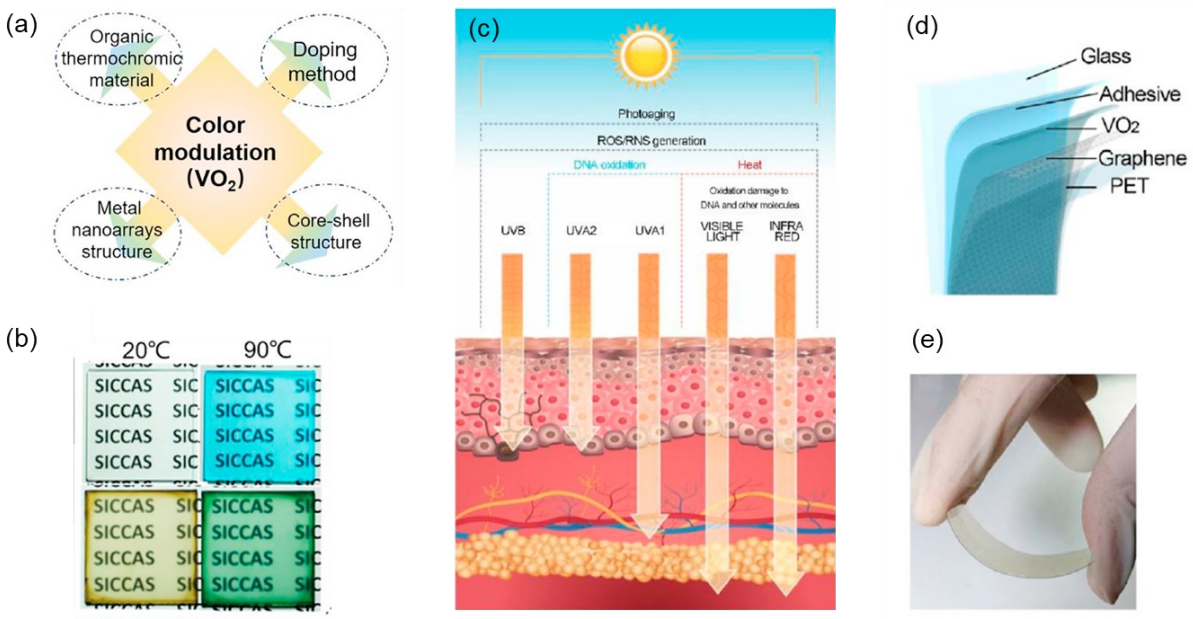


Figure 3.17. (a) Strategies of color modulation of VO_2-based smart coatings.[2] *(b) Pure hydrogel thin film, and VO_2/hydrogel hybrid at room temperature and 35°C.*[104] *(c) The solar spectrum is composed of various wavelengths, which penetrate into skin at different levels.*[103] *(d) Structure of the graphene-supported VO2 film on PET substrate.*[105] *(e) The excellent flexibility of thin VO2/mica films.*[2,105]

4.7.2.6 *Flexible fabrication*

The creation of thermochromic films on flexible polymers would boost the energy-saving applications in terms of worldwide availability and applicability, as polymeric substrates can be easily transported and arranged in multiple configurations. A common strategy to prepare thermochromic coatings on flexible substrates is to disperse VO_2 particles within a polymeric matrix, which is then used to coat the substrate. With respect to the film form, a higher sensitivity of VO_2 particles towards moisture was noticed, as well as a missing percolation path for electrical conductivity.[2] To overcome the problem, film transfer technologies[106], high-power impulse magnetron sputtering (HiPIMS)[107], or the use of inorganic muscovite substrates[108] have been proposed (Figure 3.17 (d, e)). A promising alternative is offered by unconventional photonic annealing, through lamps or lasers, which was exploited in Chapter 5. The former exploits light irradiation, at specific wavelengths or within a broader range, to induce photochemical and/or photothermal effects in the irradiated films. Through an accurate tuning of the laser sources, the heat rise can be confined within the films, without compromising the underneath substrate.[109]

4.7.2.7 *Current work*

Within this PhD, several of the above challenges were addressed. The environmental friendliness was reached by employing a CSD method (Chapter 4), in which both precursor and solvent were selected

to be non-cancerogenic and low hazard. Moreover, an unconventional annealing method was proposed in Chapter 5. With respect to furnace annealing, laser-induced crystallization was employed to lower the annealing time and hence the energy load required for the crystallization step.

Unconventional laser annealing was also chosen to aim for a flexible fabrication of VO_2 thin films. As will be reported in Chapter 5, laser annealing offers the possibility to selectively heat the film, without interacting with the substrate. The process is based on a macroscopically low-temperature crystallization of metal oxides, which allows to extend the VO_2 fabrication on flexible polymeric substrates.

Multifunctional coatings, based on the combination of VO_2 with other oxide materials, were addressed in Chapter 6. Two VO_2-related challenges were targeted, namely a higher luminous transmittance and a higher durability under high moisture conditions, exploiting the advantages offered by TiO_2 and SiO_2 coatings.

In Chapter 7, VO_2 thin films were employed as gas sensors for H_2 detection. The influence of morphology and crystallinity degree was addressed by comparing furnace- and laser-annealed samples, at different annealing conditions.

References

1. Davis, L. W. & Gertler, P. J. Contribution of air conditioning adoption to future energy use under global warming. *Proc Natl Acad Sci U S A* **112**, 5962–5967 (2015).

2. Cao, X. *et al.* Challenges and Opportunities toward Real Application of VO2-Based Smart Glazing. *Matter* **2**, 862–881 (2020).

3. Mazzone, A. *et al.* Understanding systemic cooling poverty. *Nature Sustainability 2023* 1–9 (2023) doi:10.1038/s41893-023-01221-6.

4. Bahlawane, N. & Lenoble, D. Vanadium Oxide Compounds: Structure, Properties, and Growth from the Gas Phase. *Chemical Vapor Deposition* **20**, 299–311 (2014).

5. Wang, S. *et al.* Recent progress in VO2 smart coatings: Strategies to improve the thermochromic properties. *Prog Mater Sci* **81**, 1–54 (2016).

6. Shvets, P., Dikaya, O., Maksimova, K. & Goikhman, A. A review of Raman spectroscopy of vanadium oxides. *Journal of Raman Spectroscopy* **50**, 1226–1244 (2019).

7. Gao, Y. *et al.* Nanoceramic VO 2 thermochromic smart glass: A review on progress in solution processing. *Nano Energy* **1**, 221–246 (2012).

8. Liu, K., Lee, S., Yang, S., Delaire, O. & Wu, J. Recent progresses on physics and applications of vanadium dioxide. *Materials Today* **21**, 875–896 (2018).

9. Brahlek, M. *et al.* Opportunities in vanadium-based strongly correlated electron systems. *MRS Commun* **7**, 27–52 (2017).

10. Zhang, Y., Xiong, W., Chen, W. & Zheng, Y. Recent Progress on Vanadium Dioxide Nanostructures and Devices: Fabrication, Properties, Applications and Perspectives. *Nanomaterials 2021, Vol. 11, Page 338* **11**, 338 (2021).

11. Boontan, A., Barimah, E. K., Steenson, P. & Jose, G. Stabilization of the VO2(M2) Phase and Change in Lattice Parameters at the Phase Transition Temperature of WXV1–XO2 Thin Films. *ACS Appl Mater Interfaces* **15**, 51606–51616 (2023).

12. Wu, Y. *et al.* Depressed transition temperature of WxV1−xO2: mechanistic insights from the X-ray absorption fine structure (XAFS) spectroscopy. *Physical Chemistry Chemical Physics* **16**, 17705–17714 (2014).

13. Andersson, G., Paju, J., Lang, W. & Berndt, W. Studies on Vanadium Oxides. I. Phase Analysis. *Acta Chem Scand* **8**, 1599–1606 (1954).

14. Goodenough, J. B. Anomalous properties of the vanadium oxides. *Annu. Rev. Mater. Sci.* **1**, 101–138 (1971).

15. Wu, C., Feng, F. & Xie, Y. Design of vanadium oxide structures with controllable electrical properties for energy applications. *Chem Soc Rev* **42**, 5157–5183 (2013).

16. Warwick, M. E. A. & Binions, R. Advances in thermochromic vanadium dioxide films. *J Mater Chem A Mater* **2**, 3275–3292 (2014).

17. Ordonez-Miranda, J., Ezzahri, Y., Joulain, K., Drevillon, J. & Alvarado-Gil, J. J. Modeling of the electrical conductivity, thermal conductivity, and specific heat capacity of VO2. *Phys Rev B* **98**, 075144 (2018).

18. Choi, H., Ahn, J., Jung, J., Noh, T. & Kim, D. Mid-infrared properties of a VO2 film near the metal-insulator transition. *Phys Rev B Condens Matter* **54**, 4621–4628 (1996).

19. Goodenough, J. B. The two components of the crystallographic transition in VO2. *J Solid State Chem* **3**, 490–500 (1971).

20. Eyert, V. The metal-insulator transitions of VO2: A band theoretical approach. *Ann Phys* **514**, 650–704 (2002).

21. Stoyanov, E., Langenhorst, F. & Steinle-Neumann, G. The effect of valence state and site geometry on Ti L3,2 and O K electron energy-loss spectra of TixOy phases. *American Mineralogist* **92**, 577–586 (2007).

22. Aetukuri, N. B. *et al.* Control of the metal–insulator transition in vanadium dioxide by modifying orbital occupancy. *Nature Physics 2013 9:10* **9**, 661–666 (2013).

23. Koethe, T. C. *et al.* Transfer of spectral weight and symmetry across the metal-insulator transition in VO2. *Phys Rev Lett* **97**, 116402 (2006).

24. Biermann, S., Poteryaev, A., Lichtenstein, A. I. & Georges, A. Dynamical singlets and correlation-assisted peierls transition in vo 2. *Phys Rev Lett* **94**, 1–4 (2005).

25. Brito, W. H., Aguiar, M. C. O., Haule, K. & Kotliar, G. Metal-Insulator Transition in VO2: A DFTDMFT Perspective. *Phys Rev Lett* **117**, 056402 (2016).

26. Verleur, H. W., Barker, A. S. & Berglund, C. N. Optical Properties of VO2 between 0.25 and 5 eV. *Phys. Rev.* **172**, (1968).

27. Shao, Z., Cao, X., Luo, H. & Jin, P. Recent progress in the phase-transition mechanism and modulation of vanadium dioxide materials. *NPG Asia Mater* **10**, 581–605 (2018).

28. Sood, A. *et al.* Universal phase dynamics in VO2 switches revealed by ultrafast operando diffraction. *Science (1979)* **373**, 352–355 (2021).

29. Morrison, V. R. *et al.* A photoinduced metal-like phase of monoclinic VO_2 revealed by ultrafast electron diffraction. *Science* **346**, 445–448 (2014).

30. Yuan, X., Zhang, W. & Zhang, P. Hole-lattice coupling and photoinduced insulator-metal transition in VO2. *Phys Rev B Condens Matter Mater Phys* **88**, 035119 (2013).

31. Cardona, M. & Pollak, F. H. Energy-Band Structure of Germanium and Silicon: The k·p Method. *Physical Review* **142**, 530 (1966).

32. Fujimori, A. *et al.* Electronic structure of Mott–Hubbard-type transition-metal oxides. *J Electron Spectros Relat Phenomena* **117–118**, 277–286 (2001).

33. Mott, N. F. & Friedman, L. Metal-insulator transitions in VO2, Ti2O3 and Ti2xVxO3. *Philosophical Magazine* **30**, 389–402 (1974).

34. Peierls, R. E. *More Surprises In Theoretical Physics*. vol. 19 (Princeton University Press, 1991).

35. Wegkamp, D. & Stähler, J. Ultrafast dynamics during the photoinduced phase transition in VO2. *Prog Surf Sci* **90**, 464–502 (2015).

36. Yang, Z., Ko, C. & Ramanathan, S. Oxide Electronics Utilizing Ultrafast Metal-Insulator Transitions. *Annu Rev Mater Res* **41**, 337–367 (2011).

37. Chang, T., Cao, X., Long, Y., Luo, H. & Jin, P. How to properly evaluate and compare the thermochromic performance of VO2-based smart coatings. *J Mater Chem A Mater* **7**, 24164–24172 (2019).

38. Schlag, H. J. & Scherber, W. New sputter process for VO2 thin films and examination with MIS-elements and C–V-measurements. *Thin Solid Films* **366**, 28–31 (2000).

39. Christmann, T., Felde, B., Niessner, W., Schalch, D. & Scharmann, A. Thermochromic VO2 thin films studied by photoelectron spectroscopy. *Thin Solid Films* **287**, 134–138 (1996).

40. Béteille, F. & Livage, J. Optical Switching in VO2 Thin Films. *J Solgel Sci Technol* **13**, 915–921 (1998).

41. Annasiwatta, C. *et al.* Multi-physics modeling of hysteresis in vanadium dioxide thin films. *Proceedings of the American Control Conference* **2016-July**, 6905–6910 (2016).

42. Venkat Sunil Kumar, C., Maury, F. & Bahlawane, N. *Vanadium Oxide as a Key Constituent in Reconfigurable Metamaterials*. *Metamaterials and Metasurfaces* (IntechOpen, 2019).

43. Katase, T., Endo, K. & Ohta, H. Thermopower analysis of metal-insulator transition temperature modulations in vanadium dioxide thin films with lattice distortion. *Phys Rev B Condens Matter Mater Phys* **92**, 035302 (2015).

44. Morin, F. J. Oxides Which Show a Metal-to-Insulator Transition at the Neel Temperature. *Phys Rev Lett* **3**, 34 (1959).

45. Warwick, M. E. A., Ridley, I. & Binions, R. The effect of variation in the transition hysteresis width and gradient in thermochromic glazing systems. *Solar Energy Materials and Solar Cells* **140**, 253–265 (2015).

46. Cui, Y. *et al.* Thermochromic VO2 for Energy-Efficient Smart Windows. *Joule* **2**, 1707–1746 (2018).

47. Xiong, T. H. *et al.* A temperature-tunable chirality-selective meta-absorber for electromagnetic encrypted imaging. *Appl Phys Lett* **123**, (2023).

48. Nie, G. *et al.* Monocrystalline VO2 (B) nanobelts: large-scale synthesis, intrinsic peroxidase-like activity and application in biosensing. *J Mater Chem A Mater* **2**, 2910–2914 (2014).

49. Guo, H., Si, L., Yu, J., Wang, X. & Si, Y. Phase-Engineered VO2 Metal Nanofiber Enables a Metal-Insulator Transition for Bidirectional Thermal Reallocation. *Nano Lett* **23**, 6233–6240 (2023).

50. Madiba, I. G., Mabakachacha, B., Khanyile, S., Numan, N. & Azizi, S. Nano-structured VO2 based films for space application and radiative environment. *Mater Today Proc* (2023).

51. Luo, P. *et al.* Accelerated ion/electron transport kinetics and increased active sites via local internal electric fields in heterostructured VO2-carbon cloth for enhanced zinc-ion storage. *Nano Res* **16**, 503–512 (2023).

52. Xu, Y. S. *et al.* Achieving high performance in aqueous iron-ion batteries using tunnel-like VO2 as a cathode material. *Chemical Communications* **59**, 8576–8579 (2023).

53. Zhou, W. *et al.* Crafting amorphous VO2–crystalline NiS2 heterostructures as bifunctional electrocatalysts for efficient water splitting: The different cocatalytic function of VO2. *Chemical Engineering Journal* **470**, 144146 (2023).

54. Jourshabani, M. *et al.* Advanced Functional Carbon Nitride by Implanting Semi-Isolated VO2 Active Sites for Photocatalytic H2 Production and Organic Pollutant Degradation. *Small* **19**, 2300147 (2023).

55. Cho, H. Bin *et al.* Utilizing VO2 as a Hole Injection Layer for Efficient Charge Injection in Quantum Dot Light-Emitting Diodes Enables High Device Performance. *ACS Appl Mater Interfaces* **15**, 29259–29266 (2023).

56. Li, Y. *et al.* Direct Laser Writing of Multishaped VO2 Microactuators Based on Freestanding VO2 Film. *Adv Mater Technol* **8**, 2200977 (2023).

57. Yuan, R. *et al.* A neuromorphic physiological signal processing system based on VO2 memristor for next-generation human-machine interface. *Nature Communications 2023 14:1* **14**, 1–14 (2023).

58. Wu, F. *et al.* A 3D flower-like VO2/MXene hybrid architecture with superior anode performance for sodium ion batteries. *J Mater Chem A Mater* **7**, 1315–1322 (2019).

59. Xie, B., Zhang, W., Zhao, J., Zheng, C. & Liu, L. Design of VO2-based spacecraft smart radiator with low solar absorptance. *Appl Therm Eng* **236**, 121751 (2024).

60. Weerasinghe, H., Kumarihamy, M. & Wu, H. F. Synthesis of 2D VO2 Nanosheets for the Dual Optical Sensor Method by Colorimetric and Fluorometric Sensing of Catecholamines. *ACS Appl Mater Interfaces* (2023).

61. Yahiaoui, R. *et al.* Dynamically tunable single-layer VO2/metasurface based THz cross-polarization converter. *J Phys D Appl Phys* **54**, 235101 (2021).

62. Huotari, J., Bjorklund, R., Lappalainen, J. & Lloyd Spetz, A. Pulsed Laser Deposited Nanostructured Vanadium Oxide Thin Films Characterized as Ammonia Sensors. *Sens Actuators B Chem* **217**, 22–29 (2015).

63. Jaiswal, J. *et al.* Vertically Aligned Porous VxOyNanofilms with Pt Decoration for Sub-ppm H2Gas Sensors. *ACS Appl Nano Mater* (2022).

64. Liang, J., Lou, Q., Wu, W., Wang, K. & Xuan, C. NO2Gas Sensing Performance of a VO2(B) Ultrathin Vertical Nanosheet Array: Experimental and DFT Investigation. *ACS Appl Mater Interfaces* **13**, 31968–31977 (2021).

65. Evans, G. P. *et al.* Room temperature vanadium dioxide–carbon nanotube gas sensors made via continuous hydrothermal flow synthesis. *Sens Actuators B Chem* **255**, 1119–1129 (2018).

66. Li, B. *et al.* Enhanced Pd/a-WO3/VO2 Hydrogen Gas Sensor Based on VO2 Phase Transition Layer. *Small Methods* **6**, 2200931 (2022).

67. Byon, J. W. *et al.* Electrothermally induced highly responsive and highly selective vanadium oxide hydrogen sensor based on metal-insulator transition. *Journal of Physical Chemistry C* **116**, 226–230 (2012).

68. Baik, J. M. *et al.* Pd-Sensitized single vanadium oxide nanowires: Highly responsive hydrogen sensing based on the metal-insulator transition. *Nano Lett* **9**, 3980–3984 (2009).

69. Shen, N. *et al.* Vanadium dioxide for thermochromic smart windows in ambient conditions. *Mater Today Energy* **21**, 100827 (2021).

70. Kim, J. & Paik, T. Recent advances in fabrication of flexible, thermochromic vanadium dioxide films for smart windows. *Nanomaterials* **11**, (2021).

71. Cui, Y., Shi, S., Chen, L., Luo, H. & Gao, Y. Hydrogen-doping induced reduction in the phase transition temperature of VO2: a first-principles study. *Physical Chemistry Chemical Physics* **17**, 20998–21004 (2015).

72. Cui, Y., Wang, Y., Liu, B., Luo, H. & Gao, Y. First-principles study on the phase transition temperature of X-doped (X = Li, Na or K) VO2. *RSC Adv* **6**, 64394–64399 (2016).

73. Wang, N., Liu, S., Zeng, X. T., Magdassi, S. & Long, Y. Mg/W-codoped vanadium dioxide thin films with enhanced visible transmittance and low phase transition temperature. *J Mater Chem C Mater* **3**, 6771–6777 (2015).

74. Dietrich, M. K. *et al.* Influence of doping with alkaline earth metals on the optical properties of thermochromic VO2. *J Appl Phys* **117**, 185301 (2015).

75. Dai, L. *et al.* F-doped VO2 nanoparticles for thermochromic energy-saving foils with modified color and enhanced solar-heat shielding ability. *Physical Chemistry Chemical Physics* **15**, 11723–11729 (2013).

76. Hu, L. *et al.* Porous W-doped VO2 films with simultaneously enhanced visible transparency and thermochromic properties. *J Solgel Sci Technol* **77**, 85–93 (2016).

77. Shen, N. *et al.* The synthesis and performance of Zr-doped and W–Zr-codoped VO2 nanoparticles and derived flexible foils. *J Mater Chem A Mater* **2**, 15087–15093 (2014).

78. Chen, S. *et al.* The visible transmittance and solar modulation ability of VO2 flexible foils simultaneously improved by Ti doping: an optimization and first principle study. *Physical Chemistry Chemical Physics* **15**, 17537–17543 (2013).

79. Cao, J. *et al.* Strain engineering and one-dimensional organization of metal–insulator domains in single-crystal vanadium dioxide beams. *Nature Nanotechnology 2009 4:11* **4**, 732–737 (2009).

80. Wu, J. *et al.* Strain-induced self organization of metal-insulator domains in single-crystalline VO 2 nanobeams. *Nano Lett* **6**, 2313–2317 (2006).

81. Muraoka, Y. & Hiroi, Z. Metal-insulator transition of VO2 thin films grown on TiO 2 (001) and (110) substrates. *Appl Phys Lett* **80**, 583–585 (2002).

82. Muraoka, Y., Ueda, Y. & Hiroi, Z. Large modification of the metal–insulator transition temperature in strained VO2 films grown on TiO2 substrates. *Journal of Physics and Chemistry of Solids* **63**, 965–967 (2002).

83. Powell, M. J. *et al.* Intelligent Multifunctional VO2/SiO2/TiO2 Coatings for Self-Cleaning, Energy-Saving Window Panels. *Chemistry of Materials* **28**, 1369–1376 (2016).

84. Wu, W. *et al.* Design of Antireflection and Enhanced Thermochromic Properties of TiO2/VO2 Thin Films. *Adv Mater Interfaces* **10**, 2202506 (2023).

85. Wang, M. *et al.* Novel synthesis of pure VO2@SiO2 core@shell nanoparticles to improve the optical and anti-oxidant properties of a VO2 film. *RSC Adv* **6**, 108286–108289 (2016).

86. Cool, N. I. *et al.* Thermochromic Fenestration Elements Based on the Dispersion of Functionalized VO2 Nanocrystals within a Polyvinyl Butyral Laminate. *ACS Engineering Au* **2**, 477–485 (2022).

87. Outón, J. *et al.* Novel laser texturing of W-doped VO2 thin film for the improvement of luminous transmittance in smart windows application. *Appl Surf Sci* **608**, 155180 (2023).

88. Savorianakis, G. *et al.* VO2 nanostripe-based thin film with optimized color and solar characteristics for smart windows. *J Appl Phys* **129**, (2021).

89. Zhao, X. *et al.* Thermochromic composite film of VO2 nanoparticles and [(C2H5)2NH2]2NiBr4@SiO2 nanospheres for smart window applications. *Chemical Engineering Journal* **460**, 141715 (2023).

90. Zhao, S. *et al.* Roomerature Synthesis of Inorganic-Organic Hybrid Coated VO 2 Nanoparticles for Enhanced Durability and Flexible Temperature-Responsive Near-Infrared Modulator Application. *ACS Appl Mater Interfaces* **11**, 10254–10261 (2019).

91. Liu, S. *et al.* Bio-inspired TiO2 nano-cone antireflection layer for the optical performance improvement of VO2 thermochromic smart windows. *Scientific Reports 2020 10:1* **10**, 1–14 (2020).

92. Liu, S. *et al.* Self-Densified Optically Transparent VO2Thermochromic Wood Film for Smart Windows. *ACS Appl Mater Interfaces* **13**, 22495–22504 (2021).

93. Ke, Y. *et al.* Cephalopod-inspired versatile design based on plasmonic VO2 nanoparticle for energy-efficient mechano-thermochromic windows. *Nano Energy* **73**, 104785 (2020).

94. Raut, H. K., Ganesh, V. A., Nair, A. S. & Ramakrishna, S. Anti-reflective coatings: A critical, in-depth review. *Energy Environ Sci* **4**, 3779–3804 (2011).

95. Basso, M. *et al.* Rapid laser-induced low temperature crystallization of thermochromic VO2 sol-gel thin films. *Appl Surf Sci* **631**, (2023).

96. Ji, Y. X., Li, S. Y., Niklasson, G. A. & Granqvist, C. G. Durability of thermochromic VO2 thin films under heating and humidity: Effect of Al oxide top coatings. *Thin Solid Films* **562**, 568–573 (2014).

97. Okimura, K., Mian, M. S., Yamaguchi, I. & Tsuchiya, T. High luminous transmittance and solar modulation of VO2-based smart windows with SiO2 anti-reflection coatings. *Solar Energy Materials and Solar Cells* **251**, 112162 (2023).

98. Du, Z. *et al.* VO2@SiO2Nanoparticle-Based Films with Localized Surface Plasmon Resonance for Smart Windows. *ACS Appl Nano Mater* **5**, 12972–12979 (2022).

99. Zhang, J. *et al.* Mesoporous SiO2/VO2 double-layer thermochromic coating with improved visible transmittance for smart window. *Solar Energy Materials and Solar Cells* **162**, 134–141 (2017).

100. Ke, Y. *et al.* Two-Dimensional SiO2/VO2 Photonic Crystals with Statically Visible and Dynamically Infrared Modulated for Smart Window Deployment. *ACS Appl Mater Interfaces* **8**, 33112–33120 (2016).

101. Fatola, O. I., Olaolorun, F. A., Olopade, F. E. & Olopade, J. O. Trends in vanadium neurotoxicity. *Brain Res Bull* **145**, 75–80 (2019).

102. Rehder, D. Vanadium. Its role for humans. *Met Ions Life Sci* **13**, 139–169 (2013).

103. Krutmann, J., Bouloc, A., Sore, G., Bernard, B. A. & Passeron, T. The skin aging exposome. *J Dermatol Sci* **85**, 152–161 (2017).

104. Zhu, J. *et al.* Composite Film of Vanadium Dioxide Nanoparticles and Ionic Liquid-Nickel-Chlorine Complexes with Excellent Visible Thermochromic Performance. *ACS Appl Mater Interfaces* **8**, 29742–29748 (2016).

105. Kim, H. *et al.* Flexible thermochromic window based on hybridized VO2/graphene. *ACS Nano* **7**, 5769–5776 (2013).

106. Kim, H. *et al.* Flexible thermochromic window based on hybridized VO2/graphene. *ACS Nano* **7**, 5769–5776 (2013).

107. Loquai, S., Baloukas, B., Zabeida, O., Klemberg-Sapieha, J. E. & Martinu, L. HiPIMS-deposited thermochromic VO2 films on polymeric substrates. *Solar Energy Materials and Solar Cells* **155**, 60–69 (2016).

108. Li, C. I. *et al.* Van der Waal Epitaxy of Flexible and Transparent VO2 Film on Muscovite. *Chemistry of Materials* **28**, 3914–3919 (2016).

109. Palneedi, H. *et al.* Laser Irradiation of Metal Oxide Films and Nanostructures: Applications and Advances. *Advanced Materials* **30**, 1–38 (2018).

Chapter 4

Sol-gel synthesis of VO_2 thin films

Table of contents

4 Chapter 4 – Sol-gel synthesis of VO_2 thin films 137

4.1 Introduction 139

4.2 V_2O_5 precursor 140

4.2.1 Solution stability 144

4.2.2 Film aging and moisture influence 146

4.2.3 Deposition over hot substrates and influence of drying temperature 147

4.3 $VO(acac)_2$ precursor 149

4.3.1 Solvent 149

4.3.2 Synthesis 152

4.3.2.1 Chemical composition of the solution 152

4.3.2.2 Solution aging 155

4.3.3 Thin film deposition and drying 157

4.3.4 Annealing atmosphere 161

4.3.5 Annealing temperature 166

4.3.6 Thin film thickness 170

4.3.7 Solution aging time 176

4.3.8 Atmosphere during synthesis and deposition 179

4.3.8.1 Inert atmosphere vs air 179

4.3.8.2 Moisture influence on synthesis and deposition 181

4.3.8.3 Moisture influence – conclusions 193

4.4 Conclusions 194

5.1 Introduction

As highlighted in Chapter 3, vanadium can form nearly 20 types of corresponding oxide phases. The VO_2 form displays more than 10 polymorphs, such as VO_2 (M), VO_2 (A) or VO_2 (B), which display the same chemical formula but hold totally different crystalline structure and optical and electrical properties.[1] The complexity of the vanadium-oxygen diagram, reported in Figure 3.1 in Chapter 3, imposes a strict control of the process conditions to obtain the desired vanadium oxide phase or polymorph.

Examining the literature, one aspect that clearly comes to light is the difficulty of meticulously controlling the process. Studies that employed matching conditions of synthesis, deposition, and thermal treatment, did not always produce the same vanadium oxide phases, but often led to different phases or to combinations of multiple oxides.[2–4] This highlights the need to carefully consider the influence of the multiple factors during sol-gel fabrication, such as solution aging, atmosphere during deposition, and annealing temperature, atmosphere, pressure, and time.

Concurrently, the urgency of lowering the energy consumption, with a particular focus on cooling systems, evidences the need for simple, low-cost, and straightforward solutions. As introduced in Chapter 3, thermochromic smart windows would amplify the impact on energy consumption if they could be easily processed on a wide range of substrates, including plastic panels, and worldwide distributed. Following these considerations, in Chapters 4-6 the experimental choices have been done with the ultimate goal of simplifying the process, when possible, once satisfactory functional properties were obtained.

In this chapter, the factors affecting the sol-gel processing of VO_2 thin films will be discussed. The common and overall process to produce VO_2 thin films was based on the following steps:

- the initial solution was synthesized, starting from the vanadium precursor, the solvent and eventual additives/reagents;
- the solution was aged under stirring, with the eventual addition of a reflux step at higher temperatures respect to room temperature;
- the solution was deposited on the chosen substrate by spin or dip coating, after proper cleaning of the latter;
- the as-deposited thin films were dried at mild temperatures conditions and aged for an appropriate time;
- the dried thin films were annealed in a tube furnace to induce the material's crystallization.

As mentioned in Chapter 1, many vanadium precursors, despite being widely employed, are linked to high levels of toxicity, carcinogenicity, mutagenicity, damages to the reproductive system or the aquatic environment.[5,6] This highlights the need for a safer process, in terms of both precursor and solvent. In this Chapter, two vanadium precursors were considered, vanadium pentoxide (V_2O_5) and vanadyl acetylacetonate ($VO(acac)_2$). The V_2O_5 powder, despite the carcinogenicity issues, is a widely used precursor to produce VO_2 thin films, so it was initially chosen as a reference starting point.

5.2 V_2O_5 precursor

The synthesis of VO_2 thin films was adapted from the work of Zhang *et al.*[7] and Sun *et al.*[8] and reported in Appendix A.1.3. To prepare the initial solution, 1.158 g of V_2O_5 (> 98%, Sigma-Aldrich) were mixed with 2.314 g of oxalic acid bi-hydrated ($H_2C_2O_4 \cdot 2H_2O$, 98%, Sigma-Aldrich) and 2.5 mL of bidistilled H_2O in 27.5 mL of absolute ethanol (EtOH, 99.9% purity, Emsure, Sigma Aldrich). The solution was refluxed for 18 h inside a round-bottom flask and heated in a silicon oil bath, set at 90°C. Oxalic acid acts as a reducing agent, decreasing the oxidation state of vanadium from V^{5+} to V^{4+} according to Eq. (4.1)[7]:

$$V_2O_5 + 3\ H_2C_2O_4 \leftrightarrow VOC_2O_4 + CO_2 + 3H_2O \qquad (4.1)$$

Following the aging time, the solution was spin coated on monocrystalline silicon wafers (p-type, [100] orientation, single-side polishing, Silicon Materials) and fused silica substrates (Quartz, Electro Optical Technology), previously cleaned through multiple solvent rinsing and atmospheric plasma treatment (Plasma Cleaner, PDC-002-CE, Harrick Plasma, USA). The spin coating (spin coater, WS-650MZ-23NPPB, Laurell) was performed in air, spinning the solution at 2000 rpm for 30 seconds. The thin films were then dried on a hot plate for 10 minutes at 150°C. The procedure was repeated to eventually increase the thickness of the film.

Following the reaction in Eq. (4.1) proposed by Zhang *et al.*[7], the vanadium oxidation state in the as-deposited thin films was initially assumed to be V^{4+}, already matching the target one in VO_2. The thermal treatment of the thin films was therefore performed under an inert N_2 flux. Since the thin films were spin coated in air, the possible oxidation to a higher oxidation state was considered. To eventually balance the latter, identically prepared thin films were annealed under a partially reducing

atmosphere of 5% H_2 in N_2 flux. The heat treatment was conducted in a tube furnace with a heating rate of 10°C/min for 2 h at 550°C. Initially, film cracking was seen on both silicon and fused silica substrates. This should be prevented as the presence of cracks constitutes an obstacle for electrical conductivity, as well as a light scattering source for the optical transmission. Uniform and continuous films were obtained by decreasing the heating rate during the thermal treatment to 5°C/min.

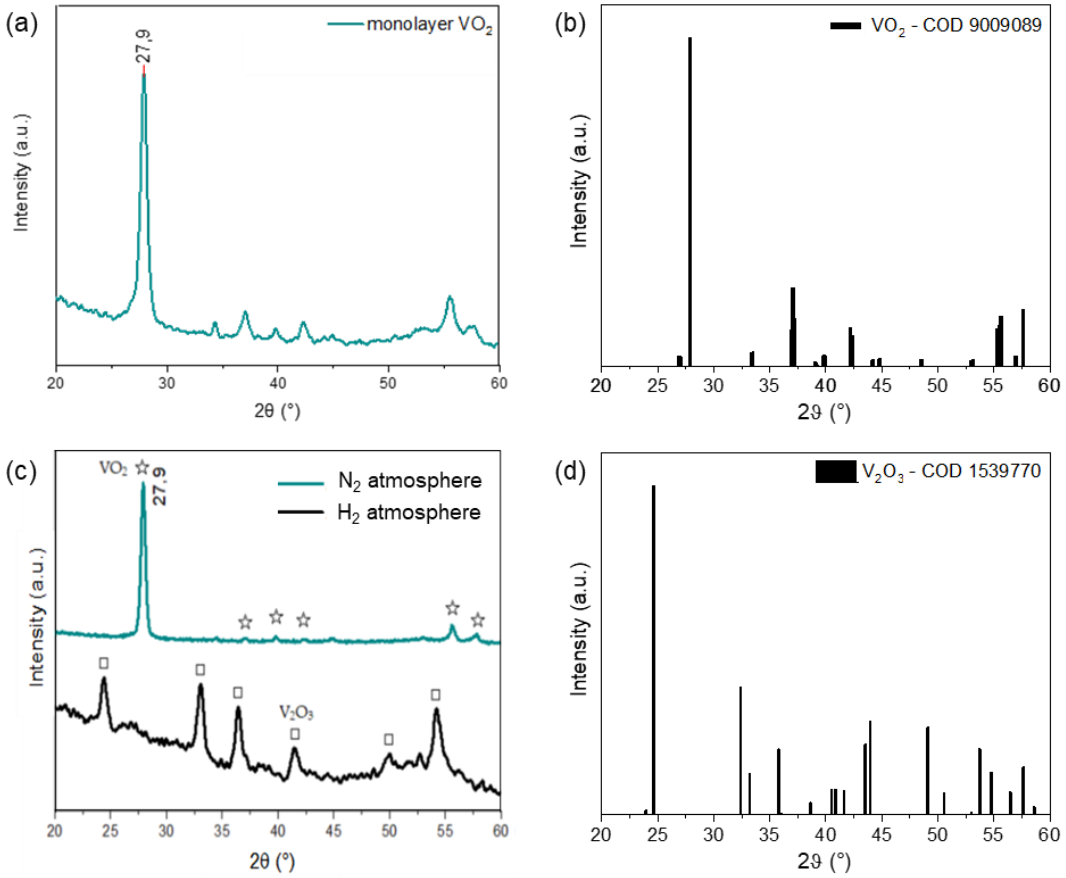


Figure 4.1. (a) Grazing incidence X-ray diffraction (GIXRD) of monoclinic VO_2 (M1) thin film. (b) Reference diffraction pattern of VO_2 (M1) - COD 9009089. (c) Vanadium-based thin films annealed under a nitrogen atmosphere or a 5% H_2 in N_2 flux. (d) Reference diffraction pattern of V_2O_3 - COD 1539770.

Figure 4.1 (a) displays the grazing incidence X-ray diffraction (GIXRD) patterns of the thin films on silicon substrate, annealed under N_2 flux. The diffraction peaks were associated to a monoclinic VO_2 (M1) crystalline structure (Figure 4.1 (b), COD 9009089). The crystalline structure of the material was characterized by a predominant orientation along the (0 1 1), as visible from the diffraction peak at 2Θ = 27.9°. Other principal orientations were detected at - 33.4° (-1 0 -2) - 37.1°(2 1 -1) - 39.9° (0 2 0) - 42.2° (2 1 -2) - 55.6° (2 1 -1) – 57.6° (0 2 2). The thin films annealed under partially reducing atmosphere were coherently reduced to a V^{3+} oxidation state (Figure 4.1 (c)). The diffraction pattern was matched to V_2O_3 (Figure 4.1 (d), COD 1539770). In the case of the reducing atmosphere, the GIXRD signal was less intense, which can be linked to a lower crystallinity, since the thin films were identically prepared and the GIXRD parameters were kept constant. Not all the diffraction peaks

matched a V_2O_3 pattern, but a mixture of multiple oxide phases was formed, with a predominant presence of V_2O_3.

The Scherrer equation (see Appendix A.2.6) was used to estimate the average crystallite dimension of the VO_2 thin films, which was found to be ~17 nm from a full width half maximum (FWHM) of 0.482. Ellipsometry measurements (J. A. Woollam Co. M2000 spectroscopic ellipsometer) were employed to determine the film's thickness of 50 ± 5 nm.

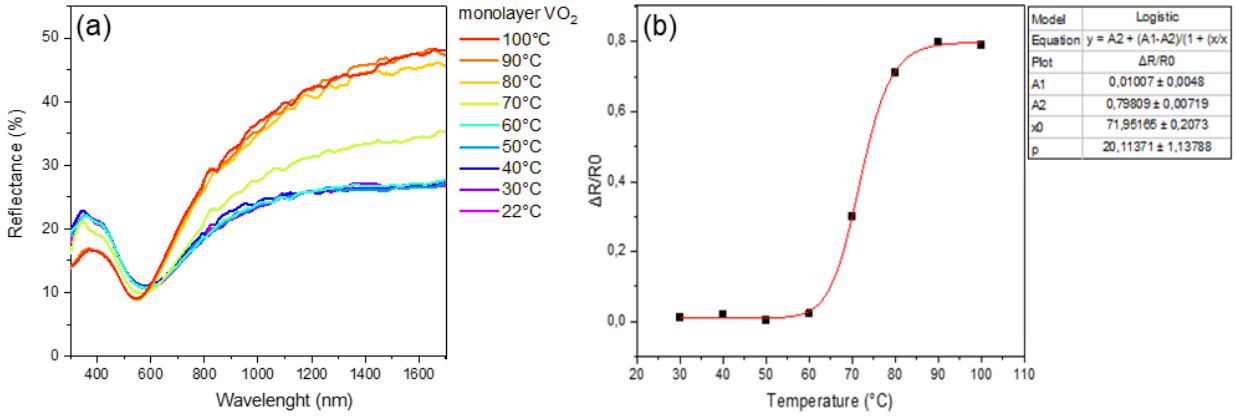


Figure 4.2. (a) Ellipsometry measurements of the reflectance of VO_2 thin film in function of increasing temperature (22-100°C) in the range 300-1700 nm. (b) Logistic model fitting of the reflectance values at 1600 nm in function of the increasing temperature.

The ellipsometer was used to measure the reflectance of the VO_2 thin films. The temperature-dependence of the optical properties was assessed *in-situ* through a heating attachment, which allowed to measure the film's reflectance while varying the temperature between room temperature and 100°C. The thermochromic performance of the sample was confirmed by the latter measurements (Figure 4.2 (a)). The reflectance shows unvaried behavior up to 60°C, above which an abrupt increase was seen. Upon further increase of the temperature to 80°C, the reflectance behavior was stabilized and remains unvaried at higher temperatures. The changes in reflectance upon a certain transition temperature further confirms the successful crystallization of the thin films into VO_2 (M1), which was previously shown by GIXRD. To determine the temperature at which the metal-insulator phase transition (MIT) is activated during heating (T_{heat}), the value of the reflectance at 1600 nm (i.e., in the near-infrared - NIR) was plotted in function of the temperature. A logistic function was applied to fit the data and the T_{heat} = 72°C was obtained from the inflection point of the corresponding curve. It should be noted that T_{heat} is not equal to the MIT transition temperature (T_c), as the former expresses the temperature at which the MIT occurs during the heating phase, whereas the latter is derived by taking into consideration the entire heating and cooling cycle. A proper control of the cooling system could not be performed, therefore preventing the measurement of the T_{cool}. The T_c is usually derived from the mean value between the transition temperatures during heating and cooling (T_{heat} and T_{cool},

respectively), therefore resulting to be $T_{heat} < T_c < T_{cool}$. A detailed explanation on the procedure to determine the T_c is reported in Appendix A.2.8.

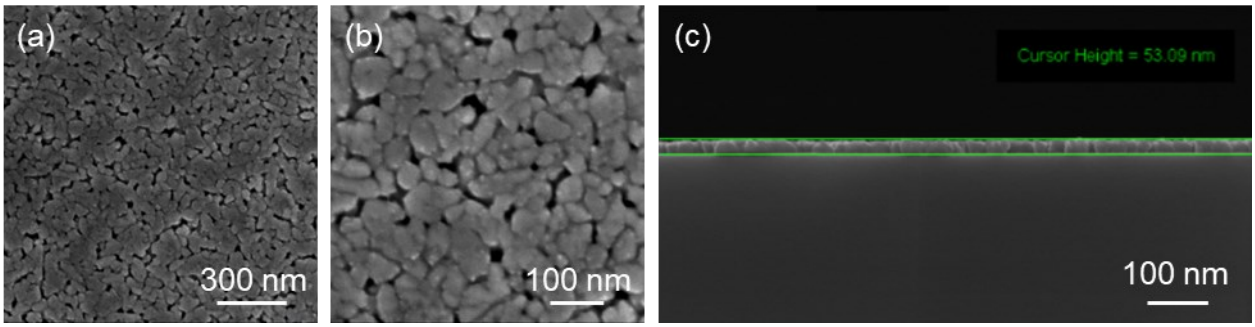


Figure 4.3. Scanning electron microscopy (SEM) images of a representative VO_2 thin film. (a, b) Surface images. (c) Cross section image. The scale bars are reported at the bottom right of each image.

The VO_2 film's morphology was studied with a scanning electron microscope (SEM), by analyzing both the surface (Figure 4.3 (a, b)) and cross section (Figure 4.3 (c)). The cross section confirmed the thickness value of 50 ± 5 nm, previously found with the ellipsometer. The film was characterized by a homogeneous distribution and surface coverage, displaying the spheroidal morphology typical of VO_2 thin films.[7,9]

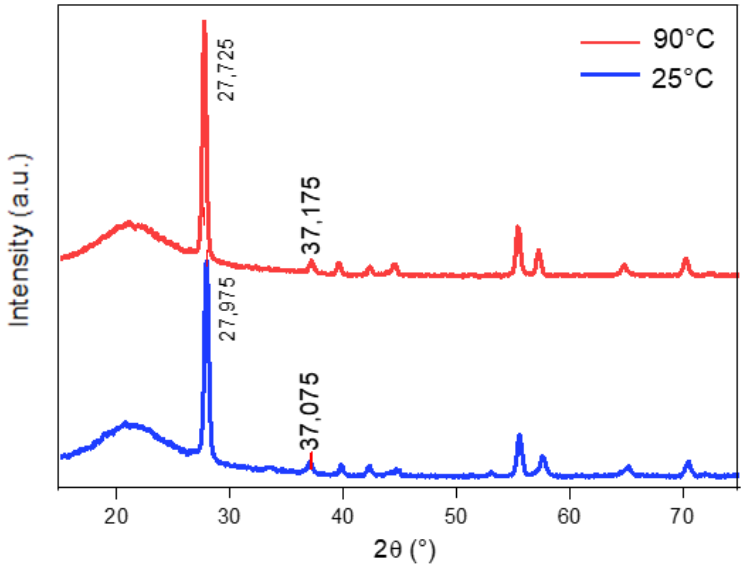


Figure 4.4. GIXRD patterns of VO_2 thin film on fused silica substrate at 25°C (monoclinic M1) and 90°C (rutile), respectively.

Table 4.1. Full-width half-maximum (FWHM) and crystallite dimensions estimated from the Scherrer equation for the monoclinic M1 and rutile VO_2 thin film.

	25°C Monoclinic (011)	90°C Tetragonal (110)
2Θ (°)	27,98	27,73
FWHM (°)	0,4543	0,4083
Crystallite dimension (nm)	19	21

Finally, the VO_2 thin films deposited on fused silica substrates were analyzed to check an eventual influence of an amorphous substrate rather than a monocrystalline silicon one. Moreover, the transparency of the former allows for a better representation of a smart windows, respect to silicon substrates. The GIXRD patterns matched the previously reported ones (Figures 4.1, 4.4) and confirmed the successful crystallization of VO_2 (M1) on fused silica (COD 9009089). The predominant orientation along the (0 1 1) direction was as well confirmed. The metal-insulator transition was assessed by *in-situ* GIXRD analysis in function of the temperature, exploiting a heating cell attachment. The monoclinic to rutile phase change is indeed visible by comparing the 25°C measurement with the 90°C one (Figure 4.4). The transition to a rutile structure is manifested with a shift towards lower 2Θ values, from the monoclinic 2Θ = 27.98° (0 1 1) to the tetragonal 2Θ = 27.73° (1 1 0), which corresponds to a slight increase in the interplanar distance. The less intense peak at 2Θ = 37.08° was seen to shift to 2Θ = 37.18°, with an opposite behavior respect the principal orientation. This trend was found in previous works.[10,11] Johnson *et al.*[12] evidenced the overall slight increase in volume of the unit cell, which was found to increase of ~1% upon the MIT from monoclinic M1 to rutile.

Following the preliminary results, additional studies were conducted to assess the reproducibility and the influence of the process parameters, such as the solution's stability, the film's stability, and the drying temperature.

5.2.1 *Solution stability*

The stability of the initial solution has a crucial influence on the reproducibility of the process. As the whole synthesis and deposition steps are performed in air, it is vital to ensure that the solution is stable under environmental conditions. As mentioned in the introduction of Paragraph 4.2, the reaction between V_2O_5 powder and oxalic acid leads to a decrease in the oxidation state of vanadium from V^{5+} to V^{4+}. Considering the typical colors of the different oxidation states of vanadium in aqueous solution, yellow corresponds to V^{5+}, green to V^{3+} and blue to V^{4+}. During the synthesis, the initial

yellow color of the solution turns to green within 1 h and then evolves to blue after the 18 h under reflux in the oil bath, further confirming the reduction of the V_2O_5 precursor in solution. While the latter was confirmed to be stable if deposited within a few hours, higher aging times led to variable color variations, highlighting the instability of the solution. In some cases, the solution turned to a dark green color, indicating that a partial change in the oxidation state was induced.

To verify the solution influence on the final thin films, two thin films were deposited and annealed under the same processing conditions. The first was deposited from the standard fresh blue solution, whereas the second was deposited from a green solution, aged for 1 day under the environmental laboratory conditions (23°C, 50% relative humidity – RH). Both films were annealed at 550°C under a N_2 flux, as previously described.

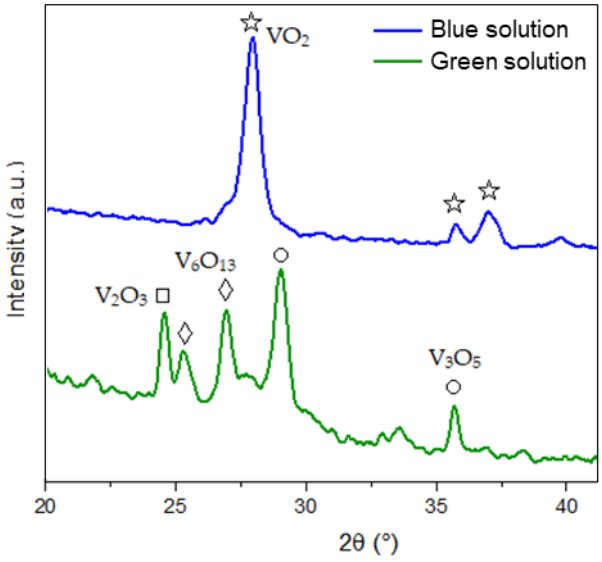


Figure 4.5. GIXRD patterns of monoclinic VO_2 (M1) thin film, obtained from the "blue" solution, and the mixture of vanadium oxides obtained from the "green" solution.

The resulting thin films were analyzed by GIXRD (Figure 4.5). While the blue solution was confirmed to led to monoclinic VO_2 (M1), the green solution led to the formation of a mixture of different oxidation states. Given the multiplicity of oxides, an accurate peak indexing could not be performed. Diffraction peaks from a mixture of V_2O_3, V_6O_{13} and V_3O_5 were detected, as reported in Figure 4.5.

The results indicate that, while the fresh solution allows the deposition of the thin films to be performed within several hours, further aging prevents the formation of the target VO_2 thin films. Therefore, a fresh solution should be prepared to ensure the crystallization into monoclinic VO_2 (M1) and avoid the concurrent formation of multiple oxide phases.

5.2.2 *Film aging and moisture influence*

Another factor influencing the reproducibility of the process is the stability of the dried films before the annealing step. To verify the effect of the film's aging, two thin films were deposited and annealed under the same processing conditions. The difference between the two was the aging time of the film before annealing, which was a few minutes in one case and 1 day for the second sample. The film's aging was conducted inside a sealed chamber under low moisture conditions of 23°C and 20% RH.

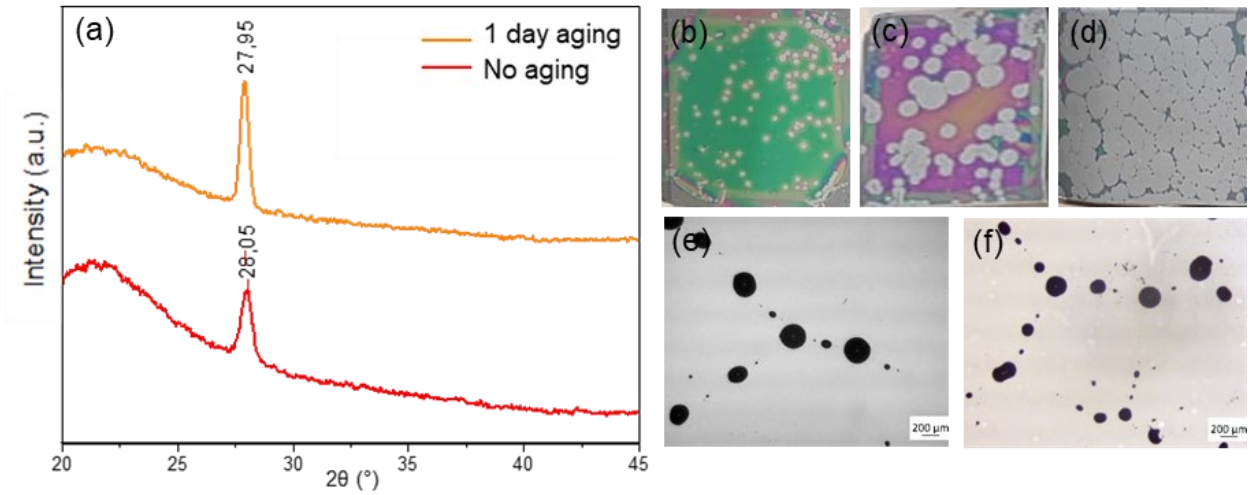


Figure 4.6. (a) GIXRD patterns of monoclinic VO_2 (M1) thin films, either aged for 1 day under low moisture conditions or immediately annealed. (b-d) Images and (e, f) optical microscopy images of the gradual dewetting of the dried thin film, upon aging under high moisture conditions.

From the GIXRD results (Figure 4.6), the crystallization into monoclinic VO_2 (M1) was confirmed and the average crystallite dimension was estimated through the Scherrer formula. The aging of 1 day led to an average crystallite dimension of ~20 nm, respect to the ~15 nm of the film annealed right after deposition. The stability under higher moisture conditions was also verified. The previous experiment was repeated, but the aging of the second sample was performed at 23°C and 45% RH. In this case, dewetting of the film was found to start within the first few minutes (Figure 4.6 (b)). The progressive withdrawal of the film led to the formation of isolated particles on the substrate (Figure 4.6 (c, d)), with complete dewetting after 1 day as visible from the optical microscope images (OM, Figure 4.6 (e, f)).

Therefore, the aging of the film induced a two-fold effect, in function of the moisture conditions. Low moisture conditions favored an increase in the average crystallite size, without affecting the homogeneous surface coverage, whereas moisture conditions higher than 45% RH at 23°C led to a progressive dewetting of the film, compromising the final surface coverage.

5.2.3 *Deposition over hot substrates and influence of drying temperature*

The dewetting of the films under high moisture conditions could be prevented by inducing a rapid evaporation of the solvent during the first phases of the deposition step. The rapid solvent evaporation is usually induced by raising the film's temperature immediately after the deposition, by rapidly transferring the sample from the spin coater to the hot plate. Even if the dewetting rate was reduced by the rapid solvent evaporation, the formation of holes within the film could not be totally prevented.

The deposition over hot substrates was tested during the spin coating step. The substrate was heated to 150°C on a hot plate and rapidly transferred to the spin coater. The solution was then dropped on the hot substrate within a few seconds and the spin coating phase was started, leading to an accelerated solvent evaporation and formation of the metal-oxide network. The dewetting was successfully prevented and a homogeneous coverage was confirmed by the OM images (Figure 4.7 (b)).

To verify whether the higher temperature had an impact on the vanadium oxide phase, two thin films were annealed under the same processing conditions. The deposition step was identical, except for the temperature during the spin coating phase, which was room temperature (RT) for the first film and ~150°C for the second film.

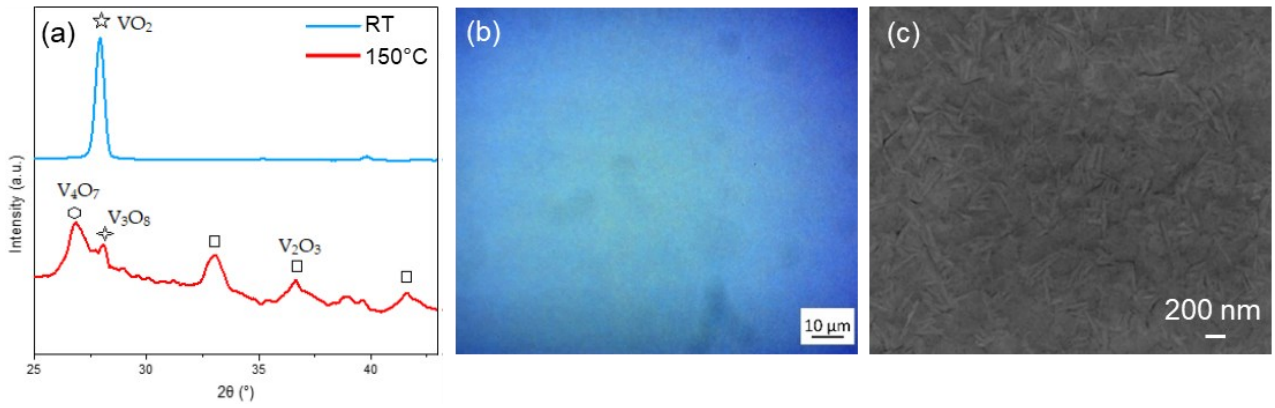


Figure 4.7. (a) GIXRD patterns of the thin films, spin coated at either room temperature (VO_2 (M1) or at ~150°C (mixed of vanadium oxides). (b) Optical microscopy and (c) scanning electron microscopy images of the thin film deposited at ~150°C and annealed at 550°C.

The analysis of the morphology at higher magnifications, i.e., with SEM, highlighted the formation of elongated needle-like morphologies (Figure 4.7 (c)), remarkably different respect to the ones found with previous samples (Figure 4.3). The GIXRD analysis (Figure 4.7 (a)) confirmed that the higher temperature during deposition led to an unfavorable alteration of the vanadium oxidation state. The standard annealing under inert atmosphere, in the case of the second sample, led to the formation of multiple oxide phases with an unclear diffraction pattern. The indexing of the diffraction peaks was proposed to be a mixture of V_4O_7, V_3O_8 and V_2O_3. The higher temperature during the deposition step

avoided the progress of film's dewetting under high moisture conditions but prevented the formation of crystalline monoclinic VO_2 (M1), leading to the formation of multiple oxide phases.

Following the studies on the film's stability, the influence of the drying temperature was considered. It was found that a drying temperature of 150°C did not lead to major increases of the film's thickness, upon increasing the number of deposited layers. To solve the issue, the drying temperature was raised to 300°C. Similarly to the previous tests, two thin films were deposited and annealed under the same processing conditions. The two samples only differed in terms of the temperature, which was 150°C for the reference sample and 300°C for the second film.

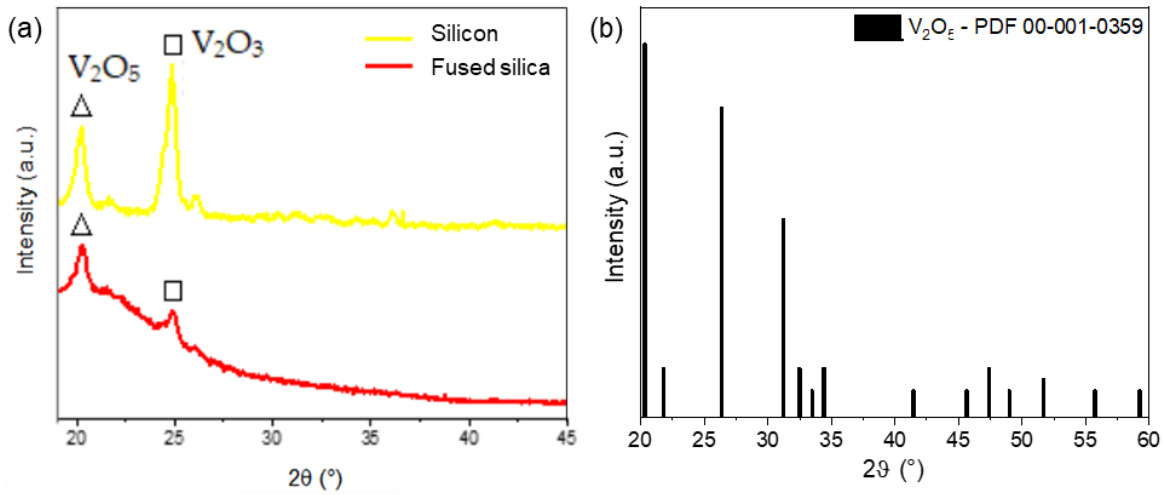


Figure 4.8. (a) GIXRD patterns of the thin films dried at 300°C and annealed at 550°C, on both silicon and fused silica substrates. (b) Reference diffraction pattern of V_2O_5.

The GIXRD was performed on both silicon and fused silica substrates (Figure 4.8 (a)). The drying temperature of 300°C led to the formation of a mixture of oxide phases, which could be attributed to the concurrent presence of V_2O_3 and V_2O_5.

Considering the overall results, the synthesis based on the V_2O_5 precursor allowed for the formation of crystalline monoclinic VO_2 (M1) thin films, which displayed the desired thermochromic properties. However, several issues regarding the stability of both the solution and the dried films were found, which limit the scalability of the process. As evidenced in Chapter 3, several vanadium precursors are highly toxic and carcinogenic, including the V_2O_5 powder. As a general approach and when possible, during the PhD research the choice of precursors, reagents and solvents was preferentially oriented towards a green chemistry route. Following these considerations, vanadyl acetylacetonate ($VO(acac)_2$) was considered as an alternative precursor for the synthesis and deposition of VO_2 thin films.

5.3 $VO(acac)_2$ precursor

The reduction of the energy load required for the process and the use of environmentally friendly and non-hazardous reagents are among the fundamental principles of green chemistry. The latter were assembled as[13]:

1. Prevention of waste.
2. Atom economy - all the materials used should be incorporated into the final product.
3. Less hazardous chemical synthesis.
4. Designing safer chemicals.
5. Safer solvents and auxiliaries.
6. Design for energy efficiency.
7. Use of renewable feedstocks.
8. Reduce derivatives.
9. Catalysts.
10. Design for degradation.
11. Real-time analysis for pollution prevention.
12. Inherently safer chemistry for accident prevention.

5.3.1 *Solvent*

The synthesis of VO_2 thin films based on the metal-organic $VO(acac)_2$ precursor started from the choice of a proper solvent. Considering the twelve principles reported above, ethanol, isopropanol and water were chosen as potential solvents. The latter were compared with less favorable solvents, such as methanol and acetonitrile, chosen according to previous literature.[14,15] Water and isopropanol were discarded, as they allowed very low solubility of the metal-organic precursor.

Ethanol was then compared to methanol and acetonitrile. Identical 100 mM solutions were freshly prepared and stirred at room temperature inside closed vials. Since the first few minutes after mixing precursor and solvent, a higher solubility of methanol was noticed with respect to the other solvents. For each solution, a single layer was deposited by spin coating after 5 days of stirring. The latter were subsequently dried at temperatures which were set to be 5°C higher with respect to the boiling point of each solvent, leading to 70-83-87°C for methanol, ethanol, and acetonitrile, respectively. The ellipsometry measurements evidenced a film's thickness around 20 nm irrespectively of the solvent. However, the data fittings of the films deposited from the methanol and acetonitrile solutions

displayed a higher mean square error (MSE) with respect to the ethanol-based film, indicating a lower quality of the film.

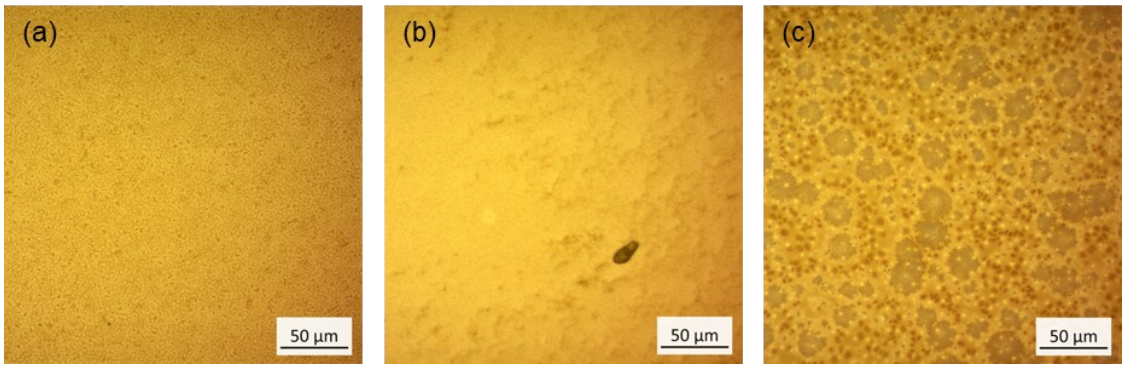


Figure 4.9. Vanadium-based dried thin films from (a) ethanol, (b) acetonitrile, (c) methanol solvent.

To explain the ellipsometry results, the quality of the as-deposited thin film was assessed from the OM images (Figure 4.9). The film from the ethanol-based solution (Figure 4.9 (a)) was characterized by a higher homogeneity respect to the acetonitrile and methanol ones (Figure 4.9 (b, c)).

The Life-Cycle Assessment (LCA) method evaluates the environmental impact of a solvent's life cycle by quantifying emissions and resource use throughout the substance's life cycle. The Environmental, Health and Safety (EHS) method evaluates organic substances according to three risk categories, namely the risk factors for the environment (persistence, airborne, aquatic hazards); health risks (acute toxicity, rashes, chronic toxicity); security risks (explosions, fires, chemical reactions). The combined ECA and EHS results indicate that ethanol and methanol are among the best organic solvents from this perspective, whereas acetonitrile is not recommended due to environmental and health issues.[16] The production of ethanol greatly relies on biomass fermentation, which allows for environmentally friendly farming practices. Conversely, methanol is mostly produced from fossil fuels, i.e., natural gas reforming, which prevents the use of sustainable and renewable resources. Methanol is responsible for chronic toxicity risks, as the human body converts it to formic acid, responsible of causing blindness through permanent optic nerve damage.

From the above results, ethanol was chosen as the solvent for the process. The lower solubility of the precursor in the latter respect to methanol was counterbalanced by the higher film quality and lower toxicity for the human health.



Figure 4.10. Color evolution with increasing aging time of the solution, from (a) solution creation to (e) solution after stirring at room temperature for 1 day.

Following the solvent choice, another aspect that was investigated was the color variation noticed in all three solvents, with increasing aging time of the solution. The typical color evolution is reported for an ethanol-based solution in Figure 4.10. The initial blue color of the precursor dissolved in ethanol evolved within 1 day to dark green, gold-brown, and finally ruby-red, while being stirred at room temperature in a round-bottom flask. The final color was seen to be stable for months if the exposure to air was not prevented. As the solution was prepared in air, the influence of moisture and oxygen was considered, besides a potential reaction between the $VO(acac)_2$ precursor and ethanol. To understand which key factor was responsible for the color change, the influence of the different parameters was considered singularly by excluding the remaining ones. First, the solution was prepared inside a glove box, with O_2 < 2 ppm and H_2O < 2 ppm. The solution did not show any variation from the initial blue color of Figure 4.10 (a) and was stable for months. Therefore, the eventual interaction between the solvent and the precursor was excluded from being responsible for the color variation. The influence oxygen on the solution was then tested. A fresh 100 mM solution of $VO(acac)_2$ in ethanol was prepared in round bottom flask inside a glove box, with O_2 < 2 ppm and H_2O < 2 ppm. The flask was sealed with a rubber Suba seal septum and subsequently transferred outside the glove box. One needle was inserted through the rubber cap and oxygen gas was bubbled through the solution, while a second needle allowed for a pressure release. The oxygen gas was flowed for 5 seconds inside the system, after which both needles were removed and the septum was further sealed with parafilm. The color evolution was monitored by acquiring photographs every 30 minutes, without exposing the solution to additional variations in atmosphere. The solution displayed the same color variations of the system prepared in air (Figure 4.10) and showed a stable ruby red color after 18 h. Oxygen was therefore proven to be the key factor responsible of the color variation. The third factor, i.e., moisture, was found to play a crucial role during the deposition phase, as will be discussed in paragraph 4.3.8.

5.3.2 *Synthesis*

5.3.2.1 *Chemical composition of the solution*

Following the identification of oxygen as the factor responsible for the color change, eventual chemical variations of the solution were studied by UV-Vis spectroscopy. The 100 mM solution led to a saturation of the signal, therefore dilutions were applied according to the range of interest (UV or Vis). A total volume of 3 mL was added within a standard quartz cuvette, with a ~0.25 mM concentration for the UV range (190–400 nm) and a ~12 mM concentration for the Vis range (400-900 nm). The cuvette was closed with a cap and the measurement of the absorbance of the solution was repeated every 15 min to monitor the solution variations induced by the exposure to air (Figure 4.11 (b)).

The crystal structure of $VO(acac)_2$ has a C_{2v} symmetry, in which the vanadium atom displays a double bond with oxygen (V=O) and is aligned perpendicularly respect to the plane defined by the four chelating oxygen atoms, resulting in ~0.3-0.6 Å distance. The vanadium atom is located at 1.59 Å distance from the double bonded oxygen and at 1.97 Å from the remaining four oxygen atoms.[17]

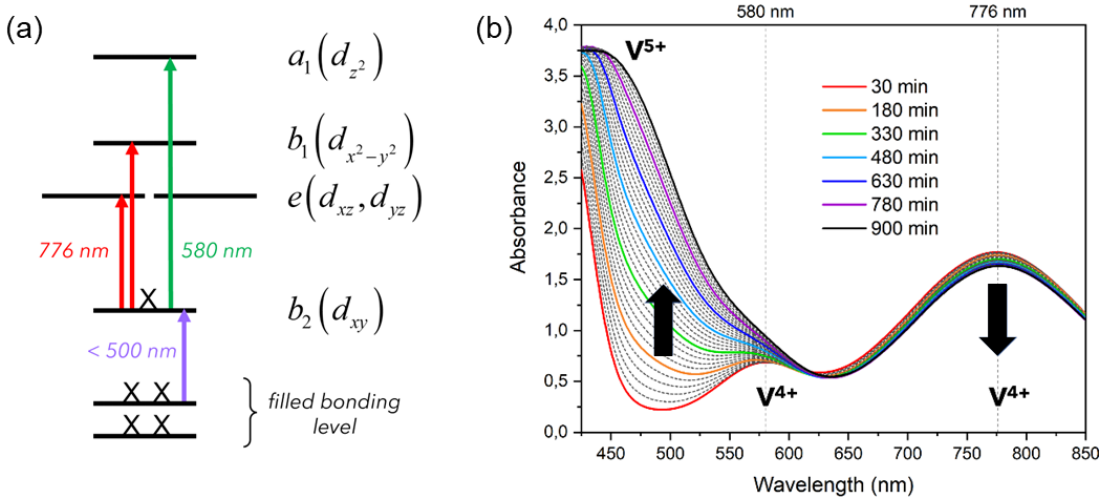


Figure 4.11. (a) Schematic of the electronic energy levels of the vanadium complex (V^{4+} with [Ar] $3d^1$) with C_{2v} symmetry, (b) UV-Vis spectroscopy of the solution, repeated every 15 min to monitor the solution variations induced by the exposure to air.

The electronic energy levels of the vanadium complex (V^{4+} with [Ar] $3d^1$) with C_{2v} symmetry for the quadratic pyramid are shown in Figure 4.11 (a). The b_2 state derives from V ($3d_{xy}$ orbital), whereas the *e* state is a combination of orbitals from V and O. Therefore, the $b_2 \rightarrow e$ transition should display a higher susceptibility to axial solvent perturbations. The ENDOR spectroscopy was used by Makinen *et al.*[17] to evaluate the structure of $VO(acac)_2$ in a methanol solution. They found that in the alcoholic solvent, the $VO(acac)_2$ does not undergo any conformational changes, but a solvent molecule

coordinate to the structure through an axial hydrogen bonding to the oxygen of the V=O bond. A second solvent molecule coordinates to the vanadyl center through the oxygen present in the alcohol molecule.

Choi *et al.*[18] and Geiser *et al.*[19] studied the behavior of vanadyl sulfate ($VOSO_4$) in sulfuric acid (H_2SO_4) for vanadium redox flow batteries. They varied the oxidation state of V by applying charge and discharge cycles, monitoring the corresponding variations in the absorption spectra. In function of the number of available electrons in the t_{2g} state, the octahedral configuration allows for *d-d* orbital transitions for oxidation states of V^{4+} ($3d^1$) or lower, whereas charge transfer transitions are induced in the case of V^{5+} ($3d^0$). They associated the *d-d* transitions to the UV-Vis peaks at 400-610 nm (V^{3+}) and 765 nm (V^{4+}), whereas the charge transfer transition was correlated to the 390 nm peak (V^{5+}).[18,19]

As previously mentioned, the $VO(acac)_2$ displays a different configurational symmetry and chemical environment respect to $VOSO_4$, therefore the peaks should not be expected at the same wavelength of the latter. Regarding the visible range, two peaks were found by measuring the solution of $VO(acac)_2$ in ethanol, respectively at ~580 e ~776 nm (Figure 4.11 (b)). According to the literature[17,20,21], the latter correspond to the $d_{xy} \rightarrow d_{z2}$ transition (Figure 4.11 (a), green) and the $d_{xy} \rightarrow d_{xz},d_{yz}$ and $d_{xy} \rightarrow d_{x2-y2}$ transitions (Figure 4.11 (a), red), respectively. The band below 500 nm is correlated with a charge transfer transition between the electrons of the ligands and the b_2 level. The band was found to progressively increase with increasing air exposition time. Compared to the initial 4+ state, the energy of the process increases in consequence of the electron transfer to the d_{xy} level. With the progress of oxidation, the electron of $3d^1$ is removed, leading to V^{5+} ($3d^0$). The resulting decrease in repulsion energy, due to the electron loss, is manifested through an in increased absorbance around 500 nm and a decrease in absorbance at 776 nm.[17,20,21]

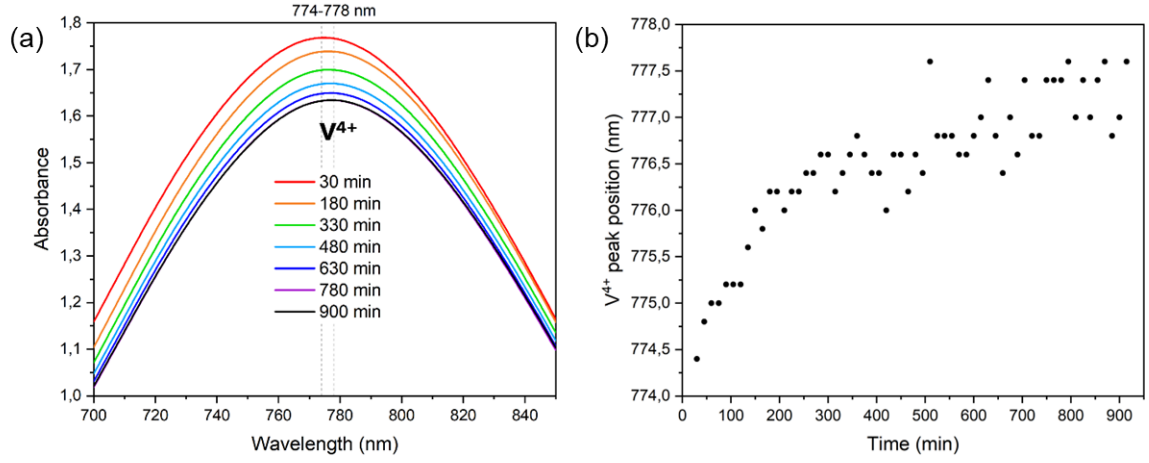


Figure 4.12. (a) UV-Vis spectroscopy in 700-860 nm range of the solution of $VO(acac)_2$ in ethanol with increasing aging time in air. (b) Plot of the V^{4+}peak position in fucntion of aging time.

The peak at ~776 nm was seen to progressively shift towards lower energies with increasing exposure to air (Figure 4.12 (a, b)). This could be related to a slight variation in the V=O bond, as the $b_2 \rightarrow e$ transition was found to be more susceptible to solvent perturbations.[17]

To further confirm the previous associations between the oxidation state and the UV-Vis peaks, oxidizing and reducing agents were separately added to the initial solution to boost the oxidation and reduction rate, respectively.

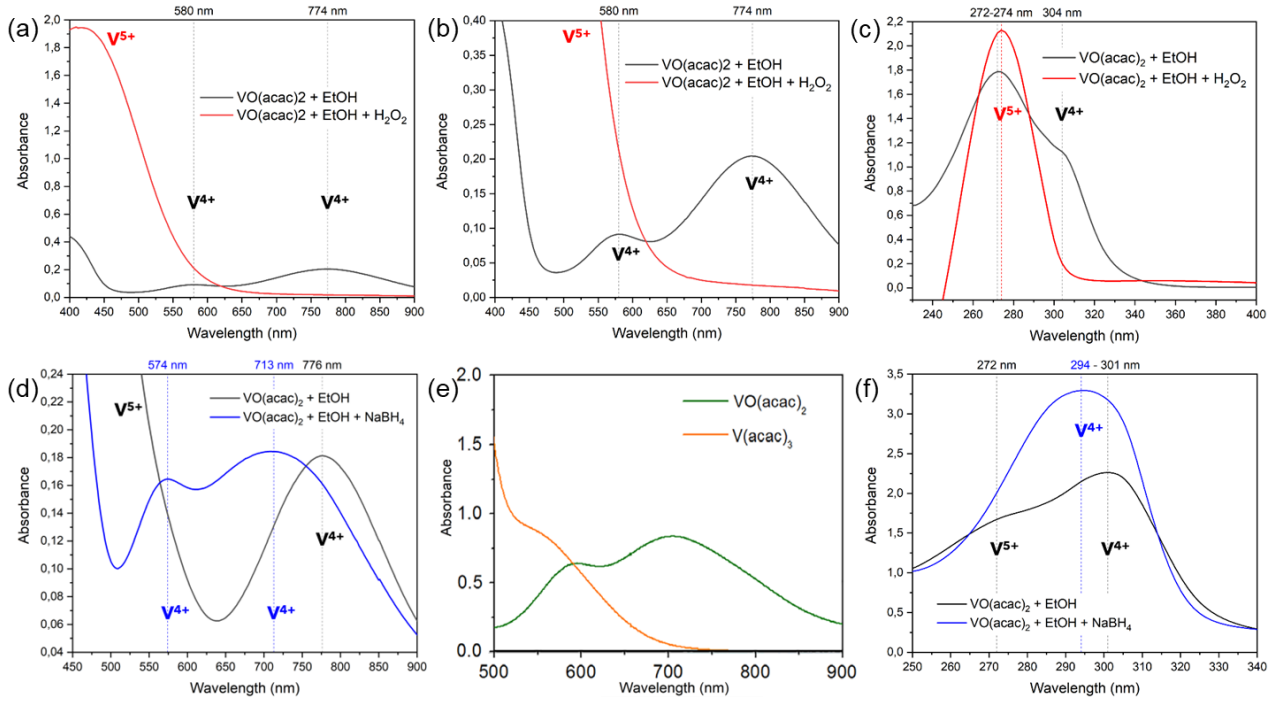


Figure 4.13. (a) Vis absorption spectra in the 400-900 nm range of the fresh solution of $VO(acac)_2$ in ethanol (black line) and of the fresh solution of $VO(acac)_2$ in ethanol with ~200 µL H_2O_2. (b) Zoom of Figure (a) in the Absorbance range below 0.4. (c) UV absorption spectra in the 190-400 nm range of the fresh solution of $VO(acac)_2$ in ethanol (black line) and of the fresh solution of $VO(acac)_2$ in ethanol with ~200 µL H_2O_2. (d) Vis absorption spectra in the 450-900 nm range of the fresh solution of $VO(acac)_2$ in ethanol (black line) and of the fresh solution of $VO(acac)_2$ in ethanol with few mg of $NaBH_4$. (f) UV absorption spectra in the 250-340 nm range of the fresh solution of $VO(acac)_2$ in ethanol (black line) and of the fresh solution of $VO(acac)_2$ in ethanol with few mg of $NaBH_4$. (e) Reference absorption spectra of $VO(acac)_2$ and $V(acac)_3$ from ref.[22]

Following the previously describe procedure, fresh solutions of $VO(acac)_2$ in ethanol were prepared and diluted according to the range under investigation (Vis or UV). The absorbance of the solution was measured before the addition of further reagents, as a reference spectrum. To analyze the oxidation of the precursor, ~200 µL of hydrogen peroxide (H_2O_2, 30% v/v in H_2O, Sigma Aldrich) were directly added to the cuvette and the absorbance measurement was repeated. Figure 4.13 (a, c) shows the absorbance spectra in the Vis and UV range, respectively, before and after the addition of H_2O_2. A higher magnification of the Vis region is reported in Figure 4.13 (b). The addition of the oxidizing agent led to the disappearance of the peaks relative to the V^{4+} state and to the formation of a predominant absorbance band centered at ~400 nm, confirming the previous associations. In the UV range, the addition of H_2O_2 led to the full disappearance of the peak at 304 nm, with a

predominant presence of the 274 nm peak. The two peaks, respectively assigned to V^{4+} and V^{5+}, are in agreement with the results of Grybos *et al.*[23], who studied the oxidation of $VO(acac)_2$ in methanol. Similarly to what observed in the Vis range (Figure 4.13 (b)), the position of the V^{5+} peak slightly shifts from 272 nm to 274 nm with the boost in oxidation.

To analyze the reduction of the precursor, the absorbance of a solution exposed to air for 4 months was measured as a reference spectrum. A few mg of sodium borohydride powder ($NaBH_4$, >98%, Sigma Aldrich) were directly added to the cuvette and the absorbance measurement was repeated. Figure 4.13 (d, f) shows the absorbance spectra in the Vis and UV range, respectively, before and after the addition of $NaBH_4$. Coherently with the previous results, the initial addition displayed the presence of a mixture of V^{5+} and V^{4+} states. The addition of the reducing agent led to a reduction of the V^{5+}, with the formation of two peaks at 574 nm and 713 nm (Figure 4.13 (d)). The position of the latter peaks is blue-shifted by 6 nm and 60 nm, respectively, with respect to the spectrum of a fresh solution (Figure 4.13 (b)). This might be caused by a further reduction from V^{4+} to V^{3+} induced by $NaBH_4$, which is a powerful reducing agent. This hypothesis is supported by the findings of Choi *et al.*[18] and Geiser *et al.*[19], who assigned a 610 nm peak to V^{3+} in the case of $VOSO_4$ precursor. Moreover, Park *et al.*[22] compared the absorbance spectrum of $V(acac)_3$ (V^{3+}) and $VO(acac)_2$ (V^{4+}) (Figure 4.13 (e)), from which a peak at 560 nm is seen in the case of the V^{3+} precursor. From these considerations, the peak at 574 nm cannot be assigned to pure V^{3+} or V^{4+}, as it could be related to the concurrent presence of both oxidation states. In the UV range, the addition of leads to the formation of a broad peak, centered at 294 nm. The blue-shift of the peak respect to the 304 nm (V^{4+}) of the fresh solution is coherent with the results seen from the Vis range. For the explanation of the shifts, the potential oxidation or reduction of the solvents should also be considered, as H_2O_2 and $NaBH_4$ represent powerful oxidating and reducing agents, respectively.

By combining the overall results, during the synthesis step of the VO_2 film fabrication, the solution of $VO(acac)_2$ in ethanol was found the be composed by a mixture of a V^{4+} and V^{5+} oxidation states.

5.3.2.2 *Solution aging*

Following the analysis of the oxidation state composition by UV-Vis spectroscopy, the solution was optimized to improve the homogeneity in terms of film deposition.

Identical 100 mM solutions in absolute ethanol were prepared and the temperature and aging time were varied to find the best combination. Considering the work of Pan *et al.*[14] and Yu *et al.*[24], four

conditions were tested, namely stirring at room temperature or at 78°C under reflux for either 2 h or 24 h. The aging time of the solution for more than 1 day was also considered. Each solution was filtered prior to the deposition with 0.2 μm pore sized filters and spin coated on silicon substrates at 2000 rpm for 30 seconds. Each layer was dried on a hot plate at 150°C for 15 min. For all five aging conditions, 1 layer and 3 layers were respectively deposited and compared. The thickness, refractive index (n) and extinction coefficient (k) of the 10 samples were characterized by ellipsometry and optical microscopy. The ellipsometry data are reported in Table 4.2.

Table 4.2. Ellipsometry data of the thin films deposited after stirring at room temperature or at 78°C under reflux for either 2 h, 24 h, or 3 weeks. Thickness (nm), refractive index (n) and extinction coefficient (k) are reported at 400 nm and 500 nm for each film. The values with the asterisk indicate that the fitting was not reliable and the value should be considered an indicative one.

	Thickness / nm	$n_{400\ nm}$	$k_{400\ nm}$	$n_{500\ nm}$	$k_{500\ nm}$
20°C - stir 2 h - 1L	20*	1.42*	0.01*	1.41*	0.00*
20°C - stir 24 h - 1L	12*	2.18*	0.95*	1.95*	0.72*
20°C - still 3 w - 1L	25*	1.71*	0.17*	1.60*	0.13*
78°C - stir 2 h - 1L	37*	1.46*	0.00*	1.43*	0.00*
78°C - stir 24 h - 1L	28	1.97*	0.10	1.90	0.03
20°C - stir 2 h - 3L	40*	1.64*	0.05*	1.60*	0.02*
20°C - stir 24 h - 3L	38*	1.52*	x*	x*	x*
20°C - still 3 w - 3L	61	1.96	0.09	1.88	0.05
78°C - stir 2 h - 3L	78	1.85	0.06	1.71	0.06
78°C - stir 24 h - 3L	91	1.90	0.07	1.81	0.07

Considering the single-layered films, the solution deposited after stirring at room temperature for 2 h led to the formation of a fragmented film, composed by isolated particles instead of a uniform layer. Similarly, inhomogeneous films were still obtained by increasing the stirring time to 24 h at room temperature or by stirring for 2 h at 78°C. The inhomogeneity of the films was confirmed by the fitting of the ellipsometry data. The values with the asterisk indicate that the fitting was not reliable and the value should be considered an indicative one. The three thin films mentioned above were indicatively ~20 nm, but the refractive index values were out of the standard range of homogeneous dried VO_2 thin films ($n_{400\ nm}$~1.7-1.9) and closer to the ones of SiO_2 ($n_{400\ nm}$~1.45). This probably resulted from the native SiO_2 layer that covers the surface of the silicon substrate, which was exposed in the case of fragmented inhomogeneous films. The film quality improved by aging the solution for 3 weeks, while the best homogeneity was reached by increasing the stirring time at 78°C to 24 h. From the above results and from additional tests (data not shown), the optimized parameters for the

synthesis of the solution were found to be stirring at 78°C for more than 2 h and subsequently aging the solution without stirring for at least 1 day at room temperature.

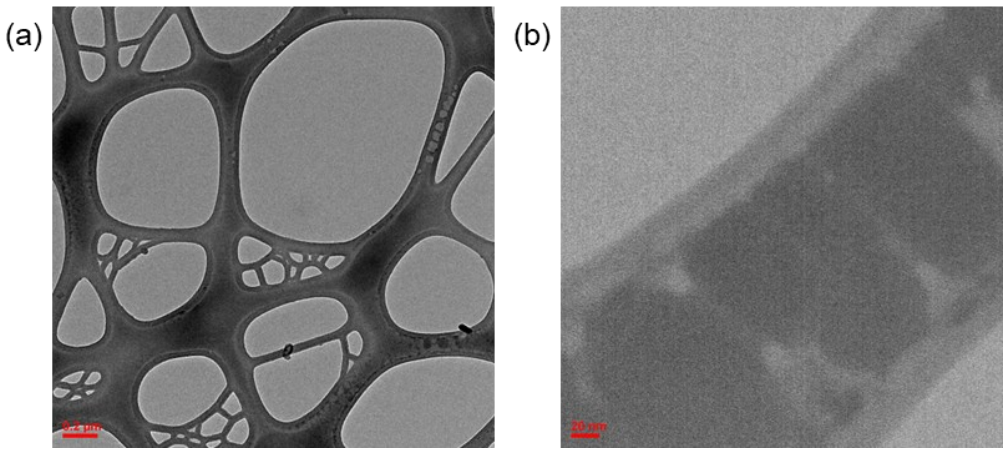


Figure 4.14. Transmission electron microscopy (TEM) of a typical process solution, i.e. stirred at 78°C for 24 h and aged for more than 3 days at room temperature. The solution was diluted and drop casted on a continuous carbon TEM grid.

Transmission electron microscopy (TEM) to verify the eventual formation of nanoparticles during the synthesis step. The typical process solution, i.e. stirred at 78°C for 24 h and aged for more than 3 days at room temperature, was diluted and 5 µL were deposited by drop casting on a continuous carbon TEM grid. The presence of nanoparticles was not detected within the solution (Figure 4.14), therefore the formation of an amorphous metal-oxide network during the deposition step was confirmed. The formation of the preliminary crystallites was detected within the dried thin films, as will be shown in the following paragraphs.

5.3.3 *Thin film deposition and drying*

Author disclosure statement: part of the data shown in this paragraph was published in the article "Basso, M. *et al.* Rapid laser-induced low temperature crystallization of thermochromic VO_2 sol-gel thin films. *Applied Surface Science*, Volume 631, 157507 (2023). ISSN 0169-4332. https://doi.org/10.1016/j.apsusc.2023.157507 ".[25]

During the fabrication of VO_2 thin films by CSD method, the thin films were generally deposited by spin coating the solution in air. To investigate the chemical and structural composition of the as-deposited thin films, X-ray photoelectron spectroscopy (XPS) was combined with TEM, ellipsometry and Rutherford backscattering (RBS).

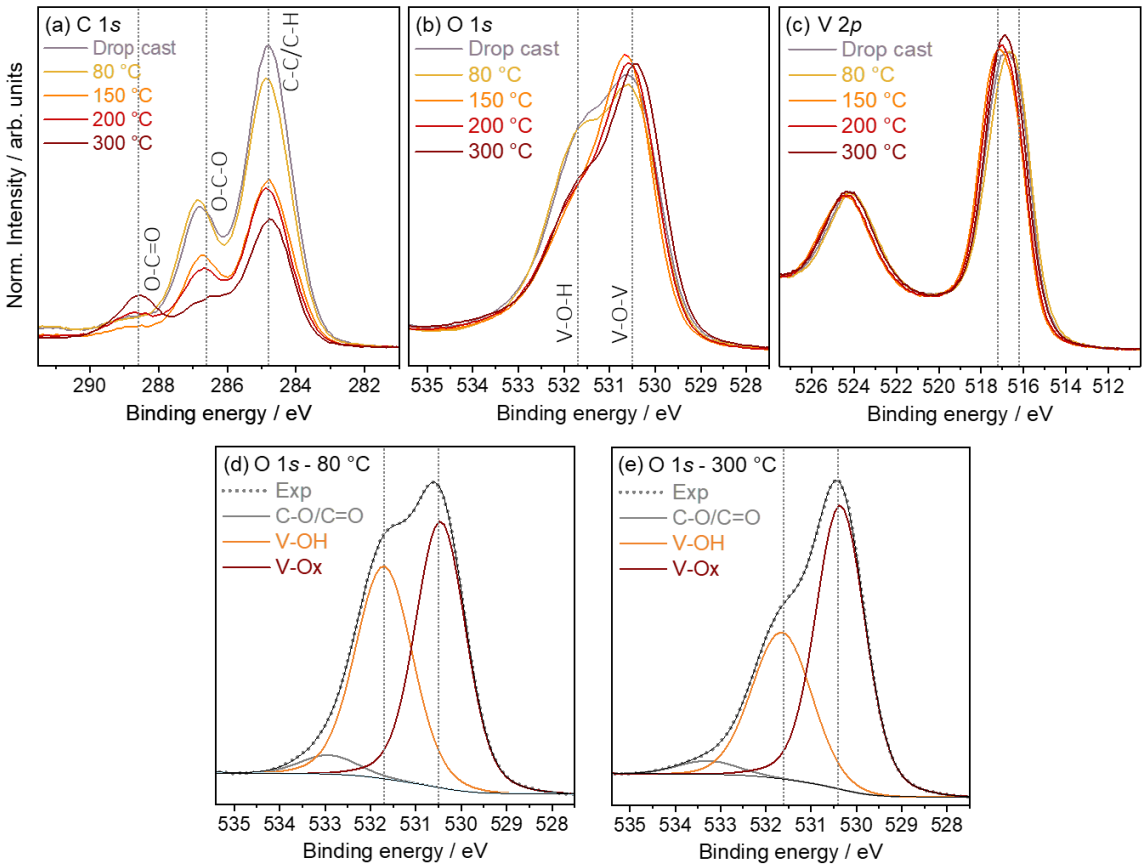


Figure 4.15. Key core level XP spectra of the drop cast solution and of the samples dried using temperatures from 80 to 300°C. (a) C 1s, (b) O 1s, (c) V 2p. (d, e) O 1s peak fit for the 80°C sample and 300°C sample, respectively. The reference lines represent the position of the main identified spectral features.[25]

Regarding the XPS analysis, single-layer films were deposited on silicon substrates and four different drying temperatures were compared, chosen between 80°C and 300°C. The former value was chosen to allow for a mild solvent evaporation, as the boiling point of ethanol is ~78°C.[26] The latter value was chosen to boost the film's condensation and densification, as well as the removal of organic components. These temperatures were verified to be lower than the minimum reported temperature for VO_2 crystallization, which is between 440-550°C when CSD is considered.[9,14]

The core level spectra of the dried samples are shown in Figure 4.15 (a-c). Regarding the C 1*s* core level, the three main features are related to adventitious carbon and C-C/C-H environments (284.8 eV), O-C-O (~286.6 eV) and O-C=O (~288.6 eV) environments, respectively.[27] With increasing drying temperature, the overall intensity of the C 1*s* spectra decreases relative to the V $2p_{3/2}$ spectral area. This can be explained by the release of the acetylacetonate ligands (acac) as acetylacetone (Hacac). The removal of Hacac during drying was found to be favored at temperatures between 150 and 200°C, which are above the boiling point of acetylacetone (~140°).[28] At the highest drying temperatures, the thermal decomposition of residual metal precursor, which was found to start at ~220°C, probably contributes to the reduction observed in the C signal intensity.[29,30] Van der Voort

et al.[31] studied the thermal decomposition of $VO(acac)_2$ in air by combining differential thermogravimetry (DTG) with Fourier-transform Infrared Spectroscopy (FTIR). They found two principal weight losses, the first at 150°C and the second at 300°C. The former is related to non-oxidative loss of the acac ligands, which result in the formation of Hacac as the main product. The second is related to oxidative decomposition of residual ligands, resulting in the formation of acetone, butane-2,3-dione, acetic acid, water, and CO_2.[31]

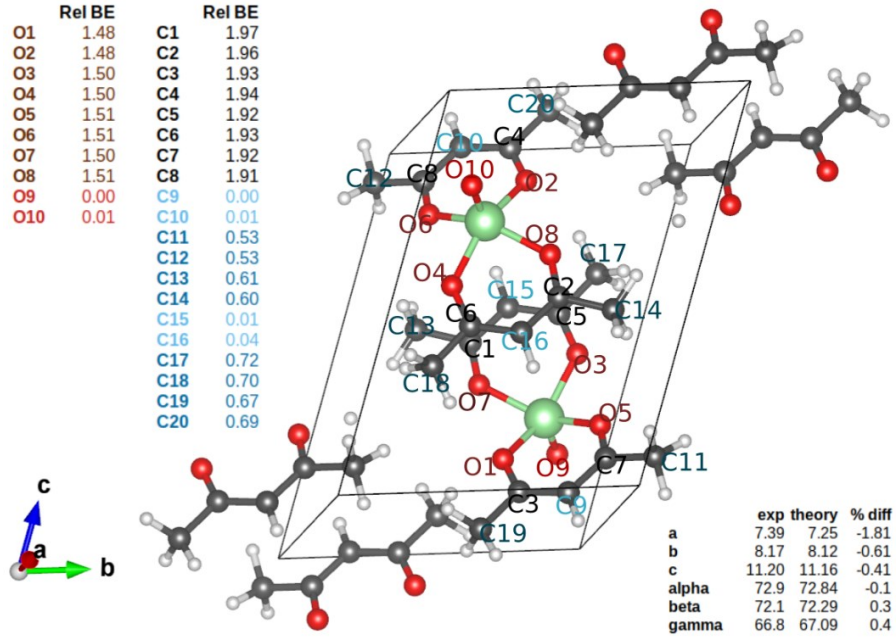


Figure 4.16. Theoretical calculations by DFT of the relative BE distance between O and C atoms in the metal-organic precursor.[25]

Alongside the observed changes in the C 1s core level, the O 1s core level was used to monitor the changes in the oxygen chemical state, namely the metal-oxide conversion and the hydroxyl contribution. Two main features were attributed to V-O-H (~531.7 eV) and V-O-V (~530.5 eV) environments, alongside with a smaller contribution from organic C-O/C=O environments (~533 eV).[27,32,33] To corroborate the peak analysis in XPS, calculations were performed using density functional theory (DFT).[25] The core binding energy (BE) calculations were used to estimate the relative BE distance between O and C atoms in the precursor structure (Figure 4.16). From the peak fit analysis (Figure 4.15 (d, e)), the presence of hydroxylated V-OH groups, strongly evident in the drop-cast solution and in the film dried at 80°C, decreases when the drying temperature is higher than 150°C. This goes hand-in-hand with a decrease in the V-O-H:V-O-V ratio, which highlights the progress of condensation reactions and the development of V-O-V networks.

The V2*p* core level (Figure 4.15 (c)) highlighted the presence of a mixed oxidation state on the surface of the dried thin films, found to be composed by both V^{5+} (~517.2 eV) and V^{4+} (~516.2 eV) from peak fitting. Hard X-ray photoelectron spectroscopy (HAXPES) was employed to probe deeper

within the film respect to soft XPS (SXPS), to ascertain a depth distribution profile of the V^{5+} oxidation state (Figure 4.17).

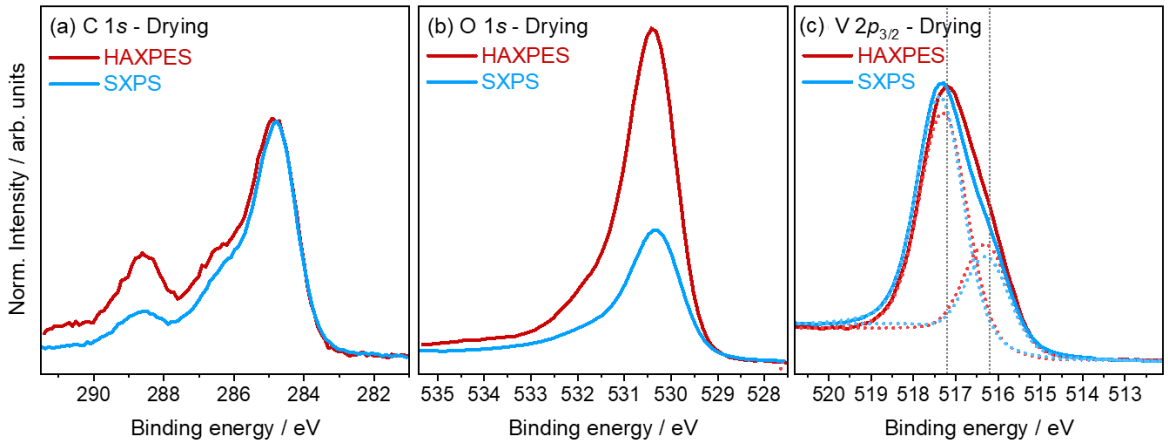


Figure 4.17. Soft X-rays photoelectron spectroscopy (SXPS) and Hard X-rays photoelectron spectroscopy (HAXPES) of (a) C 1 s, (b) O 1s and (c) V 2p core levels of the dried film.[25]

Chemical analysis using laboratory-based soft X-ray photoelectron spectroscopy (SXPS) was performed on a Thermo Scientific K-Alpha X-ray photoelectron spectrometer, whereas synchrotron-based hard X-ray photoelectron spectroscopy (HAXPES) was performed at beamline I09 at the Diamond Light Source, UK. The QUASES software package was used to estimate the maximum inelastic mean free path (λ_{IMFP}) for bulk VO_2, with values of ~3 nm at 1.5 keV (SXPS) and ~9 nm at 5.9 keV (HAXPES).[34] The total probing depth can be estimated as 95% of the signal intensity (i.e. $3\lambda_{IMFP}$), giving values of ~9 nm and ~27 nm for SXPS and HAXPES, respectively. This was done by comparing the variations in oxidation state by peak fitting the V $2p_{3/2}$ core level. From the XPS measurements on the amorphous dried sample, the V^{5+} state was confirmed to be dominant even at deeper probing depths. The V^{5+}/V^{4+} ratio did not significantly vary with increasing probing depth, as it was found to be 71%/29% by SPXS and 68%/32% by HAXPES. The presence of residual V^{4+} state could be due to incomplete oxidation of the precursor during the initial synthesis.[25]

Rutherford backscattering (RBS) was used to probe the atomic composition of the dried thin films, expressed in terms of oxygen and vanadium dose/*area*. The O/V ratio of 100°C dried thin film was found to be 2.89 ± 0.12 (Figure 5.27, paragraph 5.4.1, Chapter 5). As the O/V ratio of the original precursor would correspond to 5, the result further confirms the formation of a sol-gel network, alongside with the partial removal of the organic component.

Table 4.3. Variations of thickness, refractive index (n) and extinction coefficient (k) monitored by ellipsometry upon increasing drying temperature, from 80-300°C.[25]

Drying T_d / °C	Thickness / nm	*n* @ 300 nm	*k* @ 300 nm
80	60 ± 2	1.81 ± 0.01	0.21 ± 0.01
150	53 ± 2	1.83 ± 0.02	0.25 ± 0.02
200	54 ± 3	1.84 ± 0.03	0.25 ± 0.03
300	52 ± 1	1.86 ± 0.01	0.31 ± 0.01

Additional characterizations were performed to investigate eventual changes in thickness in function of the dying temperature. Identical thin films were deposited by dip coating and dried at temperatures between 80°C and 300°C. Ellipsometry measurements showed a moderate film densification from 80 to 300°C, with a ∼13% decrease in thickness (Table 4.3). This corresponded to a slight increase in refractive index (*n*), as well as extinction coefficient (*k*).

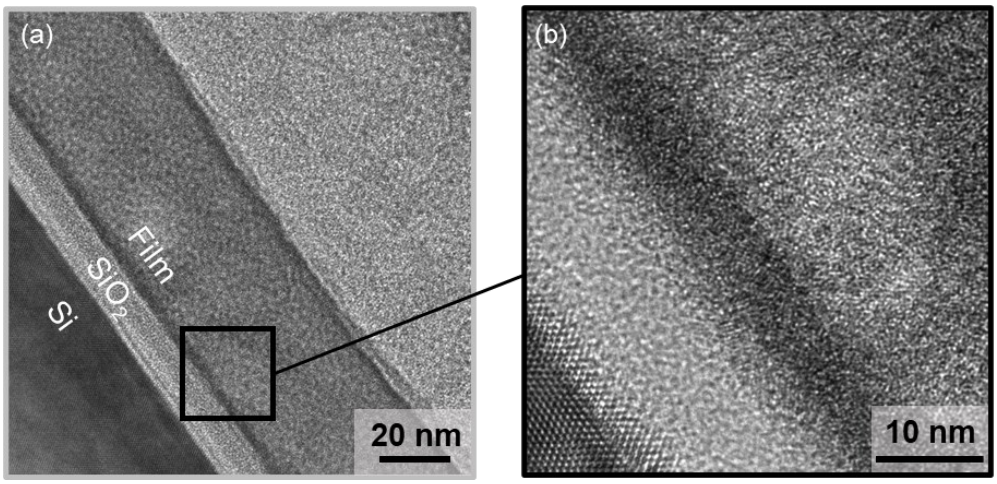


Figure 4.18. TEM cross-sections of the dried thin film at 300°C. The relative scale bars are inserted at the bottom of each image.[25]

The structural properties were evaluated by GIXRD, which was performed on the 300°C dried sample to verify the eventual undesired presence of crystalline peaks. As expected, the dried thin film displayed amorphous characteristics with no detectable diffraction peaks (Figure 5.4, paragraph 5.2.4, Chapter 5). However, the presence of small crystallites in the overall amorphous matrix was found from the TEM investigation (Figure 4.18 (a, b)). These crystallites were only ∼1-2 nm in dimension and could not be detected by GIXRD.

5.3.4 *Annealing atmosphere*

The previous GIXRD measurements on the dried thin films (paragraph 4.3.2) did not show the presence of diffraction peaks up to 300°C. Following the deposition and drying steps, thermal

annealing was applied to induce the conversion from an amorphous thin film to a crystalline one. First, the annealing atmosphere was studied, to verify which condition would allow the formation of the target vanadium oxide, namely VO_2 (M1).

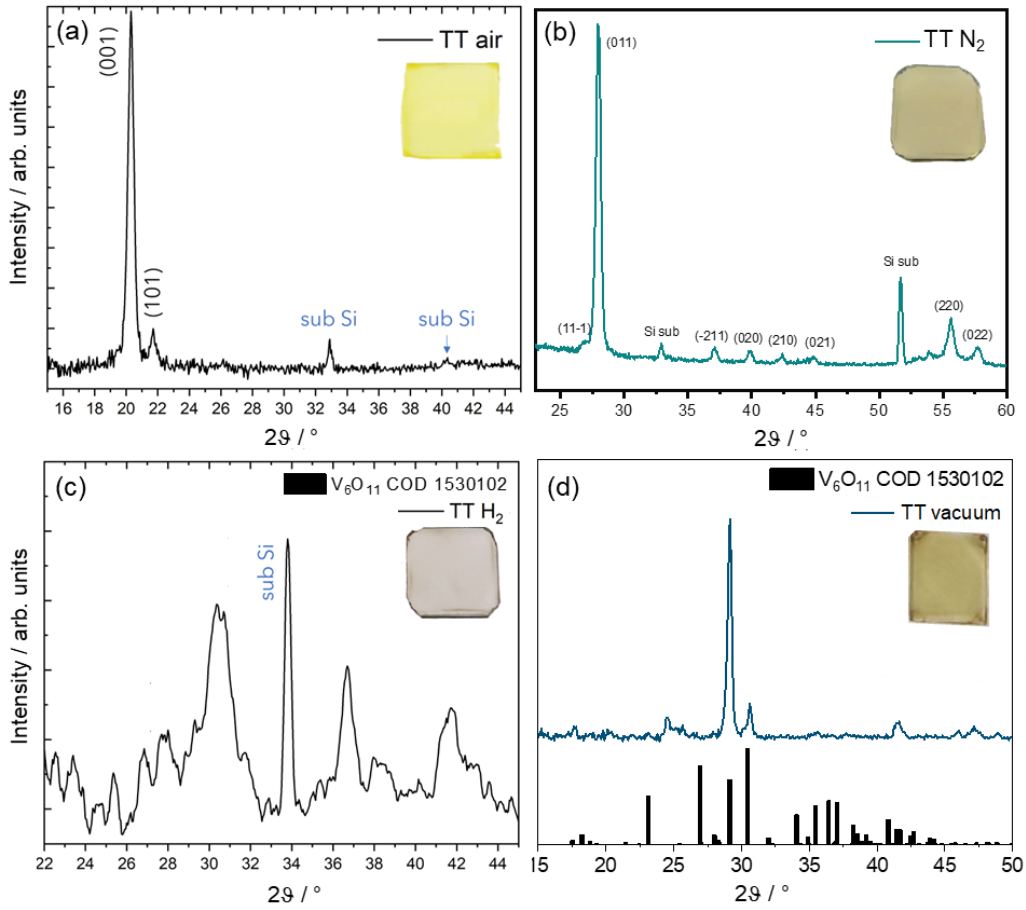


Figure 4.19. GIXRD of thin films deposited under 20°C 40% RH from a solution aged for 6 days, consisting of 3 layers dried at 150°C for 10 min. The samples were then annealed (a) in air, (b) under 0.1 lpm N_2 flux, (c) under 0.1 lpm 5% H_2 in Argon flux, (d) in vacuum with pressure below 1 mbar. The reference GIXRD patterns are reported in (b) and (d).

Identical thin films were prepared by spin coating 3 layers on both silicon and fused silica substrates, dried at 150°C for 10 minutes and annealed in a tube furnace (Lenton LTF) at 550°C for 1 h, with heating rate of 10°C/min. Four annealing atmospheres were compared, namely oxidizing, inert, vacuum, and reducing. The first sample (a) was annealed in air in a box furnace, whereas the second, third and fourth samples were annealed in a tube furnace. Sample (b) and (c) differed in terms of annealing atmosphere, which corresponded to a 0.1 lpm N_2 flux in the first case and to 0.1 lpm 5% H_2 in Argon flux in the second case. Before the start of the annealing under N_2, three cycles of vacuum/N_2 refill were conducted to ensure full removal of air (see Appendix A.1.5). The fourth sample (d) was annealed under vacuum, with pressure below 1 mbar (i.e., pressure detection limit). As expected, V_2O_5 was obtained by annealing in oxidizing atmosphere (Figure 4.19 (a)), whereas crystallization into VO_2 (M1) was induced by annealing under inert atmosphere (Figure 4.19 (b),

COD 9009089). Annealing under 5% H_2 in Argon flux or vacuum led to formation of a mixed oxide phases (Figure 4.19 (c, d)). The GIXRD measurement of sample (c) was hard to index, as the background signal was particularly intense, indicating a poor degree of crystallization within the film. In both cases, the predominant oxide phase was found to be V_6O_{11} (COD 1530102), indicating a lower oxidation state respect to V^{4+} of VO_2.

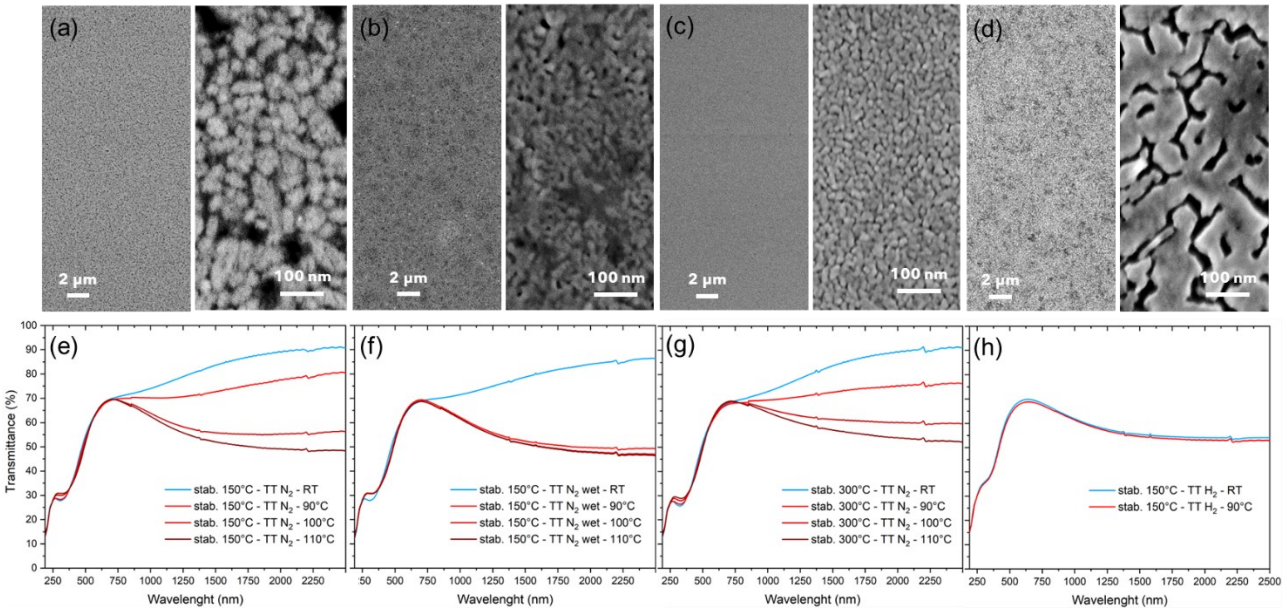


Figure 4.20. SEM images (a-d) and UV-Vis-NIR transmittance spectra (e-h) of thin films deposited under 20°C 40% RH from a solution aged for 6 days, consisting of 3 layers (a, e) dried at 150°C and annealed under N_2 flux, (b, f) dried at 150°C and annealed under wet N_2 flux, (c, g) dried at 300°C and annealed under N_2 flux, (d, h) dried at 150°C and annealed under 5% H_2 in Ar. The SEM scale bar is reported in the bottom of each image. The UV-Vis-NIR transmittance spectra are reported at room temperature (light blue lines, transmitting state) and 90-100-110°C (orange-red lines, reflecting state).

The inert N_2 atmosphere was selected to obtain the crystallization of the thin films into a VO_2 (M1) crystalline structure. To better understand the influence of the annealing atmosphere, two additional conditions were considered. Identical thin films were deposited by spin coating and annealed at 550°C under N_2 flux, as previously described. Within the inert flux, the role of moisture was considered by annealing identical thin films under "wet N_2". The latter was obtained by adding a distilled water reservoir within the annealing set up and inducing the N_2 gas to flow through it before entering the furnace. Additionally, the possible influence of residual organic matter was considered. As described in paragraph 4.3.3, the degradation of the latter might lead to the formation of CO_2 and acetone as degradation products, which in turn could create a partially reducing local atmosphere. Two different drying temperatures before annealing were considered, i.e. 150°C and 300°C, while a N_2 annealing atmosphere was used in both cases. The two temperatures were chosen according to the XPS results (paragraph 4.3.3), to investigate two different conditions of organic residuals.

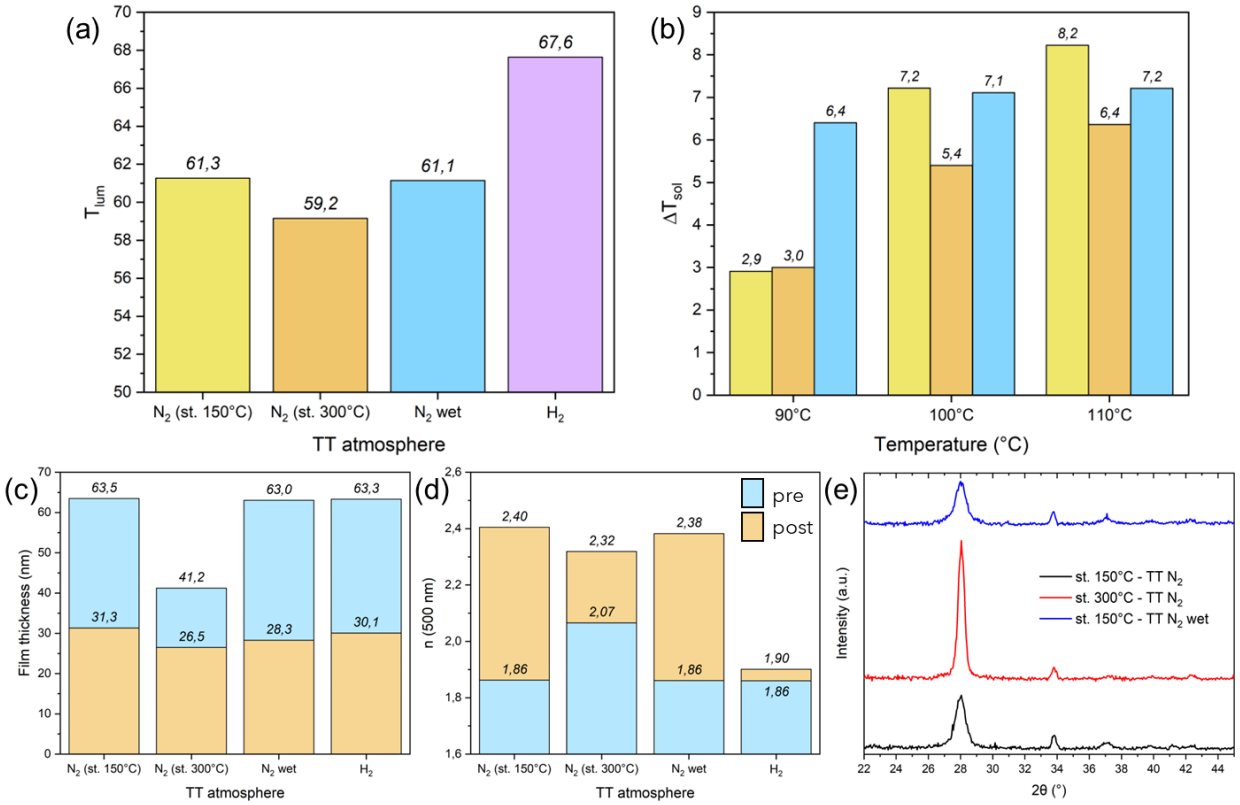


Figure 4.21. (a) Luminous transmittance (T_{lum}), (b) solar modulation efficiency (ΔT_{sol}), (c) thickness, (d) refractive index n at 550 nm, and (e) GIXRD of the thin films deposited under 20°C 40% RH from a solution aged for 6 days, consisting of 3 layers, dried and annealed under the following conditions: (i) dried at 150°C and annealed under N_2 flux, (ii) dried at 150°C and annealed under wet N_2 flux, (iii) dried at 300°C and annealed under N_2 flux, (iv) dried at 150°C and annealed under 5% H_2 in Ar. In (c, d), the ellipsometry characterizations are reported for both the dried state (light blue color) and the annealed state (light red color).

All the samples were characterized in terms of morphology and thermochromic efficiency (SEM, UV-Vis-NIR spectroscopy, respectively - Figure 4.20), thickness, optical constants, and crystallinity (ellipsometry, GIXRD, respectively - Figure 4.21 (c-e)). The thermochromic efficiency was expressed through the luminous transmittance and the solar modulation efficiency (T_{lum}, ΔT_{sol}, respectively - Figure 4.21 (a-b)), according to what reported in Appendix A.2.8. The ΔT_{sol} is based on the difference in solar transmittance below and above the transition temperature, calculated considering the solar irradiation spectrum. As 90°C might not be high enough to induce the full metal-insulator transition (MIT), 100°C and 110°C were also tested.

The reducing atmosphere (i.e., H_2 in Argon) did not show any modulation of the optical transmittance (Figure 4.20 (h)). This was expected, as the transmittance modulation is directly linked to the crystallization into VO_2 (M1), which can undergo a metal-insulator transition upon a temperature variation. The reducing atmosphere led instead to the formation of a predominant V_6O_{11} oxide phase, with a remarkably different morphology (Figure 4.20 (d)) with respect to the samples under inert N_2 atmosphere (Figure 4.20 (a-c)). The latter showed comparable morphologies, which seemed to differ in terms of film densification. After annealing under N_2 flux, the films showed a noticeable increase in refractive index values (Figure 4.21 (d)). As shown in Eq. 4.1[35], the decrease in film thickness after

thermal treatment implies an increase in mass density, which directly acts on the optical polarizability and thus the refractive index of the film:

$$A \approx \frac{M}{\rho} \frac{n^2 - 1}{3} \tag{4.1}$$

In which A represents the total polarizability of a mole of a substance, ρ the substance density, M the molecular weight and n the real part of the complex refractive index.

The sample dried at 300°C showed a higher degree of compactness, in terms of morphology, with respect to the samples dried at 150°C. However, no drastic differences were noticed in terms of refractive index, which can be correlated with the film's density. Similar thicknesses of 29 ± 2 nm within the four samples, after crystallization at 550°C (Figure 4.21 (c)). The sample dried at 300°C showed a slightly lower thickness of ~27 nm. The latter had a higher refractive index of ~2.07 before annealing, but the n after annealing had similar values for the samples annealed under N_2 ($n_{500\,nm}$ = 2.37 ± 0.04, Figure 4.21 (c)). The sample annealed under 5% H_2 in Ar was instead characterized by a notably lower $n_{500\,nm}$ ~ 1.90, that could be explained by the lower compactness found from the SEM characterizations (Figure 4.20 (d)). The GIXRD results showed analogous diffraction patterns within the three samples annealed under N_2 flux (Figure 4.21 (e)). The average crystallite dimension, calculated from the Scherrer equation, was found to be ~11 nm for the samples dried at 150°C and annealed under N_2 and wet N_2. Interestingly, the sample dried at 300°C and annealing under N_2 had an average size of ~18 nm.

Finally, the thermochromic performance was compared within the samples (Figure 4.21 (a, b)). The treatment under reducing atmosphere led to the highest T_{lum} = 68% (Figure 4.21 (a)) but could not modulate the transmittance (ΔT_{sol} = 0, Figure 4.20 (h)). The samples annealed under N_2 flux had similar T_{lum} ~ 60% (Figure 4.21 (a)). The wet N_2 flux induced the metal-insulator transition to be almost complete around 90°C, as the $\Delta T_{sol,\,90°C}$ = 6.4% is close to $\Delta T_{sol,\,110°C}$ = 7.2% (Figure 4.21 (b)). By comparing the same drying temperature of 150°C, the dry N_2 atmosphere required a higher temperature to fully induce the MIT but led to a higher thermochromic modulation ($\Delta T_{sol,\,110°C}$ = 8.2%). Considering the same dry N_2 atmosphere, a higher drying temperature of 300°C led to a lower thermochromic efficiency ($\Delta T_{sol,\,110°C}$ = 6.4%), even if compared to the wet N_2 sample (Figure 4.21 (b)).

From the overall characterizations, a drying step at 150°C and a dry N_2 atmosphere were selected as the standard condition to process VO_2 thin films, as the combination induced the highest

thermochromic modulation of the solar irradiation, while displaying a uniform surface coverage and crystallinity.

5.3.5 *Annealing temperature*

Once established the proper atmosphere during annealing, the crystallization temperature was investigated. Identical thin films were prepared from a solution aged for 3 weeks, which was spin coated to deposit 3 layers (32% RH 20°C) on both silicon and fused silica substrates. Each layer was dried at 150°C for 10 minutes and the final film was annealed in a tube furnace (Lenton LTF) for 1 h at 10°C/min, under a 0.1 lpm N_2 flux. Five temperatures were considered for annealing, namely 250-350-450-550-650°C. Prior to the start of the heat treatment, three cycles of vacuum/N_2 refill were conducted to ensure full removal of air (see Appendix A.1.5).

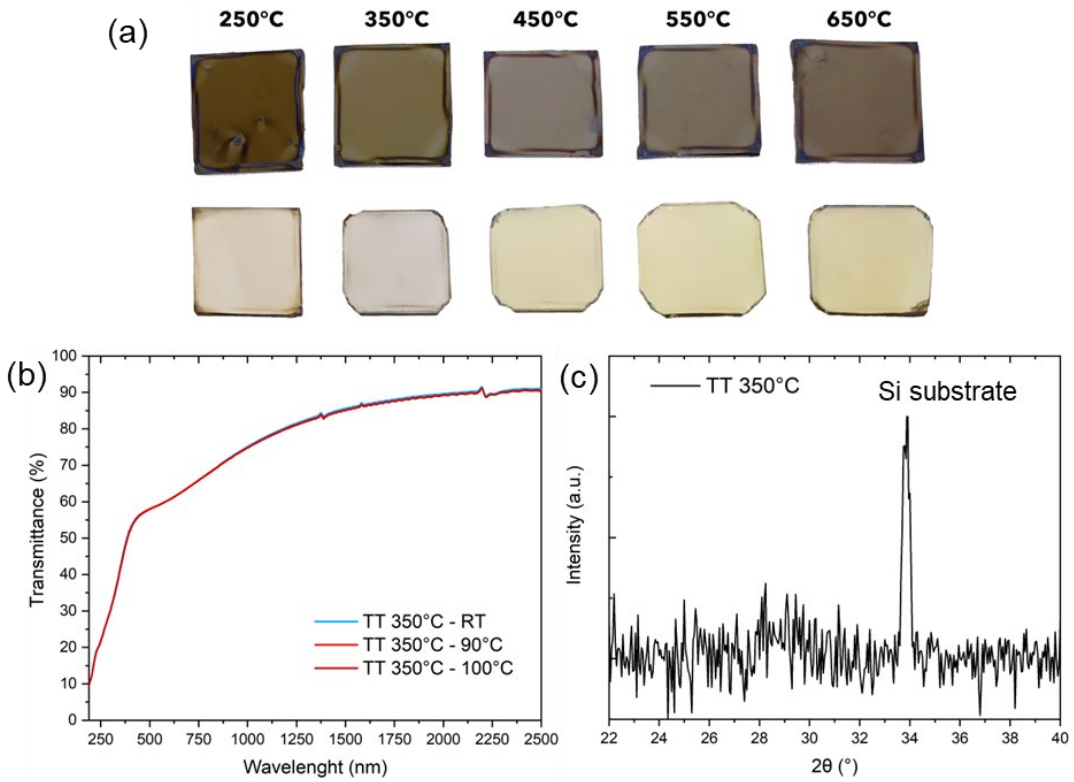


Figure 4.22. (a) Color of thin films deposited on silicon and fused silica substrates under 20°C 32% RH from a solution aged for 3 weeks, consisting of 3 layers, dried at 150°C and annealed in a tube furnace for 1 h at 10°C/min, under a 0.1 lpm N_2 flux, at five different temperatures (i.e., 250-350-450-550-650°C). (b) UV-Vis-NIR transmittance spectra of the sample annealed at 350°C. The transmittance spectrum is reported at room temperature (light blue lines, transmitting state) and 90-100-110°C (orange-red lines, reflecting state). (c) GIXRD of the sample annealed at 350°C.

The color of the annealed thin films on fused silica substrates was found to be a qualitative indicator of the successful or unsuccessful crystallization into VO_2 (M1). As visible in Figure 4.22 (a), the samples annealed at 250°C and 350°C did not show the typical light-yellow color of VO_2 (M1). The GIXRD of the 350°C sample indeed confirmed that the temperature was not sufficiently high to

induce the crystallization (Figure 4.22 (c)). An almost unperceivable shoulder could be present at 2Θ ~ 28°, which is however not discernible from the substrate signal. The shoulder would be coherent with the presence of the 1-2 nm crystallites found by TEM on the samples dried at 300°C (Figure 4.18 in paragraph 4.3.3). The absence of well-distinguished diffraction peaks of the 350°C sample is in line with the absence of thermochromic modulation (Figure 4.22 (b)).

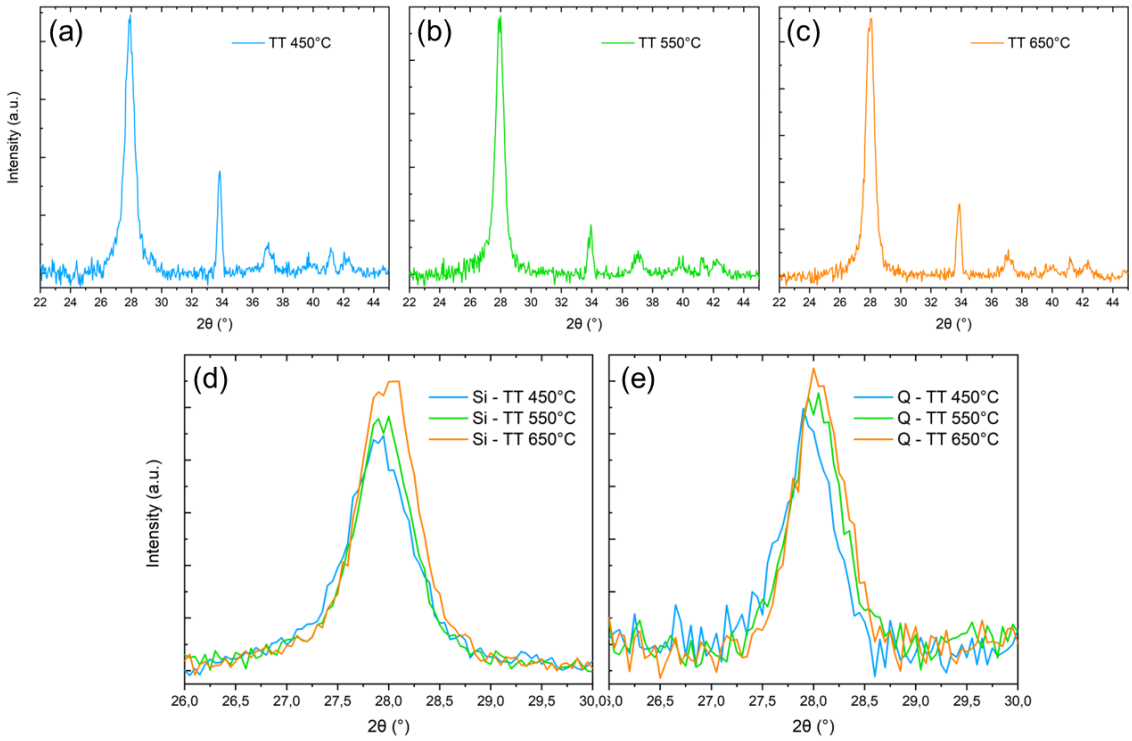


Figure 4.23. (a-c) GIXRD of the thin films deposited on silicon substrates under 20°C 32% RH from a solution aged for 3 weeks, consisting of 3 layers, dried at 150°C and annealed in a tube furnace for 1 h at 10°C/min, under a 0.1 lpm N_2 flux, at 450-550-650°C, respectively. (d, e) Comparison of the principal orientation at 2Θ ~ 28° of the three samples on silicon and fused silica substrates, respectively.

Figure 4.23 (a-c) reports the diffraction patterns of the samples annealed at temperatures between 450-650°C. All three patterns were confirmed to be monoclinic VO_2 (M1) (COD 9009089). The comparison between a silicon and fused silica substrates is reported in Figure 4.23 (d, e). The average crystallite size, estimated through the Scherrer equation, was found to slightly increase from ~11 nm (450°C) to ~12 nm (650°C) on silicon and from ~14 nm (450°C) to ~15 nm (650°C) on fused silica. Moreover, the position of the 2Θ at ~28°, which is the principal orientation, shifted from 27.90° (450°C) to 27.99° (650°C) on silicon substrates. The trend was observed to be coherent on fused silica substrate (from 27.94° at 450°C to 28.05° at 650°C), therefore it was confirmed to be induced by the temperature rather than by the substrate type. The slight shift towards higher values of the 2Θ position with increasing annealing temperature might be correlated to the slight increase in crystallite dimension. The substrate has an influence on the pattern position, which is correlated with the interplanar distance. On fused silica substrates, the principal (0 1 1) orientation is found at higher 2Θ

(e.g., 2Θ = 28.02° at 550°C) respect to silicon substrates (e.g., 2Θ = 27.94° at 550°C). This corresponds to slightly lower interplanar distances.

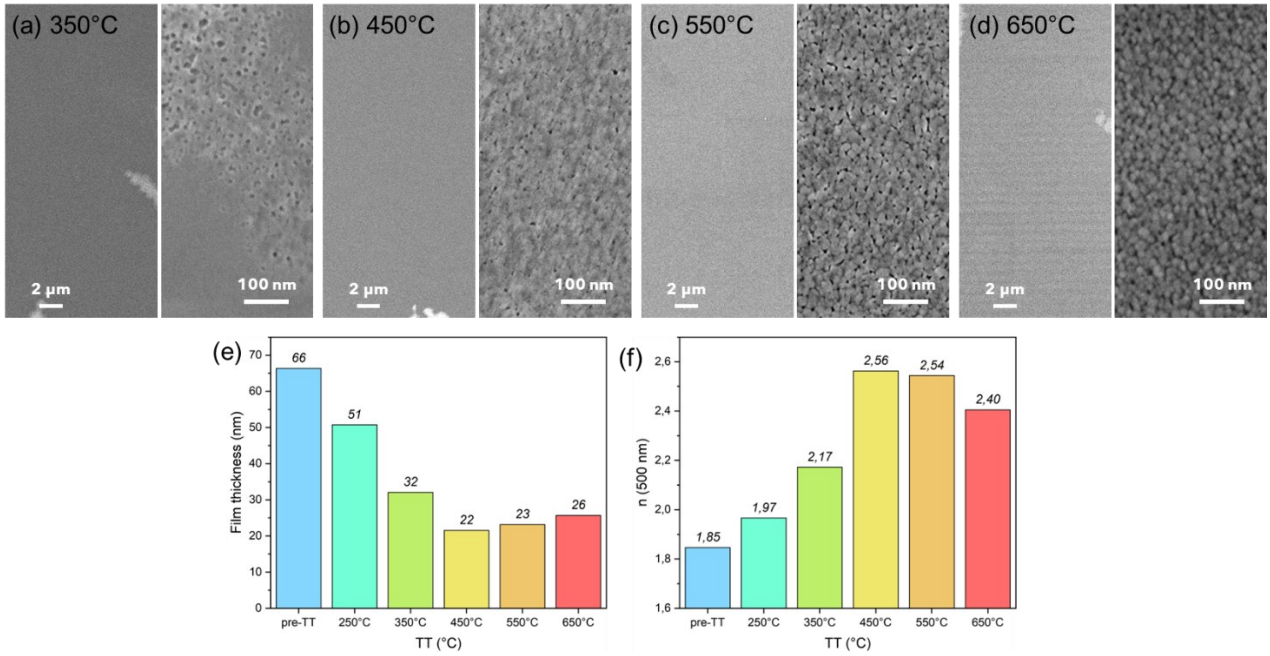


Figure 4.24. (a-d) SEM of the thin films deposited on silicon substrates under 20°C 32% RH from a solution aged for 3 weeks, consisting of 3 layers, dried at 150°C and annealed in a tube furnace for 1 h at 10°C/min, under a 0.1 lpm N_2 flux, at 350-450-550-650°C, respectively. The scale bar is reported at the bottom of each image. (e, f) Ellipsometry characterization of the film thickness and refractive index at 550 nm, respectively, of the thin films before (i.e., drying at 150°C) and after thermal annealing at 250-350-450-550-650°C.

The film thickness, as well as the optical constants, were measured by ellipsometry (Figure 4.24 (e, f)). The crystalline films (TT = 450-550-650°C) were characterized by similar thickness (24 ± 2 nm) and refractive index ($n_{500\ nm}$ = 2.50 ± 0.09). Regarding the amorphous films, the film thickness decreased with increasing temperature from ~66 nm (150°C, dried film) to ~32 nm (350°C). This decrease was correlated with an increased densification, as the refractive index increased from $n_{500\,nm}$ ~ 1.85 (150°C) to 2.17 (350°C). The refractive index variation between 350°C and 450°C matches the morphology evolution (Figure 4.24 (a, b, f)). Nanometric-sized holes within the film can be seen in the film annealed at 350°C, which were substantially reduced in dimension at 450°C (Figure 4.24 (a, b)). Annealing at 550°C led to the formation of well-defined nanoparticles, which displayed a compact and uniform surface coverage (Figure 4.24 (c)). The boundaries between nanoparticles became more clearly defined by the increased annealing temperature of 650°C (Figure 4.24 (d)).

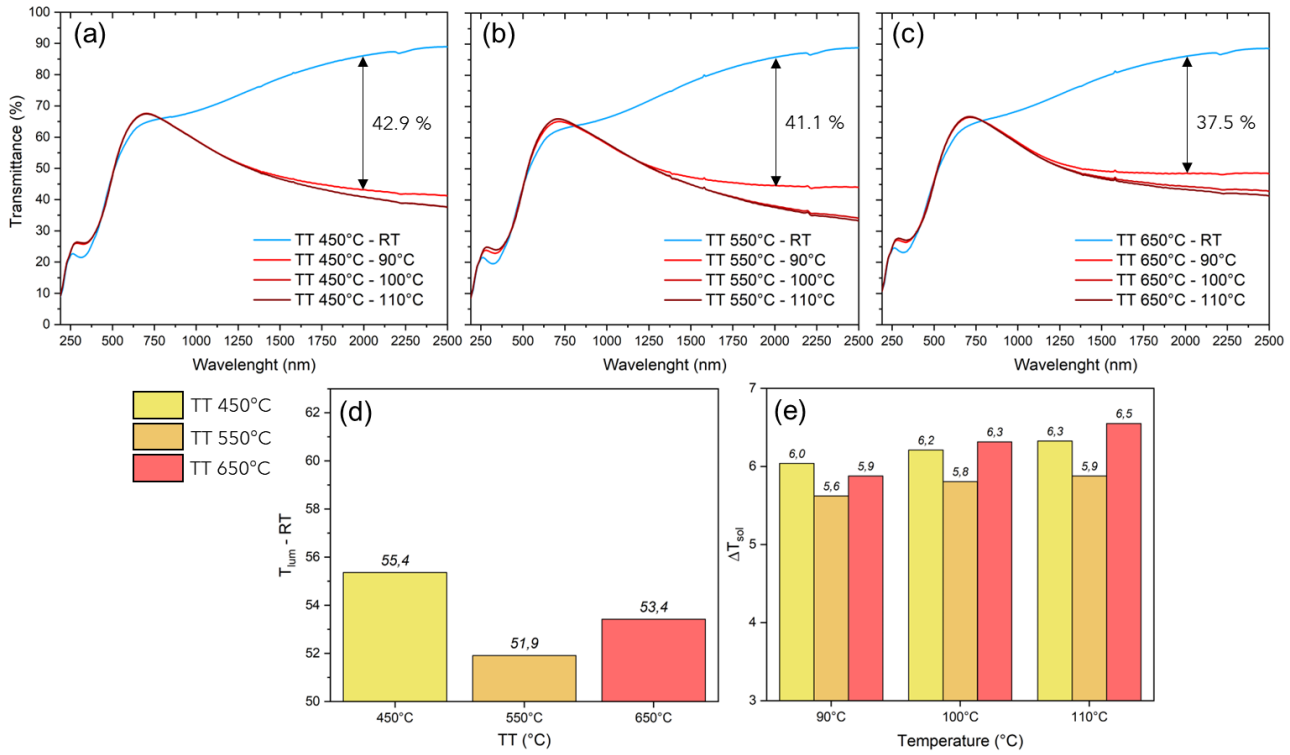


Figure 4.25. (a-c) UV-Vis-NIR transmittance spectra, (d) luminous transmittance (T_{lum}), and (e) solar modulation efficiency (ΔT_{sol}) of the thin films deposited on silicon substrates under 20°C 32% RH from a solution aged for 3 weeks, consisting of 3 layers, dried at 150°C and annealed in a tube furnace for 1 h at 10°C/min, under a 0.1 lpm N_2 flux, at 450-550-650°C, respectively. In (a-c), the UV-Vis-NIR transmittance spectra are reported at room temperature (light blue lines, transmitting state) and 90-100-110°C (orange-red lines, reflecting state).

Finally, the thermochromic performance was compared within the crystalline samples (Figure 4.25 (a-c)). The three annealing temperatures led to comparable values of both $T_{lum} = 53 \pm 2\%$ (Figure 4.25 (d)) and $\Delta T_{sol} = 6.2 \pm 0.3\%$ (Figure 4.25 (e)). The 450°C displayed a different behavior in terms of MIT. For the latter, the transformation into the rutile structure was almost completed at 90°C (Figure 4.25 (a)). The samples annealed at 550°C and 650°C showed further modulation of the NIR transmittance ($\Delta T_{2000\ nm}$) with increasing temperature from 90°C to 100°C (Figure 4.25 (b, c)). This behavior was explained by considering the transition temperature of the samples, reported in Figure 4.26.

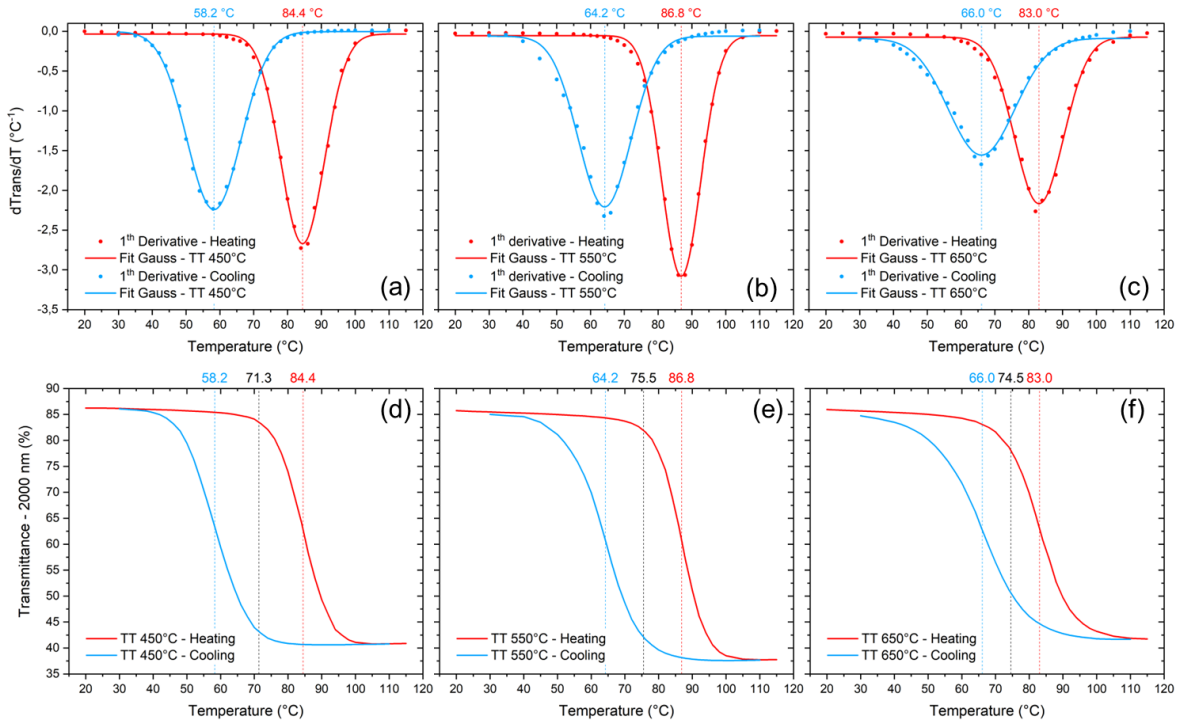


Figure 4.26. (d-e) Variation of the transmittance at 2000 nm upon heating and cooling of the thin films deposited on silicon substrates under 20°C 32% RH from a solution aged for 3 weeks, consisting of 3 layers, dried at 150°C and annealed in a tube furnace for 1 h at 10°C/min, under a 0.1 lpm N_2 flux, at 450-550-650°C, respectively. (a-c) First derivative and Gaussian fit of the corresponding curves in (d-f).

Table 4.4. Transition temperature during heating (T_{TH}) and cooling (T_{TC}), transition temperature (T_C), and hystheresis (ΔH) of the thin films deposited on silicon substrates under 20°C 32% RH from a solution aged for 3 weeks, consisting of 3 layers, dried at 150°C and annealed in a tube furnace for 1 h at 10°C/min, under a 0.1 lpm N_2 flux, at 450-550-650°C, respectively.

TT / °C	T_{TC} / °C	T_{TH} / °C	T_c / °C	ΔH / °C
450	58	84	71	26
550	64	87	76	22
650	66	83	75	17

The transition temperature (T_c) was found to increase with the annealing temperature, from T_c = 71°C of the sample annealed at 450°C to T_c = 75-76°C of the samples annealed at 650-550°C, respectively. The hysteresis (ΔH) showed an opposite trend, as the 450°C annealed sample had the highest ΔH = 26°C, which decreased to $\Delta H_{550°C}$ = 22°C and further to $\Delta H_{650°C}$ = 17°C. These results explain the different modulation of the NIR transmittance that was noticed in Figure 4.26.

5.3.6 *Thin film thickness*

The influence of film thickness on the crystallization and functional properties of VO_2 was investigated by increasing the number of deposited layers during spin coating. The thickness was progressively increased by depositing the 100 mM solution of $VO(acac)_2$ in ethanol from 1 to 5 layers. Each layer was dried at 150°C for 10 min, chosen as an intermediate temperature according to the

previous paragraph 4.3.3, and cooled before the deposition of the following one. The samples were annealed in a tube furnace at 550°C for 1 h, with 10°C/min heating rate under a N_2 flux of 0.1 lpm. The annealing parameters were chosen according to the optimization of annealing atmosphere and temperature, discussed in paragraphs 4.3.4-4.3.5.

Each sample was measured by ellipsometry before and after furnace annealing, namely after a 150°C drying step and after furnace treatment at 550°C. After the furnace treatment, the crystallinity of the samples was measured by GIXRD as well. Each sample was named with the first position to represent the substrate type (letter S = silicon, Q = fused silica), the second position to represent the number of deposited layers, and the third position to represent the material (letter V = VO_2).

Table 4.5. Thickness, refractive index (n) and extinction coefficient (k) of VO_2 thin films on silicon substrate with increasing number of layers from 1 to 5, before and after the thermal annealing.

	Before annealing (dried 150°C)			After annealing (550°C 1h)			
Sample	t (nm)	n_{600nm}	k_{600nm}	t (nm)	n_{600nm}	k_{600nm}	t reduction (%)
S1V	19	1.78	0.56	15	1.97	0.45	19
S2V	40	1.95	0.12	18	2.16	0.02	55
S3V	61	1.91	0.14	31	2.22	0.02	49
S4V	81	1.90	0.13	42	2.24	0.05	49
S5V	106	1.88	0.13	51	2.46	0.03	52

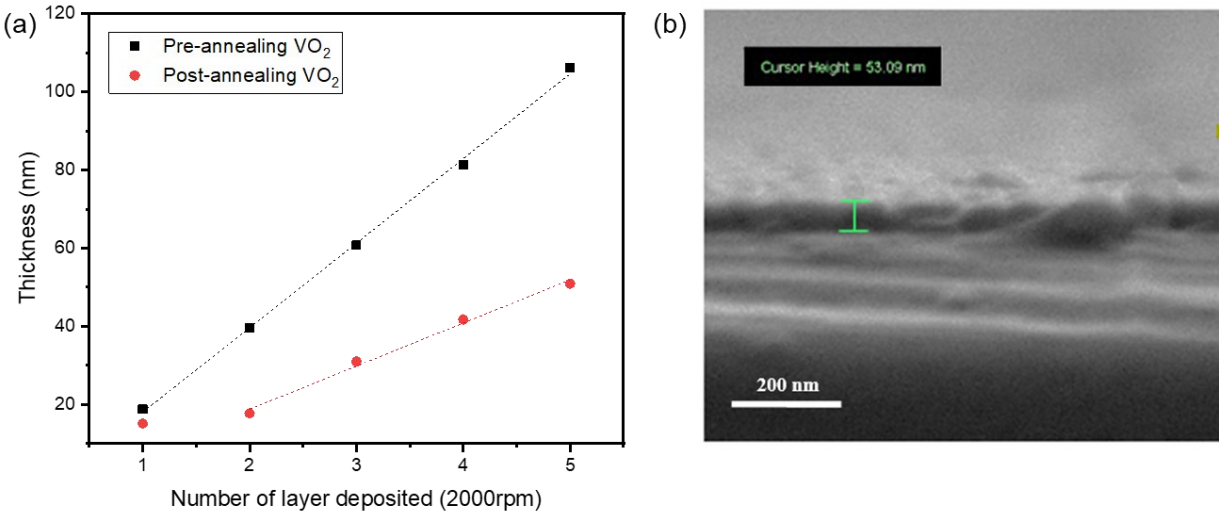


Figure 4.27. (a) Thickness dependence from the number of layers deposited by spin coating, before and after annealing. (b) SEM images of the 5-layered VO_2 thin film (S5V) in cross section, at 200 kx magnification.

The thicknesses and optical constant values at λ= 600 nm are reported in Table 4.5, for both the dried state and furnace annealed one. An increasing thickness trend with increasing number of layers was found, as reported in Figure 4.27 (a). Considering the dried state, the deposition of each additional layers was found to increase the overall film thickness by ~20 nm. A shrinkage of ~50% in thickness

was noticed when the dried thin films were furnace annealed. In the final annealed samples, each additional layer increased the VO_2 film thickness by 9-12 nm. After annealing, the films showed a noticeable increase in refractive index values (Table 4.5), which can be correlated to an increase in mass density as previously shown in Eq. 4.1.

The reliability of ellipsometry measurements was confirmed by the corresponding SEM results. From the cross-section image of sample S5V (Figure 4.27 (b)), a thickness of 53 nm was measured, which is agreement with the 51 nm found by ellipsometry measurements (Table 4.5). The drying time was also considered, by comparing 5 min to 10 min at target temperatures of both 150°C and 250°C. A few nanometers difference (~8%) was noticed between the two drying times for the as-deposited films, but no major effect on the thickness of the annealed films was found.

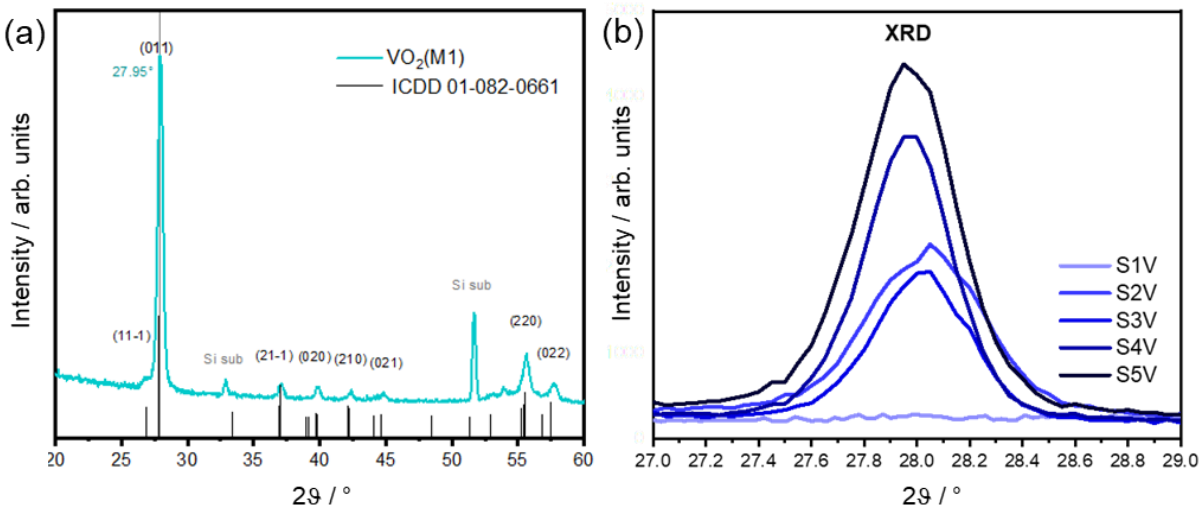


Figure 4.28 (a) GIXRD pattern of VO_2 thin films after annealing at 550°C for 1 h, with 10°C/min heating rate under a N_2 flux of 0.1 lpm, (b) GIXRD patterns at 2Θ ~28°, i.e. (011) diffraction, of the VO_2 thin films with increasing number of layers from 1 to 5.

Regarding the GIXRD results, all samples displayed the typical X-ray diffraction pattern of monoclinic VO_2 (M1) (Figure 4.28 (a), COD 9009089), characterized by a predominant (0 1 1) orientation. A comparison of the latter orientation, visible at 2Θ ~28°, is reported in Figure 4.28 (b). A progressive increase in intensity was seen from samples S2V to S5V, along with a slight shift towards lower 2Θ values. S1V did not follow the same trend in neither GIXRD nor ellipsometry results. The sample deposited with only 1 layer did not crystallize, as shown by both the absence of the main diffraction at 2Θ~28.0° (Figure 4.28 (b)) and by a significantly lower *n* at 600 nm after annealing (Table 4.5).

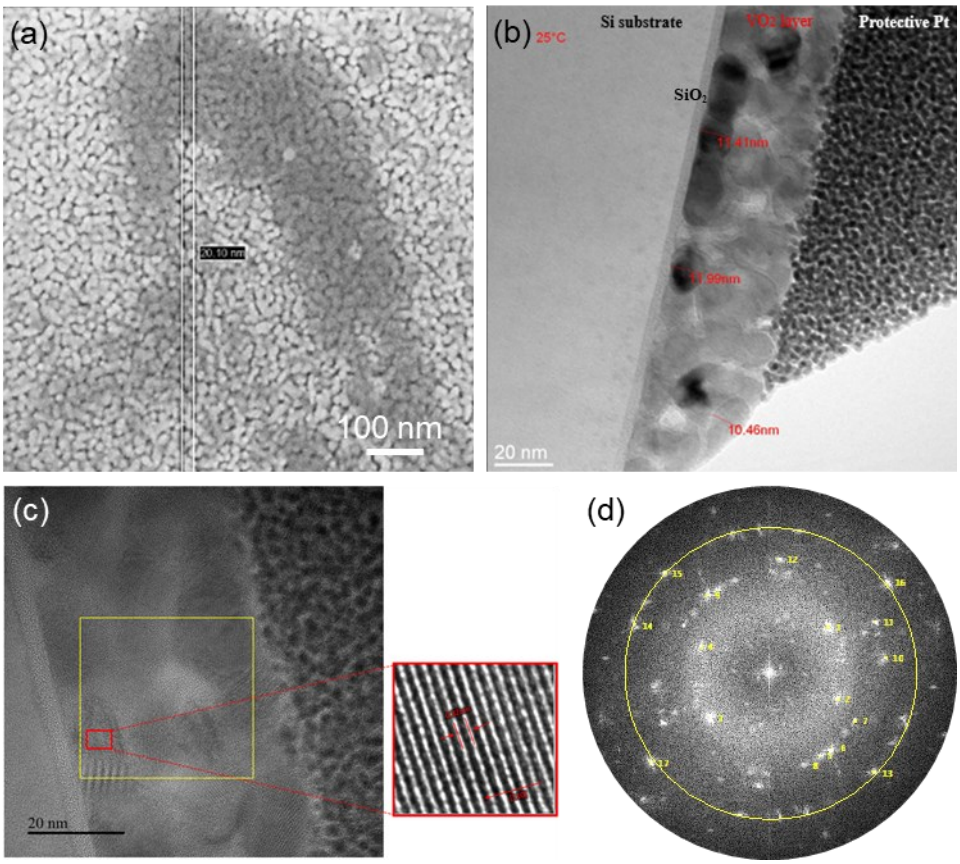


Figure 4.29 (a) SEM and (b) TEM cross section of sample 5 layered VO_2 thin film on silicon substrate (S5V) in cross-section. (c) HRTEM of cross-section of S5V and zoomed area of a [110] oriented grain corresponding to the main 28° diffraction peak of VO_2 (M1). The interplanar distances were graphically estimated by DigitalMicrograph® software. (d) Fast Fourier Transformed (FFT) obtained from a portion of crystallized VO_2 film: the multiple brights spots indicate high polycrystallinity.

SEM was employed to characterize the surface morphology of the 5-layered sample S5V, whereas the cross-section of the latter was analyzed by TEM and HRTEM. From the SEM images, irregular-shaped grain sizes of ~20 nm size were found (Figure 4.29 (a)), which displayed a ~10 nm height from the TEM analysis (Figure 4.29 (b)). Both SEM and TEM showed a residual porosity in the VO_2 thin film. Figure 4.29 (c) reports an estimation of the interplanar distance found on multiple crystalline grains, corresponding to the principal peak of VO_2 (M1) at $2\Theta = 27.9°$ which is relative to the (0 1 1) planes. The FFT analysis was used to estimate the interplanar distances shown in Figure 4.29 (d), which are reported in Table 4.6 along with the corresponding planes and diffraction patterns.

Table 4.6. Estimated d-spacing (nm) in polycrystalline VO_2 (M1) thin film, along with the corresponding diffraction peaks.

FFT spot	d spacing (nm)	hkl	Diffraction peak
1 to 4	0.3197	(0 1 1)	27.9°
5 to 9	0.2399	(2 0 0)	37.1°
10 to 12	0.2032	(0 2 1)	44.7°
13 to 15	0.1642	(2 2 0)	55.8°

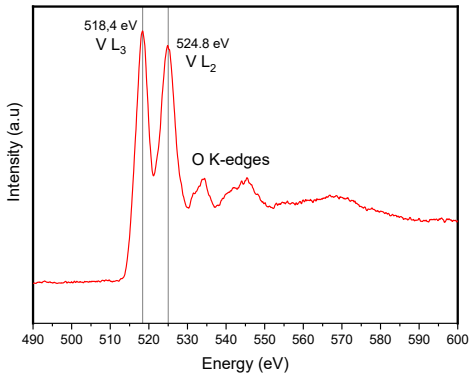


Figure 4.30. Electron energy loss spectroscopy (EELS) of the 5-layered VO_2 (M1) thin film on silicon substrate.

Electron energy loss spectroscopy (EELS) guarantees a high sensitivity to the valence band and the local atomic surroundings of the absorbing element. The vanadium L_3 ($2p_{3/2}$-> $3d$) and L_2 ($2p_{1/2}$-> $3d$) edges were found at 518.4 eV and 524.8 eV, respectively (Figure 4.30), further confirming the formation of VO_2.[36] Regarding O K-edge, the O $2p$ orbitals were mixed with the corresponding V $3d$ orbitals, giving rise to a widely spread absorption signal and highlighting the significant covalent character of the V–O bonds in the films.

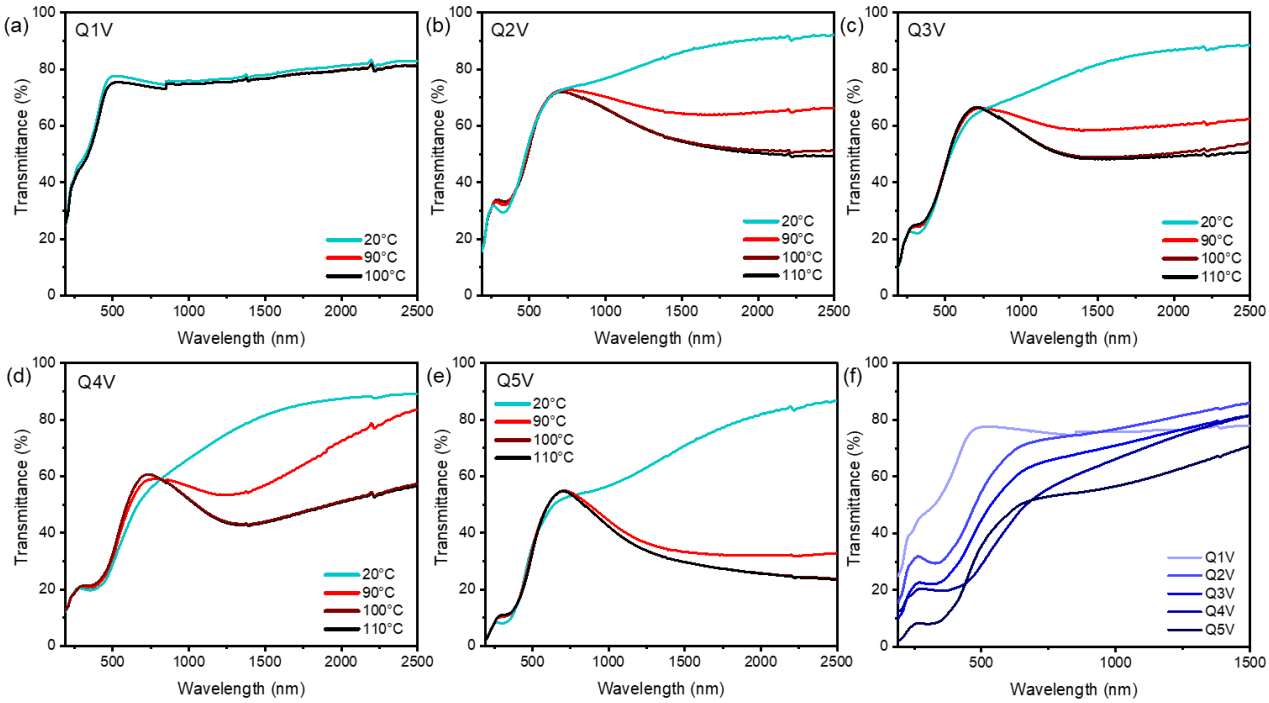


Figure 4.31. (a-e) UV-Vis-NIR spectroscopy of the VO_2 thin films of increasing thickness, i.e., number of layers, in function of the temperature. (f) Comparison of the transmittance at 20°C of the VO_2 thin films of increasing thickness, i.e., number of layers, in the 190-1500 nm range.

Table 4.7. Thermochromic performance of the VO_2 thin films of increasing thickness, i.e., number of layers, expressed in terms of luminous transmittance ($T_{lum,\ 20°C}$), solar modulation between 20°C and 90°C ($\Delta T_{sol,\ 90°C}$), maximum solar modulation ($\Delta T_{sol,\ max}$), and NIR modulation at 2000 nm ($\Delta T_{2000,\ max}$).

Sample	$T_{lum,\ 20°C}$ (%)	$\Delta T_{sol,\ 90°C}$ (%)	$\Delta T_{sol,\ max}$ (%)	$\Delta T_{2000,\ max}$ (%)
Q1V	77.3	1.7	1.8	1.6
Q2V	62.6	4.7	7.8	40.3
Q3V	52.6	4.3	6.9	37.5
Q4V	37.1	3.1	5.3	36.5
Q5V	42.5	7.9	9.4	56.3

The thermochromic behavior of the VO_2 thin films was verified by UV-Vis-NIR spectroscopy in function of the temperature (Figure 4.31, Table 4.7). The thermochromic modulation of the single-layered sample (Q1V) was almost imperceptible (Figure 4.31 (a)), which confirms the previous GIXRD results, from which no crystallization pattern was found (Figure 4.31 (b)). The samples with 2 or more layers, which did show the VO_2 (M1) diffractions peaks (Figure 4.31 (b)), successfully modulated the solar radiation (Figure 4.31 (b-e)). The 5-layered sample was characterized by a particularly high solar modulation of $\Delta T_{sol,\ max}$ = 9.4% and $\Delta T_{2000,\ max}$ = 56.3%. As expected, the luminous transmittance of the samples was seen to gradually decrease with increasing number of layers (Figure 4.31 (f), Table 4.7).

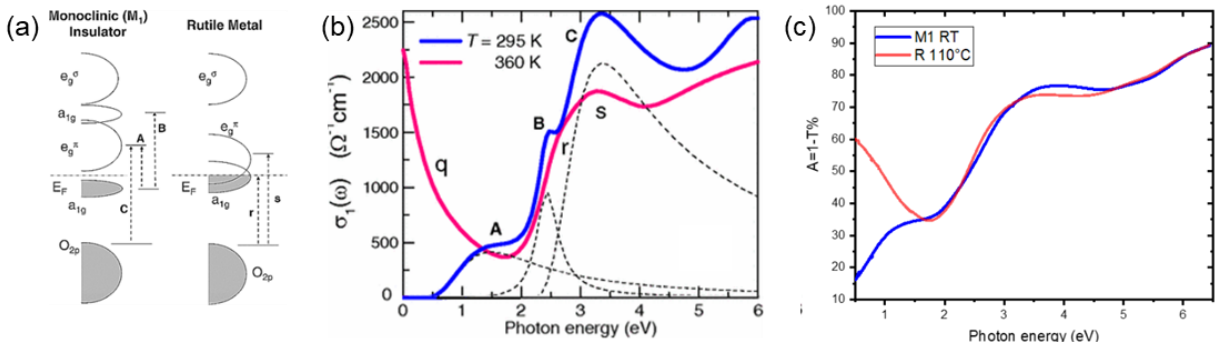


Figure 4.32 (a) Reference electronic transition of VO_2 around the Fermi level for both monoclinic and tetragonal phase, from ref.[37] (b) Optical conductivity of VO_2, ref.[37] (c) Absorbance of the 3-layered VO_2 thin film on fused silica (Q3V) at 20°C (RT) and at $T>T_c$.

The decrease in transmittance of VO_2 in the 300 – 400 nm region is mainly attributed to the transition O $2p \rightarrow e_g^{\pi}$, which is shown as transition "C" at 334 nm (3.71 eV) in Figure 4.32 (a).[37] The absorbance spectra in insulating (20°C) and transmitting state (90°C) of sample Q3V (Figure 4.32 (c)) well matches the optical conductivity behavior reported by Qazilbash *et al.*[37], which is linearly proportional to the absorbance (Figure 4.32 (b)).

5.3.7 *Solution aging time*

Following the identification of the proper annealing atmosphere (paragraph 4.3.4) and annealing temperature (paragraph 4.3.5), the influence of the solution aging on the final thermochromic properties was investigated. The effect of the former on morphology, thickness and crystallinity was also considered. In paragraph 4.3.2.2, the optimized parameters for the synthesis of the solution were found to be stirring at 78°C for more than 2 h and subsequent aging of the solution for at least 1 day. The VO_2 fabrication process was repeated numerous times throughout the experiments reported in Chapters 4-7. As a favorable outcome from the repeated experiments, it was noticed that VO_2 thin films with comparable thermochromic properties could be obtained, regardless of the exact aging time at room temperature of the solution. The solution, once stirred at 78°C for 9-24 h, was stable for months in air and could be used multiple times.

To verify this, identical thin films were deposited by spin coating 3 layers (41% RH 22°C) on both silicon and fused silica substrates. Each layer was dried at 150°C for 10 minutes and the final film was annealed in a tube furnace (Lenton LTF) for 1 h at 550°C, with heating rate of 10°C/min, under a 0.1 lpm N_2 flux. Three solutions were prepared by stirring at 78°C for 24 h and then aging at room temperature without stirring for 9 days, 36 days and 113 days, respectively.

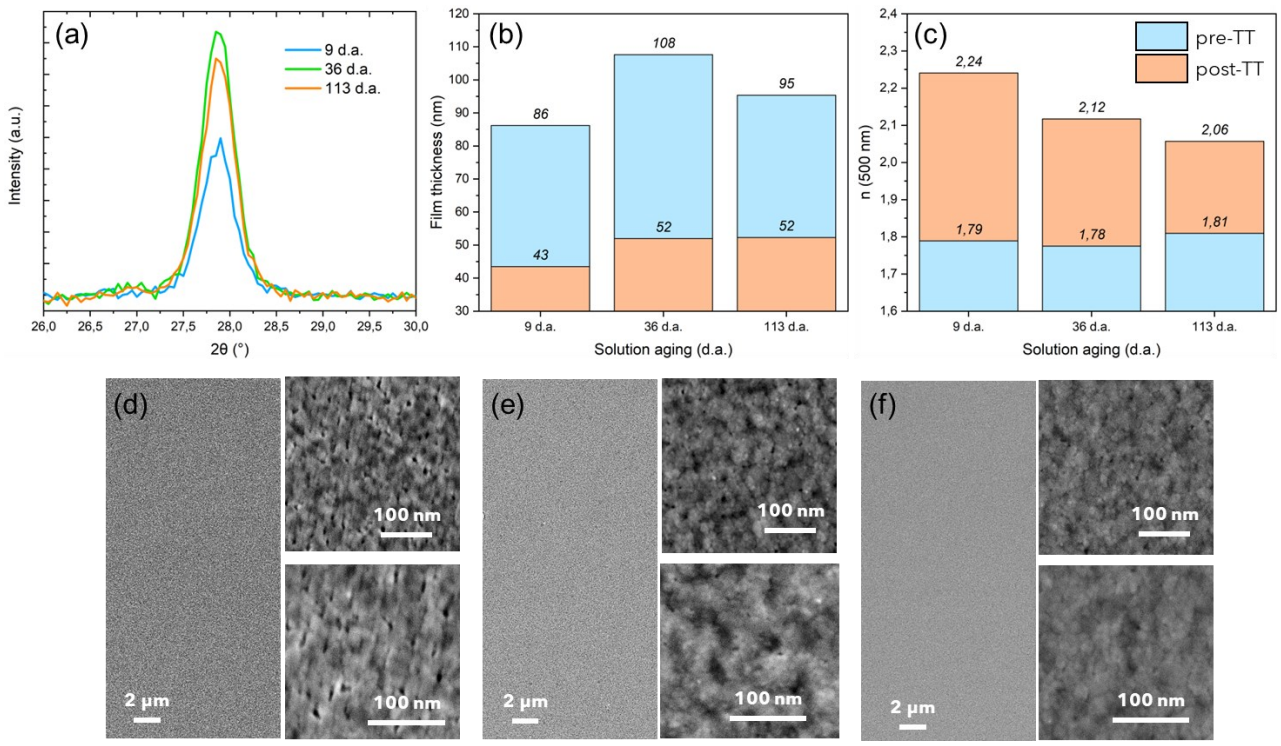


Figure 4.33. (a) GIXRD pattern at 2Θ ~ 27.9°, (b) thickness, (c) refractive index, and (d-f) SEM of the thin films deposited on silicon substrates under 20°C 41% RH, consisting of 3 layers, dried at 150°C and annealed in a tube furnace for 1 h at 10°C/min, under a 0.1 lpm N_2 flux, at 550°C. The three types of samples were deposited from solutions which were aged at room temperature for 9 days, 36 days, and 113 days, respectively. In (b, c), the ellipsometry characterizations are reported for both the dried state and the annealed state. In (d-f), the scale bar is reported at the bottom of each image.

From the GIXRD (Figure 4.33 (a)), all three samples were confirmed to possess a monoclinic VO_2 (M1) crystalline structure (COD 9009089). The aging time of the solution had no influence on the crystalline structure. The peak position of the principal (0 1 1) orientation was found at the same 2Θ = 27.87 ± 0.01° within the three samples. The average crystallite size was estimated to be 19 ± 1 nm. The sample deposited from a solution aged for 9 days showed a slightly lower thickness and higher *n* compared to the other two samples (Figure 4.33 (b, c)). The average values were measured to be 49 ± 5 nm and $n_{500\ nm}$ = 2.14 ± 0.09.

An influence of the solution aging was found on the film morphology after annealing. The higher solution aging time led to the formation of a very compact and dense film (Figure 4.33 (f)). The small holes visible in the sample deposited from the 9 days aged solution (Figure 4.33 (d)) completely disappear with increasing aging time (Figure 4.33 (e, f)). The morphology can explain the slightly different optical properties that were seen within the samples, which are reported below.

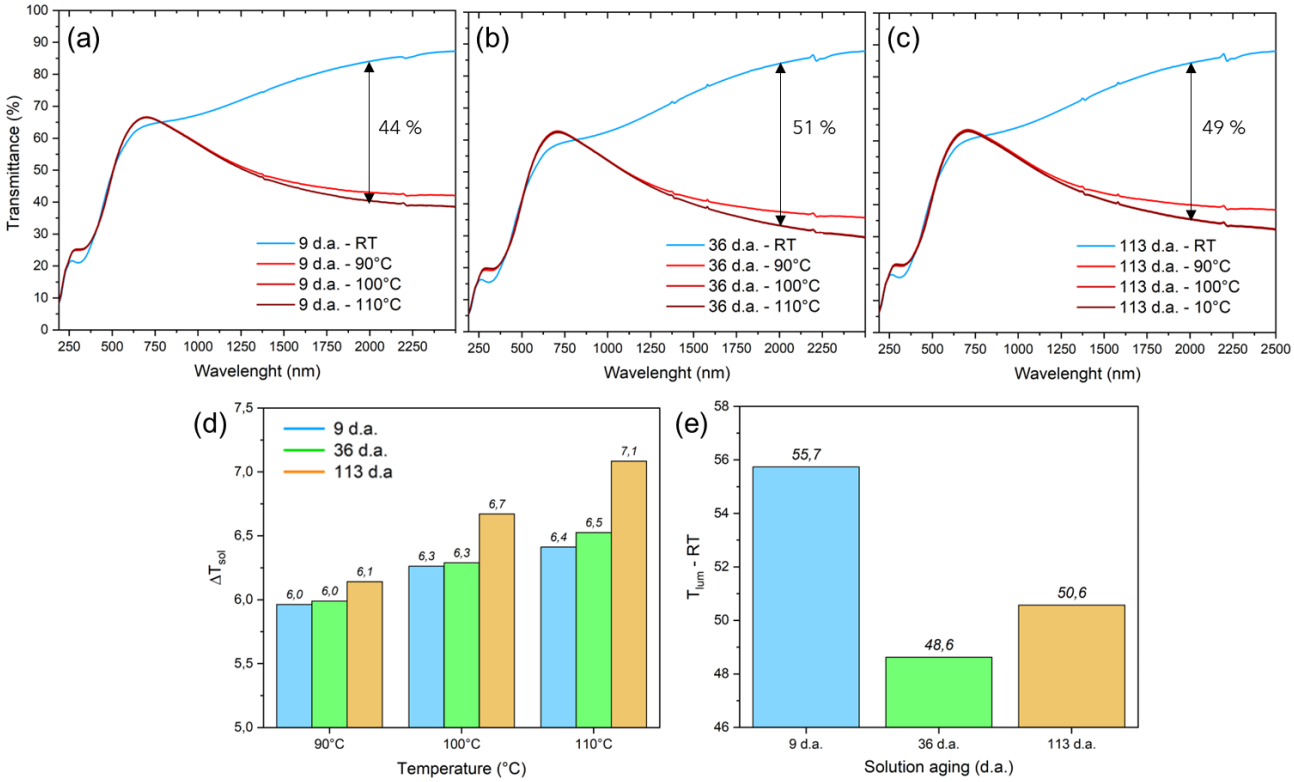


Figure 4.34. (a-c) UV-Vis-NIR transmittance spectra, (d) solar modulation efficiency (ΔT_{sol}), and (e) luminous transmittance (T_{lum}) of the thin films deposited on silicon substrates under 20°C 41% RH, consisting of 3 layers, dried at 150°C and annealed in a tube furnace for 1 h at 10°C/min, under a 0.1 lpm N_2 flux, at 550°C. The three types of samples were deposited from solutions which were aged at room temperature for 9 days, 36 days, and 113 days, respectively. In (a-c), the UV-Vis-NIR transmittance spectra are reported at room temperature (light blue lines, transmitting state) and 90-100-110°C (orange-red lines, reflecting state).

The sample deposited from the 9 days aged solution showed a higher luminous transmittance (T_{lum}, Figure 4.34 (e)), which can be correlated with the presence of small holes within the film (Figure 4.34 (d)). Among the several strategies that can be used to improve the visible transmittance, the addition of porosity with an optimized geometry was proven to favor the visible light transmittance through the film.[38] The solutions aged for ~1 or ~4 months led to comparable luminous transmittance values of $T_{lum} = 50 \pm 1$ % (Figure 4.34 (d)), which is coherent with the morphological characterization (Figure 4.34 (e, f)). The thermochromic modulation was found to slightly increase with increasing aging time of the solution, from $\Delta T_{sol,\ 9\ days} = 6.4\%$ to $\Delta T_{sol,\ 113\ days} = 7.1\%$ (Figure 4.34 (e)). By comparing the transmittance modulation at a fixed wavelength of 2000 nm ($\Delta T_{2000\ nm}$), the solutions aged for 36 or 113 days display a higher transmittance modulation between 20°C and 110°C ($\Delta T_{2000\ nm} = 50 \pm 1\%$), respect to the solution aged for 9 days ($\Delta T_{2000\ nm} = 44\%$, Figure 4.34 (e)).

From these results, the stability of the solutions in air over months was confirmed. Similar thermochromic performance could be obtained with solutions aged for more than 1 week. The solar modulation slightly improved with solution aging time, whereas the luminous transmittance decreased due to the increasing compactness of the film morphology. This confirms the possibility to achieve a simple and straightforward process, not bound to strict time schedules.

5.3.8 *Atmosphere influence on synthesis and deposition*

As previously highlighted, the development of vanadium oxides generally requires a strict control of each step of the process, from the initial solution synthesis to the film deposition and subsequent annealing. An improvement towards a real-life applicability of energy-saving applications based on VO_2 thin films would be to develop a simple and straightforward process. The use of vanadyl acetylacetonate as the precursor (paragraph 4.3) instead of vanadium pentoxide (paragraph 4.2), was proven to be more effective for the synthesis and deposition of the films without the need of a controlled atmosphere.

Once $VO(acac)_2$ was confirmed to be a valid candidate, further studies were conducted to evaluate the possible impact of the atmosphere on the final optical performance, film quality and crystallinity.

5.3.8.1 *Inert atmosphere vs air*

As a preliminary experiment, the synthesis and deposition were studied by considering two different atmospheres, i.e., inert or air. The combination of the parameters led to four different conditions (Figure 4.35 (a-d)):

a) totally inert atmosphere during both synthesis and deposition,
b) inert atmosphere during synthesis and air exposure during deposition,
c) air exposure during synthesis and inert atmosphere during deposition,
d) complete air exposure during both synthesis and deposition.

The synthesis in air of the 100 mM solution of $VO(acac)_2$ in absolute ethanol was conducted as described in paragraph 4.3.2.2. To replicate the synthesis under inert atmosphere, a sealed $VO(acac)_2$ precursor bottle was introduced inside a glove box (O_2, H_2O < 2 ppm). The precursor was mixed with anhydrous absolute ethanol to prepare a 100 mM inside a microwave reaction vessel (G30 Wide Neck), which was sealed and extracted from the glove box. The sealed vessel was heated at 78°C for 4 h by microwave heating (Anton Paar monowave 450), after which the vessel was transferred back inside a glove box to prevent any air contamination. The solution was aged for 12 days before the film deposition. The blue color of the latter solution (see Figure 4.10 paragraph 4.3.1 for reference) was stable for months, as a further confirmation that oxygen exposure was properly avoided.

Regarding the deposition of both solutions, the spin coating was either performed in a fume hood (22°C, 45% RH) or inside a glove box (O_2, H_2O < 2 ppm). Silicon substrates were cleaned following the previously described procedure. The deposition was performed within 10 minutes from the end

of the atmospheric plasma treatment, which further removes organic contaminants from the substrate and increases the hydrophilicity of the surface. The solutions were spin coated at 2000 rpm for 30 seconds to form 1 layer, after which the films were dried at 150°C for 10 minutes. The drying step was performed with the aid of a hot plate, either in fume hood or in glove box.

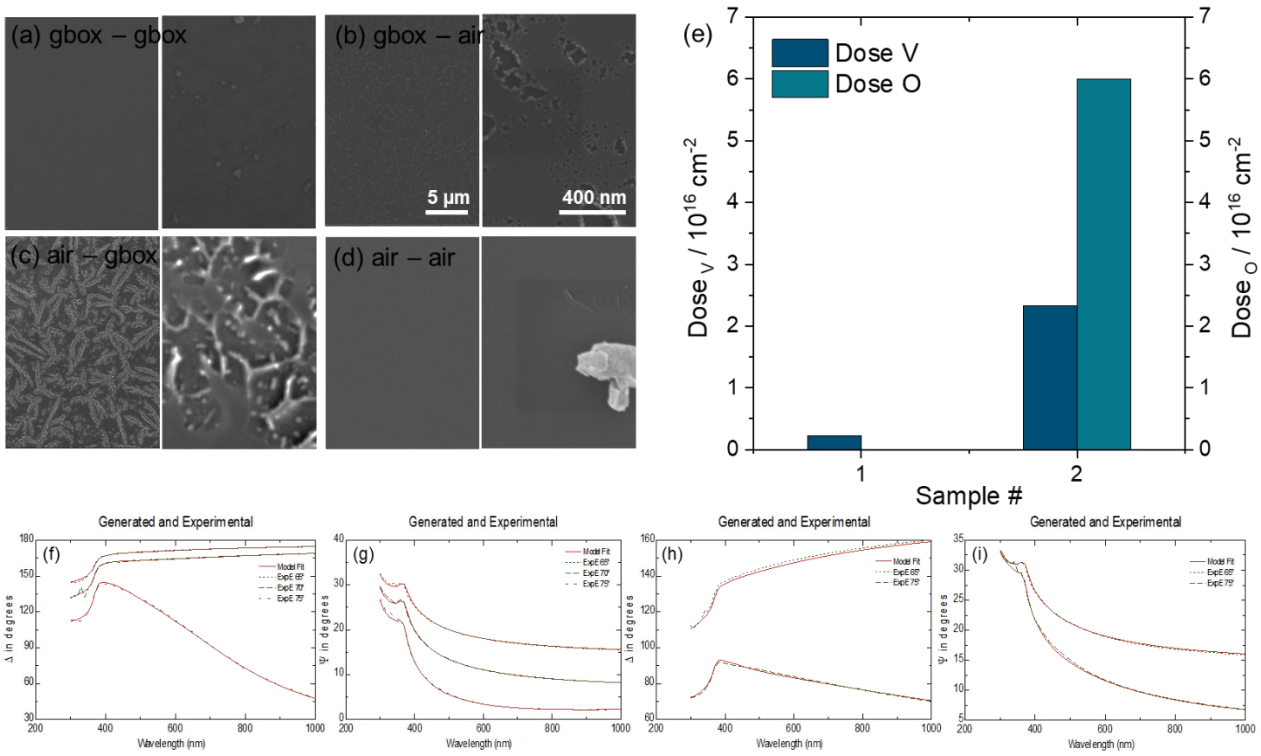


Figure 4.35. (a-d) SEM images of the thin films deposited under different conditions and from different solutions. (a) Solution prepared in glove box and deposited in glove box; (b) solution prepared in glove box and deposited in fume hood; (c) solution prepared in fume hood box and deposited in glove box; (d) solution prepared in fume hood and deposited in fume hood. The agglomerate in the magnification of figure (d) was attributed to a residual from silicon substrate, which was cut to obtain a sample for SEM. The residual was used to find the microscope focus at 200 kx magnification, as the film was smooth and uniform and did not show any morphological features. (e) Rutherford backscattering spectrometry (RBS), expressed as dose of oxygen and vanadium, of sample (a), named "1", and sample (b), named "2". In figure (e), the dose of oxygen was below the detectability limit of RBS and could not be added to the graph. (f-i) Ellipsometry data of samples (a) and (b). (f, g) Ψ and Δ functions of sample (a); (h, i) Ψ and Δ functions of sample (b).

The morphology of the dried thin films was then analyzed by SEM (Figure 4.35 (a-d)). The deposition of sample (d), synthetized and deposited under complete air exposure, led to the formation of a smooth and uniform thin film (Figure 4.35 (d)). The residual visible in the higher magnification insert (200 kx, 400 nm scale bar), which derives from the cutting process of the silicon substrate, was used to find the focus for the microscope images, as the film did not show any morphological features. The latter were instead seen in sample (b) and (c). A broken film morphology with multiple holes was found in sample (b), synthesized under inert atmosphere but deposited under air exposure (Figure 4.35 (b)). The exposure to air during the synthesis, followed by a deposition under inert atmosphere, led to an enhancement of the film's fractures (Figure 4.35 (c)). Sample (a), synthetized and deposited under complete inert atmosphere, was barely perceivable by both visual examination and SEM analysis (Figure 4.35 (a)).

To quantitatively evaluate the effectiveness of the deposition, sample (a) and (b) were analyzed with Rutherford backscattering spectrometry (RBS) and ellipsometry. RBS was used to measure the atomic composition of the dried thin films, expressed in terms of oxygen and vanadium dose/area. The samples (a) and (b), synthetized under inert atmosphere, were compared to study the influence of the atmosphere during deposition (either inert atmosphere or air). As visible in Figure 4.35 (e), the vanadium dose in sample (b) was ~$2.3*10^{16}$ atoms/cm^2, 10 times higher than sample (a). In the latter, the oxygen dose could not be detected because found to be lower than the detectability limit of the instrument. Therefore, preventing the air exposure during both synthesis and deposition was found to lead to a substantially lower quantity of material that can be deposited in form of thin film. A full air exposure during both steps, on the other hand, led to the formation of a smooth and homogeneous thin film. The ellipsometry measurements (Figure 4.35 (f-i)) confirmed the RBS results, as sample (a) displayed a thickness of 2.3 nm, whereas a thickness of 16.8 nm was found on sample (b).

5.3.8.2 *Moisture influence on synthesis and deposition*

Following the identification of the differences between an inert atmosphere and air exposure, further studies were conducted on the latter, since different air conditions can be found in terms of moisture content.

Moisture is defined as the quantity of water vapor that can be dissolved by air below the saturation limit. The latter is not a constant value but rather depends on the pressure and temperature. Humidity can be described in terms of *absolute humidity* (AH) and *relative humidity* (RH):

- absolute humidity is defined as the ratio between mass of water vapor present in air and air volume, generally expressed as g/m^3,
- relative humidity is defined as the ratio between mass of water vapor present in air and maximum water content that the air volume can withstand, before reaching the condensation point. The RH is generally expressed as % value in function of temperature (T) and pressure (p). A 100% RH means that the air volume has reached the maximum amount of water vapor at that T and p. Further increases would lead to the transformation of water vapor into liquid, i.e., to condensation.

The water vapor content that air can withstand increases with increasing temperature. This implies that, at fixed water vapor content, the RH will be higher at lower temperatures.[39] The presence of a higher or lower moisture content in air influences the wettability of the substrate during deposition of CSD methods. The surface wettability is described through the water contact angle (Θ_c), which

depends on the surface tensions between the solid, liquid and gas phases. The definition of Θ_c is reported in paragraph 2.1.1 of Chapter 2. At fixed temperature and pressure, the Θ_c was found to decrease with increasing RH, indicating a higher surface wettability with increasing relative humidity content.[40]

Besides the influence on the substrate wettability, the water vapor can play an active role to influence the sol-gel reactions, as discussed in paragraph 1.2 of Chapter 1. The overall role of moisture was considered during both the synthesis of the solution and the film deposition.

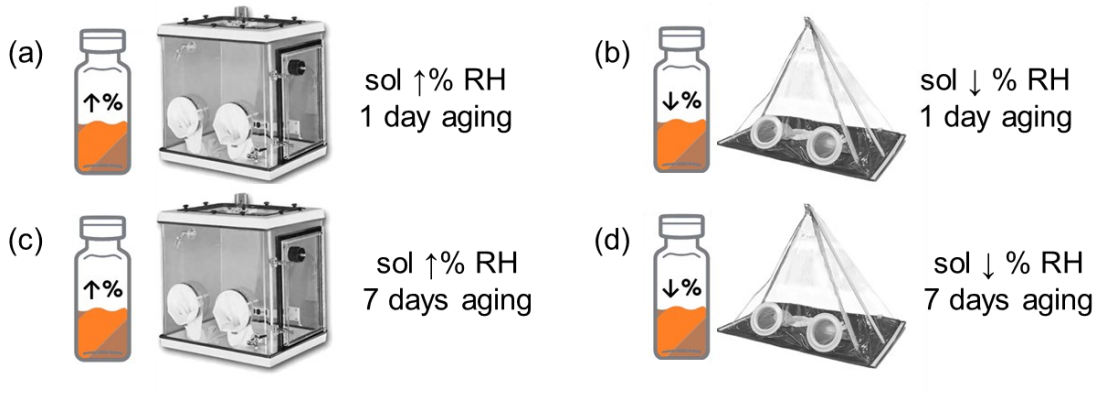


Figure 4.36. Schematic of the four environmental conditions considered during the synthesis of the solution. (a, c) glove box 90-95% at 21-23°C for1 or 7 days of aging, respectively. (b, d) glove bag 15-20% RH at 21-23°C for 1 or 7 days of aging, respectively.

The synthesis of the 100 mM solution of $VO(acac)_2$ in ethanol was developed as described in paragraph 4.3.2.2. The only difference was the environmental atmosphere during the synthesis, which was controlled by performing the steps of the solution creation and the set-up assembly either inside a glove bag (Figure 4.36 (b, d)) or a glove box (Figure 4.36 (a, c)). The moisture conditions inside the glove bag were set to be 15-20% RH at 21-23°C with the aid of zeolites, whereas the glove box was filled with air, instead of N_2, and the humidity was increased to 90-95% at 21-23°C. The latter was reached by introducing a saturated solution of KNO_3 and the moisture content was monitored through a hygrometer. For an easier discussion, the two solutions will be addressed as "↑ %RH sol" and "↓ %RH sol".

Both types of solution were refluxed at 78°C for 24 h by stirring at 500 rpm and subsequently aged at room temperature without stirring for 1 day (Figure 4.37 (a, b)) or 7 days (Figure 4.37 (c, d)), while being kept inside the corresponding compartment. Therefore, four types of solutions were considered.

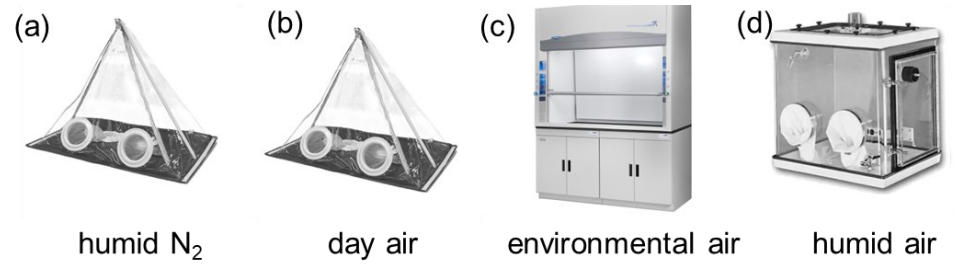


Figure 4.37. Schematic of the four environmental conditions considered during the deposition of the solution. (a) humid N_2, 11-13% RH at 22-23°C, glove bag. (b) dry air, 14-18% RH at 21-23°C, glove bag. (c) environmental air, 34-45% RH at 22°C, fume hood. (d) humid air, 85-90% RH at 20-23°C, glove box.

The deposition step was as well performed within a controlled humidity environment. Four conditions were considered and monitored through a hygrometer:

a) humid N_2, 11-13% RH at 22-23°C, glove bag,
b) dry air, 14-18% RH at 21-23°C, glove bag,
c) environmental air, 34-45% RH at 22°C, fume hood,
d) humid air, 85-90% RH at 20-23°C, glove box.

Condition (b) and (d) were created by following the same procedure described in the synthesis part. Condition (a) was created by applying vacuum to eliminate the air inside the glove bag and subsequently refilling the latter with a N_2 flux, with this procedure being applied three times. Condition (c) corresponded to the laboratory fume hood. The only step performed outside the glove bag or glove box was the cleaning of the silicon and fused silica substrates, with subsequent atmospheric plasma treatment. The substrates were then transferred inside the designated compartments. All the remaining deposition steps, from solution filtering to film drying, were performed inside the corresponding compartments. Specifically, the solution was filtered with 0.2 µm PTFE filters and spin coated at 33 rps for 30 seconds, after which the sample was dried on a hot plate at 150°C for 5 minutes. The procedure was repeated three times to increase the film thickness.

All the dried thin films were annealed in a tube furnace (Gero F-VS 100-500/13) at 550°C for 1 h, with a 5°C/min heating rate and a 1.7 L/min N_2 flux. Following the crystallization treatment, all samples were characterized with GIXRD, ellipsometry, SEM and UV-Vis-NIR spectroscopy.

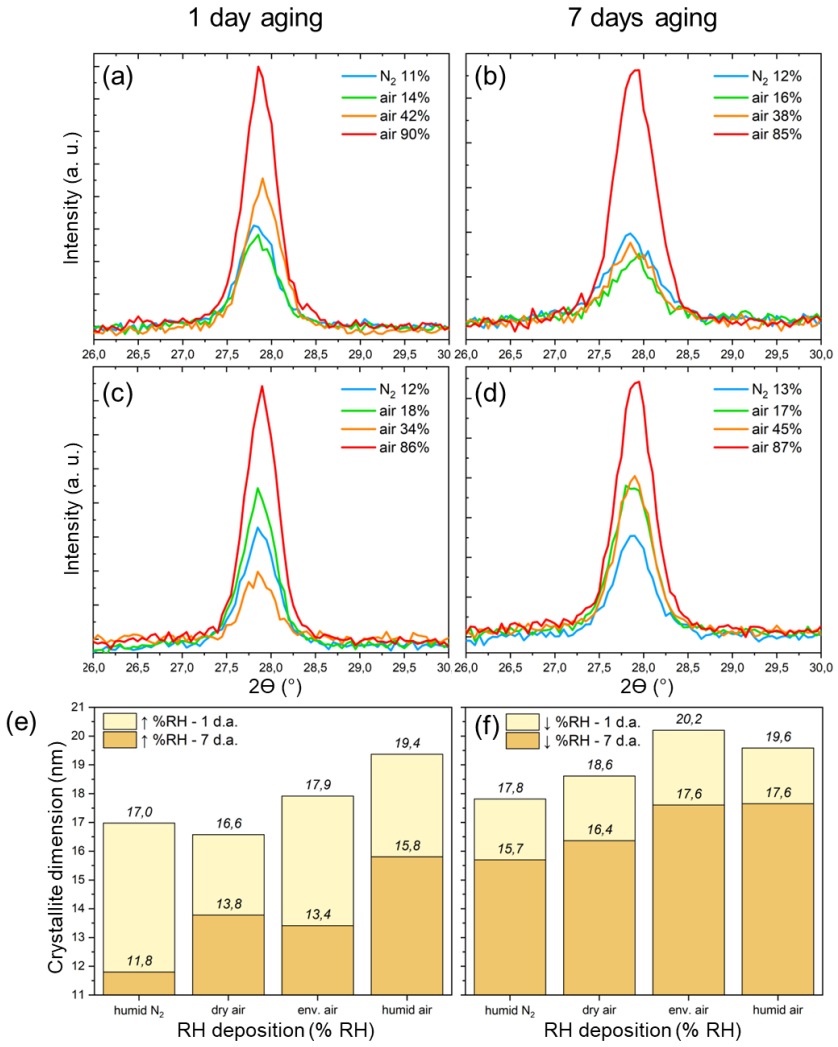


Figure 4.38. GIXRD patterns at 2Θ ~ 27.9° of the thin films synthetized under the following conditions: (a, b) ↑ %RH sol aged for 1 and 7 days, respectively. (c, d) ↓ %RH sol aged for 1 and 7 days, respectively. For each synthesis condition, the four types of atmospheric conditions during deposition are reported: humid N_2, 11-13% RH at 22-23°C (light blue line); dry air, 14-18% RH at 21-23°C (green line); environmental air, 34-45% RH at 22°C (orange line); humid air, 85-90% RH at 20-23°C (red line). (e, f) Crystallite dimension of the corresponding samples reported in (a-d). The error bar in (e, f) was calculated to be 0.3.

The GIXRD results are reported in Figure 4.38 (a-d). The full range diffraction patterns were identical to the ones reported in paragraphs 4.3.5-4.3.6 and was attributed to monoclinic VO_2 (M1) (COD 9009089). The principal (0 1 1) orientation, found to be at an average 2Θ = 27.88 ± 0.02°, was compared among the samples and the average crystallite size was calculated through the Scherrer equation. For both the ↑ %RH sol and ↓ %RH sol, the increasing solution aging time from 1 day to 7 days before deposition led to an increase in average crystallite size (Figure 4.38 (e, f)). Moreover, for all four solutions (i.e., ↑-↓ %RH sol, 1-7 d. a.), the increasing moisture during deposition led to an increasing trend in crystallite dimension.

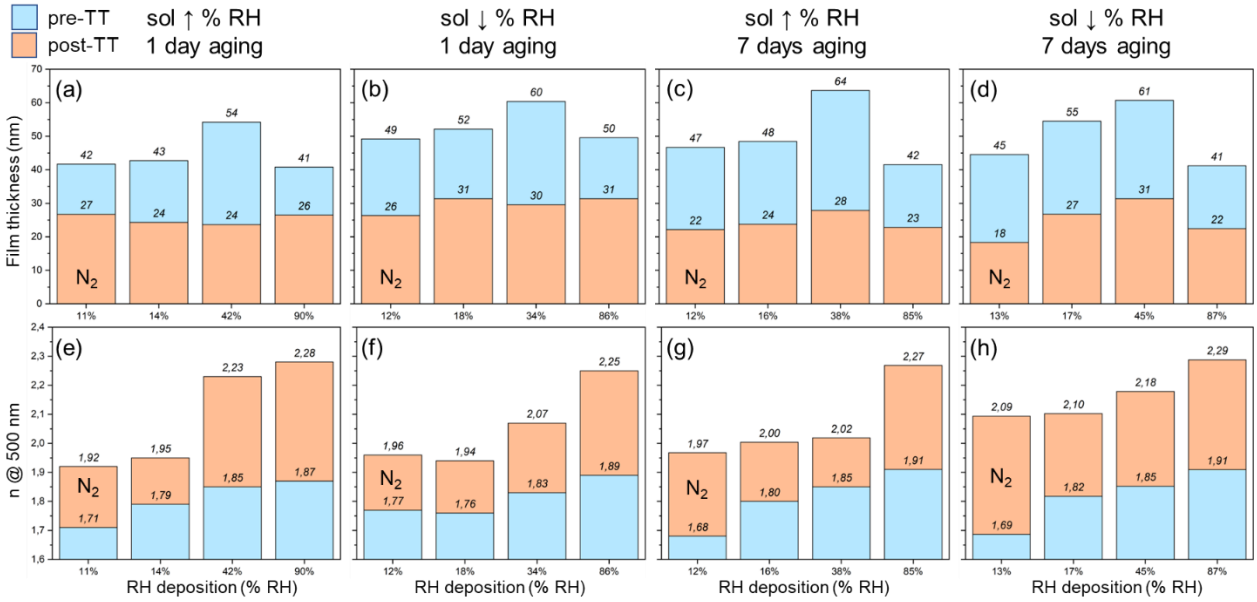


Figure 4.39. (a-d) thickness and (e-h) refractive index (n) characterized by ellipsometry of the thin films synthetized under the following conditions: (a, e) ↑ %RH sol aged for 1 day. (b, f) ↓ %RH sol aged for 1 day. (c, g) ↑ %RH sol aged for 7 days. (d, h) ↓ %RH sol aged for 7 days. For each synthesis condition, the four types of atmospheric conditions during deposition are reported: (i) humid N_2, 11-13% RH at 22-23°C; (ii) dry air, 14-18% RH at 21-23°C; (iii) environmental air, 34-45% RH at 22°C; (iv) humid air, 85-90% RH at 20-23°C. For each sample, the ellipsometry values are reported for both the dried thin film (light blue) and the thermally annealed thin film (red).

The ellipsometry results are reported in Figure 4.39. The film thickness and the refractive index (n) were measured before and after annealing. The thickness of the crystallized thin films was found to have an average value of 26 ± 4 nm. No specific influence on thickness nor n of the moisture conditions during synthesis was noticed (↑ %RH sol - Figure 4.39 (a, c, e, g) vs ↓ %RH sol - Figure 4.39 (b, d, f, h)). Viceversa, the moisture content within the deposition atmosphere influenced the refractive index of the dried thin films, which increased with increasing RH. This trend was found in all four types of solutions (Figure 4.39 (e-h)) and can be attributed to the higher hydroxyl content available to react, which in turn influence the sol-gel reactions and the forming M-O-M network. Interestingly, the same trend was maintained after the heat treatment, for all four solutions. For example, considering the ↓ %RH sol aged for 1 day (Figure 4.39 (f)), the deposition under dry air led to $n_{500\,nm} \sim 1.94$ on the crystalline film, whereas a humid air deposition led to a $n_{500\,nm} \sim 2.25$.

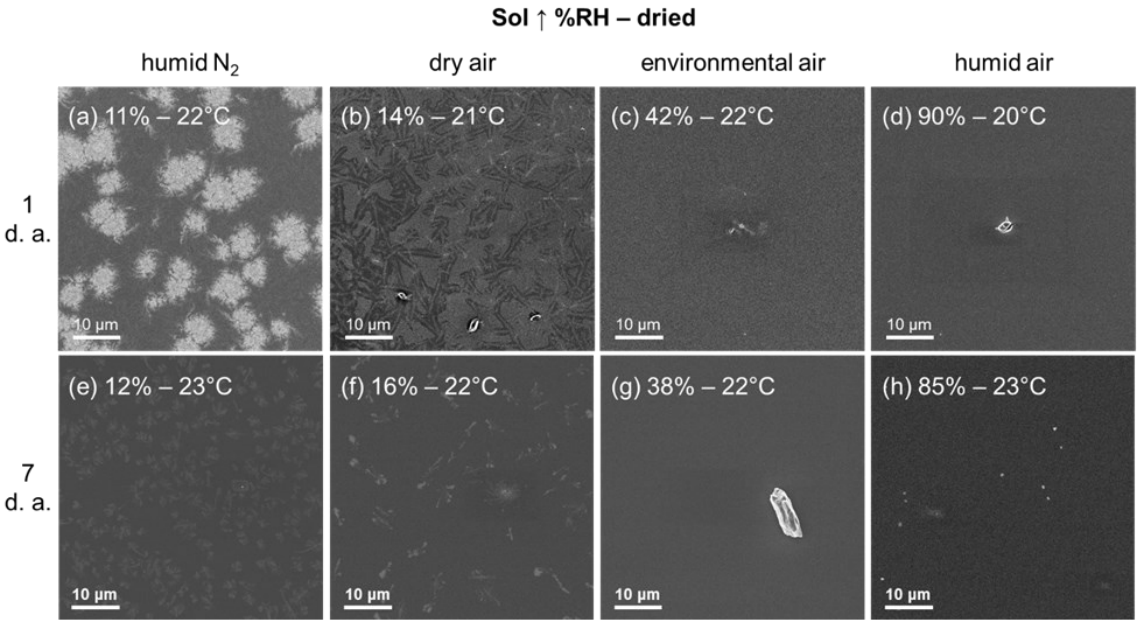


Figure 4.40. SEM images of the dried-only thin films synthetized under ↑ %RH conditions, aged for 1 and 7 days, respectively, and deposited under the four types of atmospheric conditions: (a, e) humid N_2, 11-13% RH at 22-23°C; (b, f) dry air, 14-18% RH at 21-23°C; (c, g) environmental air, 34-45% RH at 22°C; (d, h) humid air, 85-90% RH at 20-23°C. The magnification of each image is 2500 x.

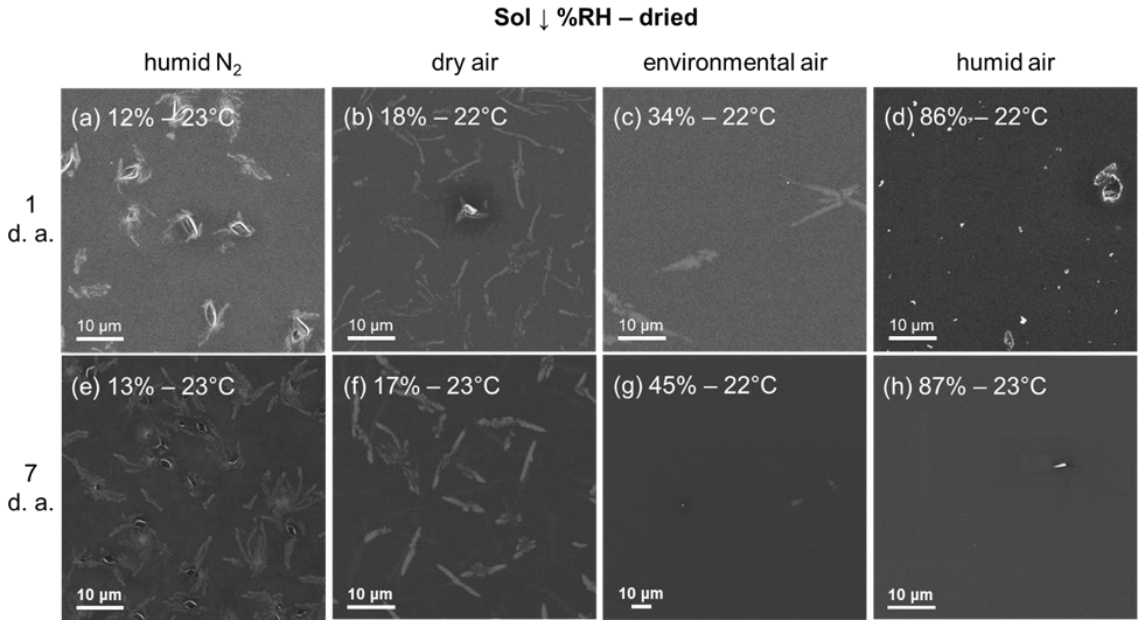


Figure 4.41. SEM images of the dried-only thin films synthetized under ↓ %RH conditions, aged for 1 and 7 days, respectively, and deposited under the four types of atmospheric conditions: (a, e) humid N_2, 11-13% RH at 22-23°C; (b, f) dry air, 14-18% RH at 21-23°C; (c, g) environmental air, 34-45% RH at 22°C; (d, h) humid air, 85-90% RH at 20-23°C. The magnification of each image is 2500 x.

Following the investigation on crystallinity, thickness and optical constants, the morphology of the films was analyzed before and after the heat treatment. The SEM of the dried thin films is reported in Figures 4.40-4.41. For all four solutions (↑-↓ %RH sol, 1-7 d. a.), the deposition under medium or high moisture conditions (environmental air or humid air) led to the formation of a smooth, compact, and uniform morphology (Figures 4.40-4.41 (c, d, g, h)). At relative humidity conditions below 20%

at 21-23°C (humid N_2 and dry air), the formation of dendritic or needle-like features was seen (Figures 4.40-4.41 (a, b, e, f)). The latter are coherent with the results found in paragraph 4.3.7.1. By comparing the secondary electron acquisition mode with the in-lens mode during SEM, these features were attributed to variations in surface morphology, rather than variations in chemical composition.

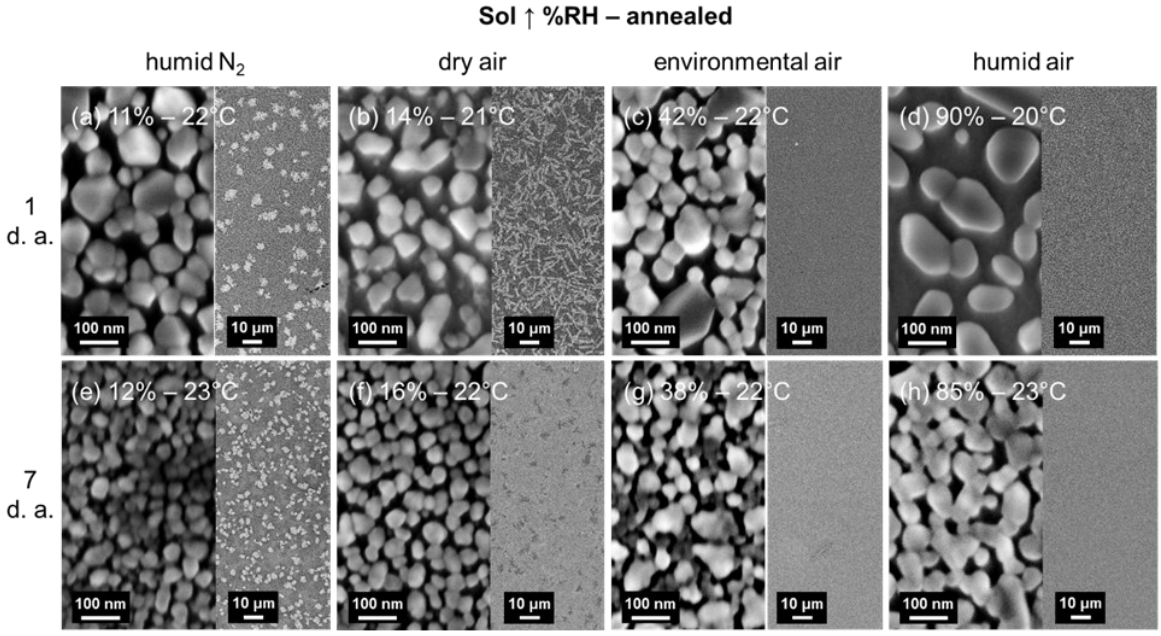


Figure 4.42. SEM images of the thermally annealed thin films synthetized under ↑ %RH conditions, aged for 1 and 7 days, respectively, and deposited under the four types of atmospheric conditions: (a, e) humid N_2, 11-13% RH at 22-23°C; (b, f) dry air, 14-18% RH at 21-23°C; (c, g) environmental air, 34-45% RH at 22°C; (d, h) humid air, 85-90% RH at 20-23°C. The magnification of the images with a 10 µm scale bar is 1000 x, whereas the magnification is 200 kx for the 100 nm scale bar.

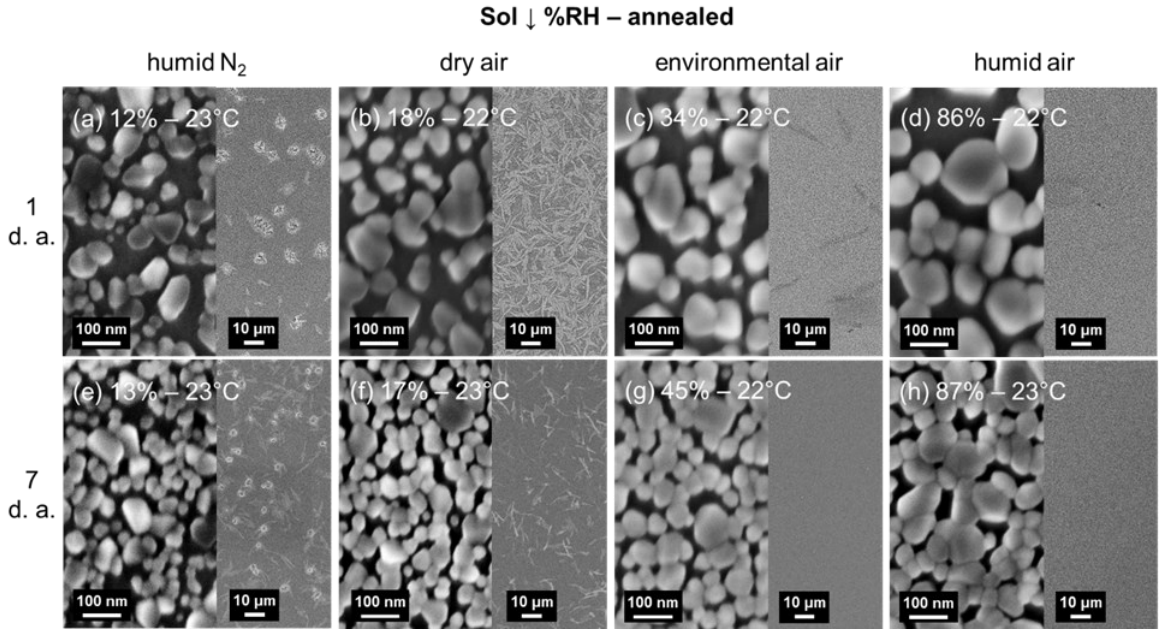


Figure 4.43. SEM images of the thermally annealed thin films synthetized under ↓ %RH conditions, aged for 1 and 7 days, respectively, and deposited under the four types of atmospheric conditions: (a, e) humid N_2, 11-13% RH at 22-23°C; (b, f) dry air, 14-18% RH at 21-23°C; (c, g) environmental air, 34-45% RH at 22°C; (d, h) humid air, 85-90% RH at 20-23°C. The magnification of the images with a 10 µm scale bar is 1000 x, whereas the magnification is 200 kx for the 100 nm scale bar.

The SEM images of the thin films after the crystallization treatment are reported in Figures 4.42-4.43. The smooth, compact, and uniform morphology at the 10 µm scale bar, previously found on the dried films under medium or high RH (environmental air or humid air, for all four solutions), was maintained after crystallization (Figures 4.42-4.43 (c, d, g, h)). At RH conditions below 20% at 21-23°C (humid N_2 and dry air), the previously found dendritic or needle-like features was maintained after crystallization (Figures 4.42-4.43 (a, b, e, f)). Observing the images at higher magnifications (200 kx, 100 nm scale bar), qualitative trends were found in terms of surface coverage and average grain size. To confirm the trend, image analysis was performed on the SEM images with the aid of ImageJ software. The detailed procedure is reported in Appendix A.2.11, whereas two examples are shown in Figure 4.44 (a-d). Figure 4.44 (a, b) shows an example of the estimation of the surface coverage, whereas Figure 4.44 (c, d) reports an example of the estimation of the average particle size and particle size distribution.

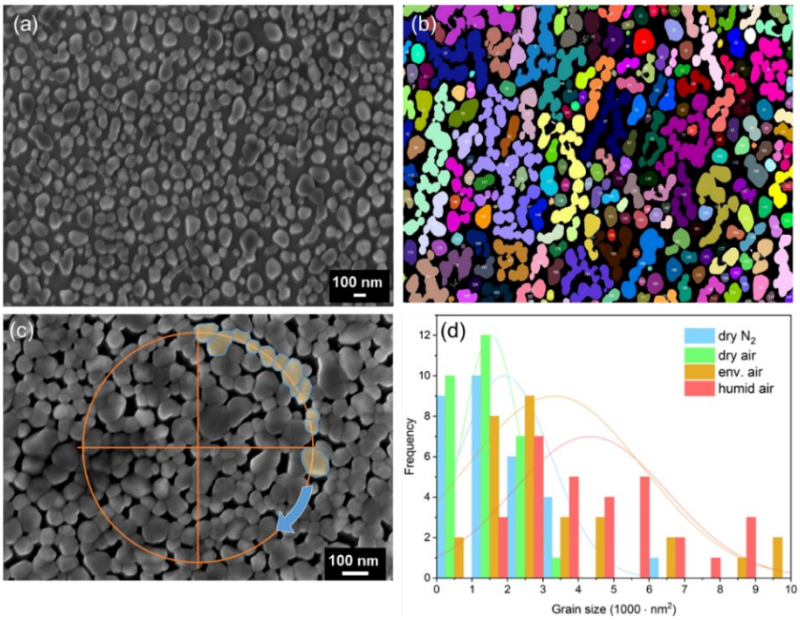


Figure 4.44. Example of the estimation method by image analysis of (b) particle surface coverage and (c, d) average particle size and particle size distribution with the ImageJ software, starting from (a) a SEM image of the films after thermal annealing.

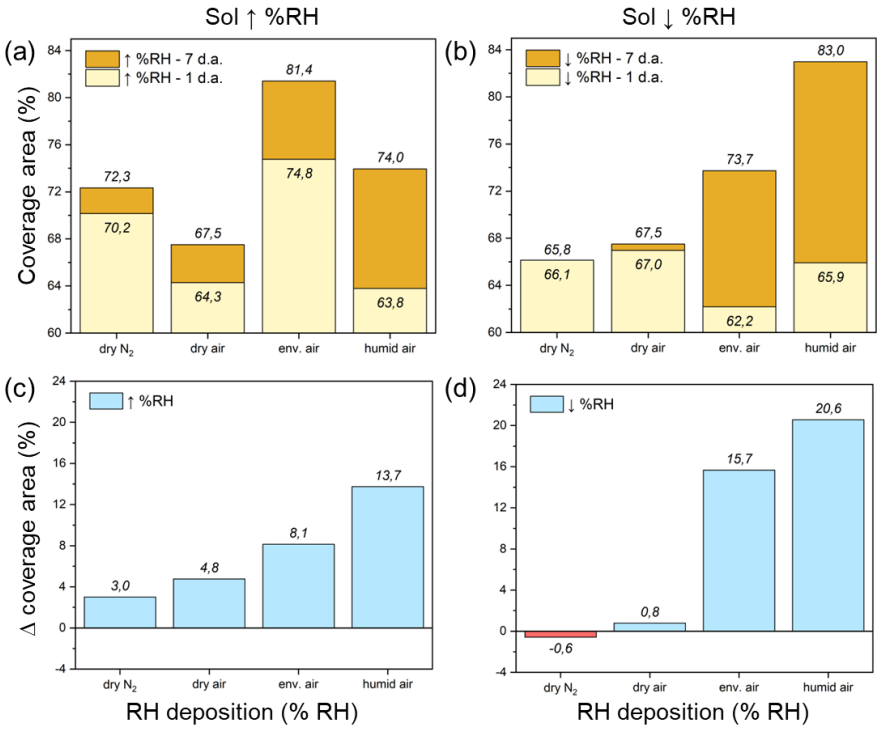


Figure 4.45. (a, b) Estimation of the coverage area of the thermally annealed thin films synthetized under ↑ and ↓ %RH conditions, respectively, aged for 1 day (light yellow) or 7 days (orange), and deposited under the four types of atmospheric conditions: (i) humid N_2, 11-13% RH at 22-23°C; (ii) dry air, 14-18% RH at 21-23°C; (iii) environmental air, 34-45% RH at 22°C; (iv) humid air, 85-90% RH at 20-23°C. (c, d) Difference (Δ) in surface coverage between 1 d and 7 days of aging for the corresponding samples reported in (a, b).

From the estimation of the surface covered by the particles, with respect to the overall area of the image, it was found that the former increased with increasing solution aging, for both ↑-↓ %RH solutions (Figure 4.45 (a, b)). For example, considering the ↓ %RH solution and humid air deposition, the particle coverage increased from ~66% to 83% with increasing solution aging time from 1 day to 7 days (Figure 4.45 (b)). The increasing trend is in well agreement with the work of Yu *et al.*[24] Moreover, for both ↑-↓ %RH solutions and for 7 days of aging, the surface coverage is higher when the deposition is performed under medium or high RH (Figure 4.45 (a, b)). Considering the difference (Δ) in surface coverage between 1 d and 7 days of aging, an increasing Δ was found with increasing moisture during deposition, for both ↑-↓ %RH solutions (Figure 4.45 (c, d)).

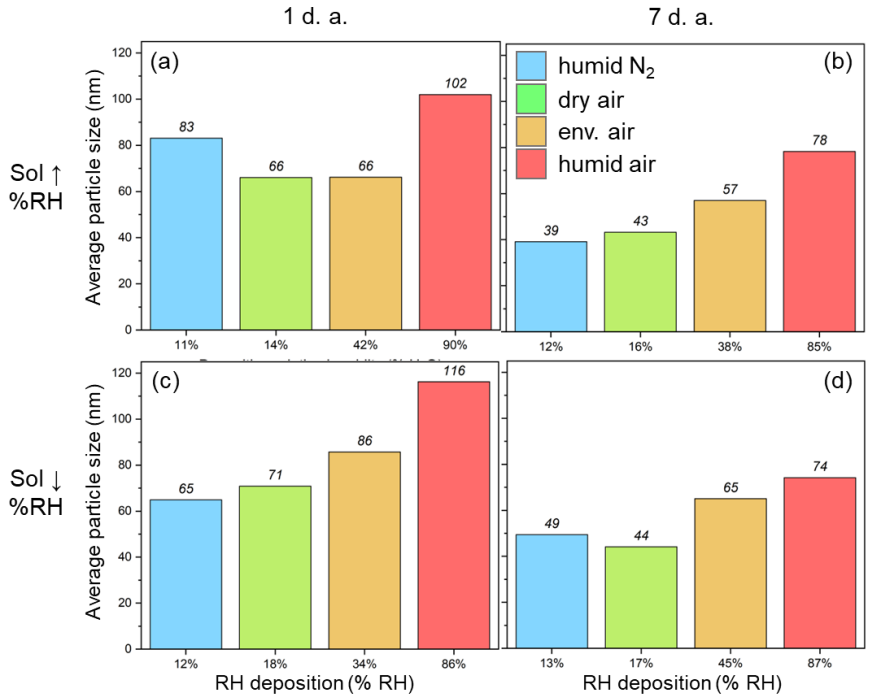


Figure 4.46. Average particle size of the thermally annealed thin films synthetized under (a, b) ↑ % RH conditions and (c, d) ↓ %RH conditions, aged for (a, c) 1 day (a, c) or (b, d) 7 days, and deposited under the four types of atmospheric conditions: humid N_2, 11-13% RH at 22-23°C (light blue); dry air, 14-18% RH at 21-23°C (green); environmental air, 34-45% RH at 22°C (orange); humid air, 85-90% RH at 20-23°C (red).

The estimated average particle size is reported in Figure 4.46. For all four RH deposition conditions and for both ↑-↓ %RH solutions, the increasing solution aging time from 1 day to 7 days led to a decrease in the particle size. For example, considering the ↑ %RH sol and the humid air deposition, the increasing solution aging time from 1 day to 7 days led to a decrease in average particle size from ~102 to ~78 nm (Figure 4.46 (a, b)). This decreasing trend with increasing aging is in well agreement with the results of the crystallite sizes calculated from the GIXRD patterns (Figure 4.38). For all four solutions, apart for one sample, the increasing moisture content during deposition led to a higher average particle size. For example, considering the ↓ %RH sol and 1 day of solution aging, the humid air deposition led to particles of 116 nm average size, respect to 65 nm of the humid N_2 deposition (Figure 4.46 (c)).

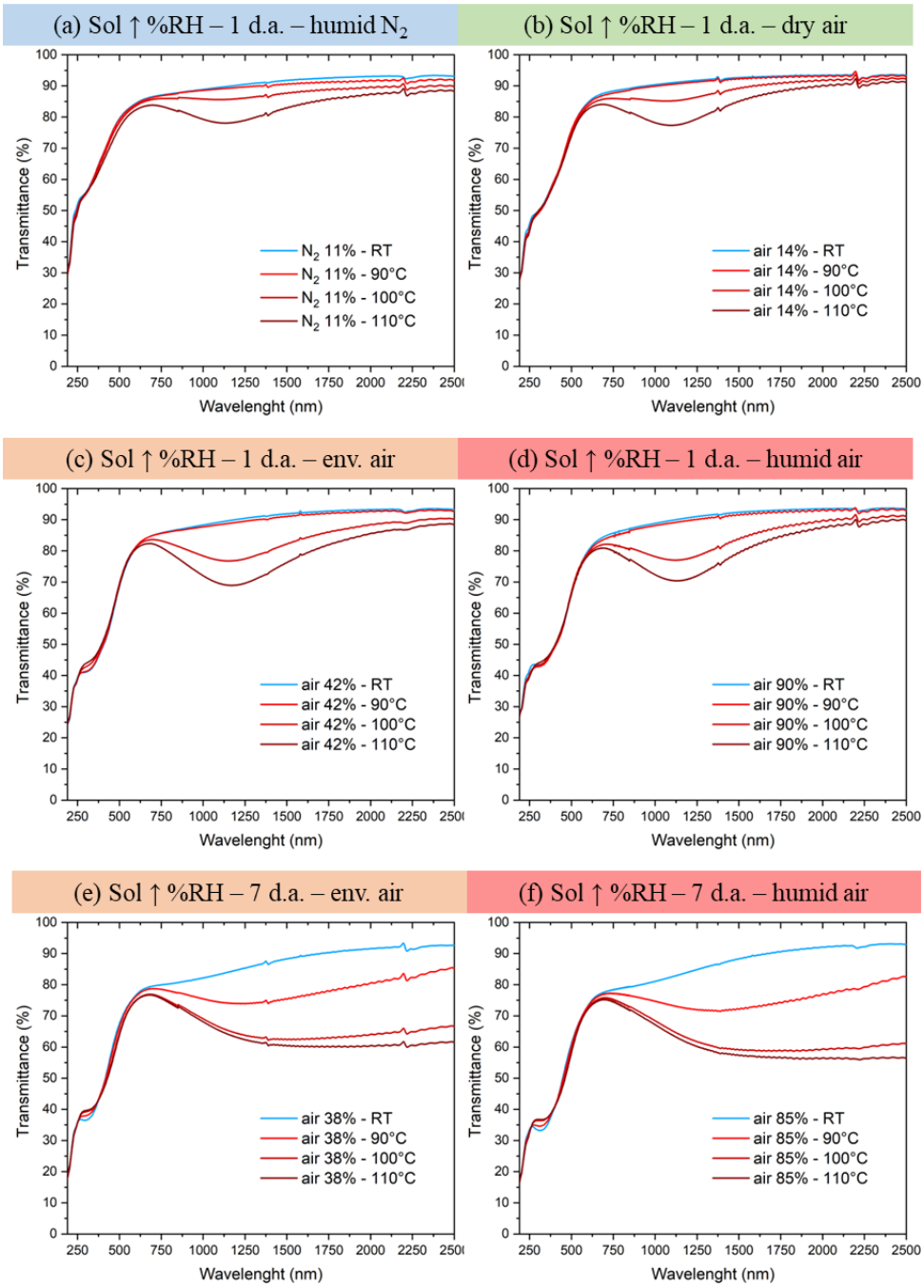


Figure 4.47. UV-Vis-NIR transmittance spectra of the thermally annealed thin films synthetized under ↑ % RH conditions, (a-d) aged for 1 day or (e, f) 7 days, and deposited under the four types of atmospheric conditions: (a) humid N_2, 11-13% RH at 22-23°C; (b) dry air, 14-18% RH at 21-23°C; (c, e) environmental air, 34-45% RH at 22°C; (d, f) humid air, 85-90% RH at 20-23°C. The transmittance spectra are reported for each sample at room temperature (light blue lines, transmitting state) and 90-100-110°C (orange-red lines, reflecting state).

Following the characterizations in terms of crystallinity, thickness, and morphology, the influence of moisture during synthesis and deposition was finally evaluated in terms of thermochromic optical performance. This was done considering an application of the VO_2 thin films for smart windows. The UV-Vis-NIR transmittance of all 16 samples was measured in the VO_2 insulating state (i.e., room temperature) and in the metallic state (i.e., 90-100-110°C). Examples of the optical spectroscopy spectra are reported in Figure 4.47, whereas the luminous transmittance (T_{lum}) and solar modulation

efficiency (ΔT_{sol}) are reported in Figures 4.48-4.49 below. A detailed explanation on how the two parameters were calculated is reported in Appendix A.2.8.

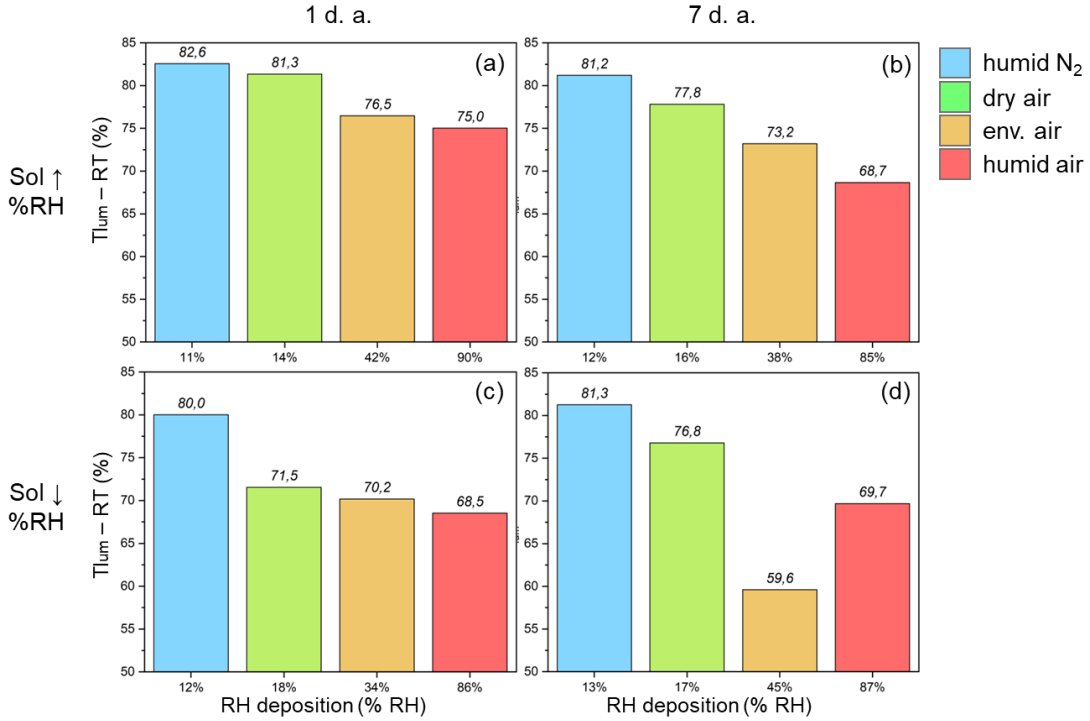


Figure 4.48. Luminous transmittance (T_{lum}) of the thin films synthetized under the following conditions: (a, b) ↑ %RH sol aged for 1 and 7 days, respectively. (c, d) ↓ %RH sol aged for 1 and 7 days, respectively. For each synthesis condition, the four types of atmospheric conditions during deposition are reported: humid N_2, 11-13% RH at 22-23°C (light blue); dry air, 14-18% RH at 21-23°C (green); environmental air, 34-45% RH at 22°C (orange); humid air, 85-90% RH at 20-23°C (red).

Considering the luminous transmittance, for all four solutions (↑-↓ %RH sol, 1-7 d. a.), a decrease in T_{lum} was observed with increasing RH during deposition (Figure 4.48 (a-d)). For example, for the ↑ %RH sol with 7 days of aging, the film deposited under humid N_2 showed a T_{lum} = 81%, whereas a deposition under humid air led to T_{lum} = 69% (Figure 4.48 (b)).

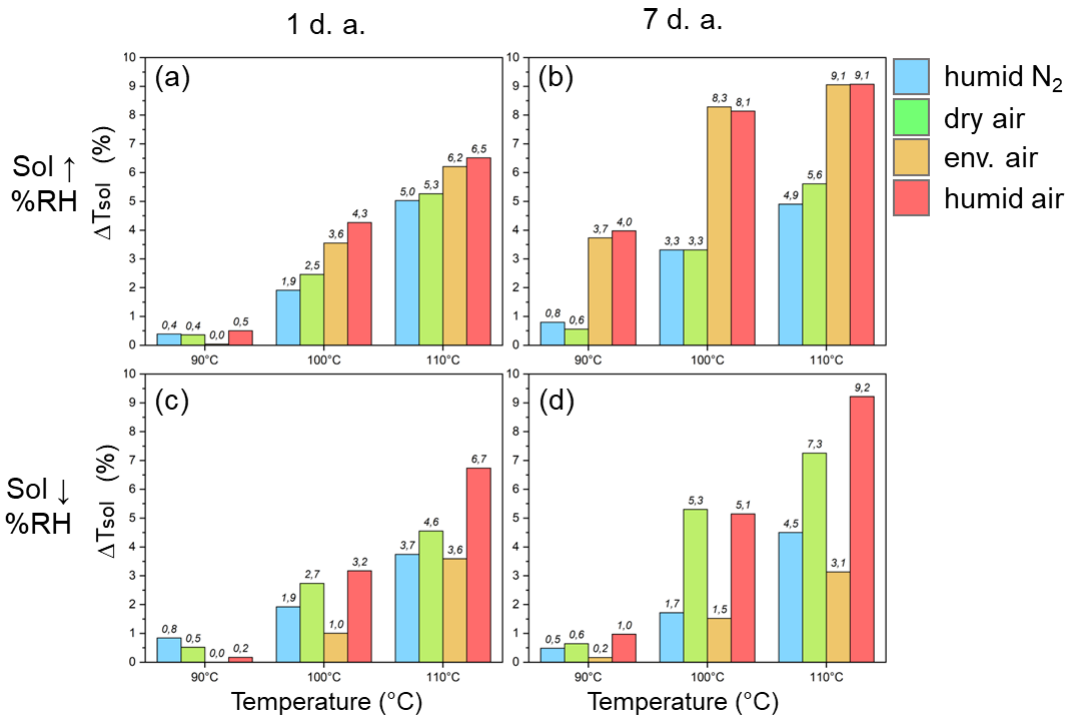


Figure 4.49. Solar modulation efficiency (ΔT_{sol}) of the thin films synthetized under the following conditions: (a, b) ↑ %RH sol aged for 1 and 7 days, respectively. (c, d) ↓ %RH sol aged for 1 and 7 days, respectively. For each synthesis condition, the four types of atmospheric conditions during deposition are reported: humid N_2, 11-13% RH at 22-23°C (light blue); dry air, 14-18% RH at 21-23°C (green); environmental air, 34-45% RH at 22°C (orange); humid air, 85-90% RH at 20-23°C (red).

Considering the modulation of the solar transmittance in function of the temperature, the maximum modulation was reached at 110°C for all samples. For all four solutions (↑-↓ %RH sol, 1-7 d. a.), an increase in ΔT_{sol} was observed with increasing RH during deposition (Figure 4.49 (a-d)). For example, for the ↑ %RH sol with 7 days of aging, the film deposited under humid N_2 showed a $\Delta T_{sol,110°C}$ = 4.1%, whereas a deposition under humid air led to $\Delta T_{sol,\ 110°C}$ = 9.1% (Figure 4.49 (b)). On average, a better solar modulation (i.e., higher $\Delta T_{sol,\ 110°C}$) was noticed with increasing solution aging from 1 day to 7 days (Figure 4.49 (a, b) and Figure 4.49 (c, d)).

5.3.8.3 *Moisture influence – conclusions*

From the overall characterizations, which were presented in the above paragraph 4.3.7.2, some key findings can be highlighted. As a general aspect, the moisture content during the synthesis step was found to have a minor influence on the final properties, in terms of crystallinity, thickness, refractive index, morphology and thermochromic efficiency. On the contrary, both the solution aging and the moisture content during deposition substantially affected the former parameters.

From the GIXRD, the increasing solution aging time led to an increase in average crystallite size, which was increased by a higher moisture during deposition as well. From ellipsometry, a higher RH

during deposition led to an increase in refractive index of the dried thin films. The same trend was maintained after the heat treatment and can be attributed to the higher hydroxyl content available to react during deposition, which in turn influence the sol-gel reactions and the forming M-O-M network.

Considering the SEM, a smooth, compact, and uniform morphology was found on films under medium or high RH, i.e., environmental air or humid air. At RH conditions below 20% at 21-23°C, i.e., humid N_2 and dry air, dendritic or needle-like features were formed. Both conditions were maintained after crystallization. From the image analysis, the particle surface coverage increased with increasing aging of the solution. Moreover, the surface coverage was higher for the deposition performed under medium or high RH. The average particle size decreased with increasing solution aging. This decreasing trend with increasing aging is in well agreement with the GIXRD results. The increasing moisture content during deposition led to a higher average particle size.

Regarding the optical performance, the luminous transmittance (T_{lum}) decreased with increasing RH during deposition. This is coherent with the surface coverage, which increases with increasing RH and leads to a lower transmission of the visible light. The decrease in T_{lum} with increasing RH during deposition is also coherent with the ΔT_{sol} trend, which increases in ΔT_{sol} with higher RH. The two parameters are known to display opposite trends, as highlighted in paragraph 3.6 of Chapter 3. A higher solar modulation was noticed with increasing solution aging.

5.4 Conclusions

The urgency of lowering the worldwide energy consumption evidences the need for simple, low-cost, and straightforward solutions. As previously mentioned, VO_2 emerges as a remarkable material for the fabrication of passive thermochromic smart windows. However, a meticulous control the process is extremely challenging to be obtained regarding the formation of the desired type and phase of vanadium oxide. Regarding the synthesis of CSD processes, many vanadium precursors, despite being widely employed, are linked to high levels of hazardousness.

To address these problems, the multiple factors which affect the fabrication of sol-gel VO_2 thin films were systematically considered in this Chapter. Parameters such as solution aging, drying temperature of the thin films, atmosphere during deposition and during annealing, and annealing temperature were optimized. Once satisfactory functional properties were obtained, additional effort was devoted to the simplification of the process. To verify the effect of each parameter, the VO_2 thin films were studied

in terms of morphology (SEM, TEM), crystallinity (GIXRD), chemical and atomic composition (XPS, RBS), optical and electrical properties (UV-Vis-NIR spectroscopy, four-point probe resistivity measurements), electron energy loss spectroscopy (EELS), Fast Fourier Transform (FFT) analysis, thickness and optical constants (ellipsometry).

Two vanadium precursors were considered, vanadium pentoxide (V_2O_5) and vanadyl acetylacetonate ($VO(acac)_2$). The V_2O_5 powder, despite the carcinogenicity issues, is a widely used precursor to produce VO_2 thin films, so it was initially chosen as a reference starting point. Following the investigation of all the process parameters, the synthesis based on the former precursor led to the formation of crystalline monoclinic VO_2 (M1) thin films, which displayed the desired thermochromic properties. However, besides the toxicity and carcinogenicity, several issues regarding the stability of both the solution and the dried films were found, which limited the scalability of the process. As a general approach and when possible in this work, the choice of precursors, reagents and solvents was oriented towards a green chemistry route. Considering this, $VO(acac)_2$ was chosen as an alternative precursor, with respect to V_2O_5.

The $VO(acac)_2$ precursor showed excellent results in terms of film quality, functional properties, versatility, and simplicity of the process. An in-depth analysis on the synthesis, deposition, and annealing parameters was conducted. Factors such as the oxidation state of the solution and thin films, solvent type, solution aging, moisture levels during deposition, drying temperature of the thin films, and annealing atmosphere were systematically varied until the optimized values were found. The results were evaluated in terms of film quality and functional properties, expressed as luminous transmittance and thermochromic solar modulation of the smart window.

As a brief overview, the chemical composition of the solution was initially studied by UV-Vis spectroscopy, which highlighted the presence of a mixed oxidation state of V^{4+} and V^{5+}. The solution was found to be stable for months in air, which guarantees flexibility in terms of industrial scalability. The resulting film quality, in terms of surface coverage, homogeneity, and optical properties, was seen to increase with the aging time of the solution. The chemical composition of the as-deposited thin films was investigated by XPS. A decrease in organic content was seen with increasing drying temperature (from 80°C to 300°C) and the presence of a mixed V^{4+} and V^{5+} in the dried films was confirmed.

Different annealing atmospheres were considered, from oxidizing to inert to reducing environments. A thermal treatment in air led to the formation of V_2O_5, whereas annealing in 5% H_2 in Ar led to a mixture of multiple vanadium oxides. The thermal annealing under a N_2 atmosphere allowed for the

formation of the target vanadium oxide, i.e., VO_2 (M1). Once the correct atmosphere was determined, the temperature during the thermal treatment was varied from 250°C to 650°C. The crystallization was found to start above 450°C and marginal differences, in terms of optical properties, were found by varying the temperature within the 450-650°C range.

Finally, the influence of moisture during the deposition step was considered. The presence of the former was found to favor the formation of homogeneous and thicker films by RBS and ellipsometry analysis, with respect to a fully inert atmosphere. The effect of moisture was further studied by comparing four different environments, from low (humid nitrogen or dry air) to high moisture conditions (85-90% RH 20-23°C). A smooth, compact, and uniform morphology was found with medium or high moisture levels during deposition, whereas below 20% RH at 21-23°C dendritic or needle-like features were formed. The particle surface coverage increased with increasing aging time of the solution and with medium or high moisture levels during deposition. The average particle size decreased with increasing solution aging, in agreement with the GIXRD results, and increased with the increasing moisture content during deposition.

The moisture influence was finally evaluated in terms of luminous transmittance (T_{lum}) and solar modulation efficiency (ΔT_{sol}), which represent the standard parameters to express the efficiency of the smart windows. The luminous transmittance (T_{lum}) decreased with increasing moisture during deposition, which was explained with the increased surface coverage and the corresponding lower transmission of the visible light. The decrease in T_{lum} with increasing moisture during deposition was linked to an increase in the solar modulation (ΔT_{sol}). A smart window operates at its maximum functionality when the highest visible transmittance (T_{lum}) is achieved simultaneously with the highest level of solar modulation (ΔT_{sol}, $\Delta T_{2000\ nm}$). These parameters are known to be inversely correlated, meaning that an increase in visible transmittance typically leads to a decrease in solar modulation, and viceversa. For smart windows based on single VO_2 films, improvement is required for both T_{lum} and ΔT_{sol} values, which should be higher than 50% and 10%, respectively.[38,41] Various approaches have been reported to simultaneously enhance both parameters, often involving the combination of multiple materials, the creation of multilayers and/or composites, and the use of nanostructuring techniques.[42] In this Chapter 4, the best solar modulation of $\Delta T_{sol,\ 110°C}$ = 9.2% and T_{lum} = 70% was reached by depositing under high moisture conditions (85-90% RH at 20-23°C) a solution aged for 7 days. Considering the reference smart windows based on single VO_2 films in the literature,[38,41] in this case quite high values of solar modulation were reached without deteriorating the luminous transmittance. Further improvements in terms of T_{lum} will be addressed in Chapter 6, by combining the VO_2 films with TiO_2 and hybrid SiO_2 coatings in bilayer configurations.

References

1. Gao, Y. *et al.* Nanoceramic VO 2 thermochromic smart glass: A review on progress in solution processing. *Nano Energy* **1**, 221–246 (2012).

2. Seyfouri, M. M. & Binions, R. Sol-gel approaches to thermochromic vanadium dioxide coating for smart glazing application. *Solar Energy Materials and Solar Cells* **159**, 52–65 (2017).

3. Kim, J. & Paik, T. Recent advances in fabrication of flexible, thermochromic vanadium dioxide films for smart windows. *Nanomaterials* **11**, (2021).

4. Liu, K., Lee, S., Yang, S., Delaire, O. & Wu, J. Recent progresses on physics and applications of vanadium dioxide. *Materials Today* **21**, 875–896 (2018).

5. Rehder, D. Vanadium. Its role for humans. *Met Ions Life Sci* **13**, 139–169 (2013).

6. Fatola, O. I., Olaolorun, F. A., Olopade, F. E. & Olopade, J. O. Trends in vanadium neurotoxicity. *Brain Res Bull* **145**, 75–80 (2019).

7. Zhang, C., Cao, W., Adedeji, A. V. & Elsayed-Ali, H. E. Preparation and properties of VO2 thin films by a novel sol-gel process. *J Solgel Sci Technol* **69**, 320–324 (2014).

8. Sun, R. *et al.* Controllable Design of Bifunctional VO2Coatings with Superhydrophobic and Thermochromic Performances. *ACS Appl Mater Interfaces* **13**, 13751–13759 (2021).

9. Seyfouri, M. M. & Binions, R. Sol-gel approaches to thermochromic vanadium dioxide coating for smart glazing application. *Solar Energy Materials and Solar Cells* **159**, 52–65 (2017).

10. Huang, Y. *et al.* Phase transition analysis of thermochromic VO2 thin films by temperature-dependent Raman scattering and ellipsometry. *Appl Surf Sci* **456**, 545–551 (2018).

11. Son, S. B., Youn, J. W., Kim, K. S. & Kim, D. U. Optical properties of periodic micropatterned VO2 thermochromic films prepared by thermal and intense pulsed light sintering. *Mater Des* **182**, 107970 (2019).

12. Johnson, A. S. *et al.* Ultrafast X-Ray hyperspectral imaging of a photo-induced phase transition with nanometer space and femtosecond time resolution.

13. Anastas, P. & Eghbali, N. Green Chemistry: Principles and Practice. *Chem Soc Rev* **39**, 301–312 (2009).

14. Pan, M. *et al.* Properties of VO2 thin film prepared with precursor VO(acac)2. *J Cryst Growth* **265**, 121–126 (2004).

15. Robert H. Lipson & Cheng Lu. Method for inhibiting the oxidization of vo(acac)2 in solution. (2009).

16. Capello, C., Fischer, U. & Hungerbühler, K. What is a green solvent? A comprehensive framework for the environmental assessment of solvents. *Green Chemistry* **9**, 927–934 (2007).

17. Makinen, M. W. & Salehitazangi, M. The Structural Basis of Action of Vanadyl (VO2+) Chelates in Cells. *Coord Chem Rev* **279**, 1–22 (2014).

18. Choi, N. H., Kwon, S. & Kim, H. Analysis of the Oxidation of the V(II) by Dissolved Oxygen Using UV-Visible Spectrophotometry in a Vanadium Redox Flow Battery. *J Electrochem Soc* **160**, A973–A979 (2013).

19. Geiser, J., Natter, H., Hempelmann, R., Morgenstern, B. & Hegetschweiler, K. Photometrical Determination of the State-of-Charge in Vanadium Redox Flow Batteries Part I: In Combination with Potentiometric Titration. *Zeitschrift fur Physikalische Chemie* (2019).

20. Nazari, S. & Charpentier, P. A. Stabilizing vanadyl acetylacetonate using imidazolium Ionic liquids for VO2 thermochromic thin films. *Thin Solid Films* **725**, 138640 (2021).

21. Ortolano, T. R., Selbin, J. & Mcglynn, S. P. Electronic Structure, Spectra, and Magnetic Properties of Oxycations. V. The Electronic Spectra of Some Vanadyl Complexes. *J Chem Phys* **41**, 262–268 (1964).

22. Park, S. K. *et al.* Effect of Functionalized Ionic Liquids on the Stability of V(acac)3. *Bull Korean Chem Soc* **39**, 1036–1040 (2018).

23. Samotus, A., Grybos, R., Popova, N. & Bogolitsyn, K. Kinetics of oxidation of vanadyl acetylacetonate by oxygen in methanolic solution. **64**, 2–5 (1997).

24. Yu, J. H. *et al.* Thermal aging effect of vanadyl acetylacetonate precursor for deposition of VO2 thin films with thermochromic properties. *Mater Res Bull* **82**, 11–15 (2016).

25. Basso, M. *et al.* Rapid laser-induced low temperature crystallization of thermochromic VO2 sol-gel thin films. *Appl Surf Sci* **631**, (2023).

26. Green, Dr. D. W. & Southard, Dr. M. Z. *Perry's Chemical Engineers' Handbook*. *Perry's Chemical Engineers' Handbook* (McGraw-Hill Education, 2019).

27. With, P. C. *et al.* Photochemical low-temperature synthesis of iron(III) oxide thin films. *Appl Surf Sci* **493**, 525–532 (2019).

28. Melia, T. P. & Merrifield, R. Thermal properties of acetylacetone. *J. Appl. Chem.* **19**, 79–82 (2007).

29. Von Hoene, J., Charles, R. G. & Hickam, W. M. Thermal decomposition of metal acetylacetonates mass spectrometer studies. *Journal of Physical Chemistry* **62**, 1098–1101 (1958).

30. Nenashev, R. N., Mordvinova, N. E., Zlomanov, V. P. & Kuznetsov, V. L. Thermal decomposition of vanadyl acetylacetonate. *Inorganic Materials* **51**, 891–896 (2015).

31. Van Der Voort, P., White, M. G. & Vansant, E. F. Thermal decomposition of VO(acac)2 deposited on the surfaces of silica and alumina. *Langmuir* **14**, 106–112 (1998).

32. Twyman, N. M., Tetzner, K., Anthopoulos, T. D., Payne, D. J. & Regoutz, A. Rapid photonic curing of solution-processed In 2 O 3 layers on flexible substrates. *Appl Surf Sci* **479**, 974–979 (2019).

33. Kim, Y. H. *et al.* Flexible metal-oxide devices made by room-temperature photochemical activation of sol-gel films. *Nature* **489**, 128–132 (2012).

34. Tanuma, S., Powell, C. J. & Penn, D. R. Calculations of electron inelastic mean free paths. V. Data for 14 organic compounds over the 50–2000 eV range. *Surface and Interface Analysis* **21**, 165–176 (1994).

35. Born, M. & Wolf, E. *Principles of Optics: Electromagnetic Theory of Propagation, Interference and Diffraction of Light*. (Cambridge University Press, 1999).

36. Jang, W. L. *et al.* Local geometric and electronic structures of gasochromic VOx films. *Physical Chemistry Chemical Physics* **16**, 4699–4708 (2014).

37. Qazilbash, M. M. *et al.* Electrodynamics of the vanadium oxides V O2 and V2 O3. *Phys Rev B Condens Matter Mater Phys* **77**, 115121 (2008).

38. Cao, X. *et al.* Challenges and Opportunities toward Real Application of VO2-Based Smart Glazing. *Matter* **2**, 862–881 (2020).

39. Greenspan, L. Humidity Fixed Points of Binary Saturated Aqueous Solutions. *J Res Natl Bur Stand A Phys Chem* **81A**, 89 (1977).

40. Alam, A. U., Howlader, M. M. R. & Deen, M. J. The effects of oxygen plasma and humidity on surface roughness, water contact angle and hardness of silicon, silicon dioxide and glass. *Journal of Micromechanics and Microengineering* **24**, 035010 (2014).

41. Santos, A. J. *et al.* Facile Fabrication of High-Performance Thermochromic VO2-Based Films on Si for Application in Phase-Change Devices. *Chemistry of Materials* **35**, 4435–4448 (2023).

42. Wang, S. *et al.* Recent progress in VO2 smart coatings: Strategies to improve the thermochromic properties. *Prog Mater Sci* **81**, 1–54 (2016).

Chapter 5
Laser annealing of VO_2 thin films

Table of contents

5 Chapter 5 – Laser annealing of VO_2 thin films 203

5.1 Introduction 205

5.2 Photonic annealing 207

5.2.1 UV continuous lamps 207

5.2.1.1 DUV lamp crystallization of MO sol gel thin films 209

5.2.1.2 DUV lamp crystallization of VO_2 thin films 209

5.2.2 Laser annealing 210

5.2.2.1 Laser irradiation of sol gel MO thin films 215

5.2.2.2 KrF excimer laser irradiation of VO_2 thin films 216

5.3 Laser-induced crystallization of VO_2 thin films 216

5.3.1 Synthesis and deposition of VO_2 thin films 217

5.3.2 Laser annealing 217

5.3.3 Low temperature drying 218

5.3.4 Laser-thin film interaction 219

5.3.5 Substrate influence 228

5.3.6 Laser-crystallization of VO_2 thin films – conclusions 236

5.4 Moisture influence on laser annealed VO_2 thin films 236

5.4.1 Synthesis, deposition, and laser-annealing of VO_2 thin films 237

5.4.2 Optimal working window for laser-processing of VO_2 thin films 237

5.4.3 Moisture influence and optimal working window – conclusions 247

5.5 Laser-induced crystallization mechanism of VO_2 thin films 247

5.5.1 GIXRD, SEM, TEM and AFM results 248

5.5.2 Laser-induced crystallization mechanism of VO_2 thin films 254

5.5.3 Laser-induced crystallization mechanism of VO_2 thin films – conclusions 257

5.6 Conclusions 258

Author disclosure statement

Part of the data and the discussion reported in paragraphs 5.1-5.3 of Chapter 5 was published in the article "Basso, M. *et al.* Rapid laser-induced low temperature crystallization of thermochromic VO_2 sol-gel thin films. *Applied Surface Science*, Volume 631, 157507 (2023). ISSN 0169-4332. https://doi.org/10.1016/j.apsusc.2023.157507 ".[1]

Part of the data and the discussion reported in paragraphs 5.4-5.5 of Chapter 5 was submitted for publication, in the draft article "Basso, M. *et al*. Ultrafast laser crystallization dynamics of thermochromic VO_2 thin films by simple moisture-assisted sol-gel. *Submitted*"

6.1 Introduction[1]

As emerged from Chapter 1 and 3, chemical solution deposition (CSD) methods for the development of metal oxides (MOs) thin films are generally based on four fundamental steps:

1. Synthesis of the initial solution: the MO precursor is properly chosen, along with suitable additives and solvent. The influence of parameters such as concentration, temperature, aging time, and atmosphere should be considered.
2. Thin film deposition: multiple techniques are available, such as spin coating, blade coating, inkjet printing, and spray coating. Optimization of the deposition parameters should be performed.
3. Thin film processing: removal of organic residuals, densification and/or crystallization of the MO network.
4. Device fabrication.

The annealing step is particularly crucial for vanadium oxides, because the annealing atmosphere usually requires high levels of precision with respect to the gas partial pressures, temperatures, and flux values. Another challenge of CSD is the reduction of the processing temperatures required for the densification and eventual crystallization of MOs. Most MOs require annealing temperatures above 250°C, which pose severe limitations to MO deposition on temperature-sensitive substrates, such as polymers or low-melting temperature metals.[2] Regarding VO_2, alternative solutions such as the incorporation of previously crystallized nanoparticles in polymeric matrices, are more sensitive to the environment and cannot achieve uniform optical or electrical performance, due to low connectivity between individual particles.[3]

The successful crystallization of uniform MO coatings on temperature-sensitive substrates would make a wide range of innovative solutions available to tackle the increasing worldwide energy demand. As introduced in Chapter 3, unconventional techniques, such as photonic curing, have gained attention for the development of actuators, memory-devices, transistors, and flexible electronics, based on VO_2 or other MOs.[3,4] Photons of appropriate wavelengths are used to induce localized photothermal and/or photochemical effects in the coating, avoiding thermal damage of the underlying substrate. The three main types of photonic curing, namely deep ultraviolet (DUV) irradiation, lasers, and flash lamps, substantially differ in terms of temporal and spatial energy distribution inside the film, process timescale, and irradiation range.[2,5,6] Among them, laser annealing is a particularly promising alternative to conventional thermal treatments, offering accurate control of the energy distribution inside the coatings in both space and time. The extremely fast laser processing allows reduced manufacturing time, roll-to-roll versatility, and scalability over large substrate areas.[2,7,8]

In this Chapter, an initial overview on photonic annealing will be discussed in paragraph 5.1, whereas the experimental results will be reported in paragraphs 5.2-5.4.

Regarding the latter, VO_2 thin films were deposited following the green sol-gel synthesis described in Chapter 4, which is based on a non-hazardous precursor ($VO(acac)_2$) and solvent (ethanol) with no supplementary additives. With respect to Chapter 4, an alternative route to induce the amorphous to crystalline conversion into VO_2 (M1) will be presented in Chapter 5, i.e., nanosecond pulsed laser irradiation. Considering the literature, the difficulty of meticulously controlling the process often emerges as a crucial aspect for vanadium oxide processing. Studies that employed matching conditions of synthesis, deposition, and thermal treatment, did not always produce the same vanadium oxide phases, but often led to different phases or to combinations of multiple oxides.[9–11] In contrast to conventional thermal treatments, which require inert atmospheres to avoid the formation of other vanadium oxides,[12] in this work the laser treatment was performed in air.

Since the interaction between ns laser pulses and sol gel thin films was not clearly understood, the laser parameters were systematically varied to gain in-depth knowledge of their effect. The influence of laser parameters and substrate type on the films' optical, chemical, and morphological properties were explored through several techniques, including grazing incidence X-ray diffraction (GIXRD), soft and hard X-ray photoelectron spectroscopy (SXPS, HAXPES), transmission and scanning electron microscopy (TEM, SEM), UV-Vis-NIR spectroscopy, ellipsometry, and Rutherford backscattering spectrometry (RBS).

6.2 Photonic annealing

Photonic annealing has progressively gained attention as a suitable alternative to conventional thermal treatments. The process is based on light irradiation, either from a narrow or broad range of wavelengths, and on the consequent absorption by the irradiated sample. Photonic annealing can be classified according to the type of light source, which can be a UV continuous lamp, a pulsed or continuous laser, or a flash lamp. The type of light source remarkably influences how the light is absorbed by the sample, as a function of wavelength range, thermal load, timescales, heating rates, temperature profiles, and substrate involvement.

The choice of irradiation wavelength is performed according to the optical properties of the materials involved, which generally consist of a thin film and a substrate. Two strategies can be adopted: the first is to match the substrate's absorbance with the irradiation wavelength(s), whereas the second is to match the film's absorbance with the irradiation source. According to the different choices, the light absorption by the film or substrate leads to photochemical and/or photothermal reactions inside the film, depending on the process timescales and heat distribution.[2,13]

6.2.1 *UV continuous lamps*

As highlighted by Yarali *et al.*[2], the UV range is broadly employed for the formation of dense amorphous MO films, due to the favorable band gap absorption. Continuous UV irradiation can be performed through gas discharge lamps, based on mercury, metal halides, excited dimers, or inorganic light-emitting diodes (LED), among which the low-pressure mercury lamps are the most common. The latter emit at two principal peaks, i.e., 90% at 254 nm and 10% at 185 nm. Besides the irradiation range, the optical power density affects the film conversion and is influenced by the device geometry (i.e., sample-source distance) and irradiance (i.e, power per unit area), which spans between 1-1000 mW/cm^2.[14,15]

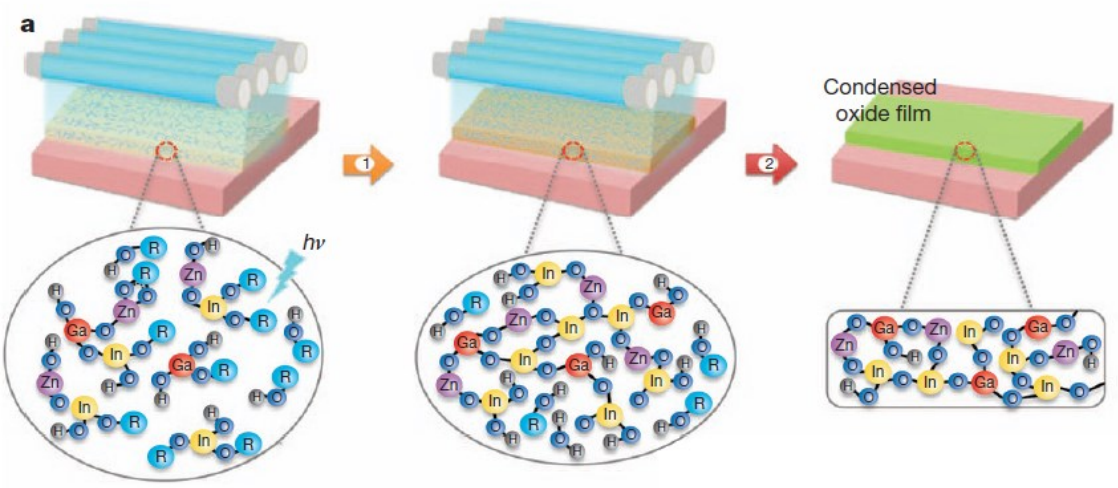


Figure 5.1. Schematic of the photochemical conversioin by UV lamps induced on CSD metal-oxide precursors.[16]

UV lamps are mainly used to induce or boost the conversion of a CSD metal-oxide precursor into a dense metal-oxide network, exploiting the photochemical conversion instead of a thermal-aided one (Figure 5.1). In some cases, the combination of both UV irradiation and thermal sources, such as hot plates, was found to be the best solution. However, the use of the latter is strictly linked to the thermal properties of the substrate. The photochemical conversion through UV lamps generally exploits the optical absorption of metal salt precursors. In case of insufficient precursor absorption at the source's spectrum, UV-absorbing compounds, such as β-diketones, can be added to maximize the UV absorption. Kim *et al*. deeply explored DUV photochemical conversion of sol-gel films. Employing multiple metal nitrates, chlorides, or alkoxides, they densified semiconducting or dielectric MO materials such as indium oxide (In_2O_3), indium-gallium zinc oxide (IGZO), AlO_x and ZrO_x.[16,17] They proposed the conversion mechanism to be based on the photolysis of metal ligands, leading to radicals reactive which promote M-O-M formation through hydrolysis and condensation reactions.

The UV-aided photochemical conversion is usually reached with irradiation times of tens of minutes to hours. Unintentional heating up to 150°C was found during DUV irradiation. The former positively contributed to the network formation and densification promoted by the UV light. The synergy between collateral heating and DUV irradiation was proven to lead to device functional properties comparable with a 350°C thermal annealing.[17] Given the long irradiation timescales, the atmosphere during UV irradiation was also considered. The formation of ozone (O_3) was proven if the irradiation was performed in air, which led to a lower photochemical conversion efficiency.[2] The use of an inert atmosphere, e.g. nitrogen, was proposed as a suitable solution to overcome the ozone formation, even though the presence of O_3 was found to be beneficial for the removal of organic residuals.[18,19]

Besides the collateral temperature rise during UV irradiation, a synergistic approach between combustion reactions and UV irradiation was proposed to further boost the precursor conversion into

a M-O-M network.[20,21] The exothermic reaction between an oxidizer reagent, typically a nitrate salt, and a fuel, e.g. urea or acetylacetone, favorably increased the conversion efficiency of the metal precursor. The release of gaseous products needed to be addressed as a possible source of cracks within the film, which might damage the functional device properties.

From an overall perspective, DUV irradiation was proven to be a solid pathway for the development of dense and amorphous MO thin films at lower temperatures respect to the thermally annealed ones. The former functional properties were proven to be comparable to the latter, in terms of final device application.

6.2.1.1 *DUV lamp crystallization of MO sol gel thin films*

While most of research on DUV irradiation focused on the low temperature densification of amorphous MO thin films, a few studies have addressed the crystallization of MO thin films by unconventional photonic annealing. For example, Akasuma *et al.*[22] crystallized ZnO thin films with the aid of a low-pressure mercury lamp. The DUV irradiated samples showed comparable crystallinity and optical properties to the conventionally thermal annealed ones, which were crystallized at 150°C.

6.2.1.2 *DUV lamp crystallization of VO_2 thin films*

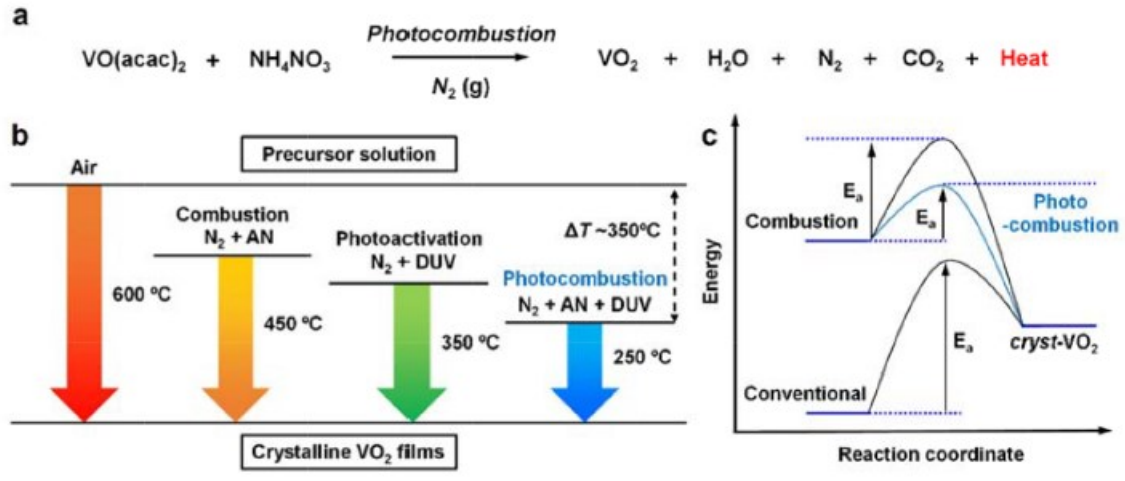


Figure 5.2. (a) Schematic of the reaction mechanism upon the photocombustion method derived from the reaction between $VO(acac)_2$ and NH_4NO_3 with additional UV irraditaion. (b) Schematic of the different annnealing conditions to induce the crystalliztion into VO_2 (M1). (c) Schematic of the energy levels during conventional annealing and photocombustion. (a-c) were adapted from ref.[23]

Regarding vanadium oxides, Jo *et al.*[23] exploited a synergic approach between DUV irradiation, inert atmosphere, and combustion reactions to lower the crystallization temperature of VO_2 to 250°C

(Figure 5.2). The initial precursor solution, consisting of $VO(acac)_2$ as fuel and NH_4NO_3 as oxidizer in methanol, was prepared and spin coated inside a glovebox. The photocombustion method, based on a low-pressure mercury lamp irradiation at 250°C under N_2, allowed to crystallize VO_2 thin films on polyimide substrates. A protective Al_2O_3 buffer layer was added between VO_2 and the substrate.

6.2.2 *Laser annealing*

Respect to other photonic annealing sources, LA offers great advantages in terms of fast processing timescales, roll-to-roll or sheet-to-sheet compatibility, low temperatures, and extreme control of the delivered energy in terms of spatial and temporal resolution. Laser systems were traditionally used for cutting, welding, or patterning purposes in industry, whereas an employment for additive manufacturing and micro-nano fabrication technologies was more recently established.[24] For example, excimer lasers are currently employed for large-area manufacturing of poly-Si transistor displays and annealing of organic light emitting diodes (OLED) or liquid crystal displays for smartphones or televisions.[25]

Laser equipment operate in continuous-wave (CW) or pulsed mode, at wavelengths from UV to Vis to NIR. Respect to DUV lamps or flash lamps, laser sources are monochromatic, coherent and collimated.[26] Their power can be tuned from a few mW to ~100 kW and delivered with extreme precision in terms of time and space distribution. Regarding MOs, LA has been exploited for applications in photocatalysis, gas sensing, chromogenic devices, field-effect transistors, solar cells.[27–30] Modifications of the material's functional properties were also targeted, from magnetic mode changes, to resistive or wettability switches, to structural distortions.[31–35]

The interaction between the laser source and the irradiated materials depends on the light absorption from the latter, which strongly relies on both the LA system and the material's properties. The way the light is absorbed determines whether effects such as heating, melting, vaporization, plasma formation or ablation are induced (Figure 5.3 (c)).[24]

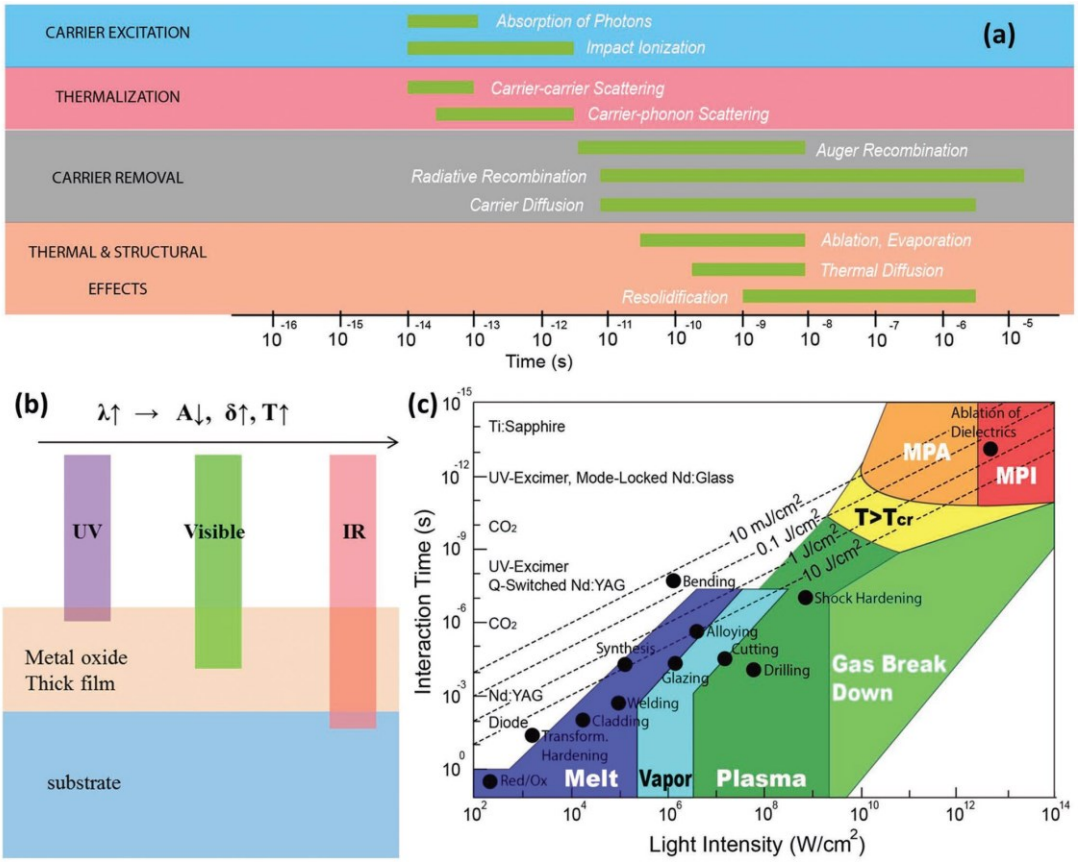


Figure 5.3. (a) Schematic of different phenomena involved upon laser irradiation, according to the different timescales.[24,36] *(b) Schematic of the different interaction between the metal oxide material and the laser source, in function of the wavelength range.* [24,37] *(c) Schematic of the interaction time in function of the light intensity.*[24,38]

Generally, scattering of laser light is induced along with absorption, which leads to the attenuation of the beam energy caused by diffusion. The light absorption depends on the material's electronic structure. Semiconductors and insulators are characterized by a band gap (E_g) value. A photon energy lower than E_g induces a weak phonon excitation, whereas a higher photon energy leads to interband excitation of electrons and consequent formation of electron-hole pairs. In the former case, interband excitation may still be induced under high laser fluence, which may induce coherent or subsequential multiphoton excitation, or due to the presence of defects, which allow sub-bandgap transitions. Lattice vibrations are increased by the phonons, which receive additional energy from the excited electronic states. The temperature rise may induce intraband excitations as well, deriving by the higher number of free electrons. In all cases of electron-electron and electron-phonon interactions, the material experiences non-equilibrium phenomena during laser irradiation, which lead to the material's thermalization. The material is brought back to equilibrium due to the electron-hole recombination, with the final effect being the conversion of laser light into heat.[24,39]

Each phenomenon involved, namely carrier excitation, thermalization, carrier removal and thermal and structural effects, is developed over considerably different timescales, which overlap in time

(Figure 5.3 (a)). The overall laser-matter interaction is developed within the femtoseconds to microseconds range and strongly depend on both the LA system and the material's properties.[36]

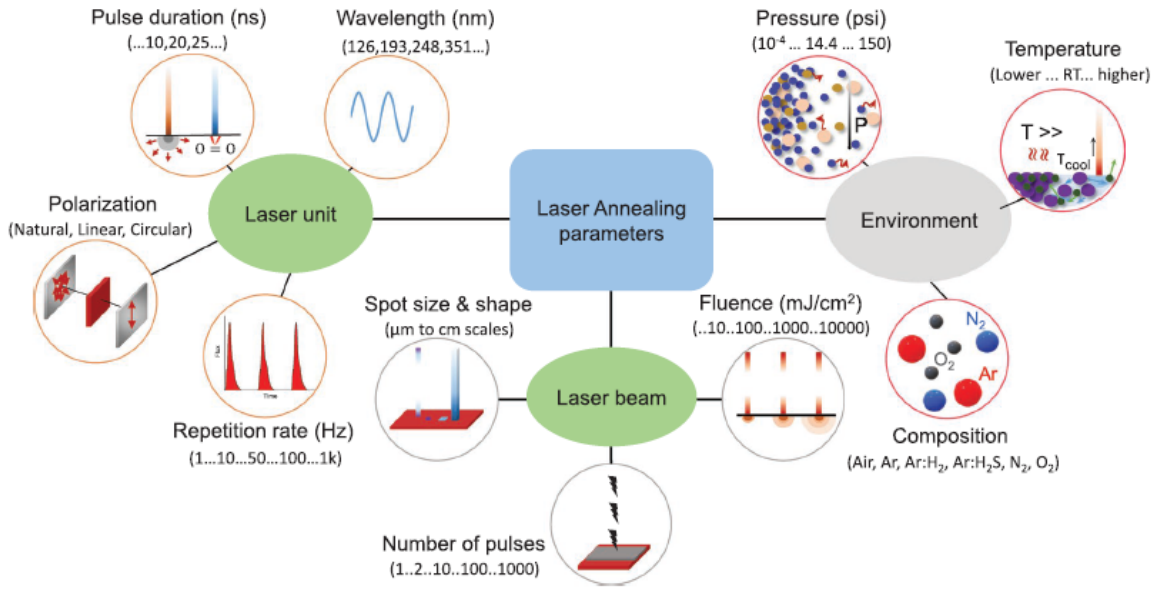


Figure 5.4. Paratmers of influence during laser annealing, grouped within three main categories, i.e., laser unit, laser beam, and environment.[2]

The laser set-up generally consists of three parts, i.e. the laser source, the beam delivery system, and the sample manipulator. The influencing factors linked to LA are grouped within three principal categories (Figure 5.4)[2]:

a. Laser unit: wavelength, polarization, pulse duration, repetition rate.
b. Laser beam: fluence, pulse number, spot size, shape.
c. Environment: atmosphere, pressure, temperature.

Laser wavelength[2,24,37]: the laser wavelength should be chosen according to the bandgap of the irradiated semiconductors/insulators. UV lasers are widely employed when MOs are considered, due to the higher absorbance of the latter in the UV region respect to Vis or IR. While UV radiation displays a limited penetration within MO of a few hundreds of nm, IR penetrates deeper, which may induce thermal damage to the underlying substrate (Figure 5.3 (b)).

Laser polarization[2]: the laser polarization influences the penetration depth within the material, as well as the heat profile. Generally, a linear polarization penetrates deeper into the sample respect to unpolarized or circularly polarized light.

Laser pulses and repetition rate[2,24,40,41]: when pulsed lasers are considered, the duration of the single pulse can either be in nanosecond (2-30 ns), femtosecond, or picosecond regime. The repetition rate expresses the pulse frequency in Hz (1 Hz = 1/s) and usually lies within a few to few hundreds of Hz.

Quasicontinuous wave (CW) lasers are also available, which operate at few hundreds of kHz and within irradiation times higher than 1 μs. CW lasers allow for fast annealing or welding but induce deeper heat penetration within both film and substrate. Pulsed lasers can be instead employed when the ablation threshold needs to be reduced or fast heat dissipation and extreme precision for localized annealing are required.

Laser fluence and number of pulses[2]*:* the amount of energy delivered by each laser pulse can be tuned within the laser system. The former is usually expressed as energy density (mJ/cm^2), to account for the exact set-up geometry. Each energy density can be delivered more than once on the same sample spot and is described through the number of pulses. Upon each pulse, the irradiated materials changes in terms of optical, thermal, structural, and morphological properties, which influence the sample's ability of absorbing the laser light and distributing the consequent heat.

Laser spot size and shape[2]: the energy density profile of the laser spot influences how the material is modified within the irradiated area. The former can range from a Gaussian shape, which results in the edges of the spot being different respect to the center, to a top-hat homogeneous profile. Particular attention should be devoted to the spot edges, especially when micro spots are employed.

Temperature, pressure, atmosphere[2,42]: LA can either be performed at room temperature or while the sample is kept at higher temperatures. This influences the cooling rates, which can reach hundreds of degrees Celsius during a single laser pulse. Pressure might be increased to reduce ablation effects, as higher pressures raise the ablation threshold and allow the use of higher laser fluences. Sample protection or specific chemical reactions might be induced through the modification of the environmental atmosphere during laser irradiation, which can for example tuned to be inert, oxidizing or reducing.

Besides the LA parameters, the material's properties play a key role on the laser-matter interaction. The principal influencing factors of the material are:

a. Optical absorption.
b. Thermal conductivity.
c. Phase structure and microstructure.
d. Morphology and surface roughness.
e. Substrate properties.

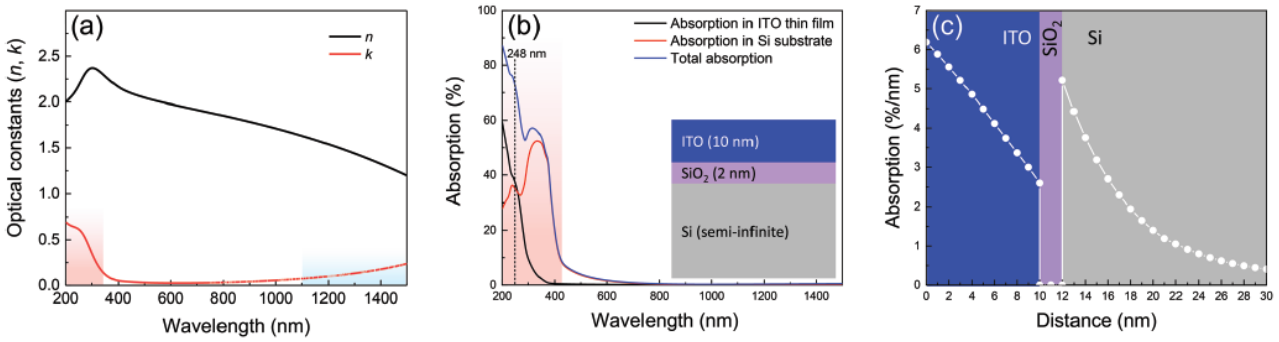


Figure 5.5. (a) Optical constants n and k in function of the wavelength for an ITO film. (b) Absorption in function of the wavelength for an ITO film deposited on silicon substrate, with a native SiO_2 layer. (c) Absorption in function of the distance for an ITO film deposited on silicon substrate, with a native SiO_2 layer. (a-c) adapted from ref.[2]

Optical absorption[2,24,39,43]: the material's optical absorption strongly influences the laser light absorption. The laser light intensity (I) is absorbed by the material according to the Beer-Lambert law: $I(t) = I_0 e^{-\alpha t}$, in which I_0 is the intensity after the initial reflection at the film's surface, t the film's thickness, α the material's absorption coefficient. The laser intensity decreases with increasing penetration depth (δ), which is linked to α and the laser wavelength (λ) according to: $\delta = 1/\alpha = \lambda/(4\pi k)$, in which k is the extinction coefficient of the material. The absorption coefficient is linked to the material's thickness and optical properties: $\alpha = -1/t \ ln(T/(1-R))$, with T and R being the materials' transmittance and reflectance, respectively. As reported above, the material's optical absorption is represented by the imaginary part of the complex refractive index ($\tilde{n}$): $\tilde{n} = n + ik$, with n refractive index and k extinction coefficient. An example of n and k of indium tin-oxide (ITO) is reported in Figure 5 (a). The laser light should be chosen in the regions in which $k > 0$. In the ITO case, the intraband absorption is visible in the UV region, whereas intraband absorption deriving from the free electrons are enabled in the NIR region. The influence of the thickness (t) on the laser intensity (I) during irradiation, expressed in the Beer-Lambert equation, is shown in Figure 5.5 (b, c).

Thermal conductivity[24,44]: the thermal conductivity (k) determines how the photogenerated heat is distributed within the material and is linked to the specific heat capacity (C_p), photon velocity (v) and phonon mean free path (l) by: $k = 1/3 \ C_p \ vl$. The heat is transported through phonon movements within dielectrics, maintained until scattering is reached through phonon-phonon interactions or at lattice defects. Ceramics typically display low k values, which lead to a lower extension of the heat affected areas.

Phase structure and microstructure[24,45,46]: the heat transport is greatly affected by microphase and phase structure. In both amorphous and partially crystalline materials the heat is constrained within smaller areas respect to fully crystalline materials. The structural disorder of amorphous materials lowers the phonon mean free path and annihilates the coherence of lattice vibrations, whereas high phonon scattering is caused by the high density of grain boundaries in partially crystalline materials.

Moreover, the presence of pores within otherwise dense MO films can favor a higher UV light penetration.

Morphology and surface roughness[24,47,48]: the laser light can undergo reflection or scattering phenomena according to the morphology of the irradiated film, through the presence of channels or voids. This could either decrease or enhance the laser light absorption, in function of the specific geometries.

Substrate properties[24,49]: the substrate can play a key role within the film-laser interaction. High substrate's *k* values can lead to increased temperature gradients within the film, while high differences in coefficient of thermal expansion can lead to film's cracking. Substrates with low lattice mismatch with the film are employed to epitaxially grow the irradiated materials, while high chemical stability of the substrate favors a lower atomic diffusion during LA.

6.2.2.1 *Laser irradiation of sol gel MO thin films*

The considerations reported above are related to the interaction between solid MO thin films and laser light. When sol-gel materials are considered, additional complexity is added to the listed parameters of influence and effects.

As discussed in Chapter 1, during the sol-gel process an initial colloidal solution is synthesized, based on the chosen MO precursor, and deposited on the target substrate. The as-deposited thin films require additional energy, which is usually delivered via conventional thermal treatments, to induce the transformation from the original precursors to a compact M-O-M network. During this step, the film is densified, the residuals of organic and hydroxyl groups are removed, and chemical-physical transformations are developed. While many applications necessitate of amorphous MO thin films, an additional crystallization step is required for other devices.

During unconventional LA, the photochemical conversion is exploited for the formation of the M-O-M network. As highlighted by Yarali *et al.*[2], an important distinction should be applied between the effect of ns or fs pulsed lasers. During LA of MO thin films, the light absorption from ns pulsed lasers lead to local temperature increases, which in turn induce the chemical conversion of the deposited precursors.[50] The ns LA effect can be related to a photothermally induced chemical conversion. Differently, material ablation can be reached during fs LA, which allow direct bond breaking and limited temperature rise.[42] In the latter case, the effect is described as a photochemical conversion, which differs from the photothermally induced chemical conversion of ns LA.

6.2.2.2 *KrF excimer laser irradiation of VO_2 thin films*

Only a few studies addressed the use of laser processing for vanadium oxide and VO_2 thin films.

Charipar *et al*.[51] exploited the pulsed laser deposition (PLD) method for the development of VO_2 thin films. A KrF excimer laser was first used to ablate a VO_2 target and grow VO_x thin films on Al_2O_3 single crystals. The films were than crystallized with the aid of a 1030 nm ytterbium-based femtosecond laser. Tsuchiya *et al*. studied the epitaxial growth of VO_2 on TiO_2 single crystals from a carboxylate solution, by irradiating the samples with a KrF excimer laser while heating at 300°C.[52] The group also spin coated the films on glass from a vanadium butyl acetate solution, which were kept at 300°C while subjected to laser irradiation.[53]

Another approach in literature is to employ UV lasers as post-crystallization treatments for VO_2 thin films. Breckenfeld *et al*.[54] deposited VO_2 particles by PAD method, which were then crystallized by conventional furnace annealing. The electrical contact between the crystalline VO_2 particles was then improved by irradiating the sample with a KrF excimer laser. Lin-Bin *et al*.[55] modified the morphology and color of VO_2 crystalline films with the aid of a XeCl excimer laser. The authors evaporated the films from a V_2O_5 target and subsequently annealed the films at 450°C under vacuum to form VO_2. The XeCl excimer laser was used to modify the color from yellow to grey, along with morphological variations. Molaei *et al*.[35] modified the magnetic behavior of epitaxial VO_2 thin films, by irradiating the already crystalline films with a single KrF laser pulse. The single pulse changed the ferromagnetic behavior into a diamagnetic one, while preserving the VO_2 crystallinity. The change in magnetic behavior was attributed to a partial surface reduction to V^{3+} oxidation state.

6.3 Laser-induced crystallization of VO_2 thin films[1]

As introduced in paragraph 5.1, VO_2 thin films were deposited following the green sol-gel synthesis described in Chapter 4, which is based on a non-hazardous precursor ($VO(acac)_2$) and solvent (ethanol) with no supplementary additives. With respect to Chapter 4, an alternative route to induce the amorphous to crystalline conversion into VO_2 (M1) was exploited in Chapter 5, i.e., nanosecond pulsed laser irradiation. A general process overview for the laser-induced crystallization of sol-gel VO_2 thin films is reported in Figure 5.6.

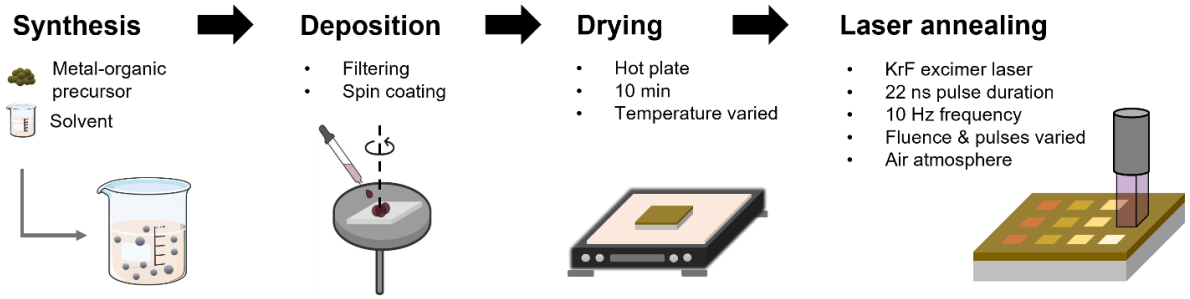


Figure 5.6. Schematics of sol-gel VO_2 thin films preparation, including the following stages from left to right: synthesis, deposition, drying and laser annealing.[1]

Following the synthesis and deposition steps, the thin films were dried at low temperature and photonically treated with a KrF excimer laser. The evolution of the sol-gel films during laser annealing was studied on silicon and fused silica substrates, exploiting different combinations of laser fluence (i.e., energy density) and number of pulses.

6.3.1 *Synthesis and deposition of VO_2 thin films*[1]

Silicon wafers (P-type, <100>, single-side polished, Silicon Materials) and fused silica substrates (Quartz, Electro optical technology) were rinsed in absolute ethanol (EtOH, 99.9%, Emsure, Sigma Aldrich, UK) and dried with nitrogen. Residual organic contaminants were removed by atmospheric plasma cleaning (Plasma Cleaner, PDC-002-CE, Harrick Plasma, USA). The starting solution was prepared following the same procedure described in paragraph 4.3.2.2 of Chapter 4. Vanadyl acetylacetonate powder ($VO(acac)_2$, 98%, Sigma-Aldrich) was dissolved in absolute ethanol in a 0.125 M concentration. The solution was stirred at 85°C in a round-bottom flask under reflux for 9 h, after which it was aged for 15 h at room temperature. Subsequently, the solution was filtered with 0.2 µm sized syringe filters and spin coated on the pre-cleaned substrates at 2000 rpm for 30 s. Only for drying temperature tests, the films were deposited by dip coating at 300 mm/min. Samples were coated from 1 to 3 layers to tune the thickness of the film. Each layer was dried at 85°C on a hot plate for 15 min prior to the deposition of the following one. After the deposition, the films were dried on a hot plate in air for 10 min, at temperatures ranging between 80-300°C.

6.3.2 *Laser annealing*[1]

The dried films were laser-annealed one day after the deposition. A KrF excimer laser system (248 nm, Coherent COMPex 201F, 22 ns pulse duration) was used to irradiate the samples in distinct and isolated parts of the total surface. Each spot had a 5×5 mm^2 size, with uniformity of 2%. The

irradiation was carried out in air at room temperature with a variable number of pulses (#), at fixed repetition rate of 10 Hz with a laser fluence between 40-700 mJ/cm^2 for the initial energy density scan and 40-200 mJ/cm^2 for the following tests. Fluence was controlled through a motorized attenuator paired with an in-line energy meter, with an accuracy of 1%. Reference samples were annealed in a tube furnace at 550°C for 1 h, with a heating ramp of 10°C/min in a nitrogen environment.

6.3.3 *Low temperature drying*[1]

As reported by Yarali *et al.*,[2] the initial film quality is expected to have a substantial influence on the final properties and application of the photonically-cured material. Past research on similar sol-gel films has evidenced the need of a low-temperature treatment prior to or during the photonic curing, with minimum temperatures of 250-300°C.[23] This step helps to reach a proper film densification and adhesion to the substrate, avoiding the film ablation observed upon direct exposure to laser light.[24] The drying temperature was firstly studied to promote sol-gel condensation and impurity removal, with the goal of simultaneously avoiding film ablation and uncontrolled crystallization. Single-layer films were deposited on silicon substrates and four different drying temperatures were considered, in the 80-300°C range. The lowest value was chosen just above the boiling point of the solvent (~78°C) to allow for a gentle evaporation.[56] The highest value was chosen to strongly promote film condensation and densification along with removal of organic components. These temperatures are lower than those used in conventional thermal treatments of similar solution-based films, where the minimum reported temperature for VO_2 crystallization is 440-550°C.[57–59]

XPS, ellipsometry and TEM were used to characterize the dried samples and the corresponding results were previously discussed in paragraph 4.3.3 of Chapter 4. From the XPS analysis, a decrease in the carbon content with increasing drying temperature was found from the C 1*s* core level. This can be explained by the release of the acetylacetonate ligands (acac) as acetylacetone (Hacac). The removal of Hacac during drying was found to be favored at temperatures between 150 and 200°C, which are above the boiling point of acetylacetone (~140°).[60] At the highest drying temperatures, the thermal decomposition of residual metal precursor, which was found to start at ~220°C, probably contributes to the reduction observed in the C signal intensity.[61,62] The O 1*s* core level was used to monitor the changes in the oxygen chemical state, namely the metal-oxide conversion and the hydroxyl contribution. The presence of hydroxylated V-OH groups, strongly evident in the drop-cast solution and in the film dried at 80°C, decreased when the drying temperature was higher than 150°C. This

corresponded to a decrease in the V-O-H:V-O-V ratio, which highlights the progress of condensation reactions and the development of V-O-V networks.

The ellipsometry analysis evidenced a moderate film densification from 80 to 300°C, with a ∼13% decrease in thickness. This corresponded to a slight increase in refractive index (*n*), as well as extinction coefficient (*k*). The structural properties were evaluated by GIXRD, which was performed on the 300°C dried sample to verify the eventual undesired presence of crystalline peaks. As expected, the dried thin film displayed amorphous characteristics with no detectable diffraction peaks (Figure 5.9 in the following paragraph 5.3.4). However, the presence of small crystallites in the overall amorphous matrix was found from the TEM investigation. These crystallites were only ∼1-2 nm in dimension and could not be detected by GIXRD.

Based on the previous results, a temperature of 300°C was selected for the drying step before the laser annealing. The latter allows for the best removal of impurities, provides good film densification, and can avoid direct ablation before the laser-induced crystallization.

6.3.4 *Laser-thin film interaction*[1]

Following the exploration of the appropriate film drying temperature, the interaction between sol-gel coating and UV laser setup was investigated for silicon substrates. The exhaustive review by Yarali *et al*. examined the complexity of laser-matter interaction in detail.[2] Numerous factors contribute to this, including pulse number, laser fluence, and energy density profile of the laser, as well as optical path, absorption coefficient, morphology, and thermal conductivity of the film material, which influence how the laser energy is distributed inside the film. Additionally, the complexity of the sol-gel process itself, which typically involves hydrolysis and condensation reactions as well as interactions with additives, further increases the challenges of understanding the mechanism of laser-matter interactions.[2]

Based on existing studies of KrF laser-treated sol-gel films, [2,52,63,64] the first sample set was prepared by exposing a dried film to single ns laser pulses (#) of increasing laser fluence, which was varied in the range of 30-700 mJ/cm^2 (Figure 5.7 (f)). The initial film thickness (*t*) was determined using ellipsometry and found to be 33 ± 3 nm. Each single pulse laser-annealed spot had an area of 5×5 mm^2 and a separation of 5 mm from the next laser spot to exclude the influence of thermal diffusion. The edges and inner surface of the laser-annealed spots were analyzed with a profilometer (Figure 5.7 (f)). A single pulse in the fluence range of 30 to 80 mJ/cm^2 led to an increase in surface roughness with unclear boundaries around the irradiated area. The edges became more defined above 100

mJ/cm^2. Above 600 mJ/cm^2 the step height at the edge of the laser-annealed area matched the film thickness (i.e., 33 nm), indicating that a complete ablation of the film material occurred. Therefore, the range of interest of the laser fluence was set to be 40-200 mJ/cm^2, to further investigate the influence of consecutive pulses and simultaneously reduce the thermal load of a single pulse. The reduction of the energy density is beneficial for the ultimate goal of extending MO densification and crystallization on polymeric substrates.

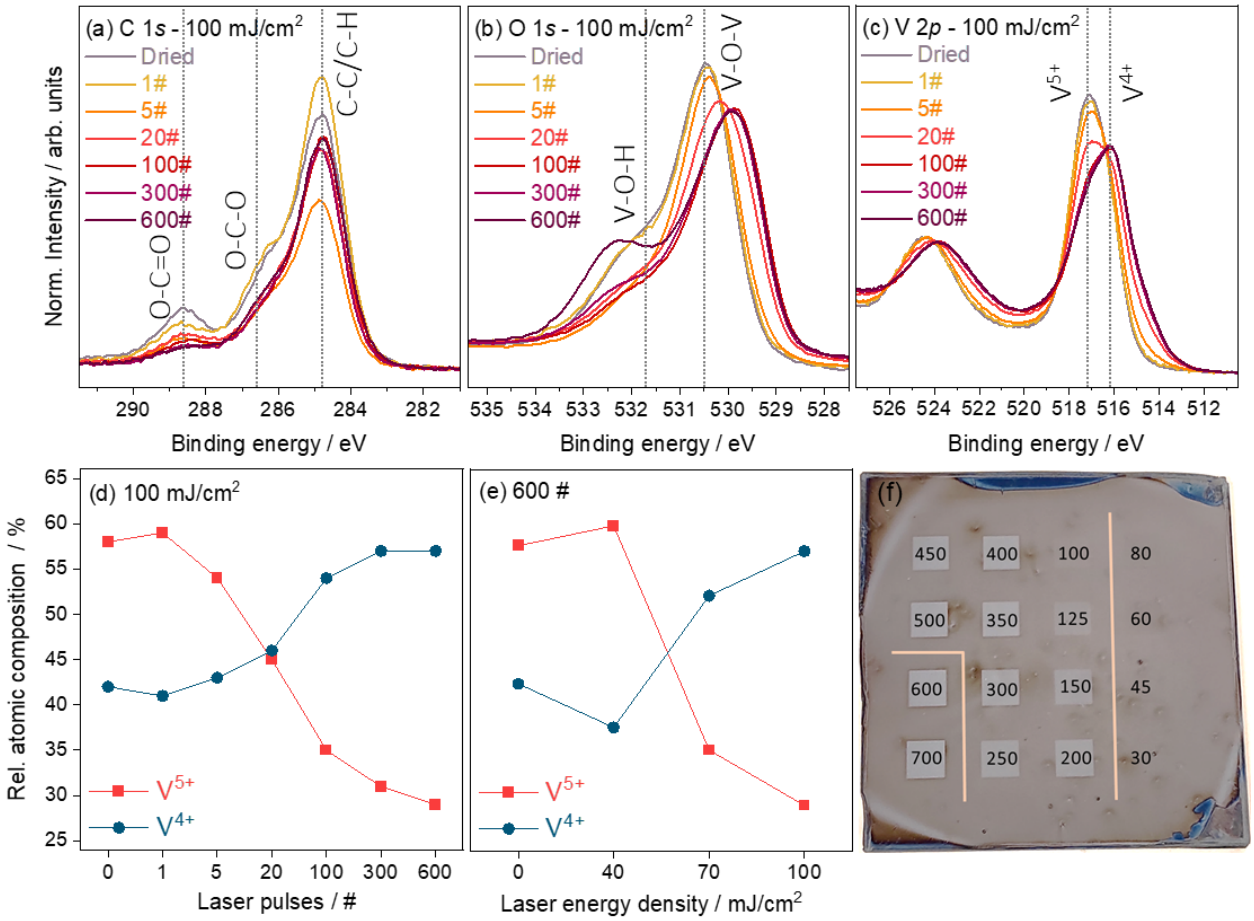


Figure 5.7. XP spectra of laser annealed thin films at 100 mJ/cm^2 with varying pulse numbers, including (a)-(c) C 1s, O 1s and V 2p core level spectra. The reference lines represent the position of the main identified spectral features. V^{4+} and V^{5+} oxidation state populations from peak fit analysis of the V $2p_{3/2}$ core level spectra, for (d) films treated at 100 mJ/cm^2 with varying pulse numbers and for (e) films treated with 600 laser pulses at varying laser fluence, respectively. (f) energy density scan at 1 pulse, with energy density increased from 30 to 700 mJ/cm^2. Each single-pulse laser-annealed film had an area of 5×5 mm^2 and a separation of 5 mm from the next laser spot.[1]

Following the findings for single pulses, the influence of increasing pulse number and fluence was separately studied using XPS. Two identical thin films with $t = 21 \pm 2$ nm were deposited on 5×5 cm^2 silicon substrates. To study the influence of the number of pulses, six spots were laser-annealed at a fixed energy density of 100 mJ/cm^2 with pulse numbers of 1, 5, 20, 100, 300 and 600.

The C 1*s*, O 1*s* and V 2*p* core levels (Figure 5.7 (a-c)), were used to monitor the chemical variations of the films. The three main features visible in the C 1*s* core levels are assigned to adventitious carbon

and C-C/C-H environments (284.8 eV), O-C-O (~286.6 eV) and O-C=O (~288.6 eV) environments, respectively.[65] As expected, the C 1*s* features (Figure 5.7 (a)) decreased in intensity with increasing pulse number. In both the O 1*s* and V 2*p* spectra (Figure 5.7 (b-c)) continuous changes up to 100 pulses were visible, which stabilized thereafter. In the O 1*s* core level, the main lowest BE feature between 529.5-530.5 eV is related to the O^{2-} ions of the amorphous or crystalline metal-oxygen network,[66] and the second feature at a BE of ~531.7 eV arises from hydroxyl groups. No clear trend could be observed between the lower BE oxide feature and the hydroxyl peak as the latter depends on a range of surface-related factors (including surface chemistry and roughness), which all change in a complex fashion when the number of laser pulses changes. The highest BE feature at ~533.5 eV, which intensity increased with increasing pulses, can be related to the native oxide layer covering the substrate.[67] The increasing pulses probably led to a reduction of film's thickness, which allowed to partially probe the silica layer below the film. A systematic shift to lower BE of the lowest BE feature is observed with increasing pulse number with a maximum BE difference of ~0.4 eV. This variation can arise from an interplay between changes in (i) the chemical environment due to differences in V-O-V network development, (ii) the V oxidation state, and (iii) the amorphous-to-crystalline structural changes. Similar shifts in O 1*s* BE were seen in other studies.[68,69]

The V 2*p* core level spectra also showed systematic changes with increasing number of pulses (Figure 5.7 (c)). They are dominated by two features at ~517.2 eV and ~516.1 eV, stemming from V^{5+} and V^{4+}, respectively. A smaller shoulder at ~514.5 eV arising after higher pulse numbers is attributed to V^{3+}.[59,70,71] From peak fit analysis of the V 2*p* spectra the contributions of the V^{5+} and V^{4+} states could be quantified (Figure 5.7 (d)). Before laser curing, the oxidized V^{5+} state was predominant in the film with a ~60% contribution. A single pulse at 100 mJ/cm^2 did not lead to significant changes, whereas with increasing pulse exposure, the population of V^{5+} decreases in favor of V^{4+}. The contribution from V^{3+} was below 10% for all samples. Above 300 pulses the V^{4+} contribution reaches a maximum at ~60%. Bordelet *et al.*[53] speculated that the reduction to V^{4+} could be favored by the decomposition of residual organic species inside the film. Considering the Ellingham diagram, VO_2 crystallization is not expected at room temperature in air but could be expected at lower oxygen partial pressures (pO_2).[72,73] Even if the 10 min drying treatment at 300°C favored a decrease in carbon content, a residual organic component was expected due to the short time and low temperature of drying as confirmed in the XPS spectra (Figure 4.15, Chapter 4). The increasing pulse numbers led to a progressive reduction in the carbon content (Figure 5.7 (a)), which was concurrent with the progressive increase in the V^{4+}/V^{5+} ratio (Figure 5.7 (c)). This could be evidence that the mechanism suggested by Bordelet *et al.* applies in the present case.

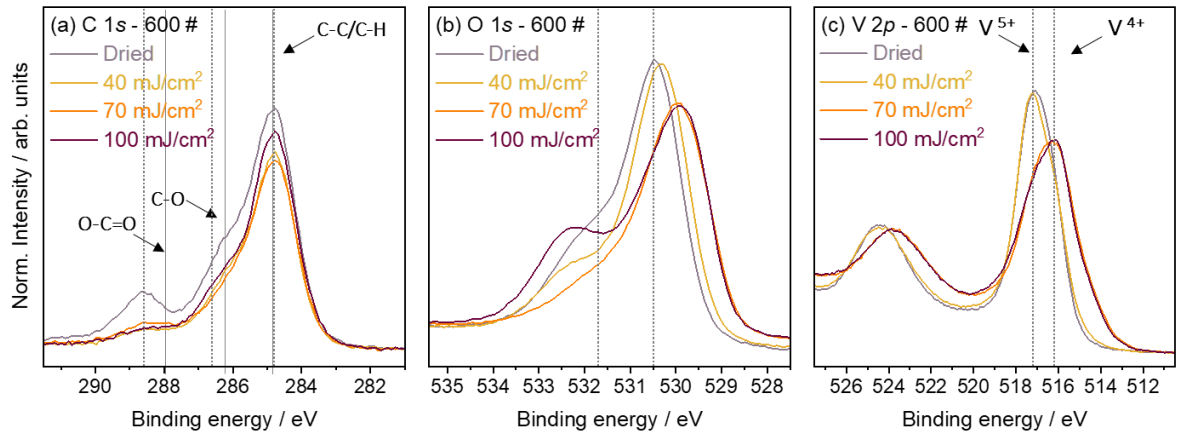


Figure 5.8. XP spectra of laser annealed thin films with 600 laser pulses at varying laser fluence, including (a-c) C 1s, O 1s and V 2p core level spectra. The reference lines represent the position of the main identified spectral features.[1]

The influence of energy density was also explored by applying a fixed pulse number of 600 and laser-curing three spots at 40, 70, and 100 mJ/cm^2, respectively. All three XPS core levels (Figure 5.8 (a-c)) presented the same features described for the pulse effect. With respect to the 100 mJ/cm^2 treated sample, a lower fluence of 40 or 70 mJ/cm^2 did not lead to higher organic residuals in the C 1*s* spectra (Figure 5.8 (a)). This can be related to the high number of pulses, which was effective in reducing the organic content even at lower energy densities. Similarly to the study on pulse influence, the V 2*p* spectra were peak fitted to evaluate the contribution of each oxidation state (Figure 5.8 (c)). Compared to the non-laser-annealed film, the V^{5+}/V^{4+} ratio did not vary significantly at 40 mJ/cm^2, with V^{5+} being predominant (~60%). In contrast at fluences of 70 and 100 mJ/cm^2 a clear increase in V^{4+} contribution was observed. A different behavior of the 40 mJ/cm^2 sample respect to the other two fluences could also be seen from the O 1*s* core level (Figure 5.8 (b)). The core level of the former sample displayed comparable features to the dried film and the first few laser pulses of Figure 5.8 (b), whereas the 70-100 mJ/cm^2 fluences had similar features to the samples above 100# of Figure 5.8 (b). These results can be explained by considering GIXRD and optical spectroscopy, which will be shown below. From the latter analysis, the VO_2 (M1) pattern and corresponding thermochromic behavior was seen above 70 mJ/cm^2, with a net change in structural and chemical environment respect to an amorphous network.

In literature, the main accepted mechanism for the densification or crystallization during photonic curing is attributed to photochemical and/or photothermal processes. The selective and extremely fast laser irradiation induces a localized heat over a nanosecond timescale, only partially involving the superficial layers of the substrate without affecting the bulk. Respect to a continuous laser, a pulsed laser irradiation allows to control the heat distribution inside the film, since the short timescales and large temperature gradients do not induce high energy transfers to the surrounding areas. This leads

to a great reduction of the heat-affected zones, both laterally and in-depth. Respect to UV lamps, which lead to continuous annealing times within seconds to minutes, the pulsed laser annealing is performed over 1-1000 ns. The heating rates differ by orders of magnitude, from 10-10^3 K/s for halogen lamps to > 10^8 K/s for pulsed lasers.[13]

Regarding laser annealing, there is no complete agreement whether the underlying mechanism is to be attributed only to photothermal effects or to photochemical reactions as well. According to Yarali *et al.*,[2] pulsed lasers induce different effects in function of the pulse duration: nanosecond pulses are mainly responsible for thermal effects, whereas femtosecond pulses can lead to cold ablation of the films. The authors highlight the difference between the two processes: the photothermal effect of ns lasers can trigger chemical reactions and precursor conversions, while photochemical reactions and metal-organic bond breaking can be reached with fs lasers. When sol-gel films are considered, the energy absorbed during the ns laser pulses leads to a local increase of temperature, which aids the conversion to a metal-oxide film.

To better investigate the chemical variations observed with XPS, the laser-annealed area for each combination of fluence-pulses was extended to 1.5×1.5 cm^2 to characterize its crystalline structure, phase, and morphological properties. A thin film was deposited on a 5.5 cm^2 silicon wafers with a thickness of 29 ± 2 nm. The film was laser-treated with four combinations of laser fluence and number of pulses, each performed on a separated area of the film. The process parameters were chosen considering the influence of pulse number and fluence previously investigated and selected to be 70 mJ/cm^2 at 100 - 300 - 600 # and 100 mJ/cm^2 at 300 #. A reference sample was prepared by thermally annealing a film at 550°C in a tubular furnace under a nitrogen atmosphere.

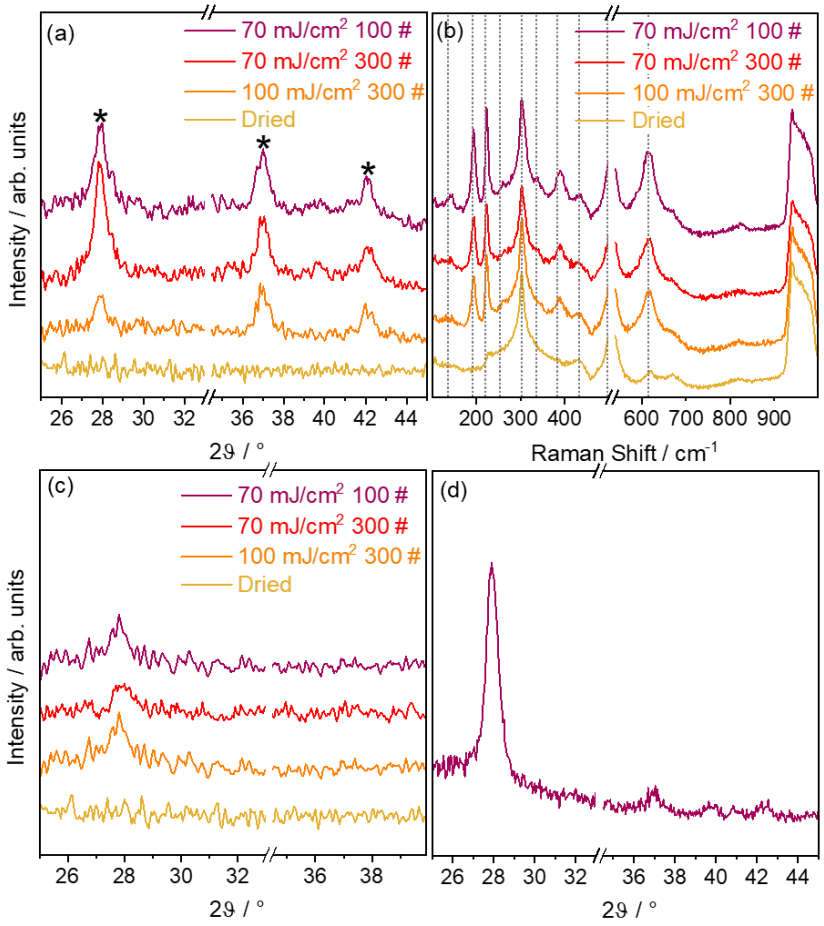


Figure 5.9. (a, c) GIXRD pattern and (b) Raman spectra of the dried film of ~90 nm and of the laser-annealed films, at laser parameters of 70 mJ/cm² 100-300 # and 100 mJ/cm² 300 #. (c) GIXRD pattern of the dried film and of the laser-annealed films, at laser parameters of 70 mJ/cm² 100-300 # and 100 mJ/cm² 300 # for thin films of ~30 nm. (d) GIXRD pattern of the reference furnace treated film at 550°C. The reference symbols and lines in (a) and (b) represent the VO_2 GIXRD pattern and Raman spectral profile, respectively.[1]

The material structure of the laser-annealed films was characterized by GIXRD (Figure 5.9 (a, c)) and Raman spectroscopy (Figure 5.9 (b)), which both confirmed the successful crystallization into monoclinic VO_2 (M1). To enhance the quality of these characterizations, the laser-annealed spots were reproduced with the same laser parameters on a thicker film (92 ± 3 nm, Figure 5.9 (a)). In the former, the main peak at 27.8° highlighted the formation of a predominant (011) orientation, while the two smaller peaks at 37.1° and 42.2° corresponded to (200) and (210) phases of VO_2 (M1).[10,74,75] The reference sample, furnace treated at 550°C, showed a more pronounced (011) orientation (Figure 5.9 (d)). The average crystallite size (~13 nm) did not vary among the samples. Coherently with GIXRD, the Raman spectra shown in Figure 5.9 (b) displayed peaks at 143, 193, 223, 261, 307, 334, 389, 437, 497 and 615 cm^{-1} which commensurate with VO_2,[70,76] whereas the other visible peaks were due to the silicon substrate.[77]

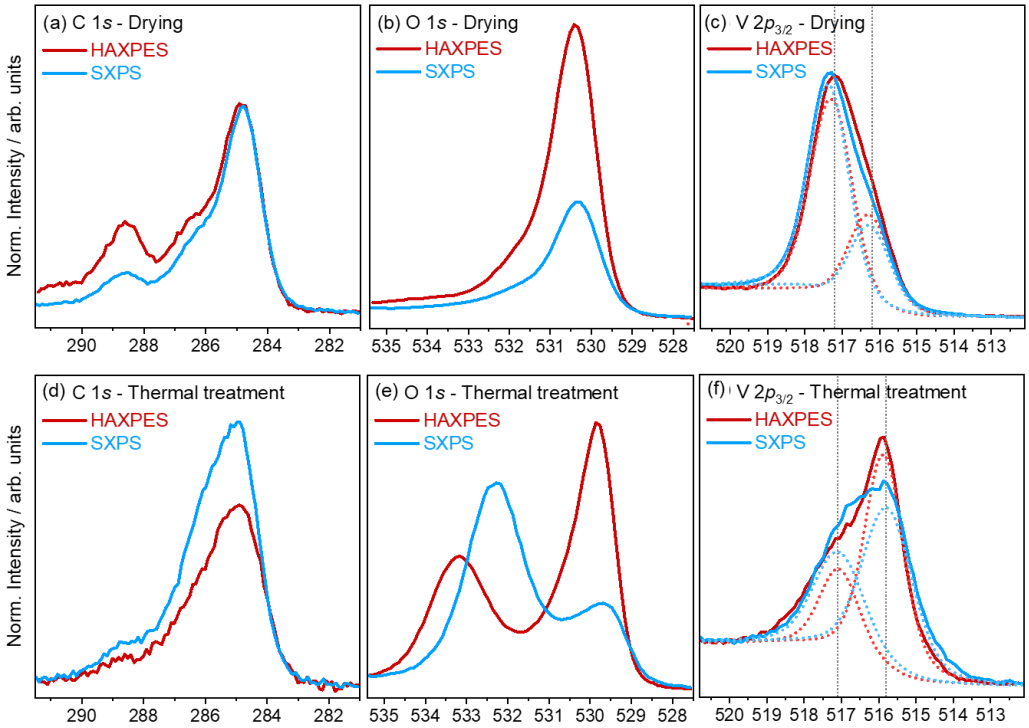


Figure 5.10. Soft X-rays photoelectron spectroscopy (SXPS) and Hard X-rays photoelectron spectroscopy (HAXPES) of (a-c) the dried thin film and (d-f) the thermally annealed VO_2 thin film. (a, d) C 1s, (b, e) O 1s, (c, f) V 2p core levels.[1]

Previous studies have shown that a thin oxidized overlayer forms when VO_2 is exposed to air and that a gradual transition to V_2O_5 can be induced in conditions of high relative humidity.[78,79] Hard X-ray photoelectron spectroscopy (HAXPES) was employed to probe deeper within the film respect to soft XPS (SXPS), to ascertain a depth distribution profile of the V^{5+} oxidation state. This was done by comparing the variations in oxidation state by peak fitting the V $2p_{3/2}$ core level. The QUASES software package was used to estimate the maximum inelastic mean free path (λ_{IMFP}) for bulk VO_2, with values of ~3 nm at 1.5 keV (SXPS) and ~9 nm at 5.9 keV (HAXPES).[80] The total probing depth can be estimated as 95% of the signal intensity (i.e. $3\lambda_{IMFP}$), giving values of ~9 nm and ~27 nm for SXPS and HAXPES, respectively.

The amorphous dried film was compared to the thermally annealed sample (Figure 5.10), on which the presence of bulk VO_2 was previously confirmed by GIXRD (Figure 5.10 (d)). From the photoelectron spectroscopy measurements on the amorphous dried sample, the V^{5+} state was confirmed to be dominant even at deeper probing depths, since the ratio between V^{5+} and V^{4+} did not significantly change with increasing probing depth (Figure 5.10 (c)). The presence of residual V^{4+} state could be due to incomplete oxidation of the precursor during the initial synthesis. On the contrary, the V^{5+} state was seen to decrease on the two crystallized samples when the probing depth was increased by HAXPES (Figure 5.10 (f)). The variations found with increasing probing depth from SXPS to HAXPES to bulk XRD confirmed the superficial nature of the oxidized state.

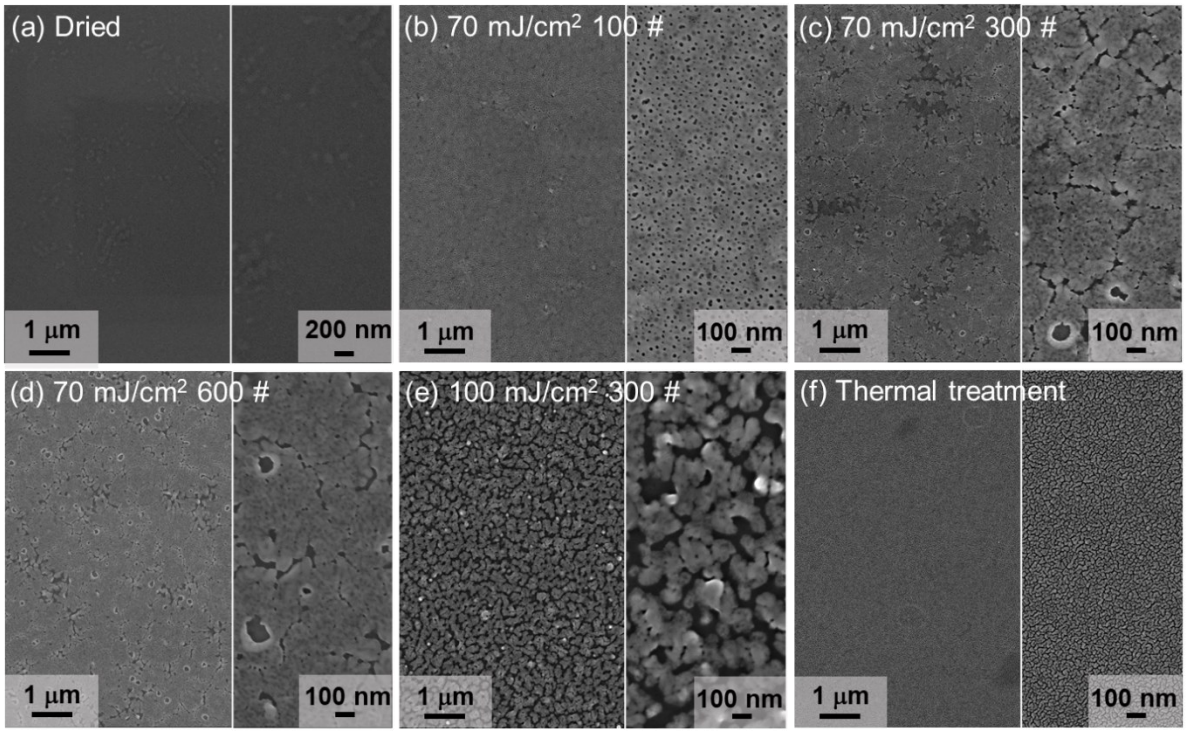


Figure 5.11. SEM images of the (a) dried thin film and of the laser-annealed spots at (b) 70 mJ/cm² 100 #, (c) 70 mJ/cm² 300 #, (d) 70 mJ/cm² 600 #, (e) 100 mJ/cm² 300 #. (f) SEM image of the reference sample thermally treated at 550°C. The relative scale bars are inserted at the bottom of each image.[1]

Following the GIXRD, Raman, and XPS characterizations, SEM and TEM analysis were employed to verify the laser effect on the film's morphology (Figures 5.11-5.12). The dried film, i.e., before laser-annealing, had a smooth, compact and uniform surface morphology (Figure 5.11 (a)). 100 laser pulses at a fluence of 70 mJ/cm^2 led to the formation of a porous surface network, containing nanometer-sized holes (Figure 5.11 (b)). Increasing the pulse number to 300 (Figure 5.11 (c)) and 600 (Figure 5.11 (d)) gradually transformed the morphology to a closely-packed structure, with fewer and smaller holes within them. Similar patterns were found after KrF laser irradiation on other metal-oxide sol-gels films.[81,82] When the fluence was increased to 100 mJ/cm^2, while keeping constant the pulse number (300 #, Figure 5.11 (e)), more pronounced variations of the surface morphology were obtained.

Table 5.1. Thickness measured before and after laser irradiation at 100 mJ/cm². Extinction coefficient, for the same samples, generated from ellipsometry data fitting at the laser wavelength (248 nm). The latter was used to estimate the optical penetration depth (δ) before and after laser irradiation, as described in the Appendix A.2.9.[1]

Fluence / mJ/cm^2	Pulses / #	Thickness / nm	$k_{248\ nm}$ / a. u.	$\delta_{248\ nm}$ / nm
/	/	29 ± 2	0.58	34
100	300	30 ± 5	0.49	40

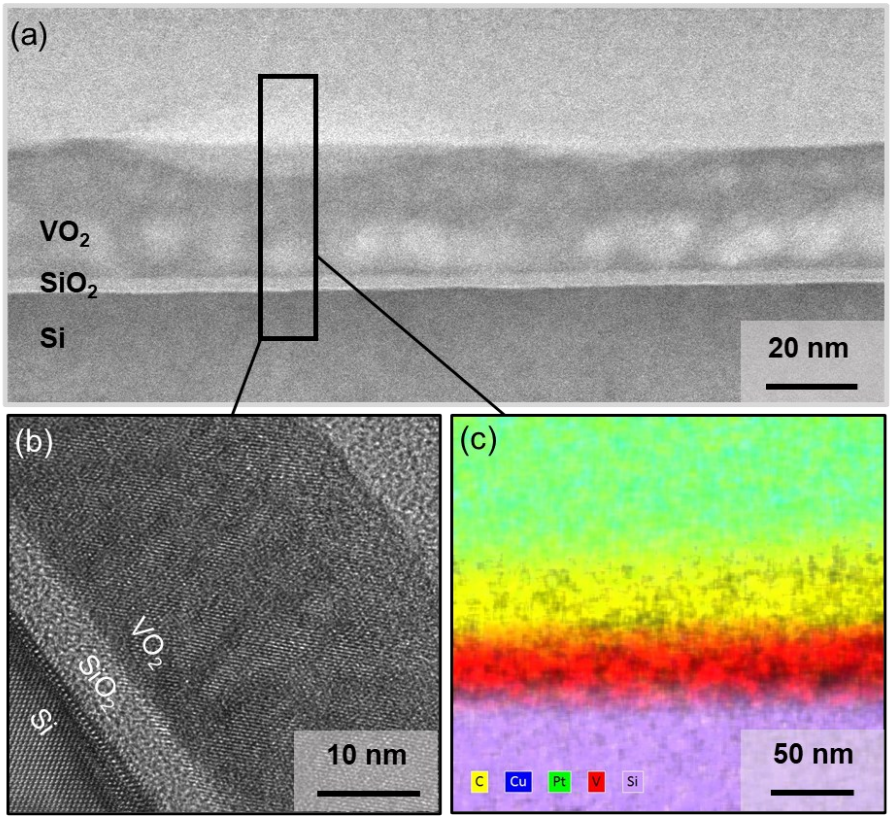


Figure 5.12. (a) STEM and (b) TEM cross-section of the laser-annealed spot at 100 mJ/cm² 300 #. (c) EDX analysis of the laser-annealed spot at 100 mJ/cm² 300 #. The relative scale bars are inserted at the bottom of each image.[1]

The STEM and TEM cross-sections (Figure 5.12 (a-c)) confirmed the film thickness measured with the ellipsometer (Table 5.1) and the successful crystallization induced by the laser irradiation. The extinction coefficient (*k*) values confirm the film's absorption at the laser wavelength (Table 5.1). Moreover, the EDX analysis (Figure 5.12 (c)) verified that major inter-diffusion between film and substrate did not occur after laser annealing. The higher fluence of 100 mJ/cm^2 induced the formation of complex-shaped packed agglomerates (Figure 5.12 (e)), which resembled the morphology of the furnace annealed VO_2 but with bigger dimensions (Figure 5.12 (f)). The reference sample showed the typical packed nanoparticle morphology of crystalline solution-based VO_2.[83,84]

The difference in nanoparticle dimension and shape can be attributed to the different heat generation and distribution in the film. During conventional furnace annealing, the heat is uniformly and isothermally distributed throughout the film, whereas the heat generated upon laser light absorption follows an adiabatic regime.[13] The amount of heat generated during laser annealing is influenced by the film's absorption.[2] High energy photons are delivered to the material within each 22 ns laser pulse: the extremely rapid heating and cooling cycles experienced by the film do not allow the gradual heat distribution typical of conventional furnace treatments. According to our simulations (Figure 5.16), which will be thoroughly discussed in the following paragraph 5.3.5, the high temperature experienced by the films during a single pulse is lowered back to room temperature within a few

hundreds of nanoseconds. Moreover, temperature gradients are generated between the surface of the film and the interface with the substrate, which enhances the complexity of the spatial and temporal heat distribution.

In conclusion, a synergistic effect of both pulse number and fluence on the film's properties was found. The starting dried film was successfully crystallized into monoclinic VO_2, by using a 70-100 mJ/cm^2 and above 100 pulses. Respect to the pulse number, the fluence had a predominant impact on the final film properties.

6.3.5 *Substrate influence*[1]

Another major factor of influence on photonic curing processing is represented by the substrate underlying the film. Depending on the optical penetration of laser radiation through the film, the UV light may penetrate enough to reach the substrate, which can in turn display different interactions with the radiation in function of its optical and thermal properties.[24]

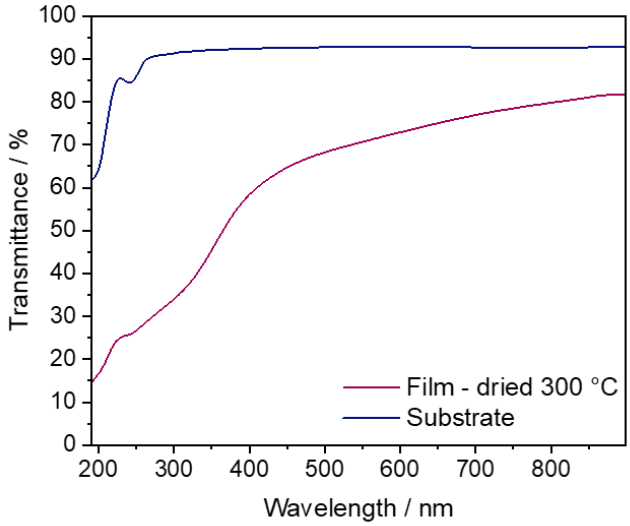


Figure 5.13. UV-Vis transmittance of the fused silica substrate and of the dried film at 300°C before laser irradiation.[1]

Fused silica was employed to consider the influence of a lower thermal diffusivity and lower laser light absorption with respect to silicon. The thermal diffusivity of fused silica is ~1.4 mm^2/s, one order of magnitude lower with respect to silicon (~88 mm^2/s). The fused silica substrate displayed a ~15% absorption at the laser wavelength (i.e., 248 nm), while the dried vanadium-based film absorbed more than 70% of the radiation (Figure 5.13). Following the previous studies on silicon, the effect of both pulse number and fluence was studied on fused silica substrates. Three identical thin films were deposited on 1.5×1.5 cm^2 substrates, with a 33 ± 5 nm thickness. The laser parameters were varied among 40-200 mJ/cm^2 and 10-1200 #, to expand the range of interest.

The thermochromic efficiency was studied by monitoring the changes in optical transmittance at 20°C and 90°C, i.e., below and above the T_c. For each sample, the luminous transmittance (T_{lum}) in the 380-770 nm range, the solar modulation ability at 2000 nm ($\Delta T_{2000\ nm}$) and in the 250-2500 nm range (ΔT_{sol}) were calculated as described in Appendix A.2.8. As discussed in Chapter 3, increases of the solar modulation ability are linked to decreases of the luminous transmittance. The latter is usually less than ~40% for films with a high magnitude of ΔT_{sol}. The current challenge is to simultaneously increase both the parameters, to guarantee a high visible transmittance through the windows (T_{lum} > 60%) as well as a robust solar modulation ability (ΔT_{sol} > 10%).[12,57]

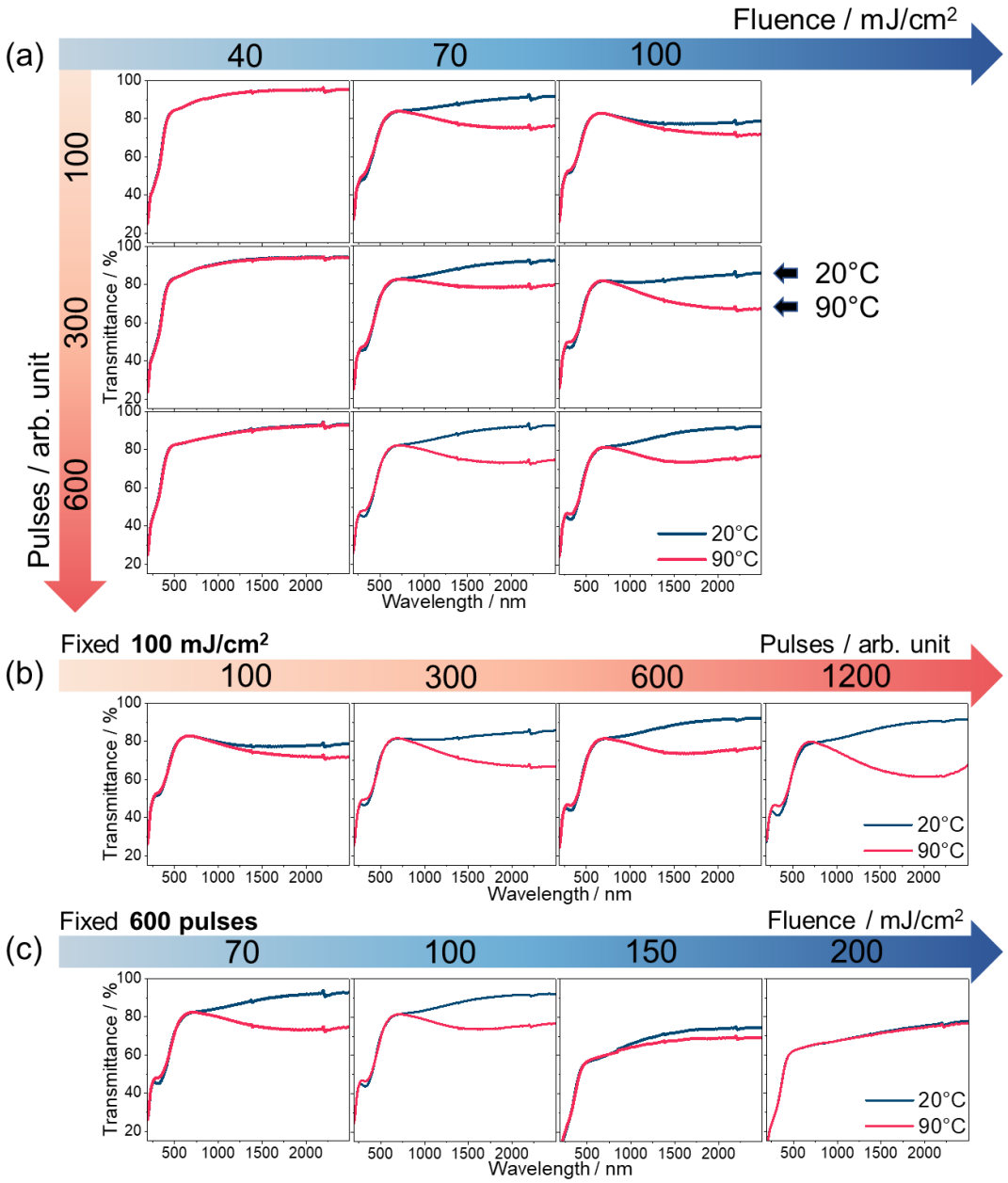


Figure 5.14. (a) UV-Vis-NIR transmittance at 20°C and 90°C of the laser-annealed films deposited on fused silica substrates, at increasing values of fluence (40-100 mJ/cm²) and pulse number (100-600), respectively. (b) Transmittance at 20°C and 90°C of the laser-annealed films at fixed fluence of 100 mJ/cm² and increasing values of pulse number (100-1200). (c) Transmittance at 20°C and 90°C of the laser-annealed films at fixed pulse number of 600 and increasing values of fluence (70-200 mJ/cm²).[1]

Table 5.2. Thermochromic efficiency values of the laser-annealed films and of the reference furnace annealed film deposited on fused silica substrates, including the luminous transmittance (T_{lum}), the transmittance modulation efficiency at 2000 nm ($\Delta T_{2000\ nm}$) and the solar modulation efficiency (ΔT_{sol}).[1]

Laser parameters (mJ/cm^2 - #)	T_{lum} (%)	$\Delta T_{2000\ nm}$ (%)	ΔT_{sol} (%)
40 - 100	85.4	< 1	< 1
40 - 300	84.5	< 1	< 1
40 - 600	83.1	< 1	< 1
70 - 100	79.5	15.4	2.6
70 - 300	77.8	12.9	2.3
70 - 600	76.8	18.5	3.1
100 - 100	80.2	5.6	< 1
100 - 300	77.2	17.0	2.7
100 - 600	75.8	16.4	3.2
100 - 1200	71.2	28.7	4.1
150 - 600	57.3	5	< 1
200 - 600	63.1	< 1	< 1
Furnace 550 °C	69.4	24.1	3.7

100 pulses at 40 mJ/cm^2 were not sufficient to reach a solar transmittance modulation, since no significant variations of the transmittance above the T_c was detected (Figure 5.14 (a), Table 5.2). The increase in pulse number (300 or 600 #) did not lead to different results. A difference in transmittance between 20 and 90°C was instead reached by increasing the fluence to 70 mJ/cm^2. At this fluence, 100 # led to $\Delta T_{2000\ nm}$ = 15.4% and ΔT_{sol} = 2.6%, with a luminous transmittance of 79.5%. Similar efficiencies were obtained by increasing the pulse number from 100 # to 600 # (Figure 5.14 (a)). At 100 #, further increasing the fluence to 100 mJ/cm^2 led to a lower thermochromicity respect to 70 mJ/cm^2 ($\Delta T_{2000\ nm}$ = 5.6% at 100 #), whereas a higher pulse number led to an increased solar modulation ($\Delta T_{2000\ nm}$ = 16.4% and ΔT_{sol} = 3.2% at 600 #). Despite the increased solar modulation, the luminous transmittance was stable around 76-80%. A considerable increase in the solar modulation was reached by doubling the pulse number from 600 # to 1200 # at 100 mJ/cm^2, which led to $\Delta T_{2000\ nm}$ = 28.7% and ΔT_{sol} = 4.1% (Figure 5.14 (b)). This laser-annealed sample exhibited a higher thermochromic performance in terms of both T_{lum} and ΔT_{sol} respect to the corresponding reference sample, which was thermally annealed in the furnace at 550°C (Table 5.2). The obtained values align well with single-layer VO_2 thin films in the literature and display a particularly high T_{lum}, which is usually compromised when high values of ΔT_{sol} are reached.[57] A common approach to

further increase ΔT_{sol} is the combination of VO_2 with other materials (e.g., TiO_2, ZnO, WO_3) in a multilayer configuration.[3,12,57]

*Table 5.3. Performance comparison between our samples and other samples from the literature. VO_2 only thin films were considered for the comparison. Legend: *[1] = deposition or annealing temperature (depending on the technique), *[2] = $\Delta T_{2500\ n}$, *[3] = High-power impulse magnetron sputtering, *[4] = theoretical values, *[5] = not given, *[6] = for 100 mJ/cm² 1200#.*[1]

Technique	Temperature*[1]	Thickness	T_{lum}	$\Delta T_{2000\ nm}$	ΔT_{sol}	Year	Ref.
DC magnetron sputtering	475-575°C	~50 nm	44-55%	7-2%	4-2%	2023	[85]
Sol gel furnace annealing	550°C	~65 nm	40%	35%*[2]	14%	2020	[86]
HiPIMS*[3]	250°C	100 nm*[4]	53%*[4]	27%*[4]	n.g.*[5]	2017	[87]
Laser annealing*[6]	300°C	~30 nm	71%	29%	4%	2023	This work

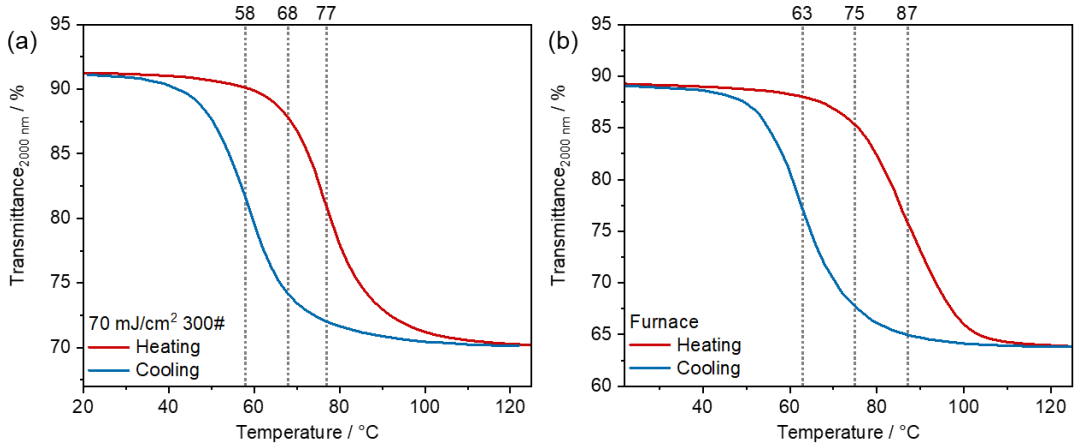


Figure 5.15. Evolution of the transmittance at 2000 nm upon heating (red lines) and cooling (blue lines) of the (a) laser annealed sample at 70 mJ/cm² at 300# and (b) furnace annealed sample.[1]

The T_c of the laser-annealed and furnace-annealed samples are reported in Figure 5.15. The T_c of the sample laser-annealed at 70 mJ/cm² with 300# was found to be ~68°C, while the T_c of the furnace annealed sample was slightly higher (~75°C).

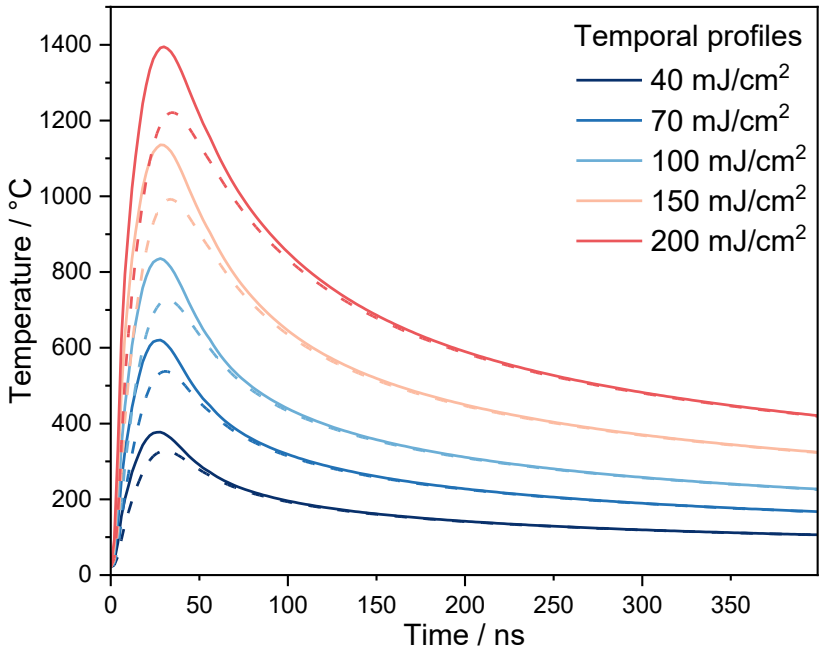


Figure 5.16. Simulations of the temperature profiles over time throughout the films on fused silica substrates, during a single pulse of laser irradiation, at increasing fluence between 40 and 200 mJ/cm2. For each fluence, the temperature was simulated at the film's surface (solid line) and at the interface between the film and the substrate (dashed line).[1]

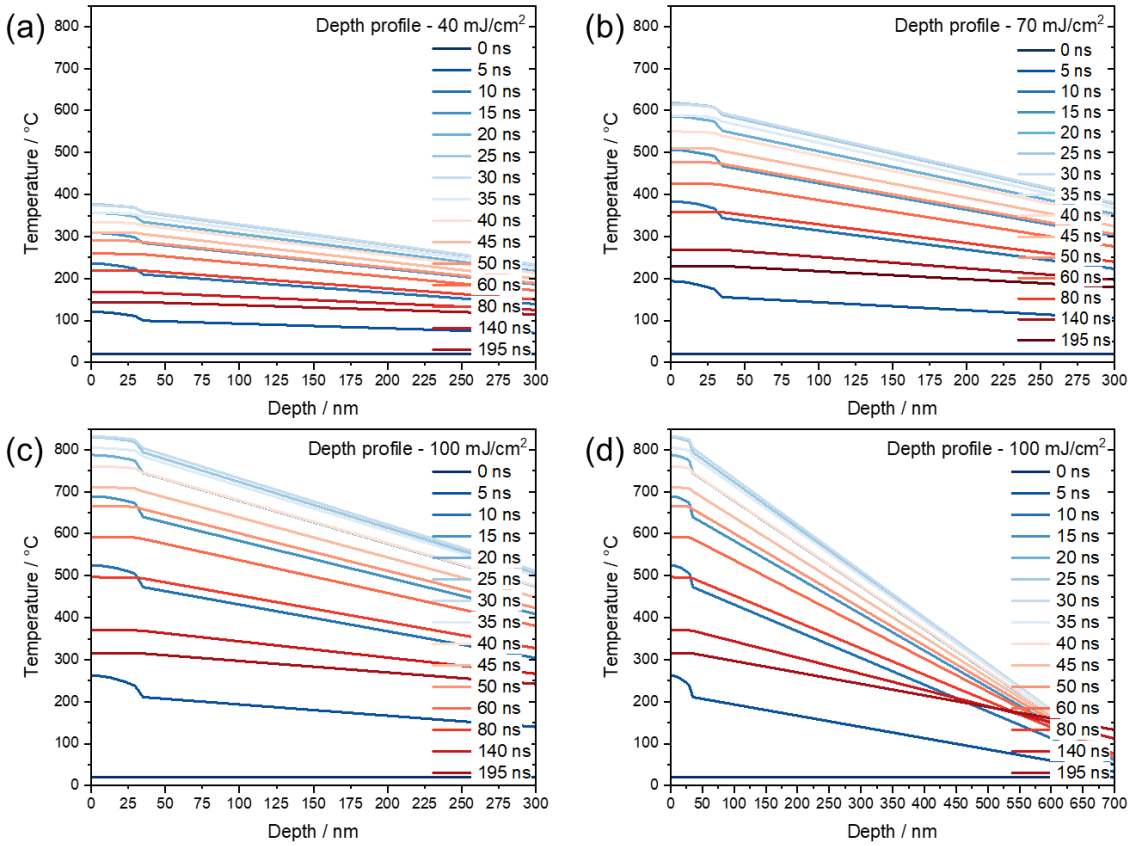


Figure 5.17. Depth profile simulations of the temperature distribution throughout the film, during a single pulse of laser irradiation and over increasing distance from the film surface (corresponding to 0 nm). The simulations are shown for increasing time values at different fluences, including (a) 40 mJ/cm², (b) 70 mJ/cm², (c) 100 mJ/cm². On (d), the x-axis of (c) is widened up to a 500 nm depth.[1]

To better understand the heat distribution throughout the film and the temporal scale involved, numerical simulations were used to compare the effect of the fluence during a single pulse. Two types

of profile were considered, the temporal profiles (Figure 5.16) and the depth ones (Figure 5.17). Numerical solutions of the heat equation based on heat flow calculations were performed by employing the LIMP software (Harvard simulation software package)[88] and calibrated on VO_2 and fused silica physical and optical data. The former were chosen from the literature,[89,90] whereas the latter were calculated from experimental data obtained in this work. The absorption coefficient (α) was calculated from the equation $\alpha = (A\lambda)/t$, in which λ is the laser wavelength (λ = 248 nm). The penetration depth (δ) of laser radiation can be calculated as the inverse of the absorption coefficient ($\delta = 1/\alpha$, Table 5.1).

As emerged from the temporal profiles, the material was subjected to a ns-scale temperature gradient of hundreds of degrees Celsius (Figure 5.16). The temperature rapidly decreased below 300°C within ~300 ns. The temporal evolution of the temperature was simulated both at the film surface and at the substrate interface (Figure 5.16). The maximum surface temperature was reached between 22 and 25 ns for all the fluences (40-200 mJ/cm^2). A single pulse at 40 mJ/cm^2 increased the surface temperature to a maximum peak of ~380°C, while fluences of 70-100 mJ/cm^2 led to peak temperatures of ~620-840°C. The simulated temperatures were close or above to the crystallization range during conventional heating, which is usually located at 400-600°C.[58,59] Considering the depth profiles (Figure 5.17), simulated for single pulses at 40, 70, and 100 mJ/cm^2 at increasing irradiation time, the temperature increase involved all the film thickness and propagated into the first few hundreds of nm of the substrate. After 22 ns, a 100 mJ/cm^2 fluence led to a peak surface temperature of ~840°C (Figure 5.17 (c)). At the same timescale, the temperature experience at 500 nm depth from the surface was ~300°C (Figure 5.17 (d)). The depth profiles confirmed the heat confinement allowed by laser annealing, which minimizes the thermal damage of the substrate respect to conventional furnace treatment.

According to recent literature, a proposed explanation regarding the amorphous-to-crystalline conversion during laser annealing is related to the effective annealing time (t_{eff}).[91] The latter is defined as the time over which the temperature experienced by the film exceeds the heat-induced crystallization temperature. The teff was found to be less than a hundred ns in several compounds. This can explain the successful crystallization of the films even within a minute of laser irradiation, since 600 pulses at 10 Hz frequency correspond to 1 min. The simulations can only describe the temperature distribution and teff during a single pulse, therefore the influence of increasing pulse number was not accounted. The physical parameters used in the simulations were chosen according to the literature, which offers a broad range of values in function of the fabrication technique,[92] whereas the optical absorption was calculated from ellipsometry data (Table 5.1). Due to the nature

of sol-gel process, the increasing number of pulses determines an evolution of the film in terms of morphological, physical, and thermal properties, which in turn influence the real temperatures experienced throughout the film. Nonetheless, the simulations offer a useful estimation of the temperature distribution during the pulsed irradiation, since the simulated temperatures match with our experimental results.

Following the identification of the crystallization threshold on fused silica substrates, the fluence was further increased to verify the eventual presence of an upper threshold (Figure 5.18 (c)). The increase of fluence to 150 mJ/cm^2 led to a decrease of the transmittance modulation ($\Delta T_{2000\ nm}$ = 5%), which almost disappeared at 200 mJ/cm^2 ($\Delta T_{2000\ nm}$ ~ 0%) (Table 5.2).

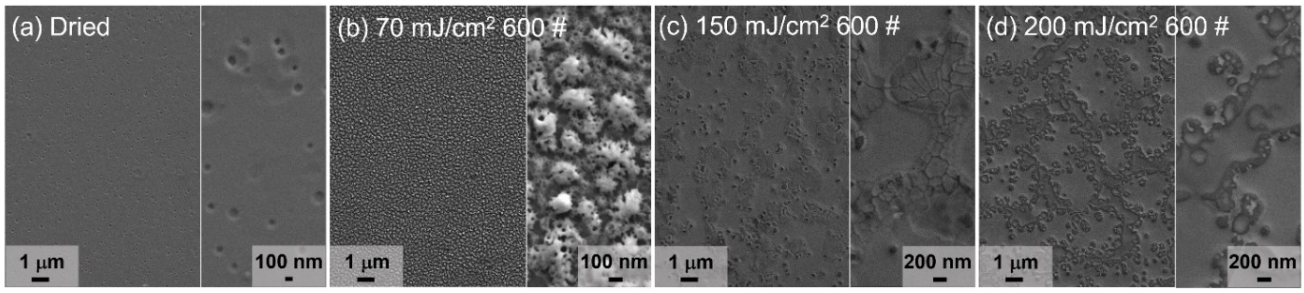


Figure 5.18. SEM images of (a) the dried film and (b-d) the laser-annealed films deposited on fused silica substrates, including (b) 70 mJ/cm² 600 #, (c) 150 mJ/cm² 600 #, (d) 200 mJ/cm² 600 #. The relative scale bars are inserted at the bottom of each image.[1]

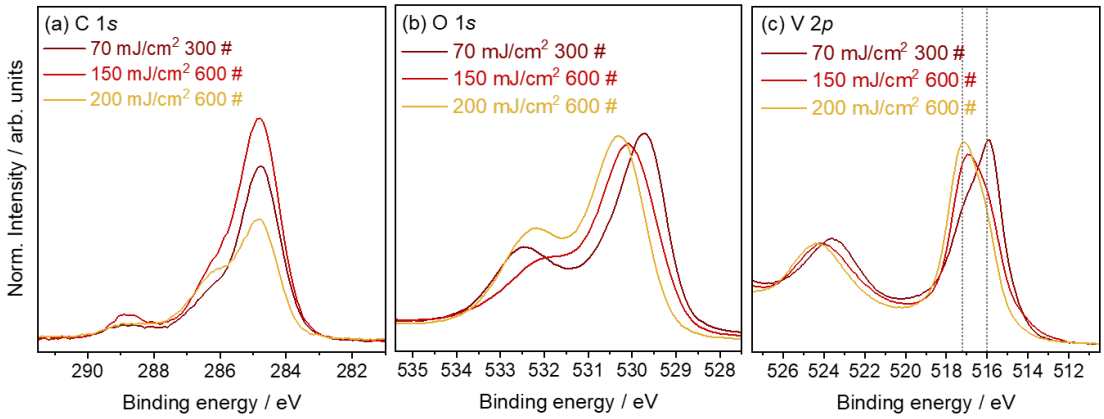


Figure 5.19. XP spectra of laser annealed thin films with 600 laser pulses at varying laser fluence, including (a)-(c) C 1s, O 1s and V 2p core level spectra.[1]

To explain the gradual decrease in thermochromic modulation and the total disappearance of the latter after 100 mJ/cm^2 (Figure 5.14 (c)), a chemical and morphological analysis were carried by XPS (Figure 5.19) and SEM (Figure 5.18).

The key core levels from XPS showed the same key features as discussed for the silicon substrate (Figure 5.19). A higher V^{5+}/V^{4+} ratio was detected on the samples which showed a degradation in the optical modulation (i.e., 150-200 mJ/cm^2, Figure 5.19 (c)). From the SEM analysis, the dried sample displayed a smooth and uniform morphology before laser curing (Figure 5.18 (a)), in analogy with

the silicon substrate (Figure 5.11 (a)). While 600 # at 70 mJ/cm^2 led to the formation of similar nanofeatures (Figure 5.18 (b)) as found for the silicon substrate (Figure 5.18 (d)), the samples cured at the two highest fluences (150-200 mJ/cm^2) displayed different morphologies. At 150 mJ/cm^2, molten-like islands were formed on the sample's surface (Figure 5.18 (c)). An increase of fluence to 200 mJ/cm^2 determined the extension of the molten area (Figure 5.18 (d)), which covered most of the surface and caused the degradation of solar modulation (Figure 5.18 (c)).

From the simulations (Figure 5.16), single pulses at 150-200 mJ/cm^2 determined increases in temperature up to ~1100-1400°C in a nanosecond timescale, respectively. The melting of bulk VO_2 happens at ~1500°C,[93] even though several studies on VO_2 thin film found that melting could occur below 1000°C.[94] The smooth interconnected island morphologies in Figure 5.18 (c, d) could be related to the partial melting of the film's surface, since the heat distribution during laser irradiation follows a non-equilibrium process, happening over an extremely fast timescale respect to conventional furnace heating. As shown before, the surface is covered by a thin oxidized layer, which could have additionally helped the non-equilibrium melting due to its lower melting temperature of ~690°C.[93] Similar superficial melted morphologies were found when threshold laser fluences were reached on both sputtered crystalline V_2O_5 films[95] and on amorphous sol gel ZnO films,[96] in which the melting threshold was found to be higher on silicon substrates respect to polyimide.

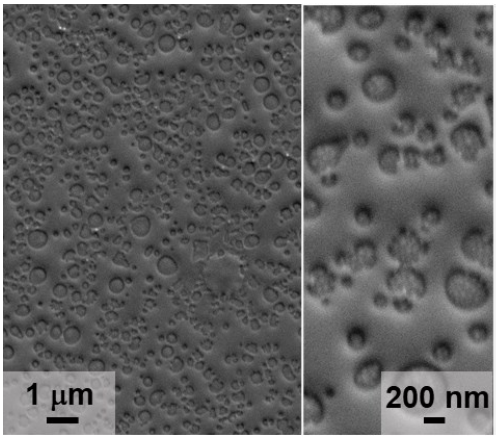


Figure 5.20. SEM image of surface melting on silicon substrate, after laser annealing at 600 pulses at 300 mJ/cm^2.[1]

To verify the influence of the substrate, the increase of the fluence above 100 mJ/cm^2 was done on the silicon substrate as well. On the latter, the molten morphology was reached with a 300 mJ/cm^2 fluence (Figure 5.20). The higher fluence required to reach the melted morphologies on silicon can be explained by the higher thermal diffusivity respect to fused silica, as well as the higher light absorption at 248 nm. The latter may have led to lower temperatures inside the film at the same fluence and lower exposure time to the photogenerated heat.

6.3.6 *Laser-crystallization of VO_2 thin films – conclusions*[1]

In this first paragraph 5.3, the possibility to crystallize VO_2 (M1) thin films by unconventional pulsed excimer laser annealing was investigated. The effect of laser fluence and pulse number was initially separately studied and then combined. The threshold laser parameters to induce the crystallization into VO_2 (M1), while avoiding surface melting, were found. The VO_2 crystallization was achieved within only 60 s of laser exposure and was performed at room temperature in air, after a 10 min drying step at 300°C. Temperature profile simulations were performed to evaluate the temperature distribution within a single pulse, in function of the ns pulse duration and the penetration depth. The simulations confirmed that the heat was confined within the film during the laser pulses, with negligible substrate heating. The thermochromic properties of the laser-annealed thin films (T_{lum} = 71.2%, $\Delta T_{2000\ nm}$ = 28.7%, ΔT_{sol} = 4.1%) displayed a high T_{lum} and were comparable with both the reference furnace-treated films and with other single-layer VO_2 thin films in literature. Further increase in ΔT_{sol}, without compromising the T_{lum}, could be obtained by combining VO_2 with other materials in multilayer configurations, which will be discussed in Chapter 6.

6.4 Moisture influence on laser annealed VO_2 thin films

Author disclosure statement. Part of the data and the discussion reported in paragraphs 5.4-5.5 of Chapter 5 was submitted for publication in the draft article "Basso, M. *et al*. Ultrafast laser crystallization dynamics of thermochromic VO_2 thin films by simple moisture-assisted sol-gel. *Submitted*"

In the previous paragraph 5.3, the possibility of crystallizing VO_2 thin films by nanosecond pulsed laser annealing (PLA) was demonstrated. Following the latter, a study on the process parameters was conducted with the goal of widening the process working window. The tunability of sol-gel reactions was combined with the rapid amorphous-crystalline conversion of PLA.

In paragraph 5.4, the influence of multiple influencing factors was considered, in terms of both sol-gel parameters and laser parameters. The effect of all parameters was evaluated in terms of functional properties of the final thin films, i.e., thermochromic efficiency for smart window applications.

In paragraph 5.5, the laser-induced crystallization mechanisms will be thoroughly investigated, by combining scanning and transmission electron microscopy (SEM/TEM), atomic force microscopy (AFM), grazing incidence X-ray diffraction (GIXRD) and Rutherford backscattering (RBS).

6.4.1 *Synthesis, deposition and laser-annealing of VO_2 thin films*

The same procedure described in paragraph 5.3.1 was applied for the development of VO_2 thin films. Vanadyl acetylacetonate powder ($VO(acac)_2$, 98% purity, Sigma-Aldrich) was dissolved in absolute ethanol to create a 100 mM solution, which was stirred at 78°C in a round-bottom flask under reflux for 1 day and aged for 2 months at room temperature in air. Subsequently, the solution was filtered using 0.2 µm sized syringe filters and deposited by spin coating onto the pre-cleaned silicon and fused silica substrates at 2000 rpm for 30 seconds. Samples were coated with 2 or 3 layers to tune the film thickness. Each layer was dried at temperatures between 100-250°C on a hot plate for 10 minutes prior to the deposition of the subsequent layer. The films, once dried, were laser annealed after a fixed time since their deposition, ranging from 2 h to 10 m. A KrF excimer laser system (248 nm, Coherent COMPex 201F, pulse duration of 22 ns) was employed to irradiate distinct and isolated areas of the overall surface. Each spot measured 5×5 mm² and exhibited a uniformity of 2%. The irradiation took place in air at room temperature, utilizing a variable number of pulses (#) at a repetition rate of 1 or 8 Hz, with a laser fluence of 70 mJ/cm². The fluence was regulated via a motorized attenuator coupled with an in-line energy meter, with an accuracy of 1%. For each sample type, multiple 5×5 mm² spots, with the same laser fluence, number of pulses and frequency, were produced to anneal the total sample area.

6.4.2 *Optimal working window for laser-processing of VO_2 thin films*

The final device properties of a thin film are highly influenced by the quality of the film, in terms of morphological, chemical, and structural homogeneity. The numerous parameters of CSD methods guarantee a great versatility but play a critical role as well, as they can either enhance or hinder the ultimate device properties. Understanding in detail the overall process parameters is essential to identify the optimal working window and exploit the maximum potential of the materials involved.

Regarding the identification of the optimal working window, parameters such as the atmosphere during deposition, drying temperature, film aging, and crystallization time play a key role. To identify the optimal combinations, all these parameters were varied within a specified range of interest. The

latter were selected to be 50-70-90% RH at 22°C for the moisture levels during spin coating deposition, T_d = 100-150-250°C for the drying temperature, 2 h - 6 d - 10 m for the aging time of the film prior to laser treatment, and 1-5-10-20-50-100-300 number of laser pulses at fixed energy density of 70 mJ/cm^2.

The effect of each parameter was assessed in terms of thermochromic performance, after subjecting each sample to a laser treatment to induce the crystallization. The thermochromic performance is directly linked to the crystallization of the film into VO_2 (M1). Among the numerous vanadium oxides and VO_2 polymorphs, the reversible M1 – R transition of VO_2 is the only one capable of modulating the NIR within this temperature range (20-100°C).[11] On the other hand, the presence of amorphous residues or other vanadium oxides leads to a degradation in terms of optical performance. As described in Chapter 3, the thermochromic performance is generally reported in function of three main parameters: the luminous transmittance (T_{lum}), the solar modulation (ΔT_{sol}) and the NIR modulation at fixed wavelength ($\Delta T_{2000\,nm}$). In this paragraph 5.4.2, the transmittance curves in both transmitting and reflecting state were reported for each sample and $\Delta T_{2000\,nm}$ was selected to better highlight the variations among the samples.

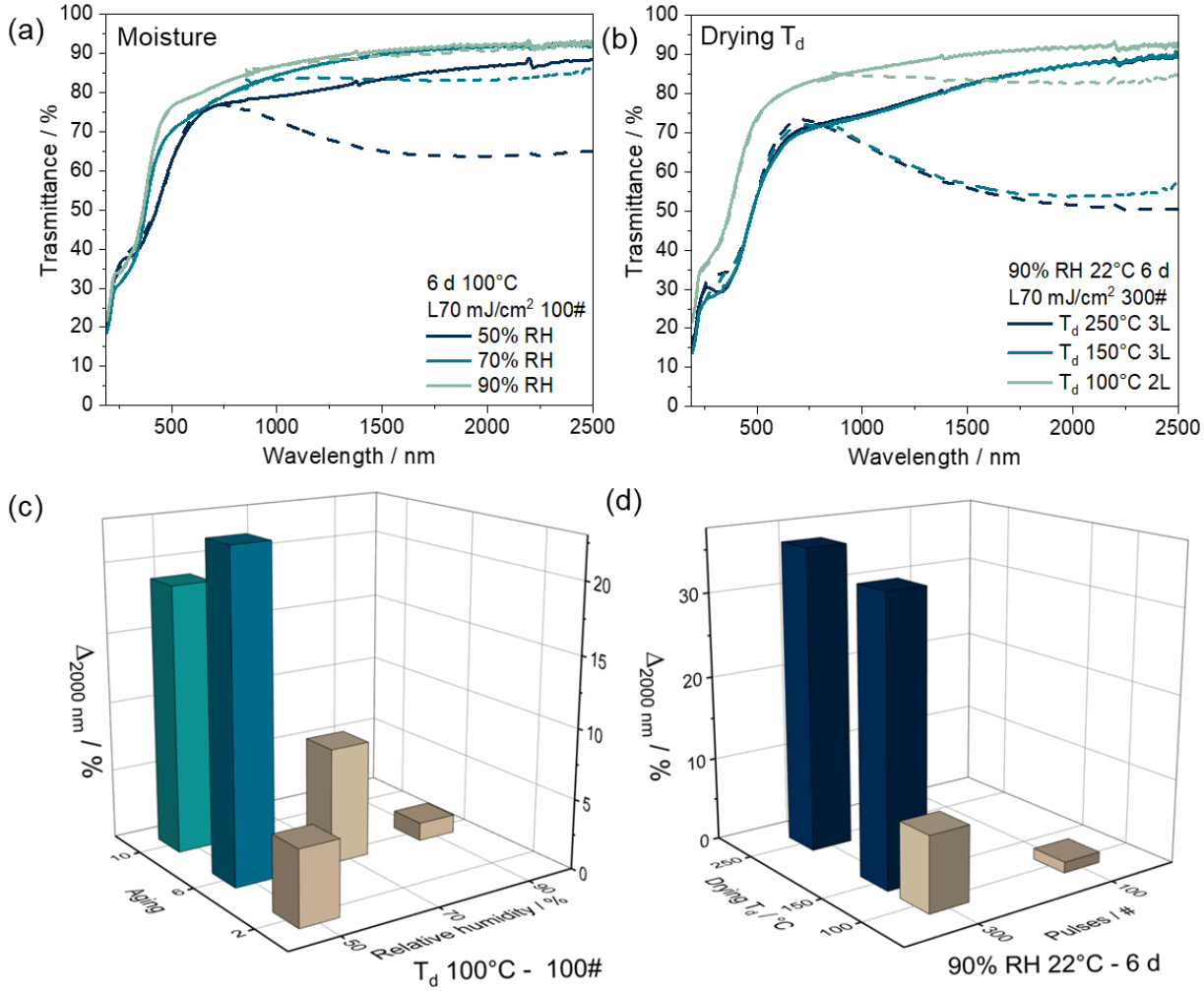


Figure 5.21. (a) UV-Vis-NIR transmittance of the samples deposited under 50-70-90% RH at 22°C, respectively, dried at 100°C, aged for 6 days before laser annealing and laser annealed with 100# laser pulses at 70 mJ/cm². (b) UV-Vis-NIR transmittance of the samples deposited under 90% RH at 22°C, dried at 100-150-250°C, respectively, aged for 6 days before laser annealing and laser annealed with 300# laser pulses at 70 mJ/cm². The solid lines represent the transmittance in the low temperature state, whereas the dashed lines represent the high temperature state. (c) Comparison of the NIR modulation at 2000 nm ($\Delta T_{2000\ nm,\ max}$) of the samples dried at 100°C and laser annealed with 100 pulses at 70 mJ/cm², with varied relative humidity during deposition (50-70-90% at 22°C) and aging time (2 h, 6 d, 10 m). (d) Comparison of the NIR modulation at 2000 nm ($\Delta T_{2000\ nm,\ max}$) of the samples deposited under 90% RH at 22°C and aged for 6 days before laser annealing at 70 mJ/cm², with varied drying temperature (100-150-250°C) and number of pulses (100-300#).

In Figure 5.21 (a) the effect of moisture during deposition (50-70-90% RH 22°C) was considered. At the lowest drying temperature (T_d = 100°C) and at fixed film aging time and laser pulses (6 d, 100 #), the best thermochromic performance was obtained with mild 50% RH at 22°C during deposition (Figure 5.21 (c), $\Delta T_{2000\ nm}$ = 22.9%, ΔT_{sol} = 4.0%, T_{lum} = 68.5%). If the drying step was kept at 100°C, increasing the RH during deposition to 70% and 90% at 22°C progressively led to a deterioration of the thermochromicity ($\Delta T_{2000\ nm}$ = 8.2-1.3%, respectively – Figure 5.21 (a, c)). Nonetheless, high thermochromic performance could still be obtained with a 90% RH deposition, by increasing the drying temperature to 150°C or above. The film deposited at 90% RH 22°C and dried at 150°C led to $\Delta T_{2000\ nm}$ = 33.5% (300 #, Figure 5.21 (b, d)), which is comparable with $\Delta T_{2000\ nm}$ = 30.6% of the film deposited at 50% RH 22°C and dried at 100°C (300 #, Figure 5.24 (x)).

The higher drying temperature allows for a residual solvent evaporation from the sol-gel network and boosts the condensation of the hydroxyl groups present in the film. Moreover, one additional layer could be deposited by drying at 150°C, without interfering with the film quality. In the previous paragraph 5.3, a major decrease in the carbon content was found by XPS with drying temperature higher than 150°C[1], i.e., above the boiling point of acetylacetone (~140°C). Further reducing the RH during deposition below 50% RH was also tested but led to barely perceivable thermochromic performance (43% RH 22°C, $\Delta T_{2000\ nm}$ = 1.7%, Table 5.4 below). As it emerges, the best thermochromic efficiency could be found with more than one combination of parameters, which favorably widens the optimal working window. The maximum NIR modulation was either obtained by mild RH during deposition and mild drying temperature (50% RH - 22°C, T_d 100°C, $\Delta T_{2000\ nm}$ = 30.6% at 300#), or by boosting both the RH and drying temperature (90% RH - 22°C, T_d 250°C, $\Delta T_{2000\ nm}$ = 35.9% at 300#). To explain this favorable behavior, the following factors were considered.

Regarding the influence of moisture on sol-gel, increasing the number of hydroxyl groups available to react boosts the kinetic of hydrolysis, and hence condensation. The higher moisture during deposition can increase the hydrolysis rate, leading to the formation of a higher number of hydroxyl groups bound to the metal-organic complex and reactive towards condensation. Regarding the $VO(acac)_2$ precursor, the sol gel pathways of synthesis and condensation have not yet been clearly established in literature. In line with the tendency of transition metals to maximize their coordination number, the available sixth coordination of the vanadyl ion in the precursor offers a possible path for the interaction with the solvent. Grybos *et al.*[97] proposed the hydrolysis and oxidation of the $VO(acac)_2$ precursor in methanol to proceed via the formation of $VO(OH)(OCH_3)(acac)$, along with the removal of an acetylacetonate ligand (acac). As shown in the previous paragraph 5.3, the surface of the dried thin films was predominantly composed of V^{5+} respect to V^{4+}, with the ratio to be inverted after the annealing step.[1] The decrease in carbon content was majorly detected after raising the drying temperature to 150°C. This result aligns with the work of Van der Voort *et al.*[98] and Nenashev *et al.*[62], who both suggested a thermolysis of $VO(acac)_2$ on silica substrates to happen above 150°C, in air or in humid nitrogen atmosphere, respectively.

On the other side, photonic annealing has been mainly exploited to convert metal-organic precursors into dense and amorphous metal oxide films, exploiting the advantage of lower temperatures respect to conventional methods. With *et al.*[65] clarified the difference between pure UV photochemical conversion and synergic interplay of hydrolysis and UV irradiation, i.e., UV-aided conversion of pre-condensed sol-gel films. Using a vacuum ultraviolet (VUV) excimer lamp, they showed the possibility of photochemically convert a metal-organic precursor under inert atmosphere.[68] An

optimized O_2% was required to induce the conversion into a densified metal oxide thin film, which would not proceed under a totally inert atmosphere. They noticed that VUV conversion would not happen if the films were previously hydrolyzed by exposure to ambient air. Park *et al*.[17] studied the DUV conversion on sol-gel films by UV mercury lamp, lower in power respect to the VUV excimer one. They combined DUV irradiation with the collateral temperature rise to 150°C, induced by the prolonged exposure (1-2 h). This resulted in an initial photochemical condensation, followed by a gradual film densification.

Besides the film densification, crystallization by photonic annealing has recently started to gain a higher focus. Under the case of water and oxygen exclusion, i.e., with the whole process performed under inert atmosphere, Jo *et al*.[23] successfully reduced the crystallization temperature of VO_2 thin films to 250°C, by combining DUV irradiation with combustion reactions. They proposed the formation of the thin films to follow the removal of both ligands from $VO(acac)_2$, with subsequent condensation and formation of the V-O-V network.

During DUV irradiation, the development of photo-induced chemical reactions is allowed both by the timescale of minutes-hours and by the power of the UV source. Pulsed laser annealing is extremely challenging to probe since the fast nano-femtosecond timescale is hard to detect with *in-situ* measurements. When pulsed lasers are employed, it is important to distinguish between the effect of ns and fs laser irradiation: the former laser light is absorbed by the film/substrate and converted into thermal energy, causing photothermally induced chemical reactions, whereas the latter induces cold ablation and extremely fast bond breaking.[2] In our case, the KrF pulsed excimer laser should therefore cause photothermally induced chemical reactions rather than photochemical reactions, which will be discussed in paragraph 5.5 below.

In this case, a synergic approach was adopted to combine the tunability of sol-gel reactions and the ultrafast amorphous-crystalline conversion of laser processing. Different degrees of precondensation on the thin films could be induced by varying the moisture content during deposition and by tuning the drying temperature accordingly. Under low moisture deposition, laser irradiation led to simultaneous conversion of both precondensed network and residual unreacted metal-organic precursor, whereas increasing the moisture content led to a decrease in residual precursor and increased the precondensed bonds due to the higher availability of hydroxyl groups. Laser irradiation was hence used to simultaneously boost the photothermal conversion and induce the amorphous-to-crystalline transition into a VO_2 (M1) structure.

Many studies on laser annealing focus on the removal of organic matter before UV exposure or perform laser irradiation while maintaining the substrate at temperatures higher than 300°C.[99,100] In this case, similar thermochromic properties were obtained both at 100°C or higher drying temperatures, after proper tuning of the other parameters (moisture, film aging and pulse number). This offers a great advantage in terms of process efficiency, since organic removal, densification and crystallization can be performed in one step, within a few seconds of laser irradiation.

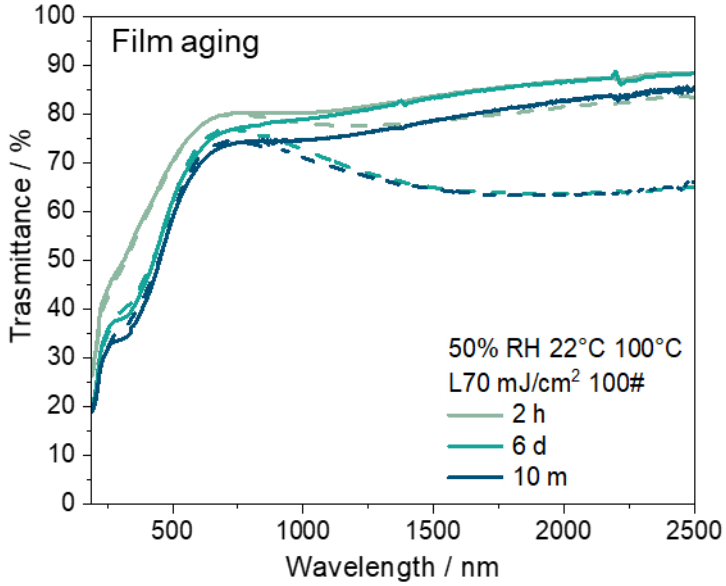


Figure 5.22. UV-Vis-NIR transmittance of the samples deposited under 50% RH at 22°C, dried at 100°C, aged for 2 hours, 6 days, or 10 months, respectively, before laser annealing with 100# laser pulses at fixed 70 mJ/cm^2. The solid lines represent the transmittance in the low temperature state, whereas the dashed lines represent the high temperature state.

Considering the effect of film aging before laser annealing (Figure 5.22, 50% RH 22°C during deposition), remarkable differences were found between a few hours and 6 days. Allowing the condensation reactions to proceed for only 2 hours is not sufficient for the formation of a stable V-O-V sol-gel network before inducing the laser photothermal conversion. An unstable and partially formed V-O-V sol-gel network leads to a scarce film crystallization and insufficient thermochromic performance (2 h, $\Delta T_{2000\ nm}$ = 5.3%, Figure 5.21 and Table 5.4 below). Under the same conditions (50% RH, T_d 100°C), increasing the film aging to 6 days allows for a proper formation and stabilization of the gel network, resulting in a remarkable boost of the final thermochromic performance ($\Delta T_{2000\ nm}$ = 22.9%, T_{lum} = 68.5%, Figure 5.22, Table 5.4 below).

Table 5.4. Luminous transmittance at room temperature ($T_{lum,\ 20°C}$), maximum solar modulation ($\Delta T_{sol,\ max}$), NIR modulation at 2000 nm ($\Delta T_{2000\ nm,\ max}$) reported for each sample. The latter two were calculated from the difference between the low temperature state (i.e., 20°C) and the high temperature state (i.e., 90-110°C). The latter temperature was chosen based on when the change in transmittance reached a steady state. The drying temperature (T_d), humidity conditions during deposition (RH at 22°C), the film aging before laser irradiation, and the number of laser pulses (#) are reported for each sample. The fluence was fixed at 70 mJ/cm^2.

T_d (°C)	RH 22°C (%)	Film aging	Pulses (#)	$T_{lum,\ 20°C}$ (%)	$\Delta T_{sol,\ max}$ (%)	$\Delta T_{2000\ nm,\ max}$ (%)
100	50	6 d	100	68.5	4.0	22.9
100	50	6 d	50	70.5	3.1	17.2
100	50	6 d	20	71.1	2.6	12.4
100	50	6 d	10	71.0	1.4	3.7
100	50	6 d	5	75.6	1.1	0.7
100	50	6 d	1	81.1	1.5	0.9
100	50	10 m	300	60.2	3.8	30.6
100	50	10 m	100	65.5	2.4	19.0
100	50	10 m	50	70.8	2.4	15.6
100	50	10 m	20	71.6	1.4	9.3
100	50	10 m	10	75.2	0.4	1.6
100	43	6 d	100	73.2	0.6	1.7
100	50	2 h	100	74.7	1.4	5.3
100	70	6 d	100	72.5	1.1	8.2
100	90	6 d	100	77.9	0.2	1.3
100	90	6 d	300	77.2	1.4	8.9
150	90	6 d	300	60.6	4.5	33.5
250	90	6 d	300	61.1	4.7	35.9

With the goal of expanding the process working window as much as possible, the dried thin films were aged for 10 months before performing the laser annealing. The thin films were aged under no specific environmental control, to check their stability and susceptibility to seasonal oscillations of both moisture and temperature. At fixed deposition RH, drying temperature, and pulse number (50% RH – 22°C, 100°C, 100#), a comparable thermochromic performance is obtained after 10 months of aging ($\Delta T_{2000\ nm}$ = 19.0%, T_{lum} = 65.5%, Figure 5.24, Table 5.4), with respect to 6 d. Both the luminous transmittance and the solar modulation are slightly lower in the former, but with minimal changes if compared to the difference between 2 h and 6 days ($\Delta T_{2000\ nm}$ = 5.3 - 22.9%, respectively, Table 5.4). This confirms the possibility to anneal the thin films within months, without the need to observe a strict time schedule or protect them with a controlled atmosphere.

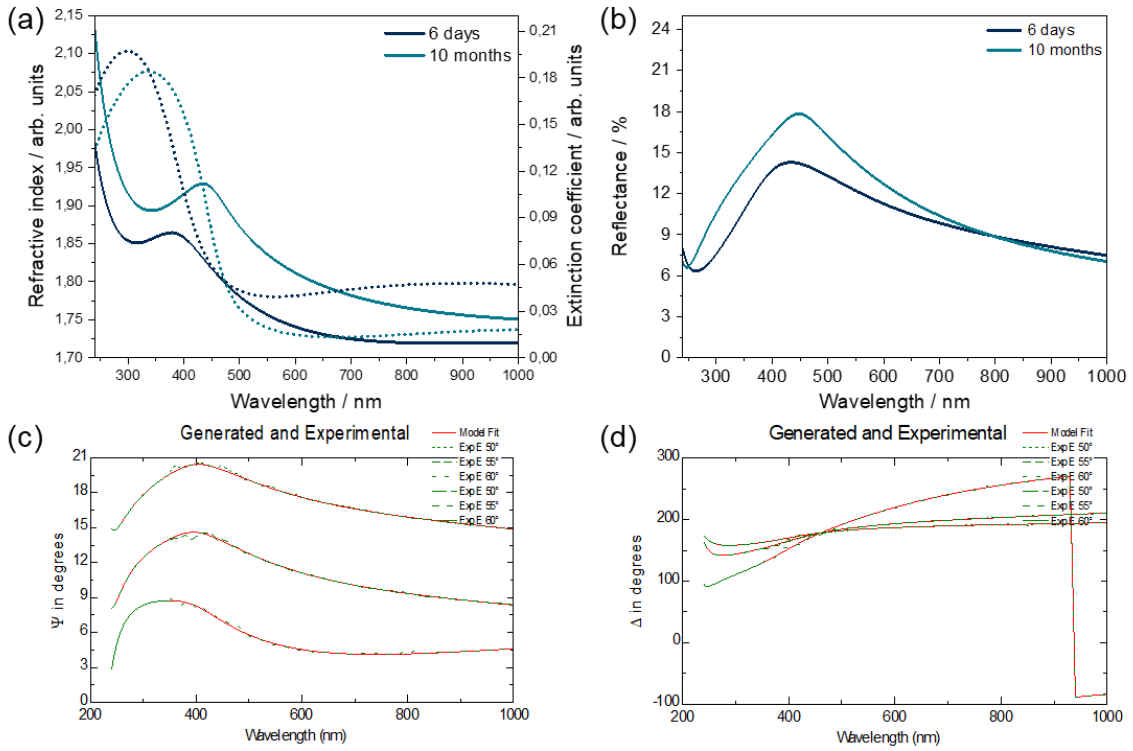


Figure 5.23. (a) Refractive index, extinction coefficient in function of the wavelength, measured on the dried samples aged for 6 d and 10 m, respectively. (b) Normal reflectance in function of the wavelength, simulated for the dried samples aged for 6 d and 10 m, respectively. (c, d) fitting and generated data of the psi and delta functions of the dried samples aged for 6 days.

The thickness (*t*), refractive index (*n*) and extinction coefficient (*k*) of the dried thin films after 6 d and 10 m were measured with ellipsometry in the 300-1000 nm range. The optical constants *n* and *k*, along with the reflectance at 90°, were generated after data fitting (Figure 5.23 (c, d)) to consider the values at the laser wavelength of 248 nm. The same trend was observed for the two aging times, indicating that the films were stable for months. As expected, a film condensation occurred after 10 m, highlighted by the decrease in thickness and concurrent increase in refractive index. The former decreased from 65 nm to 57 nm, accompanied by an increase in *n* from 1.86 to 1.92 and k from 0.11 to 0.16 (Figure 5.23 (a)).

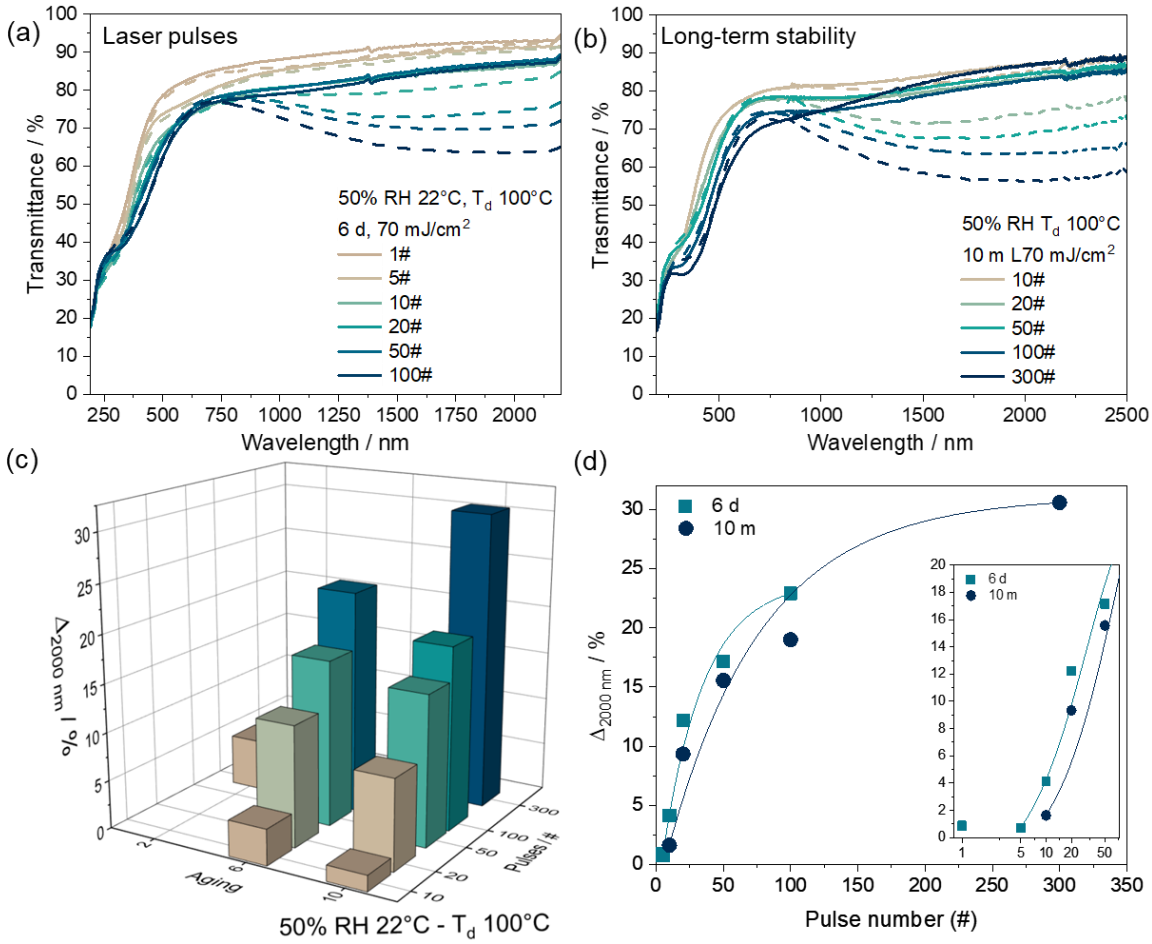


Figure 5.24. (a) UV-Vis-NIR transmittance of the samples deposited under 50% RH at 22°C, dried at 100°C, aged for 6 days before laser annealing and laser annealed with increasing number of pulses (1-100#) at 70 mJ/cm². (b) UV-Vis-NIR transmittance of the samples deposited under 50% RH at 22°C, dried at 100°C, aged for 10 months before laser annealing and laser annealed with increasing number of pulses (10-300#) at 70 mJ/cm². The solid lines represent the transmittance in the low temperature state, whereas the dashed lines represent the high temperature state. (c) Comparison of the NIR modulation at 2000 nm ($\Delta T_{2000\ nm,\ max}$) of the samples deposited under 50% RH at 22°C and dried at 100°C, with varied aging time (2 h, 6 d, 10 m) and number of laser pulses (10-300#) at 70 mJ/cm². (d) NIR modulation at 2000 nm ($\Delta T_{2000\ nm,\ max}$) reported for increasing laser pulses (1-300#). The light blue squares represent the samples deposited under 50% RH at 22°C, dried at 100°C, aged for 6 days before laser annealing and annealed with increasing laser pulses (1-100#) at fixed 70 mJ/cm², whereas the blue circles represent the samples deposited under 50% RH at 22°C, dried at 100°C, aged for 10 months before laser annealing and annealed with increasing laser pulses (10-300#) at fixed 70 mJ/cm². An exponential fitting is used to highlight the similar trend in the NIR modulation values. The insert in (c) is a zoom of Figure (c) between the 1-50 laser pulses range.

Finally, the laser pulse number was progressively increased from 1 to 300 to evaluate at which point the amorphous to crystalline conversion would start. At fixed laser fluence (70 mJ/cm^2), the thermochromic modulation increased with increasing pulse number, for both 6 d and 10 m of film aging (Figure 5.24 (a) and Table 5.4). Interestingly, the correlation between thermochromic modulation and laser pulse number followed a saturating exponential increase, rather than a linear trend (Figure 5.24 (d)): a sharp increase in $\Delta T_{2000\ nm}$ was induced within the first 10-20 laser pulses, after which the trend kept increasing but with a lower gradient. It is worth noting that the film aging before laser annealing (i.e., 6 d or 10 m) did not influence the correlation between laser pulse number and $\Delta T_{2000\ nm}$, as they displayed a similar slope within the first 50 pulses (insert of Figure 5.24 (d)). As a result, by appropriately tuning the process parameters of deposition, drying, laser annealing,

satisfactory properties can be obtained even with few pulses, according to the desired application. An example will be presented in Chapter 7, in which the gas sensing properties towards H_2 detection will be compared between a thin film laser-annealed with 10 pulses and one laser-annealed with 300 pulses.

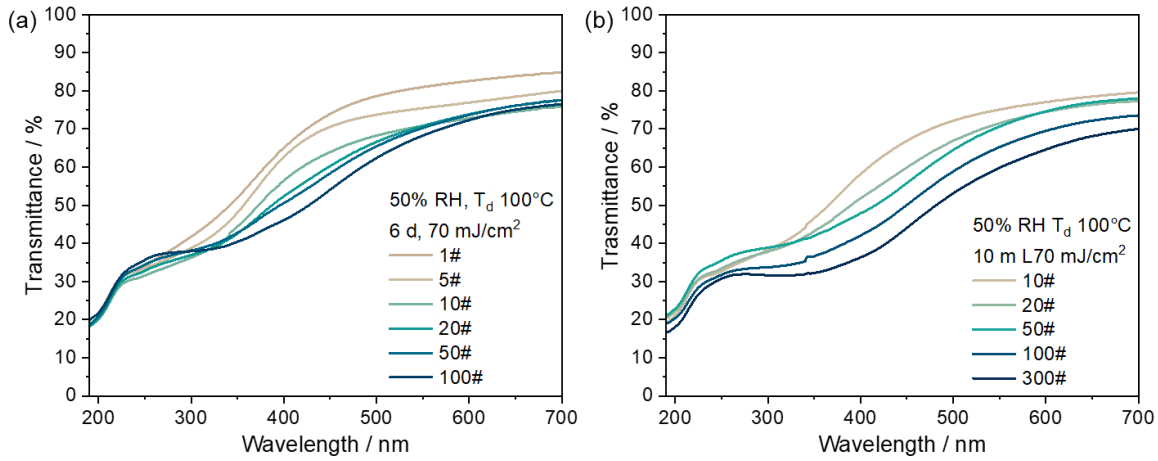


Figure 5.25. (a) UV-Vis transmittance at room temperature (i.e., semiconducting state) of the samples deposited under 50% RH at 22°C, dried at 100°C, aged for 6 days before laser annealing and annealed with increasing laser pulses (1-100#) at fixed 70 mJ/cm². (b) UV-Vis transmittance at room temperature (i.e., semiconducting state) of the samples deposited under 50% RH at 22°C, dried at 100°C, aged for 10 months before laser annealing and annealed with increasing laser pulses (10-300#) at fixed 70 mJ/cm².

As discussed in paragraph 3.6 of Chapter 3, a smart window operates at its maximum functionality when the highest visible transmittance (T_{lum}) is achieved simultaneously with the highest level of solar modulation (ΔT_{sol}, $\Delta T_{2000\ nm}$). These parameters are known to be inversely correlated, meaning that an increase in visible transmittance typically leads to a decrease in solar modulation, and viceversa. For smart windows based on solely VO_2, improvement is required for both T_{lum} and ΔT_{sol} values, which should be higher than 50% and 10%, respectively.[3,101] Various approaches have been reported to simultaneously enhance both parameters, often involving the combination of multiple materials, the creation of multilayers and/or composites, and the use of nanostructuring techniques.[12] As evidenced in paragraph 5.3 and confirmed in this paragraph 5.4 (Table 5.4, Figure 5.25), all the laser-annealed samples exhibit a T_{lum} ranging between 60-80%, which is relatively high compared to the standard reported in literature for VO_2-only smart windows (~50%).[11] From Figure 5.25, the luminous transmittance was seen to decrease with increasing laser pulses, due to gradual formation of crystalline VO_2 along with the formation of a spontaneous nanostructured morphology (see paragraph 5.5). The solar modulation (ΔT_{sol}~4.0%) should be enhanced through the several strategies proposed in literature, which will be the addressed in Chapter 6. Bhupati *et al.*[102] successfully increased the T_{lum} through the creation of nanograting structures, by irradiating an already crystalline VO_2 thin film with a fs laser. Another widely used strategy to gain the material's patterning is to exploit a polymeric template and induce its removal by etching or thermal treatment.[103] In our case,

the ns pulsed laser irradiation induces a spontaneous film patterning within few seconds, which greatly favors the achievement of high luminous transmittance (T_{lum}=60-80%). This approach is template-free and enables the simultaneous achievement of organic residue removal, densification, crystallization, and nanostructuring in a single step, allowing for time-, cost- and energy-savings.

6.4.3 *Moisture influence and optimal working window – conclusions*

As an overall view, this process offers multiple advantages, in terms of versatility, easiness and scalability. Crystallization occurs within a matter of seconds, with no need for an inert atmosphere. The process can be easily conducted in ambient air, which ease the industrial scalability. The long-term stability of the dried films offers the potential to perform the annealing step over an extended months-long period, allowing for flexibility in the process timelines. This method involves a reduced drying temperature of 100°C, which, combined with the macroscopically cold laser annealing, favors a lower thermal impact on the substrate. The approach is template-free and enables the simultaneous achievement of organic residue removal, densification, crystallization, and nanostructuring in a single step, allowing for time-, cost- and energy-savings.

6.5 Laser-induced crystallization mechanism of VO_2 thin films

In the previous paragraph 5.4, the optimal process working window was identified to exploit the maximum potential of the material. Following the investigation on the process parameters, further studies were conducted to assess the mechanism of the amorphous-crystalline transformation, dictated by the laser-film interaction.

The optical performance is strongly correlated to the crystalline composition (i.e., type of vanadium oxide and degree of crystallization) and to the film morphology. The previous optical information (Figure 5.24), function of the increasing pulse, was therefore combined with the corresponding GIXRD patterns, SEM, TEM, and AFM images. For the sake of a higher clarity, in paragraph 5.5.1 the outcomes of the distinct characterizations will initially be presented individually. In paragraph 5.5.2 the results of all characterizations will be discussed together, to provide an overall explanation of the laser-matter interaction.

6.5.1 *GIXRD, SEM, TEM and AFM results*

The GIXRD patterns of the laser-annealed thin films on fused silica substrates are reported in Figure 5.26 (a), whereas Figure 5.26 (b) displays the comparison between laser and furnace annealing.

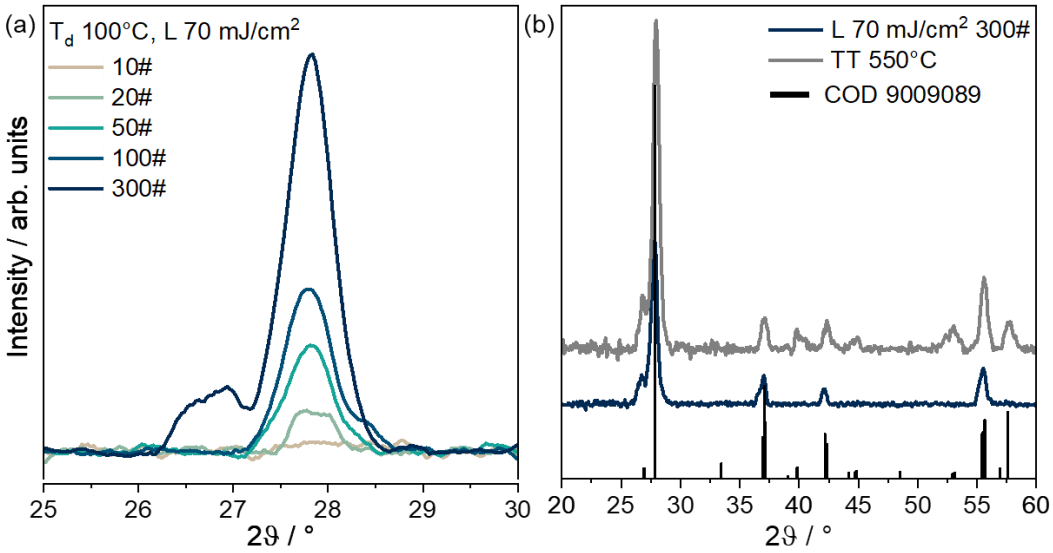


Figure 5.26. (a) Grazing-incidence X-ray diffraction (GIXRD) of the laser-annealed (L 70 mJ/cm^2) and furnace-annealed (TT 550°C) films. The former was deposited under 50% RH at 22°C, dried at 100°C, aged for 10 months and laser annealed with 300 pulses at 70 mJ/cm^2, whereas the latter was annealed in furnace at 550°C for 1 h, with 10°C/min heating rate under a N_2 flux. (b) GIXRD of the films laser-annealed at increasing laser pulses on fused silica substrates, in the range of the principal diffraction at 2Θ ~ 27.9° with (0 1 1) orientation. The films were deposited under 50% RH at 22°C, dried at 100°C, aged for 10 months before laser annealing and annealed with increasing laser pulses (10-300#) at fixed 70 mJ/cm^2.

From the GIXRD patterns, both the laser- and the furnace annealed samples display similar patterns, attributed to monoclinic VO_2 (M1) (Figure 5.26 (b), COD 9009089). Both samples displayed a preferential orientation along the (0 1 1) direction, visible at 2Θ ~ 27.9°, along with the presence of diffraction patterns at 2Θ ~ 26.9°, 36.9°, 42.2°, 55.6°, which correspond to (1 1 0), (2 0 -2), (2 1 -2), (2 2 0), respectively. The furnace annealed sample showed additional peaks, of weak intensity, at 39.9° (0 2 0), 44.8° (0 2 1), 53.0° (-1 2 2), 57.6° (0 2 2). The GIXRD of the laser-annealed samples deposited under 50% RH 22°C, dried at 100°C and aged 10 m, which optical properties were previously shown in Figure 5.24 (b), are reported in Figure 5.26 (a) (zoom on the (0 1 1) orientation). The appearance of a diffraction peak is visible between 10 and 20 pulses, after which the peak progressively increased in intensity and became more defined in shape. Between 100 and 300 pulses, the shoulder at 2Θ ~ 26.9° resulted detectable from the GIXRD pattern.

The morphological evolution under increasing laser pulses was analyzed by AFM, SEM and TEM (Figures 5.27, 5.28, 5.29, 5.31). The three characterizations allowed a progressive increase in magnification as reported from the scale bars in the images, which decreased from 2 µm (AFM, Figure 5.27) to 100 nm (SEM, Figure 5.28) to 20 nm and 5 nm (TEM, Figure 5.29, 5.31).

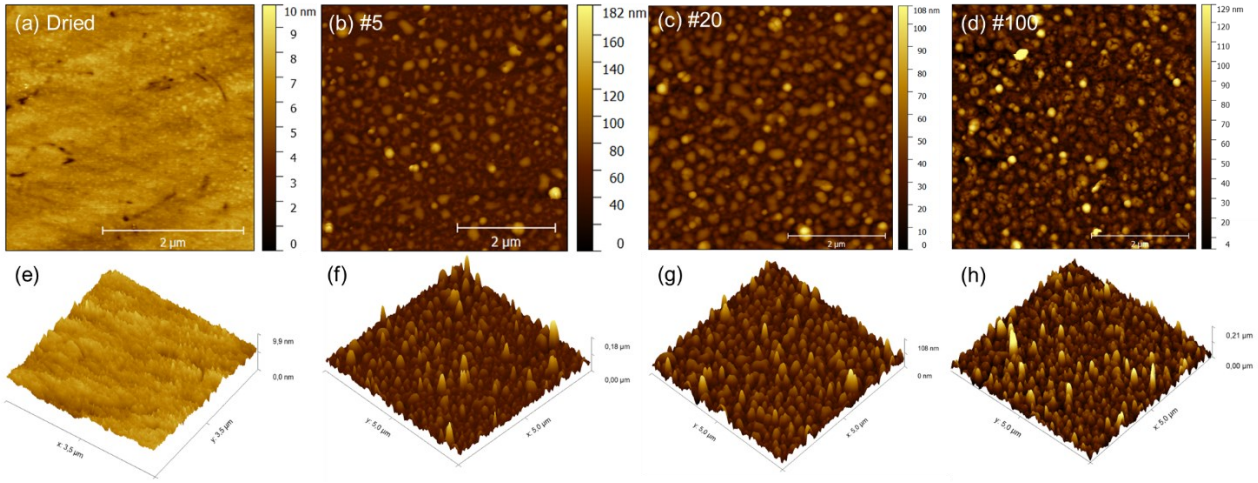


Figure 5.27. AFM images of the (a, e) dried sample, (b-h) laser annealed samples with increasing laser pulses, deposited under 50% RH at 22°C, dried at 100°C, aged for 6 days and laser annealed at 70 mJ/cm^2. (b, f) 5 pulses, (c, g) 20 pulses, (d, h) 100 pulses. Figures (a-d) display the 2D images whereas (d-h) the 3D images.

Prior to laser irradiation, the thin films were dried at 100°C for 10 min and subjected to no further thermal treatment. The samples displayed an overall flat and smooth surface from both AFM and SEM (Figure 5.27 (a), Figure 5.28 (a)), as well as a uniform film distribution along the thickness (z axis, TEM cross section, Figure 5.29 (b)). The dried films resulted to have a thickness of 65 ± 3 nm from ellipsometry analysis, with refractive index n = 1.86 ± 0.01 and extinction coefficient k = 0.11 ± 0.02 at 400 nm.

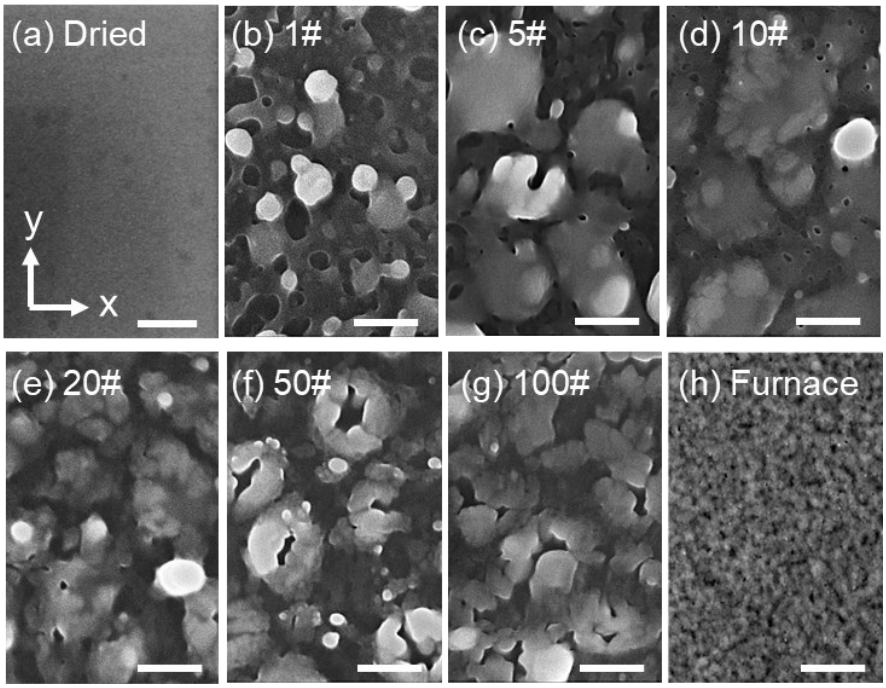


Figure 5.28. SEM images of the (a) dried sample, (b-g) laser annealed samples with increasing laser pulses, deposited under 50% RH at 22°C, dried at 100°C, aged for 6 days and laser annealed at 70 mJ/cm^2. (h) SEM image of the furnace annealed film at 550°C for 1 h, with 10°C/min heating rate under a N_2 flux. The scale bar in (a-h) is 100 nm.

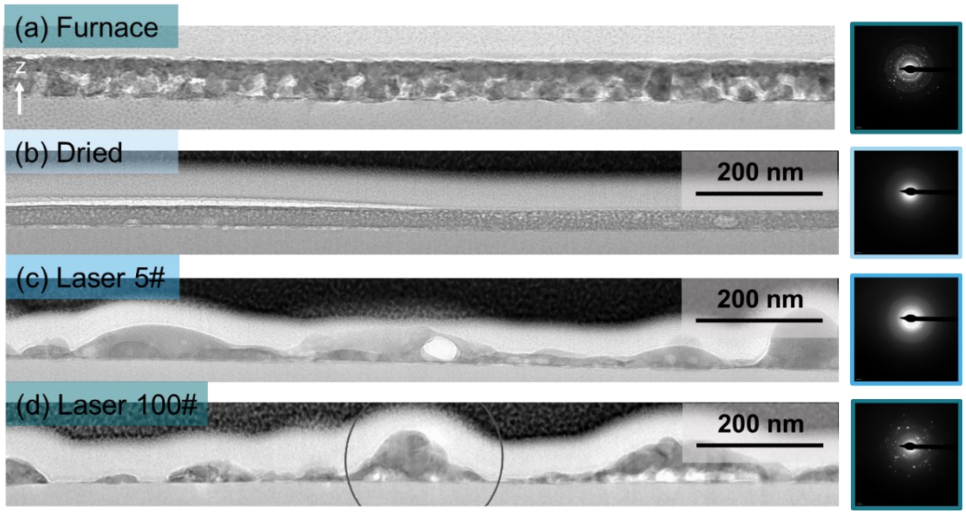


Figure 5.29. TEM images and corresponding SAED patterns of the thin films: (a) furnace annealed at 550°C for 1 h under N_2 flux, (b) dried at 100°C, (c) laser-annealed with 5 pulses at 70 mJ/cm^2, (d) laser-annealed with 100 pulses at 70 mJ/cm^2. The films were deposited under 50% RH at 22°C, dried at 100°C, aged for 6 days before laser or furnace annealing. The scale bar is 200 nm.

The initial first laser pulse induced a significant transformation in the film morphology, resulting in the formation of voids within the film (Figure 5.27 (b)). The material appeared to undergo a thermal dewetting, aggregating to form small spheres that protruded along the z-axis. From the comparison between in lens and secondary electron SEM acquisition, the lighter coloration in Figure 5.28 (b-g) is attributed to electron charge accumulation caused by the nanostructured morphology, rather than to compositional variations. Progressing from 1 to 5 pulses, larger agglomerates with a predominantly smooth surface emerged from the SEM images (Figure 5.28 (c)). From AFM (Figure 5.27 (b)) and TEM cross section (Figure 5.29 (c)), the 5 laser pulses induced a viscous flow of the material, which led to a preliminary film fragmentation and formation of distinct agglomerated areas. Temporarily isolated holes formed inside the film after 5 pulses, which then disappeared with the increasing pulse number (Figure 5.29 (c, d)). The holes are attributed to the release of gaseous products due to the decomposition of organic residuals into acetone, CO_2, and H_2O.[61,62,104] In the previous paragraphs 5.3-5.4, the organic content evolution upon drying and laser annealing was analyzed by XPS. From the C 1*s* peak, a major decrease of carbon content happened between drying temperatures of 80°C and 150°C and a further decrease, with a lower magnitude, continued within the first few laser pulses. In this section, the thin films were dried at a lower temperature (100°C) with respect to the previous case (300°C, paragraph 5.4), therefore the presence of organic residuals prior to the first laser pulse was higher, supporting the formation of intermediate holes due to gaseous release. After irradiation of 100 pulses, the film evolved into a denser nanostructured morphology with no longer visible holes, formed by smaller agglomerations closely packed together. The gradual film densification upon increasing laser pulses was confirmed by BF-DF HRTEM images. The formation of these distinctive morphologies was found to be highly dependent on the interaction between the laser beam and the

thin film and less influenced by the underlying substrate type.[1,105] On the contrary, conventional heat treatment did not lead to a film nanostructuring, resulting in a smoother morphology without specific nanostructures (Figure 5.28 (h)). The thickness distribution was found to be homogeneous and the film displayed a high porosity degree (Figure 5.29 (a)).

The AFM was used to quantitively evaluate the changes in surface roughness with increasing laser pulses, expressed in terms of root mean square (RMS) roughness. The RMS roughness increased from 0.61 nm in the dried film (Figure 5.27 (a)) to 15.94 – 11.78 – 18.89 nm in the laser-annealed films, respectively with 5 – 20 – 100 laser pulses (Figure 5.27 (b-d)).

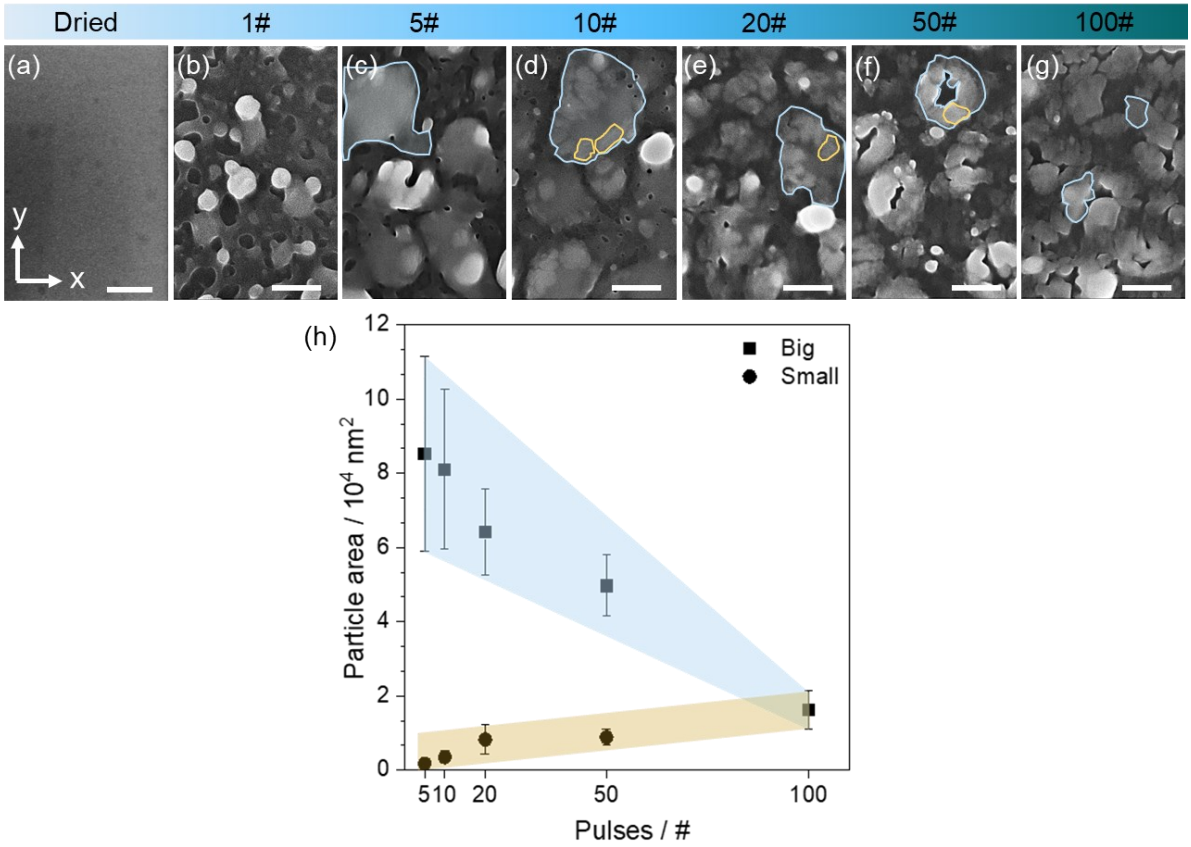


Figure 5.30. SEM images of the (a) dried sample and (b-g) laser annealed samples with increasing laser pulses. The scale bar in (a-g) is 100 nm. In figures (c-g) same examples of the particle boundaries considered for the image analysis is shown. The light blue lines refer to the "big" particles, whereas the yellow lines refer to the "small" particles. (h) Particle area estimated from the image analysis in function of the number of laser pulses. The error bar is reported for each sample type. The squares refer to the "big" particles, whereas the circles refer to the "small" ones.

A qualitative image analysis was conducted on the SEM images, to investigate eventual trends in morphology upon the increasing laser pulses. The variations were expressed in terms of an average particle dimension, as reported in Appendix A.2.11. The particle/agglomerate size was chosen at two different scales, "big" (area > $1.5*10^4$ nm^2) and "small" (area < $1.5*10^4$ nm^2) (Figure 5.30 (c-g)). Considering the former agglomerates, the average dimension was seen to gradually decrease with increasing laser pulses (Figure 5.30 (h)). The surface was predominantly smooth up to 5 pulses

(Figure 5.30 (c)), whereas after 10 pulses smaller particles emerged within the boundaries of the "big" agglomerates (Figure 5.30 (d)). The presence of the smaller nanoparticles became increasingly evident, with their size increasing with the number of pulses, while the big agglomerates were subjected to a progressive fragmentation and size reduction. Observing the two trends in function of pulse number, the two types of particles gradually converged towards a unified outcome at 100 pulses, at which no clear distinction could be seen (Figure 5.30 (g, h)).

Selected area diffraction (SAD) analysis was conducted at various locations on TEM-prepared lamellae from the dried film and the laser-annealed films at 5 and 100 pulses, respectively (Figure 5.31). The absence of diffraction spots in the dried film aligns with the absence of diffraction patterns from GIXRD (Figure 5.31 (a)). A limited number of diffraction spots were discernible in the film which was irradiated with 5 laser pulses (Figure 5.31 (b)), while the film treated with 100 laser pulses showed multiple diffraction spots (Figure 5.31 (c)). These results corroborate with both the evolution of the GIXRD patterns (Figure 5.26) and optical spectroscopy results (Figure 5.24).

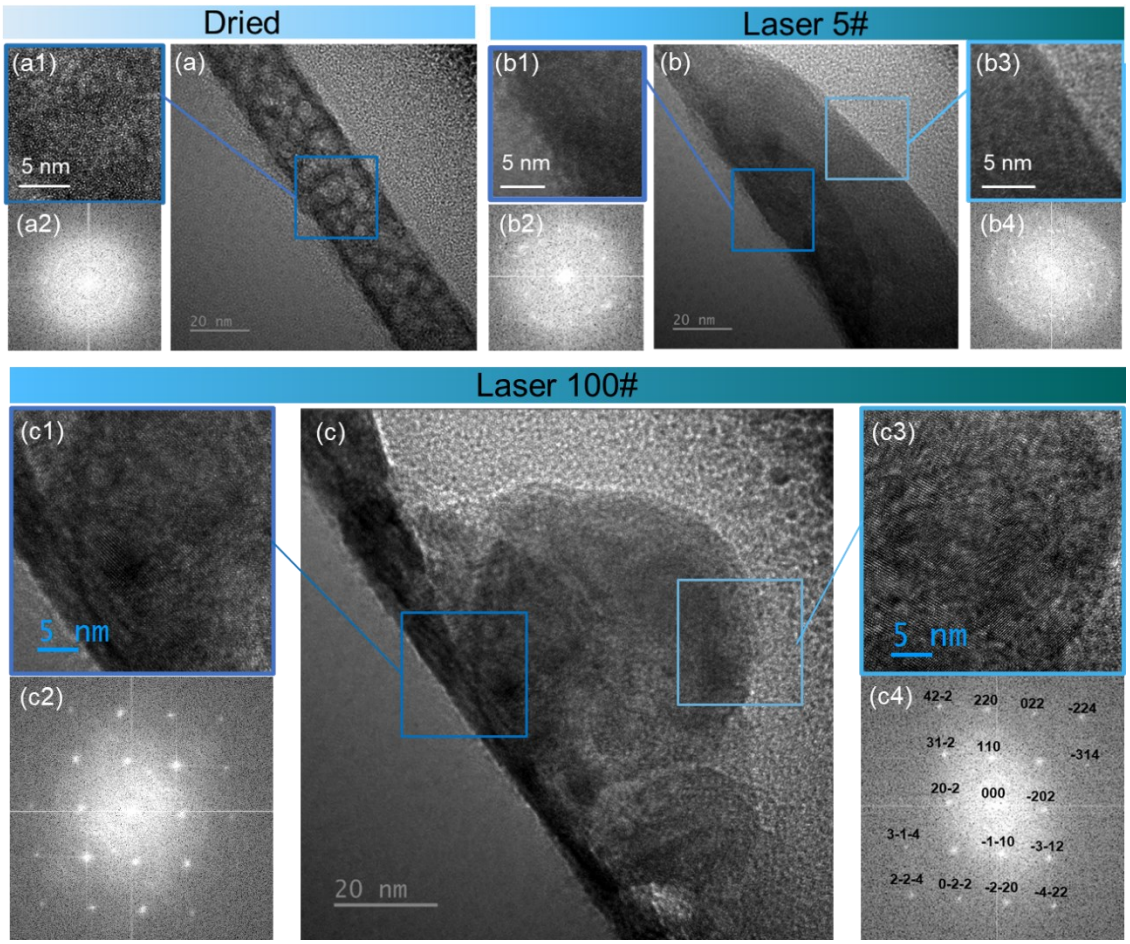


Figure 5.31. TEM images of the thin films: (a, a1) dried at 100°C, (b, b1, b3) laser-annealed with 5 pulses, (c, c1, c3) laser-annealed with 100 pulses. The films were deposited under 50% RH at 22°C, dried at 100°C, aged for 6 days before laser annealing at 70 mJ/cm². (a2) Fast Fourier Transform (FFT) analysis of the dried sample in figure (a1), (b2, b4) FFT analysis of the sample laser-annealed with 5 pulses in figure (b1, b3), respectively, (c2, c4) FFT analysis of the sample laser-annealed with 100 pulses in figure (c1, c3), respectively.

Fast Fourier Transform (FFT) analysis was performed on target areas of the dried film and laser-annealed films at 5 and 100 pulses (Figure 5.31). Consistently with previous GIXRD and SAD characterizations, the film dried at 100°C did not exhibit the presence of ordered regions (Figure 5.31 (a, a1)). FFT analysis was applied to various spots and did not reveal any diffraction spots (Figure 5.31 (a2)). Conversely, in the film subjected to 5 laser pulses, the presence of 1-2 nm crystallites was observed (Figure 5.31 (b, b1, b3)) and confirmed by the detection of a few diffraction spots from FFT (Figure 5.31 (b2, b4)). The latter were visible both at the interface with the substrate and at the film's surface. In the sample treated with 100 pulses, highly ordered regions are evident in a particle with ~60 nm height (Figure 5.31 (c)). The monoclinic pattern previously found by GIXRD was confirmed by the FFT analysis, with no remarkable differences between the film-substrate interface and the film's surface (Figure 5.31 (c1-c4)).

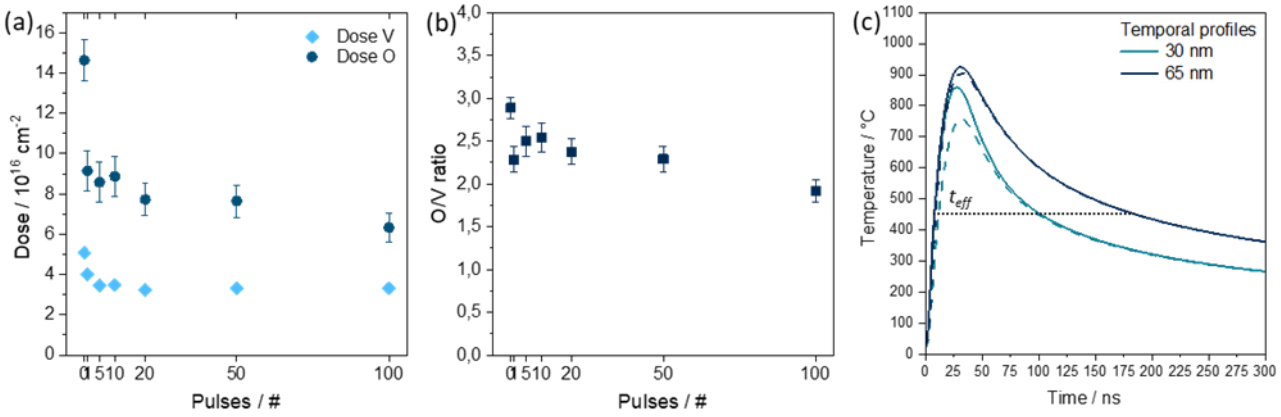


Figure 5.32. (a) Vanadium and oxygen doses measured by RBS as a function of the number of pulses used in different samples, with a fixed laser fluence of 70 mJ/cm^2.(b) Evolution of the ratio between O and V doses in function of the number of pulses. The length of the error bar of the vanadium dose is lower respect to the dimension of the representative spot. (c) Temperature profile simulations of VO_2 thin film upon a single laser pulse of 22 ns, with thickness of 30 nm and 65 nm, respectively. The solid lines represent the temperature profiles at the surface of the film, whereas the dashed lines represent the interface between the film and the substrate.

Finally, Rutherford backscattering (RBS) was used to evaluate the changes in atomic composition of the initial dried samples after laser irradiation. Figure 5.32 (a) reports the oxygen and vanadium dose variations with increasing laser pulses, which were then combined and expressed as stoichiometric variation through the O/V ratio (Figure 5.32 (b)). The initial O/V = 2.89 ± 0.12 of the dried film confirmed the formation of a partially pre-condensed film, which was dried at 100°C. If only unreacted $VO(acac)_2$ precursor was present, the ratio would have been O/V = 5. Within the first 5 pulses, the decrease of O/V ratio to 2.5 ± 0.18 highlighted the presence of V_2O_5, which is in line with the previous XPS analysis (paragraph 5.3.4).[1] With increasing pulse number, the stoichiometry was progressively reduced from 2.5 ± 0.18 (V_2O_5) to 1.92 ± 0.13 (VO_2). The progressive reduction in oxygen content and the trend of the corresponding O/V ratio match the GIXRD results, from which a gradual increase in crystalline VO_2 was seen, starting from 10 pulses. The oxygen dose showed higher changes in magnitude respect to vanadium, as expected. The latter decreased by 32% within

the first 5 pulses and was then stabilized at a constant value. The oxygen dose maintained a decreasing trend, with a higher loss of 38% within the first 5 pulses and a 57% decrease after 100 pulses.

Temperature profile simulations were performed to estimate the temperatures experienced by the film during the 22 ns laser pulse (Figure 5.32 (c)). The effect of film thickness was considered, as the initial ~65 nm thickness of the dried film evolved in an average ~30 nm nanostructured morphology shown by the TEM images (Figure 5.29). Peak temperatures of ~850-950°C were reached during a single laser pulse at 70 mJ/cm^2 for the 30-65 nm films, respectively. Both temperatures were considerably lower with respect to the melting temperature of VO_2 (1967°C in bulk state[93]). During the 22 ns pulse, temperature gradients of hundreds of degrees Celsius were developed between the film's surface and the interface with the substrate. These temperature gradients constituted the driving force for the diffusion of atoms, allowing the onset of the crystallization and boosting the conversion from the amorphous phase. The simulations were performed considering a single laser pulse and could not account for the variations of the sol-gel material upon each pulse, as different physical, optical, and thermal parameters would be needed upon each additional pulse. Physical and thermal properties of bulk VO_2 were used as the closest approximation, while ellipsometry was used to measure the optical properties of our reference crystalline VO_2 films. The simulations provide a useful tool to estimate the range of temperatures experienced by the material, which was found to be above the crystallization temperatures required for VO_2 but below the latter melting point.

6.5.2 *Laser-induced crystallization mechanism of VO_2 thin films*

The explanation of the laser-induced evolution of the thin films relies on the combination of all the characterizations, i.e., UV-Vis-NIR spectroscopy, GIXRD, SEM, TEM, AFM, and RBS. Within the initial 5-10 laser pulses, the morphology was already trending towards the final state, as the formation of small and big nanoparticles clearly appeared from AFM, SEM, and TEM and analysis. The morphological changes corresponded to slight variations in NIR transmittance, which was almost imperceptible for the first 5 pulses ($\Delta T_{2000\ nm}$ = 0.72%). This constituted an indirect proof of the formation of nanocrystallites within the amorphous network, which were then directly shown by TEM images and corresponding FFT/SAD (Figure 5.29, 5.31). The nanoscale dimension of these components prevented the crystalline phase from being detectable by GIXRD, which characterize the material at higher magnifications and only showed a peak from 20 pulses onwards. However, the presence of nanocrystallites was confirmed by NIR spectroscopy and SAD/FFT analysis.

The conventional furnace annealing led to a different morphology with respect to the laser-annealed ones, consisting of uniformly distributed bigger grains with numerous pores in between (Figure 5.29). The remarkable differences in morphology between laser- and furnace annealing confirmed that the amorphous-to-crystalline conversion did not rely on the same path. Conventional thermal annealing is based on equilibrium phenomena, during which the high temperatures induce a microstructural evolution based on sintering, grain growth and/or coarsening. Sintering is usually induced via solid-state, liquid-phase or viscous flow. During the former, atoms can migrate through the particle's surface, grain boundaries or crystal lattice, by either sublimation and recondensation or diffusion mechanisms. During sintering by viscous flow, the mass transport is highly favored by diffusion through the liquid phase, which fills the residual porosity. All these mechanisms are generated at equilibrium during furnace treatments, which usually require several minutes or hours to induce successful microstructural changes. Oppositely to conventional thermal annealing, nanosecond pulsed laser annealing is based on non-equilibrium reactions. Two key aspects are still under debate, the first is whether laser annealing is based on photochemical or photothermal-induced chemical reactions, the second is whether the ns laser pulses induce a solid-state or liquid-state driven reactions.[2,24]

Addressing the first aspect, multiple works on pulsed laser crystallization focus on epitaxial growth of thin films. According to Tsuchiya *et al.*[106], a photothermal effect cannot explain by itself the successful epitaxial crystallization of $LaMnO_3$ on $SrTiO_3$ but the failure on $LaAlO_3$ substrates. They addressed the latter to a lower laser absorption, which prevented the occurrence of photochemical reactions at the interface between film and substrate. On the contrary, Queralto *et al.*[99] attributed the epitaxial growth of several CSD thin films to a photothermal effect, after irradiating the samples at 400°C with 1000-20000 pulses of 3 ns with a Nd:YAG laser. In this work, ns pulsed laser annealing was exploited to grow polycrystalline thin films, without employing single crystal substrates nor controlled atmospheres. Fused silica substrates were chosen to exclude possible growth orientations induced by the substrate, to broaden the process applicability and allow possible extensions to polymeric supports. Crystallization on monocrystalline silicon substrates was also added as a comparison. Fused silica and monocrystalline silicon greatly differ in terms of structure (amorphous vs monocrystalline, respectively), laser wavelength absorption (~15% absorption at 248 nm vs ~1.1 eV band gap) and thermal diffusivity (~1.4 mm^2/s vs ~88 mm^2/s).[93,107] Photochemical reactions rely on the cleavage of chemical bonds, achievable when the laser photon energy overcomes the dissociation energy of the material's bonds. Most of the dissociation energies of V-O, C=O, C-O, C-C, H_3C-CH_3 (368-1077 kJ/mol[108]) were found to be higher with respect to the photon energy of the KrF excimer laser (482 kJ/mol). Even though the exact dissociation energies of the ligand bonds

might differ from the latter ones, it was previously shown that the organic component is removed within the first few pulses.[1] The film's absorption at the laser wavelength of 248 nm was ~70% (Figure 5.13) and varied by 7% at maximum with increasing laser pulses, remaining considerably higher respect to fused silica absorption. The evolution of the dried thin films under increasing laser pulses was examined by TEM, to detect the eventual formation of a preferential crystallization near the substrate and check whether the crystallization could still be influenced by the latter absorption. From the current data (Figure 5.31), no evidence of preferential crystalline growth at the interface between the thin film and the substrate was found. Even though the latter influences the temporal evolution of the generated heat, through high or low thermal diffusivity values, the VO_2 crystallization was reached on both fused silica and silicon substrates (paragraphs 5.3-5.5).

During laser irradiation, the laser photons are absorbed by the film and their energy is converted into heat. The remarkably high laser power (10^6-10^7 W/cm^2) and the local irradiation induce a thermal excitation over timescales of 10^{-3}-10^{-1} ns. The latter prevails on possible electronic excitations, which evolve over ps timescales during photochemical reactions.[109] Previous studies showed that the effective time (t_{eff}) is the key parameter during unconventional photonic annealing.[2,106,109] Several materials were found to share common t_{eff} values around 60 ns, defined as the time during which the temperature experienced by the film is higher than the crystallization temperature. In this case, the temperatures experienced by the film during the 22 ns laser pulse allowed for a sufficient t_{eff} above the crystallization threshold for VO_2 (M1). The latter is around ~450°C considering the average CSD VO_2 (M1) films in literature.[58,110]

The nucleation of the crystalline phase, i.e., the transformation from amorphous to crystalline, should be considered from both a thermodynamic and a kinetic point of view. Thermodynamically, the variations in Gibbs free energy (ΔG) are the driving force for the crystallization. ΔG is negative for spontaneous processes and lower temperatures favor the process ($\Delta G = \Delta H - T\Delta S$, with H enthalpy, T temperature and S entropy).[56] Kinetically, the diffusion of atoms governs both nucleation and consequent growth of the crystalline phase and is enhanced at high temperatures.

Considering the present case, the reaction evolution was pushed far from the equilibrium during the laser pulses. Prior to laser irradiation, the thin film displayed a gel structure, consisting of an amorphous network typical of the sol-gel process which could be related to a polymeric state. During the first few laser pulses, the polymer-like material seemed to undergo a viscous flow, which led to the initial formation of the fragmented big agglomerates as emerged from the combined results of GIXRD, AFM, SEM, TEM, FFT/SAD, RBS and previous XPS (paragraph 5.3). With increasing laser pulses, the material was transformed into a denser, prevalently inorganic, amorphous metal-oxide

network, but the transformation was not completed after 1 pulse. Upon each pulse, the material changed in terms of density, morphology, chemical composition, structural organization, electrical and thermal conductivity, which complicated the explanation of the laser-film interaction mechanism. The structural disorder present in the initially amorphous material limited the thermal diffusion of the absorbed laser energy. The initial organic component, due to the solvent residuals and the metal-organic nature of the vanadium precursor, was greatly reduced within the first few laser pulses and accompanied by a film densification. Small crystalline domains of 1-2 nm appeared within the amorphous network (Figure 5.31). The crystallinity degree gradually increased with increasing laser pulses, as confirmed both by GIXRD and UV-Vis-NIR spectroscopy (Figures 5.26, 5.24, respectively). This was accompanied by a change in chemical composition and morphology (Figures 5.7, 5.27, 5.28).

Within the first 5 pulses, a partial ~30% ablation was detected from RBS (Figure 5.32). Depending on the involved energy and material, ablation can occur through multiple mechanisms, from vaporization to sublimation to photochemical bond breaking.[2] By considering the dissociation bond energies, the KrF laser energy should not be high enough to induce direct bond breaking, at least of most bonds. The instability of the initial dried thin film, as compared to a final crystalline metal oxide, can allow for the partial photothermal ablation detected within the 1st and 5th pulses by RBS. The partial ablation was induced by the extreme temperature rise, occurring at higher temperatures respect to a glass transition one and probably leading to vaporization or sublimation. With increasing crystalline/amorphous ratio, the viscous flow would be harder to happen because a melting temperature would be established at specific values. The temperature profile simulations (Figure 6 (c)) revealed peak temperatures of ~900°C during a single laser pulse at 70 mJ/cm^2, notably lower than the melting temperature of VO_2. During the 22 ns pulse, temperature gradients of hundreds of degrees Celsius were developed between the film's surface and the interface with the substrate. These temperature gradients constituted the driving force for the diffusion of atoms, allowing the onset of the crystallization and boosting the conversion from the amorphous phase. Given the lower values with respect to the melting temperature of VO_2, it seems reasonable to consider the second stage to be governed by a solid-state diffusion.

6.5.3 *Laser-induced crystallization mechanism of VO_2 thin films – conclusions*

A synergic approach between the versatility of sol-gel reactions and ultrafast crystallization by pulsed laser annealing (PLA) was exploited for the development of VO_2 (M1) thin films. The

environmentally friendly process could be performed in air, without the need for a protected atmosphere. Similar thermochromic efficiencies could be reached through multiple combinations of parameters, highlighting the robustness of the process and the broad working window. Benefiting from the environmental moisture, the drying temperature before PLA was reduced to 100°C. This, combined with the selective film heating of PLA, enables future extension to plastic substrates.

The crystallization was found to start from the 5th pulse and full conversion to crystalline VO_2 (M1) was reached within a few seconds. The sol-gel laser-induced conversion was found to be based on two distinct mechanisms, an initial partial ablation followed by solid-state diffusion. Simulations of the temperature distribution revealed peak temperatures of ~900°C during a single laser pulse at 70 mJ/cm^2, notably lower than the melting temperature of VO_2. The temperature gradients of hundreds of degrees Celsius developed within the film constituted the driving force for the diffusion of atoms, allowing the onset of the crystallization and boosting the conversion from the amorphous phase.

6.6 Conclusions

In this Chapter 5, pulsed laser annealing was presented as an alternative to conventional furnace annealing for the crystallization of thermochromic VO_2 thin films.

In the first part (paragraph 5.3), the effect of laser fluence and pulse number was initially separately studied and then combined. The threshold laser parameters to induce the crystallization into VO_2 (M1) were found. The VO_2 crystallization was achieved within only 60 s of laser exposure and was performed at room temperature in air, after a 10 min drying step at 300°C. The eventual occurrence of surface melting was verified and the maximum fluence to avoid the former was identified. Temperature profile simulations were performed to evaluate the temperature distribution within a single pulse, in function of the ns pulse duration and the penetration depth. The simulations confirmed that the heat was confined within the film during the laser pulses, with negligible substrate heating.

All the laser-annealed samples in Chapter 5 exhibited a T_{lum} ranging between 60-80%, which is relatively high compared to the standard reported in literature for VO_2-only smart windows (~50%). The luminous transmittance was seen to decrease with increasing laser pulses, due to gradual formation of crystalline VO_2 along with the formation of a spontaneous nanostructured morphology (see paragraph 5.5). Further improvements of the thermochromic solar modulation (ΔT_{sol}~4.0%) will be discussed in Chapter 6, through the combination of VO_2 with other materials in multilayer configurations.

In the second part (paragraph 5.4), the versatility of sol-gel reactions was combined with the fast timescales of pulsed laser annealing (PLA) to investigate the width of the process working window. Similar thermochromic efficiencies could be reached through multiple combinations of parameters, highlighting the robustness of the process and the broad working window. Benefiting from the environmental moisture, the drying temperature before PLA was reduced to 100°C. This, combined with the selective film heating of PLA, enables future extension to plastic substrates. At the lowest drying temperature (T_d = 100°C) and at fixed film aging time and laser pulses (6 d, 100 #), the best thermochromic performance was obtained with mild 50% RH at 22°C during deposition ($\Delta T_{2000\ nm}$ = 22.9%, ΔT_{sol} = 4.0%, T_{lum} = 68.5%). If the drying step was kept at 100°C, increasing the RH during deposition to 70% and 90% at 22°C progressively led to a deterioration of the thermochromicity ($\Delta T_{2000\ nm}$ = 8.2-1.3%, respectively). Nonetheless, high thermochromic performance could still be obtained with a 90% RH deposition, by increasing the drying temperature to 150°C or above ($\Delta T_{2000\ nm}$ = 33.5% with T_d = 150°C and 300 pulses).

Considering the effect of film aging before laser annealing, remarkable differences were found between a few hours and 6 days. Allowing the condensation reactions to proceed for only 2 hours led to the formation of an unstable and partially formed V-O-V sol-gel network, with a resulting scarce film crystallization and insufficient thermochromic performance ($\Delta T_{2000\ nm}$ = 5.3%). Under the same conditions (50% RH, T_d 100°C), increasing the film aging to 6 days allowed for a proper stabilization of the gel network and a corresponding remarkable boost of the final thermochromic performance ($\Delta T_{2000\ nm}$ = 22.9%, T_{lum} = 68.5%).

With the goal of expanding the process working window, the dried thin films were aged for 10 months before laser annealing. At fixed deposition RH, drying temperature, and pulse number (50% RH – 22°C, 100°C, 100#), a comparable thermochromic performance was obtained after 10 months of aging ($\Delta T_{2000\ nm}$ = 19.0%, T_{lum} = 65.5%), with respect to 6 days. The dried thin films were found to guarantee a long-term stability before laser annealing, allowing for process flexibility compared to the more rigid timelines typically associated with sol-gel processes.

Since the interaction between ns laser pulses and vanadium-based sol gel thin films was not clearly understood, the results from grazing incidence X-ray diffraction (GIXRD), UV-Vis-NIR spectroscopy, atomic force microscopy (AFM), scanning and transmission electron microscopy (SEM, TEM), Rutherford backscattering spectrometry (RBS) were combined in paragraph 5.5, to gain in-depth knowledge on the laser-matter interaction.

The initial organic component, due to the solvent residuals and the metal-organic nature of the vanadium precursor, was greatly reduced within the first few laser pulses and accompanied by a film densification. Crystallization was found to start from the 5th pulse as crystalline domains of 1-2 nm appeared within the amorphous network. The crystallinity degree gradually increased with increasing laser pulses, as confirmed by GIXRD, UV-Vis-NIR spectroscopy, and TEM, and full conversion to crystalline VO_2 (M1) was reached within a few seconds.

The sol-gel laser-induced conversion was found to be based on two distinct mechanisms, an initial partial ablation followed by solid-state diffusion. Simulations of the temperature distribution revealed peak temperatures of ~900°C during a single laser pulse at 70 mJ/cm^2, notably lower than the melting temperature of VO_2. The temperature gradients of hundreds of degrees Celsius developed within the film constituted the driving force for the diffusion of atoms, allowing the onset of the crystallization and boosting the conversion from the amorphous phase.

Overall, laser annealing offers multiple advantages, in terms of versatility, easiness and scalability. Crystallization occurred within a matter of seconds and could be easily conducted in ambient air, with no need for an inert atmosphere. This constitutes a remarkable advantage when vanadium oxides are considered, as the latter usually require extremely controlled atmospheres during crystallization. The proposed approach is template-free and enables the simultaneous achievement of organic residue removal, densification, crystallization, and nanostructuring in a single step, allowing for time-, cost- and energy-savings.

References

1. Basso, M. *et al.* Rapid laser-induced low temperature crystallization of thermochromic VO2 sol-gel thin films. *Appl Surf Sci* **631**, (2023).

2. Yarali, E. *et al.* Recent Progress in Photonic Processing of Metal-Oxide Transistors. *Adv Funct Mater* **30**, 1–37 (2020).

3. Cao, X. *et al.* Challenges and Opportunities toward Real Application of VO2-Based Smart Glazing. *Matter* **2**, 862–881 (2020).

4. Li, Y. *et al.* Direct Laser Writing of Multishaped VO2 Microactuators Based on Freestanding VO2 Film. *Adv Mater Technol* **8**, 2200977 (2023).

5. Tan, G. *et al.* Broadband antireflection film with moth-eye-like structure for flexible display applications. *Optica* **4**, 678 (2017).

6. Twyman, N. M., Tetzner, K., Anthopoulos, T. D., Payne, D. J. & Regoutz, A. Rapid photonic curing of solution-processed In 2 O 3 layers on flexible substrates. *Appl Surf Sci* **479**, 974–979 (2019).

7. Carlos, E. *et al.* Laser induced ultrafast combustion synthesis of solution-based AlO: Xfor thin film transistors. *J Mater Chem C Mater* **8**, 6176–6184 (2020).

8. Chang, P. Y. *et al.* Near-Infrared Laser-Annealed IZO Flexible Device as a Sensitive H2S Sensor at Room Temperature. *ACS Appl Mater Interfaces* **12**, 24984–24991 (2020).

9. Seyfouri, M. M. & Binions, R. Sol-gel approaches to thermochromic vanadium dioxide coating for smart glazing application. *Solar Energy Materials and Solar Cells* **159**, 52–65 (2017).

10. Kim, J. & Paik, T. Recent advances in fabrication of flexible, thermochromic vanadium dioxide films for smart windows. *Nanomaterials* **11**, (2021).

11. Liu, K., Lee, S., Yang, S., Delaire, O. & Wu, J. Recent progresses on physics and applications of vanadium dioxide. *Materials Today* **21**, 875–896 (2018).

12. Wang, S. *et al.* Recent progress in VO2 smart coatings: Strategies to improve the thermochromic properties. *Prog Mater Sci* **81**, 1–54 (2016).

13. Im, T. H. *et al.* Flashlight-material interaction for wearable and flexible electronics. *Materials Today* **51**, 525–551 (2021).

14. Lee, W., Choi, S., Kim, J., Park, S. K. & Kim, Y. H. Solution-Free UV-Based Direct Surface Modification of Oxide Films for Self-Patterned Metal-Oxide Thin-Film Transistors. *Adv Electron Mater* **5**, (2019).

15. John, R. A. *et al.* Low-temperature chemical transformations for high-performance solution-processed oxide transistors. *Chemistry of Materials* **28**, 8305–8313 (2016).

16. Kim, Y. H. *et al.* Flexible metal-oxide devices made by room-temperature photochemical activation of sol-gel films. *Nature* **489**, 128–132 (2012).

17. Park, S. *et al.* In-Depth Studies on Rapid Photochemical Activation of Various Sol–Gel Metal Oxide Films for Flexible Transparent Electronics. *Adv Funct Mater* **25**, 2807–2815 (2015).

18. Kim, M. G., Kanatzidis, M. G., Facchetti, A. & Marks, T. J. Low-temperature fabrication of high-performance metal oxide thin-film electronics via combustion processing. *Nat Mater* **10**, 382–388 (2011).

19. Umeda, K. *et al.* Impact of UV/O3 treatment on solution-processed amorphous InGaZnO4 thin-film transistors. *J Appl Phys* **113**, 184509 (2013).

20. Rim, Y. S. *et al.* Direct light pattern integration of low-temperature solution-processed all-oxide flexible electronics. *ACS Nano* **8**, 9680–9686 (2014).

21. Carlos, E. *et al.* UV-Mediated Photochemical Treatment for Low-Temperature Oxide-Based Thin-Film Transistors. *ACS Appl Mater Interfaces* **8**, 31100–31108 (2016).

22. Asakuma, N. *et al.* Photocrystallization of amorphous ZnO. *J Appl Phys* **92**, 5707–5710 (2002).

23. Jo, Y. R., Lee, W. J., Yoon, M. H. & Kim, B. J. In Situ Tracking of Low-Temperature VO2Crystallization via Photocombustion and Characterization of Phase-Transition Reliability on Large-Area Flexible Substrates. *Chemistry of Materials* **32**, 4013–4023 (2020).

24. Palneedi, H. *et al.* Laser Irradiation of Metal Oxide Films and Nanostructures: Applications and Advances. *Advanced Materials* **30**, 1–38 (2018).

25. Excimer Laser Annealing (ELA) Market Size, Trend and Forecast to 2028. https://www.marketresearchintellect.com/global-excimer-laser-annealing-ela-market-size-and-forecast?utm_source=Pulse2&utm_medium=017.

26. Allemann, I. B. & Goldberg, D. J. Basics in dermatological laser applications. *Basics in Dermatological Laser Applications* **42**, 1–199 (2011).

27. Molaei, R., Bayati, M. R., Alipour, H. M., Estrich, N. A. & Narayan, J. Nanosecond laser switching of surface wettability and epitaxial integration of c-axis ZnO thin films with Si(111) substrates. *Journal of Physics: Condensed Matter* **26**, 015004 (2013).

28. Hou, Y. & Jayatissa, A. H. Effect of laser irradiation on gas sensing properties of sol–gel derived nanocrystalline Al-doped ZnO thin films. *Thin Solid Films* **562**, 585–591 (2014).

29. Kang, H. *et al.* Near-infrared light-responsive core-shell nanogels for targeted drug delivery. *ACS Nano* **5**, 5094–5099 (2011).

30. Dong, W. J., Ham, J., Jung, G. H., Son, J. H. & Lee, J. L. Ultrafast laser-assisted synthesis of hydrogenated molybdenum oxides for flexible organic solar cells. *J Mater Chem A Mater* **4**, 4755–4762 (2016).

31. Nakajima, T., Tsuchiya, T. & Kumagai, T. Pulsed laser-induced oxygen deficiency at TiO2 surface: Anomalous structure and electrical transport properties. *J Solid State Chem* **182**, 2560–2565 (2009).

32. Wang, X. *et al.* Reshaping the tips of ZnO nanowires by pulsed laser irradiation. *Nano Res* **5**, 412–420 (2012).

33. Xia, R. *et al.* Precision excimer laser annealed Ga-doped ZnO electron transport layers for perovskite solar cells. *RSC Adv* **8**, 17694–17701 (2018).

34. Park, Y. W. *et al.* Molecular beam epitaxy of large-area SnSe2 with monolayer thickness fluctuation. *2d Mater* **4**, 014006 (2016).

35. Molaei, R. *et al.* Diamagnetic to ferromagnetic switching in VO2 epitaxial thin films by nanosecond excimer laser treatment. *Appl Phys Lett* **103**, 252109 (2013).

36. Sundaram, S. K. & Mazur, E. Inducing and probing non-thermal transitions in semiconductors using femtosecond laser pulses. *Nat Mater* **1**, 217–224 (2002).

37. Palneedi, H. *et al.* Unleashing the Full Potential of Magnetoelectric Coupling in Film Heterostructures. *Advanced Materials* **29**, 1605688 (2017).

38. Bäuerle, D. Laser-CVD of Microstructures. *Laser Processing and Chemistry* 369–392 (2011).

39. Carpene, E., Höche, D. & Schaaf, P. Fundamentals of Laser-Material Interactions. *Springer Series in Materials Science* **139**, 21–47 (2010).

40. Poate, J. M. & Mayer, J. W. *Laser annealing of semiconductors*. (Academic Press, 1982).

41. Kang, B., Han, S., Kim, J., Ko, S. & Yang, M. One-step fabrication of copper electrode by laser-induced direct local reduction and agglomeration of copper oxide nanoparticle. *Journal of Physical Chemistry C* **115**, 23664–23670 (2011).

42. Brown, M. S. & Arnold, C. B. Fundamentals of Laser-Material Interaction and Application to Multiscale Surface Modification. *Springer Series in Materials Science* **135**, 91–120 (2010).

43. PE, H. G. Cm. *Manufacturing Engineering Handbook*. *Manufacturing Engineering Handbook* (McGraw-Hill Education, 2016).

44. Goddard, W. A. *Handbook of nanoscience, engineering, and technology*. (CRC Press, 2012).

45. Nakajima, T. & Tsuchiya, T. Flexible thermistors: pulsed laser-induced liquid-phase sintering of spinel Mn–Co–Ni oxide films on polyethylene terephthalate sheets. *J Mater Chem C Mater* **3**, 3809–3816 (2015).

46. Kim, W., Wang, R. & Majumdar, A. Nanostructuring expands thermal limits. *Nano Today* **2**, 40–47 (2007).

47. Otto, M., Kroll, M., Käsebier, T., Salzer, R. & Wehrspohn, R. B. Conformal Al2O3 Coatings on Black Silicon by Thermal ALD for Surface Passivation. *Energy Procedia* **27**, 361–364 (2012).

48. Li, D. & McGaughey, A. J. H. Phonon Dynamics at Surfaces and Interfaces and Its Implications in Energy Transport in Nanostructured Materials—An opinion Paper. *Nanoscale and Microscale Thermophysical Engineering* **19**, 166–182 (2015).

49. Joe, D. J. *et al.* Laser–Material Interactions for Flexible Applications. *Advanced Materials* **29**, 1606586 (2017).

50. Dellis, S. *et al.* Rapid laser-induced photochemical conversion of sol–gel precursors to In2O3 layers and their application in thin-film transistors. *J Mater Chem C Mater* **5**, 3673–3677 (2017).

51. Charipar, N. A. *et al.* Polycrystalline VO2 thin films via femtosecond laser processing of amorphous VOx. *Appl Phys A Mater Sci Process* **122**, 1–5 (2016).

52. Nishikawa, M., Nakajima, T., Manabe, T., Okutani, T. & Tsuchiya, T. High temperature coefficients of resistance of VO2 films grown by excimer-laser-assisted metal organic deposition process for bolometer application. *Mater Lett* **64**, 1921–1924 (2010).

53. Bordelet, G., Yamaguchi, I., Manabe, T. & Tsuchiya, T. Low temperature vanadium oxide thin film sintering by thermal and excimer-laser-assisted Metal-Organic Deposition (MOD). *Ceram Int* **44**, S26–S29 (2018).

54. Breckenfeld, E., Kim, H., Gorzkowski, E. P., Sutto, T. E. & Piqué, A. Laser-processing of VO 2 thin films synthesized by polymer-assisted-deposition. *Appl Surf Sci* **397**, 152–158 (2017).

55. Li-Bin, L., Tie-Cheng, L., Yong, L. & Qiang, L. Variation of morphology and color of VO2 thin films induced by excimer laser. *Nucl Instrum Methods Phys Res B* **191**, 102–105 (2002).

56. Green, Dr. D. W. & Southard, Dr. M. Z. *Perry's Chemical Engineers' Handbook*. *Perry's Chemical Engineers' Handbook* (McGraw-Hill Education, 2019).

57. Seyfouri, M. M. & Binions, R. Sol-gel approaches to thermochromic vanadium dioxide coating for smart glazing application. *Solar Energy Materials and Solar Cells* **159**, 52–65 (2017).

58. Pan, M. *et al.* Properties of VO2 thin film prepared with precursor VO(acac)2. *J Cryst Growth* **265**, 121–126 (2004).

59. Zhang, Z. *et al.* Thermochromic VO2 thin films: Solution-based processing, improved optical properties, and lowered phase transformation temperature. *Langmuir* **26**, 10738–10744 (2010).

60. Melia, T. P. & Merrifield, R. Thermal properties of acetylacetone. *J. Appl. Chem.* **19**, 79–82 (2007).

61. Von Hoene, J., Charles, R. G. & Hickam, W. M. Thermal decomposition of metal acetylacetonates mass spectrometer studies. *Journal of Physical Chemistry* **62**, 1098–1101 (1958).

62. Nenashev, R. N., Mordvinova, N. E., Zlomanov, V. P. & Kuznetsov, V. L. Thermal decomposition of vanadyl acetylacetonate. *Inorganic Materials* **51**, 891–896 (2015).

63. Sandu, C. S. *et al.* Densification and crystallization of SnO 2 :Sb sol-gel films using excimer laser annealing. *Appl Surf Sci* **208–209**, 382–387 (2003).

64. Tsay, C. Y. & Wang, M. C. Structural and optical studies on sol-gel derived ZnO thin films by excimer laser annealing. *Ceram Int* **39**, 469–474 (2013).

65. With, P. C. *et al.* Photochemical low-temperature synthesis of iron(III) oxide thin films. *Appl Surf Sci* **493**, 525–532 (2019).

66. Dupin, J. C., Gonbeau, D., Vinatier, P. & Levasseur, A. Systematic XPS studies of metal oxides, hydroxides and peroxides. *Physical Chemistry Chemical Physics* **2**, 1319–1324 (2000).

67. Çopurogìlu, M., Sezen, H., Opila, R. L. & Suzer, S. Band-bending at buried SiO2/Si interface as probed by XPS. *ACS Appl Mater Interfaces* **5**, 5875–5881 (2013).

68. With, P. C. *et al.* Low-Temperature Photochemical Conversion of Organometallic Precursor Layers to Titanium(IV) Oxide Thin Films. *Chemistry of Materials* **28**, 7715–7724 (2016).

69. Kim, H. *et al.* Flexible thermochromic window based on hybridized VO2/graphene. *ACS Nano* **7**, 5769–5776 (2013).

70. Zhang, J. *et al.* Evolution of Structural and Electrical Properties of Oxygen-Deficient VO2 under Low Temperature Heating Process. *ACS Appl Mater Interfaces* **9**, 27135–27141 (2017).

71. Silversmit, G., Depla, D., Poelman, H., Marin, G. B. & De Gryse, R. Determination of the V2p XPS binding energies for different vanadium oxidation states (V5+ to V0+). *J Electron Spectros Relat Phenomena* **135**, 167–175 (2004).

72. Lopez, R., Boatner, L. A. & Haynes, T. E. Synthesis and characterization of size-controlled vanadium dioxide nanocrystals in a fused silica matrix. *J Appl Phys* **92**, 4031 (2002).

73. Tsuchiya, T., Nakajima, T., European, Y. U.-C. & 2020, undefined. Flexible and Epitaxial Metal Oxide Thin Film Growth by Photoreaction Processing for Electrical and Optical Applications. *Wiley Online Library* **2020**, 9261–9276 (2020).

74. Rogers, K. D. An X-ray diffraction study of semiconductor and metallic vanadium dioxide. *Powder Diffr* **8**, 240–244 (1993).

75. Yao, L. *et al.* Long-Lived Multilayer Coatings for Smart Windows: Integration of Energy-Saving, Antifogging, and Self-Healing Functions. *ACS Appl Energy Mater* **2**, 7467–7473 (2019).

76. Zhang, C. *et al.* Characterization of vanadium oxide thin films with different stoichiometry using Raman spectroscopy. *Thin Solid Films* **620**, 64–69 (2016).

77. Kallel, T., Dammak, M., Wang, J. & Jadwisienczak, W. M. Raman characterization and stress analysis of AlN:Er 3+ epilayers grown on sapphire and silicon substrates. *Materials Science and Engineering B* **187**, 46–52 (2014).

78. Quackenbush, N. F. & State University of New York at Binghamton. Department of Physics, A. P. and Astronomy. The physics of ultra-thin vanadium dioxide: At the surface, interface and in-between. *PhDT* (2016).

79. Ji, Y. X., Li, S. Y., Niklasson, G. A. & Granqvist, C. G. Durability of thermochromic VO2 thin films under heating and humidity: Effect of Al oxide top coatings. *Thin Solid Films* **562**, 568–573 (2014).

80. Tanuma, S., Powell, C. J. & Penn, D. R. Calculations of electron inelastic mean free paths. V. Data for 14 organic compounds over the 50–2000 eV range. *Surface and Interface Analysis* **21**, 165–176 (1994).

81. Winfield, R. J., Koh, L. H. K., O'Brien, S. & Crean, G. M. Excimer laser processing of ZnO thin films prepared by the sol-gel process. *Appl Surf Sci* **254**, 855–858 (2007).

82. Joya, Y. F. & Liu, Z. Effect of the excimer laser irradiation on sol-gel derived tungsten-titanium dioxide thin films. *Appl Phys A* **102**, 91–97 (2011).

83. Wu, J. *et al.* Effect of annealing temperature on thermochromic properties of vanadium dioxide thin films deposited by organic sol-gel method. *Appl Surf Sci* **268**, 556–560 (2013).

84. Yu, J. H. *et al.* Thermal aging effect of vanadyl acetylacetonate precursor for deposition of VO2 thin films with thermochromic properties. *Mater Res Bull* **82**, 11–15 (2016).

85. Santos, A. J. *et al.* A simple two-step approach to the fabrication of VO2-based coatings with unique thermochromic features for energy-efficient smart glazing. *Energy Build* **285**, 112892 (2023).

86. Ersundu, A. E., Çelikbilek Ersundu, M., Doğan, E. & Güven, M. B. A comparative investigation on thermal, structural and optical properties of W and Nb-doped VO2-based thermochromic thin films. *Thin Solid Films* **700**, (2020).

87. Houska, J., Kolenaty, D., Rezek, J. & Vlcek, J. Characterization of thermochromic VO 2 (prepared at 250 °C) in a wide temperature range by spectroscopic ellipsometry. *Appl Surf Sci* **421**, 529–534 (2017).

88. Hoglund, D. E. & Thompson, M. O. Experimental test of morphological stability theory for a planar interface during rapid solidification. *Phys Rev B Condens Matter Mater Phys* **58**, 189–199 (1998).

89. Kizuka, H. *et al.* Temperature dependence of thermal conductivity of VO2 thin films across metal-insulator transition. *Jpn J Appl Phys* **54**, 053201 (2015).

90. Touloukian, Y. S., Powell, R. W., Ho, C. Y. & Klemens, P. *Thermophysical properties of matter - Thermal conductivity: nonmetallic solids*. https://www.osti.gov/biblio/5303523 (1970).

91. Matsubayashi, Y., Nomoto, J., Yamaguchi, I. & Tsuchiya, T. Control of the oxygen deficiency and work function of SrFeO3-δ thin films by excimer laser-assisted metal organic decomposition. *CrystEngComm* **22**, 4685–4691 (2020).

92. Currie, M., Mastro, M. A., Wheeler, V. D., Davis, . M K & Digonnet, M. J. F. Characterizing the tunable refractive index of vanadium dioxide. *Opt Mater Express* **7**, 1697–1707 (2017).

93. Haynes, W., Lide, D. & Bruno, T. *CRC Handbook of Chemistry and Physics*. *CRC Handbook of Chemistry and Physics* (CRC Press, 2016).

94. Maklakov, S. S. *et al.* Post-deposition annealing of thin RF magnetron sputter-deposited VO2 films above the melting point. *J Alloys Compd* **763**, 558–569 (2018).

95. Kang, M. *et al.* Optical characteristics of amorphous V2O5 thin films colored by an excimer laser. *Current Applied Physics* **12**, 489–493 (2012).

96. Fiaschi, G. *et al.* Effect of laser annealing on ZnO nanorods grown by chemical bath deposition on flexible substrate. *Appl Surf Sci* **458**, 800–804 (2018).

97. Samotus, A., Grybos, R., Popova, N. & Bogolitsyn, K. Kinetics of oxidation of vanadyl acetylacetonate by oxygen in methanolic solution. **64**, 2–5 (1997).

98. Van Der Voort, P., White, M. G. & Vansant, E. F. Thermal Decomposition of VO(acac)2 Deposited on the Surfaces of Silica and Alumina. *Langmuir* **14**, 106–112 (1998).

99. Queraltó, A. *et al.* Ultrafast Epitaxial Growth Kinetics in Functional Oxide Thin Films Grown by Pulsed Laser Annealing of Chemical Solutions. *Chemistry of Materials* **28**, 6136–6145 (2016).

100. Nakajima, T., Tsuchiya, T., Ichihara, M., Nagai, H. & Kumagai, T. Epitaxial growth mechanism for perovskite oxide thin films under pulsed laser irradiation in chemical solution deposition process. *Chemistry of Materials* **20**, 7344–7351 (2008).

101. Santos, A. J. *et al.* Facile Fabrication of High-Performance Thermochromic VO2-Based Films on Si for Application in Phase-Change Devices. *Chemistry of Materials* **35**, 4435–4448 (2023).

102. Bhupathi, S. *et al.* Femtosecond Laser-Induced Vanadium Oxide Metamaterial Nanostructures and the Study of Optical Response by Experiments and Numerical Simulations. *ACS Appl Mater Interfaces* **12**, 41905–41918 (2020).

103. Ke, Y. *et al.* Controllable Fabrication of Two-Dimensional Patterned VO2 Nanoparticle, Nanodome, and Nanonet Arrays with Tunable Temperature-Dependent Localized Surface Plasmon Resonance. *ACS Nano* **11**, 7542–7551 (2017).

104. Zimbone, M. *et al.* Low-temperature atomic layer deposition of TiO2 activated by laser annealing: Applications in photocatalysis. *Appl Surf Sci* **596**, 153641 (2022).

105. Colusso, E. *et al.* Pulsed laser crystallization of sol-gel derived cerium oxide thin films. *J Solgel Sci Technol* 1–12 (2023).

106. Tsuchiya, T., Nakajima, T. & Uzawa, Y. Flexible and Epitaxial Metal Oxide Thin Film Growth by Photoreaction Processing for Electrical and Optical Applications. *Chemistry - A European Journal* **26**, 9261–9276 (2020).

107. Battaglia, C., Cuevas, A. & De Wolf, S. High-efficiency crystalline silicon solar cells: status and perspectives. *Energy Environ Sci* **9**, 1552–1576 (2016).

108. Speight, Dr. J. G. *Lange's Handbook of Chemistry*. (McGraw-Hill Education, 2017).

109. Bretos, I., Jiménez, R., Ricote, J. & Calzada, M. L. Low-temperature crystallization of solution-derived metal oxide thin films assisted by chemical processes. *Chem Soc Rev* **47**, 291–308 (2018).

110. Gao, Y. *et al.* Nanoceramic VO 2 thermochromic smart glass: A review on progress in solution processing. *Nano Energy* **1**, 221–246 (2012).

Chapter 6
Multifunctional bilayers

Table of contents

6 Chapter 6 – Multifunctional bilayers 271

6.1 Introduction 273

6.1.1 Principles of antireflective layers 275

6.2 TiO_2 – VO_2 bilayers 276

6.2.1 Synthesis, deposition and annealing of VO_2 thin films 276

6.2.2 Synthesis and deposition of TiO_2 films 276

6.2.3 Crystallization of TiO_2 films 279

6.2.4 TiO_2 – VO_2 bilayers 282

6.2.4.1 Structural and morphological analysis of TiO_2 – VO_2 bilayers 282

6.2.4.1.1 Influence of VO_2 on the anatase-rutile transition of TiO2 282

6.2.4.1.2 Elemental interdiffusion 284

6.2.4.1.3 Influence of TiO_2 on VO_2 crystallization 287

6.2.4.2 Optical and electrical properties of TiO_2 – VO_2 bilayers 288

6.2.4.2.1 Simulations of luminous transmittance of TiO_2 – VO_2 bilayers 288

6.2.4.2.2 TiO_2 thickness influence on luminous transmittance of bilayers 290

6.2.4.2.3 Optical properties of “low diffusion” bilayers 291

6.2.4.2.4 Optical properties of “high diffusion” bilayers 292

6.2.4.2.5 Optical and electrical hysteresis of bilayers 293

6.3 VO_2 – SiO_2 bilayers 295

6.3.1 Synthesis and deposition of VO_2 films 296

6.3.2 Synthesis and deposition of hybrid SiO_2 coatings 296

6.3.2.1 Methyl-modified SiO_2 coating 296

6.3.2.2 Octyl-modified SiO_2 coating 297

6.3.3 Optical properties of VO_2 – hybrid SiO_2 bilayers 297

6.3.4 Durability tests 301

6.4 Multifunctional bilayers – conclusions 303

7.1 Introduction

VO_2 thin films display promising prospectives in terms of applicability for thermochromic smart windows. The latter is currently prevented by the unsolved challenges of VO_2 thin films, which were discussed in paragraph 3.7 of Chapter 3. One of the most crucial challenges concerns the achievement of high values of solar modulation (ΔT_{sol}) simultaneously with high luminous transmittance (T_{lum}). Multiple studies highlighted that the two parameters follow an anti-synergic behavior, as the increase in ΔT_{sol} usually leads to the decrease in T_{lum}, and viceversa. The minimum values generally required are $\Delta T_{sol} > 10\%$ along with $T_{lum} > 50\%$.[1] Another crucial challenge concerns the improvement of the coating's durability against weathering, as VO_2 can be partially oxidized to V_2O_5 under exposure to high levels of moisture.[1,2]

Most solutions involved morphological modifications, in terms of micro- or nanostructuring, as well as doping and/or combinations of multiple materials (Figure 6.1). Successful solutions include multilayered structures[3,4], nanocomposites based on VO_2 nanoparticles, core-shell particles[5], porous coatings[6], laser texturing[7], nano stripe morphologies[8], hybrid organic-inorganic coatings[9,10], and bioinspired patterns. The latter include nano cones[11], wood-based devices[12], and cephalopod-inspired[13] morphologies.

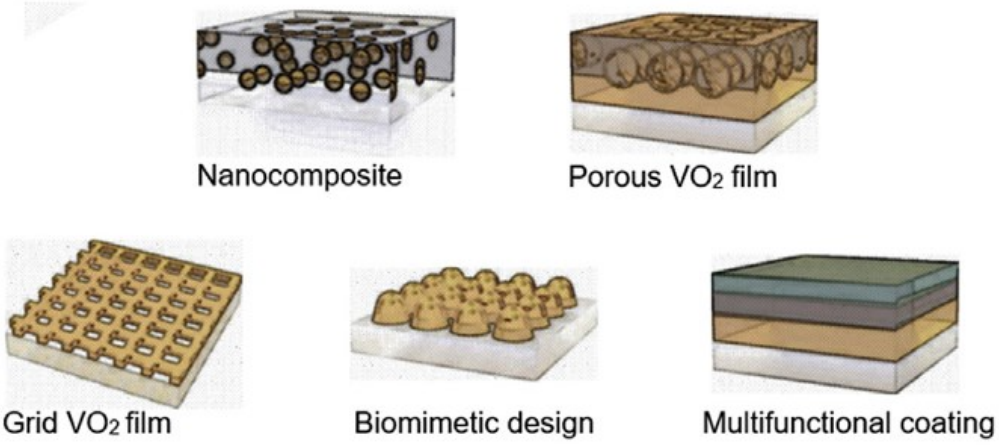


Figure 6.1. Examples of morphological modifications of the VO_2 thin films and/or combinations with different materials.[1,2]

Among the multiple available options, sol-gel based multilayered coatings offer advantages in terms of simplicity of fabrication, scalability, and mechanical resistance, with respect to micro- or nanostructuring techniques. Oxide materials such as TiO_2[14], SiO_2[15,16], ZrO_2[17], CeO_2[18], Cr_2O_3[19], Al_2O_3[20] are among the most popular choices for antireflection and/or buffer layers in a multilayered configuration. In this PhD research, TiO_2 and SiO_2 were selected to improve the luminous transmittance and durability of VO_2 in a multilayer configuration.

TiO_2 displays high chemical stability and mechanical resistance, high refractive index values and low toxicity.[21] The low lattice mismatch between rutile TiO_2 and the high-temperature metallic phase of VO_2 favors the reduction of stresses which are often induced by matching different materials.[2,22,23] The photocatalytic properties of TiO_2 offer an additional advantage for the creation of multifunctional self-cleaning and thermochromic windows. Recently, a synergy between the thermochromic, luminous and photocatalytic effects was reported by Ji *et al.*[24] for a TiO_2/VO_2 configuration.

SiO_2 displays intrinsically low refractive index values, high transparency in the visible range, excellent chemical stability, and high mechanical resistance.[25,26] The wettability of the sol-gel SiO_2 coatings can be modified by introducing organic groups within the inorganic network, leading to an increased hydrophobicity of the surface. As discussed in Chapter 2, the higher hydrophobicity allows for a more efficient removal of condensed water droplets, which in turns can enhance the durability of the smart window.

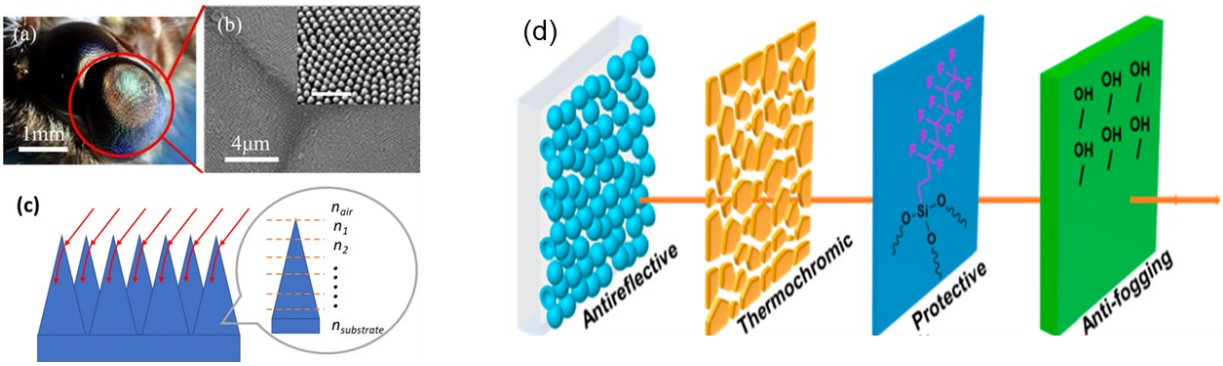


Figure 6.2. (a, b, c) Bioinspired morphological modifications combined with matching of multiple materials. Ref.[11] *(d) Schematic illustration of the design of HSi/V/FSi/P multilayer coating, consisting of an antireflective hollow SiO_2 layer, a thermochromic VO_2 layer, a protective fluorosilane−SiO_2 layer, and an antifogging cross-linked poly(vinyl alcohol) and poly(acrylic acid) layer. Ref.*[27]

Wu *et al.*[3] deposited VO_2/TiO_2 bilayers by magnetron sputtering and, following simulations on the optimal thicknesses, obtained T_{lum} = 42.29% and ΔT_{sol} = 16.03%. Liu *et al.*[11] exploited both morphological modifications and combination of multiple materials to create a bioinspired bilayered coating (Figure 6.2 (a, b)). The latter was based on a thermochromic VO_2 layer, coated by an antireflective TiO_2 layer with nano-cones structures (Figure 6.2 (c)). The optimized bilayer displayed T_{lum} = 55.4% and ΔT_{sol} = 11.3%. Mlyuka *et al.*[28] proposed a penta-layered configuration of $TiO_2/VO_2/TiO_2/VO_2/TiO_2$, with T_{lum} = 45.0% and ΔT_{sol} = 12.1%.

Powell *et al.*[4] combined the VO_2, SiO_2, and TiO_2 materials in a $VO_2/SiO_2/TiO_2$ configuration, with overall high ΔT_{sol} = 15.3% but improvable T_{lum} = 17.8%. Yao *et al.*[27] created a multifunctional coating consisting of an antireflective hollow SiO_2 layer, a thermochromic VO_2 layer, a protective fluorosilane−SiO_2 layer, and an antifogging cross-linked poly(vinyl alcohol) and poly(acrylic acid)

layer, which displayed ΔT_{sol} = 16.4% and T_{lum} = 54.0% (Figure 6.2 (d)). The VO_2 films were synthesis by CSD method, starting from the V_2O_5 powder. The same group[29] compared different morphologies, i.e. semi-domes, honeycomb, and hexagonal lattice, in a multilayered configuration. The best efficiency was reached with the hexagonal lattice, which displayed ΔT_{sol} = 9.9% and T_{lum} = 79.3%. The optimized morphologies displayed high water contact angles, along with superhydrophobicity ($\Theta > 150°$) in the case of the semi-domes configuration.

7.1.1 *Principles of antireflective layers*

The working principle underneath antireflective coatings (ARCs) is based on the proper tuning of destructive interferences, which can be achieved by choosing and designing the properties, thicknesses, and interfacial characteristics of the involved materials. The refractive index n of a material describes the light speed within the material with respect to vacuum. Considering a ray of light passing through two different materials of refractive indices n_1 and n_2, interference phenomena are generated at the interface between air (n_0) and the first material (n_1) and at interface between the latter and the second material (n_2). Generally, a perfectly antireflective material should possess broadband, omnidirectional, and polarization-insensitive anti-reflectivity.[30]

To induce the formation of destructive interferences, two key parameters can be tuned, namely the optical thickness and the refractive index of each material involved. From the Fresnel law, assuming that only a single wave with the same intensity is reflected per interface and that scattering, absorption or other optical interactions are negligible, the ideal n_c for a homogeneous ARC would need to be[31]:

1. $n_c = (n_a\, n_s)^{1/2}$, with n_a and n_s of air and substrate, respectively.
2. $d = \lambda/4n_c$, with d coating's thickness and λ incident wavelength.

Following from the above requirements, the optical thickness of the optimized ARC would need to be an odd multiple of $\lambda/4$. Two common strategies for the optimization of bilayers are hence based on tuning the optical thickness of the films in either a quarter-quarter waved structure, or a quarter-three quarter waved structures.[30]

Under the previous assumptions, the reflection (R) of a bilayer under a normal incidence is given by Eq. 6.1[30]:

$$R = \left[\frac{n_2^2 n_0 - n_s n_1^2}{n_2^2 n_0 + n_s n_1^2}\right] \tag{6.1}$$

With n_s substrate, $n_0 = 1$ air, n_1 top ARC layer, n_2 bottom layer.

Within this work, the investigated materials were VO_2, SiO_2, and TiO_2, which were deposited on either silicon or fused silica substrates. The refractive index of each material was measured by ellipsometry measurements, and the values were compared at a fixed wavelength. SiO_2 displays lower refractive index of $n_{550\ nm} = 1.4 – 1.5$ with respect to VO_2 and TiO_2 ($n_{550\ nm} = 2 – 2.5$). The above model is based on strong assumptions, such as the singular reflected wavelength per interface and the negligible remaining optical phenomena, therefore it was used as a qualitative reference for the materials' choice. Transfer-matrix model-based simulations were performed in the case of TiO_2–VO_2 bilayers, to optimize the thickness of both layers to reach the highest luminous transmittance.

7.2 TiO_2 – VO_2 bilayers

As previously mentioned, TiO_2 displays high chemical stability and mechanical resistance, high refractive index values, low toxicity, and low lattice mismatch with the metallic phase of VO_2.[2,21–23] Moreover, a favorable synergy between the thermochromic, luminous and photocatalytic properties from the TiO_2 – VO_2 configuration.[24] Therefore, TiO_2 – VO_2 bilayers were investigated to verify the eventual increase in visible transmittance of VO_2 films. The mutual influence on crystallinity and morphology was also considered.

7.2.1 *Synthesis, deposition and annealing of VO_2 thin films*

The synthesis, deposition, and furnace annealing of VO_2 thin films was performed according to the procedure reported in paragraph 4.3.2.2 of Chapter 4.

7.2.2 *Synthesis and deposition of TiO_2 films*

The synthesis of the initial solution was adapted from the work of Paz *et al.*[32] 4,5 mL of titanium (IV) isopropoxide ($Ti(OCH(CH_3)_2)_4$) were mixed with 10 mL of 1-propanol and 1,6 mL of acetylacetone. The normal propanol solvent was used to tune the viscosity of the solution, while acetylacetone was used to coordinate the titanium precursor and decrease the reactivity of the latter, as discussed in paragraph 1.2.3.1 of Chapter 1. The reaction between the two components is slightly exothermic. 1 mL of the previous solution were then extracted, and 1,615 mL of 1-propanol and 0,190 ml of

deionized water were added to the former. Water was added to induce the hydrolysis of the titanium precursor. Solution B was stirred for a few minutes to allow proper homogenization. The solution was deposited within 1 h from the water addition by spin coating. Each substrate, i.e. fused silica or single-crystalline silicon, was cleaned and treated with an atmospheric plasma cleaner before the solution deposition. The spin rate was varied from 1000 to 4000 rpm for 1 min depending on the target thickness. Each as-deposited film was dried at 200°C for 10 minutes prior to the deposition of the subsequent layer.

To find the target thicknesses for TiO_2 – VO_2 bilayers, transfer-matrix model-based simulations were performed to find the combinations with the highest luminous transmittance. To briefly anticipate the results (paragraph 6.2.4.2.1), VO_2 displayed a higher absorption in the visible range, resulting in a severe drop of luminous transmittance (T_{lum}) with increasing thickness of the VO_2 layer. On the contrary, the increasing thickness (t) of the TiO_2 layer over a fixed VO_2 layer led to the presence of two ranges of maximum T_{lum}, with t ~ 0-25 nm and t ~ 125-175 nm.

The TiO_2 film thickness was hence optimized as previously done for VO_2 thin films (paragraph 4.3.6 of Chapter 4). Two approaches were tested, i.e., varying the spin coating rate and increasing the number of layers. In the first approach, thin films were deposited at 1000, 2000 and 4000 rpm, respectively. Each film was dried at 200°C for 10 min and subsequently annealed in a box furnace in air at 550°C for 1 h at 10°C/min, which led to the crystallization into anatase TiO_2. The GIXRD results will be discussed in the following paragraph 6.2.3. Each sample was named with the first position to represent the substrate type (letter S = silicon), the second position to represent the number of deposited layers, the third position to represent the material (letter T = TiO_2), and the eventual subscript to report the spin coating rate. For example, $S1T_{4000\ rpm}$ represents 1 layer of TiO_2 film, which was spin coated at 4000 rpm on a silicon substrate.

Table6.1. Effect of spinning rate on the thickness for single-layer of TiO_2.

		Before annealing		After annealing		
Sample	Speed (rpm)	t (nm)	n_{600nm}	t (nm)	n_{600nm}	t reduction (%)
$S1T_{4000}$	4000	52	1.92	36	2.15	31
$S1T_{2000}$	2000	71	1.92	50	2.12	30
$S1T_{1000}$	1000	108	1.88	70	2.11	34

The film thickness before and after annealing is reported in Table 6.1. After annealing, a reduction in thickness of ~30% and an increase in optical constants of 11-12% were observed in all samples, regardless of the thickness.

Table 6.2. Values of the thickness for single-layer of TiO_2 of identical samples deposited on Si substrates at 1000 rpm and dried at 250°C 5 min.

	Before annealing		After annealing	
Sample	t (nm)	n_{600nm}	t (nm)	n_{600nm}
(1) S1T	90	1.96	64.5	2.13
(2) S1T	89	1.97	64.5	2.12
(3) S1T	87	1.99	64.6	2.21

The reproducibility of the thickness values was verified. Table 6.2 reports the thickness and refractive index values of 3 samples spin coated at the same condition of 1000 rpm for 1 min, dried at 250°C for 5 min and annealed at 550°C for 1 h. After annealing, the average thickness and $n_{600\,nm}$ were found to be 64.5 ± 0.1 and 2.15 ± 0.05, respectively. The results agree with the work of Londhe *et al.*[33], who reported a thickness of 55 ± 5 nm at 1000 rpm and ~40 ± 5 nm at 3000 rpm for sol-gel spin-coated TiO_2 thin films.

Table 6.3. Effect of the number of depositions on the thickness post-annealing of TiO_2 layer.

Sample	Speed (rpm)	t (nm)	n_{600nm}
S1T	2000	48	2.12
S2T	2000	95	2.24
S3T	2000	142	2.22

A second approach for a higher film thickness was tested, by increasing the number of deposited layers. Table 6.3 reports the effect on the thickness of 1 to 3 layers at spin coating rate of 2000 rpm, which were all annealed at 550°C in air for 1 h**.** After annealing, the thickness increased by ~47 nm with each deposited layer.

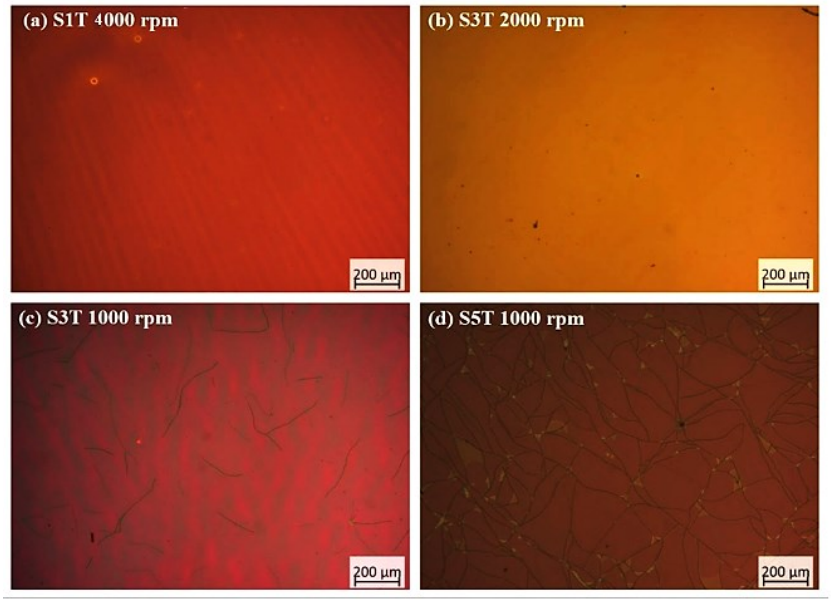


Figure 6.3. Optical microscope images of as-deposited different thicknesses layers of TiO_2: (a) ~50 nm, (b) ~140nm, (c)~300nm, starting cracking, (d) ~500nm, severely cracked.

The optical microscope was used to verify the quality of the deposited films. A single layer spin coated at 4000 rpm displayed a high homogeneity (Figure 6.3 (a)). The maximum achievable thickness of TiO_2 films, without compromising the film quality, was verified. A spin rate of 1000 rpm was initially fixed and the number of layers were consecutively increased. From the previous results (Table 6.3), each single layer was ~100 nm before annealing. Widespread cracks were formed after the 5th consecutive deposition (Figure 6.3 (d)), but smaller cracks were also detected in the S3T sample (Figure 6.3 (c)). To achieve high thickness values of hundreds of nm, higher speed rates (i.e. 2000 rpm), along with a higher number of deposited layer (i.e., 3L) were found to be a better solution. From Figure 6.3 (b), $S3T_{2000\ rpm}$ did not show any cracks.

7.2.3 *Crystallization of TiO_2 films*

Rutile TiO_2 is considered an ideal buffer layer due to the higher stability and lower lattice mismatch with the crystalline structure of monoclinic VO_2, respect to the anatase phase of TiO_2. However, the TiO_2 anatase phase is thermodynamically favored at relative low temperatures (i.e., 400-600°C) when nanometric films are deposited, due to the lower surface energy of the former.[34]

Prior to the deposition of TiO_2 – VO_2 multilayers, the TiO_2 sol gel synthesis was employed to investigate under which conditions the crystallization of TiO_2 rutile phase would be possible. For thin films, the rutile phase is usually obtained by annealing at 900-1000°C.[35]

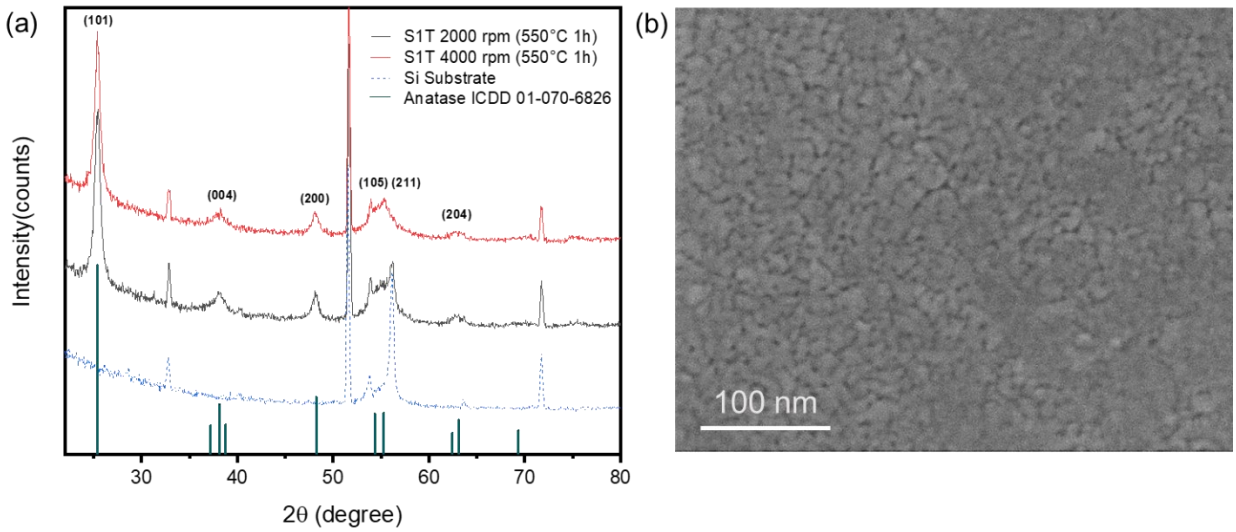


Figure 6.4. (a) GIXRD of anatase TiO_2 thin films of different thicknesses, obtained after 1 hour 550°C annealing in air, along with ICDD 01-070-6826 reference pattern.[36] *(b) SEM image (In Lens) of SIT (2000rpm) post-annealing at 550°C for 1 h.*

From the previous paragraph, the xerogels spin coated at various rotation speeds (i.e., 4000, 2000, 1000 rpm) and annealed in a box furnace in air at 550°C for 1 h displayed different thicknesses (~35, ~50, ~70 nm, respectively). The GIXRD analysis of the latter samples is reported in Figure 6.4 (a). As can be seen, the anatase phase of TiO_2 was obtained, which displays the typical predominant (1 0 1) orientation at 2Θ ~ 25.4°. The GIXRD pattern of silicon substrate is reported for reference. The TiO_2 thin film morphology of the anatase phase was found to be compact and homogeneous by SEM analysis (Figure 6.4 (b)).

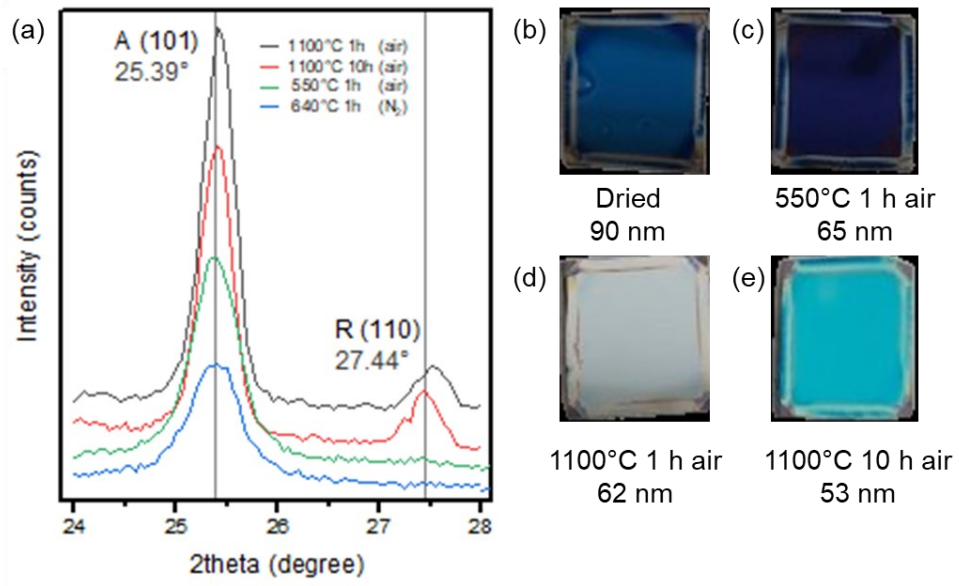


Figure 6.5. (a) GIXRD of SIT samples undergone to different thermal treatments, main peaks for anatase and rutile are shown; (b) Images of TiO_2 thin films deposited on Si and annealed under different conditions. The thickness of the TiO_2 layer was measured by ellipsometry.

Following the crystallization at 550°C of TiO_2 films of different thicknesses, different annealing atmospheres and temperatures were considered. Regarding the former, the crystallization of TiO_2 was

investigated under inert atmosphere. This was done considering the annealing atmosphere required for the VO_2 crystallization. As shown in Figure 6.5 (b), the crystallization to TiO_2 anatase phase was found to be possible under a nitrogen atmosphere as well, besides the conventional annealing in air.

Regarding the annealing temperatures, identical samples were spin coated at 1000 rpm spin rate and annealed at 550°C or 1100°C for 1 h in air. The latter temperature was chosen according to the literature, according to which temperatures higher than 800°C are required for the crystallization of the rutile phase.[37] As visible from Figure 6.5 (a), annealing at 1100°C for 1 h in air a mixed oxide phase was obtained, with the sample displaying both anatase ($2\Theta \sim 25.4°$) and rutile ($2\Theta \sim 27.5°$) phase. From ellipsometry measurements, an increase of refractive index *n* was seen by increasing the annealing temperature from 550°C ($n_{600\,nm} \sim 2.13$) to 1100°C ($n_{600\,nm} \sim 2.28$), which is consistent with the presence of rutile, besides anatase.[38] The thickness of the dried xerogel decreased from ~90 nm to ~65 nm and ~62 nm after annealing at 550°C or 1100°C for 1 h, respectively (Figure 6.5 (b)).

Following these results, the annealing time was increased to 10 h at 1100°C, aiming for an increase in rutile phase. Even though the rutile/anatase ratio increased, full rutile phase was not obtained. The SiO_2 layer on the Si wafer, which was measured to be 2 nm thick at room temperature by ellipsometry, grew during annealing to ~60 nm after 1 hour and ~240 nm after 10 hours. The presence of a 240 nm thick SiO_2 layer below the ~53 nm anatase TiO_2 film induced a modification of the sample's color to a bright green. These samples indirectly show how structural colors can be tuned (Figure 6.5 (b)). The multilayer configuration of TiO_2, SiO_2 and Si lead to light interference phenomena, which are influenced by the refractive indexes, thicknesses, and observation angle. From an industrial perspective, structural colors are widely employed for decoration purposes for automobiles or luxury jewelry.[39]

A fully rutile TiO_2 film was achieved by annealing a thicker xerogel. A 3-layer deposited TiO_2 on fused silica at 2000 rpm ($Q3T_{2000\,nm}$) was annealed at 1100°C for 1 h. The annealed film displayed a 100 nm thickness from ellipsometry and the (1 1 0) peak at $2\Theta \sim 27.5°$ from GIXRD, along with the absence of (1 0 1) anatase peak. As will be discussed in the following paragraphs, high thicknesses of TiO_2 films negatively affected both the thermochromicity of multilayers and the VO_2 crystallization. For this reason, most TiO_2 – VO_2 bilayers were based on anatase TiO_2 or a mixed anatase-rutile TiO_2.

7.2.4 *TiO_2 – VO_2 bilayers*

In this paragraph, several TiO_2 – VO_2 bilayers will be presented. To explain the different optical and electrical properties, the interaction and mutual influence of the two materials will be considered. The analysis of the structure, morphology, and elemental composition will first be discussed, followed by considerations on the optical and electrical properties.

Each sample was named with the first position to represent the substrate type (letter S = silicon, or Q = fused silica), the second position to represent the number of deposited layers, the third position to represent the material (letter T = TiO_2, or V = VO_2), and the eventual subscript to report the spin coating rate. For example, $S1T_{4000\ rpm}3V$ represents 1 layer of TiO_2 film, spin coated at 4000 rpm on a silicon substrate, on which 3 layers of VO_2 were deposited.

7.2.4.1 *Structural and morphological analysis of TiO_2 – VO_2 bilayers*

Several aspects were found to affect the interplay between VO_2 and TiO_2, during the development of the bilayer configuration. The two materials were found to critically influence each other during the crystallization step. Moreover, interdiffusion was noticed under specific deposition and annealing conditions, which in turn impacted the final optical and electrical properties, as will be discussed in the following paragraph 6.2.4.2. The specific deposition and annealing conditions will be stated in each paragraph.

7.2.4.1.1 Influence of VO_2 on the anatase-rutile transition of TiO_2

Initially, the crystallization of a single layer of TiO_2 ($S1T_{4000\ rpm}$) was compared to a TiO_2–VO_2 bilayer ($S1T_{4000\ rpm}1V$) by GIXRD. Regarding the TiO_2 film, a single layer was spin coated at 4000 rpm, which corresponds to ~35 nm after annealing (paragraph 6.2.2). For the bilayer configuration, 1 layer of TiO_2 was spin coated at 4000 rpm and annealed at 550°C in air for 1 h. The annealed sample was then coated by 1 layer of VO_2 and annealed in a tubular furnace, at the same conditions used for VO_2 single layers (inert gas flux at 0.1 lpm, 640° for 1h, 10°C/min ramp).

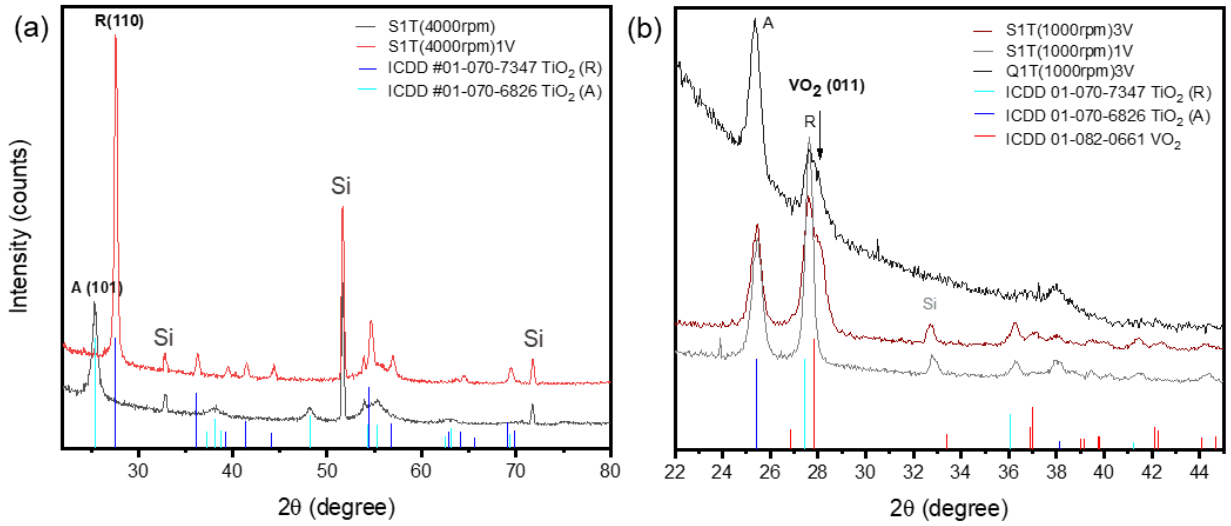


Figure 6.6. (a) GIXRD of S1T$_{4000\ rpm}$1V after 640°1 h in N_2 compared to S1T$_{4000\ rpm}$ after 550°C 1h. (b) GIXRD of different bilayers with a ~70 nm TiO_2 buffer layer, showing both anatase and rutile presence after final annealing and lack of VO_2 crystallization for 1-layer deposition of VO_2 precursor solution.

In the S1T$_{4000\ rpm}$1V bilayer, the (0 1 1) diffraction of VO_2 (M1) was not detected, presumably due to the presence of insufficient quantity of material to trigger the VO_2 crystallization. This was previously noticed when only 1 layer of VO_2 was deposited, with respect to the deposition of 2 or more layers (paragraph 4.3.6 of Chapter 4).

Nonetheless, the ~30 nm VO_2 layer deposited on TiO_2 was found to promote the TiO_2 crystallization into the rutile phase. Before the deposition of the VO_2 layer, the ~35 nm TiO_2 layer of sample S1T$_{4000\ rpm}$1V was initially anatase. As shown in Figure 6.6 (a), the TiO_2 was subjected to a phase transformation into rutile following the formation of the TiO_2–VO_2 bilayer (sample S1T$_{4000\ rpm}$1V). In paragraph 6.2.3, the challenge of crystallizing thin layers of TiO_2 in the rutile phase was highlighted, as the thinner films were shown to be preferentially crystallized into the anatase phase. For TiO_2 single films, only a few % of rutile phase was obtained at 1100°C, even for thicker films of ~70 nm. In the same paragraph (paragraph 6.2.3), it was demonstrated that TiO_2 single layers could be crystallize into anatase if annealed under the same conditions used for VO_2 annealing.

A mixed phase of both rutile and anatase TiO_2 was instead reached with a thicker TiO_2 layer (~70 nm) in the bilayer, as can be seen from both samples S1T$_{1000\ rpm}$3V and S1T$_{1000\ rpm}$1V (Figure 6.6 (b)). By comparing the latter two samples, the deposition of a higher amount of VO_2 (3 layers instead of 1 layer) on the TiO_2 layer, led to the successful crystallization of VO_2 as well. In sample S1T$_{1000\ rpm}$3V (Figure 6 (b)), the (1 1 0) TiO_2 (R) peak is visible at 2Θ ~ 27.7°, slightly shifted respect to reference rutile diffraction. This shift will be shown to be caused by diffusion in the following paragraph 6.2.4.1.2. The latter peak displays a shoulder at 2Θ ~ 27.9°, which corresponds to the (0 1 1) peak of VO_2 (M1). Minor diffractions were also found at 2Θ ~ 37.1°, 42.4°, corresponding to the (2 0 0) and

(2 1 0) planes of VO_2 (M1). On the bilayer with only 1 layer of VO_2 ($S1T_{1000\ rpm}1V$, Figure 6.6 (b)), the shoulder could not be seen, confirming the results of Figure 6.6 (a). Under the presence of vanadium atoms, Depero *et al.*[40] observed a lower transition temperature for the anatase-to-rutile transformation of TiO_2, due to the distortions induced by V ions in the anatase structure of TiO_2.

7.2.4.1.2 Elemental interdiffusion

Several studies have reported the high solubility between TiO_2 and VO_2 over an entire range of compositions,[40,41] which is favored by the similar ionic radii of Ti^{4+} (74.5 pm) and V^{4+} (72 pm) in the octahedral field.[42]

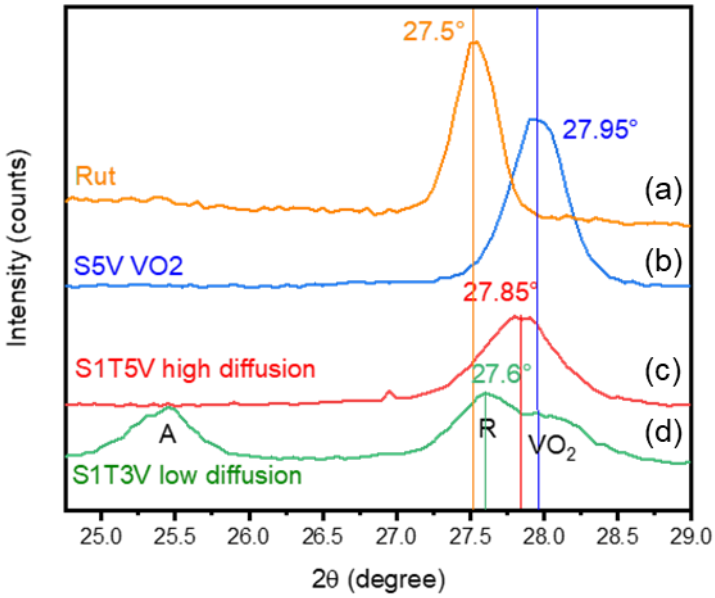


Figure 6.7. Comparison between GIXRD patterns of a "low diffusion" and "high diffusion" TiO_2-VO_2 bilayers. (a) Rutile TiO_2, (b) monoclinic VO_2,(c) "high diffusion" TiO_2-VO_2 bilayer S1T5V (30nm TiO_2-50nm VO_2), (d) "low diffusion" TiO_2-VO_2 bilayer S1T3V (65nm TiO_2-30nm VO_2).

In several TiO_2–VO_2 bilayer samples within this work, a single diffraction peak with a broad FWHM was observed at $2\Theta \sim 27.8°$ by GIXRD, instead of a TiO_2 rutile peak at $2\Theta \sim 27.5°$ and a separate shoulder at $2\Theta \sim 27.95°$ of VO_2 (M1) (Figure 6.7 (b)). In other bilayers, the (1 1 0) diffraction peak of TiO_2 (R) could be evidently identified respect to the (0 1 1) of VO_2 (M1) (Figure 6.7 (d)). In the latter case, a peak shift from $2\Theta \sim 27.5°$ (Figure 6.7 (a)) of TiO_2 (R) to 27.6° of TiO_2–VO_2 bilayer could still be detected. Both cases were attributed to doping-induced lattice distortions. The first sample type, characterized by a single broad diffraction peak, was identified as "high diffusion" bilayer, whereas the second case as "low diffusion" bilayer. Similar trends were reported by Nishikawa *et al.*[43], who noticed a progressive overlap between the two peaks with increasing titanium content in $Ti_xV_{(1-x)}O_2$.

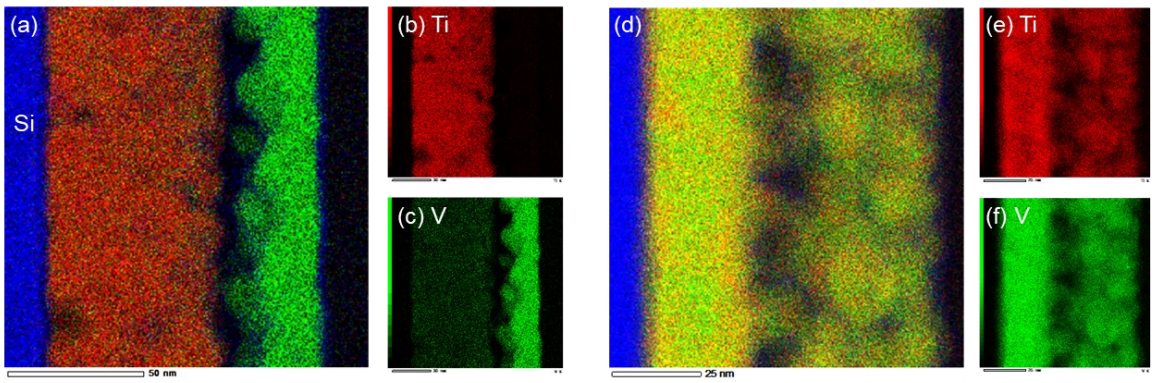


Figure 6.8. EDX maps for (a) "low diffusion" sample S1T3V (65nm TiO_2-30nm VO_2), (b) "high diffusion" sample S1T5V (30nm TiO_2-50nm VO_2).

EDX analyses was performed to investigate the diffusion of the two sample types, namely the "low diffusion" (Figure 6.8 (a)) and the "high diffusion" (Figure 6.8 (b)). As evidenced in the latter, remarkable diffusion of both Ti and V was seen in the bilayer which previously displayed a single broad peak from GIXRD (S1T5V, Figure 6.8 (c)). In this case, the overall sample would be more appropriately defined as $Ti_xV_{(1-x)}O_2$, instead of a $TiO_2 - VO_2$ bilayer. In the "low diffusion" sample (S1T3V, Figure 6.8 (a)), a lower diffusion of V atoms inside the TiO_2 layer was confirmed.

The EDX analysis is characterized by a low energy resolution (125 eV), which might be an issue as Ti and V have very close L edges. EELS analysis, which guarantee a 0.6 eV resolution, was performed to confirm the EDX results.

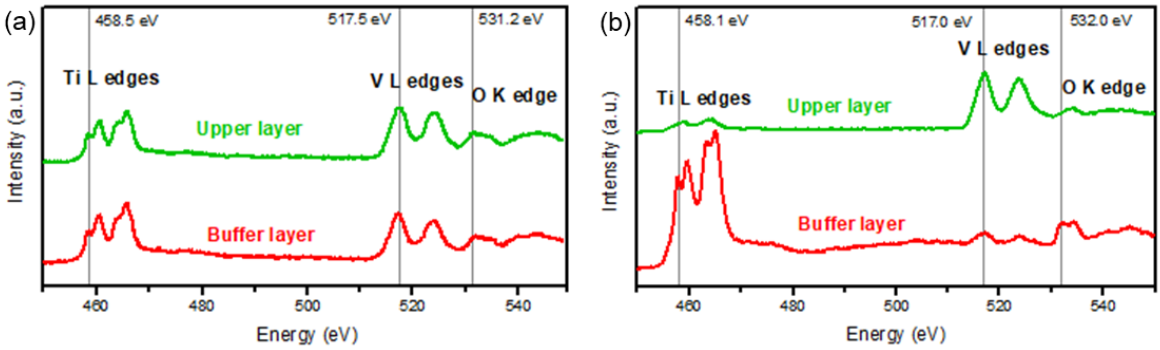
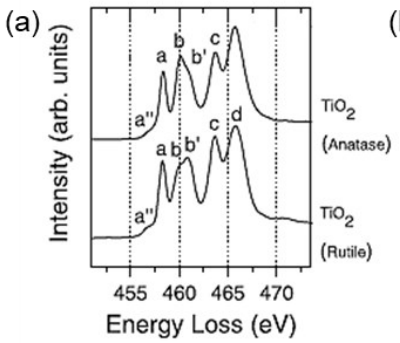


Figure 6.9. EELS comparison between (a) "high diffusion" sample S1T5V (30nm TiO_2-50nm VO_2), (b) "low diffusion" sample S1T3V (65nm TiO_2-30nm VO_2).

(a)



(b)

Oxide	Ti L_3 edge peak positions (eV)			
	a	*a'*	*b*	*b'*
TiO_2 rutile	458.3	–	460.0	460.8
TiO_2 anatase	458.3	–	460.0	460.7
Ti_3O_5	456.4	–	459.0	–
Ti_4O_7	456.6	–	459.5	–
Ti_5O_9	456.4	458.2	459.7	–
Ti_2O_3	456.3	458.1	458.9	–
TiO	–	–	457.4	–

Figure 6.10. (a) EELS spectra for TiO_2 anatase and rutile phase in Ti L_3 and L_2 region. Ref.[44] *(b) Comparison of the experimentally determined energy positions of the peaks a, a', b, and b' within L_3 edges of Ti Oxides. Ref.*[44]

The EELS results of the "high diffusion" sample (Figure 6.9 (a)) highlight a homogeneous composition throughout the whole double layer, confirming the EDX results. In the "low diffusion" sample (Figure 6.9 (b)), almost imperceptible peaks due to Ti presence can be seen in the VO_2 layer, and viceversa. The well-resolved *t2g* and *eg* peaks in the Ti L-edges indicate that the Ti cations display a 4+ oxidation state. The shape and energy of the EELS peaks are highly consistent with both the rutile and anatase phase reported in literature, as can be seen from the peak "a" in Figure 6.10 (a) (558.3 eV from Figure 6.10 (b)).[44] A slight shift towards a higher energy was noticed for the "high diffusion" sample, which typically highlights a change in the chemical surrounding and may be due to the high V doping found in the TiO_2 lattice.

Doping was found to severely affect the functional optical and electrical properties, in terms of thermochromicity of the samples. As will be shown in paragraph 6.2.4.2, a general reduction of ΔT_{sol} was found with increasing thickness of the TiO_2 layer, along with a lower variation in electrical resistivity. The reduction in thermochromic efficiency was found to be more significant in the "high diffusion" samples respect to the "low diffusion" ones. This was attributed to the cationic substitution along vanadium chains, which introduced defects, hindered the electron delocalization, and led to a consequent reduction of the metallic behavior in the NIR spectrum. The identification of the key parameters responsible for diffusion was not straightforward. Following a consideration of all the experimental tests on TiO_2 – VO_2 bilayers, the drying temperature before annealing was identified as the most probable one. In the case of the "low diffusion" samples, a temperature of 150°C was employed to dry the as-deposited VO_2 layer on top of the TiO_2 layer. In the case of the "high diffusion" ones, the drying temperature of VO_2 films was 250°C. The higher drying temperature may have boosted a higher migration of the cations in the amorphous phase. With a higher drying temperature, the preliminary thermal treatment of the amorphous TiO_2 xerogel before the deposition of VO_2 was not sufficient to prevent diffusion. The annealing temperatures of the previously shown samples (S1T3V and S1T5V) were set to be identical.

7.2.4.1.3 Influence of TiO_2 on VO_2 crystallization

The influence of TiO_2 layer buffers on the VO_2 morphology was investigated by SEM analysis. The images were acquired on different TiO_2 – VO_2 bilayers, characterized by TiO_2 layers of increasing thickness, i.e., 0 nm, ~35 nm, ~50 nm, ~70 nm.

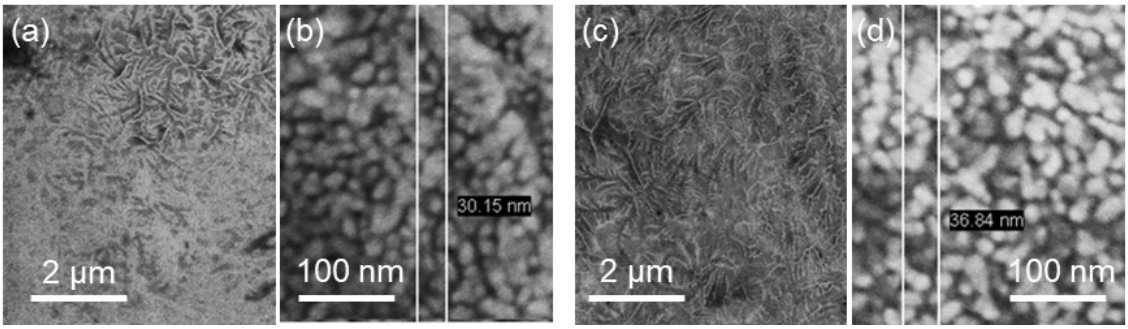


Figure 6.11. SEM images of samples (a, b) 50 nm VO_2 layer on fused silica, (c, d) VO_2 (50nm)-TiO_2 (35nm) on fused silica.

The morphology of the VO_2 film (Figure 6.11 (a, b)) was not affected by the presence of the TiO_2 sublayer (Figure 6.11 (c, d)). Considering the higher magnifications of both sample types (Figure 6.11 (b, d)), the grains displayed multi-shaped morphologies with average dimensions between 20 and 40 nm. On these samples, the presence of dendritic-like structures was attributed to the deposition under low moisture conditions (25% RH 19°C), as discussed in paragraph 4.3.8 of Chapter 4.

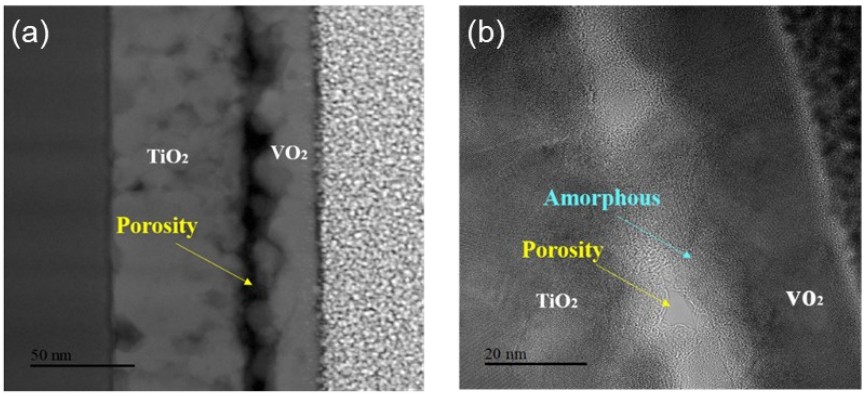


Figure 6.12. (a) HAADF-STEM image of S1T3V cross section;(b) Zoomed double layer interface area.

The cross-section of the "low diffusion" S1T3V bilayer (Figure 6.12 (a)), which displayed both diffraction peaks by GIXRD (Figure 6.12 (d)), was analyzed by high angle annular dark field (HAADF) HRTEM. The interface between the VO_2 and TiO_2 layers displayed a high porosity, besides the presences of amorphous regions. A flattening of the EELS peaks was noticed while measuring on these areas, confirming the absence of Ti, V, and O within the porous areas. On this sample, the VO_2 layer did not reach a sufficient adhesion on the TiO_2 layer below. Further characterizations would be needed to verify the adhesion of other bilayers.

7.2.4.2 *Optical and electrical properties of TiO_2 – VO_2 bilayers*

Following the GIXRD and morphological characterizations, the optical and electrical properties of the bilayers TiO_2 – VO_2 bilayers were analyzed by UV-VIS-NIR spectroscopy, FTIR spectroscopy, and four-point probe measurements. The luminous transmittance (T_{lum}), solar modulation ability (ΔT_{sol}), transition temperature (T_c) and emittance of the double layers were compared to the ones of VO_2 films. Initially, simulations on the visible transmittance (T_{lum}) were employed to identify the best thickness combination of the TiO_2 and VO_2 films.

7.2.4.2.1 Simulations of luminous transmittance of TiO_2 – VO_2 bilayers

To identify the best thickness combination for the TiO_2 – VO_2 bilayers, transfer-matrix model based simulations were performed.

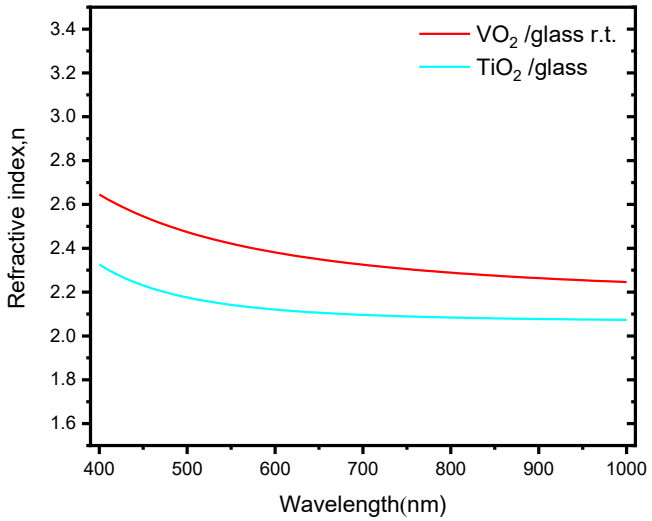


Figure 6.13. Refractive index of crystalline sol-gel based monoclinic VO_2 and anatase TiO_2 thin films, determined by spectroscopic ellipsometry.

The refractive index (n) of the sol-gel anatase TiO_2 and monoclinic VO_2, as well as of the 1 mm fused silica substrate, was measured by spectroscopic ellipsometry (Figure 6.13). The thickness of both TiO_2 and VO_2 was chosen to be varied between 0 and 200 nm.

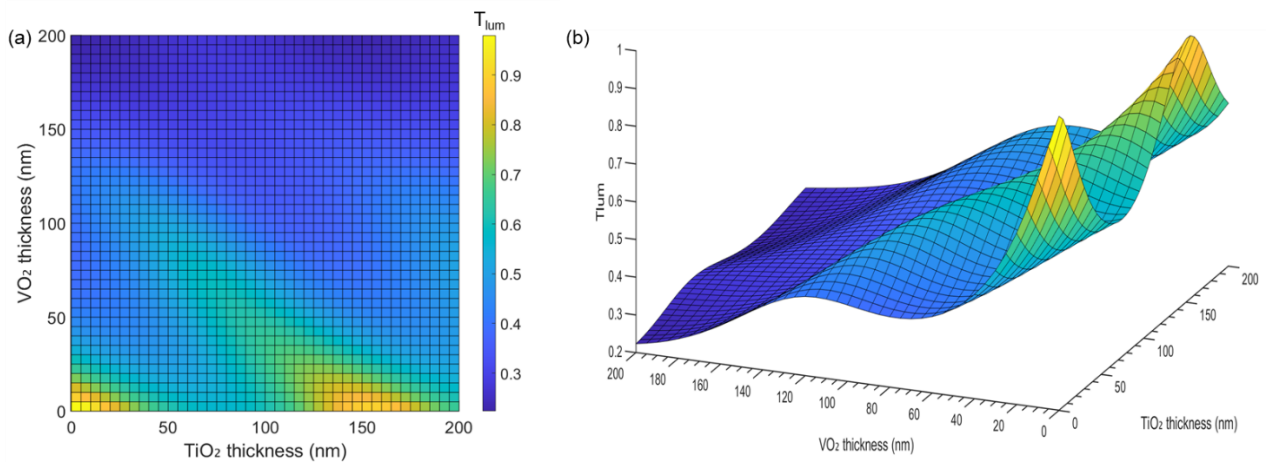


Figure 6.14. (a) 2D and (b) 3D graph of luminous transmittance in function of thickness of both TiO_2 and VO_2 layers in the TiO_2-VO_2 bilayer configuration. The transfer-matrix model based simulations were performed in collaboration with the group of prof. David Horwat from the Institut Jean Lamour of University of Loraine.

VO_2 displayed a higher absorption in the visible range, resulting in a severe drop of luminous transmittance (T_{lum}) with increasing thickness of the VO_2 layer (Figure 6.14 (a)). On the contrary, the increasing thickness of the TiO_2 layer showed a different influence on the luminous transmittance. Considering the 3D version of the graph (Figure 6.14 (b)), the yellow maxima represent the regions of enhanced luminous transmittance and highlight the target thickness for the bilayer. These results agree with the work of Wu *et al.*[45], who simulated the T_{lum} for VO_2 and ARC TiO_2 – VO_2 via the transfer matrix method using the experimental optical constant for glass, VO_2 and TiO_2. Their results show a similar drop of T_{lum} for thick VO_2 films, as well as the wave interference pattern which was noticed by varying the TiO_2 thickness.

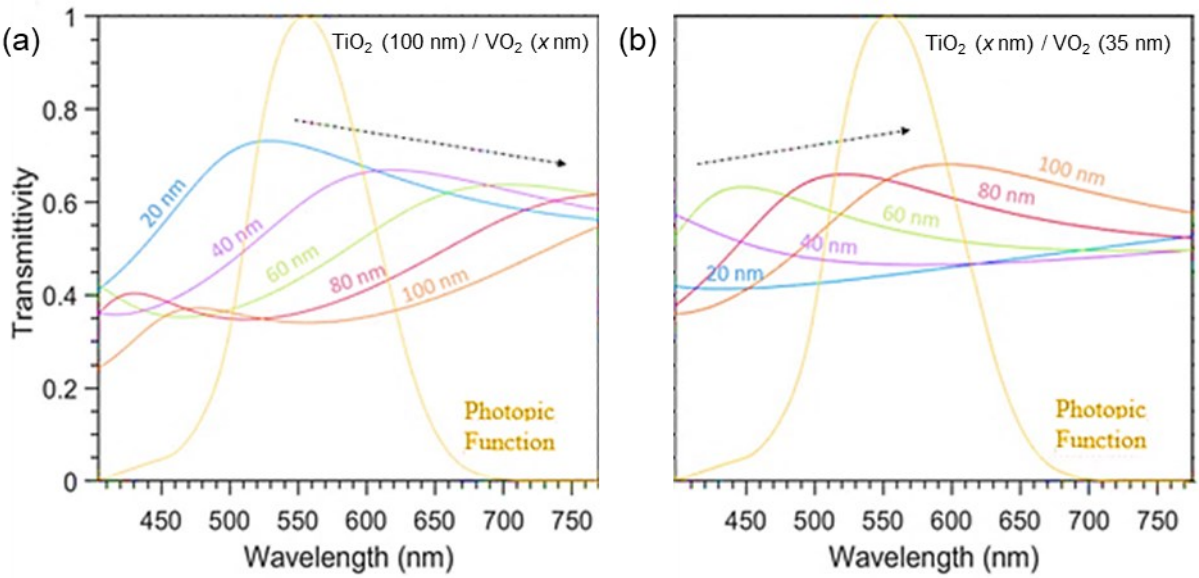


Figure 6.15. Shift of the transmissivity maximum with (a) increasing VO_2 layer thickness, deposited on a 100nm TiO_2 buffer layer; (b) increasing TiO_2 layer thickness, with a fixed 35nm of VO_2. The transfer-matrix model based simulations were performed in collaboration with the group of prof. David Horwat from the Institut Jean Lamour of University of Loraine.

The luminous transmittance (T_{lum}) is defined by the transmittance in the visible spectrum, weighted by the photopic efficiency of the human eye (Appendix A.2.8). The maximum increase in T_{lum} is therefore linked to the region in which the photopic function is maximized, i.e., around 550 nm. The influence of an increasing VO_2 thickness on a 100 nm TiO_2 film is reported in Figure 6.15 (a), whereas the effect of the increasing TiO_2 thickness with a constant 35 nm VO_2 film is shown in Figure 6.15 (b). As the thickness of VO_2 increased, the transmittance was seen to decrease, whereas an inverse trend was found with increasing thickness of TiO_2. Interestingly, a synergistic effect was found by the combination of the two materials in a bilayer configuration. While the simulated T_{lum} of a 35 nm VO_2 film and a 100 nm TiO_2 films were respectively 50% and 60% (Figure 6.15 (a)), the simulated T_{lum} of a 100 nm TiO_2 – 35 nm VO_2 bilayer was found to be 66% (Figure 6.15 (b)).

Following the theoretical simulations, the separate influence of the thickness of VO_2 and TiO_2 layers on the luminous transmittance was experimentally verified. The former was previously shown in paragraph 4.3.6 of Chapter 4, whereas the latter is reported in the following paragraph 6.2.4.2.2.

7.2.4.2.2 TiO_2 thickness influence on T_{lum} of bilayers

To assess the influence of TiO_2 thickness on the luminous transmittance, three TiO_2 films of increasing thickness were deposited on fused silica substrates and annealed at 550°C for 1 h in air. The detailed characterization of the films was previously shown in paragraph 6.2.2. The final thicknesses of the anatase TiO_2 films were 35 nm, 70 nm, and 140 nm, respectively.

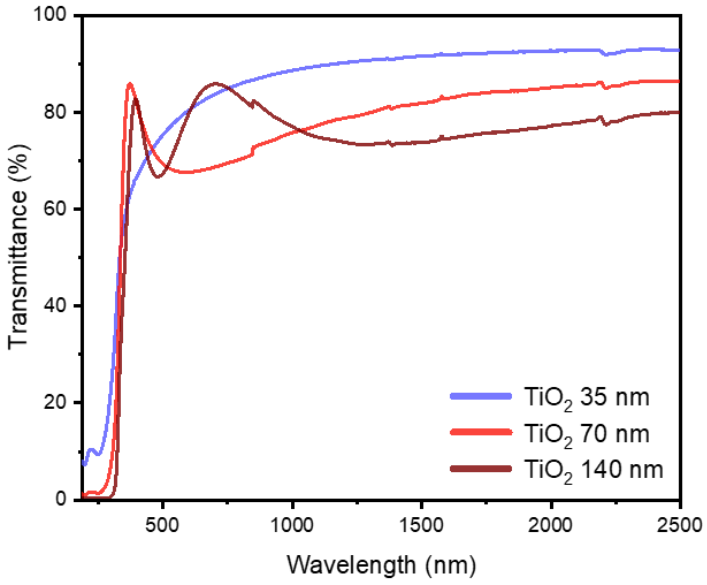


Figure 6.16. Transmittance spectra of the 35 nm, 70 nm,140 nm TiO_2 films on fused silica at 20°C.

Table 6.4. Luminous transmittance values of the 35 nm, 70 nm,140 nm TiO_2 films on fused silica at 20°C.

Sample	$T_{lum,\ 20°C}$ (%)
$Q1T_{4000\ rpm}$ – 35 nm	78.2
$Q1T_{1000\ rpm}$ – 70 nm	68.1
$Q1T_{2000\ rpm}$ – 140 nm	74.1

The transmittance spectra of the three TiO_2 films is shown in Figure 6.16, whereas the calculated luminous transmittance ($T_{lum,\ 20°C}$) is reported in Table 6.4. As can be seen, the increasing film thickness did not show a corresponding decreasing trend in T_{lum}. The experimental results confirmed the theoretical ones from the simulations, which showed the presence of two range of thicknesses in which the luminous transmittance could be maximized.

7.2.4.2.3 Optical properties of "low diffusion" bilayers

Following the optical characterization on single TiO_2 films (paragraph 6.2.4.2.2) and single VO_2 films (paragraph 4.3.6 of Chapter 4), the effect of the TiO_2 presence on the optical properties of VO_2 films was investigated. Similarly to the discussion of the GIXRD results (paragraph 6.2.4.1.2), both the "low diffusion" bilayers and the "high diffusion" ones were characterized by UV-Vis-NIR spectroscopy.

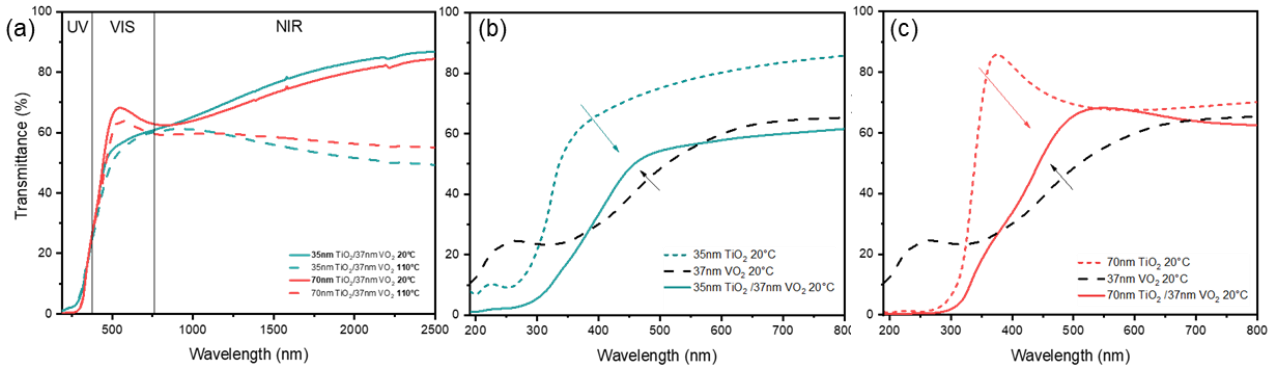


Figure 6.17. (a) Transmittance spectra of 35 nm TiO_2 -37 nm VO_2 bilayer and 70 nm TiO_2 -37 nm VO_2 bilayer on fused silica at 20°C. (b) Transmittance enhancement of the 35 nm TiO_2 -37 nm VO_2 bilayer respect to the VO_2 film. (c) Transmittance enhancement of the 70 nm TiO_2 -37 nm VO_2 bilayer respect to the VO_2 film.

Table 6.5. Luminous transmittance of VO_2 film ($T_{lum,\ VO2}$), TiO_2 film($T_{lum,\ TiO2}$) and TiO_2–VO_2 bilayers (T_{lum}). Solar modulation ($\Delta T_{sol,\ max}$) and NIR modulation at 2000 nm ($\Delta T_{2000,\ max}$) of the TiO_2–VO_2 bilayers.

Sample	T_{lum} (%)	$\Delta T_{sol,\ max}$ (%)	$\Delta T_{2000\ nm,\ max}$ (%)
35 nm TiO_2 – 37 nm VO_2	56.3	5.7	31.8
70 nm TiO_2 – 37 nm VO_2	66.9	5.9	24.0

The transmittance spectra of the "low diffusion" bilayers are reported in Figure 6.17, whereas the calculated luminous transmittance ($T_{lum,\ 20°C}$) and solar modulation (ΔT_{sol}, ΔT_{2000}) are shown in Table 6.5. For both bilayers, the luminous transmittance was increased respect to the VO_2-only film (Q3V). The latter film of 37 nm displayed a $T_{lum,\ 20°C}$ = 55.4%, whereas a combination with either 35 nm or 70 nm of TiO_2 led to $T_{lum,\ 20°C}$ = 56.3%, 66.9% respectively. The thermochromic modulation of VO_2 films ($\Delta T_{sol,max}$ = 6.3%) was only partially affected by the bilayer configuration, since the value decreased to $\Delta T_{sol,max}$ = 5.7% and 5.9%, for the 35 nm and 70 nm thicknesses of TiO_2, respectively. Compared to the 35 nm TiO_2 film, the 70 nm film displayed a better performance in the bilayer configuration, since it led to a 21% increase of the luminous transmittance, while maintaining a satisfactory thermochromic modulation. As highlighted in Chapters 4-5, the latter two parameters (T_{lum} and ΔT_{sol}) usually display an opposite trend, whereas the final goal for smart window applications must be the simultaneous increase of both values.

7.2.4.2.4 Optical properties of "high diffusion" bilayers

Following the optical characterization of the "low diffusion" bilayers, the transmittance spectra of the "high diffusion" bilayers are reported in Figure 6.18, while the calculated luminous transmittance ($T_{lum,\ 20°C}$) and solar modulation (ΔT_{sol}, ΔT_{2000}) are shown in Table 6.6.

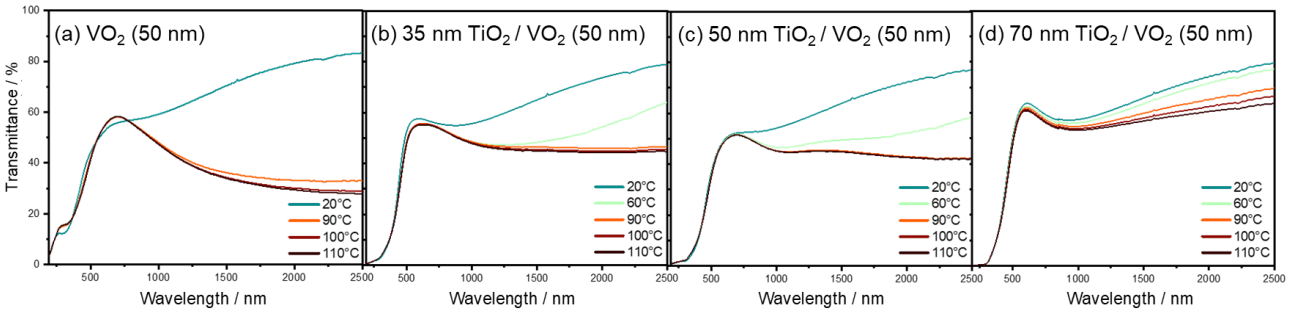


Figure 6.18. Transmittance spectra of (a) 5-layered VO_2 film (Q5V) and of TiO_2–VO_2 bilayers, respectively (b) 35 nm TiO_2 – 50 nm VO_2, (c) 50 nm TiO_2 – 50 nm VO_2, (d) 70 nm TiO_2 – 50 nm VO_2.

Table 6.6. Luminous transmittance (T_{lum}), Solar modulation ($\Delta T_{sol,\ 90°C}$, $\Delta T_{sol,\ max}$) and NIR modulation at 2000 nm ($\Delta T_{2000,\ max}$) of TiO_2–VO_2 bilayers and of Q5V VO_2 film.

Sample	T_{lum} (%)	$\Delta T_{sol,\ 90°C}$ (%)	$\Delta T_{sol,\ max}$ (%)	$\Delta T_{2000\ nm,\ max}$ (%)
50 nm VO_2 (Q5V)	49.2	7.9	8.6	49.8
35 nm TiO_2 – 50 nm VO_2 ($Q1T_{4000\ rpm}5V$)	55.9	6.0	6.7	29.3
50 nm TiO_2 – 50 nm VO_2 ($Q1T_{2000\ rpm}5V$)	44.7	5.6	5.8	29.6
70 nm TiO_2 – 50 nm VO_2 ($Q1T_{1000\ rpm}5V$)	59.1	2.6	4.0	13.8

As expected, the "high diffusion" samples were more affected in terms of optical properties with respect to the "low diffusion" ones, particularly regarding the thermochromic solar modulation. The increasing thickness of the TiO_2 layer induced a progressive deterioration of the solar modulation. The latter decreased from $\Delta T_{sol,max}$ = 8.6% of the 5-layered VO_2 film to $\Delta T_{sol,max}$ = 6.7%, 5.8%, 4% for TiO_2 thicknesses of 35 nm, 50 nm, 70 nm, respectively. As discussed in paragraph 6.2.4.1.2, the solar modulation reduction could be related to a random cationic substitution along vanadium chains, which introduces defects and hinders the electron delocalization, with a consequent reduction of the metallic behavior in the NIR spectrum.

Nonetheless, for TiO_2 thicknesses of 35 nm and 70 nm, the deterioration of the thermochromic modulation was balanced by a higher $T_{lum,\ 20°C}$ in the bilayer configuration, respect to VO_2 films. Overall, the 35 nm TiO_2 – 50 nm VO_2 bilayer offered the most favorable compromise, with a 14% increase of $T_{lum,\ 20°C}$ and a 22% decrease of $\Delta T_{sol,max}$.

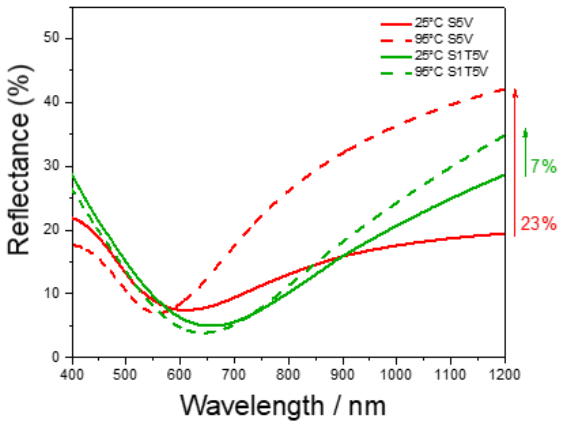


Figure 6.19. Reflectance spectra of (red curves) 5-layered VO_2 film S5V, and (green curves) 35 nm TiO_2 – 50 nm VO_2 bilayer.

The reduction of the thermochromic properties induced by the elemental diffusion was also proved by the specular reflectance measurements on silicon substrates, as reported in Figure 6.19.

7.2.4.2.5 Optical and electrical hysteresis of bilayers

Two important parameters which affect the applicability of thermochromic smart windows are represented by the hysteresis (ΔH) during the heating/cooling cycles and by the transition temperature (T_c). The ΔH and T_c values can be derived from both optical and electrical characterizations, i.e., by measuring the optical transmittance variations or the electrical resistivity changes in function of the temperature.

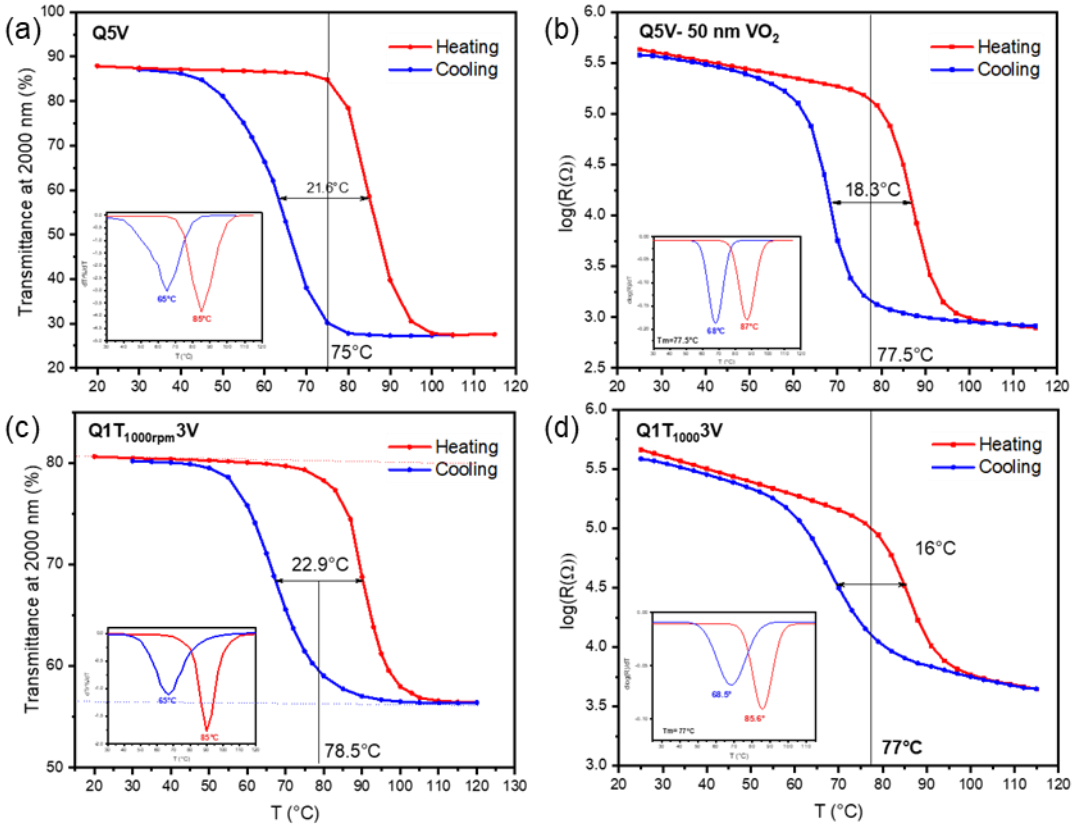


Figure 6.20. Comparison between optical (a, c) and electrical (b, d) hysteresis for samples (a, b) Q5V VO_2 film, and (c, d) Q1T$_{1000\ rpm}$3V bilayer.

A comparison between the hysteresis obtained from either optical or electrical characterizations is reported in Figure 6.20. Two samples were compared, namely the VO_2-only film (Q5V, Figure 6.20 (a, b)) and the 70 nm TiO_2 – 37 nm VO_2 bilayer (Q1T$_{1000\ rpm}$3V, Figure 6.20 (c, d)). The two types of hysteresis (i.e., from optical or electrical characterizations) displayed well matched results, with T_c variations of only a few degrees Celsius. The optical and electrical-based hysteresis curves are usually not identical, as they rely on a different characterization mechanism, as explained in paragraph 3.6.3 of Chapter 3.

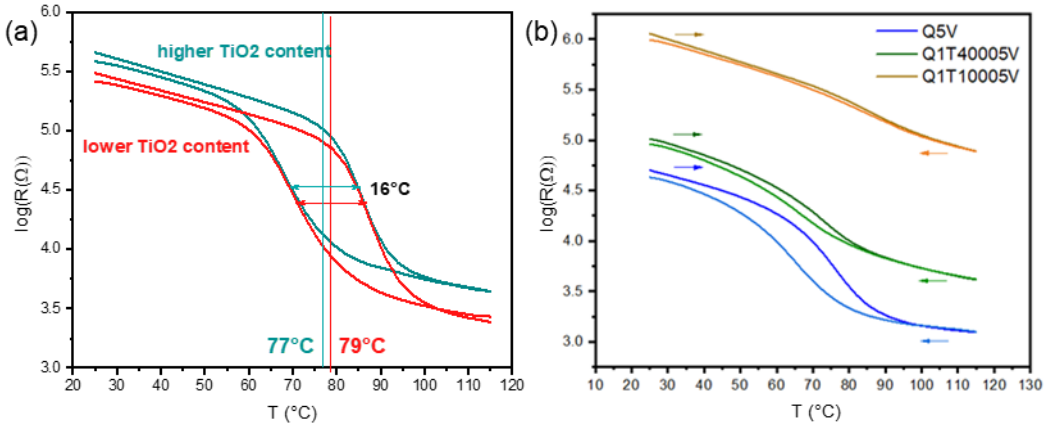


Figure 6.21. (a) Comparison between the hysteresis for "low diffusion" samples: 35 nm TiO_2-37 nm VO_2 (red curve), 70 nm TiO_2-37 nm VO_2 (red curve). (b) Comparison between the hysteresis for "high diffusion" samples at different TiO_2 thicknesses.

Several factors are known to influence both the T_c and the hysteresis width, including the purity and quality of the crystal lattice, doping, substrate-induced strain, non-stoichiometric compositions, film thickness, and annealing conditions.[46–49] Substitutional Ti cations in VO_2 lattice can hinder the electron delocalization on the c_R rutile axis and compromise the metallic behavior of VO_2. To investigate the influence of diffusion on the hysteresis of VO_2 (M1), the variation of the electrical resistivity in function of the temperature was analyzed for both the "low diffusion" and "high diffusion" bilayers (Figure 6.21 (a) and (b), respectively).

Considering the former (Figure 6.21 (a)), doubling the thickness of the TiO_2 layer from 35 nm to 70 nm led to a slight increase in sheet resistance, but did not significantly affect the hysteresis loop. The slight increase in resistance was caused by the higher content of TiO_2 insulating phase in the overall bilayer. Both samples showed a decrease in sheet resistance of 2 orders of magnitude, a hysteresis width of 16°C and T_c = 77-79°C. The "high diffusion" samples induced more significant effects on the hysteresis loop (Figure 6.21 (b)). The increasing TiO_2 thickness led to a progressive deterioration of the metal-insulator transition. This was probably induced by an increasing Ti diffusion in the VO_2 layer, which was shown in paragraph 6.2.4.1.2. The cationic substitution along vanadium chains created defects in the rutile structure and led to the progressive disappearance of the metal-insulator transition (MIT). An analogous trend was found for $Ti_xV_{(1-x)}O_2$ at different values of x[50], confirming the role of doping in suppressing the thermochromicity of the "high diffusion" samples.

7.3 VO_2 – SiO_2 bilayers

The addition of TiO_2 coatings on VO_2 films successfully lead to an increase in the luminous transmittance of the latter. However, under specific circumstances, elemental diffusion severely affected the optical and electrical properties of the resulting samples. The former could be reduced by accurately tuning the deposition parameters, but it could not be totally avoided. SiO_2 was hence selected as a promising alternative to increase the optical transmittance of VO_2 films.

As previously mentioned, SiO_2 displays low refractive index values, high transparency in the visible range, excellent chemical stability, and high mechanical resistance.[25,26] With respect to previous TiO_2 – VO_2 bilayers, VO_2 – SiO_2 bilayers were synthetized by first crystallizing VO_2 films and then depositing amorphous SiO_2 layers on top. A low temperature drying was employed to avoid diffusion due to high-temperature annealing. The wettability of the sol-gel SiO_2 coatings was modified by introducing organic groups within the inorganic network, leading to an increased hydrophobicity of the surface. As discussed in Chapter 2, the higher hydrophobicity allows for a more efficient removal

of condensed water droplets, which in turns can be exploited to enhance the durability of the smart window.

7.3.1 *Synthesis and deposition of VO_2 films*

The synthesis and deposition of VO_2 thin films was performed according to the procedure reported in paragraph 4.3.2.2 of Chapter 4. Briefly, a 2 months aged solution was spin coated on previously cleaned fused silica and silicon substrates. The procedure was performed at 73-85% RH at 22-28°C and repeated three times, with a drying step of 250°C for 10 min. All films were aged for 6 days in air at 30-45% RH 22°C, followed by a crystallization step performed either by furnace or laser annealing. Furnace annealing was performed at 550°C for 1 h at 10°C/min under a 0.1 lpm N_2 flux, whereas laser annealed films were irradiated for 300 pulses at 70 mJ/cm^2 with 8 Hz frequency in air. The detailed furnace annealing procedure is reported in Appendix A.1.5, whereas the laser annealing one in Appendix A.1.6.

7.3.2 *Synthesis and deposition of hybrid SiO_2 coatings*

Two different hybrid SiO_2 coatings were selected, namely methyl-modified SiO_2 (M_5T_5) and octyl-modified SiO_2 (O_2T_8), which were previously employed for the condensation of humid air and saturated vapor in Chapter 2. With respect to the previous studies, the concentrations and aging time of the solutions were varied to modify the final thickness of the sol-gel coatings. All the synthesis and deposition parameters were optimized for a spin coating procedure, with respect to the previous dip coating process.

7.3.2.1 *Methyl-modified SiO_2 coating*[51]

An acid-catalyzed solution was prepared by mixing tetraethylortosilicate (TEOS), methyltriethoxysilane (MTES), ethanol (EtOH), hydrochloric acid 1 M (HCl) and water (H_2O), in molar ratios of (TEOS+MTES):EtOH:H_2O:HCl=1:2:4:0.01, respectively. The TEOS:MTES molar ratio of 1 (M_5T_5) was chosen according to the previous optimization of paragraph 2.3.1 of Chapter 2. The solution was stirred for 30 min at 400 rpm at room temperature, following which theoretical final SiO_2 concentrations of 0.49 M and 0.67 M were reached by solvent dilution. The solution was aged for 15 min prior to deposition. During the initial optimization part, the hybrid sol-gel coatings were deposited on silicon wafers, previously cleaned through sonication in ethanol followed by

atmospheric plasma treatment (Plasma Cleaner, PDC-002-CE, Harrick Plasma). The coatings were deposited by spin coating at 3000 rpm for 30 s and then annealed on a hot plate at 250°C for 15 min. Once the optimized synthesis and deposition parameters were found, the procedure was repeated to deposit two types of hybrid M_5T_5 coatings, respectively 66 nm and 120 nm thick, on previously crystallized VO_2 films, either by furnace annealing or laser annealing.

7.3.2.2 *Octyl-modified SiO_2 coating*[52]

Tetraethyl orthosilicate (TEOS), octyltriethoxysilane (OTES), absolute ethanol (EtOH), 1 M hydrochloric acid (HCl) and milliQ water (H_2O, 18.2 MΩ) were mixed in molar ratios of (TEOS+OTES):EtOH:H_2O:HCl=1:2:2:0.01, respectively. The TEOS:OTES molar ratio was selected to be 8:2 (O_2T_8) from the optimization discussed in paragraph 2.2.2 of Chapter 2. The solution was stirred for 30 min at 400 rpm at room temperature and diluted to reach a theoretical final concentration of SiO_2 of 0.49 M. The diluted solution was stirred for 1 h 30 min at 400 rpm, aged still for 2 h, stirred for 20 h at 400 rpm prior to the deposition. During the initial optimization part, the hybrid sol-gel coatings were deposited on silicon wafers, previously cleaned through sonication in ethanol followed by atmospheric plasma treatment (Plasma Cleaner, PDC-002-CE, Harrick Plasma). The coatings were deposited by spin coating at 3000 rpm for 1 min and then annealed on a hot plate at 200°C for 15 min. Once the optimized synthesis and deposition parameters were found, the procedure was repeated to deposit the hybrid O_2T_8 coatings on previously crystallized VO_2 films, either by furnace annealing or laser annealing.

7.3.3 *Optical properties of VO_2 – hybrid SiO_2 bilayers*

The effect of hybrid SiO_2 coatings on the optical properties on VO_2 films was considered on both laser- and furnace annealed films. Several identical VO_2 films were prepared following the procedure of paragraph 6.3.1. The successful crystallization into VO_2 (M1) was verified by GIXRD, SEM, and UV-Vis-NIR spectroscopy. All films displayed the typical morphology of either furnace annealed (Figure 6.22 (a, b)) or laser annealed (Figure 6.22 (c, d)) VO_2 films, reported for both silicon and fused silica substrates. All films displayed thicknesses of 28 ± 2 nm and reproducible optical properties, as shown in Figure 6.23 (a, c, e).

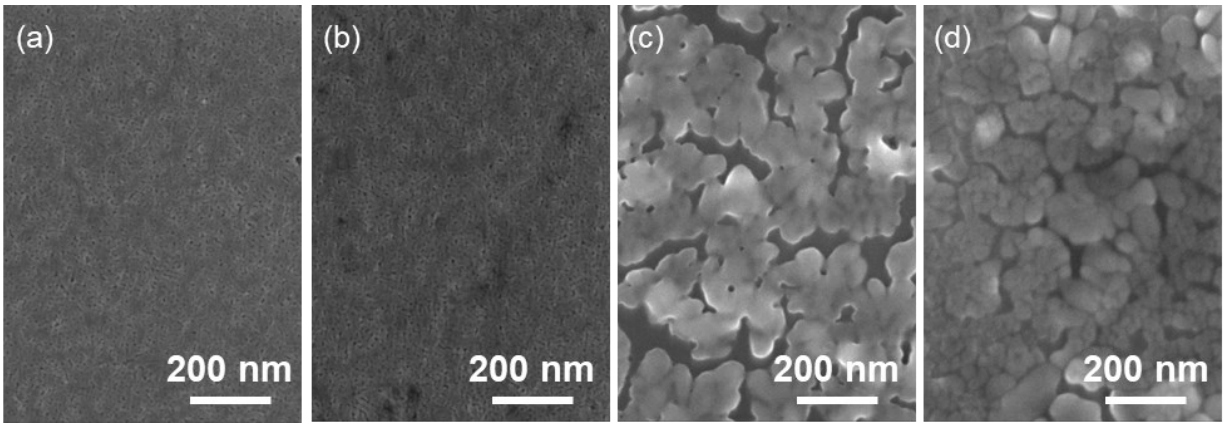


Figure 6.22. (a, b) furnace annealed VO_2 films, on silicon and fused silica substrates, respectively. (c, d) Laser annealed VO_2 films, on silicon and fused silica substrates, respectively.

Initially, three furnace annealed VO_2 films were coated with a ~66 nm M_5T_5 layer, a ~120 nm M_5T_5 layer, and a ~70 nm O_2T_8 layer, respectively. The UV-Vis-NIR transmittance of the pristine VO_2 films is visible in Figure 6.23 (a, c, e), whereas the corresponding bilayers are shown in Figure 6.23 (b, d, f). For the sake of a higher clarity, the pristine furnace annealed VO_2 films were named "V_{Fx}", with *x* sample number, whereas the hybrid SiO_2 coatings were respectively named "M_1" for ~66 nm M_5T_5, "M_2" for ~120 nm M_5T_5, and "O" for ~70 nm O_2T_8 layer.

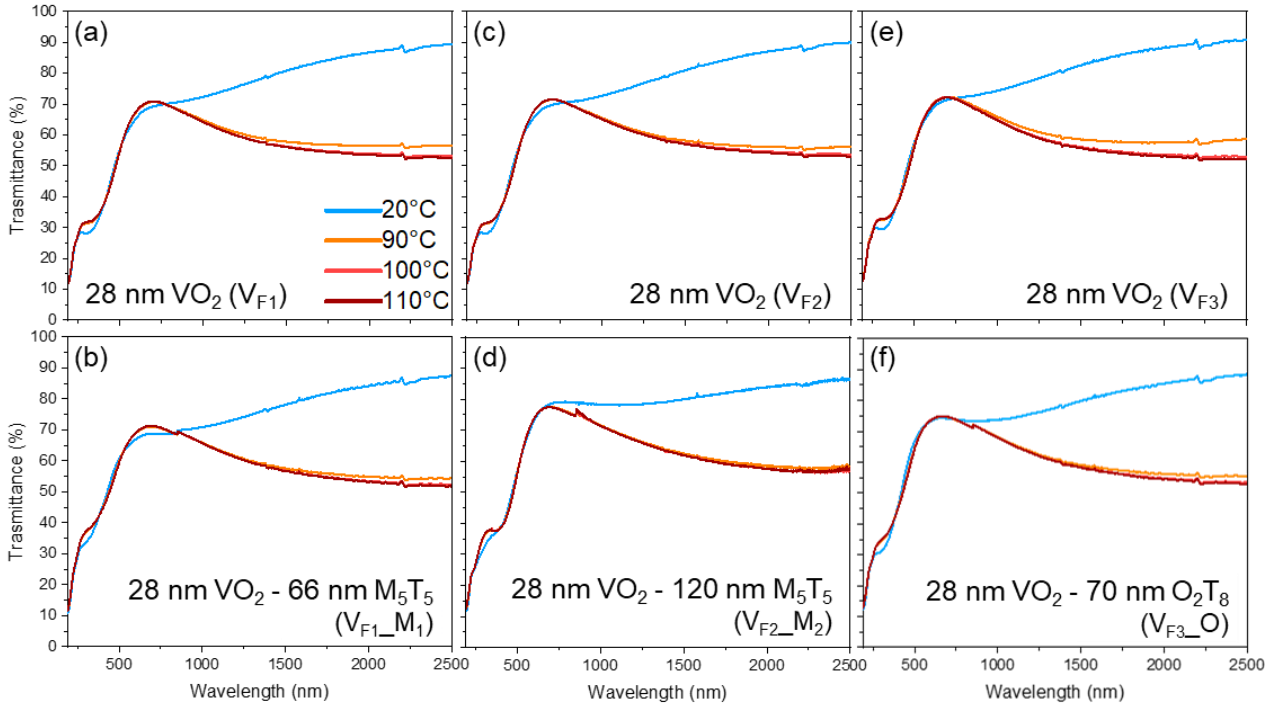


Figure 6.23. (a, c, e) Three pristine furnace annealed VO_2 films. (b, d, f) VO_2 films were coated with a ~66 nm M_5T_5 layer, a ~120 nm M_5T_5 layer, and a ~70 nm O_2T_8 layer, respectively.

Coherently with what reported in Chapter 4 and 5, the thermochromic efficiency of the potential smart windows was expressed in terms of luminous transmittance (T_{lum}), solar modulation ($\Delta T_{sol,\ 90°C}$, $\Delta T_{sol,\ max}$) and NIR modulation at 2000 nm ($\Delta T_{2000,\ max}$). Table 6.7 reports the parameters for each sample,

before and after the addition of the hybrid SiO_2 coating. For each sample, the increment of decrement with respect to the original VO_2 film is expressed with the Δ (%) parameter.

Table 6.7. Luminous transmittance (T_{lum}), solar modulation ($\Delta T_{sol,\ 90°C}$, $\Delta T_{sol,\ max}$) and NIR modulation at 2000 nm ($\Delta T_{2000,\ max}$) of VO_2–SiO_2 bilayers and of reference VO_2 films, before and after bilayer creation. Legend: F = furnace annealed, L = laser annealed, V = VO_2, M = methyl-modified hybrid SiO_2, O = octyl-modified hybrid SiO_2.

Sample	T_{lum} (%)	$\Delta T_{sol,\ 90°C}$ (%)	$\Delta T_{sol,\ max}$ (%)	$\Delta T_{2000\ nm,\ max}$ (%)
28 nm VO_2 (V_{F1})	61.3	4.7	5.2	32.9
28 nm VO_2 – 66 nm M_5T_5 ($V_{F1}_M_1$)	64.6	4.0	4.2	31.1
Δ (%)	**+5.4**	-14.9	-19.2	**-5.5**
28 nm VO_2 (V_{F2})	62.4	4.7	5.1	32.8
28 nm VO_2 – 120 nm M_5T_5 ($V_{F2}_M_2$)	67.0	4.7	4.9	26.3
Δ (%)	**+7.4**	0	-3.9	**-19.8**
28 nm VO_2 (V_{F3})	62.4	4.9	5.6	33.2
28 nm VO_2 – 70 nm O_2T_8 (V_{F3}_O)	71.0	5.0	5.3	30.9
Δ (%)	**+13.8**	+2.0	+5.4	**-6.9**
27 nm VO_2 (V_{L1})	60.8	4.1	4.5	32.2
27 nm VO_2 – 66 nm M_5T_5 ($V_{L1}_M_1$)	74.5	3.4	3.4	26.9
Δ (%)	**+22.5**	-17.1	-24.4	**-16.5**
31 nm VO_2 (V_{L2})	57.6	4.3	4.9	38.0
31 nm VO_2 – 74 nm O_2T_8 (V_{L2}_O)	68.1	3.4	3.4	30.5
Δ (%)	**+18.2**	-20.9	-30.6	**-19.7**

Considering the furnace-annealed VO_2 films (V_{Fx}, x = 1-3, first three rows of Table 6.7), the addition of all three types of hybrid SiO_2 coatings led to an increase in luminous transmittance, with respect to the original uncoated VO_2 film. The two M_5T_5 coatings led to comparable T_{lum} increases of +5.4% ($V_{F1}_M_1$) and +7.4% ($V_{F2}_M_2$), whereas the O_2T_8 layer (V_{F3}_O) led to the highest increase of +13.8% with respect to the uncoated VO_2 film. A crucial aspect which must be considered when multilayers are created is the possible loss of thermochromic efficiency. As discussed in Chapters 4-5, the increase of luminous transmittance is often linked to a reduction in solar modulation, which should be minimized. Comparing the three bilayers, M_2 (i.e., ~120 nm M_5T_5) induced the most severe reduction of thermochromicity in the $V_{F2}_M_2$ bilayer, with a -19.8% decrease in $\Delta T_{2000,\ max}$ with respect to the original V_{F2}. The $V_{F1}_M_1$ (~66 nm M_5T_5) and V_{F3}_O bilayers only decreased the NIR modulation by -5.5% and -6.9%, respectively, which is an acceptable compromise considering the simultaneous increase in luminous transmittance.

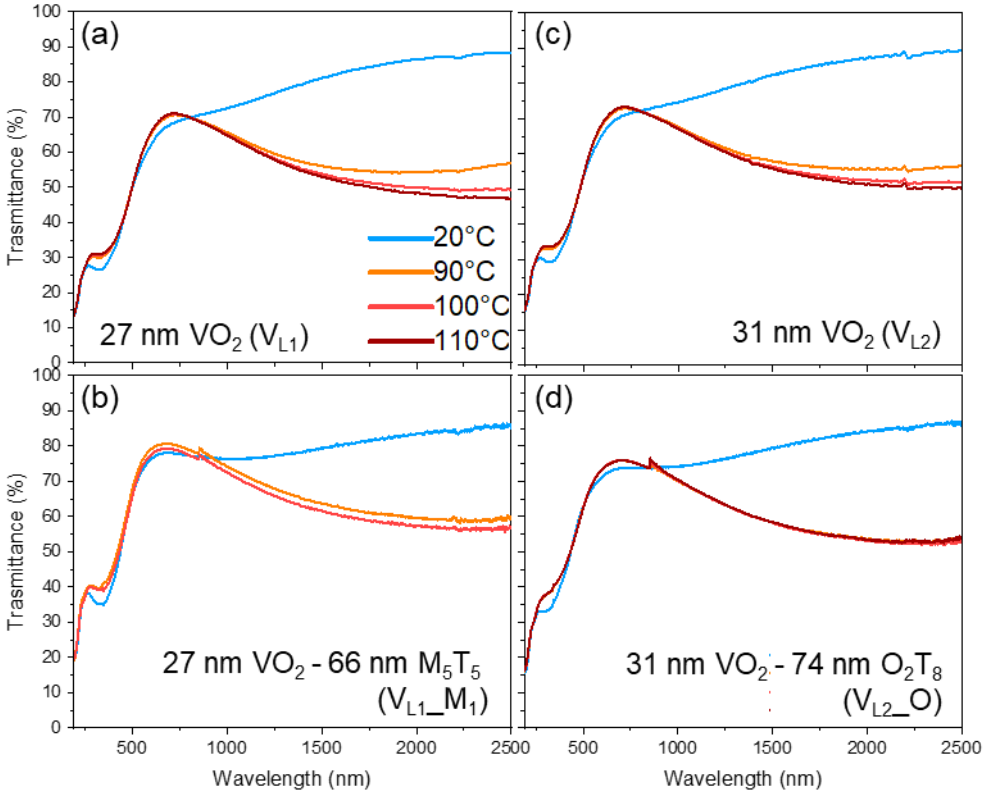


Figure 6.24. (a, c) Two pristine laser annealed VO_2 films. (b, d) VO_2 films were coated with a ~66 nm M_5T_5 layer, and a ~70 nm O_2T_8 layer, respectively.

Following the results for the furnace-annealed VO_2 films, the ~66 nm M_5T_5 and the ~70 nm O_2T_8 coatings were selected to coat two laser-annealed VO_2 films, leading to the formation of $V_{L1}_M_1$ bilayer (27 nm VO_2 – 66 nm M_5T_5, Figure 6.24 (b)) and V_{L2}_O bilayer (31 nm VO_2 – 74 nm O_2T_8, Figure 6.24 (d)). The variations in luminous transmittance and solar modulation with respect to the original laser-annealed VO_2 films is reported in Table 6.7 (V_{Lx}, x = 1-2, last two rows of Table 6.7). With respect to the furnace-annealed samples, the addition of a hybrid SiO_2 coating led to a higher increase in T_{lum}. The latter remarkably increased by +22.5% with the $V_{L1}_M_1$ configuration and by +18.2% with the V_{L2}_O bilayer. The highest luminous transmittance (T_{lum} = 74.5%) was reached with the $V_{L1}_M_1$ bilayer, with respect to the original T_{lum} = 60.8% of the lasered VO_2 film. In accordance with the literature and with the previous furnace-annealed samples, the high increase in T_{lum} was accompanied by a decrease in solar modulation.

Following the optical characterization, the five bilayers and the reference pristine VO_2 films were subjected to durability tests under high moisture conditions, described in the following paragraph 6.3.4.

7.3.4 *Durability tests*

The durability tests under high moisture content were performed in a sealed glove box. The glove box was filled with air, instead of N_2, and the humidity was set to be 90-95% at 22-24°C by introducing a saturated solution of KNO_3, with the moisture content monitored through a hygrometer. The samples, consisting of the five bilayers, a reference laser-annealed VO_2 film and a furnace-annealed one, were maintained under static conditions inside the glove box for 1 month. Following the prolonged exposure to high moisture conditions, the optical transmittance was measured to verify eventual degradation of the performance.

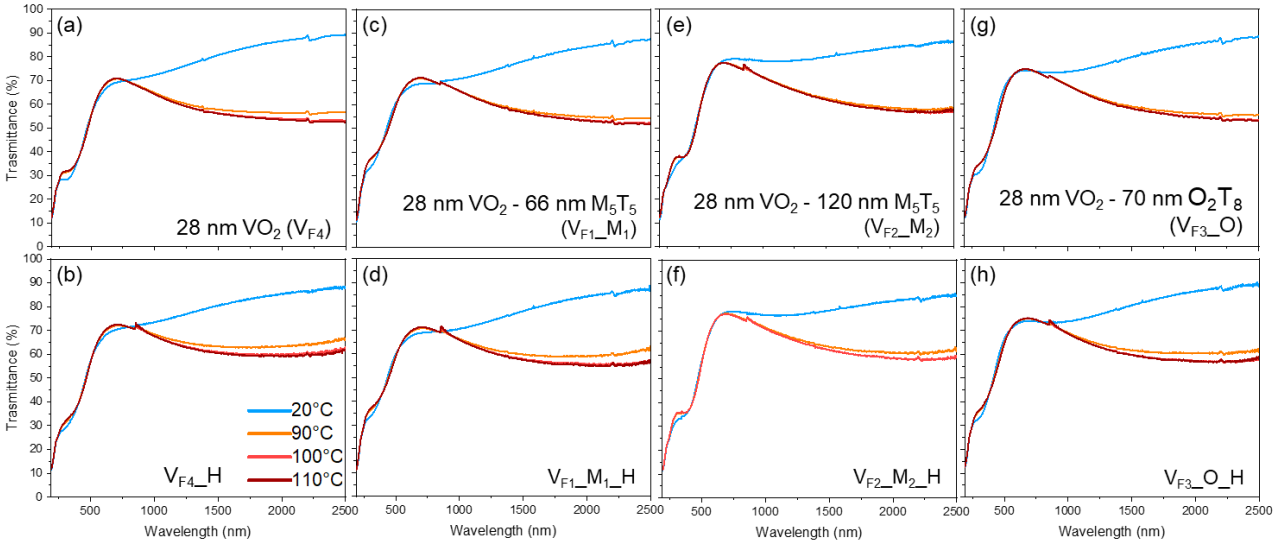


Figure 6.25. Durability tests: (a, c, e, g) before and (b, d, f, h) after the durability tests. (a) pristine furnace-annealed VO_2 film and (c, e, g) coated with a ~66 nm M_5T_5 layer, a ~120 nm M_5T_5 layer, and a ~70 nm O_2T_8 layer, respectively. (b) pristine furnace-annealed VO_2 film after the durability tests and (d, f, h) VO_2 films coated with a ~66 nm M_5T_5 layer, a ~120 nm M_5T_5 layer, and a ~70 nm O_2T_8 layer, respectively, after the durability tests.

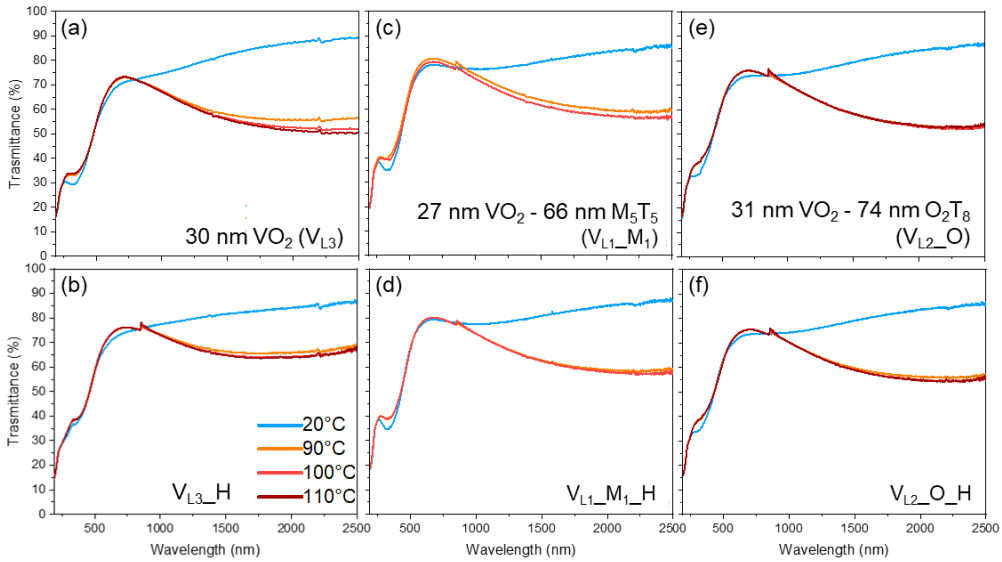


Figure 6.26. Durability tests: (a, c, e) before and (b, d, f) after the durability tests. (a) pristine laser-annealed VO_2 film and (c, e, g) coated with a ~66 nm M_5T_5 layer and a ~74 nm O_2T_8 layer, respectively. (b) pristine laser-annealed VO_2 film after the durability tests and (d, f) VO_2 films coated with a ~66 nm M_5T_5 layer and a ~74 nm O_2T_8 layer, respectively, after the durability tests.

The transmittance curves before and after the durability tests are reported in Figure 6.25 and 6.26. The former is related to the furnace annealed samples, whereas the latter to the laser annealed ones. The luminous transmittance and the solar modulation are reported in Table 6.8, before and after the durability tests.

Table 6.8. Luminous transmittance (T_{lum}), solar modulation ($\Delta T_{sol,\ 90°C}$, $\Delta T_{sol,\ max}$) and NIR modulation at 2000 nm ($\Delta T_{2000,\ max}$) of VO_2–SiO_2 bilayers and of reference VO_2 films, before and after the durability tests. Legend: F = furnace annealed, L = laser annealed, V = VO_2, M = methyl-modified hybrid SiO_2, O = octyl-modified hybrid SiO_2, H = humidity durability tests.

Sample	T_{lum} (%)	$\Delta T_{sol,\ 90°C}$ (%)	$\Delta T_{sol,\ max}$ (%)	$\Delta T_{2000\ nm,\ max}$ (%)
28 nm VO_2 (V_{F4})	62.4	4.9	5.6	33.2
V_{F4}_H	63.4	3.2	3.7	26.1
Δ	**+1.6%**	-34.7%	-33.9%	**-21.4%**
28 nm VO_2 – 66 nm M_5T_5 ($V_{F1}_M_1$)	64.6	4.0	4.2	31.1
$V_{F1}_M_1_H$	64.2	3.4	3.8	29.0
Δ	**-0.6%**	-15.0%	-9.5%	**-6.8%**
28 nm VO_2 – 120 nm M_5T_5 ($V_{F2}_M_2$)	67.0	4.7	4.9	26.3
$V_{F2}_M_2_H$	60.0	3.9	4.5	31.8
Δ	**-10.4%**	-17.0%	-8.2%	**+20.9%**
28 nm VO_2 – 70 nm O_2T_8 (V_{F3}_O)	71.0	5.0	5.3	30.9
$V_{F3}_O_H$	70.4	4.1	4.5	29.4
Δ	**-0.8%**	-18.0%	-15.1%	**-4.9%**
30 nm VO_2 (V_{L3})	61.1	4.3	4.7	35.9
V_{L3}_H	65.1	2.2	2.5	20.0
Δ	**+6.5%**	-48.8%	-46.8%	**-44.3%**
27 nm VO_2 – 66 nm M_5T_5 ($V_{L1}_M_1$)	74.5	3.4	3.4	26.9
$V_{L1}_M_1_H$	70.9	3.0	3.1	26.8
Δ	**-4.8%**	-11.8%	-8.8%	**-0.4%**
31 nm VO_2 – 74 nm O_2T_8 (V_{L2}_O)	68.1	3.4	3.4	30.5
$V_{L2}_O_H$	*68.5*	*3.2*	*3.4*	*28.8*
Δ	**+0.6%**	-5.9%	0%	**-5.6%**

According to the literature (see paragraph 2.2 of Chapter 2), the exposure to high moisture conditions is expected to lead to the coating's degradation, which can result in a loss of thermochromicity. Considering the results from Table 6.8, all the hybrid SiO_2 coatings preserved the NIR modulation ($\Delta T_{2000,\ max}$), with respect to the uncoated VO_2 films. The uncoated furnace-annealed and laser-annealed VO_2 films were severely affected by the 1 month exposure to high moisture conditions, displaying losses in $\Delta T_{2000,\ max}$ of -21.4% and -44.3%, respectively. Among the bilayered samples, the $V_{F2}_M_2$ sample (28 nm VO_2 – 120 nm M_5T_5) led to the worse performance, as the luminous transmittance decreased by -10.4%. The two coated lasered sample ($V_{L1}_M_1$ and V_{L2}_O) displayed the best performance, with a decrease in $\Delta T_{2000,\ max}$ of only -0.4% and -5.6%, respectively, with respect

to the corresponding bilayers on the furnace annealed VO_2 films. The latter ($V_{F1}_M_1$ and V_{F3}_O) were characterized by a decrease in $T_{2000,\,max}$ of only -6.8% and -4.9%, respectively. As an overall result, the ~66 nm hybrid M_5T_5 coating and the 70-74 nm O_2T_8 coating favorably enhanced the durability under high moisture conditions of VO_2 films, both laser- and furnace-annealed.

7.4 Multifunctional bilayers - conclusions

VO_2 thermochromic thin films offer great opportunities regarding in terms of a lower reliance on HVAC systems, as they guarantee a passive modulation of the solar irradiation which does not require active energy inputs for its functioning. However, several factors need to be improved for a real-life application of VO_2 films for smart windows, among which the improvement of the optical properties and the coating durability are particularly important. The multilayer configuration represents one of the most extensively investigated strategies for the efficiency optimization of VO_2 thermochromic thin films, in terms of both optical properties and coating durability.

In this Chapter, a green sol-gel approach was employed for the deposition of VO_2, $TiO_2 – VO_2$, and $VO_2 – SiO_2$ samples. In line with the approach used for VO_2 films, the bilayers were synthesized aiming for a reduction of costs and energy load required for the fabrication, along with the choice of low hazardous chemicals. The optical and electrical response of the fabricated coatings was estimated by UV-VIS-NIR spectroscopy, reflectance measurements, and four-point probes technique, concurrent with the investigation of the coatings' morphology, crystalline structure, and optical constants.

In literature, TiO_2 coatings were demonstrated to synergistically enhance the transmittance of VO_2 films in the visible range. In this Chapter, the thickness of polycrystalline TiO_2 buffer layers was initially optimized and several $TiO_2 – VO_2$ bilayers were tested.

The deposition and annealing parameters were found to crucially influence several factors, particularly regarding the crystallization of VO_2 and the extension of the Ti ions diffusion into the VO_2 lattice. The elemental diffusion was confirmed by GIXRD, EELS and EDX-HRTEM analysis, and was found to severely impact the thermochromic efficiency of same samples, particularly the ones which were dried at higher temperatures before annealing. For the "high diffusion" samples, the increasing TiO_2 thickness led to a gradual disappearance of the metal-insulator transition, which was assessed with both optical transmittance and electrical resistivity measurements. To compensate for diffusion phenomena, the use of intermediate barrier layers could be used as a possible solution.

Nonetheless, regarding the "low diffusion" samples, a 70 nm TiO_2 – 35 nm VO_2 configuration was found to successfully increase the luminous transmittance by ~20% respect to the pristine VO_2 film. The increase in luminous transmittance was reached without deteriorating the thermochromic modulation of the latter. The latter two parameters (T_{lum} and ΔT_{sol}) usually display an opposite trend, whereas the final goal for smart window applications must be the simultaneous increase of both values.

Following the studies on TiO_2 – VO_2 bilayers, a different approach was tested by employing hybrid SiO_2 coatings. Previously crystallized VO_2 films were coated with amorphous anti-reflective silica coatings. Two types of hybrid SiO_2 coatings were selected, a methyl-modified SiO_2 (M_5T_5) and an octyl-modified one (O_2T_8). All the hybrid SiO_2 coatings led to an increase in luminous transmittance with respect to the original uncoated VO_2 films, for both furnace-annealed and laser-annealed films. As expected, the increased T_{lum} was linked to a decrease in solar modulation, which was however limited to a ~5-6% decrease for the most performing bilayers. Considering the laser-annealed VO_2 films, the T_{lum} remarkably increased by +22.5% with the addition of ~66 nm M_5T_5 coating and by +18.2% with the ~74 nm O_2T_8 coating. The highest luminous transmittance (T_{lum} = 74.5%) was reached with the 27 nm VO_2 – 66 nm M_5T_5 bilayer, with respect to the original T_{lum} = 60.8% of the lasered VO_2 film.

The five bilayers, along with the reference laser-annealed and furnace-annealed VO_2 films, were subjected to durability tests under high moisture conditions. According to the literature, the exposure to high moisture conditions was expected to lead to the coating's degradation, which can result in a loss of thermochromicity. The uncoated furnace-annealed and laser-annealed VO_2 films were severely affected by the 1 month exposure to high moisture conditions, displaying losses in $\Delta T_{2000,\ max}$ of -21.4% and -44.3%, respectively. With respect to the uncoated VO_2 films, all the hybrid SiO_2 coatings preserved the NIR modulation. The two coated lasered sample ($V_{L1}_M_1$ and V_{L2}_O) displayed the best performance, with a decrease in $\Delta T_{2000,\ max}$ of only -0.4% and -5.6%, respectively. As an overall result, the ~66 nm hybrid M_5T_5 coating and the 70-74 nm O_2T_8 coating favorably enhanced the durability under high moisture conditions of VO_2 films, both laser- and furnace-annealed.

References

1. Cao, X. *et al.* Challenges and Opportunities toward Real Application of VO2-Based Smart Glazing. *Matter* **2**, 862–881 (2020).

2. Cui, Y. *et al.* Thermochromic VO2 for Energy-Efficient Smart Windows. *Joule* **2**, 1707–1746 (2018).

3. Wu, W. *et al.* Design of Antireflection and Enhanced Thermochromic Properties of TiO2/VO2 Thin Films. *Adv Mater Interfaces* **10**, 2202506 (2023).

4. Powell, M. J. *et al.* Intelligent Multifunctional VO2/SiO2/TiO2 Coatings for Self-Cleaning, Energy-Saving Window Panels. *Chemistry of Materials* **28**, 1369–1376 (2016).

5. Wang, M. *et al.* Novel synthesis of pure VO2@SiO2 core@shell nanoparticles to improve the optical and anti-oxidant properties of a VO2 film. *RSC Adv* **6**, 108286–108289 (2016).

6. Cool, N. I. *et al.* Thermochromic Fenestration Elements Based on the Dispersion of Functionalized VO2 Nanocrystals within a Polyvinyl Butyral Laminate. *ACS Engineering Au* **2**, 477–485 (2022).

7. Outón, J. *et al.* Novel laser texturing of W-doped VO2 thin film for the improvement of luminous transmittance in smart windows application. *Appl Surf Sci* **608**, 155180 (2023).

8. Savorianakis, G. *et al.* VO2 nanostripe-based thin film with optimized color and solar characteristics for smart windows. *J Appl Phys* **129**, (2021).

9. Zhao, X. *et al.* Thermochromic composite film of VO2 nanoparticles and [(C2H5)2NH2]2NiBr4@SiO2 nanospheres for smart window applications. *Chemical Engineering Journal* **460**, 141715 (2023).

10. Zhao, S. *et al.* Roomerature Synthesis of Inorganic-Organic Hybrid Coated VO 2 Nanoparticles for Enhanced Durability and Flexible Temperature-Responsive Near-Infrared Modulator Application. *ACS Appl Mater Interfaces* **11**, 10254–10261 (2019).

11. Liu, S. *et al.* Bio-inspired TiO2 nano-cone antireflection layer for the optical performance improvement of VO2 thermochromic smart windows. *Scientific Reports 2020 10:1* **10**, 1–14 (2020).

12. Liu, S. *et al.* Self-Densified Optically Transparent VO2Thermochromic Wood Film for Smart Windows. *ACS Appl Mater Interfaces* **13**, 22495–22504 (2021).

13. Ke, Y. *et al.* Cephalopod-inspired versatile design based on plasmonic VO2 nanoparticle for energy-efficient mechano-thermochromic windows. *Nano Energy* **73**, 104785 (2020).

14. Zheng, J., Bao, S. & Jin, P. TiO2(R)/VO2(M)/TiO2(A) multilayer film as smart window: Combination of energy-saving, antifogging and self-cleaning functions. *Nano Energy* **11**, 136–145 (2015).

15. Ke, Y. *et al.* Two-Dimensional SiO2/VO2 Photonic Crystals with Statically Visible and Dynamically Infrared Modulated for Smart Window Deployment. *ACS Appl Mater Interfaces* **8**, 33112–33120 (2016).

16. Okimura, K., Mian, M. S., Yamaguchi, I. & Tsuchiya, T. High luminous transmittance and solar modulation of VO2-based smart windows with SiO2 anti-reflection coatings. *Solar Energy Materials and Solar Cells* **251**, 112162 (2023).

17. Zong, H. *et al.* Tuning the electrical and optical properties of ZrxOy/VO2 thin films by controlling the stoichiometry of ZrxOy buffer layer. *Appl Surf Sci* **487**, 138–145 (2019).

18. Saitzek, S., Guinneton, F., Sauques, L., Aguir, K. & Gavarri, J. R. Thermochromic CeO2–VO2 bilayers: Role of ceria coating in optical switching properties. *Opt Mater (Amst)* **30**, 407–415 (2007).

19. Chang, T. *et al.* Facile and Low-Temperature Fabrication of Thermochromic Cr2O3/VO2 Smart Coatings: Enhanced Solar Modulation Ability, High Luminous Transmittance and UV-Shielding Function. *ACS Appl Mater Interfaces* **9**, 26029–26037 (2017).

20. Yang, Y. *et al.* Controlling metal-insulator transition in (010)-VO2/(0001)-Al2O3 epitaxial thin film through surface morphological engineering. *Ceram Int* **44**, 3348–3355 (2018).

21. Meng, A. *et al.* Dual Cocatalysts in TiO2 Photocatalysis. *Advanced Materials* **31**, 1807660 (2019).

22. Miyazaki, K., Shibuya, K., Suzuki, M., Wado, H. & Sawa, A. High temperature coefficient of resistance of low-temperature-grown VO2 films on TiO2-buffered SiO2/Si (100) substrates. *J Appl Phys* **118**, (2015).

23. Qiu, H. *et al.* The tetragonal-like to rutile structural phase transition in epitaxial VO2/TiO2 (001) thick films. *New J Phys* **17**, 113016 (2015).

24. Ji, Y., Mattsson, A., Niklasson, G. A., Granqvist, C. G. & Österlund, L. Synergistic TiO2/VO2 Window Coating with Thermochromism, Enhanced Luminous Transmittance, and Photocatalytic Activity. *Joule* **3**, 2457–2471 (2019).

25. Wang, X. *et al.* Reducing Optical Reflection Loss for Perovskite Solar Cells Via Printable Mesoporous SiO2 Antireflection Coatings. *Adv Funct Mater* **32**, 2203872 (2022).

26. Ruud, C. J., Cleri, A., Maria, J. P. & Giebink, N. C. Ultralow Index SiO2Antireflection Coatings Produced via Magnetron Sputtering. *Nano Lett* **22**, 7358–7362 (2022).

27. Yao, L. *et al.* Long-Lived Multilayer Coatings for Smart Windows: Integration of Energy-Saving, Antifogging, and Self-Healing Functions. *ACS Appl Energy Mater* **2**, 7467–7473 (2019).

28. Mlyuka, N. R., Niklasson, G. A. & Granqvist, C. G. Thermochromic multilayer films of VO2 and TiO2 with enhanced transmittance. *Solar Energy Materials and Solar Cells* **93**, 1685–1687 (2009).

29. Sun, R. *et al.* Controllable Design of Bifunctional VO2Coatings with Superhydrophobic and Thermochromic Performances. *ACS Appl Mater Interfaces* **13**, 13751–13759 (2021).

30. Raut, H. K., Ganesh, V. A., Nair, A. S. & Ramakrishna, S. Anti-reflective coatings: A critical, in-depth review. *Energy Environ Sci* **4**, 3779–3804 (2011).

31. Yao, L. & He, J. Recent progress in antireflection and self-cleaning technology – From surface engineering to functional surfaces. *Prog Mater Sci* **61**, 94–143 (2014).

32. Paz, Y., Luo, Z., Rabenberg, L. & Heller, A. Photooxidative self-cleaning transparent titanium dioxide films on glass. *J Mater Res* **10**, 2842–2848 (1995).

33. Londhe, P., Chaure, N. B. & Athawale, A. TiO2 thin films derived by facile sol-gel method: Influence of spin rate and Al-doping on the optical and electronic properties. *Mater Today Commun* **29**, 102924 (2021).

34. Zhu, S. C., Xie, S. H. & Liu, Z. P. Nature of Rutile Nuclei in Anatase-to-Rutile Phase Transition. *J Am Chem Soc* **137**, 11532–11539 (2015).

35. Heo, C. H., Lee, S. B. & Boo, J. H. Deposition of TiO2 thin films using RF magnetron sputtering method and study of their surface characteristics. *Thin Solid Films* **475**, 183–188 (2005).

36. Weirich, T. E., Winterer, M., Seifried, S., Hahn, H. & Fuess, H. Rietveld analysis of electron powder diffraction data from nanocrystalline anatase, TiO2. *Ultramicroscopy* **81**, 263–270 (2000).

37. Wetchakun, N. & Phanichphant, S. Effect of temperature on the degree of anatase–rutile transformation in titanium dioxide nanoparticles synthesized by the modified sol–gel method. *Current Applied Physics* **8**, 343–346 (2008).

38. Tanemura, S. *et al.* Optical properties of polycrystalline and epitaxial anatase and rutile TiO2 thin films by rf magnetron sputtering. *Appl Surf Sci* **212–213**, 654–660 (2003).

39. Yasuda, T., Nishikawa, K. & Furukawa, S. Structural colors from TiO2/SiO2 multilayer flakes prepared by sol–gel process. *Dyes and Pigments* **92**, 1122–1125 (2012).

40. Depero, L. E., Bonzi, P., Musci, M. & Casale, C. Microstructural Study of Vanadium—Titanium Oxide Powders Obtained by Laser-Induced Synthesis. *J Solid State Chem* **111**, 247–252 (1994).

41. Zhao, G., Han, G., Takahashi, M. & Yoko, T. Photoelectrochemical properties of sol–gel-derived Ti1−xVxO2 solid solution film photoelectrodes. *Thin Solid Films* **410**, 14–20 (2002).

42. Shannon, R. D. Revised effective ionic radii and systematic studies of interatomic distances in halides and chalcogenides. *Acta Cryst.* **A32**, 751–767 (1976).

43. Nishikawa, M., Nakajima, T., Kumagai, T., Okutani, T. & Tsuchiya, T. Ti-doped VO2 films grown on glass substrates by excimer-laser-assisted metal organic deposition process. *Jpn J Appl Phys* **50**, (2011).

44. Stoyanov, E., Langenhorst, F. & Steinle-Neumann, G. The effect of valence state and site geometry on Ti L3,2 and O K electron energy-loss spectra of TixOy phases. *American Mineralogist* **92**, 577–586 (2007).

45. Wu, W. *et al.* Design of Antireflection and Enhanced Thermochromic Properties of TiO2/VO2 Thin Films. *Adv Mater Interfaces* **10**, 2202506 (2023).

46. Warwick, M. E. A., Ridley, I. & Binions, R. The effect of variation in the transition hysteresis width and gradient in thermochromic glazing systems. *Solar Energy Materials and Solar Cells* **140**, 253–265 (2015).

47. Koo, H. *et al.* Thermochromic properties of VO2 thin film on SiNx buffered glass substrate. *Appl Surf Sci* **277**, 237–241 (2013).

48. Du, J. *et al.* Significant changes in phase-transition hysteresis for Ti-doped VO2 films prepared by polymer-assisted deposition. *Solar Energy Materials and Solar Cells* **95**, 469–475 (2011).

49. Yoon, J., Park, C., Park, S., Mun, B. S. & Ju, H. Correlation between surface morphology and electrical properties of VO2 films grown by direct thermal oxidation method. *Appl Surf Sci* **353**, 1082–1086 (2015).

50. Béteille, F., Morineau, R., Livage, J. & Nagano, M. Switching properties of V1-XTiXO2 thin films deposited from alkoxides. *Mater Res Bull* **32**, 1109–1117 (1997).

51. Basso, M. *et al.* Bioinspired silica-based sol–gel micropatterns on aluminium for humid air condensation. *J Solgel Sci Technol* **102**, 466–477 (2022).

52. Basso, M. *et al.* Hydrophobic hybrid silica sol-gel coating on aluminium: Stability evaluation during saturated vapour condensation. *Journal of Non-Crystalline Solids: X* **17**, 100143 (2023).

Chapter 7
VO_2 thin films for H_2 gas sensing

Table of contents

7 Chapter 7 – VO_2 thin films for H_2 gas sensing 311

7.1 Introduction 313

7.1.1 Properties of gas sensors 314

7.1.2 Gas sensing mechanism 314

7.1.3 Vanadium oxides as gas sensors 315

7.2 VO_2 thin films for H_2 gas sensing 316

7.2.1 Device fabrication 316

7.2.2 Device characterization 317

7.2.3 Electrical and optical H_2 gas sensing 322

7.2.4 H_2 gas sensing – discussion 327

7.3 Conclusions 329

Author disclosure statement

The data and the discussion reported in Chapter 7 are part of a manuscript under preparation, which will be submitted for publication in the draft article "Influence of morphology and crystallinity degree of VO_2 thin films on H_2 gas sensing. *Manuscript under preparation.*"

8.1 Introduction

As previously introduced in Chapter 3, the reversible metal-insulator transition of VO_2 can be activated by multiple stimuli, including temperature, pressure, strain, electric or magnetic fields.[1,2] As a result, the optical and electrical properties of VO_2 have been exploited in a wide range of applications, including radiative space applications, thermal controllers, cathode materials for aqueous batteries, H_2 production by photocatalysis, electrocatalytic water splitting, neuromorphic memristors, microactuators, optical filters, polarization converters, and gas sensors.[3–26] While Chapters 4-6 have been focused on VO_2-based smart windows, in this Chapter 7 different types of VO_2 thin films have been employed as gas sensors for hydrogen detection.

The importance of gas detection has been growing with the progress of industrialization and urbanization. The applications of gas sensors include the control of emissions in the automotive industry, leak detection in the petrochemical industry, and breath diagnosis tools in the medical field.[27–29] Moreover, household appliances increasingly require the presence of detectors to monitor the air quality, humidity, or CO_2 presence.[30,31] Among the several gases, H_2 is becoming increasingly important in the field of decarbonization and implementation of low-impact renewable energy.[32]

Metal oxide (MOs) semiconductors are among the most popular materials employed as conductometric gas sensors. This class of materials are sometimes affected by a low selectivity and sensitivity to humidity, but simultaneously offer a high sensitivity and short response time. Among the most exploited materials figure TiO_2, ZrO_2, SnO_2 CeO_2, ZnO, and CuO, which sensing properties arise from stoichiometric variations upon gas exposure.[33–39] Besides the conventional electrical-based gas sensors, which are based on the variation of electrical conductivity upon gas exposure, opto-chemical gas sensors offer advantages in terms of process parameters, as variations in intensity, wavelength, or probing light polarization can be monitored.[40]

8.1.1 *Properties of gas sensors*

The efficiency of a gas sensor is evaluated by considering specific key features, such as the sensitivity, selectivity, response time, reversibility, recovery time, stability, energy consumption and fabrication costs.[29,41] Sensitivity describes the sensor's capability of identifying a specific gas within a mixture, whereas selectivity expresses the minimum gas volume required for detection by the sensor. The response time describes the time required for the sensor to generate a signal since the start of gas exposure, whereas the reversibility and recovery time express the capability and time required for the sensor to return to the pristine state after gas exposure. Finally, the stability is evaluated in terms of stability during working conditions, which generally involve high temperatures and analyte presence, and during storage at standard conditions.

8.1.2 *Gas sensing mechanism*

The underlying mechanism which allows the MOs response upon gas exposure is still under debate. Two key models are generally accepted and combined to explain the sensing mechanism, namely the ionosorption model and the oxygen-vacancy model.

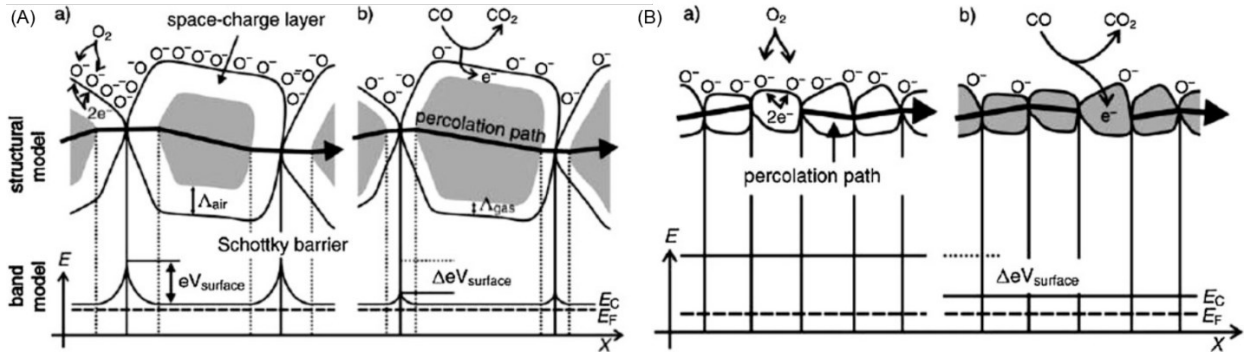


Figure 7.1. Mechanism controlling the conductivity change and its magnitude in function of the ratio between grain size (D) and Debye screening length (Λ): (A) D>2Λ, (B) D<2Λ.[42]

According to the ionosorption model, redox reactions are developed between the target gas and the ionosorbed oxygen ions on the MO surface. A variation in the electronic configuration of the MO is induced by the redox reactions, which leads to a variation of the sensor's electrical resistance. Oxygen molecules are adsorbed on the MO surface in either the molecular form ($O_2^-{}_{,ads}$, 150-200°C) or dissociated form (O^-_{ads} or O^{2-}_{ads}, 200-400°C). Consequently, the MO surface is negatively charged and a formation of a positively charged electron-depleted region is induced below the surface, to balance the negatively charged region (space charge region, Λ, Figure 7.1). The adsorbed oxygen species can react with reducing gases or compete in adsorption with oxidizing ones, leading to variations in band bending and electrical conductivity.[42]

The micro- and nanostructure of the gas sensor crucially influence the sensing dynamics. The decreasing size of the crystalline grain boundaries can enhance the sensor's response. The space charge region (SCR) displays a higher electrical resistance with respect to the bulk and therefore highly affects the charge transport. For grain size (D) lower than the double of the SCR length ($D>2\Lambda$, Figure 7.1 (B)), the whole grain actively participates in the charge transfer. Small grain sizes allow high sensitivity, due to the considerable impact of the charge depletion layer on the conduction channel.[41,42]

According to the oxygen-vacancy model, reducing gases do not react with ionosorbed oxygen on the MO surface, but instead remove the oxygen of the MO lattice. For example, CO gas would react with the latter oxygen to form CO_2, along with an oxygen vacancy on the surface of the MO. Upon the ionization of the oxygen vacancy, electrons are then released into the conduction band, with a resulting increase in conductivity. Gaseous oxygen subsequently fills the oxygen vacancies, extracting electrons from the MO conduction band and hence decreasing the conductivity.[42]

8.1.3 *Vanadium oxides as gas sensors*

Multiple vanadium oxides have been employed and eventually combined as gas sensors. Most of the studies highlight the crucial importance of creating nanostructured metal oxides, to increase the surface able to react with the gaseous species. Babar *et al*.[43] employed nanoplatelets and sponge-like V_2O_5 for NO_2 sensing at 150°C, highlighting the crucial role of porosity. Sanger *et al*.[44] combined Pd and V_2O_5 thin films for H_2 detection, exploiting the hydrogen spillover induced by the Pd layer. Han *et al*.[45] combined the nanostructured morphology of V_2O_5 nanocolumns with the presence of residual monoclinic VO_2. The porous V_2O_5 *n*-type semiconductor, along with the presence of narrow necks, favored a high selectivity towards NO_2 at low temperature. The residual VO_2 acted as an electron donor, which extended the depletion region and favored the oxygen adsorption.

Among the multiple VO_2 polymorphs, VO_2 (B) particularly emerges for gas sensing applications. VO_2 (B) ultrathin vertical nanosheets were employed by Liang *et al*.[46] for room temperature detection of NO_2. The band gap of VO_2 was found to become narrower upon NO_2 adsorption, with a shift of the Fermi level towards the valence band along with an increase in the density of states near the Fermi level. In another work[47], the sensitivity of VO_2 (B) nanorods towards NH_3 detection at room temperature was enhanced through the addition of In_2O_3 nanoparticles. Evans *et al.*[48] combined VO_2 (B) with carbon nanotubes for water vapor and NH_3 sensing, by appropriately tuning both the surface composition and the microstructure.

Fewer studies exploited the metal-insulator transition (MIT) of VO_2 (M1) for gas sensing. Strelcov *et al*.[49] and Baik *et al*.[50] were the first to report hydrogen sensing based on VO_2 (M1) nanowires. The second group highlighted the key role of Pd nanoparticles in inducing the dissociative chemisorption of hydrogen, which was then incorporated in the VO_2 in the atomic form. A two-step variation in electronic conduction was found, i.e., a rapid decrease in MIT transition temperature by 10°C, followed by hours-long hydrogen diffusion accompanied by a modest change in MIT temperature but significant increase in conductivity. The recovery was however noticed to be quite slow. The authors proposed the interaction to be based on two distinct mechanisms. The first involved electron-phonon coupling due to the introduction of H impurities, whereas the second involved the modification of the material's band structure, due to the release of electrons following the diffusion of interstitial H.

8.2 VO_2 thin films for H_2 gas sensing

To test the efficiency of VO_2 towards H_2 gas sensing, the influence of crystallinity, morphology, and chemical composition was considered. Overall, three types of thin films were fabricated, with different degrees of crystallinity, nanostructured morphology, and chemical composition. A furnace-annealed VO_2 thin film was compared to a laser-annealed one. The two samples are characterized by a remarkably different morphology, as shown in Chapters 4-5. A third sample was fabricated by laser-annealing the films with only 10 laser pulses. As discussed in Chapter 5, this leads to the formation of a few crystallites within the remaining amorphous matrix. Besides the presence of a lower degree of crystallinity, the latter samples display a different chemical composition in terms of oxidation state, with respect to fully crystallized VO_2 films. As emerged from the XPS analysis displayed in Chapter 5, the samples irradiated with 10 laser pulses display a higher V^{5+} state with respect to the V^{4+} state of the crystalline VO_2 samples. The differences in terms of morphology, chemical composition, and crystallinity were expected to lead to different responses during the gas sensing tests.

8.2.1 *Device fabrication*

Three types of thin films were compared, namely a furnace-annealed VO_2 thin film, a fully laser-annealed VO_2 thin film, and a partially laser-annealed VO_2 thin film. The three types will be addressed as "Furnace – TT", "Laser high cryst. – L70 300#" and "Laser low cryst. – L70 10#", with "TT" standing for thermal treatment, "high/low cryst" for high/low crystallinity, "L70 300/10#" for laser annealed at 70 mJ/cm^2 for 300 or 10 pulses, respectively. All three types of films were deposited on four types of substrates, namely monocrystalline silicon wafer ("S"), fused silica ("Q"), a silicon

nitride (Si_3N_4) film on silicon substrate ("SN"), and a Si_3N_4 film on silicon substrate with platinum electrodes ("SNE"). The latter substrates were used for the electrical resistance measurements during the gas sensing tests, whereas the fused silica ones were used for the optical gas sensing tests. The additional substrates were fabricated as a reference for the characterizations of the VO_2 thin films, as some of the latter require the presence of smooth and/or bigger sized substrates. Two lengths were considered for the squared silicon substrates, i.e., 0.5 cm ("S") and 1.5 cm ("Sg").

The VO_2 thin films were deposited according to the standard procedure described in paragraph 4.3.2.2 of Chapter 4. Briefly, a 100 mM solution of $VO(acac)_2$ in ethanol was aged 4 months, filtered with 0.2 µm pore-sized filters and deposited by spin coating under ~85 RH% 24°C moisture conditions. The spin coating was performed three times at 2000 rpm for 30 seconds, with each layer being dried at 150°C for 10 min. The samples were aged for 6 days under low moisture conditions, i.e. below 30% RH 22°C. The furnace-annealed samples were crystallized in a tubular furnace at 550°C for 1 h, with a heating ramp of 10°C/min under a 0.1 lpm N_2 flux. The laser-annealed samples were irradiated with a KrF excimer laser in air at 70 mJ/cm^2 for 300 pulses at 8 Hz or 10 pulses at 1 Hz, respectively. The detailed furnace annealing procedure is reported in Appendix A.1.5, whereas the laser annealing one in Appendix A.1.6.

Platinum nanoparticles were deposited on some of the annealed VO_2 thin films. The Pt nanoparticles were obtained following the procedure described in Appendix A.1.7. A 30 mM solution of Pt nanoparticles in ethanol was spin coated at 2000 rpm for 30 s. The samples were dried on a hot plate at 200°C for 1 h and treated with a UV lamp (Hamamatsu Lightningcure LC5 UV, Model L8333-01) for 7 min.

8.2.2 *Device characterization*

Prior to the gas sensing tests, techniques such as grazing incidence X-ray diffraction (GIXRD), Raman spectroscopy, scanning electron microscopy (SEM), UV-Vis-NIR spectroscopy, and ellipsometry were employed to characterize the three types of VO_2 thin films on all substrate types.

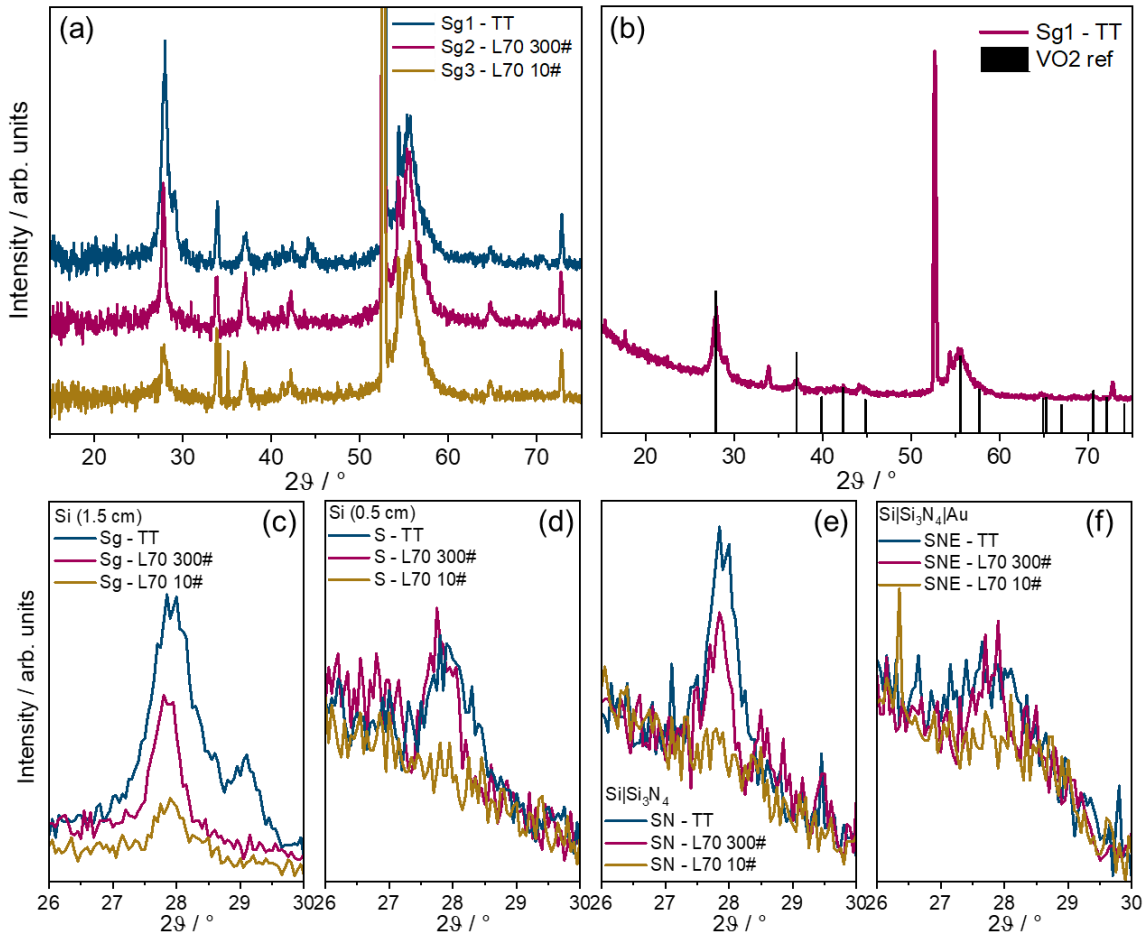


Figure 7.2. (a) Grazing incidence X-ray diffraction (GIXRD) of the furnace annealed sample (TT), the high crystallinity laser-annealed sample (L70 300#) and the low crystallinity laser-annealed sample (L70 10#) on silicon substrate (Sg, 1.5 cm²). (b) Reference GIXRD pattern of monoclinic VO_2 (M1). (c-f) Focus on the 26-30° diffraction range to highlight the differences in the principal diffraction at $2\Theta \sim 27.9°$ of the three sample types, on (c) silicon (Sg, 1.5 cm²), (d) silicon (S, 0.5 cm²), (e) Si_3N_4 film on silicon (SN), and (f) Si_3N_4 film on silicon with platinum electrodes (SNE).

The GIXRD patterns are reported in Figure 7.2. The full range pattern of the furnace annealed film (TT) and laser annealed films with 300 (L70 300#) and 10 (L70 10#) pulses is shown in Figure 7.2 (a), whereas the reference VO_2 (M1) pattern is visible in Figure 7.2 (b). The reference diffraction pattern on the silicon substrate, which is detectable in all three samples, was previously reported in Chapter 4. A focus on the principal (0 1 1) orientation at $2\Theta \sim 27.9°$ is shown for the four substrate types, i.e. Sg, S, SN, and SNE (Figure 7.2 (c-f)). All three types of thin films were confirmed to be monoclinic VO_2 (M1). While the furnace annealed film and the film lasered with 300# displayed a high crystallinity, the films lasered with 10# displayed a weak (Figure 7.2 (c, f)) or almost imperceptible (Figure 7.2 (d, e)) diffraction.

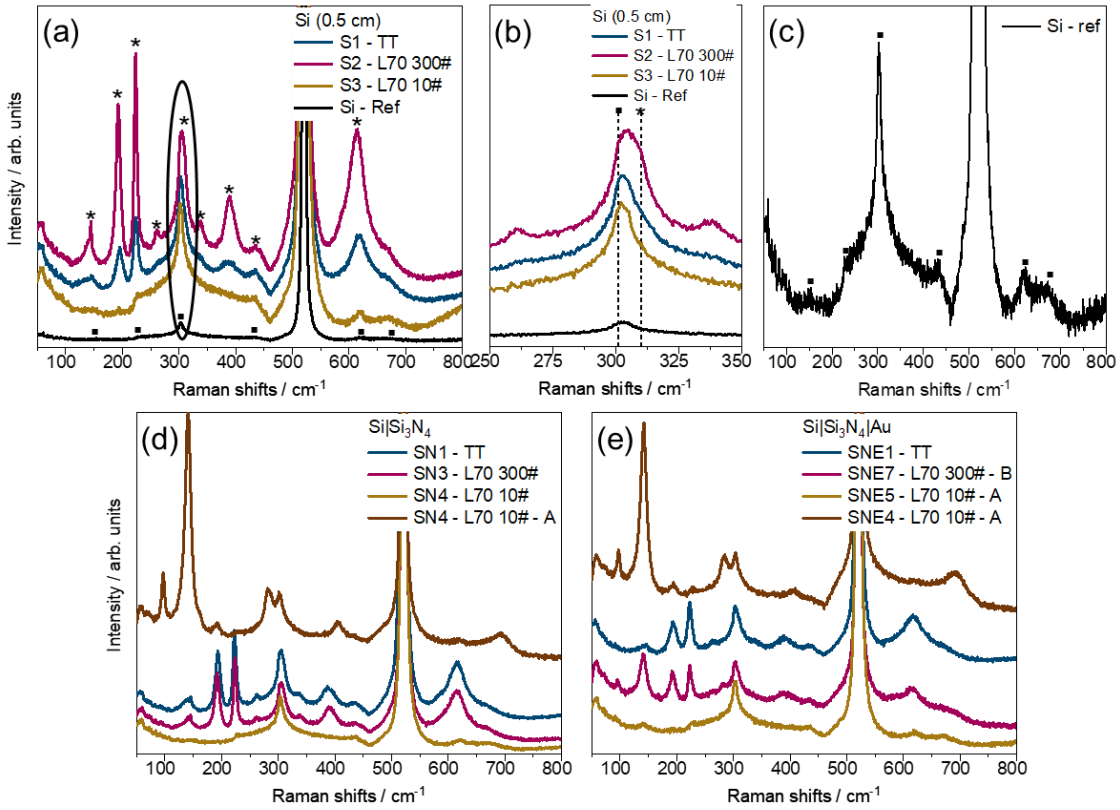


Figure 7.3. (a) Raman spectroscopy of the furnace annealed sample (TT), the high crystallinity laser-annealed sample (L70 300#) and the low crystallinity laser-annealed sample (L70 10#) on silicon substrate (S, 0.5 cm²). (b) Focus on the 250-350 cm⁻¹ range to highlight the difference between the silicon and VO_2 shifts. (c) Reference Raman shifts of the silicon substrate. (d) Raman spectroscopy of the furnace annealed sample (TT), the high crystallinity laser-annealed sample (L70 300#) and the low crystallinity laser-annealed sample (L70 10#) on Si_3N_4 film on silicon substrate (SN). Two different areas are shown for the L70 10# sample, indicating the amorphous region (yellow curve, L70 10#) and the V_2O_5 region (brown curve, L70 10# - A). (e) Reference Raman shifts of the silicon substrate. (d) Raman spectroscopy of the furnace annealed sample (TT), the high crystallinity laser-annealed sample (L70 300#) and the low crystallinity laser-annealed sample (L70 10#) on Si_3N_4 film on silicon substrate with platinum electrodes (SNE). Two different areas are shown for the L70 300# sample, indicating the amorphous region (yellow curve, SNE5 - L70 10#) and the V_2O_5 region (brown curve, SNE4 - L70 10#).

Micro-Raman spectroscopy was employed to verify on multiple locations of the thin films the type of vanadium oxides which were generated after furnace or laser annealing. Similarly to the GIXRD analysis, the three thin film types were analyzed by Raman spectroscopy on silicon (S, Figure 7.3 (a, b)), SN (Figure 7.3 (d)), and SNE (Figure 7.3 (e)) substrates. The reference shifts of the silicon substrates are reported in Figure 7.3 (c), as well as in Figures 7.3 (a, b). Considering the reference silicon substrates (Figure 7.3 (a)), the shifts of the TT and L70 300# films were attributed to monoclinic VO_2 (M1).[51] A zoom around the shift at 300 cm^{-1} is reported in Figure 7.3 (b), to highlight the difference between the shifts of silicon and VO_2, respectively. The L70 10# sample did not display other shifts besides the ones attributed to the underlying silicon substrate. On SN and SNE substrates, on the other hand, different areas were found within the thin films. On both substrate types, the L70 10# sample displayed either amorphous areas, evidenced by the presence of the silicon shifts, or Raman shifts attributed to V_2O_5 (brown lines, L70 10# - A, Figure 7.3 (d, e)). This result well agrees with the X-ray spectroscopy analysis (XPS), which was previously discussed in paragraph 5.3.4 of

Chapter 5. In the latter, the presence of a V^{5+} oxidation state was found on the dried thin film, which was gradually seen to be reduced to a V^{4+} oxidation state upon increasing laser pulses. On the SNE substrates, which were the ones employed during the electrical resistance-based gas sensing tests, the L70 300# thin film displayed two different types of Raman shifts. Most analyzed areas displayed the typical VO_2 shifts, but a few areas with a mixed VO_2 and V_2O_5 composition were found (purple line, Figure 7.3 (e)).

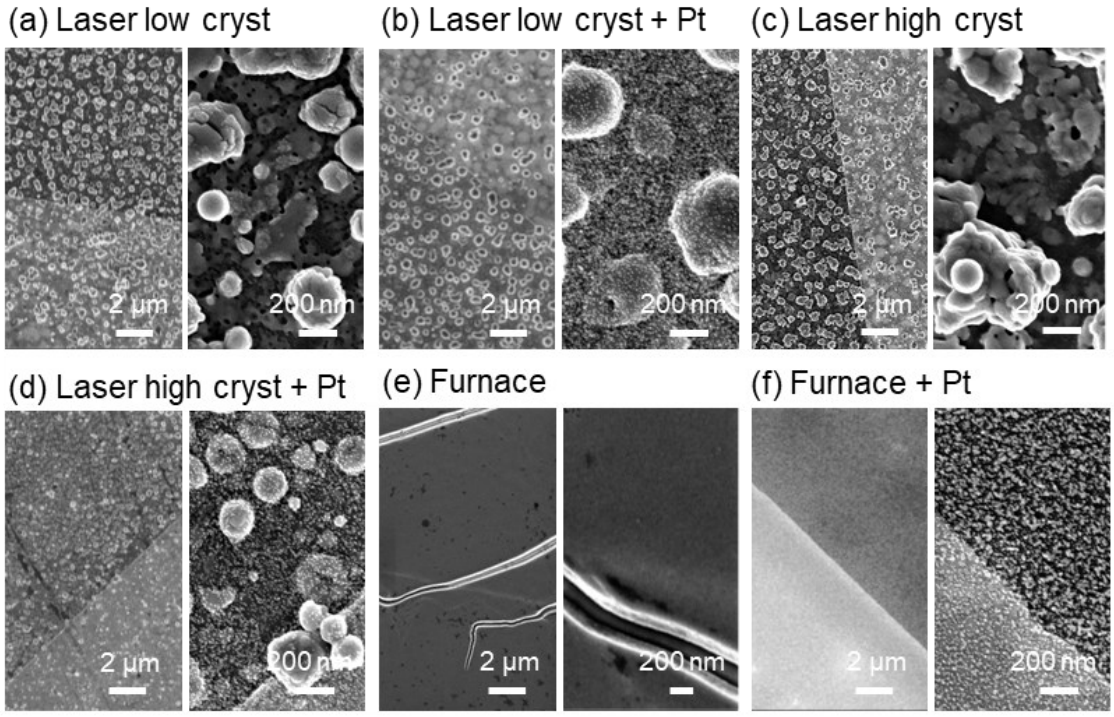


Figure 7.4. Scanning electron microscopy (SEM) images of the thin films on SNE substrates: (a, b) laser-annealed low crystallinity without and with Pt nanoparticles, respectively; (c, d) laser-annealed high crystallinity without and with Pt nanoparticles, respectively; (e, f) furnace annealed without and with Pt nanoparticles, respectively. The scale bar is reported in each image and the Pt electrodes are visible in the images at higher magnifications (i.e., 2 µm).

As discussed in the Introduction, the thin film morphology is known to greatly affect the gas sensing properties. SEM was employed to analyze the morphology of each sample type, both with and without the Pt nanoparticles. The morphology of the samples used during the gas sensing tests, i.e., on the SNE substrates, are reported in Figure 7.4. The furnace annealed samples (Figure 7.4 (e, f)) confirmed the typical smooth morphology, along with a uniform surface coverage, of the optimized VO_2 thin films discussed in Chapter 4. The different substrate type upon laser annealing, with respect to previously shown silicon and fused silica ones (Chapter 5), was confirmed to have a marginal influence on the film's morphology, as the former was found to be highly dependent on the matter-laser interaction. Slight differences were found between the two laser-annealed thin films, with the 10# one displaying the presence of nanometric sized holes due to gaseous release (Figure 7.4 (a)), as discussed in Chapter 5. The disappearance of the latter holes was confirmed upon increasing number of laser pulses (300#, Figure 7.4 (c)). The presence of Pt nanoparticles, with a uniform surface

coverage in all samples, was clearly visible from Figure 7.4 (b, d, f). Both the electrodes and the underlying Si_3N_4/Si substrate were uniformly covered by the VO_2 thin films, even though the furnace annealed samples displayed some dewetted and/or cracked areas.

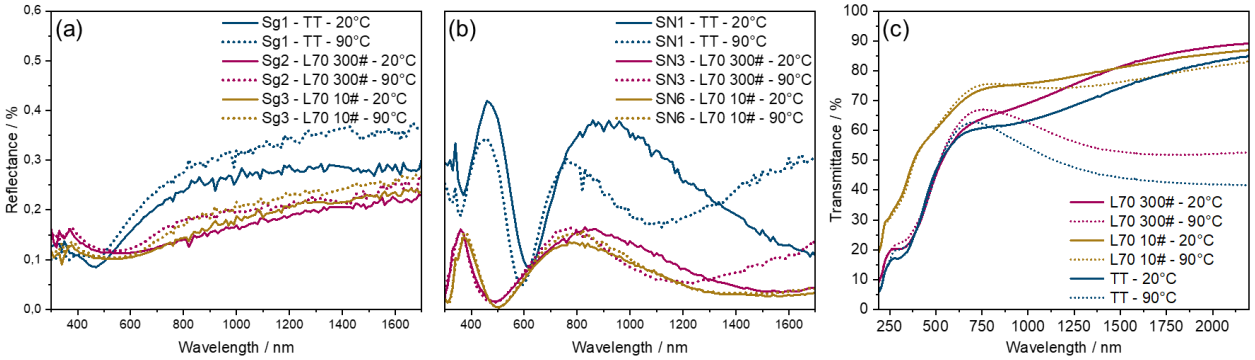


Figure 7.5. Reflectance and transmittance variations at 20°C (solid lines) and 90°C (dotted lines). (a) Reflectance of the furnace annealed sample (TT), the high crystallinity laser-annealed sample (L70 300#) and the low crystallinity laser-annealed sample (L70 10#) on silicon substrate (Sg, 1.5 cm^2). (b) Reflectance of the furnace annealed sample (TT), the high crystallinity laser-annealed sample (L70 300#) and the low crystallinity laser-annealed sample (L70 10#) on Si_3N_4 film on silicon (SN) substrate. (c) Transmittance of the furnace annealed sample (TT), the high crystallinity laser-annealed sample (L70 300#) and the low crystallinity laser-annealed sample (L70 10#) on the fused silica substrates.

To further verify the presence of monoclinic VO_2 (M1), optical characterization was performed at different temperatures with the aid of a UV-Vis-NIR spectrophotometer and an ellipsometer. The former was employed for the films deposited on fused silica substrates, which were then used for the optical gas sensing tests. The ellipsometer was used to test the silicon (S, Sg) and Si_3N_4/Si (SN) substrates. The latter were considered the closest approximation of the SNE substrates, which were used for the electrical resistance-based gas sensing tests. The SNE samples could not be directly measured by ellipsometry, as the latter is highly influenced by the presence of inhomogeneous morphology and reflecting materials (i.e., Pt electrodes). Considering the fused silica substrates (Figure 7.5 (c)), the furnace-annealed sample and the laser-annealed film with 300# both displayed a well-defined solar modulation, as visible from the difference between the low-temperature spectra (solid lines) and high-temperature ones (dotted lines). The sample laser-annealed with 10# displayed a weak, but clearly visible, solar modulation (yellow lines, Figure 7.5 (c)), which confirms the weak diffraction peaks of VO_2 (M1) previously found by GIXRD. Coherent results were found on fused silica substrates, a solar modulation was found on the silicon and SN substrates as well, in which the metallic state led to a higher reflectance in the NIR range (Figure 7.5 (a, b)). The modulation was higher in the case of the furnace annealed samples with respect to the laser-annealed ones at 300#. The weak solar modulation of the L70 10# sample was confirmed on both silicon and SN substrates.

8.2.3 *Electrical and optical H_2 gas sensing*

Following the materials' characterization, the response of the samples to H_2 detection was tested considering both the variations in electrical resistance and in optical transmission. The former were measured on SNE substrates and will be reported in the first part of paragraph 7.2.3, whereas the latter were performed on fused silica substrates and will be shown in the second part of the paragraph. Paragraph 7.2.4 will be devoted to the discussion of both gas sensing results.

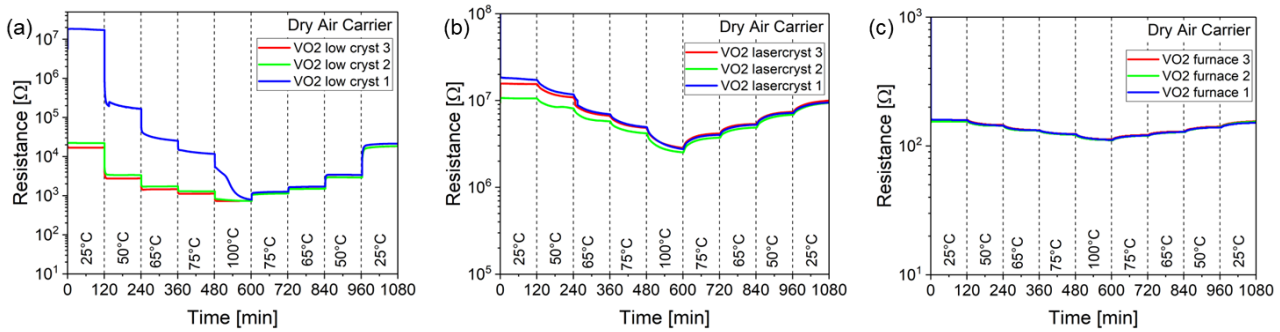


Figure 7.6. Resistance variations in function of the temperature (25-100°C) in dry air carrier of the (a) low crystallinity laser-annealed sample (L70 10#), (b) high crystallinity laser-annealed sample (L70 300#), (c) furnace annealed sample (TT), on SNE substrates. Three cycles were applied for each sample, represented respectively by the blue (1st cycle), green (2nd cycle), and red (3rd cycle)) curves.

The detailed procedure of the conductometric gas sensing tests is reported in Appendix A.2.17. The electrical resistance was initially characterized in function of the temperature, by applying three heating and cooling cycles (Figure 7.6). The electrical behavior of the low crystallinity sample, i.e., the sample lasered with 10 pulses, was stabilized after the first cycle, which was attributed to the initial presence of organic residues.

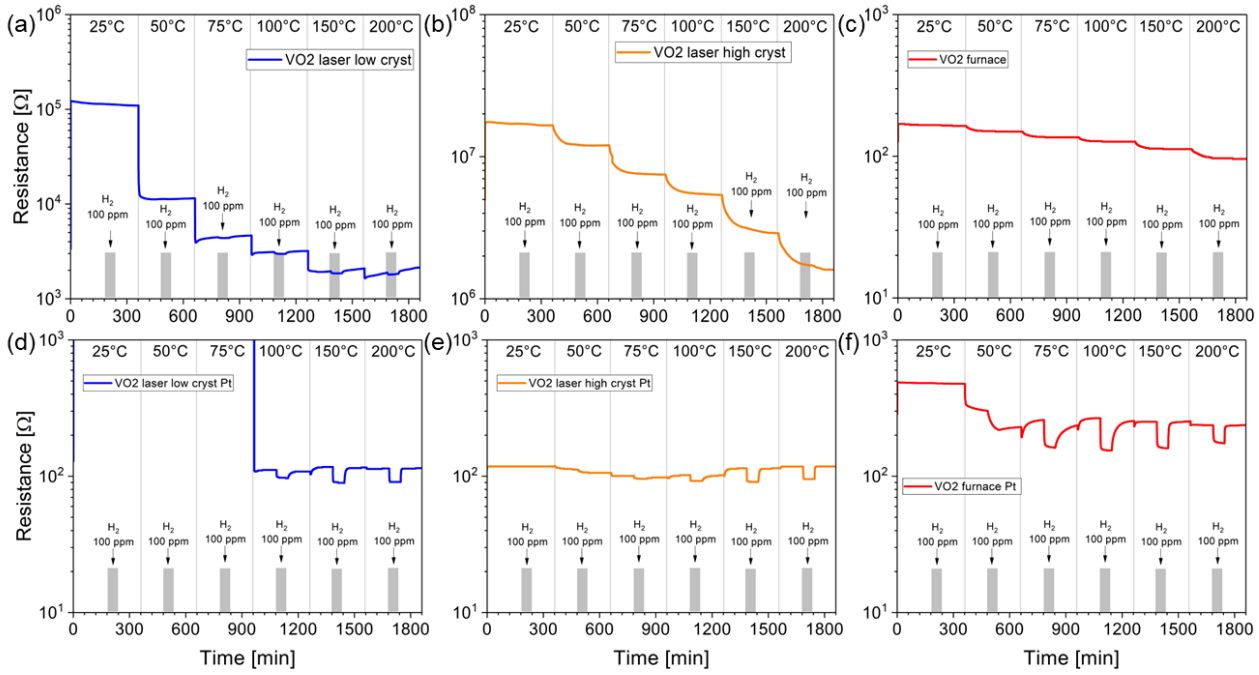


Figure 7.7. Resistance variations of the samples on SNE substrates in function of the temperature (25-200°C) upon exposure to 100 ppm of H_2 in dry air carrier, with alternating cycles of gas desorption in dry air. (a, d) Low crystallinity laser-annealed sample (L70 10#) without and with Pt nanoparticles, respectively. (b, e) High crystallinity laser-annealed sample (L70 300#), without and with Pt nanoparticles, respectively. (c, f) Furnace annealed sample (TT), without and with Pt nanoparticles, respectively.

In Figure 7.7 the static H_2 gas sensing tests are reported for samples with and without Pt nanoparticles. Initially, the optimal sensing temperature (OT) was tested, by repeatedly exposing all samples to 100 ppm of H_2 and varying the temperature from 25°C to 200°C. The OT was evaluated by considering two aspects of the sensor's response. The first aspect was the sensor's signal amplitude (relative response ratio, $RR = R_{air}/R_{gas}$), while the second was the recovery of the baseline resistance after gas desorption (resistance of air at equilibrium, BRL). Considering the samples without Pt nanoparticles, the low crystalline sample was the only one to display a weak response above 100°C, even if almost imperceptible (Figure 7.7 (a)). With increasing temperature, the two laser-annealed samples showed a monotonic decrease in the BRL, which is typical of semiconducting materials.[52] When the Pt nanoparticles were added on the VO_2 thin films, all three sample types displayed a response to 100 ppm of H_2 gas, through a decrease in resistance upon gas exposure above a certain OT (Figure 7.7 (d-f)). Both the low and high crystallinity laser-annealed samples showed a low signal response at 100°C, along with a slow recovery of the BLR (Figure 7.7 (d, e)). With a 150°C OT, the sensor's response was higher and the desorption kinetics considerably improved in both cases. In the case of the furnace annealed VO_2 film covered with Pt nanoparticles (Figure 7.7 (f)), the sensor responded to H_2 gas exposure below 100°C, but with the BLR was not fully recovered before the following H_2 exposure. A temperature of 150°C was confirmed to be the optimal temperature for this sample as well.

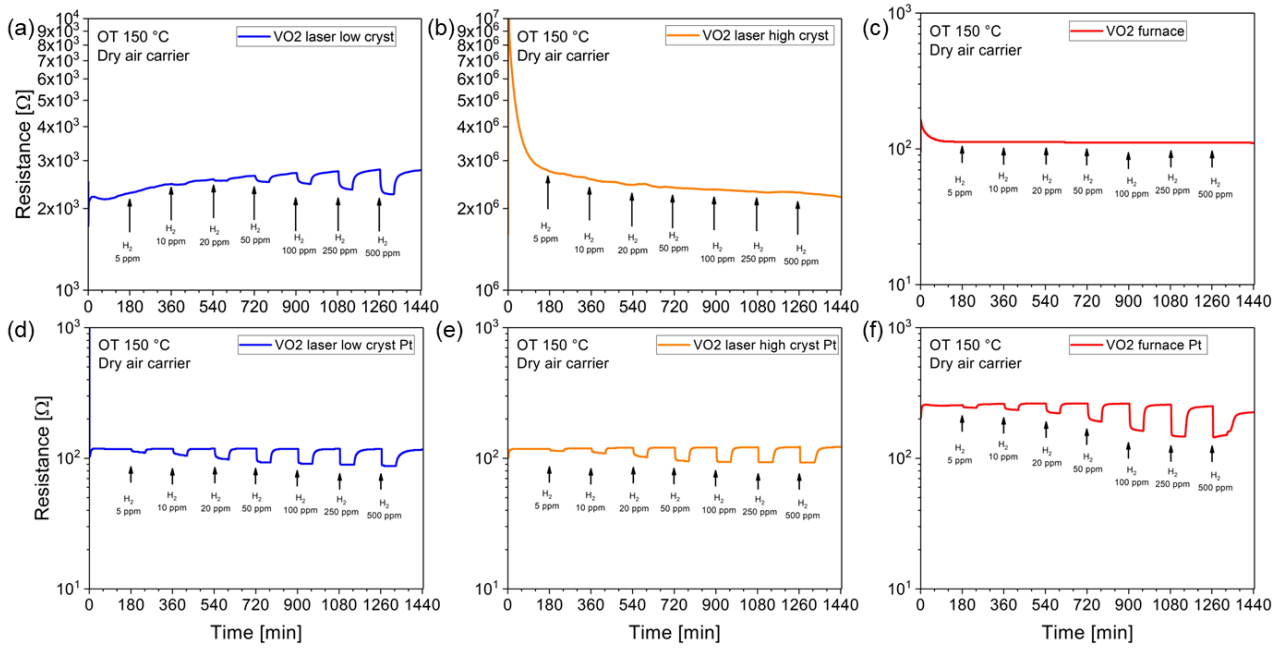


Figure 7.8. Resistance variations of the samples on SNE substrates at the optimal temperature of 150°C upon exposure to increasing levels of H_2 (5-500 ppm) in dry air carrier, with alternating cycles of gas desorption in dry air. (a, d) Low crystallinity laser-annealed sample (L70 10#) without and with Pt nanoparticles, respectively. (b, e) High crystallinity laser-annealed sample (L70 300#), without and with Pt nanoparticles, respectively. (c, f) Furnace annealed sample (TT), without and with Pt nanoparticles, respectively.

Following the determination of the OT, dynamic gas sensing tests were performed on each sample type. The resistance was monitored at fixed OT = 150°C, by varying the H_2 gas concentration from 5 to 500 ppm in dry air carrier. The low crystallinity laser-annealed sample, without Pt nanoparticles, displayed an H_2 detection up to 20 ppm, even if with a weak sensor's signal (Figure 7.8 (a)). The high-crystallinity laser-annealed sample and the furnace annealed one, without Pt nanoparticles, did not respond to a higher H_2 concentration (Figure 7.8 (b, c)), with respect to the previous static tests. The VO_2 films covered with Pt nanoparticles displayed an excellent recovery of the BLR after each H_2 exposure, along with a fast sensors' response. The detection limit was found to be 5 ppm in all three samples (Figure 7.8 (d-f)).

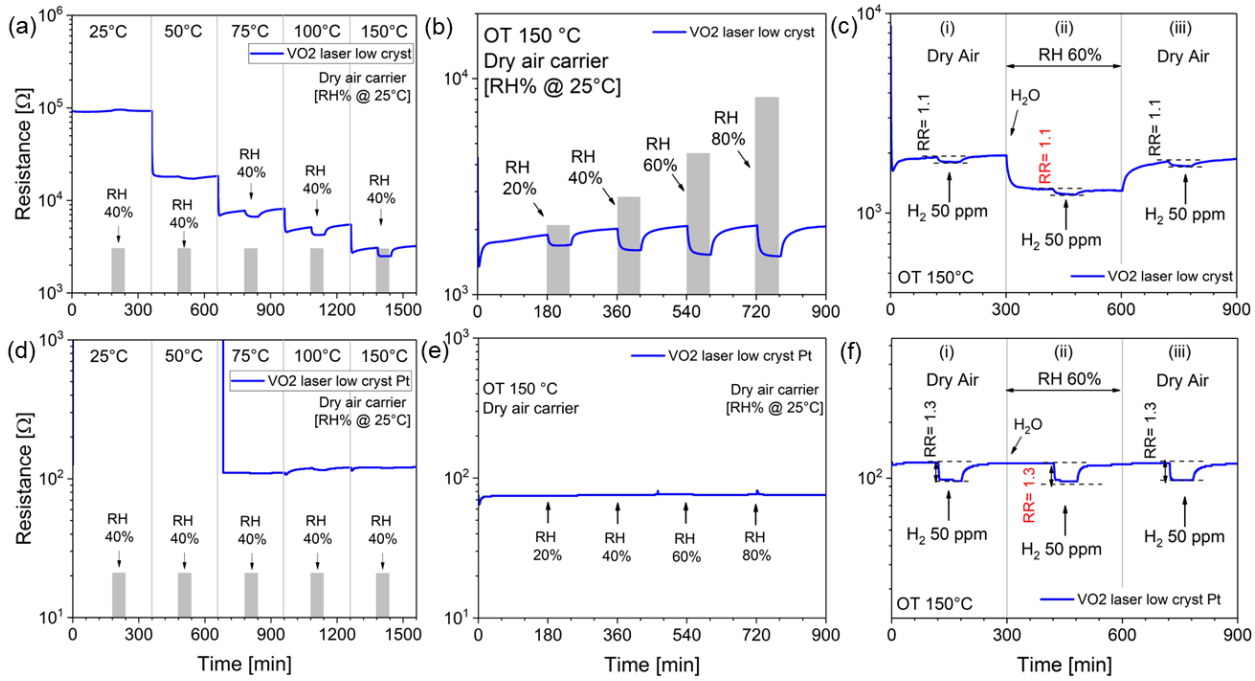


Figure 7.9. (a, d) Resistance variations of the low crystallinity laser-annealed sample (L70 10#) on SNE substrates without and with Pt nanoparticles, respectively, with increasing temperature (25-200°C) upon exposure to 40% RH 25°C in dry air carrier, with alternating cycles of gas desorption in dry air. (b, e) Resistance variations of the low crystallinity laser-annealed sample (L70 10#) on SNE substrates without and with Pt nanoparticles, respectively, with increasing RH levels at the optimal temperature of 150°C, with alternating cycles in dry air. (c, f) Cross sensitivity tests on the low crystallinity laser-annealed sample (L70 10#) on SNE substrates without and with Pt nanoparticles, respectively, at the optimal temperature of 150°C, with 50 ppm H_2 in dry air and 60% RH.

Air humidity is known to affect the sensor's response as it can either improve or hinder the latter performance. The sensor's response to 40% RH at 25°C air was tested at increasing temperature on the low crystallinity sample, with and without Pt nanoparticles. The two samples were chosen to verify the role of the VO_2 thin film and the beneficial effect of Pt nanoparticles. As visible from Figure 7.9 (a, c), only the sample without Pt nanoparticles did detect the moisture presence, when the temperature was raised to 75°C. The sample with Pt nanoparticles was confirmed to be selective towards H_2 and not sensible to the presence of moisture. Considering the BLR recovery, the OT was selected to be 150°C and dynamic tests were performed by exposing the two samples to increasing RH levels at 25°C. The low crystallinity laser-annealed VO_2 thin films displayed a higher decrease in resistance with increasing RH levels (Figure 7.9 (b)), whereas the sample with Pt nanoparticles did not respond to the exposure (Figure 7.9 (d)). Finally, cross-sensitivity tests between moisture (air 60% RH at 25°C) and H_2 were performed on both sample types. The low crystallinity laser-annealed sample with Pt nanoparticles confirmed the selectivity towards H_2 gas, as the simultaneous exposure to moisture did not affect the BLR (Figure 7.9 (f)). On the other hand, the response of the sample without Pt to H_2 was affected by the simultaneous presence of moisture. As visible from Figure 7.9 (c), a first decrease in the sample's BLR was noticed upon exposure to air with 60% RH at 25°C, followed by a further decrease after H_2 exposure.

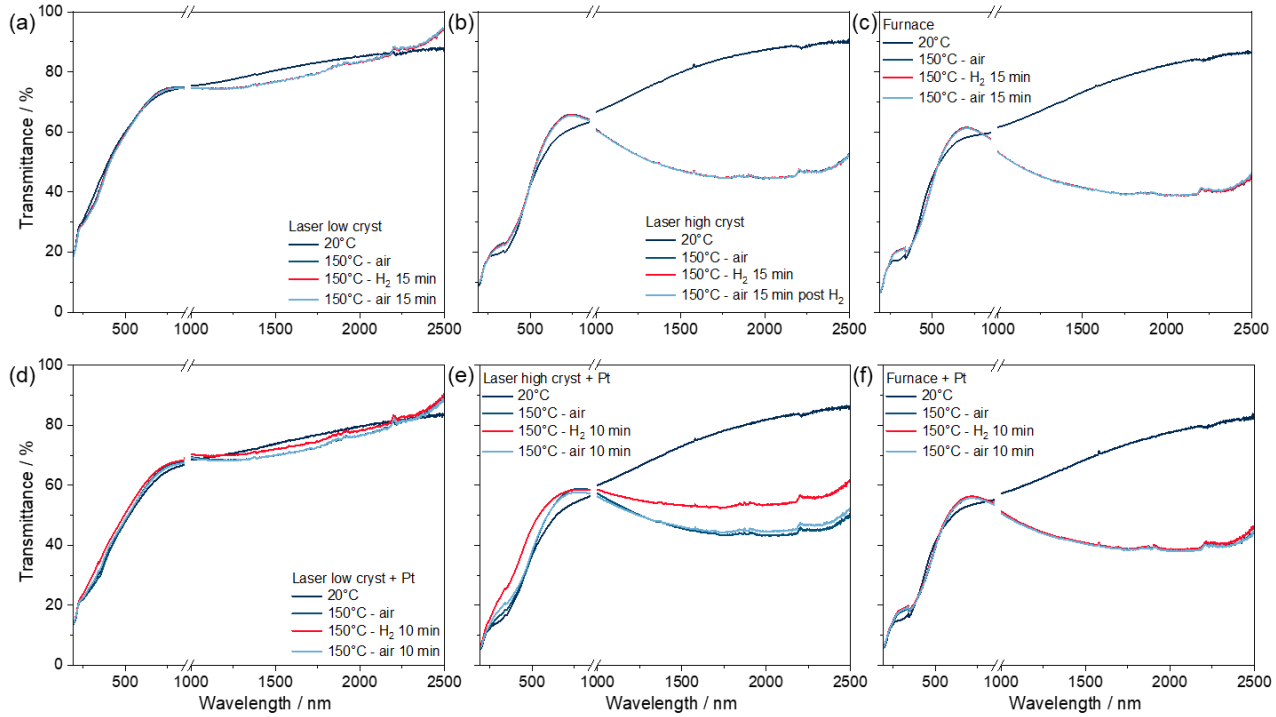


Figure 7.10. Transmittance variations of the samples on fused silica substrates at OT = 150°C upon exposure to 1000 ppm of H_2 in dry air carrier (red lines, 150°C – H_2 10 min), with following cycle of gas desorption in dry air (light blue lines, 150°C – air 10 min). (a, d) Low crystallinity laser-annealed sample (L70 10#) without and with Pt nanoparticles, respectively. (b, e) High crystallinity laser-annealed sample (L70 300#), without and with Pt nanoparticles, respectively. (c, f) Furnace annealed sample (TT), without and with Pt nanoparticles, respectively.

Following the electrical resistance-based gas sensing tests, optical gas sensing tests were performed on the fused silica substrates at OT = 150°C, which was chosen considering the previous results. The detailed procedure of the optical gas sensing tests is reported in Appendix A.2.17. The transmittance of the VO_2 thin films was initially measured in air at 20°C and 150°C, respectively, to evaluate the solar modulation upon the metal-insulator transition (Figure 7.10). All three sample types were considered, namely the furnace-annealed, the high crystallinity laser-annealed with 300 pulses, and the low crystallinity laser-annealed with 10 pulses. The gas sensing response of the three VO_2 thin films was considered both with and without Pt nanoparticles. The samples were exposed to 1000 ppm of H_2 in dry air gas carrier and the transmittance was measured before and after 15 min of exposure. The sensor's recovery after gas desorption was also considered, in comparison with the transmittance curves before H_2 exposure. Initially, the VO_2 thin films were tested without the Pt nanoparticles, but the response was almost imperceptible (Figure 7.10 (a-c)). Upon the deposition of the former, all three samples did respond to the H_2 gas exposure but displayed different degrees of transmittance changes. The furnace-annealed one showed a very weak increase in transmittance, even though reversible, in the 2200-2500 nm range (Figure 7.10 (f)). The low crystallinity laser-annealed sample displayed a higher increase in transmittance upon H_2 exposure, over the whole solar range of 190-2500 nm (Figure 7.10 (d)). The variation was reversible, as shown by the transmittance spectrum after gas desorption (light-blue line, Figure 7.10 (d)). With respect to the other two samples, the high

crystallinity laser-annealed VO_2 film with Pt displayed the highest optical modulation upon H_2 exposure (Figure 7.10 (e)). The transmittance reversibly increased over the whole solar range, with the highest change displayed in the NIR range (~2000 nm).

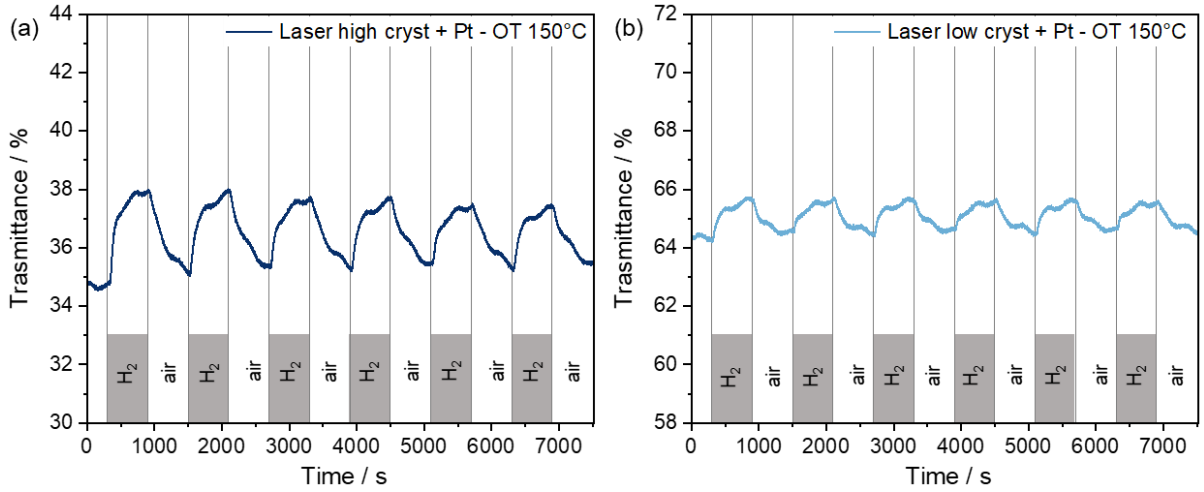


Figure 7.11. Transmittance variations of the (a) high crystallinity laser-annealed sample (L70 300#) with Pt nanoparticles and (b) low crystallinity laser-annealed sample (L70 10#) with Pt nanoparticles samples on fused silica substrates, at the optimal temperature of 150°C, upon exposure to alternating cycles of 1000 ppm H_2 in dry air carrier and dry air.

Following the static optical gas sensing tests, time-resolved optical measurements were performed at OT = 150°C by monitoring the transmittance at 2000 nm over time. The latter wavelength was chosen from the maximum modulation in transmittance in Figure 7.10 (e). Since the furnace annealed sample showed only a barely perceivable response, the two laser-annealed samples were compared, both with the presence of Pt nanoparticles. The samples were exposed to several adsorption/desorption cycles, by alternating 10 minutes of 1000 ppm H_2 in dry air gas carrier with 10 minutes of dry air, respectively. A relatively fast response time was found for the high crystallinity sample, even though the recovery times were not ideal as several minutes occurred for gas desorption (Figure 7.11 (a)). Nonetheless, the repeated cycles confirmed the signal variations to be reversible, with a well-defined signal amplitude and good recovery of the BLR after each H_2 exposure cycle.

8.2.4 *H_2 gas sensing – discussion*

In the previous paragraph, the H_2 sensing response of three types of VO_2 thin films was measured by both optical and electrical characterizations. The three sample types, namely a furnace-annealed, a high crystallinity laser-annealed with 300 pulses, and a low crystallinity laser-annealed with 10 pulses, displayed a different response according to the characterization type. Considering the electrical resistance tests, the low crystallinity laser-annealed sample was the only one to display a H_2 sensitivity without Pt nanoparticles. When Pt nanoparticles were added on the surface of the films,

all three samples displayed resistance variations upon H_2 exposure. The role of noble metal nanoparticles in favoring the dissociative chemisorption of H_2, which was highlighted by previous works[44,50], was confirmed by these results.

During the optical gas sensing tests, the samples displayed a response to H_2 exposure under the presence of Pt nanoparticles. The furnace-annealed sample weakly varied the transmittance upon gas exposure, even if reversibly, whereas the two laser-annealed samples displayed well-defined and reversible transmittance changes. In particular, the high crystallinity laser-annealed sample showed a remarkably high increase in transmittance upon H_2 exposure.

The different behavior of the samples should be explained by considering both the testing mode, i.e. based on optical transmittance or electrical resistance, and the morphological, structural, and chemical properties of the thin films. Further investigations are currently being carried to further explain the results, but preliminary considerations can be evidenced. Considering the testing mode, the electrical and optical characterizations are based on a different mechanism. As discussed in Chapter 3, during optical characterizations each light ray interacts with single domains, whereas during electrical measurements each current streamline passes through multiple domains. A percolation path is required for electrical conduction, to avoid the deterioration of the electrical properties.[15,53] Besides the testing mode, the underlying mechanism of the metal-insulator transition of VO_2 is still an open question in literature, due to the extreme complexity of the phenomenon involving multiscale factors. Considering the differences between the three samples, both the furnace annealed film and the laser-annealed one with 300 pulses consisted of crystalline VO_2 (M1). The sample annealed with 10 laser pulses displayed a lower degree of crystallinity, which presence was however confirmed by GIXRD, transmittance and reflectance measurements. From the results displayed in Chapter 5, a few nanometers layer of V_2O_5 was confirmed to be present on the surface of both the furnace and laser-annealed samples. The V_2O_5 layer naturally forms when VO_2 films are exposed to air, especially over prolonged timescales. The Raman spectroscopy results (Figure 7.3) on the films deposited on SNE substrates confirmed the V_2O_5 presence within the low crystallinity laser-annealed sample (10 pulses). On the high crystallinity laser-annealed sample (300 pulses), the predominant presence of VO_2 (M1) confirmed the GIXRD results, along with a minor component of V_2O_5 found in part of the analyzed spots. Considering the gas sensing results, the combination of V_2O_5 and VO_2 (M1) seem to have favored the H_2 detection. At the operating temperature of 150°C, the metallic phase of VO_2 may have provided an additional source of pseudo-free electrons able to participate in the sensing mechanism upon H_2 exposure. Regarding the optical sensing tests, the nanostructured morphology of

the laser-annealed sample may also have been responsible for the successful H_2 detection, with respect to the furnace-annealed sample.

8.3 Conclusions

In this Chapter, the H_2 sensing response of three types of VO_2 thin films was measured by both optical and electrical characterizations. The influence of both crystallinity degree and nanostructured morphology of VO_2 films on gas sensing was considered. The three sample types, namely a furnace-annealed, a high crystallinity laser-annealed with 300 pulses, and a low crystallinity laser-annealed with 10 pulses, displayed a different response according to the characterization type.

Considering the electrical resistance tests, the low crystallinity laser-annealed sample was the only one to display a H_2 sensitivity without Pt nanoparticles. The former could be detected up to 20 ppm. When Pt nanoparticles were added on the surface of the films, all three samples displayed resistance variations upon H_2 exposure, with an excellent recovery of the BLR during gas desorption, fast sensors' response, and 5 ppm detection limit. Considering the optical tests, all three samples displayed a response to H_2 exposure under the presence of Pt nanoparticles, which was particularly evident in the two laser-annealed samples. The role of noble metal nanoparticles in favoring the dissociative chemisorption of H_2, which was highlighted by previous works[44,50], was confirmed by these results.

The different behavior of the samples should be explained according to both the testing mode, i.e. optical transmittance or electrical resistance, and the morphological, structural, and chemical properties of the thin films. Additional investigations are currently being carried to further explain the results, but preliminary considerations were evidenced. The presence of crystalline VO_2 (M1) was confirmed in all three sample types. The former resulted predominant in both the furnace annealed film and the high crystallinity laser-annealed one, whereas a lower degree of crystallinity was found in the sample annealed with 10 laser pulses. As evidenced by the Raman spectroscopy, in the latter sample the few VO_2 crystallites coexisted with V_2O_5. A minor V_2O_5 component was found in the high crystallinity laser-annealed sample as well. Considering the gas sensing results, the combination of V_2O_5 and VO_2 (M1) seem to have favored the H_2 detection. At the operating temperature of 150°C, the metallic phase of VO_2 may have provided an additional source of pseudo-free electrons able to participate in the sensing mechanism upon H_2 exposure. Regarding the optical sensing tests, the nanostructured morphology of the laser-annealed sample may also have been responsible for the successful H_2 detection, with respect to the furnace-annealed sample.

References

1. Wang, S. *et al.* Recent progress in VO2 smart coatings: Strategies to improve the thermochromic properties. *Prog Mater Sci* **81**, 1–54 (2016).

2. Liu, K., Lee, S., Yang, S., Delaire, O. & Wu, J. Recent progresses on physics and applications of vanadium dioxide. *Materials Today* **21**, 875–896 (2018).

3. Xiong, T. H. *et al.* A temperature-tunable chirality-selective meta-absorber for electromagnetic encrypted imaging. *Appl Phys Lett* **123**, (2023).

4. Nie, G. *et al.* Monocrystalline VO2 (B) nanobelts: large-scale synthesis, intrinsic peroxidase-like activity and application in biosensing. *J Mater Chem A Mater* **2**, 2910–2914 (2014).

5. Guo, H., Si, L., Yu, J., Wang, X. & Si, Y. Phase-Engineered VO2 Metal Nanofiber Enables a Metal-Insulator Transition for Bidirectional Thermal Reallocation. *Nano Lett* **23**, 6233–6240 (2023).

6. Madiba, I. G., Mabakachacha, B., Khanyile, S., Numan, N. & Azizi, S. Nano-structured VO2 based films for space application and radiative environment. *Mater Today Proc* (2023).

7. Luo, P. *et al.* Accelerated ion/electron transport kinetics and increased active sites via local internal electric fields in heterostructured VO2-carbon cloth for enhanced zinc-ion storage. *Nano Res* **16**, 503–512 (2023).

8. Xu, Y. S. *et al.* Achieving high performance in aqueous iron-ion batteries using tunnel-like VO2 as a cathode material. *Chemical Communications* **59**, 8576–8579 (2023).

9. Zhou, W. *et al.* Crafting amorphous VO2–crystalline NiS2 heterostructures as bifunctional electrocatalysts for efficient water splitting: The different cocatalytic function of VO2. *Chemical Engineering Journal* **470**, 144146 (2023).

10. Jourshabani, M. *et al.* Advanced Functional Carbon Nitride by Implanting Semi-Isolated VO2 Active Sites for Photocatalytic H2 Production and Organic Pollutant Degradation. *Small* **19**, 2300147 (2023).

11. Cho, H. Bin *et al.* Utilizing VO2 as a Hole Injection Layer for Efficient Charge Injection in Quantum Dot Light-Emitting Diodes Enables High Device Performance. *ACS Appl Mater Interfaces* **15**, 29259–29266 (2023).

12. Li, Y. *et al.* Direct Laser Writing of Multishaped VO2 Microactuators Based on Freestanding VO2 Film. *Adv Mater Technol* **8**, 2200977 (2023).

13. Yuan, R. *et al.* A neuromorphic physiological signal processing system based on VO2 memristor for next-generation human-machine interface. *Nature Communications 2023 14:1* **14**, 1–14 (2023).

14. Béteille, F. & Livage, J. Optical Switching in VO2 Thin Films. *J Solgel Sci Technol* **13**, 915–921 (1998).

15. Venkat Sunil Kumar, C., Maury, F. & Bahlawane, N. *Vanadium Oxide as a Key Constituent in Reconfigurable Metamaterials*. *Metamaterials and Metasurfaces* (IntechOpen, 2019).

16. Wu, F. *et al.* A 3D flower-like VO2/MXene hybrid architecture with superior anode performance for sodium ion batteries. *J Mater Chem A Mater* **7**, 1315–1322 (2019).

17. Xie, B., Zhang, W., Zhao, J., Zheng, C. & Liu, L. Design of VO2-based spacecraft smart radiator with low solar absorptance. *Appl Therm Eng* **236**, 121751 (2024).

18. Weerasinghe, H., Kumarihamy, M. & Wu, H. F. Synthesis of 2D VO2 Nanosheets for the Dual Optical Sensor Method by Colorimetric and Fluorometric Sensing of Catecholamines. *ACS Appl Mater Interfaces* (2023).

19. Yahiaoui, R. *et al.* Dynamically tunable single-layer VO2/metasurface based THz cross-polarization converter. *J Phys D Appl Phys* **54**, 235101 (2021).

20. Huotari, J., Bjorklund, R., Lappalainen, J. & Lloyd Spetz, A. Pulsed Laser Deposited Nanostructured Vanadium Oxide Thin Films Characterized as Ammonia Sensors. *Sens Actuators B Chem* **217**, 22–29 (2015).

21. Jaiswal, J. *et al.* Vertically Aligned Porous VxOyNanofilms with Pt Decoration for Sub-ppm H2Gas Sensors. *ACS Appl Nano Mater* (2022).

22. Liang, J., Lou, Q., Wu, W., Wang, K. & Xuan, C. NO2Gas Sensing Performance of a VO2(B) Ultrathin Vertical Nanosheet Array: Experimental and DFT Investigation. *ACS Appl Mater Interfaces* **13**, 31968–31977 (2021).

23. Evans, G. P. *et al.* Room temperature vanadium dioxide–carbon nanotube gas sensors made via continuous hydrothermal flow synthesis. *Sens Actuators B Chem* **255**, 1119–1129 (2018).

24. Li, B. *et al.* Enhanced Pd/a-WO3/VO2 Hydrogen Gas Sensor Based on VO2 Phase Transition Layer. *Small Methods* **6**, 2200931 (2022).

25. Byon, J. W. *et al.* Electrothermally induced highly responsive and highly selective vanadium oxide hydrogen sensor based on metal-insulator transition. *Journal of Physical Chemistry C* **116**, 226–230 (2012).

26. Baik, J. M. *et al.* Pd-Sensitized single vanadium oxide nanowires: Highly responsive hydrogen sensing based on the metal-insulator transition. *Nano Lett* **9**, 3980–3984 (2009).

27. Moos, R. A Brief Overview on Automotive Exhaust Gas Sensors Based on Electroceramics. *Int J Appl Ceram Technol* **2**, 401–413 (2005).

28. Chraim, F., Erol, Y. B. & Pister, K. Wireless Gas Leak Detection and Localization. *IEEE Trans Industr Inform* **12**, 768–779 (2016).

29. Hodgkinson, J. & Tatam, R. P. Optical gas sensing: A review. *Meas Sci Technol* **24**, (2013).

30. Kumar, R., Al-Dossary, O., Kumar, G. & Umar, A. Zinc Oxide Nanostructures for NO2 Gas–Sensor Applications: A Review. *Nano-Micro Letters 2014 7:2* **7**, 97–120 (2014).

31. Xiao, Z. *et al.* Recent development in nanocarbon materials for gas sensor applications. *Sens Actuators B Chem* **274**, 235–267 (2018).

32. Hren, R. *et al.* Hydrogen production, storage and transport for renewable energy and chemicals: An environmental footprint assessment. *Renewable and Sustainable Energy Reviews* **173**, 113113 (2023).

33. Li, Z. *et al.* Resistive-type hydrogen gas sensor based on TiO2: A review. *Int J Hydrogen Energy* **43**, 21114–21132 (2018).

34. Srinivasa Varaprasad, H., Sridevi, P. V. & Satya Anuradha, M. Optical, morphological, electrical properties of ZnO-TiO2-SnO2/CeO2 semiconducting ternary nanocomposite. *Advanced Powder Technology* **32**, 1472–1480 (2021).

35. Chitoria, A. K., Mir, A. & Shah, M. A. A review of ZrO2 nanoparticles applications and recent advancements. *Ceram Int* **49**, 32343–32358 (2023).

36. Das, S. & Jayaraman, V. SnO2: A comprehensive review on structures and gas sensors. *Prog Mater Sci* **66**, 112–255 (2014).

37. Samadi, S., Asadi Cordshooli, G., Yousefi, M., Kalateh, K. & Zakaria, S. A. CeO2/TiO2 core/shell nanoparticles as quantitative gas sensor at room temperature. *Sensor Review* **38**, 458–466 (2018).

38. Bhati, V. S., Hojamberdiev, M. & Kumar, M. Enhanced sensing performance of ZnO nanostructures-based gas sensors: A review. *Energy Reports* **6**, 46–62 (2020).

39. Umar, A., Alshahrani, A. A., Algarni, H. & Kumar, R. CuO nanosheets as potential scaffolds for gas sensing applications. *Sens Actuators B Chem* **250**, 24–31 (2017).

40. Manera, M. G. *et al.* Optical gas sensing of TiO2 and TiO2/Au nanocomposite thin films. *Sens Actuators B Chem* **132**, 107–115 (2008).

41. Dey, A. Semiconductor metal oxide gas sensors: A review. *Materials Science and Engineering: B* **229**, 206–217 (2018).

42. Carpenter, M. A., Mathur, S. & Kolmakov, A. *Metal Oxide Nanomaterials for Chemical Sensors*. (Springer New York, 2013).

43. Babar, B. M. *et al.* Concentration modulated vanadium oxide nanostructures for NO2 gas sensing. *Sens Actuators B Chem* **351**, 130947 (2022).

44. Sanger, A., Kumar, A., Kumar, A., Jaiswal, J. & Chandra, R. A fast response/recovery of hydrophobic Pd/V2O5 thin films for hydrogen gas sensing. *Sens Actuators B Chem* **236**, 16–26 (2016).

45. Han, S. D. *et al.* Self-doped nanocolumnar vanadium oxides thin films for highly selective NO2 gas sensing at low temperature. *Sens Actuators B Chem* **241**, 40–47 (2017).

46. Liang, J., Lou, Q., Wu, W., Wang, K. & Xuan, C. NO2Gas Sensing Performance of a VO2(B) Ultrathin Vertical Nanosheet Array: Experimental and DFT Investigation. *ACS Appl Mater Interfaces* **13**, 31968–31977 (2021).

47. Liang, J. *et al.* High-sensitivity NH3 gas detection at room temperature using In2O3 nanoparticles-modified VO2(B) nanorods heterojunction. *Appl Surf Sci* **649**, 159170 (2024).

48. Evans, G. P. *et al.* Room temperature vanadium dioxide–carbon nanotube gas sensors made via continuous hydrothermal flow synthesis. *Sens Actuators B Chem* **255**, 1119–1129 (2018).

49. Strelcov, E., Lilach, Y. & Kolmakov, A. Gas sensor based on metal-insulator transition in VO 2 nanowire thermistor. *Nano Lett* **9**, 2322–2326 (2009).

50. Baik, J. M. *et al.* Pd-Sensitized single vanadium oxide nanowires: Highly responsive hydrogen sensing based on the metal-insulator transition. *Nano Lett* **9**, 3980–3984 (2009).

51. Shvets, P., Dikaya, O., Maksimova, K. & Goikhman, A. A review of Raman spectroscopy of vanadium oxides. *Journal of Raman Spectroscopy* **50**, 1226–1244 (2019).

52. Paolucci, V. *et al.* Bidimensional Engineered Amorphous a-SnO2Interfaces: Synthesis and Gas Sensing Response to H2S and Humidity. *ACS Sens* **7**, 2058–2068 (2022).

53. Katase, T., Endo, K. & Ohta, H. Thermopower analysis of metal-insulator transition temperature modulations in vanadium dioxide thin films with lattice distortion. *Phys Rev B Condens Matter Mater Phys* **92**, 035302 (2015).

Chapter 8

Conclusions and future perspectives

The reduction of the energy consumption, targeted in multiple fields, has been the overall theme of this doctoral research. As highlighted throughout the different Chapters, even slight improvements in the efficiency of heat exchangers, water collectors, and smart windows could have a powerful impact on reducing the massive global energy consumption. The optimization of the latter three applications has been the focus of this doctoral research, exploring several oxide coatings.

In the first experimental part (Chapter 2), the functional properties of hybrid silica (SiO_2) coatings were tuned and exploited to control the efficiency of heat exchangers and moisture collectors. Several HVAC systems rely on metallic substrates, which typical hydrophilicity is unfavorable in terms of heat exchange efficiency due to the formation of a liquid film upon vapor condensation (filmwise condensation, FWC).[1] In Chapter 2, the condensation mode was controlled through the modification of both the chemical composition and the morphology of the substrate's surface, to induce a dropwise condensation (DWC). Silica-based sol-gel coatings were employed to control the condensation mode of both saturated vapor and humid air. The wettability of the coatings was optimized exploiting a hybrid organic-inorganic composition, in which organic groups were introduced to increase the hydrophobicity of plain SiO_2 coatings. The introduction of organic chains within the silica networks was proven to enhance the durability of the latter in water-based environments.[2] Indeed, a major challenge regarding the real-life application of heat exchangers is the durability of such coatings, as they face severe environmental conditions such as fouling, scratching, corrosion or high thermal stresses.[3]

In paragraph 2.2, the efficiency of hybrid octyl-modified SiO_2 coatings was assessed during saturated vapor condensation, in terms of both thermal exchange and coating's durability. The heat exchanged over time was examined on aluminum substrates in a custom-made heat exchange apparatus. The coatings successfully promoted the DWC with heat transfer coefficient (HTC) values of ~90 kW m^{-2} K^{-1}, an average 9-fold increase with respect to FWC under similar heat flux conditions.[4] The heat transfer performance remained consistent throughout the overall duration of the condensation experiments, which were stopped prior to any potential failure to investigate the detected changes in

wettability and morphology. Straightforward accelerated degradation tests were performed on silicon substrates, to separate the different influencing factors, to evaluate the coating's resistance prior to its real industrial application. If singularly applied, the degradation conditions did not lead to significant variations on the coating's properties, whereas the interaction with water at high temperature induced different degrees of degradation whether if bubble nucleation was present or avoided. The similar changes in wettability and morphology observed in the coatings deposited on aluminum and silicon substrates indicated that the latter tests could effectively estimate the coating's durability across a wide range of liquid-vapor phase change applications.[5]

In the second part of Chapter 2 (paragraph 2.3), bioinspired hybrid patterned coatings were employed to optimize the collection of moisture from humid air. Hydrophobic methyl-modified SiO_2 coatings with hydrophilic bumps were developed via a sol-gel process, leveraging a dewetting mechanism to achieve the patterned morphology. To validate the practical application in real-world settings, the hybrid coatings were deposited and optimized on metallic aluminum surfaces. The diameter and the density of distribution of the dewetted droplets was controlled and tuned between nearly 26-52 μm and 53-11 particles/mm^2, respectively. The drainage rate of the patterned coatings during condensation from humid air was assessed in a custom-made apparatus and expressed in terms of condensed mass. During the first 15 minutes of the condensation tests at 50% RH at 28°C and ΔT = 4-10 K, the hydrophilic bumps of the pattern favored the formation of droplets with respect to the surrounding hydrophobic areas. With respect to the bare aluminum, the patterned coating at subcooling degrees of 4-10 K enhanced the condensation performance by 21-24%, confirming the crucial role of the coatings in controlling the condensation dynamics. Future goals will be devoted to the investigation of different geometries and wettability contrasts of the pattern, to assess their impact on the condensation dynamics of the humid air.[6]

The second applications which was targeted during this doctoral research was related to the fabrication of VO_2-based thermochromic smart windows. As reported in Chapter 3, the temperature-dependent nature of the optical and electrical properties of VO_2 offers a passive and clean way to modulate the solar irradiation, without relying on active energy inputs.

Examining the literature, one aspect that clearly comes to light is the difficulty of meticulously controlling the process. Studies that employed matching conditions of synthesis, deposition, and thermal treatment, did not always produce the same vanadium oxide phases, but often led to different phases or to combinations of multiple oxides.[7–9] This highlights the need to carefully consider the influence of the multiple factors during sol-gel fabrication, such as solution aging, atmosphere during deposition, and annealing temperature, atmosphere, pressure, and time. The numerous parameters

influencing the CSD method were optimized in Chapter 4, from which homogeneous and thermochromic VO_2 thin films were obtained. Two vanadium precursors were considered, vanadium pentoxide (V_2O_5) and vanadyl acetylacetonate ($VO(acac)_2$). The V_2O_5 powder, despite the carcinogenicity issues, is a widely used precursor to produce VO_2 thin films, so it was initially chosen as a reference starting point (paragraph 4.2). Following the investigation of all the process parameters, the synthesis based on the former precursor led to the formation of crystalline monoclinic VO_2 (M1) thin films, which displayed the desired thermochromic properties. However, besides the toxicity and carcinogenicity, several issues regarding the stability of both the solution and the dried films were found, which limited the scalability of the process. As a general approach and when possible in this work, the choice of precursors, reagents and solvents was oriented towards a green chemistry route. Considering this, $VO(acac)_2$ was chosen as an alternative precursor, with respect to V_2O_5.

The $VO(acac)_2$ precursor showed excellent results in terms of film quality, functional properties, versatility, and simplicity of the process (paragraph 4.3). To provide a brief overview, the starting solution of the precursor in ethanol was found to be stable for months in air, ensuring flexibility in terms of industrial scalability. The resulting film quality, in terms of surface coverage, homogeneity, and optical properties, was seen to increase with the aging time of the solution. Different annealing atmospheres were considered, from oxidizing to inert to reducing environments. A thermal treatment in air led to the formation of V_2O_5, whereas annealing in 5% H_2 in Ar led to a mixture of multiple vanadium oxides. The thermal annealing under a N_2 atmosphere allowed for the formation of the target vanadium oxide, i.e., VO_2 (M1). Once the correct atmosphere was determined, the temperature during the thermal treatment was varied from 250°C to 650°C. The crystallization was found to start above 450°C and marginal differences, in terms of optical properties, were found by varying the temperature within the 450-650°C range. Finally, the influence of moisture during the deposition step was considered. The presence of the former was found to favor the formation of homogeneous and thicker films, with respect to a fully inert atmosphere. The effect of moisture was further studied by comparing four different environments, from low to high moisture conditions. A smooth, compact, and uniform morphology was found with medium or high moisture levels during deposition, whereas at low moisture conditions dendritic or needle-like features were formed. The particle surface coverage increased with increasing aging time of the solution and with medium or high moisture levels during deposition. The average particle size decreased with increasing solution aging, in agreement with the GIXRD results, and increased with the increasing moisture content during deposition.

The moisture influence was evaluated in terms of luminous transmittance (T_{lum}) and solar modulation efficiency (ΔT_{sol}), which represent the standard parameters to express the efficiency of the smart windows. The T_{lum} decreased with increasing moisture during deposition, which was explained with the increased surface coverage and the corresponding lower transmission of the visible light. The decrease in T_{lum} with increasing moisture during deposition was linked to an increase in ΔT_{sol}. A smart window operates at its maximum functionality when the highest visible transmittance is achieved simultaneously with the highest level of solar modulation. These parameters are known to be inversely correlated, meaning that an increase in visible transmittance typically leads to a decrease in solar modulation, and viceversa. For smart windows based on single VO_2 films, improvement is required for both T_{lum} and ΔT_{sol} values, which should be higher than 50% and 10%, respectively.[10,11] Various approaches have been reported to simultaneously enhance both parameters, often involving the combination of multiple materials, the creation of multilayers and/or composites, and the use of nanostructuring techniques.[12] In Chapter 4, the best solar modulation of $\Delta T_{sol,\ 110°C} = 9.2\%$ and $T_{lum} = 70\%$ was reached by depositing under high moisture conditions (85-90% RH at 20-23°C) a solution aged for 7 days. Considering the reference smart windows based on single VO_2 films in the literature,[10,11] in this case quite high values of solar modulation were reached without deteriorating the luminous transmittance. Further improvements in terms of T_{lum} were addressed in Chapter 6, by combining the VO_2 films with TiO_2 and hybrid SiO_2 coatings in bilayer configurations.

The urgency of lowering the energy consumption, with a particular focus on cooling systems, evidences the need for simple, clean, low-cost, and straightforward solutions. Thermochromic smart windows would amplify their impact if they could be easily processed on a wide range of substrates, including plastic panels, and worldwide distributed. In this perspective, a currently unsolved challenge involves the reduction of the crystallization temperature below 400°C. In Chapter 5, an unconventional nanosecond pulsed laser annealing (PLA) method was exploited to remarkably reduce the crystallization temperature of VO_2 thin films.[19]

In the first part (paragraph 5.3), the effect of the different laser parameters was investigated and the threshold to induce the crystallization into VO_2 (M1) was found. The VO_2 crystallization was achieved within only 60 s of KrF excimer laser exposure and was performed at room temperature in air, after a 10 min drying step at 300°C. The eventual occurrence of surface melting was verified and the maximum fluence to avoid the former was identified. Temperature profile simulations were performed to evaluate the temperature distribution within a single pulse, in function of the ns pulse duration and the penetration depth. The simulations confirmed that the heat was confined within the film during the laser pulses, with negligible substrate heating. All the laser-annealed samples in

Chapter 5 exhibited a T_{lum} ranging between 60-80%, which is relatively high compared to the standard reported in literature for VO_2-only smart windows (~50%). The luminous transmittance was seen to decrease with increasing laser pulses, due to gradual formation of crystalline VO_2 (M1) along with the formation of a spontaneous nanostructured morphology (paragraph 5.5).[19] Analogously to Chapter 4, further improvements of the thermochromic solar modulation (ΔT_{sol}~4.0%) were addressed in Chapter 6.

In the second part (paragraph 5.4), the versatility of sol-gel reactions was combined with the fast timescales of PLA to investigate the width of the process working window. Similar thermochromic efficiencies were reached through multiple combinations of parameters, highlighting the robustness of the process and the broad working window. The beneficial effect of environmental moisture was exploited to lower the drying temperature before PLA down to 100°C. This, combined with the selective film heating of PLA, enables future extension to plastic substrates. Concurrently with the beneficial reduction of the drying temperature and the use of PLA technique, satisfactory optical properties were obtained $\Delta T_{2000\ nm}$ = 22.9%, ΔT_{sol} = 4.0%, T_{lum} = 68.5%. The dried thin films were found to guarantee a long-term stability before laser annealing, which expanded the working window by allowing a higher flexibility in the process timelines.

Since the interaction between the ns laser pulses and the vanadium-based sol gel thin films was not clearly understood in literature, an in-depth investigation on the laser-matter interaction was conducted in paragraph 5.5. The initial organic component, due to the solvent residuals and the metal-organic nature of the vanadium precursor, was greatly reduced within the first few laser pulses and accompanied by a film densification. Crystallization was found to start from the 5th pulse as crystalline domains of 1-2 nm appeared within the amorphous network. The crystallinity degree gradually increased with increasing laser pulses and full conversion to crystalline VO_2 (M1) was reached within a few seconds. The sol-gel laser-induced conversion was found to be based on two distinct mechanisms, an initial partial ablation followed by solid-state diffusion. Simulations of the temperature distribution revealed peak temperatures of ~900°C during a single laser pulse at 70 mJ/cm^2, notably lower with respect to the melting temperature of VO_2. The temperature gradients of hundreds of degrees Celsius developed within the film constituted the driving force for the diffusion of atoms, allowing the onset of the crystallization and boosting the conversion from the amorphous phase.

Overall, laser annealing was found to offer multiple advantages, in terms of versatility, easiness and scalability. Crystallization occurred within a matter of seconds and could be easily conducted in ambient air, with no need for an inert atmosphere. This constitutes a remarkable advantage when

vanadium oxides are considered, as the latter usually require extremely controlled atmospheres during crystallization. The proposed approach is template-free and enables the simultaneous achievement of organic residue removal, densification, crystallization, and nanostructuring in a single step, allowing for time-, cost- and energy-savings.

Additional challenges regarding VO_2-based smart windows are related to two key features which must be guaranteed for a real-life application of the former, namely the transmission of visible light and the resistance against weatherability. Both challenges were addressed in Chapter 6, though the combination of VO_2 with titanium dioxide (TiO_2) and hybrid SiO_2 coatings in bilayer configurations. In paragraph 6.2, polycrystalline TiO_2 buffer layers were initially optimized and tested in multiple TiO_2 – VO_2 bilayers configurations. The deposition and annealing parameters were found to crucially influence several factors, particularly regarding the crystallization of VO_2 and the extension of the Ti ions diffusion into the VO_2 lattice. The elemental diffusion severely impacted the thermochromic efficiency of same samples, particularly the ones which were dried at higher temperatures before annealing. To compensate for diffusion phenomena, the use of intermediate barrier layers could be used as a possible solution. Nonetheless, regarding the samples with lower diffusion, a 70 nm TiO_2 – 35 nm VO_2 configuration was found to successfully increase the luminous transmittance by ~20% with respect to the pristine VO_2 film. The increase in luminous transmittance was reached without deteriorating the thermochromic modulation of the latter.

Following the studies on TiO_2 – VO_2 bilayers, a different approach was tested by employing hybrid SiO_2 coatings (paragraph 6.3). Previously crystallized VO_2 films, both furnace-annealed and laser-annealed, were coated with amorphous anti-reflective silica coatings. Two types of hybrid SiO_2 coatings were selected, a methyl-modified SiO_2 (M_5T_5) and an octyl-modified one (O_2T_8). All the hybrid SiO_2 coatings led to an increase in luminous transmittance with respect to the original uncoated VO_2 films. As expected, the increased T_{lum} was linked to a decrease in solar modulation, which was however limited to a ~5-6% decrease for the most performing bilayers. Considering the laser-annealed VO_2 films, the highest luminous transmittance (T_{lum} = 74.5%) was reached with the 27 nm VO_2 – 66 nm M_5T_5 bilayer, a +22.5% increase with respect to the original T_{lum} = 60.8% of the lasered VO_2 film. The five bilayers, along with the reference laser-annealed and furnace-annealed VO_2 films, were subjected to durability tests under high moisture conditions. According to the literature, the exposure to high moisture conditions was expected to lead to the coating's degradation, which can result in a loss of thermochromic performance. The uncoated furnace-annealed and laser-annealed VO_2 films were severely affected by the 1 month exposure to high moisture conditions, displaying losses in $\Delta T_{2000,\,max}$ of -21.4% and -44.3%, respectively. With respect to the uncoated VO_2 films, all

the hybrid SiO_2 coatings preserved the NIR modulation. The VO_2 layers coated with ~66 nm M_5T_5 coating and 70-74 nm O_2T_8 coating, respectively, displayed the best durability performance, with a decrease in $\Delta T_{2000,\,max}$ of only -0.4% and -5.6%, respectively.

As highlighted in Chapter 3, the optical and electrical properties of VO_2 have been exploited in a wide range of applications, from radiative space applications to electrocatalytic water splitting or gas sensors.[13–15] In the final Chapter 7, the efficiency of VO_2 thin films towards H_2 gas detection was considered. The latter is becoming increasingly important in the field of decarbonization and implementation of low-impact renewable energy.[16] Different morphologies and crystallinity degrees were considered by comparing three samples, a furnace-annealed, a high crystallinity laser-annealed with 300 pulses, and a low crystallinity laser-annealed with 10 pulses. The impact on the H_2 gas sensing efficiency was investigated in terms of both electrical and optical response. Considering the electrical resistance tests, the low crystallinity laser-annealed sample was the only one to display a H_2 sensitivity without Pt nanoparticles. The former could be detected up to 20 ppm. When Pt nanoparticles were added on the surface of the films, all three samples displayed resistance and optical variations upon H_2 exposure, with an excellent recovery of the BLR during gas desorption, fast sensors' response, and 5 ppm detection limit. The role of noble metal nanoparticles in favoring the dissociative chemisorption of H_2, which was highlighted by previous works[17,18], was confirmed by these results. Additional investigations are currently being carried to further explain the results, but preliminary considerations were evidenced. The presence of crystalline VO_2 (M1) was confirmed in all three sample types. The former resulted predominant in both the furnace annealed film and the high crystallinity laser-annealed one, whereas a lower degree of crystallinity was found in the sample annealed with 10 laser pulses. In the latter sample the few VO_2 crystallites coexisted with V_2O_5, while a minor V_2O_5 component was found in the high crystallinity laser-annealed sample as well. Considering the gas sensing results, the combination of V_2O_5 and VO_2 (M1) seem to have favored the H_2 detection. At the operating temperature of 150°C, the metallic phase of VO_2 may have provided an additional source of pseudo-free electrons able to participate in the sensing mechanism upon H_2 exposure. Regarding the optical sensing tests, the nanostructured morphology of the laser-annealed sample may also have been responsible for the successful H_2 detection, with respect to the furnace-annealed sample.

References

1. Rose, J. W. Dropwise condensation theory and experiment: A review. *Proceedings of the Institution of Mechanical Engineers, Part A: Journal of Power and Energy* **216**, 115–128 (2002).

2. Metroke, T. L., Gandhi, J. S. & Apblett, A. Corrosion resistance properties of Ormosil coatings on 2024-T3 aluminum alloy. *Prog Org Coat* **50**, 231–246 (2004).

3. Jin, H. *et al.* Recent advances in emerging integrated antifouling and anticorrosion coatings. *Mater Des* **213**, 110307 (2022).

4. FAO. *The State of Food and Agriculture 2020. Overcoming water challenges in Agriculture*. *Fao* (2020).

5. Basso, M. *et al.* Hydrophobic hybrid silica sol-gel coating on aluminium: Stability evaluation during saturated vapour condensation. *Journal of Non-Crystalline Solids: X* **17**, 100143 (2023).

6. Basso, M. *et al.* Bioinspired silica-based sol–gel micropatterns on aluminium for humid air condensation. *J Solgel Sci Technol* **102**, 466–477 (2022).

7. Seyfouri, M. M. & Binions, R. Sol-gel approaches to thermochromic vanadium dioxide coating for smart glazing application. *Solar Energy Materials and Solar Cells* **159**, 52–65 (2017).

8. Kim, J. & Paik, T. Recent advances in fabrication of flexible, thermochromic vanadium dioxide films for smart windows. *Nanomaterials* **11**, (2021).

9. Liu, K., Lee, S., Yang, S., Delaire, O. & Wu, J. Recent progresses on physics and applications of vanadium dioxide. *Materials Today* **21**, 875–896 (2018).

10. Santos, A. J. *et al.* Facile Fabrication of High-Performance Thermochromic VO2-Based Films on Si for Application in Phase-Change Devices. *Chemistry of Materials* **35**, 4435–4448 (2023).

11. Cao, X. *et al.* Challenges and Opportunities toward Real Application of VO2-Based Smart Glazing. *Matter* **2**, 862–881 (2020).

12. Wang, S. *et al.* Recent progress in VO2 smart coatings: Strategies to improve the thermochromic properties. *Prog Mater Sci* **81**, 1–54 (2016).

13. Xie, B., Zhang, W., Zhao, J., Zheng, C. & Liu, L. Design of VO2-based spacecraft smart radiator with low solar absorptance. *Appl Therm Eng* **236**, 121751 (2024).

14. Zhou, W. *et al.* Crafting amorphous VO2–crystalline NiS2 heterostructures as bifunctional electrocatalysts for efficient water splitting: The different cocatalytic function of VO2. *Chemical Engineering Journal* **470**, 144146 (2023).

15. Han, S. D. *et al.* Self-doped nanocolumnar vanadium oxides thin films for highly selective NO2 gas sensing at low temperature. *Sens Actuators B Chem* **241**, 40–47 (2017).

16. Hren, R. *et al.* Hydrogen production, storage and transport for renewable energy and chemicals: An environmental footprint assessment. *Renewable and Sustainable Energy Reviews* **173**, 113113 (2023).

17. Baik, J. M. *et al.* Pd-Sensitized single vanadium oxide nanowires: Highly responsive hydrogen sensing based on the metal-insulator transition. *Nano Lett* **9**, 3980–3984 (2009).

18. Sanger, A., Kumar, A., Kumar, A., Jaiswal, J. & Chandra, R. A fast response/recovery of hydrophobic Pd/V2O5 thin films for hydrogen gas sensing. *Sens Actuators B Chem* **236**, 16–26 (2016).

19. Basso, M. *et al.* Rapid laser-induced low temperature crystallization of thermochromic VO2 sol-gel thin films. *Appl Surf Sci* **631**, (2023).

Appendix A

Materials and Methods

Table of contents

A Appendix 349

A.1 Materials recipes 351

A.1.1 Optimized recipe for the synthesis and deposition of octyl-modified SiO_2 coatings 351

A.1.2 Optimized recipe for the synthesis and deposition of methyl-modified SiO_2 coatings 351

A.1.3 Optimized recipe for the synthesis and deposition of VO_2 thin films from V_2O_5 353

A.1.4 Optimized recipe for the synthesis and deposition of VO_2 thin films from $VO(acac)_2$ 353

A.1.5 Conventional thermal annealing of VO_2 thin films 353

A.1.6 Laser annealing of VO_2 thin films 354

A.1.7 Optimized recipe for the synthesis Pt nanoparticles 355

A.2 Characterizations 355

A.2.1 Dynamic contact angle and contact angle hysteresis 355

A.2.2 Saturated vapor condensation tests 355

A.2.3 Coating degradation tests 357

A.2.4 Durability tests under high moisture conditions 358

A.2.5 Humid air condensation tests 358

A.2.6 Grazing incidence X-ray diffraction (GIXRD) 359

A.2.7 Raman spectroscopy 359

A.2.8 Optical spectroscopy 359

A.2.9 Ellipsometry 360

A.2.10 Four point probe characterization 361

A.2.11 Electron microscopy and image analysis 361

A.2.12 Atomic force microscopy (AFM) 362

A.2.13 X-ray photoelectron spectroscopy (XPS) 363

A.2.14 Density-functional theory (DFT) 363

A.2.15 Temperature profile simulations 364

A.2.16 Rutherford Backscattering Spectrometry (RBS) 364

A.2.17 Gas sensing tests 364

A.1 Materials recipes

A.1.1 Optimized recipe for the synthesis and deposition of octyl-modified SiO_2 coatings[1]

Tetraethyl orthosilicate (TEOS, 98%; Sigma Aldrich), octyltriethoxysilane (OTES, 98%; Sigma Aldrich), absolute ethanol (EtOH, Emsure; Sigma-Aldrich), concentrated hydrochloric acid (HCl, 37%; Sigma Aldrich), milliQ water (H_2O, 18.2 MΩ). All employed materials were used as purchased, except for hydrochloric acid which was diluted to obtain a 1 M concentration. Silicon wafers, aluminum with high purity (AW1050, 99.50% minimum aluminum content), 20 x 20 mm^2 and 20 x 50 mm^2 dimensions. Aluminum was polished to obtain a smooth mirror-like surface, following a standard metallographic technique. The octyltriethoxysilane-based solution was prepared adapting a recipe from De Ferri *et al*.[2] TEOS, OTES, EtOH, HCl 1 M and H_2O were mixed in molar ratios of (TEOS+OTES):EtOH:H_2O:HCl=1:2:2:0.01, respectively, with varied TEOS:OTES molar ratio. The solution was stirred for 2 h at 400 rpm at room temperature, during which additional solvent was added after 30 min, to reach a theoretical final concentration of SiO_2 of 1.3 M. The solution was aged still for 2 additional hours and then filtrated with syringe filters of 0.2 μm pores prior to the deposition. The sol-gel coatings were deposited on polished aluminum substrates and silicon wafers, both previously cleaned through sonication in ethanol followed by atmospheric plasma treatment (Plasma Cleaner, PDC-002-CE, Harrick Plasma). The deposition was done inside a custom-made dip-coater, by withdrawing the substrates from the solution at 4.8 cm/min. The solvent evaporation was induced gradually, together with the evolution of condensation reactions, by aging the coatings at room temperature for 24 h. The coatings were then annealed in a furnace at 200°C for 2 h, with a heating ramp of 10°C/min.

A.1.2 Optimized recipe for the synthesis and deposition of methyl-modified SiO_2 coatings[3]

All the employed materials were used as received, except if otherwise stated: TEOS (98%; Sigma Aldrich), MTES (98%; Sigma Aldrich), absolute ethanol (EtOH, Emsure; Sigma-Aldrich). The hydrochloric acid dilution (1 M) was obtained from concentrated hydrochloric acid (HCl, 37%; Sigma Aldrich) and milliQ water (18.2 MΩ). The metallic substrates used were made of aluminum with high purity (AW1050, 99.50% minimum aluminum content). The dimensions of the squared aluminum substrates were 20 x 20 mm^2 in the case of the static tests and 40 x 40 mm^2 for the humid air condensation tests, respectively. The side exposed to the condensation phenomenon was polished following a standard metallographic technique to obtain a smooth mirror-like surface.

The patterned coatings were synthetized following the procedure described by Colusso *et al*.[4] The patterned coatings were developed starting from a sol-gel bilayer. To synthetize the bottom CH_3-silica layer, an acid-catalyzed solution was prepared by mixing tetraethylortosilicate (TEOS), methyltriethoxysilane (MTES), ethanol (EtOH), hydrochloric acid 1 M (HCl) and water (H_2O) for 1 h at 400 rpm at room temperature, in molar ratios of (TEOS+MTES):EtOH:H_2O:HCl=1:2:4:0.01, respectively, with a TEOS:MTES molar ratio of 1. After the first 30 min of mixing, the solvent was additionally added to reach a theoretical final concentration of SiO_2 of 1.3 M. Following the first hour of stirring, the solution was aged for 30 min, filtrated with syringe filters with 0.2 μm pores and deposited on the polished aluminum substrates, which were previously cleaned through sonication in ethanol followed by atmospheric plasma cleaning (Plasma Cleaner, PDC-002-CE, Harrick Plasma). The deposition was done by spin coating at 2000 rpm for 30 s, after which the film was aged at room temperature for 24 h to allow a gradual solvent evaporation and a proper evolution of the condensation reactions and then annealed at 200°C for 4 h. The above hydrophilic silica-layer was synthetized following an analogous acid-catalyzed sol gel process. The solution was prepared by mixing EtOH:TEOS:H_2O:HCl of 2:1:4:0.01, respectively, which was stirred for 30 min and diluted with the solvent to gain a final theoretical concentration of silica between 0.75 M and 2 M. After 24 h of aging, the solution was filtered (0.2 μm pore size) and deposited on the bottom hydrophobic layer. To induce the dewetting, the as-deposited unstable film was exposed to a solvent-saturated atmosphere by enclosing the bilayered sample inside a closed-cell. The destabilization of the upper film determined the formation of growing holes, which eventually allowed the evolution of the film into isolated droplets. The as-created patterned coatings were aged at room temperature for 24 h in air to favor a gradual solvent evaporation. The films were then annealed at 200°C to reach the film densification while avoiding the thermal degradation of the organic groups. The elimination of the latter would compromise the hydrophobicity of the coating, leading to an increase of the coating wettability.

To extend the comprehension and control of the dewetting mechanism and to gain a deeper knowledge on how different morphologies and chemical compositions influence the condensation from humid air, plain silica and plain CH_3-silica coatings were also deposited on the aluminum substrates. The plain CH_3-silica coating was synthetized and deposited following the same procedure as described for the bottom-layer of the patterned coating. Regarding the plain silica films, the synthesis described for the top-layer in the pattern was identically reproduced, but after the deposition by spin coating, the silica films of different concentrations were aged for one day and then annealed in a furnace for their densification and stabilization.

A.1.3 Optimized recipe for the synthesis and deposition of VO_2 thin films from V_2O_5

The synthesis of VO_2 thin films was adapted from the work of Zhang *et al*.[7] and Sun *et al*.[8] To prepare the initial solution, 1.158 g of V_2O_5 (> 98%, Sigma-Aldrich) were mixed with 2.314 g of oxalic acid bi-hydrated ($H_2C_2O_4 \cdot 2H_2O$, 98%, Sigma-Aldrich) and 2.5 mL of bidistilled H_2O in 27.5 mL of absolute ethanol (EtOH, 99.9% purity, Emsure, Sigma Aldrich). The solution was refluxed for 18 h inside a round-bottom flask and heated in a silicon oil bath, set at 90°C. Oxalic acid acts as a reducing agent, decreasing the oxidation state of vanadium from V^{5+} to V^{4+} according to Eq. (A.1)[7]:

$$V_2O_5 + 3\ H_2C_2O_4 \leftrightarrow VOC_2O_4 + CO_2 + 3H_2O \qquad (A.1)$$

Following the aging time, the solution was spin coated on monocrystalline silicon wafers (p-type, [100] orientation, single-side polishing, Silicon Materials) and fused silica substrates (Quartz, Electro Optical Technology), previously cleaned through multiple solvent rinsing and atmospheric plasma treatment (Plasma Cleaner, PDC-002-CE, Harrick Plasma, USA). The spin coating (spin coater, WS-650MZ-23NPPB, Laurell) was performed in air, spinning the solution at 2000 rpm for 30 seconds. The thin films were then dried on a hot plate for 10 minutes at 150°C. The procedure was repeated to eventually increase the thickness of the film.

A.1.4 Optimized recipe for the synthesis and deposition of VO_2 thin films from $VO(acac)_2$[5]

Silicon wafers (P-type, <100>, single-side polished, Silicon Materials) and fused silica substrates (Quartz, Electro optical technology) were rinsed in absolute ethanol (EtOH, 99.9%, Emsure, Sigma Aldrich, UK) and dried with nitrogen. Residual organic contaminants were removed by atmospheric plasma cleaning (Plasma Cleaner, PDC-002-CE, Harrick Plasma, USA). The starting solution was prepared by dissolving vanadyl acetylacetonate powder ($VO(acac)_2$, 98%, Sigma-Aldrich) in absolute ethanol in a 100 mM concentration. The solution was stirred at 78°C in a round-bottom flask under reflux for 24 h, after which it was aged for more than 1 day at room temperature. Subsequently, the solution was filtered with 0.2 µm sized syringe filters and spin coated on the pre-cleaned substrates at 2000 rpm for 30 s. Samples were coated with multiple layers to tune the thickness of the film. Each layer was dried at 100-250°C on a hot plate for 10 min prior to the deposition of the following one.

A.1.5 Conventional thermal annealing of VO_2 thin films

VO_2 thin films and TiO_2 - VO_2 bilayers were annealed in a tubular quartz furnace, employing a Lenton LTF 16/180 furnace**.** The dried thin films were inserted inside an alumina sample holder, which was

collocated at the midpoint of the tubular quartz furnace (Figure A.1). A custom-made set up was built to ensure a proper control of the gas flow, as well as a proper removal of residual oxygen and residual contaminants before the start of the thermal annealing treatment.

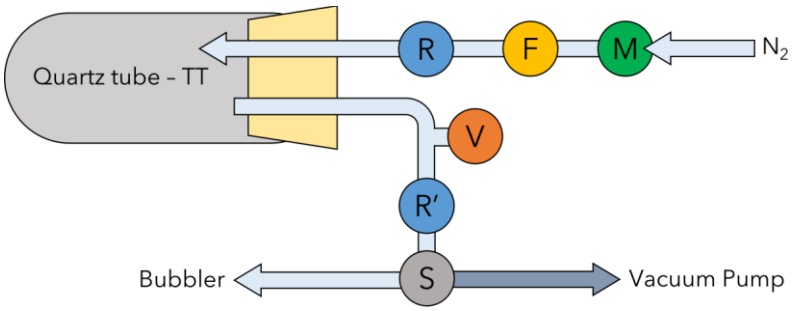


Figure A.7.4. Schematic of the tubular quartz furnace set up employed for thermal annealing of VO_2 thin films and TiO_2 - VO_2 bilayers.

During the thermal annealing, a constant nitrogen flow was streamed through the quartz tube. The open end of the tube was sealed with a rubber plug, on which the inlet and outlet quartz tubes were inserted. The nitrogen source was connected to a gauge (M) regulating the pressure, which allowed to set the system pressure to 0.2 bar. A flowmeter (F) was used to set the gas flow to 0.1 lpm. A valve (R) was inserted to enable or disable the gas flow inside the system. In the outlet position, a manometer (V) was employed to measure the vacuum level induced by the connected vacuum pump (-1 bar detection limit). The manometer was connected to a three-way valve (S) which allowed to alternate the connection of the system to the bubbler or to the vacuum pump, respectively. To ensure a proper removal of residual oxygen or residual contaminants, three consecutive vacuum cycles were alternated with nitrogen refill at room temperature, before the start of the thermal annealing treatment. The latter was performed at temperatures between 450-650°C, according to the specific test, with a heating ramp of 10°C/min for 1 h. Upon cooling, the gas flow was interrupted when the internal temperature reached 100°C.

With respect to the VO_2 thin films of Chapters 4-5-6-7, the VO_2 thin films discussed in paragraph 4.3.8 of Chapter 4 were annealed in a Gero F-VS 100-500/13 tubular furnace, with a linear geometry. The thermal annealing was performed at 550°C for 1 h, with a 5°C/min heating ramp and a 1.7 lpm nitrogen flux.

A.1.6 Laser annealing of VO_2 thin films[5]

A KrF excimer laser system (248 nm, Coherent COMPex 201F, 22 ns pulse duration) was used to irradiate the samples in distinct and isolated parts of the total surface. Each spot had a 5 × 5 mm^2 size, with uniformity of 2%. The irradiation was carried out in air at room temperature with a variable

number of pulses (#), at fixed repetition rate of 10 Hz with a laser fluence between 40 and 700 mJ/cm^2 for the initial energy density scan and 40–200 mJ/cm^2 for the following tests. Fluence was controlled through a motorized attenuator paired with an in-line energy meter, with an accuracy of 1%.

A.1.7 Optimized recipe for the synthesis Pt nanoparticles

In a 10 mL round-bottom flask, 67 mg of H_2PtCl_6 and 18.7 mg of NaCl were dissolved in 3 mL of ethylene glycol, followed by degassing and placement in nitrogen. In a 50 mL 3-neck round bottom flask, 150 mg $NaNO_3$ and 55 mg PVP-10K were dissolved into 13 mL ethylene glycol. The solution was degassed and the temperature increased up to 160°C under nitrogen. After 20 minutes, the first solution was quickly injected into the second, from which a color change was noticed from pale orange to brown-black within a few minutes. The Pt colloidal solution was kept at 160°C in a nitrogen atmosphere for 30 min and cooled to room temperature. The solution was then precipitated with excess acetone (~2:1 in volume), centrifuged at 4000 rpm for 5 minutes and redispersed in ethanol, resulting in a 30 mM nominal concentration.

A.2 Characterizations

A.2.1 Dynamic contact angle and contact angle hysteresis[3]

The dynamic contact angles were measured with the aid of a goniometer and an addition-removal method, by dispersing and subsequently withdrawing a water droplet of approximately 5 μL volume. The measurements were conducted with a home-made set-up consisting of a DCC1545M CMOS sensor camera (Thorlabs GmbH®, Bergkirchen, Germany) and MVL7000 sensor lens (Thorlabs GmbH®, Bergkirchen, Germany).

A.2.2 Saturated vapor condensation tests[1]

The hybrid silica coatings deposited on aluminium substrates were tested in a two-phase thermosyphon designed for the investigation of water vapour condensation on vertical metallic substrates. The test rig, the experimental procedure, the data reduction technique, and the uncertainty analysis are described in Mirafiori *et al.*[6] The experimental apparatus consists of three main components: a boiling chamber, a test section, and a post-condenser (Figure A.2). The design of the

test section allows to simultaneously measure the heat transfer and visualize the condensation phenomenon. The vapor produced inside the boiling chamber flows into the test section where it is partially condensed over a metallic sample (condensing area: 50 mm high, 20 mm wide). Inside this component, condensation is driven by the action of the cooling water supplied on the back surface of the sample by a thermostatic bath at controlled temperature and flowrate. Downstream the test section, the two-phase mixture (vapor and liquid) is completely condensed in the post-condenser before returning to the boiling chamber. The video acquisition system consists of a powerful LED and a high-speed camera Photron FASTCAM UX100 coupled with a macrolens.

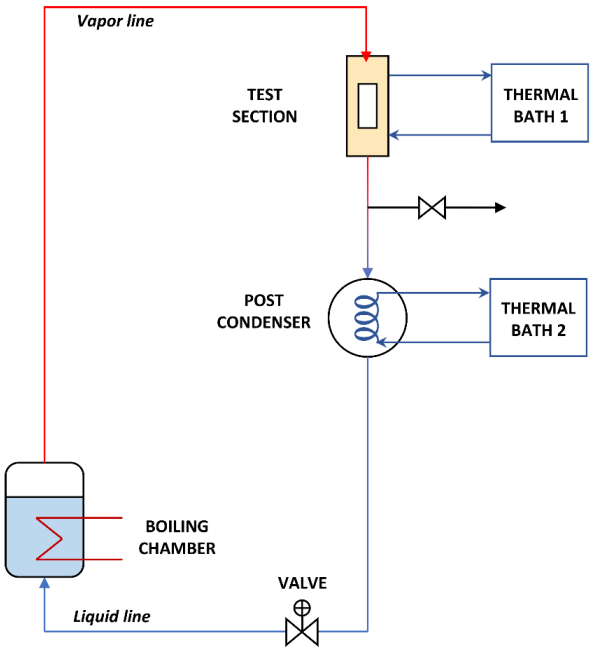


Figure A7.5. Layout of the thermosiphon loop used during DWC tests.[1]

Since the temperature difference between the inlet and outlet of the test section and the water mass flow rate are measured, the average condensation heat flux during DWC (q_{mean}) can be evaluated from the thermal balance at the coolant side of the test section. Each substrate is equipped with six T-type thermocouples arranged at two different depths from the coated surface (z_1 = 1.3 mm and z_2 = 2.8 mm) and in correspondence of three longitudinal positions along the sample (top, middle, and bottom). According to the Fourier's law for thermal conduction, the thermocouples inserted in the sample at depth z_1 and the temperature gradient associated to the mean condensation heat flux q_{mean} give the local surface temperature ($T_{wall,loc}$) for each of the three longitudinal positions. In the present work, the three temperature differences between the saturation temperature and the local surface temperature ($\Delta T_{loc} = T_{sat} - T_{wall,loc}$) are used to calculate the average wall subcooling over the whole condensing surface (ΔT). Hence, the mean HTC during dropwise condensation is evaluated as Eq. A.2:

$$\mathrm{HTC} = \frac{q_{mean}}{\Delta T} \tag{A.2}$$

Each experimental data reported in this paper is the mean of 480 readings acquired at 1 Hz with error bars representing the expanded combined uncertainty calculated considering a coverage factor $k = 2$.

Condensation tests to assess the coating robustness over time were performed at the following thermodynamic conditions: 106 °C of saturation temperature (which corresponds to a saturation pressure of 1.24 bar), 2.9 m s^{-1} of steam velocity, heat flux in the range 250-550 kW m^{-2}. As previously said, the test rig is a two-phase thermosiphon and, therefore, the velocity of the vapor inside the test section cannot be zero. However, since the vapor velocity is maintained below 3 m s^{-1}, its effect on the HTC can be considered negligible as shown in previous works[7]. To avoid the penalizing effect of non-condensable gases on the heat transfer coefficient, the experimental apparatus always works at a pressure higher than the atmospheric one.

A.2.3 Coating degradation tests[3]

The coatings deposited on silicon substrates were tested under five different environments that could affect the coating's degradation and could be related to the conditions present during the condensation experiments. The tests were chosen to be straightforward to perform and easily replicable. The exposure time of each tested condition was set to 7 h, to be comparable to the condensation experiments. Three main factors were considered separately and then combined: the chemical-mechanical interaction with water, the effect of temperature and the role of defects. The effect of the hot water on the coatings was considered both in the case of liquid and vapor phase (i.e., steam-air mixture). The five different tests are summarised in Figure A.3.

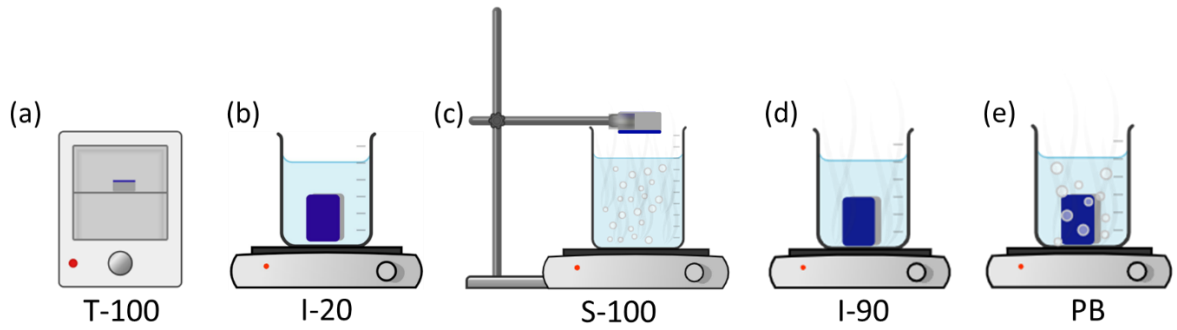


Figure A.7.6. Different conditions used in the degradation tests on silicon substrates: (a) heat treatment at 100 °C in furnace (T-100); (b) immersion in deionised water at 20 °C (I-20); exposure to mixed air-steam (S-100); (d) immersion in deionised water at 90 °C (I-90); (e) immersion in boiling water at 100 °C (I-100).[1] *Scheme drawn using Chemix.org editor.*[8]

A first sample was heat treated at 100 °C in a standard heating furnace (T-100). A second specimen was exposed to an air-steam mixture, during which the coated surface was held downside in a horizontal position, 3 cm above a glass beaker containing boiling deionized water (S-100). The third and fourth samples were fully immersed in a glass beaker containing deionized water at 20 °C (I-20) and 90 °C (I-90), respectively, whereas the last sample was immersed in boiling water (pool boiling, PB). To further correlate the influence of the substrate type on the coating's stability, the PB test was carried on a reference coated aluminium sample as well (PB-Al).

A.2.4 Durability tests under high moisture conditions[3]

The patterned coatings and the plain CH_3-silica films, deposited on the smaller square substrates, were enclosed inside a home-made humidity test chamber for increasing exposure times of 1 day, 14 days and 30 days, respectively. The VO_2 – SiO_2 bilayers were exposed for 1 month. The chamber consisted of a sealed glass vessel and the humidity was controlled by a saturated salt solution (potassium nitrate, 94–96% RH, 20–25 °C). The RH was monitored by a commercial sensor (Bel-Art, Scienceware digital hygrometer). Three samples for each type of coating were tested.

A.2.5 Humid air condensation tests[3]

The square aluminum substrates were placed in a wind tunnel developed for the study of condensation from humid air over vertical metallic surfaces. After the conditioning stage, the air enters the wind tunnel and it flows over the aluminum surface (A=16 cm^2), where a fraction of the water vapor present in the airflow is condensed. The condensate water is collected in a receiver that is weighed continuously by a high precision balance. Condensation tests were performed at constant air conditions (temperature of 28 °C, relative humidity of 50%, and velocity of 1 ms^{-1}), while the dew-to-wall temperature difference (ΔT) was varied in the range 4−10 K by controlling the air-cooled Peltier device connected to the substrate. The tests started with the condensing surface dry. After the air inside the wind tunnel reached steady-state conditions, the Peltier element was activated to lower the temperature of the substrate. At this point, all experimental data, in particular the mass of the condensate produced, were recorded for 90 min. Each experimental data set was given as the average of 30 measurements recorded over 1 min with error bars representing the combined uncertainty, calculated considering the "Type A" and "Type B" components as described in the ISO Guide.[9]

A.2.6 Grazing incidence X-ray diffraction (GIXRD)

The crystallinity of the thin films was characterized by grazing incidence X-Ray diffraction (GIXRD) using a Philips PW1710 diffractometer equipped with grazing incidence X-Ray optics. The measurements were performed at an incidence angle of 0.5°, using Cu Kα Ni filtered radiation at 30 kV and 40 mA. The average crystallite size *D* was calculated from the Scherrer equation (Eq. A.3):

$$D = \frac{K\lambda}{w\ cos\theta} \tag{A.3}$$

after fitting the experimental profiles with Lorentzian functions. In this relationship, 1.54 Å is the wavelength, Θ the diffraction angle, *w* the full width at half maximum (FWHM) of the diffraction peak, and $K = 0.94$ is the shape factor.

A.2.7 Raman spectroscopy

Raman spectroscopy was performed with a Renishaw inVia Raman Microscope with a 633 nm He:Ne laser. Three iterations were employed with 30 s accumulation time in the range 100-540 cm^{-1} and 540-1000 cm^{-1}, to exclude the signal from the silicon substrate.

A.2.8 Optical spectroscopy

The transmittance spectra were analyzed with a UV-Vis-NIR spectrophotometer (Jasco V770), in the wavelength range 190-2500 nm at 200 nm/min. The transmittance was measured at 20°C (transmitting state) and 90-110°C (reflecting state) with the aid of a custom-made heating cell attachment. The luminous transmittance (T_{lum}) and the solar modulation ability (ΔT_{sol} and $\Delta T_{2000\ nm}$) were used to express the thermochromic performance of the VO_2 thin films. The integrated luminous transmittance (T_{lum}) was obtained by Eq. A.4:

$$T_{lum} = \frac{\int \emptyset_{lum}(\lambda)\, T(\lambda) d(\lambda)}{\int \emptyset_{lum}(\lambda)\, d(\lambda)} \tag{A.4}$$

in which $\emptyset_{lum}$ is the photonic vision luminous efficiency function and T_λ is the transmittance at the wavelength λ. The standard integration range for the luminous transmittance is 380 to 780 nm. The solar modulation ability (ΔT_{sol}) was obtained by Eq. A.5:

$$\Delta T_{sol} = T_{sol,lt} - T_{sol,ht} \tag{A.5}$$

in which $T_{sol,lt}$ represents the solar transmittance at low temperature (i.e., semiconducting state – 20°C) and $T_{sol,ht}$ represents the solar transmittance at high temperature (i.e., metallic state – 90-110°C). The solar transmittance (T_{sol}) was calculated as Eq. A.6:

$$T_{sol} = \frac{\int \emptyset_{sol}(\lambda)\, T(\lambda) d(\lambda)}{\int \emptyset_{sol}(\lambda)\, d(\lambda)} \quad \text{(A.6)}$$

with $\emptyset_{sol}$ the standard solar radiation spectrum for the air mass 1.5 (AM 1.5). The standard integration range was 250 - 2500 nm. The NIR modulation ability was calculated at 2000 nm by $\Delta T_{2000\ nm} = T_{2000\ nm,\ lt} - T_{2000\ nm,\ ht}$.

The optical hysteresis was obtained by collecting transmittance of the thin films at 2000 nm every 2°C in the 20°-115°C temperature range. The transition temperature (T_c) was obtained from the middle point of the hysteresis, calculated by averaging the $T_{heating}$ (T_{TH}) and $T_{cooling}$ (T_{TC}). The latter were obtained from the minimum of the 1st derivative of the log(R) curve, which was calculated for each transmittance curve.

The chemical bonds were characterized via Fourier transform infra-red spectroscopy (Jasco FTIR 4200). The range of interest was 4500–400 cm^{-1} and the measurements were performed with 64 scans min^{-1} with a 2 cm^{-1} resolution. The absorption spectra were collected in attenuated total reflectance (ATR) mode with air as the reference.

A.2.9 Ellipsometry

The ellipsometry parameters (Ψ, Δ) were measured with a J.A. Woollam V-VASE Spectroscopic ellipsometer in a vertical configuration. The angles of incidence were set to 65°-70°-75° for silicon substrate and 50°-55°-60° for fused silica substrates, in the wavelength range of 300-1700 nm. The refractive index *n*, absorption coefficient *k*, and film thickness *t* were obtained by fitting of the experimental data (Ψ, Δ), employing a WVASE32 ellipsometry data analysis software. The data were fitted with the three-parameter Cauchy model or the GenOsc model, employing Gaussian, Tauc-Lorentz, and/or Drude oscillators. On silicon substrates, the absorption coefficient (α) was calculated from Eq. A.7:

$$\alpha = \frac{4\pi k_{\lambda}}{\lambda} \quad \text{(A.7)}$$

with k_λ extinction coefficient and λ laser wavelength (λ = 248 nm). The penetration depth (δ) of the laser radiation was calculated as δ = 1/α. The extinction coefficients at 248 nm were generated from the ellipsometry fittings.

A.2.10 Four point probe characterization

The variation of the electrical properties in function of the temperature was studies by coupling a Linkam® HFS600E heating plate with a Jandel four-point probe head (probe spacing of 1 mm). The temperature was varied between 25 and 115°C while the sheet resistance of the films was measured every 3°C. The transition temperature (T_c) was obtained from the middle point of the hysteresis, calculated by averaging the $T_{heating}$ (T_{TH}) and $T_{cooling}$ (T_{TC}). The latter were obtained from the minimum of the 1st derivative of the log(R) curve, which was calculated for each resistance curve.

A.2.11 Electron microscopy and image analysis

Optical micrographs of the samples were collected with a Leica DMRE optical microscope, with a Zeiss AxioCam ERc5s camera and Zeiss ZEN core software.

Scanning Electron Microscope (SEM) was used to evaluate the surface morphology of the thin films using a FE-SEM, Zeiss Sigma HD operating at 3-5 kV and collecting signal with InLens detector or secondary electron detector. The film's surface coverage, the average particle dimension and the size distribution were estimated with the aid of ImageJ software. It is important to note that the image analysis is intrinsically qualitative, as the selection of the analyzed particles depends on the initially defined contrast and on the operator's sensitivity. For the estimation of the film's surface coverage, the SEM images acquired at a 100 kx magnification were selected (Figure A.4 (a, b)). The images were initially calibrated using the scale bar reported in the bottom-right part of the picture. The brightness and contrast values were manually optimized to enhance the difference in color between the particles and the substrate. For the estimation of the particle size, the SEM images acquired at a 200 kx magnification were selected (Figure A.4 (c)). A circular shape was manually added on each image and the area of the first 30 particles intersecting the former was evaluated. The circular shape was chosen to avoid directional bias stemming from potential elongations along one dimension.



Figure A.7.7. Example of the estimation method by image analysis of (b) particle surface coverage and (c) average particle size and particle size distribution with the ImageJ software, starting from (a) a SEM image of the films after thermal annealing.

The cross-section of the films was obtained with a Thermo Scientific Helios 5 UX FIB-SEM. Carbon and platinum protective layers were deposited to protect the film's surface. The transmission electron microscopy (TEM) images were acquired with a FEI Tecnai G2 F20 S-TWIN transmission electron microscopy with the Bruker X-ray detector. Scanning TEM mode was employed in both bright-field (BF) and high-angle annular dark-field (HAADF) modes. Crystallographic information was obtained from Fast Fourier transform (FFT) analysis on a high-resolution TEM (HRTEM) micrograph. Electron Energy Loss Spectroscopy (EELS) was coupled with HRTEM to record the energy loss by the incident electron beam, using an ARM 200-Cold FEG microscope.

A.2.12 Atomic force microscopy (AFM)

Atomic force microscopy (AFM) measurements were performed using an NT-MDT (Solver PRO) AFM microscope operated in semi-contact mode. The scan speed was set to 0.7 Hz, on a 5 × 5 µm scan area, with an image resolution of 300 x 300 pixels. The average surface roughness was calculated from the images by using the statistical analysis tool on Gwyddion software. The experimental data were elaborated by subtracting a first-order polynomial background.

A.2.13 X-ray photoelectron spectroscopy (XPS)[5]

Chemical analysis using laboratory-based soft X-ray photoelectron spectroscopy (SXPS) was performed on a Thermo Scientific K-Alpha X-ray photoelectron spectrometer, with a 2×10^{-9} mbar base pressure. A monochromated Al Kα was used as the X-ray source ($h\nu$ = 1486.7 eV, further referred to as 1.5 keV for simplicity). Survey and key core level spectra were collected using 200 eV and 20 eV pass energy, respectively, with a 400 µm spot size. A flood gun was used to minimize sample charging. Synchrotron-based hard X-ray photoelectron spectroscopy (HAXPES) was performed at beamline I09 at the Diamond Light Source, UK, using an X-ray photon energy of 5927.4

eV (further referred to as 5.9 keV for simplicity). The analysis chamber of the beamline end station has a base pressure of ~3.5×10^{-10} mbar and measurements were performed in grazing incidence and near normal emission geometry to allow efficient spectra collection. Survey and core level spectra were collected using a pass energy of 200 eV. For both SXPS and HAXPES, the binding energy (BE) scale of all spectra was aligned to the adventitious carbon peak in the C 1*s* spectra at a binding energy (BE) of 284.8 eV (determined after peak-fit analysis). The spectra were normalized to the total V $2p_{3/2}$ spectral area, after the removal of a Shirley-type background. The Avantage software package was used to analyze the data. The QUASES software package was used to estimate the maximum inelastic mean free path (λ_{IMFP}) for bulk VO_2, with values of ~3 nm at 1.5 keV (SXPS) and ~9 nm at 5.9 keV (HAXPES).[10] The total probing depth can be estimated as 95% of the signal intensity (i.e. $3\lambda_{IMFP}$), giving values of ~9 nm and ~27 nm for SXPS and HAXPES, respectively.

A.2.14 Density-functional theory (DFT)[5]

Density-functional theory calculations were performed by Prof. L. Ratcliff from the University of Bristol, UK. To corroborate peak analysis in SXPS and HAXPES, core BE calculations were performed to estimate the relative BE distance between O and C atoms in the precursor structure. Calculations were performed using density functional theory (DFT),[11,12] using the CASTEP plane wave DFT code.[13] The PBE exchange-correlation functional[14] was used alongside norm-conserving pseudopotentials with 13 valence electrons for V, a kinetic energy cut-off of 1200 eV (1000 eV) for the geometry optimization (core BE calculations) and a Monkhorst-Pack[15] *k*-point grid of 2 × 2 × 1. The geometry optimization employed the empirical dispersion correction scheme of Tkatchenko-Scheffler,[16] while both the atomic positions and unit cell were allowed to relax. Relative core BEs were then calculated for the relaxed structure, using the ΔSCF approach with on-the-fly generated core hole PSPs. The core BE calculations were performed using spin polarization; this was found to have little impact on the geometry optimization, and so was neglected in the latter case.

A.2.15 Temperature profile simulations[5]

Simulations of the temperature profiles and their evolution during laser processing were produced as a function of both depth (i.e. film thickness) and laser irradiation time. Numerical solutions of the heat equation based on heat flow calculations were performed by employing the LIMP software

(Harvard simulation software package)[17] and calibrated on VO_2 and fused silica physical and optical data. The former were chosen from the literature,[18,19] whereas the latter were calculated from experimental data obtained in this work. The absorption coefficient (α) was calculated from the equation $\alpha = (A\lambda)/t$, in which λ is the laser wavelength (λ = 248 nm). The penetration depth (δ) of laser radiation can be calculated as the inverse of the absorption coefficient ($\delta = 1/\alpha$).

A.2.16 Rutherford Backscattering Spectrometry (RBS)

Rutherford Backscattering Spectrometry (RBS) analysis was used to calculate the overall dose of oxygen and vanadium inside the films. The RBS analysis was conducted using a collimated 2.0 MeV $^4He^+$ beam at the AN2000 Van de Graaff accelerators located at the Laboratori Nazionali di Legnaro (LNL-INFN). The experiment utilized a scattering angle of 160°, employing both random and aligned channeling conditions to acquire distinct spectra. Random spectra were generated through rotating random procedures using a high-resolution goniometer with an angular resolution of 0.01°, while channeling measurements (c-RBS) were performed by aligning the beam with the <001> substrate sample axis (axial channeling). Thanks to channeling conditions, the Si substrate signal is partially suppressed, allowing the oxygen signal to emerge.

A.2.17 Gas sensing tests

Chemoresistive gas sensing tests were performed on different VO_2 thin films spin coated on Si/Si_3N_4 substrates with comb-like Pt interdigitated electrodes (30 μm apart) and back side heaters, inserted in a 500 cm^3 Teflon chamber. Electrical responses were collected using an automated volt-amperometric system (Agilent 34970A), measuring the electrical resistance of the film at different operating temperatures (25–150°C) and different environments. Gas concentrations were obtained by diluting H_2 (500 ppm in air) certified mixtures (Nippon gases-IT) with synthetic dry air utilizing MKS147 mass flow controllers, setting the total flow rate at 500 sccm/min. Different relative humidities (RH%) were obtained by mixing dry with water-saturated air at 25 °C and measuring RH% at 25 °C before injection into the test chamber by means of a HI9564 thermohygrometer (Hannah Instruments). To characterize and compare gas responses properties of the different VO_2 samples, the following definitions apply: (i) baseline resistance (BLR): the resistance in dry air at equilibrium; (ii) relative response (RR): defined as (R_{Gas}/R_{Air}) and (R_{Air}/R_{Gas}) depending on the oxidizing/reducing nature of the gases; (iii) Sensor's Sensitivity (SS): the slope of the calibration curve (i.e. RR versus gas concentration); (iv) response time (τ_{ADS}) and recovery time (τ_{DES}) defined as the time required for the

current to reach 90% of the equilibrium value after injecting the gas and the time necessary for the sensor to return to 10% above the original current value in air after releasing the gas from the test chamber, respectively.

The optical response of the VO_2 samples to H_2 exposure was tested by measuring the transmittance variations, using a Harrick gas flow cell coupled with a Jasco V-770 spectrophotometer. The cell was provided with a heater with three thermocouples, which allowed to vary the temperature between room temperature and 200°C.

References

1. Basso, M. *et al.* Hydrophobic hybrid silica sol-gel coating on aluminium: Stability evaluation during saturated vapour condensation. *Journal of Non-Crystalline Solids: X* **17**, 100143 (2023).

2. De Ferri, L., Lottici, P. P., Lorenzi, A., Montenero, A. & Vezzalini, G. Hybrid sol-gel based coatings for the protection of historical window glass. *J Solgel Sci Technol* **66**, 253–263 (2013).

3. Basso, M. *et al.* Bioinspired silica-based sol–gel micropatterns on aluminium for humid air condensation. *J Solgel Sci Technol* **102**, 466–477 (2022).

4. Colusso, E., Martucci, A. & Neto, C. Fabrication of Biomimetic Micropatterned Surfaces by Sol–Gel Dewetting. *Adv Mater Interfaces* **6**, 1–11 (2019).

5. Basso, M. *et al.* Rapid laser-induced low temperature crystallization of thermochromic VO2 sol-gel thin films. *Appl Surf Sci* **631**, (2023).

6. Mirafiori, M., Parin, R., Bortolin, S. & Del Col, D. Experimental analysis of drop-size density distribution during dropwise condensation of steam. *J Phys Conf Ser* **1599**, (2020).

7. Tancon, M., Parin, R., Bortolin, S., Martucci, A. & Del Col, D. Effect of steam velocity during dropwise condensation. *Int J Heat Mass Transf* **165**, 120624 (2021).

8. Chemix - Draw Lab Diagrams. Simply. https://chemix.org/.

9. *JCGM 100:2008 - Evaluation of measurement data - Guide to the expression of uncertainty in measurement*.

10. Tanuma, S., Powell, C. J. & Penn, D. R. Calculations of electron inelastic mean free paths. V. Data for 14 organic compounds over the 50–2000 eV range. *Surface and Interface Analysis* **21**, 165–176 (1994).

11. Hohenberg, P. & Kohn, W. Inhomogeneous electron gas. *Physical Review* **136**, B864 (1964).

12. Kohn, W. & Sham, L. J. Self-consistent equations including exchange and correlation effects. *Physical Review* **140**, A1133 (1965).

13. Clark, S. J. *et al.* First principles methods using CASTEP. *Zeitschrift fur Kristallographie* **220**, 567–570 (2005).

14. Perdew, J. P., Burke, K. & Ernzerhof, M. Generalized Gradient Approximation Made Simple. *Phys Rev Lett* **77**, 3865 (1996).

15. Monkhorst, H. J. & Pack, J. D. Special points for Brillouin-zone integrations. *Phys Rev B* **13**, 5188 (1976).

16. Tkatchenko, A. & Scheffler, M. Accurate molecular van der Waals interactions from ground-state electron density and free-atom reference data. *Phys Rev Lett* **102**, 073005 (2009).

17. Hoglund, D. E. & Thompson, M. O. Experimental test of morphological stability theory for a planar interface during rapid solidification. *Phys Rev B Condens Matter Mater Phys* **58**, 189–199 (1998).

18. Kizuka, H. *et al.* Temperature dependence of thermal conductivity of VO2 thin films across metal-insulator transition. *Jpn J Appl Phys* **54**, 053201 (2015).

19. Touloukian, Y. S., Powell, R. W., Ho, C. Y. & Klemens, P. *Thermophysical properties of matter - Thermal conductivity: nonmetallic solids*. (1970).